ŠARŪNĖ DAŠKEVIČIŪTĖ

FLUORENO, KARBAZOLO IR SPIROBISINDANO CHROMOFORUS TURINČIŲ ORGANINIŲ PUSLAIDININKIŲ EFEKTYVIEMS NAUJOS KARTOS SAULĖS ELEMENTAMS SINTEZĖ IR TYRIMAS

DAKTARO DISERTACIJA

Kaunas
2024

KAUNO TECHNOLOGIJOS UNIVERSITETAS

ŠARŪNĖ DAŠKEVIČIŪTĖ

FLUORENO, KARBAZOLO IR SPIROBISINDANO CHROMOFORUS TURINČIŲ ORGANINIŲ PUSLAIDININKIŲ EFEKTYVIEMS NAUJOS KARTOS SAULĖS ELEMENTAMS SINTEZĖ IR TYRIMAS

Daktaro disertacija
Gamtos mokslai, chemija (N 003)

2024, Kaunas

Disertacija rengta 2020–2024 metais Kauno technologijos universiteto Cheminės technologijos fakultete, Organinės chemijos katedroje. Mokslinius tyrimus rėmė Lietuvos mokslo taryba.

Mokslinis vadovas:
prof. dr. Vytautas GETAUTIS (Kauno technologijos universitetas, gamtos mokslai, chemija, N 003).

Redagavo: anglų kalbos redaktorius dr. Armandas Rumšas (leidykla „Technologija“), lietuvių kalbos redaktorė Aurelija Gražina Rukšaitė (leidykla „Technologija“).

Chemijos mokslo krypties disertacijos gynimo taryba:
prof. dr. Saulius GRIGALEVIČIUS (Kauno technologijos universitetas, gamtos mokslai, chemija, N 003) – **pirmininkas**;
prof. dr. Eglė ARBAČIAUSKIENĖ (Kauno technologijos universitetas, gamtos mokslai, chemija, N 003);
prof. dr. Vytas MARTYNAITIS (Kauno technologijos universitetas, gamtos mokslai, chemija, N 003);
prof. dr. Edvinas ORENTAS (Vilniaus universitetas, gamtos mokslai, chemija, N 003);
doc. dr. Jolanta ROUSSEAU (Artua universitetas, Prancūzija, technologijos mokslai, chemijos inžinerija, T 005).

Disertacija bus ginama viešame Chemijos mokslo krypties disertacijos gynimo tarybos posėdyje 2024 m. rugsėjo 27 d. 11.00 val. Kauno technologijos universiteto Rektorato salėje.

Adresas: K. Donelaičio g. 73-402, LT-44249 Kaunas, Lietuva.
Tel: (+370) 608 28 527; el. paštas doktorantura@ktu.lt

Disertacija išsiųsta 2024 m. rugpjūčio 27 d.
Su disertacija galima susipažinti interneto svetainėje http://ktu.edu ir Kauno technologijos universiteto bibliotekoje (Gedimino g. 50, LT-44239 Kaunas, Lietuva).

KAUNAS UNIVERSITY OF TECHNOLOGY

ŠARŪNĖ DAŠKEVIČIŪTĖ

SYNTHESIS AND INVESTIGATION OF FLUORENE, CARBAZOLE, AND SPIROBISINDANE-BASED SEMICONDUCTORS FOR APPLICATION IN NEXT-GENERATION SOLAR CELLS

Doctoral dissertation
Natural Sciences, Chemistry (N 003)

2024, Kaunas

The dissertation has been prepared at the Department of Organic Chemistry of the Faculty of Chemical Technology of Kaunas University of Technology in 2020-2024. The research has been sponsored by the Research Council of Lithuania.

Research supervisor:
Prof. Dr. Vytautas GETAUTIS (Kaunas University of Technology, Natural Sciences, Chemistry, N 003).

Edited by: English language editor Dr. Armandas Rumšas (Publishing House *Technologija*), Lithuanian language editor Aurelija Gražina Rukšaitė (Publishing House *Technologija*)

Dissertation Defence Board of Chemistry Science Field:
Prof. Dr. Saulius GRIGALEVIČIUS (Kaunas University of Technology, Natural Sciences, Chemistry, N 003) – **chairperson**;
Prof. Dr. Eglė ARBAČIAUSKIENĖ (Kaunas University of Technology, Natural Sciences, Chemistry, N 003);
Prof. Dr. Vytas MARTYNAITIS (Kaunas University of Technology, Natural Sciences, Chemistry, N 003);
Prof. Dr. Edvinas ORENTAS (Vilnius University, Natural Sciences, Chemistry, N 003);
Doc. Dr. Jolanta ROUSSEAU (Artois University, France, Technological Sciences, Chemical Engineering, T 005).

The dissertation defence will be held on 27 September 2024, at 11 a.m. in a public meeting of the Dissertation Defence Board of the Chemistry science field at the Rectorate hall of Kaunas University of Technology.

Address: K. Donelaičio 73-402, LT-44249 Kaunas, Lithuania.
Phone: (+370) 608 28 527; e-mail doktorantura@ktu.lt

The dissertation was sent out on 27 August, 2024.
The dissertation is available on http://ktu.edu and at the Library of Kaunas University of Technology (Gedimino 50, LT-44239 Kaunas, Lithuania).

TURINYS

LENTELIŲ SĄRAŠAS 7
PAVEIKSLŲ SĄRAŠAS 9
SCHEMŲ SĄRAŠAS 12
SANTRUMPŲ SĄRAŠAS 13
1. ĮVADAS 15
2. MOKSLINĖS LITERATŪROS DISERTACIJOS TEMA APŽVALGA 21
2.1. Perovskitas ir jo sandara 21
2.2. Perovskitiniai saulės elementai 22
2.2.1. Skaidrūs elektrodai / anodai 22
2.2.2. Elektronų transportinis sluoksnis 23
2.2.3. Šviesą absorbuojantis sluoksnis – perovskitas 23
2.2.4. Skylių transportinis sluoksnis 24
2.2.5. Skaidrūs elektrodai / katodai 27
2.3. Molekulinė skylių transportinių medžiagų inžinerija perovskitiniams saulės elementams 27
2.3.1. Fluoreno centrinį fragmentą turinčios skylių transportinės medžiagos 27
2.3.2. Spirobisindano centrinį fragmentą turinčios skylių transportinės medžiagos 33
2.3.3. Karbazolo chromoforus turinčios skylių transportinės medžiagos 34
2.3.4. Polimerinės skylių transportinės medžiagos 37
2.4. Mokslinės literatūrinės dalies apibendrinimas 35
3. MOKSLINIŲ STRAIPSNIŲ APŽVALGA 42
3.1. Fluoreno centrą turintys mažamolekuliniai organiniai puslaidininkiai ir jų panaudojimas skyles transportuojantiems sluoksniams gauti efektyviuose ir stabiliuose perovskitiniuose saulės elementuose 42
3.2. Fluoreno enaminų sintezė bei jų panaudojimas skyles transportuojantiems sluoksniams gauti efektyviuose ir stabiliuose perovskitiniuose saulės elementuose 45
3.3. Fluoreno chromoforus su akceptorinėmis grupėmis turinčių enaminų sintezė ir panaudojimas efektyviems ir stabiliems perovskitiniams saulės elementams 51
3.4. Spirobisindano centrinį fragmentą turinčių enaminų sintezė ir panaudojimas perovskitiniuose saulės elementuose 57
3.5. Žaliosios chemijos principais susintetintų skylių transportinių medžiagų panaudojimas efektyviuose ir stabiliuose saulės elementuose ir moduliuose 61
3.6. Tinklintis galinčių skyles transportuojančių medžiagų su karbazolilchromoforais sintezė bei panaudojimas invertuotos struktūros perovskitiniuose saulės elementuose 67
3.7. Tinklintis galinčio puslaidininkio, turinčio spirobifluoreno centrinį fragmentą, sintezė bei panaudojimas skirtingų konfigūracijų perovskitiniuose saulės elementuose 71
4. IŠVADOS 79

5. SUMMARY 82
5.1. Introduction 82
5.2. Review of Published Articles 85
5.2.1. Fluorene-based organic semiconductors for hole transporting layers in efficient and stable perovskite solar cells 85
5.2.2. Fluorene-based enamines as hole transporting layers in efficient and stable perovskite solar cells 89
5.2.3. Synthesis and application of enamines with fluorene chromophores and acceptor groups for efficient and stable perovskite solar cells 95
5.2.4. Synthesis of spirobisindane-based enamines and their application in perovskite solar cells 101
5.2.5. Green-chemistry-inspired synthesis of hole transporting materials for efficient and stable perovskite solar cells and modules 104
5.2.6. Synthesis and application of cross-linkable carbazole-based hole transporting materials for inverted perovskite solar cells 109
5.2.7. Synthesis and application of 9,9ˋ-spirobifluorene-based thermal cross-linking semiconductor for various configurations of perovskite solar cells .. 113
5.3. Conclusions 118
6. LITERATŪROS SĄRAŠAS 122
7. MOKSLINIAI STRAIPSNIAI 137
8. CURRICULUM VITAE 232
9. PADĖKA 240

LENTELIŲ SĄRAŠAS

1 lentelė. Perovskitinių saulės elementų, kuriuose naudoti puslaidininkiai **HT1**, **HT2** ir **YT3**, fotovoltinės charakteristikos ir efektyvumai …….....28
2 lentelė. Perovskitinių saulės elementų, kuriuose naudoti puslaidininkiai **FH-0**, **FH-3**, **FDT-DMP** ir **F2DT**, fotovoltinės charakteristikos ir efektyvumai 30
3 lentelė. Perovskitinių saulės elementų, kuriuose naudoti puslaidininkiai **V1257**, **V1258** ir **V1269**, fotovoltinės charakteristikos ir efektyvumai 32
4 lentelė. Perovskitinio saulės elemento, kuriame naudotas puslaidininkis **Spiro-I**, fotovoltinės charakteristikos ir efektyvumai 34
5 lentelė. Perovskitinių saulės elementų, kuriuose naudoti puslaidininkiai **V886** ir **GJ-pp**, fotovoltinės charakteristikos ir efektyvumai 35
6 lentelė. Perovskitinio saulės elemento, kuriame naudotas puslaidininkis **EtCz-3EHCz**, fotovoltinės charakteristikos ir efektyvumai 37
7 lentelė. Perovskitinių saulės elementų, kuriuose naudoti polimeriniai puslaidininkiai, fotovoltinės charakteristikos ir efektyvumai 38
8 lentelė. Perovskitinio saulės elemento, kuriame naudotas polimerinis puslaidininkis **MCz-VPOZ**, fotovoltinės charakteristikos ir efektyvumai 39
9 lentelė. Perovskitinio saulės elemento, kuriame naudotas vinilgrupes turintis puslaidininkis **V-TPAFDPA**, fotovoltinės charakteristikos ir efektyvumai 40
10 lentelė. Organinių puslaidininkių **STM1** ir **STM2** terminės, optinės ir fotofizikinės savybės 43
11 lentelė. Perovskitinių saulės elementų, kuriuose naudoti puslaidininkiai **STM1**, **STM2** ir Spiro-OMeTAD, fotovoltinės charakteristikos ir efektyvumai 45
12 lentelė. Naujų enaminų terminės ir optinės savybės 47
13 lentelė. Naujų enaminų **STM3** – **STM7** fotofizikinės savybės 49
14 lentelė. Perovskitinių saulės elementų, kuriuose naudoti skirtingi enaminai ir Spiro-OMeTAD, fotovoltinės charakteristikos ir efektyvumai 50
15 lentelė. Naujų D-A-D tipo puslaidininkių **STM8** – **STM14** terminės, optinės ir fotofizikinės savybės 54
16 lentelė. Perovskitinių saulės elementų, kuriuose naudoti D-A-D tipo puslaidininkiai ir Spiro-OMeTAD, fotovoltinės charakteristikos ir efektyvumai 56
17 lentelė. Naujų puslaidininkių **STM15** ir **STM16** terminės, optinės ir fotofizikinės savybės 59
18 lentelė. Perovskitinių saulės elementų, kuriuose naudoti puslaidininkiai **STM15** ir **STM16**, fotovoltinės charakteristikos ir efektyvumai 60
19 lentelė. Naujų fotodimerizuoto karbazolo pagrindu susintetintų STM terminės, optinės ir fotofizikinės savybės 63
20 lentelė. Perovskitinių saulės elementų, kuriuose naudoti fotodimerizuoto karbazolo pagrindu susintetinti puslaidininkiai, fotovoltinės charakteristikos ir efektyvumai ...66
21 lentelė. Organinių puslaidininkių **STM24** ir **STM25** terminės, optinės ir fotofizikinės savybės 68
22 lentelė. Perovskitinių saulės elementų, kuriuose naudoti puslaidininkiai **STM24** ir **STM25**, fotovoltinės charakteristikos ir efektyvumai 71
23 lentelė. Puslaidininkio **STM26** terminės, optinės ir fotofizikinės savybės 73

24 lentelė. Skirtingų konstrukcijų perovskitinių saulės elementų, kuriuose naudotas puslaidininkio **STM26** ir ditiolio kopolimeras, fotovoltinės charakteristikos 77
Table 25. Thermal, optical, and photoelectrical properties of **STM1**, **STM2**, and Spiro-OMeTAD 87
Table 26. Photovoltaic parameters of the new HTMs **STM1**, **STM2** and Spiro-OMeTAD extracted from the best-performing devices 89
Table 27. Thermal, optical, and photoelectrical properties of fluorene enamines HTMs 91
Table 28. Photoelectrical properties of the new fluorene enamines HTMS 93
Table 29. Photovoltaic parameters of new fluorene enamines HTMs extracted from the best-performing devices 94
Table 30. Thermal, optical, and photoelectrical properties of new D-A-D type HTMs 98
Table 31. Photovoltaic parameters of the new D-A-D type HTMs extracted from the best-performing devices 100
Table 32. Thermal, optical, and photoelectrical properties of new HTMs **STM15** and **STM16** 102
Table 33. Photovoltaic parameters of new HTMs **STM15** and **STM16** extracted from the best-performing devices 104
Table 34. Thermal, optical, and photoelectrical properties of new HTMs based on substituted cyclobutane 106
Table 35. Photovoltaic parameters of new HTMs based on substituted cyclobutane extracted from the best-performing devices 108
Table 36. Thermal, optical, and photoelectrical properties of HTMs **STM24** and **STM25** 110
Table 37. Photovoltaic parameters of the new HTMs **STM24** and **STM25** extracted from the best-performing devices 112
Table 38. Thermal, optical, and photoelectrical properties of novel organic semiconductor **STM26** 114
Table 39. Photovoltaic parameters of the new HTM **STM26** and dithiol copolymer extracted from the best-performing devices 117

PAVEIKSLŲ SĄRAŠAS

1 pav. Kristalinė 3D perovskito struktūra: A – organinis katijonas, B – dvivalentis katijonas, X – anijonas ……..22
2 pav. PSE *n-i-p* ir *p-i-n* struktūros konstrukcijos ……..22
3 pav. Skylių transportiniam sluoksniui naudojamų legiruojančių priedų cheminės formulės 26
4 pav. Polimerinio puslaidininkio PTAA cheminė struktūra 26
5 pav. Polimerinio puslaidininkio PEDOT:PSS cheminė struktūra 27
6 pav. Fluoreno centrinį fragmentą turinčių organinių molekulių **HT1**, **HT2** ir **YT3** cheminės struktūros 28
7 pav. Organinių puslaidininkių, turinčių fluoreno centrą, **FH-0**, **FH-3**, **FDT-DMP** ir **F2DT** cheminės struktūros 29
8 pav. Fluoreno centrinį fragmentą turinčių organinių molekulių **V1257**, **V1258** ir **V1269** cheminės struktūros 32
9 pav. Spirobisindano centrinį fragmentą turinčios organinės molekulės **Spiro-I** cheminė struktūra 33
10 pav. Karbazolo chromoforus turinčių organinių molekulių **V886** ir **GJ-pp** cheminės struktūros 35
11 pav. Karbazolo chromoforus turinčių organinių molekulių **EH44** ir **EtCz-3EHCz** cheminės struktūros 36
12 pav. Vinilgrupes turinčių organinių molekulių **VB-MeO-FDPA**, **VB-Me-FDPA** ir **DH-MeO-FDPA** cheminės struktūros 37
13 pav. Tinklintis galinčios organinės molekulės **MCz-VPOZ** cheminė struktūra ...38
14 pav. Vinilgrupes turinčios organinės molekulės **V-TPAFDPA** cheminė struktūra 39
15 pav. Principinė **V-TPAFDPA** ir PETMP kopolimero susidarymo schema 40
16 pav. Naujų organinių puslaidininkių **STM1** ir **STM2** struktūros 42
17 pav. Naujų organinių puslaidininkių **STM1**, **STM2** ir Spiro-OMeTAD: a) UV-RŠ spinduliuotės sugerties spektrai THF tirpiklyje (10^{-4} M); b) dreifinio judrio priklausomybė nuo elektrinio lauko stiprio 44
18 pav. Perovskitinių saulės elementų su tirtais puslaidininkiais stabilumas 45
19 pav. Naujai susintetintų enaminų **STM3** – **STM7** struktūros 46
20 pav. Naujų enaminų **STM3** – **STM7**: a) UV-RŠ spinduliuotės sugerties (ištisinė linija) ir fluorescencijos (punktyrinė linija) spektrai THF tirpiklyje (10^{-4} M); b) dreifinio judrio priklausomybė nuo elektrinio lauko stiprio 48
21 pav. Perovskitinių saulės elementų su skirtingais enaminais **STM3** – **STM6** ir Spiro-OMeTAD stabilumų tyrimų rezultatai 51
22 pav. Susintetintų D-A-D tipo organinių puslaidininkių **STM8** – **STM14** struktūros 52
23 pav. Naujų D-A-D tipo puslaidininkių **STM8** – **STM14**: a) UV-RŠ spinduliuotės sugerties spektrai THF tirpiklyje (10^{-4} M); b) dreifinio judrio priklausomybė nuo elektrinio lauko stiprio 54

24 pav. Perovskitinių saulės elementų su puslaidininkiais **STM13** ir Spiro-OMeTAD stabilumų tyrimų rezultatai 56
25 pav. Spirobifluoreno ir spirobisindano centrinių fragmentų struktūros 57
26 pav. Naujų organinių puslaidininkių **STM15** ir **STM16** struktūros 58
27 pav. Naujų organinių puslaidininkių **STM15** ir **STM16**: a) UV-RŠ spinduliuotės sugerties (ištisinė linija) ir fluorescencijos (punktyrinė linija) spektrai THF tirpiklyje (10^{-4} M); b) dreifinio judrio priklausomybė nuo elektrinio lauko stiprio 60
28 pav. Naujų fotodimerizuoto karbazolo pagrindu susintetintų skylių transportinių medžiagų struktūros 62
29 pav. Puslaidininkio **STM18** kristalografinė analizė 64
30 pav. Naujų fotodimerizuoto karbazolo pagrindu susintetintų puslaidininkių: a) UV-RŠ spinduliuotės sugerties (ištisinė linija) ir fluorescencijos (punktyrinė linija) spektrai THF tirpiklyje (10^{-4} M); b) dreifinio judrio priklausomybė nuo elektrinio lauko stiprio 65
31 pav. Perovskitinių saulės elementų su **STM22** ir Spiro-OMeTAD stabilumų tyrimų rezultatai 66
32 pav. Polimerintis galinčių puslaidininkių **STM24** ir **STM25** struktūros 67
33 pav. Naujų organinių puslaidininkių **STM24** ir **STM25**: a) UV-RŠ spinduliuotės sugerties (ištisinė linija) ir fluorescencijos (punktyrinė linija) spektrai THF tirpiklyje (10^{-4} M); b) diferencinės skenuojamosios kalorimetrijos kreivės (10 °C/min, N_2 atmosfera) 69
34 pav. **STM24** (a) ir **STM25** (b) terminės polimerizacijos tyrimo UV-RŠ sugerties spektrai 70
35 pav. Naujo Spiro-OMeTAD analogo su polimerintis galinčiomis grupėmis struktūra 71
36 pav. **STM26** (a) ir **STM26+ditiolis** (b) diferencinės skenuojamosios kalorimetrijos kreivės (10 °C/min, N_2 atmosfera) 75
37 pav. Naujo organinio puslaidininkio **STM26**: a) UV-RŠ spinduliuotės sugerties (ištisinė linija) ir fluorescencijos (punktyrinė linija) spektrai THF tirpiklyje (10^{-4} M); b) dreifinio judrio priklausomybė nuo elektrinio lauko stiprio 77
38 pav. **STM26** (a) ir **STM26+ditiolis** (b) terminės polimerizacijos tyrimo UV-RŠ sugerties spektrai 76
39 pav. Perovskitinių saulės elementų konstrukcijos *p-i-n* (a) ir *n-i-p* (b) 77
40 pav. Perovskitinių saulės elementų *p-i-n* (a) ir *n-i-p* (b) struktūros stabilumų tyrimai 78
Figure 41. Structures of new HTMs **STM1** and **STM2** 86
Figure 42. New HTMs **STM1**, **STM2** and Spiro-OMeTAD: a) UV-vis absorption spectra in THF solution (10^{-4} M); b) Electric field dependencies of the hole-drift mobilities 88
Figure 43. Stability test of PSCs devices with **STM1**, **STM2**, and Spiro-OMeTAD 89
Figure 44. Structures of new enamines 90

Figure 45. New enamines HTMs: a) UV-vis absorption (solid line) and photoluminescence (dashed line) spectra in THF solution (10^{-4} M); b) Electric field dependencies of hole-drift mobilities 92
Figure 46. Stability test of the PSCs devices with new enamines and Spiro-OMeTAD 95
Figure 47. Chemical structures of synthesized D-A-D type organic semiconductors 96
Figure 48. New D-A-D type HTMs: a) UV-vis absorption spectra in THF solution (10^{-4} M); b) Electric field dependencies of the hole-drift mobilities 99
Figure 49. Stability test of PSCs with **STM13** and Spiro-OMeTAD 100
Figure 50. Structures of new HTMs **STM15** and **STM16** 101
Figure 51. New HTMs **STM15** and **STM16**: a) UV-vis absorption (solid line) and photoluminescence (dashed line) spectra in THF solution (10^{-4} M); b) Electric field dependencies of the hole-drift mobilities 103
Figure 52. Structures of new HTMs based on substituted cyclobutane 105
Figure 53. New HTMs based on substituted cyclobutane: a) UV-vis absorption (solid line) and photoluminescence (dashed line) spectra in THF solution (10^{-4} M); b) Electric field dependencies of the hole-drift mobilities 107
Figure 54. Stability test of PSCs with **STM22** and Spiro-OMeTAD 108
Figure 55. Molecular structures of the synthesized cross-linkable HTMs **STM24** and **STM25** 109
Figure 56. New HTMs **STM24** and **1206**: a) First and second scan heating curves (heating rate 10 ^{o}C/min, N_2, atmosphere, the *y*-axis is showing a heat flux); b) UV-vis absorption (solid line) and photoluminescence (dashed line) spectra in THF solution (10^{-4} M) 111
Figure 57. UV-vis absorption spectra after thermal cross-linking study of **STM24** (a) and **STM25** (b) 112
Figure 58. Structure of new Spiro-OMeTAD analogue with vinyl groups 113
Figure 59. First and second scan heating curves (heating rate 10 ^{o}C/min, N_2, atmosphere, the *y*-axis is showing heat flux) for **STM26** (a) and **STM26+dithiol** (b) 115
Figure 60. New HTM **STM26**: a) UV-vis absorption (solid line) and photoluminescence (dashed line) spectra in THF solution (10^{-4} M); b) Electric field dependencies of the hole-drift mobilities 116
Figure 61. UV-vis absorption spectra after thermal cross-linking study of **STM26** (a) and **STM26+dithiol** (b) 116
Figure 62. Structures of *p-i-n* and *n-i-p* PSCs 117
Figure 63. Stability test of the PSCs devices of *p-i-n* (a) and *n-i-p* (b) architectures 118

SCHEMŲ SĄRAŠAS

1 schema. Puslaidininkio Spiro-OMeTAD sintezės schema …….....25
2 schema. Mažamolekulinių puslaidininkių **STM1** ir **STM2** sintezės schema 43
3 schema. Naujų enaminų **STM3** – **STM7** sintezės schema 47
4 schema. Naujų D-A-D tipo puslaidininkių sintezės schema 53
5 schema. Naujų puslaidininkių **STM15** ir **STM16** sintezės schema 58
6 schema. Naujų žaliosios chemijos principais gautų puslaidininkių sintezės schema 63
7 schema. Naujų puslaidininkių su vinilgrupėmis **STM24** ir **STM25** sintezės schema 68
8 schema. Organinių puslaidininkių **STM24** ir **STM25** polimerizacijos schema 69
9 schema. Organinio puslaidininkio su vinilgrupėmis **STM26** sintezės schema 72
10 schema. Spiro-OMeTAD analogo su vinilgrupėmis **STM26** sintezės schema 73
11 schema. Organinio puslaidininkio **STM26** ir 4,4‘-tiobisbenzentiolio polimerizacijos schema 74
Scheme 12. Synthesis route to new HTMs **STM1** and **STM2** 87
Scheme 13. Reaction scheme of fluorene enamines HTMs 91
Scheme 14. Reaction scheme for fluorenone/dicianofluorenylidene enamine-based HTMs 97
Scheme 15. Synthesis route to new HTMs **STM15** and **STM16** 102
Scheme 16. Synthesis route to novel HTMs based on substituted cyclobutane 106
Scheme 17. Synthesis route to novel HTMs **STM24** and **STM25** 110
Scheme 18. Synthetic route and polymerization scheme of the organic semiconductor with vinyl groups **STM26** 114

SANTRUMPŲ SĄRAŠAS

AcOH – acto rūgštis;
Ar – argonas;
BCP – batokuproinas;
BTEAC – benziltrietilamonio chloridas;
C_{60} – fulerenas;
D-A-D – donoras-akceptorius-donoras;
DME – dimetoksietanas;
DMF – *N*,*N*-dimetilformamidas;
DMSO – dimetilsulfoksidas;
DSK – diferencinė skenuojamoji kalorimetrija;
DSSC – dažikliais įjautrintas saulės elementas;
$EDAI_2$ – etilendiamonio dijodidas;
E_{ea} – elektronų gimiringumas;
E_g – draustinė energijos juosta;
EGZO – egzoterminis procesas;
ETM – elektronų transportinės medžiagos;
FA – formamidžio organinis katijonas;
FF – užpildymo faktorius;
FK209 – tris[2-(1*H*-pirazol-1-il)-4-*tret*-butilpiridin]kobalto (III) druska;
FL – fluorescencija;
FTO – fluoru legiruotas alavo oksidas;
HBr HOAc – vandenilio bromidas acto rūgštyje;
HOMO – aukščiausia užimta molekulinė orbitalė;
$HO(CH_2O)_nH$ – paraformaldehidas;
I_P – jonizacijos potencialas;
ITO – indžiu legiruotas alavo oksidas;
J_{SC} – trumpojo jungimo srovės stipris;
J-*V* – fotosrovės-įtampos kreivės;
KSR – (+/-) kamparo-10-sulfonrūgštis;
k. t. – kambario temperatūra;
LiTFSI – ličio bis(trifluormetansulfonil)imido druska;
LUMO – žemiausia neužpildyta molekulinė orbitalė;
MA – metilamonio organinis katijonas;
NaO*t*-Bu – natrio *tret*-butoksidas;
NBS – *N*-bromsukcinimidas;
PC-Z – bisfenolio-Z polikarbonatas;
$PdCl_2(PPh_3)_2$ – bis(trifenilfosfino)paladžio (II) chloridas;
$Pd_2(dba)_3$ – tris(dibenzilidenacetono)dipaladis (0);
$Pd(OAc)_2$ – paladžio (II) acetatas;
$Pd(PPh_3)_4$ – tetrakis(trifenilfosfino)paladis (0);
PEDOT:PSS – poli(3,4-etilendioksitiofenas):poli(stireno sulfonatas);
PESA – fotoelektronų spektroskopija ore;
PETMP – pentaeritritolio tetrakis(3-merkaptopropionatas);

PSE – perovskitinis saulės elementas;
PTAA – poli-[bis(4-fenil)(2,4,6-trimetilfenil)aminas];
P3HT – poli-3-heksiltiofeno polimeras;
SE – saulės elementas;
SEM – skenuojamoji elektroninė mikroskopija;
Spiro-OMeTAD – 2,2ˋ,7,7ˋ-tetrakis[*N*,*N*-di(4-metoksifenil)amino]-9,9ˋ-spirobifluorenas;
STM – skylių transportinė medžiaga;
*t*BP – 4-*tret*-butilpiridinas;
tBu_3P – tri-*tret*-butilfosfinas;
TGA – termogravimetrinė analizė;
THF – tetrahidrofuranas;
T_{kr} – kristalizacijos temperatūra;
T_{lyd} – lydymosi temperatūra;
T_{poli} – polimerizacijos temperatūra;
T_{sk} – 5 % bandinio masės nuostolių temperatūra;
T_{st} – stiklėjimo temperatūra;
$[(t\text{-}Bu)_3PH]BF_4$ – tri-*tret*-butilfosfonio tetrafluoroboratas;
UV-RŠ – ultravioletinės ir regimosios šviesos spinduliuotės sugerties spektras;
V_{OC} – atviros grandinės įtampa;
v.t. – virimo temperatūra;
XPhos – 2-dicikloheksilfosfino-2′,4′,6′-triizopropilbifenilas;
λ_{abs} – absorbcijos maksimumas;
λ_{em} – emisijos maksimumas;
μ_0 – dreifinis judris esant nuliniam elektrinio lauko stipriui;
^1H – vandenilio ^1H branduolių magnetinis rezonansas;
^{13}C – anglies ^{13}C izotopo branduolių magnetinis rezonansas.

1. ĮVADAS

Pastaraisiais dešimtmečiais energijos suvartojimas kelia didelį susirūpinimą visame pasaulyje. Jos išgavimas sudaro daugiau nei tris ketvirtadalius Europos Sąjungos (ES) išmetamų šiltnamio efektą sukeliančių dujų. Norint sumažinti energetikos sektoriaus išmetamų teršalų kiekį, svarbu išnaudoti atsinaujinančios energijos potencialą. Šiuo metu ES tik daugiau nei 20 % energijos yra išgaunama iš atsinaujinančių šaltinių. Nustatytas tikslas, kad iki 2030 m. atsinaujinančios energetikos dalis sudarytų 42,5 % viso ES suvartojimo, o iki 2050 m. būtų neutralizuotas klimatas, t. y. pasiektas nulinis šiltnamio efektą sukeliančių dujų emisijos lygis[1].

Vienas iš galingiausių atsinaujinančios energetikos išteklių yra Saulė, kurios energijai išgauti yra naudojami saulės elementai (SE). Prognozuojama, jog iki XXI a. vidurio SE galėtų patenkinti apie 45 % viso pasaulio energijos poreikio[2]. Šiuo metu daugiausia (~ 90 %) naudojami polikristalinio silicio saulės elementai, tačiau juos gaminti brangu ir sudėtinga[3]. Kaip pigi alternatyva sparčiai kelią skinasi organiniai bei hibridiniai trečios kartos saulės elementai. Tarp pastarųjų proveržiu išsiskiria perovskitiniai saulės elementai (PSE), kurių efektyvumas per pastarąjį dešimtmetį sensacingai išaugo nuo 3,8 %[4] iki daugiau nei 26 %[5].

PSE pasižymi konstrukcijos paprastumu, pigiomis žaliavomis bei perovskito sluoksnio absorbcija plačiame šviesos bangos ilgių diapazone[6]. Labai svarbi PSE konstrukcijos dalis yra skyles transportuojantis sluoksnis, atsakingas už skylių ištraukimą iš perovskitinio sluoksnio ir jų transportavimą link elektrodo. Šiuo metu skylių transportui dažniausiai naudojamas organinis puslaidininkis kodiniu pavadinimu Spiro-OMeTAD. Deja, ši medžiaga yra labai brangi, nes sintetinama daugiapakope sinteze, kuriai reikalingi brangūs retųjų metalų katalizatoriai, agresyvūs ir itin jautrūs aplinkos poveikiui reagentai[7-8]. Bene didžiausia problema – nepakankamas PSE prietaisų stabilumas. Visi šie išvardinti minusai skatina ieškoti perspektyvesnių skylių transportinių medžiagų (STM).

Šioje disertacijoje apžvelgtos autorės susintetintos ir ištirtos STM, turinčios fluoreno, karbazolo ir spirobisindano fragmentus. Pigios ir komercinės pradinės medžiagos, paprastesnė sintezė, mažesni gamybos kaštai, geresni PSE efektyvumo ir stabilumo rezultatai daugeliui jų suteikia patrauklumą ir perspektyvumą šiuolaikinėje PSE rinkoje.

Darbo tikslas – efektyvių ir ekonomiškų skyles transportuojančių medžiagų su fluoreno, karbazolo ir spirobisindano chromoforais sintezė, savybių ištyrimas ir pritaikymas hibridiniuose perovskitiniuose saulės elementuose.

Darbo tikslui pasiekti buvo išsikelti šie uždaviniai:

1. Susintetinti naujus mažamolekulinius fluoreno centrinį fragmentą turinčius organinius puslaidininkius, ištirti jų termines, optines ir fotofizikines savybes bei įvertinti perovskitinių saulės elementų, kuriuose panaudoti šie junginiai, fotovoltines charakteristikas.
2. Susintetinti naujas fluoreno centrinį fragmentą ir difeniletenilgrupes turinčias skylių transportines medžiagas, charakterizuoti jų savybes ir ištirti molekulių

pritaikymo galimybes perovskitiniuose saulės elementuose su legiruojančiais priedais ir be jų.

3. Susintetinti naujus mažamolekulinius fluoreno su akceptorine grupe centrinį fragmentą ir difeniletenilgrupes turinčius organinius junginius, charakterizuoti jų savybes, ištirti skirtingų akceptorių įtaką perovskito pasyvavimui ir saulės elementų efektyvumui bei stabilumui.

4. Susintetinti naujus spirobisindano centrinį fragmentą ir difeniletenilgrupes turinčius organinius puslaidininkius, ištirti junginių termines, optines ir fotofizikines savybes bei įvertinti jų pritaikymo galimybes perovskitiniuose saulės elementuose.

5. Ištirti žaliosios sintezės pritaikymo galimybes naujoms skylių transportinėms medžiagoms su karbazolo centriniu fragmentu gauti, charakterizuoti junginių savybes ir nustatyti jų panaudojimo efektyvumą perovskitiniuose saulės elementuose.

6. Susintetinti naujus karbazolo centrinį fragmentą turinčius ir tinklintis galinčius organinius puslaidininkius, ištirti jų termines, optines ir fotofizikines savybes bei nustatyti perovskitinių saulės elementų efektyvumus.

7. Susintetinti naują 9,9′-spirobifluoreno centrinį fragmentą ir polimerintis galinčias grupes turinčią skylių transportinę medžiagą, charakterizuoti puslaidininkio savybes ir ištirti pritaikymo galimybes skirtingų konstrukcijų perovskitiniuose saulės elementuose.

Darbo naujumas ir ryšys tarp publikacijų

Hibridiniai PSE šiuo metu yra viena sparčiausiai besivystančių SE rūšių. Šiuose elementuose STM sluoksnis yra vienas pagrindinių prietaiso komponentų, lemiančių efektyvų Saulės energijos konvertavimą. Organiniai puslaidininkiai turi pasižymėti gana aukštu dreifiniu judriu, tinkamais energetiniais lygmenimis (HOMO, LUMO), aukšta skilimo temperatūra, amorfine būsena bei ekonomiškumu[9-11]. Nepaisant reikšmingų mokslininkų pastangų kuriant naujas STM, šiuo metu didžiausiu efektyvumu (26,1 %[5]) pasižymi brangi molekulė 2,2ʿ,7,7ʿ-tetrakis[*N*,*N*-di(4-metoksifenil)amino]-9,9ʿ-spirobifluorenas (Spiro-OMeTAD). Jos aukštą kainą lemia penkių žingsnių sintezė, kuriai reikalingos inertinės sąlygos, žema temperatūra, aplinkai jautrūs ir agresyvūs reagentai bei sudėtinga, ilga ir brangi gryninimo sublimacijos procedūra[7-8]. Kitas svarbus Spiro-OMeTAD trūkumas – kristališkumas, turintis neigiamą įtaką PSE stabilumui ir šviesos konversijos efektyvumui[12]. Todėl vis dar ieškoma naujų organinių puslaidininkių, kurių sintezė būtų paprastesnė, ekologiškesnė ir ekonomiškesnė, o jų pagrindu sukonstruoti PSE pasižymėtų geresniu stabilumu ir efektyvumu. Atsižvelgiant į šiuos kriterijus buvo susintetintos naujos STM, ištirtos jų savybės ir sukonstruoti PSE. Visi tyrimų rezultatai aprašyti septyniuose šios disertacijos autorės moksliniuose straipsniuose.

Pirmoje publikacijoje pristatomi du nauji organiniai puslaidininkiai, kurių centrinis fragmentas – fluorenas. Mažamolekuliniai junginiai susintetinti naudojant nesudėtingą trijų pakopų sintezės kelią. Ištyrus savybes paaiškėjo, kad STM yra amorfinės ir pasižymi aukšta stiklėjimo temperatūra, tinkamu terminiu stabilumu ir geromis fotoelektrinėmis savybėmis. Sukonstruotas PSE, kuriame panaudotas

junginys su padidinta π konjuguotąja dvigubųjų ryšių sistema, pasižymėjo 18,3 % energijos konversijos efektyvumu ir didesniu ilgalaikiu terminiu stabilumu, palyginti su etaloniniu Spiro-OMeTAD.

Antroje publikacijoje pateikiama serija junginių su difenileteniilgrupėmis ir fluoreno chromoforu molekulės centre. Šio chromoforo 9-oje padėtyje esantys vandenilio atomai yra chemiškai aktyvūs ir puikiai tinka alkilinimo reakcijoms, kurios įgalina funkcionalizuoti junginius ir gauti tikslines fotolaidžias STM. Svarbu paminėti, kad geriausiu efektyvumu pasižymėjo PSE su organiniu puslaidininkiu **STM3**, susintetintu iš komercinių pradinių medžiagų ekonomiškos kondensacijos reakcijos metu. Jo pagrindu sukonstruotas PSE pasižymėjo daug žadančiais efektyvumo rezultatais legiruotoje struktūroje (19,3 %) ir konfigūracijoje be priedų (17,1 %). Tai buvo geresnis rezultatas nei PSE su Spiro-OMeTAD.

Trečioje publikacijoje taip pat pristatoma serija STM su difenileteniilgrupėmis bei molekulės centre esančiu fluoreno chromoforu, 9-oje padėtyje turinčiu stiprias akceptorines grupes. Šiame moksliniame straipsnyje tiriama donoro-akceptoriaus-donoro sąveika, akceptoriaus įtaka perovskito pasyvavimui ir PSE efektyvumui bei stabilumui. Naudojant junginį **STM13** buvo pasiektas didesnis nei 22 % elemento efektyvumas, o praėjus 500 valandų jis sumažėjo tik 4 %. Svarbu tai, kad šie rezultatai pranoko Spiro-OMeTAD pagrindu sukonstruoto ir identiškomis aplinkos sąlygomis testuoto PSE. Be to, mažamolekulinis junginys **STM13** buvo gautas naudojant paprastą sintezės kelią, todėl yra pigi alternatyva šiandieniniam STM etalonui.

Ketvirtajame moksliniame straipsnyje pateikiami nauji spirobisindano centrinį fragmentą ir difenileteniilgrupes turintys organiniai puslaidininkiai. Junginiai pasižymi aukštu terminiu stabilumu, geromis optinėmis ir fotofizikinėmis savybėmis bei patvaria amorfine būsena, užtikrinančia gerą PSE morfologinį stabilumą. Saulės elemento, kuriame kaip teigiamus krūvininkus transportuojanti medžiaga buvo panaudotas mažamolekulinis junginys **STM15,** efektyvumo rezultatai buvo daug žadantys, todėl šis puslaidininkis gali būti puiki alternatyva etalonui Spiro-OMeTAD.

Penktojoje publikacijoje STM centriniu fragmentu buvo pasirinktas fotodimerizuotas karbazolas. Pastarasis buvo gautas nesudėtingos žaliosios chemijos principais paremtos sintezės metu. Darbe aprašytas sistemingas skirtingų pakaitų įtakos naujų organinių puslaidininkių terminėms, optinėms ir fotofizikinėms savybėms bei PSE fotovoltiniams parametrams tyrimas. Buvo pasiektas 21 % efektyvumas ir, palyginti su Spiro-OMeTAD, pagerintas ilgalaikis elemento stabilumas atmosferos aplinkoje. Geriausi efektyvumo rezultatai buvo PSE su **STM22**, todėl pastarasis buvo panaudotas konstruojant perovskitinį saulės modulį (6,5×7 cm), pasiekusį 19 % efektyvumą. Tai tuo metu buvo rekordas ne spiro klasės junginiuose. Šių puslaidininkių praktinę reikšmę demonstruoja JAV (US2023157158), Japonijos (JP2023072638), Kinijos (CN116133444) ir Europos (EP4181225) patentų biuruose užregistruotos patentinės paraiškos.

Šeštame moksliniame straipsnyje pristatyti organiniai puslaidininkiai, turintys komerciškai pigaus karbazolo chromoforą ir tinklintis galinčias funkcines grupes. Po terminio apdorojimo molekulės buvo panaudotos invertuotos struktūros (*p*-*i*-*n*) PSE formuoti. Tokioje sandaroje naudojant polimerus galima atsisakyti legiruojančių priedų, kurie ilgainiui prisideda prie elemento stabilumo mažėjimo. Buvo ištirtos

naujai susintetintų junginių optinės, terminės ir fotofizikinės savybės bei sukonstruoti PSE, pasižymėję daug žadančiais efektyvumo ir stabilumo rezultatais.

Paskutinėje publikacijoje aprašomas naujas Spiro-OMeTAD analogas **STM26**, turintis tinklintis galinčias grupes. Po terminio kryžminio sujungimo susidaro lygus ir tirpikliams atsparus trimatis (3D) polimerinis tinklas. Pastarasis buvo panaudotas kaip STM invertuotos struktūros (*p*-*i*-*n*) ir kaip tarpsluoksnis tarp šviesą absorbuojančio sluoksnio ir skylių transportinės medžiagos įprastos konfigūracijos (*n*-*i*-*p*) PSE. Abu įrenginiai pasižymėjo rekordiniais galios konversijos ir ilgalaikio stabilumo rezultatais, palyginti su atitinkamais etalonais PTAA ir Spiro-OMeTAD. Organinis puslaidininkis buvo užpatentuotas registruojant patentines paraiškas JAV (USPTO, Reg. Nr. 18/134,751), Japonijos (JP, Reg. Nr. 2023-068376) ir Europos (EPO, Reg. Nr. EP23168712.0) patentiniuose biuruose.

Mokslinių publikacijų disertacijos tema sąrašas:

1. **Daškevičiūtė, Šarūnė**; Sakai, Nobuya; Franckevičius, Marius; Daškevičienė, Marytė; Magomedov, Artiom; Jankauskas, Vygintas; Snaith, Henry J.; Getautis, Vytautas. Nonspiro, fluorene-based, amorphous hole transporting materials for efficient and stable perovskite solar cells // Advanced science. ISSN 2198-3844. 2018, vol. 5, iss. 4, art. no. 1700811, p. 1-7. (Web of Science). DOI: 10.1002/advs.201700811. [IF: 15,804; Q1].
2. **Daskeviciute, Sarune**; Momblona, Cristina; Rakstys, Kasparas; Sutanto, Albertus Adrian; Daskeviciene, Marytė; Jankauskas, Vygintas; Gruodis, Alytis; Bubniene, Giedre; Getautis, Vytautas; Nazeeruddin, Mohammad Khaja. Fluorene-based enamines as low-cost and dopant-free hole transporting materials for high performance and stable perovskite solar cells // Journal of materials chemistry A. ISSN 2050-7488. 2021, vol. 9, iss. 1, p. 301-309. (Web of Science). DOI: 10.1039/D0TA08452B. [IF: 14,511; Q1].
3. **Daskeviciute-Geguziene, Sarune**; Zhang, Yi; Rakstys, Kasparas; Xiao, Chuanxiao; Xia, Jianxing; Qiu, Zhiheng; Daskeviciene, Maryte; Paskevicius, Tomas; Jankauskas, Vygintas; Asiri, Abdullah M.; Getautis, Vytautas; Nazeeruddin, Mohammad Khaja. Passivating defects of perovskite solar cells with functional donor-acceptor-donor type hole transporting materials // Advanced functional materials. ISSN 1616-301X. 2023, vol. 33, iss. 1, p. 1-8. (Web of Science). DOI: 10.1002/adfm.202208317. [IF: 19,000; Q1].
4. **Daskeviciute-Geguziene, Sarune**; Daskeviciene, Maryte; Kantminiene, Kristina; Jankauskas, Vygintas; Kamarauskas, Egidijus; Gruodis, Alytis; Karazhanov, Smagul; Getautis, Vytautas. Design, Synthesis and Theoretical Simulations of Novel Spiroindane-Based Enamines as *p*-Type Semiconductors // Royal Society Open Science. 2024, vol. 11, iss. 5, p. 1-11. (Web of Science). DOI: 10.1098/rsos.232019. [IF: 3,500; Q2].
5. **Daskeviciute-Geguziene, Sarune**; Zhang, Yi; Rakstys, Kasparas; Kreiza, Gediminas; Khan, Sher Bahadar; Kanda, Hiroyuki; Paek, Sanghyun; Daskeviciene, Maryte; Kamarauskas, Egidijus; Jankauskas, Vygintas; Asiri, Abdullah M.; Getautis, Vytautas; Nazeeruddin, Mohammad Khaja. Green-chemistry-inspired synthesis of cyclobutane-based hole-selective materials for highly efficient perovskite solar cells

and modules // Angewandte chemie. ISSN 1433-7851. 2022, vol. 61, iss. 5, p. 1-9. (Web of Science). DOI: 10.1002/anie.202113207. [IF: 16,600; Q1].

6. **Daskeviciute-Geguziene, Sarune**; Magomedov, Artiom; Daskeviciene, Maryte; Genevičius, Kristijonas; Nekrašas, Nerijus; Jankauskas, Vygintas; Kantminiene, Kristina; McGehee, Michael D.; Getautis, Vytautas. Cross-linkable carbazole-based hole transporting materials for perovskite solar cells // Chemical communications. ISSN 1359-7345. 2022, vol. 58, iss. 54, p. 7495-7498. (Web of Science). DOI: 10.1039/D2CC02612K. [IF: 4,900; Q2].

7. **Daskeviciute-Geguziene, Sarune**; Truong, Minh Anh; Rakštys, Kasparas; Daškevičienė, Marytė; Hashimoto, Ruito; Murdey, Richard; Yamada, Takumi; Kanemitsu, Yoshihiko; Jankauskas, Vygintas; Wakamiya, Atsushi; Getautis, Vytautas. In situ thermal cross-linking of 9,9′-spirobifluorene-based hole-transporting layer for perovskite solar cells // ACS Applied Materials & Interfaces. ISSN 1944-8252. 2024, vol. 16, iss. 1, p. 1206-1216. (Web of Science). DOI: 10.1021/acsami.3c13950. [IF: 9,500; Q1].

Disertanto ir bendraautorių mokslinis indėlis straipsniuose

Disertacijos autorė susintetino ir išgrynino visus organinius puslaidininkius ir pateikė išsamius sintezės aprašymus visose septyniose publikacijose. Ji atliko geriausiai veikusių STM kainos įvertinimus, visus optinius, fluorescencijos, polimerizacijos ir vilgymo kampų tyrimus, išanalizavo bei pateikė juos grafiškai. Taip pat autorė interpretavo ir grafiškai pateikė terminius, fotofizikinius ir fotovoltinius PSE tyrimus. Dr. Nobuya Sakai (Fizikos katedra, Oksfordo universitetas) konstravo SE prietaisus, tyrė jų fotovoltines savybes, efektyvumą ir stabilumą. Dr. Vygintas Jankauskas, dr. Kristijonas Genevičius ir dr. Nerijus Nekrašas (Cheminės fizikos institutas, Vilniaus universitetas (VU)) atliko skylių dreifinio judrio matavimus. Jonizacijos potencialo matavimus atliko dr. Marius Franckevičius ir dr. Egidijus Kamarauskas (Cheminės fizikos institutas, VU). Dr. Marytė Daškevičienė ir dr. Giedrė Bubnienė konsultavo dėl naujų organinių puslaidininkių sintezės (Organinės chemijos katedra, KTU). Dr. Artiom Magomedov (Organinės chemijos katedra, KTU) padėjo ruošiant publikacijos rankraštį ir konstravo PSE, tyrė jų efektyvumą bei stabilumą. Prof. dr. Henry J. Snaith (Fizikos katedra, Oksfordo universitetas) konsultavo ruošiant publikacijos rankraštį. Dr. Cristina Momblona, dr. Albertus Adrian Sutanto, dr. Yi Zhang, dr. Jianxing Xia ir dr. Hiroyuki Kanda (Chemijos mokslų ir inžinerijos institutas, Lozanos federalinis politechnikos institutas) konstravo PSE, tyrė jų fotovoltines savybes, efektyvumą ir stabilumą. Dr. Kasparas Rakštys (Organinės chemijos katedra, KTU) kontaktavo su užsienio partneriais dėl tyrimų ir dalyvavo publikacijų ruošime. Dr. Alytis Gruodis (Cheminės fizikos institutas, VU) atliko molekulių struktūrų išsidėstymo erdvėje kompiuterinius skaičiavimus. Prof. dr. Mohammad Khaja Nazeeruddin (Chemijos mokslų ir inžinerijos institutas, Lozanos federalinis politechnikos institutas) konsultavo ruošiant publikacijų rankraščius. Dr. Chuanxiao Xiao ir dr. Zhiheng Qiu (Ningbo medžiagų technologijos ir inžinerijos institutas, Kinijos mokslų akademija) konstravo PSE, tyrė jų fotovoltines savybes, efektyvumą bei stabilumą. Prof. dr. Abdullah M. Asiri (Karaliaus Abdulos mokslo ir technologijų universitetas) konsultavo ruošiant

publikacijų rankraščius. Dr. Smagul Karazhanov (Energetikos technologijos institutas, IFE) prisidėjo prie publikacijos rankraščio ruošimo. Dokt. Tomas Paškevičius (Organinės chemijos katedra, Fizinių ir technologijos mokslų centras) susintetino vieną pradinę medžiagą. Dr. Gediminas Kreiza (Fotonikos ir nanotechnologijų institutas, VU) nustatė STM geometriją naudojant rentgenografinę analizę. Dr. Sher Bahadar Khan (Karaliaus Abdulos mokslo ir technologijų universitetas) ir dr. Sanghyun Paek (Chemijos ir energetikos inžinerijos katedra, Sangmyung universitetas) konstravo PSE prototipinį modulį, tyrė jo efektyvumą ir stabilumą. Dr. Kristina Kantminienė (Fizikinės ir neorganinės chemijos katedra, KTU) redagavo rankraštį anglų kalba. Prof. dr. Michael D. McGehee (Chemijos ir bioinžinerijos katedra, Kolorado universitetas) konsultavo ruošiant publikacijos rankraštį. Dr. Minh A. Truong, dr. Ruito Hashimoto, dr. Richard Murdey, dr. Takumi Yamada ir dr. Yoshihiko Kanemitsu (Cheminių tyrimų institutas, Kioto universitetas) konstravo skirtingų konstrukcijų perovskitinius saulės elementus, ieškojo optimaliausių veikimo sąlygų, tyrė prietaisų stabilumus. Prof. dr. Atsushi Wakamiya (Cheminių tyrimų institutas, Kioto universitetas) konsultavo ruošiant publikacijos rankraštį. Prof. dr. Vytautas Getautis (Organinės chemijos katedra, KTU) pasiūlė naujų molekulių struktūras ir padėjo rengiant mokslines publikacijas.

2. MOKSLINĖS LITERATŪROS DISERTACIJOS TEMA APŽVALGA

Per didelis iškastinio kuro naudojimas sukėlė didelę problemą Žemės atmosferoje – šiltnamio efektą. Dėl to pakilo atmosferos temperatūra, kuri savo ruožtu sukėlė sausros, potvynių, atšiaurios žiemos pasikartojimą skirtingose Žemės rutulio dalyse. Vienas iš didžiausių iššūkių, su kuriuo šiuo metu susiduria mūsų visuomenė, – atsinaujinančių energijos šaltinių paieška, galinti sušvelninti sparčiai didėjantį energijos poreikį augančiam gyventojų skaičiui ir industrializacijai. Daug dėmesio skiriama Saulės energijos panaudojimui. Per pastaruosius šešis dešimtmečius sparčiai evoliucionavo fotovoltinės SE technologijos, ir šiuo metu yra žinomos keturios jų raidos fazės[13-14]:

1. Pirmos kartos SE. Jie gaminami monokristalinio arba polikristalinio silicio pagrindu. Tokių SE gamybos technologija reikalauja daug energijos sąnaudų ir yra labai brangi.
2. Antros kartos SE. Antros kartos fotoelektronikos technologijoje naudojami plonasluoksniai neorganiniai junginiai, tokie kaip a-Si:H (amorfinis hidrogenizuotas silicis), CdTe ir CIGS ($Cu(In,Ga)(SSe)_2$). Nors šie elementai pasižymi paprastesne ir pigesne gamybos technologija, jie turi ir keletą trūkumų – ruošiant SE plėvelę yra reikalingas brangus vakuuminis garų nusodinimo metodas, indžio ištekliai yra riboti.
3. Trečios kartos SE. Tai plonasluoksniai elementai, kurie yra sukurti taip, kad būtų pasiektas didelis galios konversijos efektyvumas, esant mažoms įrenginių gamybos sąnaudoms. Šiai klasei priskiriami organiniai fotovoltiniai bei dažikliais įjautrinti saulės elementai.
4. Ketvirtos kartos SE. Tai PSE, kurie gali užtikrinti aukštą galios konversijos efektyvumą. Juose šviesos absorberio vaidmenį atlieka perovskitas. Tai sparčiausiai besivystanti SE rūšis.

2.1. Perovskitas ir jo sandara

Perovskitas – tai oksidų klasės mineralas kalcio titanatas $CaTiO_3$, kuris 1839 m. Gustavo Roso buvo atrastas Uralo kalnuose. Vėliau visi jo kristalinę struktūrą atitinkantys junginiai rusų mineralogo Levo Perovskio garbei buvo pavadinti perovskitais. Fotovoltiniuose prietaisuose naudojamo organinio-neorganinio šviesą absorbuojančio perovskito struktūros formulė yra ABX_3, kur A – metilamonio $CH_3NH_3^+$ (MA) arba formamidžio $NH_2{=}CH_3NH_2^+$ (FA) organiniai katijonai, B – švino arba alavo dvivalenčiai metalų katijonai ir X – I^-, Br^- ir Cl^- anijonai (žr. 1 pav.)[15]. Svarbu tai, kad pasirenkant skirtingus katijonus arba anijonus galima reguliuoti perovskito laidumo juostos tarpą 1,6–2,3 eV diapazone[17].

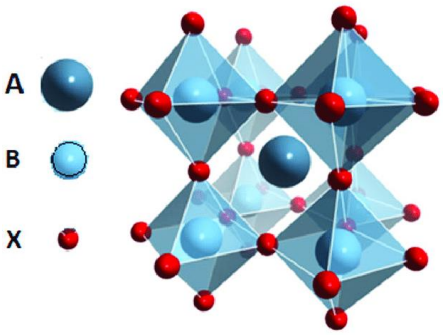

1 pav. Kristalinė 3D perovskito struktūra: A – organinis katijonas, B – dvivalentis katijonas, X – anijonas[16]

Metilamonio švino jodido ($MAPbI_3$) perovskito absorbentas yra žinomas dėl plataus sugerties diapazono, kuris apima beveik visą regimosios šviesos spektro dalį ir pasiekia artimąją infraraudonąją sritį (800 nm)[18]. Dėl šios priežasties jis plačiausiai taikomas PSE gamyboje.

2.2. Perovskitiniai saulės elementai

PSE gali būti dviejų pagrindinių konstrukcijų – reguliariosios (*n-i-p*) ir invertuotos (*p-i-n*) struktūros. *n-i-p* atveju STM sluoksnis dengiamas ant šviesą absorbuojančio perovskito, o *p-i-n* struktūroje – lokalizuotas po absorbentu. Įprastiniu atveju konstrukciją sudaro penki pagrindiniai sluoksniai: skaidrus elektrodas (FTO arba ITO), elektronų transportinis sluoksnis, perovskitas, skylių transportinis sluoksnis ir metalinis elektrodas (Au arba Ag) (žr. 2 pav.)[19].

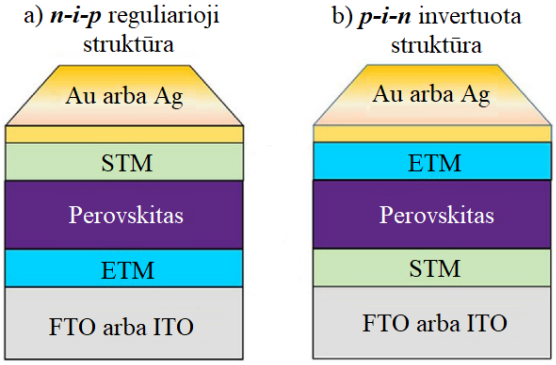

2 pav. PSE *n-i-p* ir *p-i-n* struktūros konstrukcijos

Detalūs PSE *n-i-p* ir *p-i-n* konstrukcijų sudedamųjų dalių aprašymai pateikti tolimesniuose poskyriuose.

2.2.1. Skaidrūs elektrodai / anodai

Kaip anodai naudojami skaidrūs laidūs oksidai, kurie paprastai padengiami ant stiklo plokštelės. Šie elektrodai paprastai turi platų laidumo juostos tarpą ($E \geq 3{,}1$ eV), todėl gali efektyviai perduoti regimosios ir infraraudonosios šviesos spindulius[20]. Taip

pat labai svarbios savybės – didelis laidumas, maža savitoji varža bei nedidelė oksido kaina. Skaidrių laidžių oksidų pavyzdžiai: cinko oksidas (ZnO)[21], alavo dioksidas (SnO_2)[22], indžio oksidas (In_2O_3), indžiu legiruotas alavo oksidas (ITO), fluoru legiruotas alavo oksidas (FTO) ir kt. Šiuo metu PSE gamyboje dažniausiai naudojami laidūs oksidai yra FTO ir ITO, todėl pastarieji buvo pasirinkti šioje disertacijoje apžvelgtų saulės elementų anodais.

2.2.2. Elektronų transportinis sluoksnis

Elektronų transportinės medžiagos (ETM) perneša fotogeneruotus elektronus iš fotoaktyvių PSE sluoksnių link katodo. Jos turi pasižymėti dideliu elektronų mobilumu, suderintais energijos lygmenimis su perovskitu, lengvai ištirpti organiniame tirpiklyje arba sublimuotis bei būti stabilios ore[23].

ETM gali būti skirstomos į dvi grupes – organines ir neorganines. Kaip organinės kilmės ETM, kurios labiau pritaikytos invertuotos struktūros *p-i-n* saulės elementams, gali būti naudojami fulerenas (C_{60}) arba jo dariniai, pvz., [6,6]-fenil-C_{61}-metilbutanoatas (PCBM)[24]. Deja, šios medžiagos pasižymi keliais trūkumais, kurie riboja jų komercinį pritaikymą – nepakankamas morfologinis stabilumas, brangi sintezė ir gryninimo procedūros, ribotas LUMO lygio suderinamumas[25-26]. Dėl šių priežasčių šiuo metu daug dėmesio sulaukia nefulereninės kilmės ETM, tokios kaip perileno diimidas (PDI), substituoti perileno diimidai (*N*-PDI), naftaleno diimidas (NDI) ir jo dariniai. Šios medžiagos pasižymi dideliu elektronų mobilumu (>$1{,}0\times10^{-3}$ cm^2/Vs) ir geru terminiu stabilumu[27-28]. Neorganinės kilmės ETM dažniau naudojamos konstruojant įprastinės konstrukcijos *n-i-p* saulės elementus. Tokios medžiagos gali būti titano dioksidas (TiO_2)[29], alavo (IV) dioksidas (SnO_2)[30], cinko oksidas (ZnO)[31], kadmio sulfidas (CdS)[32], kadmio selenidas (CdSe)[33] ir kt. Reguliarios konstrukcijos PSE dažniausiai naudojamos ETM yra titano ir alavo oksidai. TiO_2 yra plačiai taikomas dėl savo laidumo juostos energijos (4,4 eV), kuri yra šiek tiek mažesnė nei perovskito, todėl yra užtikrinamas efektyvus elektronų perdavimas[34]. SnO_2 – perspektyvi ETM dėl didelio stabilumo, laidumo juostos energijos (4,2–4,5 eV)[35] ir didelio elektronų mobilumo (240 cm^2/Vs)[36].

2.2.3. Šviesą absorbuojantis sluoksnis – perovskitas

Hibridinis organinis-neorganinis perovskitas atlieka svarbų vaidmenį PSE ir yra būtinas šviesos absorbcijai ir elektronų fotogeneracijai. Didelis šviesos konversijos efektyvumas saulės elementuose gali būti siejamas su tinkamomis optoelektroninėmis perovskito savybėmis[37].

Organinių-neorganinių perovskito plėvelių gavimas yra svarbus aspektas, norint jas pritaikyti saulės energijos konvertavimo elementuose. Šiuo metu laboratorijose yra naudojama daug įvairių perovskito plėvelių sintezės metodų, tokių kaip vienpakopis nusodinimas, dviejų pakopų nusodinimas, greitas nusodinimas-kristalizacija, terminis garinimas, impulsinis lazerinis purškimas, elektropurškimas ir kt[38]. Dažniausiai naudojamo organinių-neorganinių perovskito plėvelių vienpakopio sintezės metodo esmė yra gauti plėvelę tiesiai iš druskos tirpalo, naudojant sukamojo dengimo metodą (angl. *spin-coating*)[39-40]. Perovskito gavimas paremtas tirpiklio išgarinimu ir medžiagos nusodinimu vienu metu. Prekursoriai, dažniausiai MAX, kur X = Cl, Br, I

ir PbI_2, ištirpinami tame pačiame arba skirtinguose organiniuose tirpikliuose. Dažniausiai pradinėms medžiagoms ištirpinti naudojami tirpikliai yra *N*,*N*-dimetilformamidas (DMF) ir dimetilsulfoksidas (DMSO). Įrodyta, kad DMSO tirpiklis gali sudaryti DMSO-PbI_2 kompleksus, kurie pagerina perovskito paviršių[41-42].

2.2.4. Skylių transportinis sluoksnis

Labai svarbi PSE konstrukcijos dalis yra skyles transportuojantis sluoksnis, atsakingas už skylių ištraukimą iš perovskitinio sluoksnio ir jų transportavimą link elektrodo. Idealiu atveju STM turėtų atitikti šiuos reikalavimus:

- Efektyviam skylių transportavimui HOMO energetinis lygmuo turėtų būti šiek tiek aukštesnis (ne daugiau nei 0,3 eV) nei perovskito ($MAPbI_3$ atveju apie -5,2 eV) valentinės juostos energija[43];
- Pasižymėti geromis krūvio pernašos savybėmis. Mažą krūvininkų mobilumą galima pagerinti ličio ir kobalto druskomis bei piridino dariniais. Tačiau šie priedai yra higroskopiniai ir ilgainiui kenkia SE prietaiso stabilumui[44-45];
- Pasižymėti geru terminiu stabilumu ir atsparumu drėgmei[44];
- Puslaidininkiai turėtų tirpti tokiuose organiniuose tirpikliuose, kurie konstruojant PSE nepažeistų perovskito sluoksnio. Geros medžiagų tirpumo savybės sumažina gamybos sąnaudas[44];
- Pasižymėti geromis plėvelių formavimo galimybėmis, užpildyti perovskito sluoksnio poras, taip suformuodami efektyvų krūvininkų perdavimą. Puslaidininkiai turi turėti stabilią amorfinę būseną ($>T_g$ = 100 °C)[44,46];
- Puslaidininkiai turėtų būti lengvai sintetinami, netoksiški, nekenksmingi aplinkai ir ekonomiški[44].

STM skirstomos į dvi pagrindines grupes – neorganines ir organines medžiagas, kurios gali būti mažamolekuliniai arba polimeriniai junginiai.

Neorganinės STM pasižymi paprastomis sintezės procedūromis, žema kaina, geru cheminiu stabilumu, dideliu optiniu pralaidumu, tinkamais energetiniais lygmenimis ir dideliu krūvininkų mobilumu, palyginti su organinės kilmės puslaidininkiais[47-48]. Daugiau nei 20 % PSE konversijos efektyvumo rezultatas pasiektas naudojant $CuGaO_2$ ir CuSCN kaip STM mezoporinėje *n*-*i*-*p* konfigūracijoje[49]. Kitas perspektyvus neorganinis puslaidininkis yra NiO_x. Jis pasižymi svarbiomis *p*-tipo puslaidininkio charakteristikomis – E_g > 3,5 eV, dideliu optiniu pralaidumu, cheminiu stabilumu, energetinių lygmenų suderinimu su įvairiais perovskito absorbentais[50]. Pastarąjį panaudojus PSE buvo pasiektas daugiau nei 18 % efektyvumas[51]. Taip pat buvo pastebėta, jog naudojant NiO_x pagerėja SE ilgalaikis stabilumas, kuris po 60 dienų sumažėjo tik iki 90 %[52].

Šiuo metu *n*-*i*-*p* konstrukcijos PSE kaip organinis mažamolekulinis puslaidininkis dažniausiai naudojamas junginys kodiniu pavadinimu Spiro-OMeTAD. Pastarasis pirmą kartą kaip kietos būsenos STM buvo panaudotas dažikliais įjautrintame saulės elemente (DSSC) 1998 m.[53] ir iki šių dienų vis dar yra laikomas etaloniniu *p*-tipo puslaidininkiu. Spirobifluoreno centrinis fragmentas suteikia junginiui terminį stabilumą, keturios difenilamino grupės atsakingos už skylių transportavimą, o metoksigrupės gerina organinio puslaidininkio tirpumą,

užtikrina energetinių lygmenų suderinamumą ir dėl deguonies atomų sąveikauja su perovskitu[44]. Mažamolekulinis organinis junginys turi platų energijos juostos tarpą (~3 eV) ir lengvai suderinamą HOMO lygmenį su perovskitu[54-55], pasižymi geru tirpumu, aukšta stiklėjimo temperatūra, prisidedančia prie SE šiluminio stabilumo[56-58], o jo sintezė yra gerai ištyrinėta.

Nepaisant šių Spiro-OMeTAD privalumų, jis turi keletą trūkumų. Vienas iš jų – penkių pakopų sintezė (žr. 1 schemą)[59-60], kuriai reikalingi retųjų metalų katalizatoriai, agresyvūs ir itin jautrūs aplinkos poveikiui reagentai. Sudėtinga sublimacijos gryninimo procedūra taip pat prisideda prie galutinės aukštos ir komercinį prieinamumą mažinančios Spiro-OMeTAD kainos, kuri gali siekti ~300 Eur/g[61].

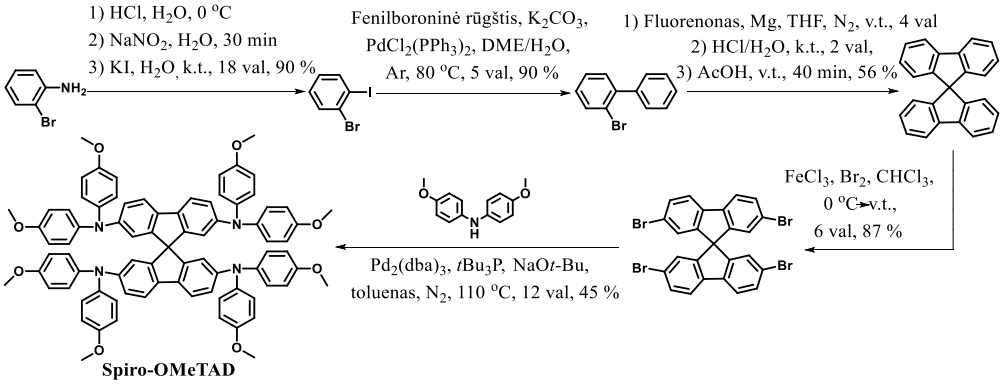

1 schema. Puslaidininkio Spiro-OMeTAD sintezės schema

Kitas svarbus šio puslaidininkio neigiamas aspektas – jo kristališkumas. Dėl centrinio spirobifluoreno fragmento organinis puslaidininkis linkęs kristalintis, t. y. vyksta terminis virsmas iš amorfinės į kristalinę būseną[62]. Ši tendencija riboja jo gebėjimą formuoti tolygias plėveles PSE ir daro neigiamą įtaką įrenginio stabilumui[63]. Taip pat yra žinoma, jog Spiro-OMeTAD skylių transportinis sluoksnis pasižymi mažu krūvininkų mobilumu[64], todėl norint pagerinti puslaidininkio elektrines savybes dažniausiai konstruojant PSE yra naudojami ličio (ličio bis(trifluormetansulfonil)imido druska (LiTFSI)) ir kobalto (tris[2-(1*H*-pirazol-1-il)-4-*tret*-butilpiridin]kobalto (III) druska (FK209)) druskų bei 4-*tret*-butilpiridino (*t*BP) organiniai ir neorganiniai priedai[65-67] (žr. 3 pav). Atlikus mokslinius tyrimus buvo pastebėta, kad *t*BP naudojimas labai pagerina LiTFSI tirpumą, todėl suformuojamos homogeniškesnės skylių transportinio sluoksnio plėvelės[68]. Nors šie priedai pagerina Spiro-OMeTAD elektrines savybes, tačiau dėl jų higroskopiškumo ir jautrumo aplinkos sąlygoms prastėja PSE ilgalaikis stabilumas[69].

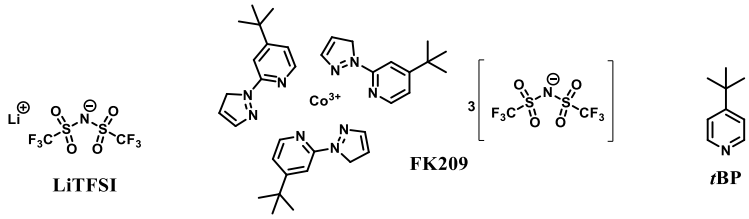

3 pav. Skylių transportiniam sluoksniui naudojamų legiruojančių priedų cheminės formulės

Vienas iš perspektyviausių polimerinių puslaidininkių yra poli[bis(4-fenil)(2,4,6-trimetilfenil)aminas] (PTAA) (žr. 4 pav.)[70-71]. Per pastaruosius metus buvo atlikta daugybė mokslinių tyrimų naudojant šį junginį *n-i-p* ir *p-i-n* konstrukcijų lanksčiuose ir didelio ploto PSE. PSE su polimeru PTAA efektyvumas 2013 m. siekė 12 %, o šiomis dienomis daugiau nei 23 %[72-73]. Vienas iš PTAA privalumų yra tai, jog *n-i-p* konfigūracijos PSE polimero sluoksnis gali būti nusodinamas naudojant žemos temperatūros apdorojimo procesą, kuris termiškai nepažeidžia perovskito[72,74]. Polimerinis puslaidininkis yra stabilus aplinkos sąlygoms, todėl jo gamybos procesas tampa lengvesnis[75]. PTAA pasižymi dideliu atsparumu mechaniniams įtempimams ir gali būti pritaikomas lanksčiuose PSE[76]. Šio polimero HOMO energetinis lygmuo apie -5,2 eV[77], todėl yra puikiai suderinamas su $MAPbI_3$ (-5,4 eV[78]) arba mišriu perovskitu (nuo -5,4 eV iki -5,7 eV[79]). Verta paminėti, kad polimerinis puslaidininkis pasižymi labai geromis elektrinėmis savybėmis, jo krūvininkų dreifinis judris lygus 4×10^{-3} cm^2/Vs[80]. Nors ši STM turi nemažai privalumų, jos komercinį pritaikymą smarkiai riboja didelė junginio kaina, kuri siekia daugiau nei 3000 Eur/g[81].

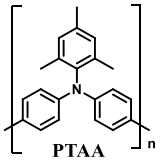

4 pav. Polimerinio puslaidininkio PTAA cheminė struktūra

Kitas invertuotoje PSE konfigūracijoje dažnai naudojamas polimerinis puslaidininkis yra poli(3,4-etilendioksitiofenas):poli(stireno sulfonatas) (PEDOT:PSS) (žr. 5 pav.). Grynas PEDOT turi geras elektrines savybes, tačiau jo tirpumas yra labai prastas. Norint tai pagerinti, jis yra maišomas su PSS. PEDOT:PSS pasižymi geromis plėvėdaros savybėmis. Plėvelė paprastai būna vienoda ir lygi[82], išsiskirianti dideliu skaidrumu regimosios šviesos diapazone, pvz., 100 nm storio PEDOT:PSS plėvelės pralaidumas prie 550 nm yra >90 %[83]. Krūvininkų dreifinis judris, priklausomai nuo polimero apdorojimo metodų ir priedų, gali svyruoti nuo 10^{-2} cm/Vs iki 10^{-3} cm/Vs[84]. Puslaidininkio jonizacijos potencialas – 5,0-5,2 eV. Stambiamolekulinis junginys pasižymi dideliu mechaniniu lankstumu, terminiu stabilumu ir mažais gamybos kaštais[85]. Pirmą kartą organinis puslaidininkis kaip STM *p-i-n* PSE buvo išbandytas 2016 metais. Tuo metu sukonstruoto elemento konversijos efektyvumas siekė 15,7 %, o šiomis dienomis optimizavus apdorojimo metodus ir sąlygas – daugiau nei 20 %[86].

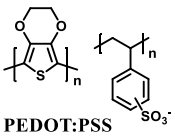

5 pav. Polimerinio puslaidininkio PEDOT:PSS cheminė struktūra

2.2.5. Skaidrūs elektrodai / katodai

Nors elektrodų medžiagos tiesiogiai nesiliečia su perovskito sluoksniu, tačiau jų stabilumas taip pat daro įtaką efektyviam PSE veikimui. Auksas (Au) arba sidabras (Ag) paprastai naudojami kaip galinis PSE elektrodas. Dažniausias nusodinimo būdas yra terminis garinimas kai gaunama plona metalinė plėvelė. Sidabro elektrodai paprastai linkę reaguoti su iš perovskito sluoksnio migruojančiu jodu ir sudaryti metalo jodidus ant elektrodo paviršiaus[87]. Dėl to akivaizdžiai keičiasi spalva ir gali prasidėti prietaiso degradacija[88]. Aukso elektrodai stabilesni, tačiau jų kaina yra daug didesnė nei Ag.

2.3. Molekulinė skylių transportinių medžiagų inžinerija perovskitiniams saulės elementams

Skyriuje 2.2.4. buvo aptarta, kad STM tam tikros savybės lemia jų pritaikymą efektyviuose ir stabiliuose PSE. Nors prieš daugelį metų susintetinti puslaidininkių etalonai vis dar yra naudojami konstruojant SE, tačiau mokslininkai nenuilsdami ieško naujų STM, kurios būtų stabilesnės, pasižymėtų geresnėmis puslaidininkinėmis ir fotovoltinėmis savybėmis, taip pat būtų pigios ir komerciškai lengvai prieinamos.

2.3.1. Fluoreno centrinį fragmentą turinčios skylių transportinės medžiagos

Šios disertacijos 3.1.–3.3. skyriuose yra nagrinėjamos autorės susintetintos ir ištirtos fluoreno centrinį fragmentą turinčios STM. Dėl šios priežasties organinių puslaidininkių inžinerijos literatūrinė apžvalga pradedama nuo efektyviuose PSE panaudotų molekulių su fluoreno centru.

Y. Huja kartu su bendraautoriais paskelbė apie dvi naujas **HT1** ir **HT2** fluoreno centrinį fragmentą turinčias STM (žr. 6 pav.). Naudojant pigias komercines pradines medžiagas lengvos dvipakopės sintezės metodu susintetinti organiniai puslaidininkiai, kurių suminė išeiga siekė net 90 %. Šie junginiai turi trimatę, panašią į Spiro-OMeTAD, struktūrą. **HT1** yra pusinė etalono molekulė, su 9-oje fluoreno padėtyje prijungtais metoksifenilradikalais. O **HT2** junginys yra Spiro-OMeTAD analogas, neturintis vieno ryšio tarp spirobifluoreno molekulės benzeno žiedų.

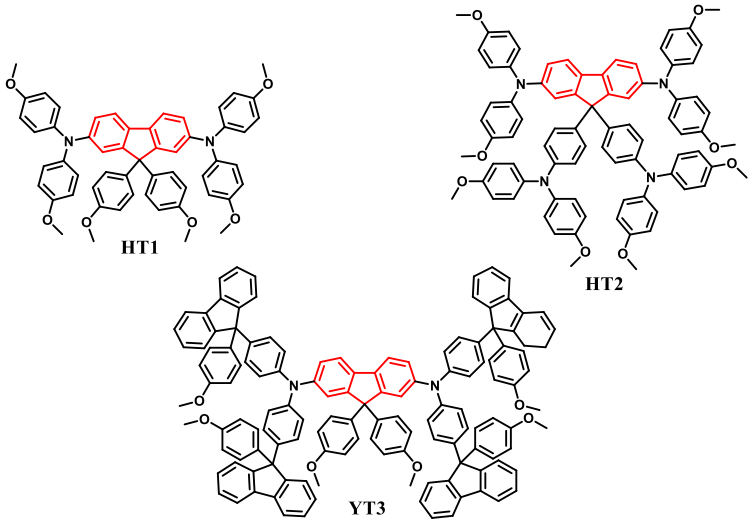

6 pav. Fluoreno centrinį fragmentą turinčių organinių molekulių **HT1**, **HT2** ir **YT3** cheminės struktūros

Junginiai pasižymėjo geru tirpumu įprastiniuose organiniuose tirpikliuose. **HT1** ir **HT2** turėjo geras elektrines savybes – šių puslaidininkių generuojamas skylių dreifinis judris atitinkamai buvo $1{,}12\times10^{-4}$ ir $1{,}01\times10^{-4}$ cm^2/Vs ir aplenkė Spiro-OMeTAD ($\mu_0=8{,}25\times10^{-5}$ cm^2/Vs[90]). Abu nauji organiniai puslaidininkiai buvo panaudoti konstruojant *n-i-p* konfigūracijos PSE su mišriu perovskitu – $(FAPbI_3)_{0,85}(MAPbBr_3)_{0,15}$. Saulės elementų optimizuoti fotovoltinių charakteristikų duomenys iš fotosrovės-įtampos (*J-V*) kreivių susisteminti ir pateikti 1 lentelėje. Puslaidininkio **HT2** pagrindu sukonstruoto įrenginio galios konversijos efektyvumas siekė 18,04 % ir buvo labai panašus į Spiro-OMeTAD (18,27 %). **HT1** atveju buvo užfiksuotas šiek tiek mažesnis efektyvumas (17,18 %). Atsižvelgus į gautus rezultatus galima teigti, kad junginys **HT2**, turintis didesnę molekulinę masę, užtikrina geresnes fotovoltines savybes ir gali būti efektyvi brangaus Spiro-OMeTAD alternatyva.

1 lentelė. Perovskitinių saulės elementų, kuriuose naudoti puslaidininkiai **HT1**, **HT2** ir **YT3**, fotovoltinės charakteristikos ir efektyvumai

STM	V_{OC}, V	J_{SC}, mA/cm^2	*FF*	STM PSE, %	Etalono PSE, %
HT1	1,12	21,91	0,70	17,18	18,27
HT2	1,11	22,26	0,73	18,04	18,27
YT3	1,13	23,25	0,77	20,23	19,18

D. Zhang kartu su bendraautoriais išleido mokslinį straipsnį[91], kuriame PSE su aprašytu organiniu puslaidininkiu **YT3** pasiekė rekordinį energijos konversijos efektyvumą. **YT3** centrinio fluoreno 9-oje padėtyje įvesti du metoksibenzeno žiedai,

o šoniniais fragmentais pasirinkti difenilaminai su fluoreno ir metoksibenzeno pakaitais (žr. 6 pav.).

Užrašius UV-RŠ sugerties spektrus buvo užfiksuoti puslaidininkio absorbcijos smailių maksimumai ties 379, 387 ir 400 nm. Junginys pasižymėjo silpna sugertimi regimojoje srityje, todėl nekonkuravo su perovskito sluoksniu dėl šviesos sugerties PSE. STM **YT3** nustatytas HOMO energetinis lygmuo (-5,21 eV) yra aukštesnis nei mišraus perovskito $(FAPbI_3)_{0,85}(MAPbBr_3)_{0,15}$ (-5,65 eV)[92-93], todėl buvo užtikrintas efektyvus skylių transportas. Organinio puslaidininkio dreifinis judris siekė $1,6\times10^{-4}$ cm^2/Vs vertę ir aplenkė Spiro-OMeTAD ($\mu_0=8,25\times10^{-5}$ cm^2/Vs).

Puslaidininkis **YT3** buvo panaudotas *n-i-p* architektūros PSE skyles transportuojančiame sluoksnyje. Prietaiso konstrukcija: FTO / kompaktiškas TiO_2 sluoksnis / mezoporinis TiO_2 / perovskitas – $(FAPbI_3)_{0,85}(MAPbBr_3)_{0,15}$ / STM / Au. Saulės elementų optimizuoti fotovoltinių charakteristikų duomenys iš fotosrovės-įtampos (*J-V*) kreivių susisteminti ir pateikti 1 lentelėje. PSE su puslaidininkiu **YT3** pasižymėjo rekordiniu efektyvumu, kuris siekė net 20,23 %, o įrenginio su Spiro-OMeTAD galios konversija buvo tik 19,18 %. Taip pat buvo ištirtas abiejų sukonstruotų PSE prietaisų stabilumas. Įrenginiai buvo neįkapsuliuoti, santykinė oro drėgmė 30–35 %. Po 600 valandų Spiro-OMeTAD pagrindu pagaminto PSE efektyvumas nukrito 13 %, o įrenginio su puslaidininkiu **YT3** atveju buvo matomas tik 5 % šviesos konversijos efektyvumo sumažėjimas. Stabilumo tyrimo rezultatai gali būti siejami su geresne STM morfologija – naujasis puslaidininkis tolygiau pasidengia ant perovskito paviršiaus, taip apsaugodamas jį nuo drėgmės poveikio. Taigi, apibendrinant rezultatus galima teigti, kad fluoreno, kaip šoninio fragmento, įtraukimas į molekulę turėjo teigiamos įtakos PSE efektyvumui ir stabilumui. **YT3** yra daugeliu aspektų pranašesnė STM už etalonu laikomą Spiro-OMeTAD ir turi dideles galimybes būti komercializuota.

W. Chen kartu su bendraautoriais aprašė dvi vienpakopės Suzuki kryžminio jungimo reakcijos metu gautas STM **FH-0** ir **FH-3**[94] (žr. 7 pav.). **FH-0** molekulė turi fluoreno centrą ir šoninius trifenilamino su metoksipakaitais fragmentus. **FH-3** puslaidininkio struktūra yra analogiška, tik fluoreno 9-oje padėtyje prijungtas alkilpakaitas.

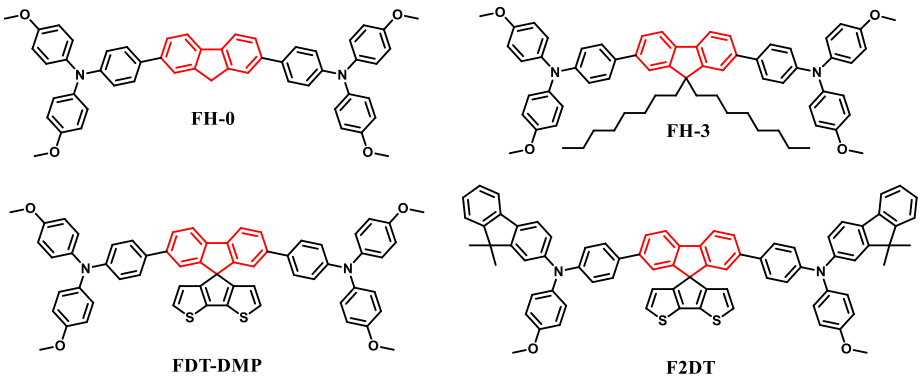

7 pav. Organinių puslaidininkių, turinčių fluoreno centrą, **FH-0**, **FH-3**, **FDT-DMP** ir **F2DT** cheminės struktūros

Atlikus medžiagų optinius tyrimus absorbcijos maksimumo smailės UV/RŠ spektruose buvo užfiksuotos ultravioletinės elektromagnetinės spinduliuotės srityje ties ~380 nm. Norint įvertinti medžiagų terminį stabilumą buvo atlikti termogravimetrinės analizės (TGA) tyrimai. Buvo nustatyta, kad organinis puslaidininkis **FH-0** 5 % savo masės svorio praranda ties 300 °C temperatūra, o jo analogas su alkilpakaitu – 400 °C temperatūroje. **FH-0** ir **FH-3** HOMO energetiniai lygmenys atitinkamai buvo -5,24 ir -5,26 eV. Junginių mobilumo vertės buvo panašios į Spiro-OMeTAD ir stipriame elektriniame lauke siekė $1{,}04\times10^{-4}$ (**FH-0**) ir $1{,}88\times10^{-4}$ cm^2/Vs (**FH-3**).

Darbe buvo atlikti molekulių struktūrų išsidėstymo erdvėje kompiuteriniai skaičiavimai. Tarp fluoreno centro ir molekulių galinių fragmentų buvo pastebėti dideli sukimosi kampai (~35°), o tai reiškia, kad molekulės pasižymi neplokštumine geometrija. Tai užtikrina glaudžius molekulių susipakavimo procesus kietoje būsenoje ir STM plėvelių susidarymą esant mažai kristalizacijai[95-96].

Organiniai puslaidininkiai buvo panaudoti *n-i-p* architektūros PSE skyles transportuojančiame sluoksnyje. Prietaiso konstrukcija: FTO / kompaktiškas TiO_2 sluoksnis / mezoporinis TiO_2 / perovskitas – $(FAPbI_3)_{0,85}(MAPbI_3)_{0,15}$ / STM / Au. Naudojant skenuojamąją elektroninę mikroskopiją buvo nustatyta **FH-0**, **FH-3** ir Spiro-OMeTAD plėvelių kokybė. PSE su naujomis STM geriausi efektyvumo rezultatai gauti, kai plėvelių storis buvo 200 nm, o tai yra daug plonesnis sluoksnis nei efektyviai veikiančio įrenginio su Spiro-OMeTAD (~300 nm). Saulės elementų optimizuoti fotovoltinių charakteristikų duomenys iš fotosrovės-įtampos (*J-V*) kreivių susisteminti ir pateikti 2 lentelėje. PSE su puslaidininkiu **FH-0** pasižymėjo sąlyginai nedideliu efektyvumu, kuris siekė 14,9 %. O SE, pagaminto naudojant junginį su alkilpakaitu **FH-3**, konversijos efektyvumas buvo daug geresnis (18,4 %). Jis gali būti lyginamas su prietaisu, kuriame kaip STM naudojamas etalonas Spiro-OMeTAD (19,6 %). Taigi, galima padaryti išvadą, kad alifatinio pakaito įterpimas į molekulę turėjo teigiamos įtakos medžiagos elektrinėms ir fotovoltinėms savybėms.

2 lentelė. Perovskitinių saulės elementų, kuriuose naudoti puslaidininkiai **FH-0**, **FH-3**, **FDT-DMP** ir **F2DT**, fotovoltinės charakteristikos ir efektyvumai

STM	V_{OC}, V	J_{SC}, mA/cm^2	*FF*	STM PSE, %	Etalono PSE, %
FH-0	0,99	19,50	0,77	14,9	19,6
FH-3	1,07	22,10	0,78	18,4	19,6
FDT-DMP	0,97	22,40	0,56	12,3	–
F2DT	1,08	23,60	0,70	18,0	–

R. D. Gayathri kartu su bendraautoriais pristatė dvi naujas STM[97]. **FDT-DMP** yra puslaidininkio **FH-0** analogas su ditiofeno fragmentu fluoreno centre, o su tokiu pačiu centru junginyje **F2DT** šoninis metoksifenilžiedas pakeistas metilfluorenu (žr. 7 pav.).

Buvo užrašyti naujų organinių puslaidininkių ultravioletinės ir regimosios šviesos spinduliuotės sugerties spektrai (UV-RŠ). **FDT-DMP** absorbcijos maksimumo smailė fiksuota ties 380 nm. Dėl papildomų fluoreno fragmentų molekulės galuose susidarė didesnė π konjuguotoji sistema, todėl junginys **F2DT** pasižymėjo batochrominiu poslinkiu ties 460 nm. Šoninių fluoreno fragmentų prijungimas į molekulę taip pat padidino terminį junginio stabilumą, t. y. **F2DT** skilimo temperatūra buvo 433 °C, o **FDT-DMP** – 414 °C. Iš diferencinės skenuojamosios kalorimetrijos (DSK) analizės rezultatų matyti, kad organiniai puslaidininkiai **FDT-DMP** ir **F2DT** egzistuoja amorfinės būsenos. Jų stiklėjimo temperatūros atitinkamai yra 148 ir 157 °C. Buvo įvertintos STM elektrinės savybės ir nustatyta, kad **FDT-DMP** ir **F2DT** jonizacijos potencialai lygūs 4,93 ir 5,02 eV. Puslaidininkių mobilumo reikšmės stipriame elektriniame lauke atitinkamai siekė $8{,}08\times10^{-5}$ ir $1{,}3\times10^{-4}$ cm^2/Vs.

Nauji puslaidininkiai buvo panaudoti formuojant PSE *n-i-p* konstrukciją. Prietaiso konstrukcija: FTO / kompaktiškas TiO_2 sluoksnis / mezoporinis TiO_2 / perovskitas – $FAPbI_3$ / STM / Au. SE fotovoltinės charakteristikos pateiktos 2 lentelėje. Geriausiu efektyvumu pasižymėjo PSE, kuriame kaip skylių transportinis sluoksnis naudotas puslaidininkis **F2DT**. Pastarojo įrenginio šviesos konversijos efektyvumas siekė 18,0 %. Deja, elementas su mažamolekuliniu junginiu **FDT-DMP** nepasižymėjo geru efektyvumu (12,3 %). Tai galėjo būti dėl mažos užpildymo faktoriaus reikšmės. Taip pat buvo ištirtas **F2DT** pagrindu sukonstruoto PSE stabilumas. Įrenginys buvo neįkapsuliuotas, santykinė oro drėgmė 40 %. Eksperimentas vykdytas 300 valandų 25 °C temperatūroje. Buvo nustatyta, kad įrenginys išlaikė 80 % savo pradinio konversijos efektyvumo.

A. Jegorovė kartu su bendraautoriais paskelbė apie tris naujas fluoreno centrinį fragmentą su skirtingais alkilpakaitais turinčias STM[98]. Kaip šoniniai fragmentai pasirinkti etilkarbazolo chromoforai (žr. 8 pav.). Organiniai puslaidininkiai gauti naudojant komerciškai prieinamas pradines medžiagas Buchwaldo kryžminio sujungimo reakcijos metu.

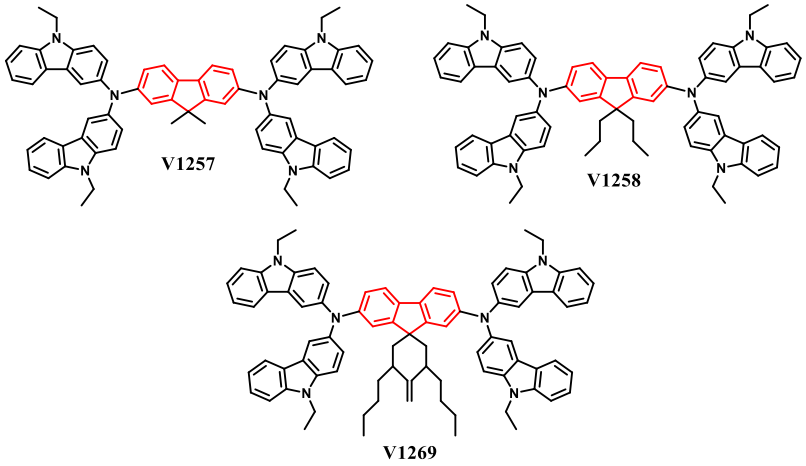

8 pav. Fluoreno centrinį fragmentą turinčių organinių molekulių **V1257**, **V1258** ir **V1269** cheminės struktūros

Terminiam medžiagų stabilumui įvertinti buvo atlikta TGA, kuri parodė, kad visos medžiagos 5 % savo masės svorio praranda aukštesnėje nei 450 °C temperatūroje ir yra pakankamai stabilios. Taip pat labai svarbu, kad atlikus DSK tyrimus buvo nustatyta, jog visi trys organiniai puslaidininkiai egzistuoja amorfinės būsenos. Buvo pastebėta tendencija, kad ilgesnių alifatinių pakaitų įterpimas į molekulę sumažino stiklėjimo temperatūras. Junginių **V1257**, **V1258** ir **V1269** T_g atitinkamai lygios 196, 183 ir 127 °C.

Išmatuoti organinių puslaidininkių jonizacijos potencialai buvo labai panašūs – 4,85; 4,85 ir 4,96 eV. Junginių **V1257**, **V1258** ir **V1269** mobilumo vertės silpname elektriniame lauke atitinkamai siekė $3{,}6\times10^{-5}$, $1{,}2\times10^{-5}$ ir 3×10^{-5} cm^2/Vs.

Panaudojus junginius skylių transportiniam sluoksniui, buvo sukonstruoti *n-i-p* struktūros prototipiniai PSE. Konstrukciją sudarantys sluoksniai: FTO / kompaktiškas TiO_2 sluoksnis / mezoporinis TiO_2 / perovskitas – $[(FAPbI_3)_{0,87}(MAPbBr_3)_{0,13}]_{0,92}(CsPbI_3)_{0,08}$ / STM / Au. Fotovoltinės charakteristikos susistemintos 3 lentelėje.

3 lentelė. Perovskitinių saulės elementų, kuriuose naudoti puslaidininkiai **V1257**, **V1258** ir **V1269**, fotovoltinės charakteristikos ir efektyvumai

STM	V_{OC}, V	J_{SC}, mA/cm^2	*FF*	STM PSE, %	Etalono PSE, %
V1257	1,03	23,37	0,71	17,2	20,1
V1258	1,05	23,32	0,73	17,8	20,1
V1269	1,05	23,35	0,74	18,1	20,1

Pastebėta, kad ilgesnis alkilpakaitas neturi įtakos prietaisų trumpojo jungimo srovės tankio vertėms. Tačiau pastebima tendencija, kad ilgėjant alifatinei grandinėlei didėja užpildymo faktorius, dėl to didėja SE prietaiso našumas. Geriausi energijos konversijos efektyvumo rezultatai – 18,1 % – buvo PSE su puslaidininkiu **V1269**. Jo

efektyvumas tik 2 % nusileido etaloniniam prietaisui, todėl pastarasis puslaidininkis galėtų būti alternatyva brangiam Spiro-OMeTAD.

2.3.2. Spirobisindano centrinį fragmentą turinčios skylių transportinės medžiagos

Šios disertacijos 3.4. skyriuje yra nagrinėjamos autorės susintetintos ir ištirtos spirobisindano centrinį fragmentą turinčios STM, todėl toliau literatūrinėje apžvalgoje aptariamos molekulės su spirobisindano centru.

X. Wang kartu su bendraautoriais pateikė naują Spiro-I organininį puslaidininkį[99]. Sumažinus Spiro centrinio fragmento simetriją, buvo susintetinta spirobisindano centrą ir karbazolo bei difenilamino chromoforus turinti STM (žr. 9 pav.). Mažamolekulinis junginys buvo gautas per kelias reakcijų stadijas iš pigaus komercinio pradinio reagento bisfenolio A. Apskaičiuotos Spiro-I gamybos sąnaudos yra tik ¼ galutinės Spiro-OMeTAD kainos.

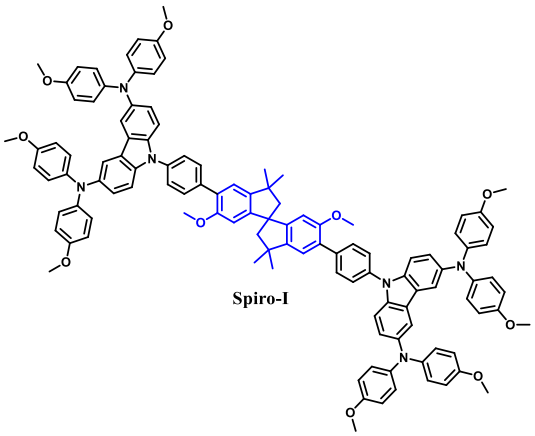

9 pav. Spirobisindano centrinį fragmentą turinčios organinės molekulės **Spiro-I** cheminė struktūra

Užrašius UV/RŠ spinduliuotės sugerties spektrus buvo nustatyta, kad junginio absorbcijos maksimumas yra ties 307 nm. Atlikus junginio **Spiro-I** DSK analizę nebuvo aptikta jokių kristalizacijos virsmų, priešingai nei etalono atveju. Galima teigti, kad spirobifluoreno centrinio fragmento modifikavimas į spirobisindaną turėjo teigiamos įtakos medžiagos amorfiškumui. Junginio jonizacijos potencialas buvo 5,2 eV, ir tai yra šiek tiek mažesnė vertė nei Spiro-OMeTAD (5,22 eV)[100].

Junginių **Spiro-I** ir Spiro-OMeTAD plėvelių morfologijai nustatyti buvo atlikti mikroskopijos tyrimai. Be legiruojančių priedų (*t*-BP ir Li-TFSI) abiejų organinių puslaidininkių plėvelės pasižymėjo lygiu paviršiumi, tačiau po priedų įdėjimo atsirado morfologijos skirtumų – **Spiro-I** plėvelė vis dar išlaikė lygų paviršių, o Spiro-OMeTAD atveju atsirado daug netolygumų, kurie išsivysto dėl medžiagos gebėjimo kristalintis[101-102].

Tiek **Spiro-I**, tiek etalonas buvo panaudoti kaip STM konstruojant *n-i-p* konfigūracijos PSE. Prietaiso konstrukciją sudarantys sluoksniai: FTO / TiO_2 / perovskitas – $[(FAPbI_3)_{0,87}(MAPbBr_3)_{0,13}]_{0,92}(CsPbI_3)_{0,08}$ / STM / Au. Visos

fotovoltinės charakteristikos pateiktos 4 lentelėje. PSE su puslaidininkiu **Spiro-I** pasižymėjo dideliu energijos konversijos efektyvumu (18,57 %), kuris nedaug nusileido įrenginio su Spiro-OMeTAD efektyvumui (19,17 %). Svarbu pažymėti, kad buvo optimizuotos medžiagų koncentracijos ir plėvelių storiai. Nustatyta, jog naujo organinio puslaidininkio optimali koncentracija (20 mg/ml) ir plėvelės storis (60 nm) yra daug mažesni nei etalono Spiro-OMeTAD (90 mg/ml ir 200 nm), o tai reiškia daug mažesnes STM sąnaudas.

4 lentelė. Perovskitinio saulės elemento, kuriame naudotas puslaidininkis **Spiro-I**, fotovoltinės charakteristikos ir efektyvumai

STM	V_{OC}, V	J_{SC}, mA/cm^2	*FF*	STM PSE, %	Etalono PSE, %
Spiro-I	1,06	24,68	0,71	18,57	19,17

Sukonstravus prietaisus buvo tirtas jų ilgalaikis terminis stabilumas. Po 2400 val. PSE su **Spiro-I** išlaikė net 80 % pradinio savo efektyvumo, o įrenginio su Spiro-OMeTAD konversijos našumas nukrito iki 27 % pradinio efektyvumo. Dėl visų išvardintų **Spiro-I** privalumų galima teigti, kad spirobisindano centrinis fragmentas gali būti naudojamas kaip amorfinių STM karkasas efektyviems ir stabiliems PSE gauti.

2.3.3. Karbazolo chromoforus turinčios skylių transportinės medžiagos

Šios disertacijos 3.5. skyrelyje yra nagrinėjamos autorės susintetintos ir ištirtos karbazolo chromoforus turinčios STM. Dėl karbazolo darinių tinkamų elektrinių savybių, lengvo modifikavimo, terminio ir cheminio stabilumo bei pigumo šios klasės organinių puslaidininkių yra labai daug, todėl šioje literatūros apžvalgos dalyje yra aptariamos tik į autorės junginius labai panašių struktūrų molekulės[103-104].

P. Gratia kartu su kolegomis aprašė mažamolekulinį junginį **V886**, kurio struktūra susideda iš dviejų 4,4ˈ-dimetoksidifenilaminu 3,6-dipakeisto karbazolo fragmentų, sujungtų benzeno žiedu (žr. 10 pav.)[105]. STM buvo susintetinta dviejų etapų sintezės metu iš komerciškai prieinamų ir sąlyginai nebrangių pradinių reagentų.

Atlikti DSK ir TGA tyrimai parodė, kad medžiaga **V886** yra amorfinės būsenos ir pasižymi geru terminiu stabilumu. Užfiksuota junginio stiklėjimo temperatūra 141 ^oC. Pastaroji yra didesnė nei Spiro-OMeTAD (125 ^oC[106]), todėl naujas organinis puslaidininkis demonstruoja stabilesnę amorfinę būseną. Organinis puslaidininkis 5 % savo masės svorio praranda ties 390 ^oC temperatūra. Junginio **V886** jonizacijos potencialas buvo 5,04 eV, o krūvininkų dreifinis judris silpname elektriniame lauke siekė 2×10^{-5} cm^2/Vs.

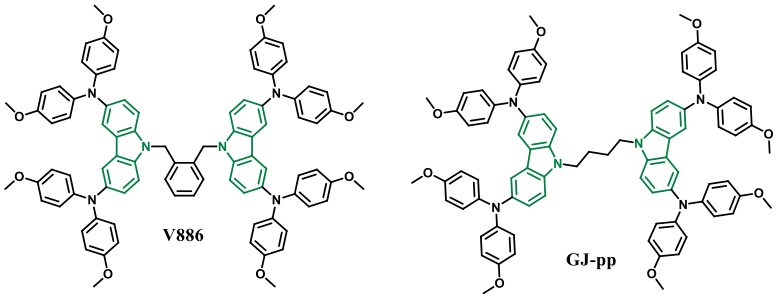

10 pav. Karbazolo chromoforus turinčių organinių molekulių **V886** ir **GJ-pp** cheminės struktūros

V886 pasižymėjo labai geru tirpumu organiniuose tirpikliuose, tokiuose kaip THF ir chlorbenzenas (> 100 mg/ml). Tai labai svarbi savybė konstruojant PSE. Junginį panaudojus skylių transportiniame sluoksnyje buvo sukonstruotas *n-i-p* struktūros prototipinis PSE. Konstrukciją sudarantys sluoksniai: FTO / kompaktiškas TiO_2 sluoksnis / mezoporinis TiO_2 / perovskitas – $MAPbI_3$ / STM / Au. Fotovoltinės charakteristikos pateiktos 5 lentelėje. Įrenginio su **V886** konversijos efektyvumas siekė beveik 17 %. Tuo metu tai buvo rekordinis našumo rezultatas tarp ne spiro klasės junginių. Organinis puslaidininkis buvo užpatentuotas ir komercializuotas tarptautinėje kompanijoje „Tokyo Chemical Industry Co, Ltd. (TCI)“.

5 lentelė. Perovskitinių saulės elementų, kuriuose naudoti puslaidininkiai **V886** ir **GJ-pp**, fotovoltinės charakteristikos ir efektyvumai

STM	V_{OC}, V	J_{SC}, mA/cm^2	*FF*	STM PSE, %	Etalono PSE, %
V886	1,09	21,38	0,73	16,91	18,36
GJ-pp	1,02	23,22	0,73	17,23	17,96

W.-J. Gao kartu su bendraautoriais supažindino su nauju ir PSE efektyviai veikiančiu organiniu puslaidininkiu **GJ-pp** (žr. 10 pav.)[107]. Pastarasis yra **V886** analogas, kurio molekulėje karbazolo chromoforai, sujungti ne konjuguotu benzeno žiedu, o butilpakaitu. Autoriai teigia, kad naujosios STM sintezė yra paprasta, o gryninimo būdai lengvi. Buvo apskaičiuota, kad **GJ-pp** laboratorinės sintezės kaina yra ~ 40 Eur/g ir sudaro tik 29 % bendros Spiro-OMeTAD kainos.

Karbazolo dariniai dėl savo terminio ir cheminio stabilumo yra gerai žinomi kaip STM, efektyviai pritaikomos PSE[108]. Junginys **GJ-pp** 5 % savo masės svorio praranda ties 426 ºC temperatūra. Puslaidininkis pasižymi stabilia amorfine būsena (T_g = 122 ºC). Atlikus naujo puslaidininkio optinius tyrimus buvo užfiksuotas didelis Stokso poslinkis (126 nm), o tai reiškia, kad sužadinimo būsenoje galima tikėtis reikšmingų molekulės konformacijų. **GJ-pp** nustatytas HOMO energetinis lygmuo yra -5,19 eV. Pastarasis efektyvaus krūvio transporto užtikrinimui tinkamai suderintas su perovskito $MAIPbI_3$ HOMO lygmeniu (-5,43 eV[109]). Organinio puslaidininkio

krūvininkų dreifinis judris (μ_0=1,22×10^{-5} cm^2/Vs) buvo labai artimas Spiro-OMeTAD vertei (μ_0=2,68×10^{-5} cm^2/Vs).

Mažamolekulinis junginys **GJ-pp** buvo išbandytas kaip STM *n-i-p* konstrukcijos PSE. Įrenginio struktūra: FTO / SnO_2 / perovskitas – $MAPbI_3$ / STM / Au. PSE, pagamintas naudojant **GJ-pp**, pasižymėjo dideliu konversijos efektyvumu (17,23 %) ir gali būti lyginamas su prietaisu, kuriame kaip STM yra etalonas Spiro-OMeTAD (17,96 %). Sukonstruotų prietaisų ilgalaikio terminio stabilumo tyrimai buvo atliekami 85 ^{o}C temperatūroje. Įrenginiai buvo neįkapsuliuoti ir laikyti Ar atmosferoje 240 val. Spiro-OMeTAD pagrindu sukonstruoto PSE efektyvumas sumažėjo ~50 %. O įrenginys su puslaidininkiu **GJ-pp** yra daug stabilesnis, nes matomas 19 % galios konversijos efektyvumo sumažėjimas. Galima teigti, kad aromatiniai arba alifatiniai pakaitai yra perspektyvūs centriniai fragmentai karbazolo chromoforams sujungti.

L. Gao su kolegomis paskelbė apie dvi naujas karbazolo chromoforus turinčias STM (žr. 11 pav.)[110]. Organinis puslaidininkis **EH44** turi centrinį karbazolo fragmentą su 2-oje ir 7-oje padėtyse prijungtais dimetoksidifenilamino pakaitais. **EtCz-3EHCz** yra pastarojo analogas, turintis didesnę konjuguotą sistemą – tris karbazolo chromoforus. Junginiuose skiriasi alifatiniai pakaitai ir jų kiekis. Buvo apskaičiuota, kad šių mažamolekulinių junginių sintezės kaina sudaro $^1/_5$ bendros Spiro-OMeTAD kainos.

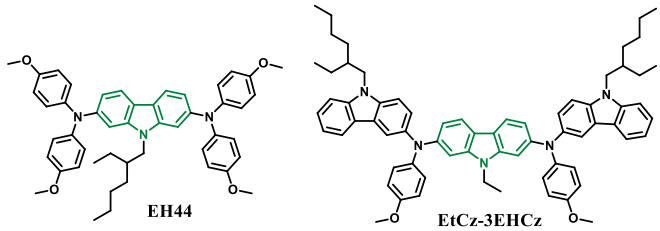

11 pav. Karbazolo chromoforus turinčių organinių molekulių **EH44** ir **EtCz-3EHCz** cheminės struktūros

DSK analizės metodu buvo nustatytos **EH44** ir **EtCz-3EHCz** junginių stiklėjimo temperatūros, kurios atitinkamai lygios 88 ir 98 ^{o}C. Abiejų puslaidininkių nustatytas jonizacijos potencialas buvo 5,4 ir 4,9 eV. Deja, bet mažamolekulinio junginio **EH44** stiklėjimo temperatūra yra per žema, o jonizacijos potencialo vertė per aukšta, kad jis galėtų būti pritaikytas efektyviuose PSE. Dėl šios priežasties tik organinis puslaidininkis **EtCz-3EHCz** buvo panaudotas konstruojant *n-i-p* konfigūracijos su priedais PSE. Konstrukciją sudarantys sluoksniai: FTO / kompaktiškas TiO_2 sluoksnis / mezoporinis TiO_2 / perovskitas – $Cs_{0,05}(MA_{0,13}FA_{0,87})_{0,95}Pb(I_{0,83}Br_{0,17})_3$ / STM / Au.

6 lentelė. Perovskitinio saulės elemento, kuriame naudotas puslaidininkis **EtCz-3EHCz**, fotovoltinės charakteristikos ir efektyvumai

STM	V_{OC}, V	J_{SC}, mA/cm^2	*FF*	STM PSE, %	Etalono PSE, %
EtCz-3EHCz	1,06	22,00	0,72	17,37	18,57

Nors įrenginio su junginiu **EtCz-3EHCz** efektyvumas (17,37 %) šiek tiek nusileidžia etalono prietaiso našumui (18,57 %), jis yra pigi alternatyva kaip STM PSE.

Toliau modifikuojant karbazolo chromoforus turinčius junginius galima pasiekti daug žadančių efektyvumo, stabilumo ir komercializavimo rezultatų PSE gamybos technologijose.

2.3.4. Polimerinės skylių transportinės medžiagos

Autorės disertacijoje 3.6. ir 3.7. skyriuose yra aprašomi naujai susintetinti polimerintis galintys organiniai puslaidininkiai. Junginiai buvo panaudoti *n-i-p* arba *p-i-n* konstrukcijų PSE kaip STM arba tarpsluoksnis tarp perovskito ir STM. Literatūrinės dalies apžvalga baigiama aukštus efektyvumo rezultatus PSE pasiekusiomis besipolimerinančiomis molekulėmis.

Y. Zhang ir kt. paskelbė apie tris naujas polimerintis galinčias STM (žr. 12 pav.)[111]. Organiniai puslaidininkiai turi fluoreno centrą, prie kurio aromatinių arba alifatinių pakaitų prijungtos vinilgrupės. Kaip fluoreno šoniniai fragmentai pasirinkti difenilaminai su metoksi- arba metilpakaitais.

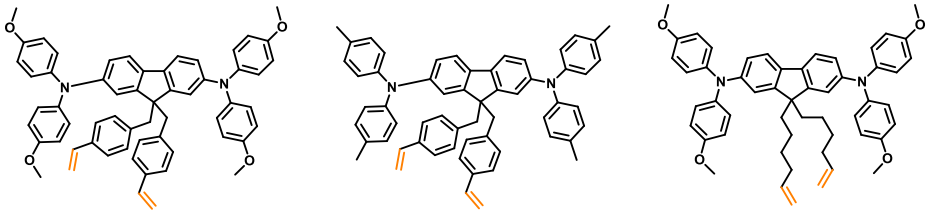

12 pav. Vinilgrupes turinčių organinių molekulių **VB-MeO-FDPA**, **VB-Me-FDPA** ir **DH-MeO-FDPA** cheminės struktūros

Visų STM polimerizacija vykdyta 160 ºC temperatūroje. Terminio proceso metu vyksta polimerizacijos reakcija tarp vinilo grupių, ir susidaro netirpus 3D struktūros polimerinis tinklas. Ši polimerizacija nereikalauja jokių papildomų priedų ar iniciatorių, kurie galėtų pakenkti PSE efektyvumui ir stabilumui. Po polimerizacijos **VB-MeO-FDPA**, **VB-Me-FDPA** ir **DH-MeO-FDPA** medžiagų mobilumo vertės padidėjo ir buvo lygios 3×10^{-4} cm^2/Vs, $1{,}4\times10^{-4}$ cm^2/Vs ir 5×10^{-5} cm^2/Vs. Pastebima tendencija, kad geresnes elektrines savybes turi junginiai, kuriuose vinilo grupė prijungta per aromatinį pakaitą.

Visi organiniai puslaidininkiai panaudoti *p-i-n* konstrukcijos PSE. Elemento struktūra: ITO / STM / perovskitas – $MAPbI_{3-x}Cl_x$ / C_{60} / Ag.

7 lentelė. Perovskitinių saulės elementų, kuriuose naudoti polimeriniai puslaidininkiai, fotovoltinės charakteristikos ir efektyvumai

STM	V_{OC}, V	J_{SC}, mA/cm^2	*FF*	STM PSE, %	Etalono PSE, %
VB-MeO-FDPA	1,15	20,89	0,78	18,7	13,7
VB-Me-FDPA	1,16	20,17	0,77	17,9	13,7
DH-MeO-FDPA	1,09	19,54	0,75	15,9	13,7

PSE su etaloniniu polimeru PEDOT:PSS efektyvumas buvo tik 13,17 %, o įrenginio su **VB-MeO-FDPA** konversijos našumas buvo rekordinis ir siekė net 18,7 %. PSE su **VB-Me-FDPA** ir **DH-MeO-FDPA** efektyvumas buvo 17,9 ir 15,9 %. Taip pat buvo atlikti **VB-MeO-FDPA** ir PEDOT:PSS pagrindu pagamintų prietaisų ilgalaikiai terminio stabilumo tyrimai. Po 200 val. etalono įrenginio efektyvumas nukrito iki 46 % pradinės savo našumo vertės, o PSE su nauju puslaidininkiu išlaikė 85 % pradinio efektyvumo. Akivaizdu, kad naujos polimerinės medžiagos pagerino prietaisų efektyvumus, stabilumus ir smarkiai sumažino įrenginių histerizę.

C. Zhang ir kt. paskelbė apie STM, turinčią karbazolo chromoforą ir vinilo grupes (žr. 13 pav.)[112]. Pastaroji buvo panaudota *p-i-n* konstrukcijos PSE, kurio efektyvumas buvo rekordinis – 23,9 %.

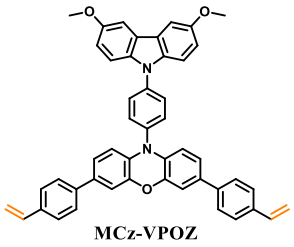

13 pav. Tinklintis galinčios organinės molekulės **MCz-VPOZ** cheminė struktūra

Atlikus DSK analizę buvo nustatyta, kad 150 °C temperatūroje lengvai vyksta junginio kryžminių ryšių susidarymas ir gaunamas trimatis polimeras. TGA tyrimas parodė, kad polimeras yra stabilus net iki 465 °C. **MCz-VPOZ** užfiksuotas aukštas skylininkų dreifinis judris (μ_0=5,2×10^{-4} cm^2/Vs), kuris buvo viena eile aukštesnis nei etalono PTAA (μ_0=2,03×10^{-5} cm^2/Vs).

Naujas polimerinis puslaidininkis buvo panaudotas invertuotos konstrukcijos PSE. Konstrukciją sudaro: ITO / STM / perovskitas – $(FA_{0,17}MA_{0,94}PbI_{3,11})_{0,95}(PbCl_2)_{0,05}$ / C_{60} / Ag. Dėl didelių energijos nuostolių, kuriuos dažniausiai lemia STM optoelektroninės savybės, ir dėl prastesnės sąsajos su perovskitu invertuotos konstrukcijos SE galios konversijos efektyvumas retai viršydavo 23 %[113-114]. Tačiau kaip STM panaudojus polimerą **MCz-VPOZ** buvo pasiekti rekordiniai efektyvumo rezultatai (23,9 %). Tuo metu tai buvo didžiausias elementų, kuriuose naudotas ne etalonas PTAA, energijos konversijos efektyvumas.

8 lentelė. Perovskitinio saulės elemento, kuriame naudotas polimerinis puslaidininkis **MCz-VPOZ**, fotovoltinės charakteristikos ir efektyvumai

STM	V_{OC}, V	J_{SC}, mA/cm^2	*FF*	STM PSE, %	Etalono PSE, %
MCz-VPOZ	1,17	24,15	0,84	23,9	20,9

Atliekant prietaisų ilgalaikio stabilumo testus įrenginiai buvo neįkapsuliuoti ir nuolatos apšviečiami LED (400–800 nm) lempa. Įrenginys su 3D polimeru **MCz-VPOZ** po 560 val. išlaikė 91 % pradinio savo efektyvumo, o elementas su PTAA – tik 70 %. **MCz-VPOZ** daugeliu aspektų pranašesnis nei PTAA, todėl lengvai galėtų būti pritaikomas PSE komercinėje rinkoje.

Literatūroje [115] pristatoma STM, kurios centrinio fragmento fluoreno 9-oje padėtyje yra prijungti trifenilaminai su polimerintis galinčiomis vinilgrupėmis (žr. 14 pav.). Šis organinis puslaidininkis buvo panaudotas efektyviuose *n-i-p* konstrukcijos PSE.

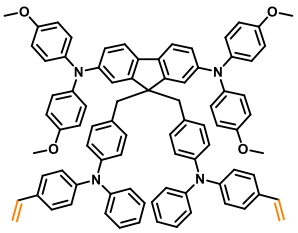

14 pav. Vinilgrupes turinčios organinės molekulės **V-TPAFDPA** cheminė struktūra

Atlikus DSK analizę buvo nustatyta **V-TPAFDPA** polimerizacijos temperatūra. Pirmojo kaitinimo metu užfiksuota, jog monomeras polimerinasi 200–240 ^{o}C temperatūroje. Antrojo kaitinimo metu jokių virsmų nepastebėta, todėl galima teigti, kad polimerizacijos procesas iki galo įvyko pirmo kaitinimo metu. Norint panaudoti organinį puslaidininkį *n-i-p* konstrukcijos PSE reikėjo sumažinti kryžminio susijungimo temperatūrą iki 150 ^{o}C, kurią gali toleruoti perovskitas. Dėl šios priežasties buvo atlikta organinio puslaidininkio **V-TPAFDPA** ir mažos molekulės pentaeritritolio tetrakis(3-merkaptopropionato) (PETMP) kopolimerizacijos reakcija (žr. 15 pav.). Esant švelnioms reakcijos sąlygoms, be papildomų iniciatorių merkaptogrupėms reaguojant su vinilo grupėmis susidaro 3D struktūros tinklas. DSK analizė parodė, kad kopolimerizacija įvyko 100–120 ^{o}C temperatūroje. Po plėvelių atkaitinimo iš polimerų tirpalų užrašius UV/RŠ sugerties spektrus buvo nustatyta, kad kaitinant 200 ^{o}C temperatūroje 30 min. susidaro 80 %, o 240 ^{o}C – 95 % **V-TPAFDPA** polimero. **V-TPAFDPA**/PETMP kopolimero 95 % susidarymo laipsnis gautas kaitinant 100 ^{o}C temperatūroje.

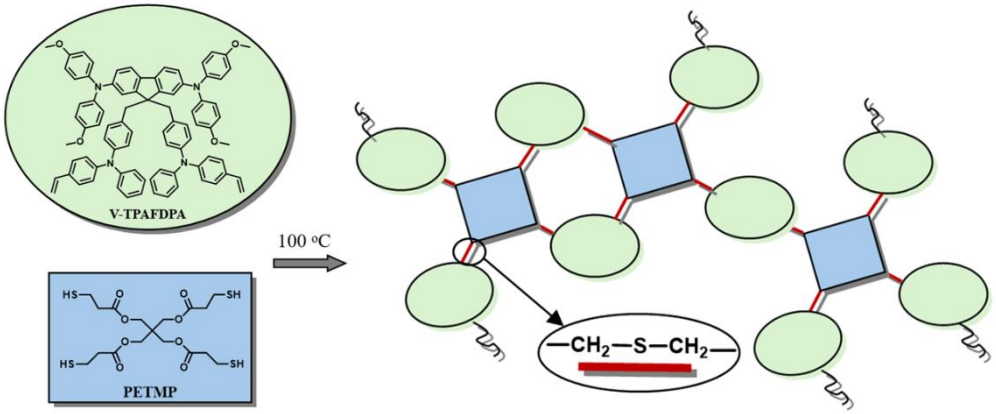

15 pav. Principinė **V-TPAFDPA** ir PETMP kopolimero susidarymo schema

Kadangi skersiniais ryšiais susietos polimerinės medžiagos pasižymi idealiu šviesos, šilumos ir mechaniniu stabilumu bei puikiu atsparumu organiniams tirpikliams, manoma, kad jos apsaugotų perovskitinį sluoksnį nuo drėgmės, taip išsaugant PSE efektyvumą ir stabilumą[116-117]. Nors dėl geresnių prietaisų stabilumo rezultatų polimerinės STM, pakeičiančios legiruotą Spiro-OMeTAD, sulaukia vis didesnio susidomėjimo, jų pagrindu sukonstruotų prietaisų efektyvumas vis dar yra šiek tiek mažesnis nei naudojant etaloną[118-119]. Vis labiau populiarėja nauja strategija, polimerinė STM yra naudojama kaip tarpsluoksnis tarp perovskito ir Spiro-OMeTAD, taip išlaikant ilgalaikį prietaiso stabilumą. **V-TPAFDPA** ir PETMP kopolimeras panaudotas kaip tarpsluoksnis *n-i-p* konstrukcijos PSE. Konstrukciją sudaro: FTO / kompaktiškas TiO_2 sluoksnis / mezoporinis TiO_2 / perovskitas – $Cs_{0,05}(FA_{0,83}MA_{0,17})_{0,95}Pb(I_{0,83}Br_{0,17})_3$ / **V-TPAFDPA**+PETMP (kopolimeras) / Spiro-OMeTAD / Au. Sukonstruoto elemento su tarpsluoksniu efektyvumas siekė 21,19 % ir pralenkė palyginamojo elemento be tarpsluoksnio konversijos efektyvumą (20,18 %).

9 lentelė. Perovskitinio saulės elemento, kuriame naudotas vinilgrupes turintis puslaidininkis **V-TPAFDPA**, fotovoltinės charakteristikos ir efektyvumai

STM	V_{OC}, V	J_{SC}, mA/cm^2	*FF*	STM PSE, %	Etalono PSE, %
V-TPAFDPA	1,13	23,9	0,79	21,19	20,18

Akivaizdu, kad **V-TPAFDPA** ir PETMP kopolimeras apsaugojo perovskitą nuo drėgmės, todėl PSE pasižymėjo daug geresniu stabilumu (86 % pradinio efektyvumo) nei elementas be tarpsluoksnio (69 % pradinio efektyvumo). Stabilumo tyrimas buvo vykdytas 1032 valandas esant 40–60 % santykinei drėgmei ir 60 °C temperatūrai. Galima teigti, kad ši polimerinio tarpsluoksnio įterpimo technologija yra labai perspektyvi norint pasiekti gerus efektyvumo ir stabilumo rezultatus.

2.4. Mokslinės literatūrinės dalies apibendrinimas

Per pastarąjį dešimtmetį kuriant naujos kartos SE didelio susidomėjimo objektu tapo PSE, kurių efektyvumas jau viršijo 26 %. Palyginti su komerciniais silicio SE, šie elementai pasižymi konstrukcijos paprastumu bei pigiomis žaliavomis. Žinomos kompanijos intensyviai darbuojasi optimizuojant SE. Konstruojant PSE išbandomi žinomi puslaidininkiai bei kuriamos ir patentuojamos naujos STM. Nors per pastaruosius metus PSE pasiekė rekordinius efektyvumus, jų komercializavimui yra keletas kliūčių. Visų pirma, skylių transportui *n-i-p* konstrukcijos prietaisuose dažniausiai naudojamas organinis puslaidininkis kodiniu pavadinimu Spiro-OMeTAD yra brangus, nes jo penkiapakopei sintezei reikalingi brangūs ir jautrūs reagentai ir sudėtinga sublimacijos procedūra. Be to, šis mažamolekulinis junginys pasižymi nestabilia amorfine būsena. Todėl pasaulyje kuriamos naujos lengvai susintetinamos, amorfinės, pigios ir efektyvios STM. Kitas didelis PSE trūkumas – nepakankamas šių prietaisų stabilumas, kurį daugiausia lemia aplinkos veikiamo perovskito skilimas. Vyksta intensyvios polimerinių STM, dengiamų ant perovskitinio sluoksnio *p-i-n* konstrukcijoje, paieškos. Supolimerintas organinis puslaidininkis gali efektyviai apsaugoti perovskitą nuo drėgmės, taip išsaugant ilgalaikį SE efektyvumą ir stabilumą.

3. MOKSLINIŲ STRAIPSNIŲ APŽVALGA

3.1. Fluoreno centrą turintys mažamolekuliniai organiniai puslaidininkiai ir jų panaudojimas skyles transportuojantiems sluoksniams gauti efektyviuose ir stabiliuose perovskitiniuose saulės elementuose

Šis skyrius yra parašytas remiantis publikuotu straipsniu: „Nonspiro, Fluorene-Based, Amorphous Hole Transporting Materials for Efficient and Stable Perovskite Solar Cells“, *Adv. Sci.*, 2018, 5, 1700811, Š. Daškevičiūtė, N. Sakai, M. Franckevičius, M. Daškevičienė, A. Magomedov, V. Jankauskas, H. J. Snaith, V. Getautis; cituota 44 kartus.

Kaip jau buvo minėta ankstesniuose skyriuose, PSE skylių transportiniame sluoksnyje kaip etalonas yra naudojamas organinis puslaidininkis Spiro-OMeTAD. Apskaičiuota, kad STM sudaro didelę dalį saulės elemento kainos[120], todėl dėl sudėtingos sintezės, apsunkintų gryninimo stadijų ir išaugusių gamybos kaštų Spiro-OMeTAD vis dar nėra naudojamas komercinių prietaisų gamyboje. Sukurta daugybė organinių puslaidininkių, kurių sintezės kelias daug paprastesnis. Vienas iš tokių pavyzdžių – mažamolekulinis junginys **V886**[105]. Jo struktūra susideda iš dviejų 4,4`-dimetoksidifenilamino ir 3,6-dipakeisto karbazolo fragmentų, sujungtų benzeno žiedu. Šio puslaidininkio sintezė labai paprasta, o jo pagrindu sukonstruoto kietos būsenos saulės elemento efektyvumas buvo beveik lygus prietaisui su Spiro-OMeTAD. Atsižvelgiant į tai, buvo susintetinti nauji mažamolekuliniai junginiai **STM1** ir **STM2**, turintys du ir tris karbazolilo chromoforus ir fluoreno fragmentą molekulės centre (žr. 16 pav.). Šie organiniai puslaidininkiai susintetinti naudojant paprastą trijų pakopų sintezės metodą. Jie yra amorfinės būsenos, termiškai stabilūs ir pasižymi aukštu galios konversijos efektyvumu. Svarbu tai, kad įrenginiai su šiomis medžiagomis pasižymėjo geresniu stabilumu nei prietaisas su Spiro-OMeTAD.

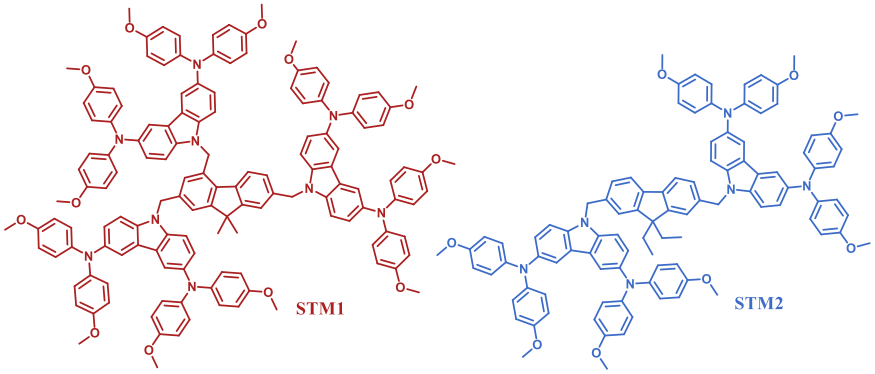

16 pav. Naujų organinių puslaidininkių **STM1** ir **STM2** struktūros

Kaip centriniai fragmentai tikslinių produktų sintezėje naudoti komerciškai prieinami skirtingai alkilinti fluorenai. Pastaruosius pagal žinomą literatūroje metodiką[121] paveikus paraformaldehidu ir HBr acto rūgštyje buvo gauti tarpiniai junginiai **1** ir **3** su skirtingu brommetilpakaitų skaičiumi. Jiems THF tirpiklyje reaguojant su 3,6-dibromkarbazolu, reakcijoje dalyvaujant KOH, išskirti fluoreno

dariniai **2** ir **4** su trimis ir dviem karbazolilo chromoforais. Galutiniai produktai **STM1** ir **STM2** buvo gauti paladžio katalizuojamos Buchwaldo kryžminio sujungimo reakcijos metu (žr. 2 schemą). Naujų junginių struktūros buvo patvirtintos ^{1}H ir ^{13}C BMR spektroskopijos bei elementinės analizės būdais.

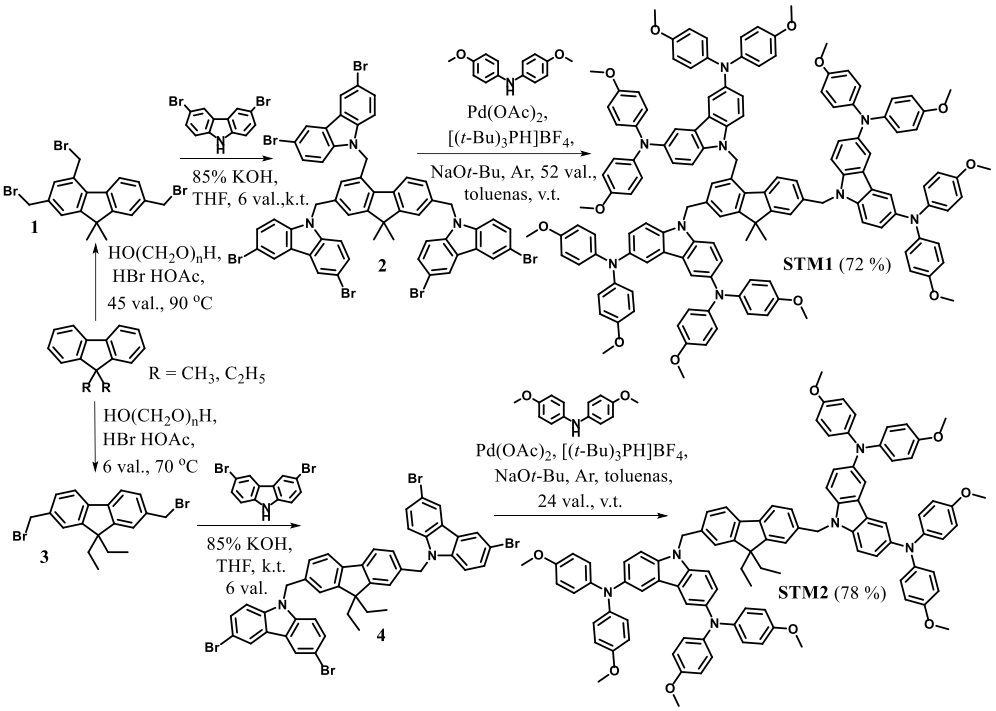

2 schema. Mažamolekulinių puslaidininkių **STM1** ir **STM2** sintezės schema

Ištyrus susintetintų STM optines, termines bei fotofizikines savybes (žr. 10 lentelę), buvo įvertintos jų panaudojimo galimybės PSE.

10 lentelė. Organinių puslaidininkių **STM1** ir **STM2** terminės, optinės ir fotofizikinės savybės

STM	T_{st} [a], °C	T_{sk} [a], °C	λ_{abs} [b], nm	I_P [c], eV	μ_0 [d], cm^2/Vs
STM1	166	400	305, 375	5,11	$1,5\times10^{-6}$
STM2	146	420	303, 373	5,10	$3,0\times10^{-6}$
Spiro-OMeTAD	126	449	303, 387	5,00	$4,1\times10^{-5}$

[a]Stiklėjimo (T_{st}) ir 5 % masės praradimo (T_{sk}) temperatūros, nustatytos iš DSK bei TGA kreivių (10 °C/min, N_2 atmosfera); [b]absorbcijos spektrų maksimumai (THF, 10^{-4} M); [c]jonizacijos potencialas, išmatuotas iš puslaidininkių plėvelių PESA metodu; [d]dreifinio judrio reikšmės esant 0 elektrinio lauko stiprio reikšmei.

STM terminiam stabilumui nustatyti buvo taikomi TGA ir DSK metodai. TGA duomenys parodė, kad tris pakaitus turintis junginys **STM1** 5 % savo masės svorio

praranda ties 400 °C temperatūra, o jo analogas su dviem karbazolilo chromoforais **STM2** – ties 420 °C. Junginiai yra pakankamai termiškai patvarūs ir gali būti panaudoti konstruojant PSE. Iš DSK analizės rezultatų matyti, kad organiniai puslaidininkiai **STM1** ir **STM2** egzistuoja amorfinės būsenos. Jų stiklėjimo temperatūros atitinkamai yra 166 ir 146 °C. Šios temperatūros labai gerai patvirtina vieną iš Wirtho postulatų, pagal kurį stiklėjimo temperatūra didėja, didėjant molekulei, t. y. centrinio fragmento 4-oje padėtyje prijungiant papildomą pakaitą[122]. Mažamolekulinio junginio **STM1** stiklėjimo temperatūra yra net 40 °C didesnė nei Spiro-OMeTAD. Tai puikus rodiklis, kuris užtikrina stabilesnę amorfinę būseną ir sumažina kristalizacijos tikimybę.

Naujų fluoreno centrinį fragmentą turinčių STM ir etalono Spiro-OMeTAD ultravioletinės ir regimosios šviesos spinduliuotės sugerties spektrai (UV-RŠ) buvo išmatuoti THF tirpaluose ir pateikti 17 pav., a. Puslaidininkių **STM1** ir **STM2** sugerties spektrai beveik identiški, ir tai patvirtina, kad nėra konjugacijos tarp atskirų dipakeistų karbazolilšakų. Abiejų junginių spektruose yra matoma intensyvi sugerties juosta ties 305 nm. Ji atspindi π-π^* elektronų perėjimus. Silpnos sugertys ties 375 nm atitinka n-π^* perėjimus. Kadangi naujų STM didžiausia absorbcija yra UV srityje ir tik labai nedidelė regimajame diapazone, jos tampa labai patrauklios naudoti PSE [123].

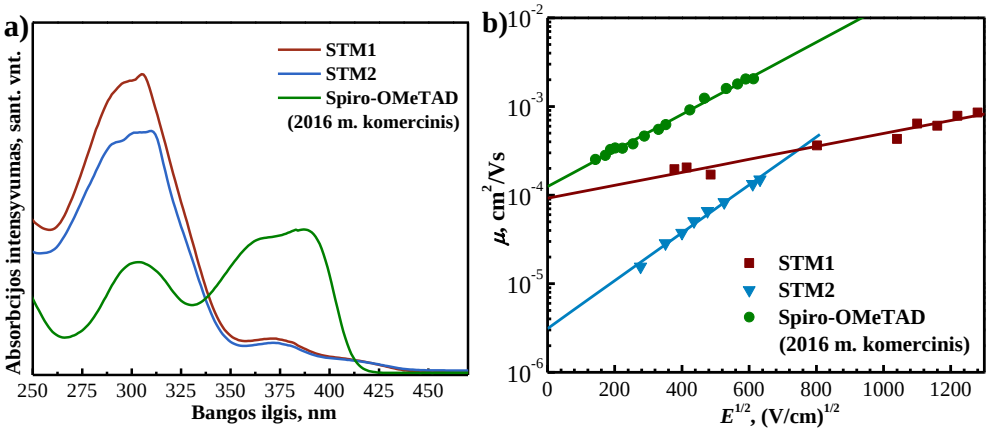

17 pav. Naujų organinių puslaidininkių **STM1**, **STM2** ir Spiro-OMeTAD: a) UV-RŠ spinduliuotės sugerties spektrai THF tirpiklyje (10^{-4} M); b) dreifinio judrio priklausomybė nuo elektrinio lauko stiprio

Naudojant elektronų fotoemisijos ore metodą buvo išmatuoti susintetintų puslaidininkių jonizacijos potencialai (I_P) – HOMO energetiniai lygmenys. Rezultatai pateikti 10 lentelėje. Junginių **STM1** ir **STM2** I_P reikšmės yra beveik vienodos, atitinkamai 5,11 ir 5,10 eV. Apskaičiuotos reikšmės yra labai artimos etalono Spiro-OMeTAD jonizacijos potencialo vertei (5,00 eV). Nauji puslaidininkiai galėtų užtikrinti efektyvų skylių perdavimą prietaisuose, todėl yra tinkami naudoti PSE. Dar viena svarbi puslaidininkių fotofizikinė savybė – dreifinis judris. Jis buvo išmatuotas naudojant kserografinį laiko lėkio metodą (žr. 17 pav., b). Junginių **STM1** ir **STM2** mobilumo vertės buvo panašios į Spiro-OMeTAD ir silpname elektriniame lauke atitinkamai siekė $1{,}5\times10^{-6}$ ir $3{,}0\times10^{-6}$ cm²/Vs.

Nauji V-serijos junginiai buvo panaudoti *n-i-p* architektūros PSE skyles transportuojančiame sluoksnyje. Prietaiso konstrukcija: FTO / SnO_2 / perovskitas – $FA_{0,83}Cs_{0,17}Pb(I_{0,8}Br_{0,2})_3$ / STM / Au. Saulės elementų optimizuoti fotovoltinių charakteristikų duomenys iš fotosrovės-įtampos (*J-V*) kreivių susisteminti ir pateikti 11 lentelėje. Puslaidininkio **STM1** pagrindu sukonstruoto įrenginio galios konversijos efektyvumas siekė 18,3 % ir buvo labai panašus į Spiro-OMeTAD (18,9 %). **STM2** atveju buvo užfiksuotas šiek tiek mažesnis efektyvumas (16,7 %).

11 lentelė. Perovskitinių saulės elementų, kuriuose naudoti puslaidininkiai **STM1**, **STM2** ir Spiro-OMeTAD, fotovoltinės charakteristikos ir efektyvumai

STM	V_{OC}, V	J_{SC}, mA/cm^2	*FF*	PSE, %
STM1	1,05	22,0	79,5	18,3
STM2	0,96	21,6	79,7	16,7
Spiro-OMeTAD	1,08	22,4	77,9	18,9

Taip pat buvo ištirtas visų sukonstruotų PSE prietaisų stabilumas (žr. 18 pav.). Įrenginiai buvo neįkapsuliuoti, santykinė oro drėgmė ~ 60 %, temperatūra 22 °C. Po 270 valandų Spiro-OMeTAD pagrindu pagaminto PSE efektyvumas nukrito 20 %. O įrenginiai su puslaidininkiais **STM1** ir **STM2** yra daug stabilesni, nes matomas tik 6 % galios konversijos efektyvumo sumažėjimas. Stabilumo tyrimo rezultatai gali būti siejami su geresne STM morfologija – nauji puslaidininkiai tolygiai pasidengia ant perovskito paviršiaus, taip apsaugodami jį nuo drėgmės poveikio.

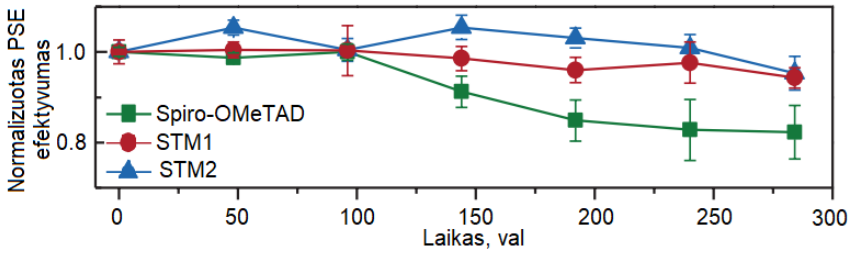

18 pav. Perovskitinių saulės elementų su tirtais puslaidininkiais stabilumas

Apibendrinant visus gautus rezultatus galima teigti, kad organinis puslaidininkis **STM1** galėtų būti puiki alternatyva etalonui Spiro-OMeTAD. Tai priartintų perovskitinių saulės elementų komercializaciją.

3.2. Fluoreno enaminų sintezė bei jų panaudojimas skyles transportuojantiems sluoksniams gauti efektyviuose ir stabiliuose perovskitiniuose saulės elementuose

Šis skyrius yra parašytas remiantis publikuotu straipsniu: „Fluorene-based enamines as low-cost and dopant-free hole transporting materials for high performance and stable perovskite solar cells“, *J. Mater. Chem. A*, 2021, 9, 301-309, Š. Daškevičiūtė, C. Momblona, K. Rakštys, A. A. Sutanto, M. Daškevičienė, V.

Jankauskas, A. Gruodis, G. Bubnienė, V. Getautis, M. K. Nazeeruddin; cituota 30 kartų.

Didelio efektyvumo PSE dažniausiai gaunami naudojant organinius puslaidininkius, sintetintus kryžminimo reakcijų metu. Sintezė vykdoma naudojant brangius ligandus ar paladžio katalizatorius inertiškomis reakcijos sąlygomis, o galutinių produktų gryninimo procedūros yra sudėtingos. Siekiant ekonomiškos ir efektyvios sintezės buvo atlikta paprasta kondensacijos reakcija, naudojant pigias pradines medžiagas ir išskiriant geromis puslaidininkinėmis savybėmis pasižyminčius enaminus (žr. 19 pav.). Šių galutinių skylių transportinių medžiagų kaina yra vos keli eurai už gramą, o etaloninis Spiro-OMeTAD kainuoja ~92 Eur/g[124]. Iš fluoreno diaminų susintetinti enaminai pasižymėjo ypač aukštais skylių dreifiniais judriais, kurie siekė net iki $3{,}3 \times 10^{-4}$ $cm^2V^{-1}s^{-1}$. Tai viena iš svarbiausių puslaidininkių fizikinių charakteristikų, todėl ir sukonstruoti PSE pasižymėjo puikiu efektyvumu – legiruotoje struktūroje 19,3 %, o konfigūracijoje be priedų 17,1 %. Be to, abiejų struktūrų SE turi puikų ilgalaikį stabilumą, palyginti su Spiro-OMeTAD.

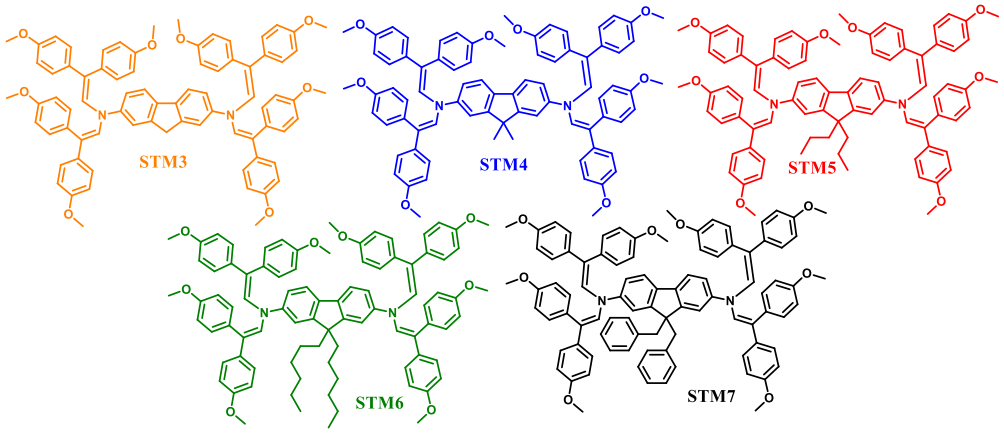

19 pav. Naujai susintetintų enaminų **STM3** – **STM7** struktūros

Tikslinių fluoreno chromoforą turinčių enaminų sintezei buvo naudojama pirminio amino reakcijos su acetaldehidais metodika. Tuo tikslu 2,7-diamino-9*H*-fluorenas THF virimo temperatūroje buvo veikiamas 2,2-bis(4-metoksifenil)acetaldehidu, reakcijoje dalyvaujant katalizatoriui kamparo-10-sulfonrūgščiai (KSR). Tokiu būdu buvo gautas enaminas **STM3**, kurio 9-oji padėtis kitame etape alkilinama įvairaus grandinėlės ilgio halogenidais, išskiriant tikslinius produktus **STM4**, **STM5**, **STM6** ir **STM7** (žr. 3 schemą). Susintetintų junginių struktūros buvo patvirtintos ^1H ir ^{13}C BMR spektroskopijos bei elementinės analizės metodais.

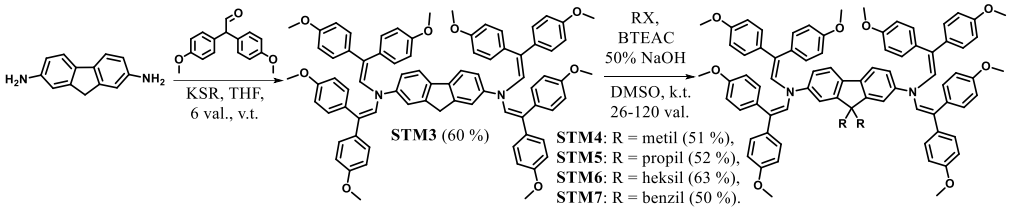

3 schema. Naujų enaminų **STM3** – **STM7** sintezės schema

Siekiant įvertinti naujų medžiagų kainą, buvo atlikta sintezės kaštų analizė. Puslaidininkio **STM3** prognozuojama kaina yra ~10 Eur/g, o alkilinto analogo **STM5** – ~22 Eur/g, kas sudaro tik ketvirtadalį Spiro-OMeTAD kainos.

Darbe buvo ištirtos naujai susintetintų STM optinės, terminės ir fotofizikinės savybės (žr. 12 lentelę) bei įvertintos panaudojimo galimybės PSE.

12 lentelė. Naujų enaminų terminės ir optinės savybės

STM	T_{lyd} [a], °C	T_{kr} [a], °C	T_{st} [a], °C	T_{sk} [a], °C	λ_{abs} [b], nm	λ_{em} [b], nm	E_g [c], eV
STM3	255	–	150	403	262, 381, 401	508	2,79
STM4	247, 267, 272	198	153	285	265, 382, 404	510	2,79
STM5	272	159	120	399	266, 382, 404	509	2,81
STM6	173, 195	–	90	393	265, 383, 404	508	2,79
STM7	330	–	116	321	265, 384, 400	507	2,79

[a]Lydymosi (T_{lyd}), kristalizacijos (T_{kr}), stiklėjimo (T_{st}) ir 5 % masės praradimo (T_{sk}) temperatūros, nustatytos iš DSK bei TGA kreivių (10 °C/min, N_2 atmosfera); [b]absorbcijos bei emisijos spektrų maksimumai (THF, 10^{-4} M); [c]*Eg*, nustatytas iš medžiagų plėvelių absorbcijos bei emisijos spektrų susikirtimo.

Pirmiausia buvo atlikti terminiai tyrimai, kurių metu įvertintos medžiagų būsenos bei atsparumas aukštoms temperatūroms. TGA parodė, kad junginys **STM3** 5 % savo svorio masės praranda 403 °C temperatūroje ir turi didžiausią terminį stabilumą tarp šios serijos enaminų. Pastebima tendencija, kad alifatinių pakaitų įterpimas į 9-ąją fluoreno padėtį pablogino naujų puslaidininkių terminį stabilumą, tačiau jų visų skilimo temperatūra yra daug aukštesnė nei Spiro-OMeTAD (T_{sk} = 288 °C[125]). Puslaidininkių terminiai virsmai buvo nustatyti naudojant DSK metodą. Įdomu tai, kad junginiai **STM3**, **STM6** ir **STM7** egzistuoja tiek kristalinės, tiek ir amorfinės būsenos, o **STM4** ir **STM5** labiau linkę kristalintis. Tačiau po antro kaitinimo ir juose fiksuojama tik stiklėjimo temperatūra, kuri parodo, kad visi junginiai turi ir amorfinę būseną. Stabiliausia amorfine būsena pasižymi organinis puslaidininkis **STM4**, nes jo stiklėjimo temperatūra yra aukščiausia 153 °C (žr. 12 lentelę).

Skyles transportuojančių medžiagų krūvio pernešimo procese ypač svarbūs yra π elektronai[126]. Norint detaliau išnagrinėti jų būseną buvo užrašyti organinių puslaidininkių, gautų iš fluoreno diaminų, elektromagnetinės spinduliuotės sugerties

spektrai (žr. 20 pav., a). Visos STM turi dvi pagrindines sugerties smailes, kurios yra ties ~260 nm ir ~400 nm. Mažiau intensyvi absorbcijos smailė prie trumpesniųjų bangų atspindi lokalizuotus elektronų π-π^* perėjimus. O ~400 nm bangos ilgio smailė atsiranda dėl intensyvesnės delokalizacijos nuo centrinio molekulės fragmento ir yra priskiriama n-π^* perėjimams. Taip pat pastebima, kad skirtingų alkilfragmentų prijungimas neturėjo ryškios įtakos konjuguotai sistemai, todėl absorbcijos spektrai išlieka beveik identiški. Atlikus valentinių elektronų sužadinimą buvo užrašyti FL spektrai (žr. 20 pav., a). Visų enaminų FL spektrai yra panašūs ir emisijos maksimumas fiksuojamas ~510 nm. Matomi labai dideli Stokso poslinkiai (~100 nm) rodo, kad sužadinimo būsenoje medžiagai yra būdingi dideli geometriniai pokyčiai. Kuo Stokso poslinkis yra didesnis, tuo labiau junginys tinkamesnis skylėms transportuoti, nes galima tikėtis didesnio krūvininkų judrio[127].

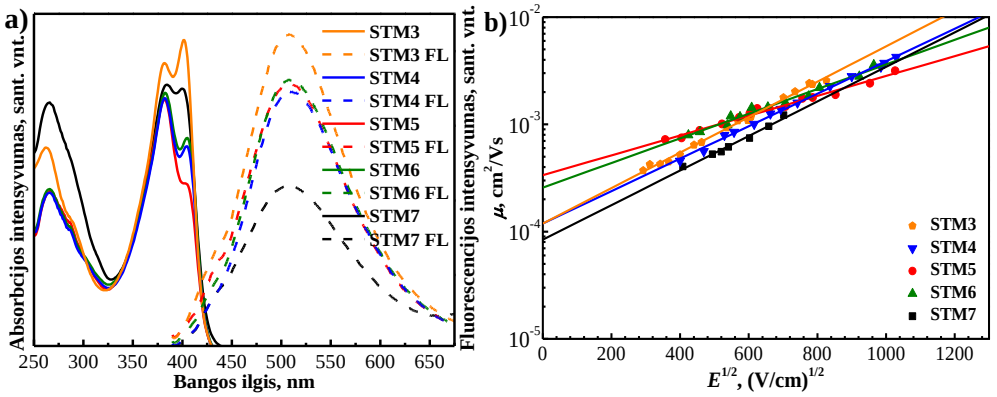

20 pav. Naujų enaminų **STM3** – **STM7**: a) UV-RŠ spinduliuotės sugerties (ištisinė linija) ir fluorescencijos (punktyrinė linija) spektrai THF tirpiklyje (10^{-4} M); b) dreifinio judrio priklausomybė nuo elektrinio lauko stiprio

Naudojant elektronų fotoemisijos ore metodą STM energetinių lygmenų suderinamumui išsiaiškinti buvo išmatuoti jonizacijos potencialai (I_P) – HOMO energetiniai lygmenys (žr. 13 lentelę). **STM3**, **STM4**, **STM5**, **STM6** ir **STM7** I_P reikšmės atitinkamai buvo 5,01, 5,0, 5,03, 5,03 ir 4,9 eV. Jos idealiai suderinamos su perovskito valentinės juostos energija (5,70 eV). Šis suderinamumas užtikrina efektyvų skylių perdavimą iš perovskito link katodo[128]. Naudojant E_g ir I_P reikšmes buvo apskaičiuotos E_{ea} (LUMO energetinio lygmens) vertės (žr. 13 lentelę). Visų junginių elektronų gimiringumo vertės buvo nuo 2,1 iki 2,2 eV. Svarbu tai, kad jos yra daug mažesnės nei perovskito laidumo juostos energija (4,1 eV), todėl yra užtikrinamas veiksmingas elektronų blokavimas nuo perovskito link anodo[128].

13 lentelė. Naujų enaminų **STM3** – **STM7** fotofizikinės savybės

STM	I_P [a], eV	I_P [b], eV	E_{ea} [c], eV	μ_0 [d], cm^2/Vs
STM3	5,01	5,39	2,22	$1,2\times10^{-4}$
STM4	5,0	5,32	2,21	$1,2\times10^{-4}$
STM5	5,03	5,39	2,22	$3,3\times10^{-4}$
STM6	5,03	5,25	2,24	$2,6\times10^{-4}$
STM7	4,9	5,34	2,11	8×10^{-5}

[a]Jonizacijos potencialas, išmatuotas iš puslaidininkių plėvelių PESA metodu be legiruojančių priedų; [b]jonizacijos potencialas, išmatuotas iš puslaidininkių plėvelių PESA metodu su legiruojančiais priedais; [c]$E_{ea} = I_P - E_g$; [d]dreifinio judrio reikšmės esant 0 elektrinio lauko stiprio reikšmei.

Naudojant kserografinį laiko lėkio metodą buvo išmatuoti naujų organinių puslaidininkių teigiamų krūvių dreifiniai judriai. Jų priklausomybė nuo elektrinio lauko stiprio yra pavaizduota 20 pav., b. Silpname elektriniame lauke (μ_0) junginių **STM3**, **STM4**, **STM5** ir **STM6** dreifinis judris buvo 10^{-4} $cm^2V^{-1}s^{-1}$ eilės, o propilpakaitą turinčio puslaidininkio **STM5** buvo užfiksuota didžiausia reikšmė – $3,3 \times 10^{-4}$ $cm^2V^{-1}s^{-1}$. Svarbu atkreipti dėmesį, kad buvo pasiektas didesnis skylininkų mobilumas nei etaloninio Spiro-OMeTAD ($\mu_0 = 1,3 \times 10^{-4}$ $cm^2V^{-1}s^{-1}$)[129] atveju. Aromatinio benzilpakaito įterpimas į fluoreno 9-ą padėtį turėjo neigiamos įtakos skylių dreifiniam judriui – palyginti su kitais analogais, jis sumažėjo daugiau nei viena eile.

Apžvelgiant visų atliktų tyrimų rezultatus galima teigti, kad gauti fluoreno enaminai yra termiškai stabilūs, turi amorfinę būseną ir aukštą skylių dreifinį judrį silpnuose elektriniuose laukuose. Šių organinių puslaidininkių HOMO/LUMO energetiniai lygmenys leidžia juos panaudoti konstruojant perovskitinius saulės elementus.

Naujosios STM buvo išbandytos kaip teigiamus krūvininkus transportuojančios medžiagos *n-i-p* architektūros PSE. Šių SE konstrukcija: FTO / kompaktiškas TiO_2 sluoksnis / mezoporinis TiO_2 / amorfinis SnO_2 / perovskitas – $[(FAPbI_3)_{0,87}(MAPbBr_3)_{0,13}]_{0,92}(CsPbI_3)_{0,08}$ / STM / Au. STM buvo legiruotos *t*BP, LiTFSI ir FK209 priedais. Visiems organinių puslaidininkių pagrindu sukonstruotiems PSE buvo atlikta skerspjūvio skenuojamoji elektroninė mikroskopija (SEM). Ši analizė parodė, kad skylių transportiniai sluoksniai iš enaminų yra kompaktiškai pasidengę ant perovskito ir yra ~ 120 nm storio, o Spiro-OMeTAD sluoksnis – ~260 nm. Geriausiu efektyvumu pasižymėjo PSE, sukonstruotas **STM3** puslaidininkio pagrindu (19,3 %). Alkilintų enaminų analogų **STM4**, **STM5** ir **STM6** SE efektyvumai atitinkamai buvo 19,2, 19,2 ir 19,1 %. Tik junginio, turinčio benzilpakaitą, PSE efektyvumas buvo daug mažesnis ir siekė vos 12,6 %. Galima teigti, kad tai yra dėsninga, nes būtent šio puslaidininkio skylių dreifinis judris ir užpildymo faktorius buvo nepalyginti mažesni nei jo analogų. Svarbu paminėti, kad tomis pačiomis sąlygomis sukonstruoto PSE su Spiro-OMeTAD efektyvumas buvo

19,7 % ir tik 0,4 % lenkė paprastos kondensacijos reakcijos metu gauto junginio **STM3** PSE efektyvumą.

Yra žinoma, kad legiruojantys priedai daro neigiamą įtaką PSE ilgalaikiam stabilumui. Ličio druskos yra higroskopiškos, o 4-*tret*-butilpiridinas yra linkęs formuoti kompleksus su PbI_2, kas lemia greitesnį perovskito irimą[130]. Todėl buvo sukonstruoti SE ir be priedų. Pažymėtina tai, kad, matuojant priedų neturinčios kompozicijos PSE, naujai susintetintų junginių SE efektyvumai smarkiai viršijo etaloninio puslaidininkio Spiro-OMeTAD. Geriausiu efektyvumu pasižymėjo junginys **STM3** (17,1 %). Visi rezultatai surinkti iš *J-V* kreivių grafikų ir pateikti 14 lentelėje.

14 lentelė. Perovskitinių saulės elementų, kuriuose naudoti skirtingi enaminai ir Spiro-OMeTAD, fotovoltinės charakteristikos ir efektyvumai

	STM	V_{OC}, V	J_{SC}, mA/cm^2	*FF*	PSE, %
Su priedais	**STM3**	1,077	23,24	0,77	19,3
	STM4	1,090	22,97	0,76	19,2
	STM5	1,089	22,86	0,77	19,2
	STM6	1,094	22,95	0,76	19,1
	STM7	1,024	22,32	0,55	12,6
	Spiro-OMeTAD	1,115	22,97	0,77	19,7
Be priedų	**STM3**	1,033	22,95	0,72	17,1
	STM4	1,038	22,98	0,71	16,9
	STM5	1,029	23,09	0,70	16,6
	STM6	1,022	23,02	0,69	16,2
	Spiro-OMeTAD	0,972	22,83	0,47	10,4

Buvo įvertintas visų sukonstruotų PSE stabilumas, išskyrus iš junginio **STM7** padaryto SE, nes jo efektyvumo rezultatai buvo mažesni. Palyginimui buvo įvertintas ir su Spiro-OMeTAD gauto įrenginio stabilumas. Visi prietaisai buvo neįkapsuliuoti, nuolat apšviečiami saulės spinduliais azoto atmosferoje 500 valandų. Ilgalaikiai prietaisų stabilumo rezultatai pateikti 21 pav. Visų naujų enaminų klasės junginių PSE stabilumo rezultatai buvo geresni nei etaloninio Spiro-OMeTAD SE.

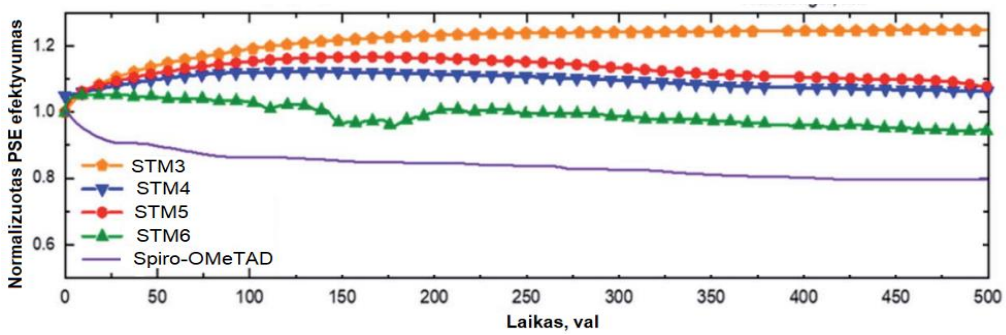

21 pav. Perovskitinių saulės elementų su skirtingais enaminais **STM3** – **STM6** ir Spiro-OMeTAD stabilumų tyrimų rezultatai

Šios V-serijos enaminų funkcionalumo galimybes įrodo ir jų panaudojimas pusiau skaidrių Sb_2S_3 konstrukcijos saulės elementuose, kurių pritaikymas šiuo metu yra gana ribotas dėl mažo konversijos efektyvumo ir brangių STM. Dažniausiai kaip etaloninė STM yra naudojamas poli-3-heksiltiofeno polimeras (P3HT). Moksliniame straipsnyje „Sb_2S_3 solar cells with a cost-effective and dopant-free fluorene-based enamine as a hole transport material“, *Sustainable Energy Fuels*, 2022, 6, 3220-3229, N. Juneja, S. Daskeviciute-Geguziene ir kt., puslaidininkis **STM6** ir P3HT buvo panaudoti stibio sulfidų SE konstravimui. Saulės elemento su enaminu **STM6** konversijos efektyvumas buvo 17 % didesnis nei su P3HT, o įrenginių skaidrumas padidėjo 20 %. Taip pat šio prietaiso kaina buvo daug mažesnė (P3HT ~45 Eur/g, **STM6** ~17 Eur/g).

Naujų enaminų klasės puslaidininkių pritaikymo galimybės buvo aprašytos ir dar viename moksliniame straipsnyje – „Employment of dopant-free fluorene-based enamines as innovative hole transport materials to boost the transparency and performance of Sb_2S_3 based solar cells“, *Materials Science in Semiconductor Processing*, 2024, 169, 107934, N. Juneja, S. Daskeviciute-Geguziene ir kt. Nauji organiniai puslaidininkiai **STM3** ir **STM5** taip pat buvo pritaikyti Sb_2S_3 saulės elementų skyles transportuojančiuose sluoksniuose. Atitinkamai SE konversijos efektyvumai buvo 3,9 ir 4,3 % ir viršijo etalono P3HT pagrindu sukonstruoto prietaiso efektyvumą, kuris buvo lygus 3,8 %.

3.3. Fluoreno chromoforus su akceptorinėmis grupėmis turinčių enaminų sintezė ir panaudojimas efektyviems ir stabiliems perovskitiniams saulės elementams

Šis skyrius yra parašytas remiantis publikuotu straipsniu: „Passivating Defects of Perovskite Solar Cells with Functional Donor-Acceptor-Donor Type Hole Transporting Materials“, *Adv. Funct. Mater.*, 2022, 3, 1-8, Š. Daškevičiūtė-Gegužienė, Y. Zhang, K. Rakštys, C. Xiao, J. Xia, Z. Qiu, M. Daškevičienė, T. Paškevičius, V. Jankauskas, A. M. Asiri, V. Getautis, M. K. Nazeeruddin; cituota 10 kartų.

Šiame skyriuje yra aprašytas sąveikos donoras-akceptorius-donoras (D-A-D) įtakos perovskito defektų pasyvavimui tyrimas. Šiam tikslui buvo susintetinti nauji

organiniai puslaidininkiai – enaminai, turintys difeniletenilgrupes ir fluoreno chromoforą su akceptorine grupe molekulės centre (žr. 22 pav.). Puslaidininkio **STM13** pagrindu veikiantis PSE pasiekė didžiausią galios konversijos efektyvumą, kuris viršijo 22 % ir pralenkė Spiro-OMeTAD identiškomis sąlygomis testuotą saulės elementą. Malononitrilo akceptorius puslaidininkio molekulėje ne tik pagerino skylių transportą, bet ir prisidėjo prie perovskito defektų pasyvavimo, o tai leido pasiekti geresnį SE stabilumą. Buvo apskaičiuota STM **STM13** sintezės kaina, kuri siekė vos 21 Eur/g. Akivaizdu, kad šie organiniai puslaidininkiai yra puiki alternatyva sudėtingos sintezės metu gaunamam brangiam Spiro-OMeTAD.

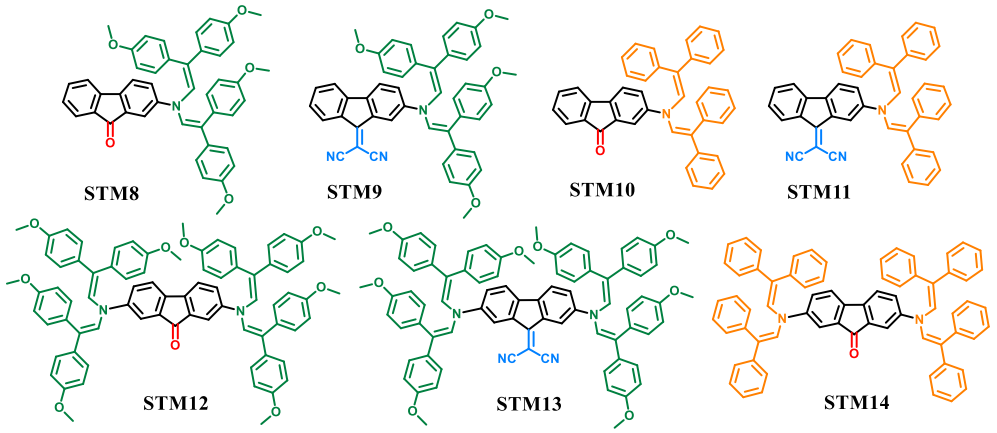

22 pav. Susintetintų D-A-D tipo organinių puslaidininkių **STM8** – **STM14** struktūros

Naudojant paprastą kondensacijos reakciją, kurios šalutinis produktas yra tik vanduo, kondensuojant pigius komercinius 2-aminofluorenoną arba 2,7-diaminofluorenoną su 2,2-bis-(4-metoksifenil)aceltadehidu, reakcijoje dalyvaujant KSR, buvo susintetinti fluorenono chromoforą turintys organiniai puslaidininkiai su vienu (**STM8** ir **STM10**) arba dviem (**STM12** ir **STM14**) enaminų fragmentais. Norint gauti junginius su stipresnėmis akceptorinėmis ciano grupėmis, keto grupė Knoevenagelio kondensacijos būdu konvertuota į malononitrilinę grupę, išskiriant puslaidininkius **STM9**, **STM11** ir **STM13**. Detalios junginių sintezės pateiktos 4 schemoje. Svarbu paminėti, kad pritaikytos kondensacijos reakcijos yra labai perspektyvios, leidžiančios išvengti sudėtingų reakcijų ir brangių metalų katalizatorių naudojimo, o tikslinių produktų išskyrimo ir gryninimo procedūros yra nesudėtingos. Susintetintų junginių struktūros buvo patvirtintos ^{1}H ir ^{13}C BMR, masių ir infraraudonosios spektroskopijų bei elementinės analizės metodais.

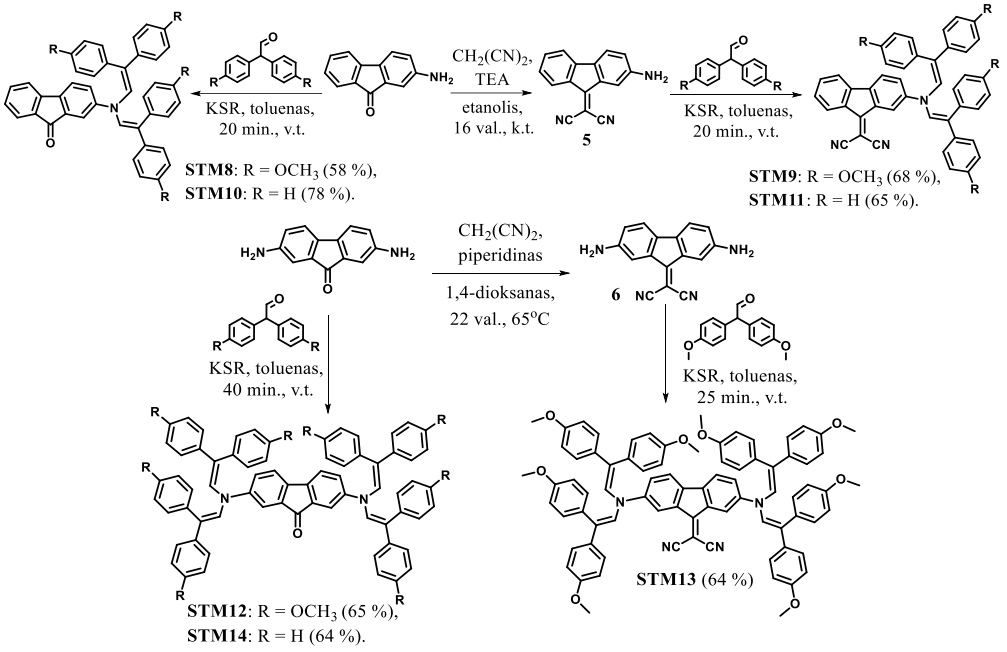

4 schema. Naujų D-A-D tipo puslaidininkių sintezės schema

Siekiant įvertinti susintetintų *p*-tipo puslaidininkių kainą, buvo atlikta sintezės kaštų analizė. Numatoma puslaidininkio **STM13** su dviem enaminų fragmentais kaina yra ~21 Eur/g, o su vienu enamino fragmentu **STM10** – ~18 Eur/g, kas sudaro tik ketvirtadalį Spiro-OMeTAD kainos.

Darbe buvo ištirtos naujų fluorenono ir dicianofluorenilidino enaminų optinės, terminės, fotofizikinės savybės (žr. 15 lentelę) bei jų panaudojimo galimybės PSE. Terminės junginių savybės buvo įvertintos naudojant TGA ir DSK (žr. 15 lentelę) tyrimų metodus. Termogravimetrinė analizė parodė, kad organiniai puslaidininkiai, turintys didesnę aromatinę sistemą, pasižymi aukštesniu terminiu stabilumu[131-133]. Aukščiausia skilimo temperatūra, kai junginys netenka 5 % savo masės, pasižymėjo puslaidininkis **STM14** (T_{sk} = 412 °C). Visų susintetintų STM skilimo temperatūra buvo daug didesnė nei Spiro-OMeTAD[125]. Junginių terminiai virsmai buvo nustatyti iš DSK kreivių. Buvo pastebėta aiški tendencija tarp metoksipakeistų ir metoksigrupių neturinčių junginių. Organiniai puslaidininkiai **STM10**, **STM11** ir **STM14** yra kristaliniai, nes abiejų kaitinimų metu yra fiksuojamos lydymosi temperatūros. Metoksigrupės suteikia junginiams tiek kristalinę, tiek ir amorfinę būsenas. Visiems junginiams, kurių struktūroje yra metoksigrupių, antro kaitinimo metu buvo fiksuota stiklėjimo temperatūra. Organiniai puslaidininkiai **V1351** ir **STM13** turi stabiliausią amorfinę būseną – stiklėjimo temperatūra fiksuota ties 140 °C.

15 lentelė. Naujų D-A-D tipo puslaidininkių **STM8** – **STM14** terminės, optinės ir fotofizikinės savybės

STM	T_{lyd} [a], °C	T_{kr} [a], °C	T_{st} [a], °C	T_{sk} [a], °C	λ_{abs} [b], nm	I_P [c], eV	μ_0 [d], cm^2/Vs
STM8	171, 186, 208	–	92	376	259, 299, 313, 370, 538	5,44	$1,3\times10^{-7}$
STM9	245	–	111	379	265, 345	5,44	$1,1\times10^{-7}$
STM10	244, 247	202	111	338	255, 285, 313, 363, 513	5,49	$1,4\times10^{-6}$
STM11	236, 248, 239, 248	175	115	347	268, 341	5,53	$1,3\times10^{-6}$
STM12	221, 232	–	143	403	261, 299, 313, 385, 403, 598	5,43	4×10^{-6}
STM13	166	–	134	389	263, 323, 349, 409	5,41	$4,6\times10^{-6}$
STM14	339, 351, 348	217	157	412	270, 288, 311, 378, 395, 570	5,39	$2,8\times10^{-6}$

[a]Lydymosi (T_{lyd}), kristalizacijos (T_{kr}), stiklėjimo (T_{st}) ir 5 % masės praradimo (T_{sk}) temperatūros, nustatytos iš DSK bei TGA kreivių (10 °C/min, N_2 atmosfera); [b]absorbcijos spektrų maksimumai (THF, 10^{-4} M); [c]jonizacijos potencialas, išmatuotas iš puslaidininkių plėvelių PESA metodu; [d]dreifinio judrio reikšmės esant 0 elektrinio lauko stiprio reikšmei.

Susintetintų STM ultravioletinės ir regimosios šviesos spinduliuotės sugerties spektrai (UV-RŠ) THF tirpaluose yra pateikti 23 pav., a.

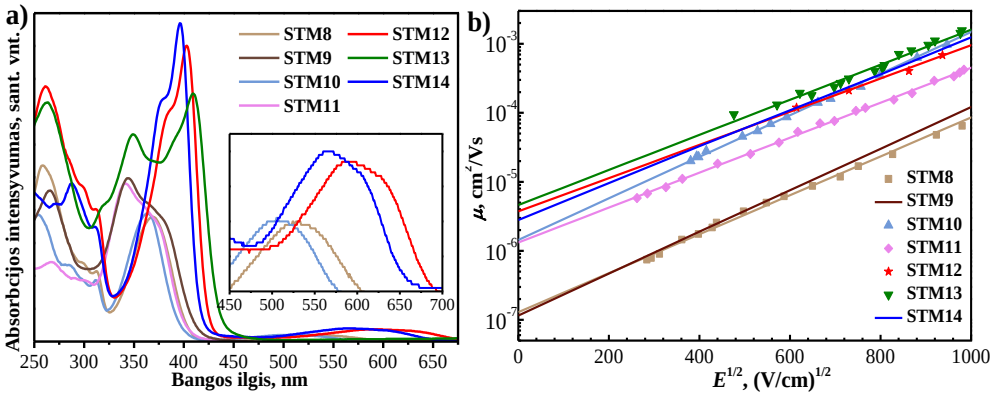

23 pav. Naujų D-A-D tipo puslaidininkių **STM8** – **STM14**: a) UV-RŠ spinduliuotės sugerties spektrai THF tirpiklyje (10^{-4} M); b) dreifinio judrio priklausomybė nuo elektrinio lauko stiprio

Tarpusavyje lyginant **STM8** su **STM9**, **STM10** su **STM11** ir **STM12** su **STM13** galima pastebėti absorbcijos maksimumų poslinkius tolimesnių bangų link. Absorbcijos maksimumų skirtumų atsiranda dėl skirtingų C=O ir C=C-$(CN)_2$ akceptorių fragmentų. Malononitrilo funkcinė grupė pasižymi stipresnėmis akceptorinėmis savybėmis. Junginiai **STM12**, **STM14** ir **STM13** turi dvigubai didesnę konjuguotą sistemą, todėl jų absorbcijos maksimumai pasižymi hiperchrominiu poslinkiu, palyginti su vieno fragmento enaminais. Plati sugerties juosta regimojoje srityje atitinka donoro-akceptoriaus krūvio pernašos sąveiką[134-135]. THF tirpaluose buvo išmatuoti visų molekulių fluorescencijos (FL) spektrai, tačiau emisija neužfiksuota.

Siekiant nustatyti puslaidininkių energijos lygmenis buvo atlikti jonizacijos potencialo matavimai naudojant elektronų fotoemisijos ore metodą. Eksperimentiniai duomenys pateikti 15 lentelėje. D-A-D tipo puslaidininkiams buvo nustatytos skirtingos I_P reikšmės, kurios varijavo ~5,4–5,5 eV intervale.

Susintetintų molekulių krūvio pernašos greitis buvo išmatuotas kserografiniu laiko lėkio metodu. Dreifinio judrio priklausomybė nuo elektrinio lauko stiprumo yra pateikta 23 pav., b, ir susisteminta 15 lentelėje. Junginių **STM9** ir **STM14** dreifinio judrio nebuvo galima išmatuoti, todėl buvo daryti skirtingų koncentracijų mišiniai su *Z*-polikarbonatu (1:1, 1:2, 1:3, 1:4). Gautų sluoksnių kokybė buvo tinkama matavimams atlikti. Remiantis eksponentine krūvininkų judrumo priklausomybe nuo vidutinio atstumo tarp krūvį pernešančių molekulių, buvo ekstrapoliuotos mobilumo reikšmės, kai medžiaga yra gryna[136]. Silpnuose elektriniuose laukuose didžiausiu krūvio pernašos greičiu pasižymėjo junginys **STM13** $\mu_0 = 4\times10^{-6}$ cm^2/Vs. Mažesnė molekulių konjugacija turėjo neigiamos įtakos dreifiniam judriui. Organinis puslaidininkis su vienu enamino fragmentu **STM9** pasižymėjo prasčiausiu krūvininkų mobilumu, kuris siekė $1{,}1\times10^{-7}$ cm^2/Vs.

Ištyrus naujos V-serijos junginių savybes ir jas išanalizavus buvo konstruojami PSE. *n-i-p* įrenginio konstrukcijos eiliškumas – FTO / SnO_2 / perovskitas – $(FAPbI_3)_{0,85}(MAPbBr_3)_{0,15}$ / STM / Au. Buvo atlikta visų elementų skerspjūvio SEM nuotrauka. Puslaidininkiais padengtų sluoksnių storis tik 80 nm, o Spiro-OMeTAD – 220 nm. Tai labai svarbu, nes konstruojant SE buvo optimizuotos naujai susintetintų junginių tirpalų koncentracijos. Duomenys apie PSE našumo parametrus yra surinkti iš *J-V* kreivių, susisteminti ir pateikti 16 lentelėje. Galima teigti, kad prietaisų našumo parametrams didelę įtaką daro molekulės struktūra, o ypač didesnė konjugacija. Puslaidininkių su mažesne dvigubų ryšių konjuguota sistema (**STM8**, **STM9**, **STM10** ir **STM11**) SE fotovoltinės charakteristikos neprilygo etalonui Spiro-OMeTAD. Priešinga situacija yra su didesnę konjuguotą sistemą turinčiais puslaidininkiais. STM **STM12** ir **STM14** prietaisų efektyvumo rezultatai atitinkamai buvo 19,92 ir 20,53 % ir beveik prilygo Spiro-OMeTAD efektyvumo vertei. Didžiausias našumo rezultatas buvo pasiektas su puslaidininkiu **STM13**, kuris buvo lygus 22,03 % ir buvo rekordinis, nes aplenkė etaloną. Šio rekordinio efektyvumo priežastis galėjo būti aukštas užpildymo faktorius (*FF*), kuris parodo gerą skyles transportuojančio sluoksnio kokybę. Akceptorinė C=C-$(CN)_2$ grupė sąveikauja su nekoordinuotais švino jonais (Pb^{2+}). Ši sąveika sumažina perovskito defektus, dėl ko gerėja PSE efektyvumo ir stabilumo rezultatai[137-139].

16 lentelė. Perovskitinių saulės elementų, kuriuose naudoti D-A-D tipo puslaidininkiai ir Spiro-OMeTAD, fotovoltinės charakteristikos ir efektyvumai

STM	V_{OC}, V	J_{SC}, mA/cm^2	*FF*	PSE, %
STM8	0,963	22,80	0,687	14,97
STM9	0,991	23,25	0,670	15,37
STM10	0,895	23,01	0,662	13,54
STM11	0,871	1,59	0,497	0,68
STM12	1,089	23,77	0,769	19,92
STM13	1,112	24,34	0,813	22,03
STM14	1,070	24,2	0,792	20,53
Spiro-OMeTAD	1,121	24,16	0,793	21,48

Norint komercializuoti puslaidininkius, labai svarbu ištirti jų pagrindu pagaminto prietaiso efektyvumą ne tik laboratorijos sąlygomis, bet ir didelio masto gamyboje. Todėl naudojant junginį **STM13** buvo pagamintas 6,5 × 7 cm dydžio perovskitinis saulės modulis ir pasiektas 18,61 % efektyvumas.

Buvo įvertinti puslaidininkio **STM13** ir Spiro-OMeTAD pagrindu sukonstruotų PSE stabilumai (žr. 24 pav.). Prietaisai neįkapsuliuoti, nuolat apšviečiami ir laikyti kambario temperatūroje 500 valandų, esant 12 % santykinei drėgmei. Po 500 valandų įrenginys su naujai susintetintu junginiu išlaikė 95 % savo pradinio efektyvumo, o Spiro-OMeTAD našumo rodmenys nukrito iki 85 %.

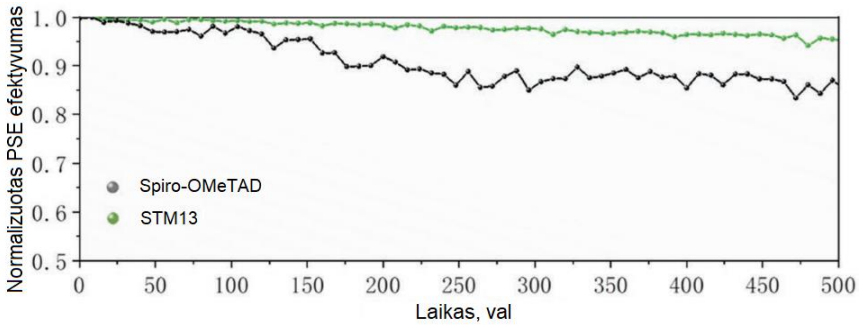

24 pav. Perovskitinių saulės elementų su puslaidininkiais **STM13** ir Spiro-OMeTAD stabilumų tyrimų rezultatai

Šiame skyriuje buvo aprašytos fluoreno pagrindo D-A-D tipo skylių transportinės medžiagos, kurių sintezei naudotos paprastos kondensacijos reakcijos. Atlikus terminius, optinius, fotofizikinius ir fotovoltinius matavimus nustatyta, kad malono nitrilas kaip akceptorius organinio puslaidininkio struktūroje buvo naudingas ne tik skylių transportui, bet ir PSE efektyvumui ir stabilumui. Iš organinio puslaidininkio **STM13** sukonstruoto įrenginio efektyvumas ir stabilumas buvo

geresni nei palyginamojo Spiro-OMeTAD. Šio tyrimo rezultatai parodė, kad paprastų skylių transportinių medžiagų molekulinė inžinerija prisidėjo prie reikšmingų PSE stabilumo ir efektyvumo patobulinimų.

3.4. Spirobisindano centrinį fragmentą turinčių enaminų sintezė ir panaudojimas perovskitiniuose saulės elementuose

Šis skyrius yra parašytas remiantis publikuotu straipsniu: „Design, Synthesis and Theoretical Simulations of Novel Spiroindane-Based Enamines as *p*-Type Semiconductors“, *R. Soc. Open Sci.*, 2024, 11, 232019, Š. Daškevičiūtė-Gegužienė, M. Daškevičienė, K. Kantminienė, V. Jankauskas, E. Kamarauskas, A. Gruodis, S. Karazhanov, V. Getautis.

Kaip jau buvo minėta, šiuo metu PSE kaip etaloninė STM yra naudojamas organinis puslaidininkis Spiro-OMeTAD. Šis junginys neturi stabilios amorfinės būsenos, todėl prietaiso veikimo metu vyksta terminis perėjimas iš amorfinės į kristalinę fazę. Šis virsmas yra sąlygotas didelės spirobifluoreno šerdies simetrijos. Tokia tendencija riboja puslaidininkio gebėjimą formuoti plėveles ir neigiamai veikia ilgalaikį PSE įrenginio stabilumą. Norint, kad junginys turėtų stabilią amorfinę būseną, reikia centrinį spirobifluoreno fragmentą pakeisti mažesne simetrija pasižyminčiu spirobisindanu (žr. 25 pav.).

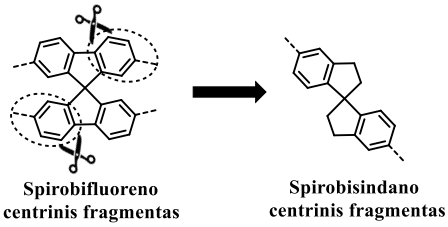

25 pav. Spirobifluoreno ir spirobisindano centrinių fragmentų struktūros

Šiame skyriuje aprašomi du nauji organiniai puslaidininkiai **STM15** ir **STM16**, turintys spirobisindano fragmentą molekulės centre (žr. 26 pav.). Nauji junginiai buvo gauti iš komerciškai prieinamų medžiagų, atsisakant brangių metalų katalizatorių ir panaudojant skirtingai substituotus anilinus. Ištyrus termines savybes buvo nustatyta, jog puslaidininkiai egzistuoja tik amorfinės būsenos, todėl jie yra puiki alternatyva kristalintis linkusiam Spiro-OMeTAD.

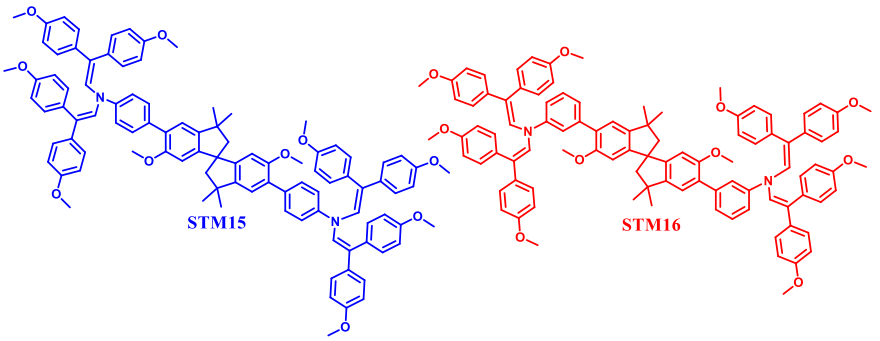

26 pav. Naujų organinių puslaidininkių **STM15** ir **STM16** struktūros

Bendra naujų STM **STM15** ir **STM16** sintezės procedūra parodyta 5 schemoje. Kaip pradinis reagentas naudotas pigus ir komerciškai prieinamas bisfenolis A. Pradiniame ciklizacijos etape jis buvo kaitinamas metansulfonrūgštyje. Gautas spirobisindanas **7** buvo alkilintas jodmetanu DMF-e, reakcijoje dalyvaujant kalio karbonatui. Atsisakius agresyvaus bromo išskirtas tarpinis junginys **8** buvo brominamas *N*-bromsukcinimidu. Šios trys sintezės stadijos atliktos pagal literatūroje žinomą metodiką[99]. Enaminų pirmtakai **10** ir **11** su skirtingose padėtyse (*para*- ir *meta*-) esančiais benzeno pakaitais buvo gauti atliekant Suzuki kryžminio jungimo reakciją. Naudojant paprastą kondensacijos reakciją, kurios šalutinis produktas yra tik vanduo, pastariesiems pirmtakams reaguojant su 2,2-bis-(4-metoksifenil)acetaldehidu, reakcijoje dalyvaujant KSR, buvo susintetinti tiksliniai organiniai puslaidininkiai **STM15** ir **STM16**. Naujų junginių struktūros buvo patvirtintos ^{1}H ir ^{13}C BMR, masių spektroskopijų bei elementinės analizės metodais.

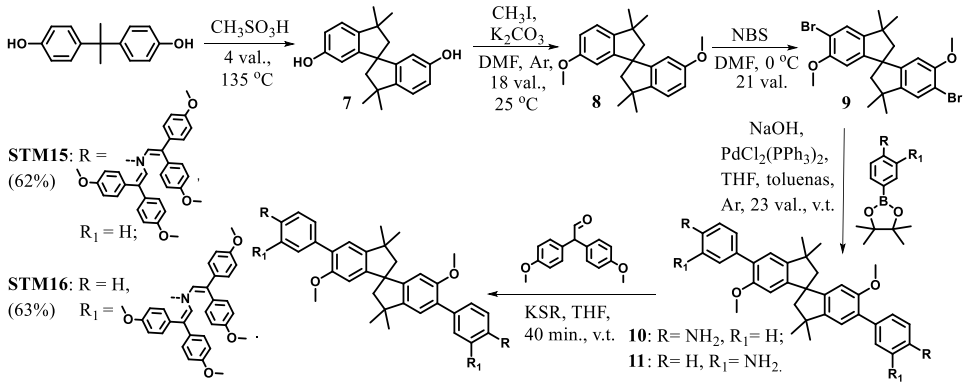

5 schema. Naujų puslaidininkių **STM15** ir **STM16** sintezės schema

Darbe buvo ištirtos naujai susintetintų STM optinės, terminės ir fotofizikinės savybės (žr. 17 lentelę) ir įvertintos jų panaudojimo galimybės PSE.

17 lentelė. Naujų puslaidininkių **STM15** ir **STM16** terminės, optinės ir fotofizikinės savybės

STM	T_{st} [a], °C	T_{sk} [a], °C	λ_{abs} [b], nm	λ_{em} [b], nm	I_P [c], eV	E_g [d], eV	E_{ea} [e], eV	μ_0 [f], cm^2 /Vs
STM15	167	403	265, 355	502	5,34	3,02	2,32	$9{,}0\times10^{-6}$
STM16	157	389	260, 335, 365	502	5,30	3,07	2,23	$2{,}6\times10^{-6}$

[a]Stiklėjimo (T_{st}) ir 5 % masės praradimo (T_{sk}) temperatūros, nustatytos iš DSK bei TGA kreivių (10 °C/min, N_2 atmosfera); [b]absorbcijos bei emisijos spektrų maksimumai (THF, 10^{-4} M); [c]jonizacijos potencialas, išmatuotas iš puslaidininkių plėvelių PESA metodu; [d]*Eg*, nustatytas iš medžiagų plėvelių absorbcijos bei emisijos spektrų susikirtimo; [e]$E_{ea} = I_P - E_g$; [f]dreifinio judrio reikšmės esant 0 elektrinio lauko stiprio reikšmei.

Atlikus TGA ir DSK tyrimus buvo įvertintos organinių puslaidininkių terminės charakteristikos. TGA analizė parodė, kad junginys **STM15** 5 % savo svorio masės praranda 403 °C temperatūroje ir turi didesnį terminį stabilumą nei analogas su metapakaitu **STM16** (T_{sk} = 389 °C). Pažymėtina, kad abiejų STM skilimo temperatūra yra daug aukštesnė nei Spiro-OMeTAD (T_{sk} = 288 °C[125]). Tikslinių junginių terminiams virsmams nustatyti buvo panaudotas DSK metodas. Iš DSK analizės rezultatų matyti, kad abu junginiai egzistuoja tik amorfinės būsenos. **STM15** ir **STM16** užfiksuotos stiklėjimo temperatūros atitinkamai yra 167 ir 157 °C. Svarbu tai, kad naujų STM T_{st} yra aukštesnės nei etaloninio Spiro-OMeTAD (T_{st} = 124 °C). Tai rodo, kad spirobisindano centrinį fragmentą turintys mažamolekuliniai junginiai gali turėti geresnį morfologinį stabilumą.

Spirobisindano centrinį fragmentą turinčių STM UV-RŠ spinduliuotės spektrai buvo užrašyti iš THF tirpalų (žr. 27 pav., a). Abu organiniai puslaidininkiai turi dvi pagrindines sugerties smailes, kurios yra ties ~265 ir ~360 nm. Absorbcijos smailė ties 265 nm atitinka lokalizuotus π-π^* elektronų perėjimus, atsiradusius dėl centrinio spirobisindano fragmento. O esant ~360 nm bangos ilgiui nevienodo intensyvumo smailės atsiranda dėl skirtingų pakaitų (*meta*- ir *para*-) delokalizacijos ir yra priskiriamos π-π^* ir n-π^* elektronų perėjimams. Atlikus valentinių elektronų sužadinimą buvo užrašyti FL spektrai (žr. 17 lentelę). Emisijos maksimumai abiejų junginių fiksuojami ties 502 nm. Pastebimi labai dideli Stokso poslinkiai (~150 nm) rodo, kad sužadinimo būsenos molekulėms yra būdingi reikšmingi geometriniai pokyčiai. **STM15** ir **STM16** draustinių energijų juostų (E_g) vertės buvo apskaičiuotos iš sugerties ir emisijos spektrų sankirtų ir atitinkamai yra 3,02 ir 3,07 eV (žr. 17 lentelę).

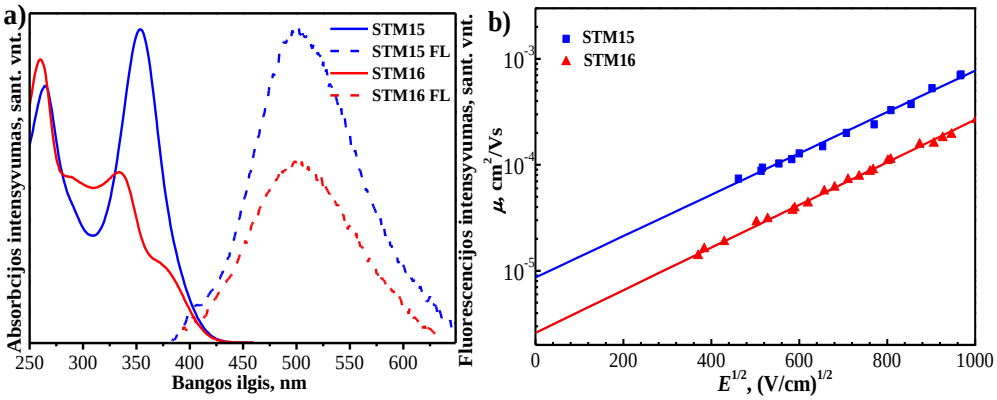

27 pav. Naujų organinių puslaidininkių **STM15** ir **STM16**: a) UV-RŠ spinduliuotės sugerties (ištisinė linija) ir fluorescencijos (punktyrinė linija) spektrai THF tirpiklyje (10^{-4} M); b) dreifinio judrio priklausomybė nuo elektrinio lauko stiprio

Norint nustatyti naujų STM energijos lygmenis, elektronų fotoemisijos ore metodu buvo išmatuoti jonizacijos potencialai (I_P) – HOMO energetiniai lygmenys. **STM15** ir **STM16** I_P reikšmės atitinkamai yra 5,34 ir 5,30 eV ir patenka į pageidaujamą STM HOMO lygmens verčių intervalą. LUMO energetinio lygmens vertės buvo nustatytos apskaičiavus E_{ea} (**STM15** 2,32 ir **STM16** 2,23 eV) (žr. 17 lentelę).

Kserografiniu laiko lėkio metodu buvo išmatuoti naujų organinių puslaidininkių teigiamų krūvių dreifiniai judriai. Eksperimentiniai duomenys, iliustruojantys skylių dreifinio judrio priklausomybę nuo elektrinio lauko stiprumo, yra pavaizduoti 27 pav., b. Junginio **STM15** silpname elektriniame lauke dreifinis judris lygus beveik 10^{-5} cm^2/Vs eilės, o jo metapakeisto analogo – **STM16** šiek tiek mažesnis (μ_0 = 2,6×10^{-6} cm^2/Vs).

Atlikus visus terminius, optinius ir fotofizikinius tyrimus bei išanalizavus gautus rezultatus galima teigti, kad mažamolekuliniai junginiai atitinka visus reikiamus parametrus, kad galėtų būti pritaikyti PSE gamyboje.

18 lentelė. Perovskitinių saulės elementų, kuriuose naudoti puslaidininkiai **STM15** ir **STM16**, fotovoltinės charakteristikos ir efektyvumai

STM	V_{OC}, V	J_{SC}, mA/cm^2	*FF*	PSE, %
STM15	1,11	22,6	0,66	16,4
STM16	1,10	22,3	0,60	14,7
Spiro-OMeTAD	1,09	22,8	0,77	19,1

Naujieji spirobisindano centrinį fragmentą turintys enaminai buvo panaudoti kaip teigiamus krūvininkus transportuojančios medžiagos *n-i-p* architektūros PSE. Elementų konstrukcija: ITO / SnO_2 / perovskitas – $Cs_{0,05}FA_{0,87}MA_{0,08}PbI_{2,76}Br_{0,24}$ / STM / Au. Visos PSE fotovoltinės charakteristikos susistemintos ir pateiktos 18 lentelėje. PSE su teigiamus krūvininkus transportuojančiu junginiu **STM15**

pasižymėjo perspektyviausiais rezultatais – efektyvumas siekė 16,4 %. Šis puslaidininkis termiškai patvaresnis nei Spiro-OMeTAD ir turi tik amorfinę būseną, todėl, tinkamai ištobulinus PSE gamybos sąlygas, jis gali būti perspektyvi etalono alternatyva.

3.5. Žaliosios chemijos principais susintetintų skylių transportinių medžiagų panaudojimas efektyviuose ir stabiliuose saulės elementuose ir moduliuose

Šis skyrius yra parašytas remiantis publikuotu straipsniu: „Green-Chemistry-Inspired Synthesis of Cyclobutane-Based Hole-Selective Materials for Highly Efficient Perovskite Solar Cells and Modules“, *Angew. Chem. Int. Ed.*, 2022, 61, e202113207, Š. Daškevičiūtė-Gegužienė, Y. Zhang, K. Rakštys, G. Kreiza, S. B. Khan, H. Kanda, S. Paek, M. Daškevičienė, E. Kamarauskas, V. Jankauskas, A. M. Asiri, V. Getautis, M. K. Nazeeruddin; cituota 20 kartų.

Šiame skyriuje aprašomos STM, kurių sintezei buvo panaudoti žaliosios chemijos principai, leidžiantys atsisakyti pavojingų ir agresyvių reagentų bei tirpiklių. Yra žinoma, kad fotodimerizuotas karbazolas yra gaunamas nesudėtingos žaliosios chemijos principais paremtos sintezės metu. Jo įvairūs dariniai pasižymi dideliu skylių dreifiniu judriu[140-142]. Todėl buvo susintetinti nauji organiniai puslaidininkiai, molekulės centre turintys ciklobutano fragmentą ir savo energetiniais lygmenimis tinkantys PSE gamybai (žr. 28 pav.).

Sistemingai buvo ištirta skirtingų karbazolo pakaitų įtaka naujų skylių transportinių medžiagų savybėms. Naujos ciklobutano pagrindu susintetintos STM buvo išbandytos konstruojant saulės elementus. Pasiektas 21 % efektyvumas ir pagerintas prietaiso stabilumas, palyginti su Spiro-OMeTAD. Taip pat naudojant puslaidininkį **STM22** buvo pagamintas perovskitinis saulės modulis (6,5 cm × 7 cm), kurio efektyvumas viršijo 19 % ir tuo metu buvo rekordinis tokio ploto moduliams.

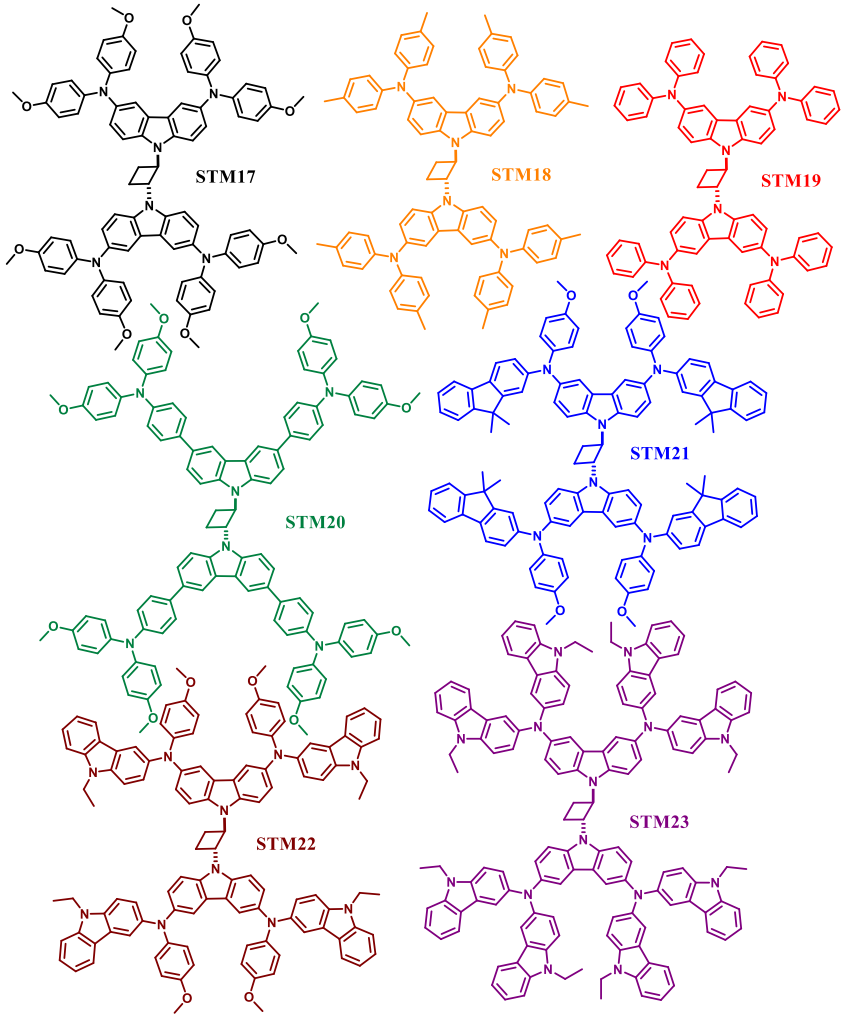

28 pav. Naujų fotodimerizuoto karbazolo pagrindu susintetintų skylių transportinių medžiagų struktūros

Bendra žaliosios chemijos principais susintetintų ciklobutano pagrindu pagamintų STM sintezės procedūra parodyta 6 schemoje. Kaip pradinis reagentas naudotas pigus ir komerciškai prieinamas 9-vinilkarbazolas. Jo fotodimerizacija lengvai vyko kambario temperatūroje, naudojant UV spinduliuotę ir reakciją vykdant acetono tirpiklyje. Gautas *trans*-1,2-bis(9-karbazolil)ciklobutanas **(12)** buvo brominamas, naudojant vandeninį kalio bromato ir bromido tirpalą, taip atsisakant agresyvaus bromo. Toliau vandens ir THF mišinyje buvo atliekama Suzuki kryžminio jungimo reakcija ir išskirta tikslinė skylių transportinė medžiaga **STM20**. Šie trys sintezės žingsniai parodė, kad, norint gauti junginį **STM20,** galima pritaikyti žaliosios chemijos sintezės principus ir nebenaudoti pavojingų aplinkai bei žmogaus sveikatai medžiagų. Kitų šiame darbe aprašytų skylių transportinių medžiagų galutinei sintezės stadijai buvo naudotos standartinės Buchwaldo reakcijos sąlygos. Susintetintų

junginių struktūros buvo patvirtintos ^{1}H ir ^{13}C BMR spektroskopijos, masių spektrometrijos ir elementinės analizės metodais.

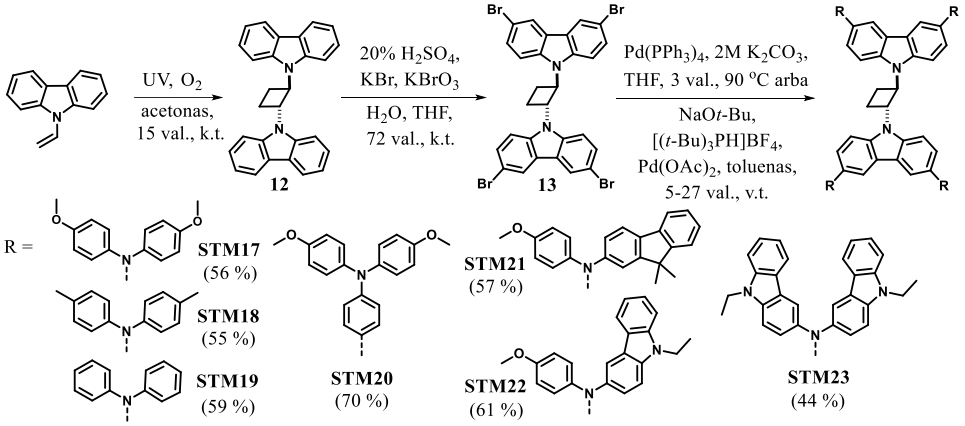

6 schema. Naujų žaliosios chemijos principais gautų puslaidininkių sintezės schema

Buvo atlikti susintetintų STM įvairūs terminiai, optiniai ir fotofizikiniai tyrimai (žr. 19 lentelę) ir įvertintos panaudojimo galimybės PSE.

19 lentelė. Naujų fotodimerizuoto karbazolo pagrindu susintetintų STM terminės, optinės ir fotofizikinės savybės

STM	T_{lyd} [a], °C	T_{st} [a], °C	T_{sk} [a], °C	λ_{abs} [b], nm	λ_{em} [b], nm	I_P [c], eV	E_g [d], eV	E_{ea} [e], eV	μ_0 [f], cm^2/Vs
STM17	–	122	416	291, 303	450	5,07	2,91	2,12	$7,9\times10^{-6}$
STM18	320	159	406	291, 304	435	5,37	2,98	2,48	$1,7\times10^{-4}$
STM19	–	162	382	289, 302	427	5,48	3,05	2,43	$3,3\times10^{-7}$
STM20	–	148	421	291, 306, 334	420	5,34	3,13	2,21	1×10^{-5}
STM21	–	157	432	291, 315, 354	445	5,28	2,93	2,35	$2,5\times10^{-5}$
STM22	–	173	439	291, 309	459	4,77	2,83	1,94	$3,5\times10^{-5}$
STM23	–	215	477	291, 318	471	4,78	2,79	1,99	$2,5\times10^{-6}$

[a]Lydymosi (T_{lyd}), stiklėjimo (T_{st}) ir 5 % masės praradimo (T_{sk}) temperatūros, nustatytos iš DSK bei TGA kreivių (10 °C/min, N_2 atmosfera); [b]absorbcijos bei emisijos spektrų maksimumai (THF, 10^{-4} M); [c]jonizacijos potencialas, išmatuotas iš puslaidininkių plėvelių PESA metodu; [d]*Eg*, nustatytas iš medžiagų plėvelių absorbcijos bei emisijos spektrų susikirtimo; [e]$E_{ea} = I_P - E_g$; [f]dreifinio judrio reikšmės esant 0elektrinio lauko stiprio reikšmei.

Iš termogravimetrinės analizės rezultatų matyti, kad STM 5 % masės nuostoliai atsiranda ties 380–480 °C, o tai yra daug aukštesnė temperatūra už įprastinio įrenginio veikimo temperatūrą (žr. 19 lentelę). Matoma akivaizdi tendencija – kuo didesnė molekulinė masė, tuo didesnė ir terminio skilimo temperatūra. DSK matavimai parodė, kad visi nauji junginiai yra amorfiniai, išskyrus puslaidininkį **STM18**, kuris turi tiek amorfinę, tiek kristalinę būseną. Svarbu tai, kad visos naujai susintetintos skylių transportinės medžiagos turi didesnes stiklėjimo temperatūras nei Spiro-OMeTAD (124 °C). Tai reiškia, kad nauji organiniai puslaidininkiai su ciklobutano fragmentu turėtų turėti geresnį morfologinį stabilumą.

Nustačius, kad junginys **STM18** turi kristalinę būseną, buvo išaugintas šio puslaidininkio monokristalas rentgeno kristalografinei ciklobutano konfigūracijai nustatyti. Kristalas buvo auginamas acetono ir chloroformo mišinyje 7 °C temperatūroje. 29 pav., a, matyti, kad dviejų karbazolo chromoforų, prisijungusių prie ciklobutano centrinio fragmento, ryšio kampai (119° ir -119°) identifikavo molekulės *trans*-konfigūraciją. Išmatuotas 98° kampas tarp dviejų karbazolo fragmentų įrodė pseudospiro konformaciją (žr. 29 pav., b). 29 pav., c, matomos kampų vertės patvirtino, kad centrinis ciklobutano fragmentas nėra visiškai plokščias.

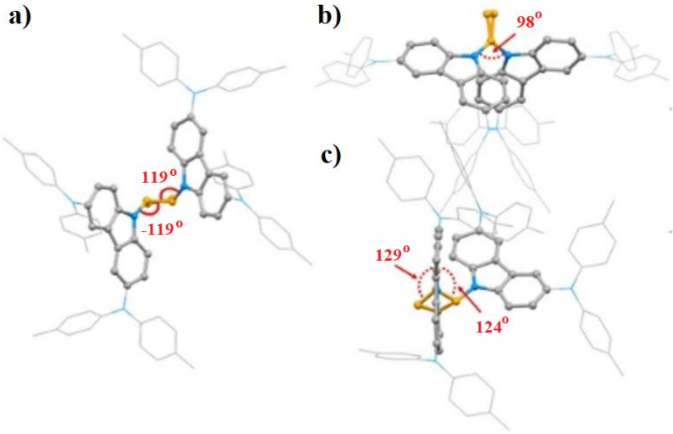

29 pav. Puslaidininkio **STM18** kristalografinė analizė

30 pav., a, pavaizduoti naujų STM optiniai tyrimai THF tirpaluose. Visi junginiai turi bent dvi pagrindines absorbcijos smailes. Ties 290 nm matomas absorbcijos maksimumas, atsiradęs dėl centrinio fragmento π-π^* valentinių elektronų šuolių. Absorbcijos smailių maksimumai, užfiksuoti srityje nuo 303 nm iki 354 nm, yra priskiriami n-π^* delokalizuotiems elektronų šuoliams. UV-RŠ spektrų skirtumų atsiranda dėl skirtingų konjuguotų pakaitų organiniuose puslaidininkiuose. FL spektrai parodė, kad visų medžiagų atveju yra matomi reikšmingai dideli Stokso poslinkiai (100–150 nm), todėl sužadinimo būsenoje galima tikėtis molekulių geometrinių pokyčių. Draustinių energijų juostų (E_g) vertės buvo apskaičiuotos iš sugerties ir emisijos spektrų susikirtimo vietos ir jos varijuoja 2,79–3,13 eV (žr. 19 lentelę).

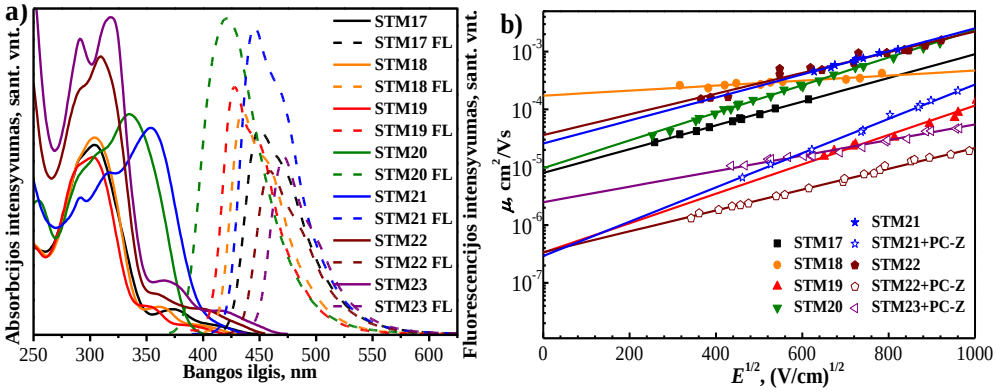

30 pav. Naujų fotodimerizuoto karbazolo pagrindu susintetintų puslaidininkių: a) UV-RŠ spinduliuotės sugerties (ištisinė linija) ir fluorescencijos (punktyrinė linija) spektrai THF tirpiklyje (10^{-4} M); b) dreifinio judrio priklausomybė nuo elektrinio lauko stiprio

Naudojant elektronų fotoemisijos ore metodą buvo išmatuotas organinių puslaidininkių HOMO energetinis lygmuo. Visų junginių I_P vertės svyravo 4,7–5,5 eV (žr. 19 lentelę). Remiantis I_P ir E_g duomenimis buvo apskaičiuotos elektronų gimiringumo vertės (E_{ea}), kurios kito 1,9–2,5 eV diapazone. Šios vertės taip pat nurodo ir LUMO energijos lygmenį. Jis turi būti mažesnis nei perovskito sluoksnio laidumo juosta (4,1 eV), kad būtų užtikrinamas elektronų pernašos blokavimas iš perovskito į elektrodą.

Naujų STM dreifinių judrių priklausomybė nuo elektrinio lauko stiprumo parodyta 30 pav., b. **STM18** pasižymėjo didžiausiu dreifiniu judriu silpnuosiuose elektriniuose laukuose (μ_0 = 1,7×10^{-4} cm^2/Vs) ir pranoksta Spiro-OMeTAD (μ_0 = 1,3×10^{-4} cm^2/Vs)[129]. Junginiai **STM20**, **STM21** ir **STM22** pasižymėjo viena eile mažesnėmis μ_0 dreifinių judrių vertėmis.

Atlikus visus reikalingus STM tyrimus buvo sukonstruoti *n-i-p* struktūros prototipiniai saulės elementai. Konstrukciją sudarantys sluoksniai: FTO / SnO_2 / perovskitas – $(FAPbI_3)_{0,85}(MAPbBr_3)_{0,15}$ / STM / Au. Konstruojant prietaisus optimizuotos puslaidininkių tirpalų koncentracijos. Sluoksnio storis elementuose buvo 100 nm, o Spiro-OMeTAD – 200 nm. **STM22** ir etalono energijos konversijos efektyvumai buvo labai panašūs, atitinkamai 21 % ir 21,64 %. Dideliu įrenginių efektyvumu taip pat pasižymėjo ir junginiai **STM17** (19,11 %) bei **STM20** (18,53 %). Deja, bet PSE su puslaidininkiais **STM18** ir **STM19** pasižymėjo labai mažu konversijos efektyvumu. Tai gali būti dėl gana žemo šių junginių HOMO lygmens. Be to, yra pastebimos ir labai mažos įrenginio užpildymo faktoriaus reikšmės (žr. 20 lentelę).

20 lentelė. Perovskitinių saulės elementų, kuriuose naudoti fotodimerizuoto karbazolo pagrindu susintetinti puslaidininkiai, fotovoltinės charakteristikos ir efektyvumai

STM	V_{OC}, V	J_{SC}, mA/cm^2	*FF*	PSE, %
STM17	1,073	24,01	0,750	19,11
STM18	0,942	6,49	0,198	1,21
STM19	0,506	12,00	0,217	1,32
STM20	1,057	24,22	0,752	18,53
STM21	1,061	21,11	0,693	15,26
STM22	1,092	24,38	0,791	21,00
STM23	0,927	22,99	0,584	12,44
Spiro-OMeTAD	1,114	24,17	0,803	21,64

Buvo įvertintas **STM22** ir **Spiro-OMeTAD** pagrindu sukonstruotų elementų stabilumas. Eksperimentas vyko aplinkos sąlygomis 550 valandų, esant santykinei drėgmei 15–20 %. Etaloniniame įrenginyje, kuriame kaip STM naudotas Spiro-OMeTAD, konversijos efektyvumas sumažėjo daugiau nei 1,5 %, o **STM22** pagrindu veikiančiame įrenginyje beveik nepastebėta jokio pokyčio (žr. 31 pav.).

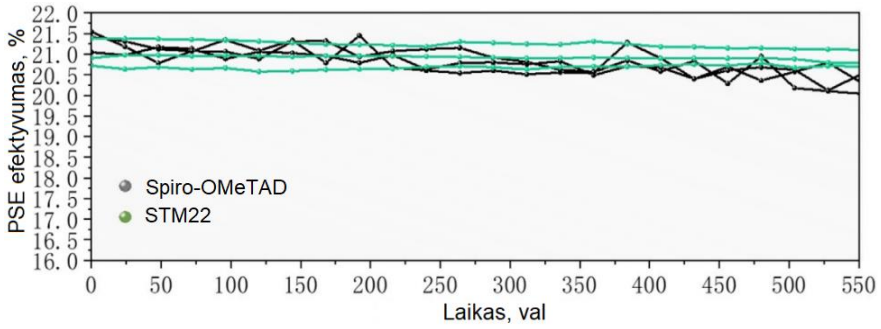

31 pav. Perovskitinių saulės elementų su **STM22** ir Spiro-OMeTAD stabilumų tyrimų rezultatai

Visuomet svarbiu aspektu saulės elementų gamyboje išlieka komercializavimo klausimas. Laboratorijos sąlygomis gavus puikius PSE prietaiso su puslaidininkiu **STM22** efektyvumo rezultatus buvo nuspręsta sukonstruoti prototipinius 6,5 × 7 cm dydžio saulės elemento modulius. Būtent iš tokio dydžio modulių yra konstruojamos saulės celės pramoninėje gamyboje. Modulio efektyvumas siekė 19,06 %. Pasiektas rekordinis rezultatas, nes tuo metu tai buvo didžiausias užfiksuotas saulės modulio efektyvumas ne Spiro-OMeTAD klasės junginiuose.

Šio tyrimo rezultatai patvirtina galimybę sėkmingai vystyti perovskitinių saulės elementų gamybos technologijas, naudojant ekologiškomis sąlygomis gautus puslaidininkius.

V-serijos organinių puslaidininkių praktinę svarbą liudija keturios tarptautinės patentinės paraiškos „Photovoltaic Devices Containing Cyclobutane-Based Hole Transporting Materials“, kurios priimtos skirtinguose patentų biuruose – JAV (US2023157158), Japonijos (JP2023072638), Kinijos (CN116133444) ir Europos (EP4181225).

3.6. Tinklintis galinčių skyles transportuojančių medžiagų su karbazolilchromoforais sintezė bei panaudojimas invertuotos struktūros perovskitiniuose saulės elementuose

Šis skyrius yra parašytas remiantis publikuotu straipsniu: „Cross-linkable carbazole-based hole transporting materials for perovskite solar cells“, *Chem. Commun.*, 2022, 58, 7495-498, Š. Daškevičiūtė-Gegužienė, A. Magomedov, M. Daškevičienė, K. Genevičius, N. Nekrašas, V. Jankauskas, K. Kantminienė, M. D. McGehee, V. Getautis; cituota 6 kartus. Šio numerio žurnalo „Chemical Communications“ viršelis buvo iliustruotas pastarojo straipsnio tematika.

Šiame skyriuje yra aprašomos naujos STM, kurios buvo panaudotos konstruojant vis labiau populiarėjančius atvirkštinės konfigūracijos (*p*-*i*-*n*) perovskitinius saulės elementus. Šiuo atveju *p*-tipo puslaidininkis padengiamas prieš perovskito sluoksnį, todėl privalo būti atsparus DMSO:DMF tirpiklių mišiniui, kuris naudojamas liejant šviesą absorbuojantį sluoksnį. Būtent dėl šios priežasties dažniausiai yra naudojamos polimerinės medžiagos, ypač galinčios sudaryti tirpikliams atsparias 3D struktūras. Tam tikslui šiame darbe buvo susintetinti du nauji karbazolilchromoforus ir vinilgrupes turintys junginiai (žr. 32 pav.).

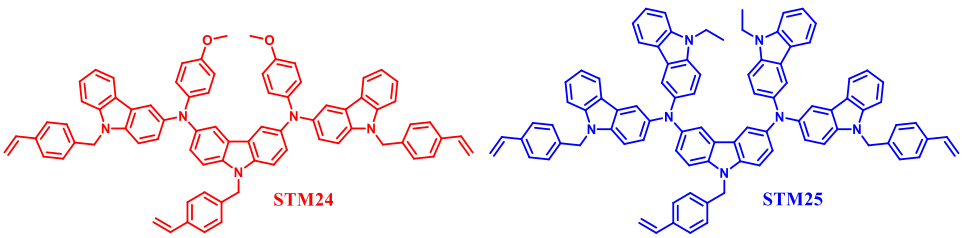

32 pav. Polimerintis galinčių puslaidininkių **STM24** ir **STM25** struktūros

Bendra naujų polimerintis galinčių STM sintezės eiga parodyta 7 schemoje. Kaip pradiniai reagentai buvo pasirinkti komerciškai prieinami 3-brom-9*H*-karbazolas ir 3,6-dibrom-9*H*-karbazolas. Naudojant alkilinimo metodiką buvo susintetinti tarpiniai junginiai **14** ir **16**, turintys vinilgrupes. Tuomet buvo atliktos Buchwaldo paladžio katalizuojamos reakcijos. Junginys **14** buvo sujungtas su *p*-anizidinu ir gautas antrinis aminas **15**, kuris toliau reagavo su pirmtaku **16**, susidarant tiksliniam junginiui **STM24** su trimis polimerintis galinčiomis vinilgrupėmis. 3-amino-9-etilkarbazolui reaguojant su junginiu **14** susidarė antrinis aminas **17**, kurį prijungus prie pirmtako **16** buvo išskirtas antras tikslinis junginį **STM25**. Susintetintų

junginių struktūros buvo patvirtintos ^{1}H ir ^{13}C BMR spektroskopijos bei elementinės analizės metodais.

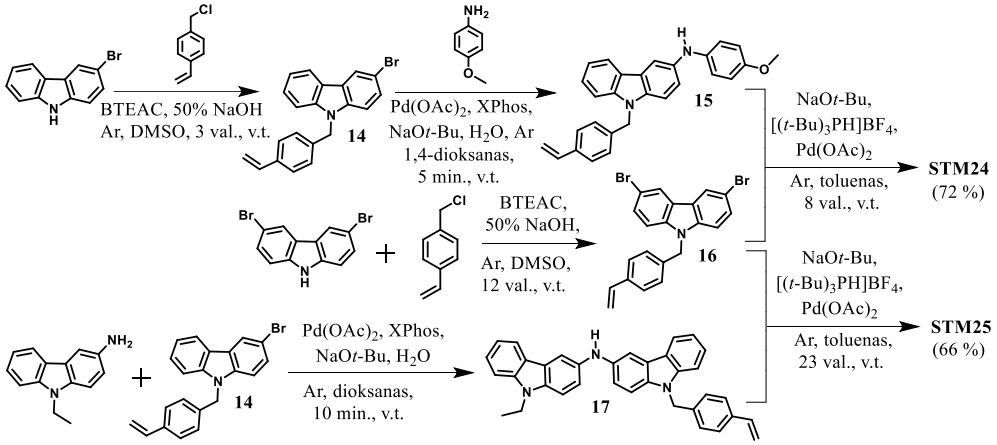

7 schema. Naujų puslaidininkių su vinilgrupėmis **STM24** ir **STM25** sintezės schema

Buvo atlikti naujų STM terminiai, optiniai ir fotofizikiniai tyrimai (žr. 21 lentelę) ir įvertintos jų panaudojimo galimybės *p-i-n* konfigūracijos PSE.

21 lentelė. Organinių puslaidininkių **STM24** ir **STM25** terminės, optinės ir fotofizikinės savybės

STM	T_{st} [a], °C	T_{poli} [a], °C	T_{sk} [a], °C	λ_{abs} [b], nm	λ_{em} [b], nm	I_P [c], eV	E_g [d], eV	E_{ea} [e], eV	μ_0 [f], cm^2/Vs
STM24	117	196	443	295, 309	458	4,84	2,90	1,94	$1,8\times10^{-6}$
STM25	56	300	404	291, 319	470	4,82	2,84	1,98	$2,4\times10^{-5}$

[a]Stiklėjimo (T_{st}), polimerizacijos (T_{poli}) ir 5 % masės praradimo (T_{sk}) temperatūros, nustatytos iš DSK bei TGA kreivių (10 °C/min, N_2 atmosfera); [b]absorbcijos bei emisijos spektrų maksimumai (THF, 10^{-4} M); [c]jonizacijos potencialas, išmatuotas iš puslaidininkių plėvelių PESA metodu; [d]*Eg*, nustatytas iš medžiagų plėvelių absorbcijos bei emisijos spektrų susikirtimo; [e]$E_{ea} = I_P - E_g$; [f]Dreifinio judrio reikšmės esant 0 elektrinio lauko stiprio reikšmei.

Termogravimetrinės analizės rezultatai parodė, kad abiejų junginių terminis stabilumas yra pakankamai aukštas – puslaidininkio **STM24** 5 % masės nuostoliai atsiranda ties 443 °C**,** o junginio **STM25** – ties 404 °C (žr. 21 lentelę). Atlikus DSK analizę buvo nustatyta, kad tiksliniai junginiai yra amorfiniai ir pirmojo kaitinimo metu buvo užfiksuotos polimerizacijos temperatūros. Mažesnės molekulinės masės junginys **STM24** polimerinasi 196 °C temperatūroje, o analogo su didesne konjuguota dvigubų ryšių sistema tinklinimosi procesas pastebimas ties 300 °C temperatūra. Antrojo kaitinimo metu jokių virsmų nepastebėta, todėl galima teigti, kad tinklinimosi procesai iki galo įvyko pirmo kaitinimo metu (žr. 33 pav., a). Svarbu paminėti, kad

šis tinklinimo procesas vyksta be papildomų iniciatorių ar priedų, kurie turėtų įtakos SE efektyvumui ar stabilumui (žr. 8 schemą).

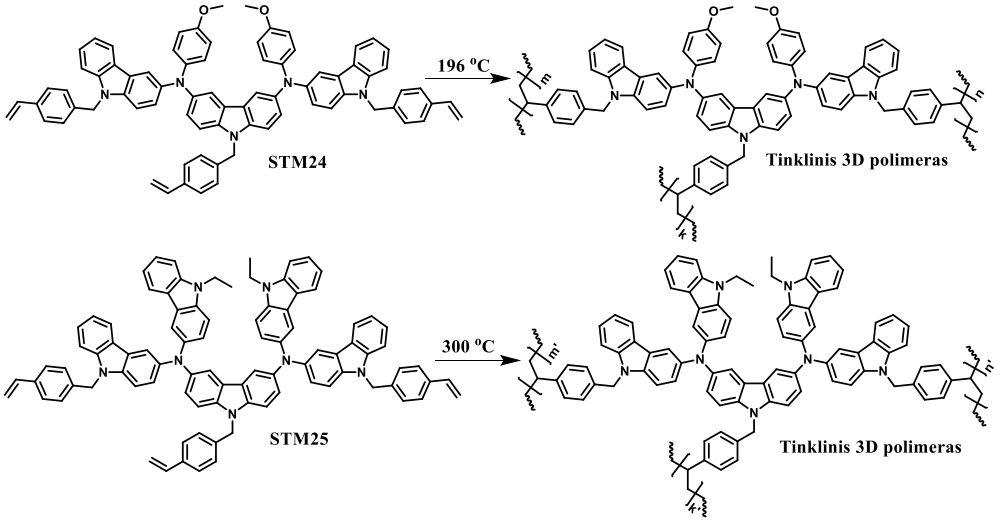

8 schema. Organinių puslaidininkių **STM24** ir **STM25** polimerizacijos schema

Norint įvertinti susintetintų puslaidininkių optines savybes, buvo užrašyti UV-RŠ absorbcijos ir FL emisijos spektrai iš tirpalų (žr. 33 pav., b). Jie parodė, kad abiejų monomerų absorbcijos maksimumai yra UV srityje ~ 320 nm, o sugertis RŠ elektromagnetinės spinduliuotės diapazone labai nereikšminga. Dėl didesnės konjuguotos sistemos junginio **STM25** absorbcijos ir emisijos maksimumai yra ~ 10 nm pasislinkę ilgesniųjų bangų link.

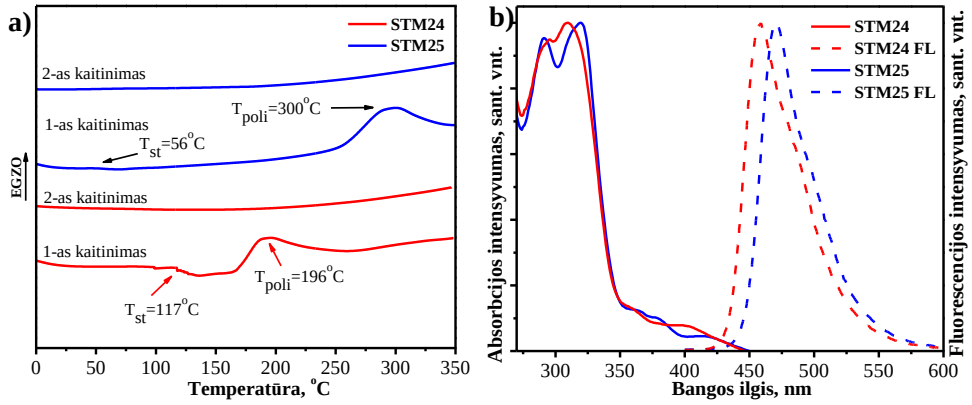

33 pav. Naujų organinių puslaidininkių **STM24** ir **STM25**: a) UV-RŠ spinduliuotės sugerties (ištisinė linija) ir fluorescencijos (punktyrinė linija) spektrai THF tirpiklyje (10^{-4} M); b) diferencinės skenuojamosios kalorimetrijos kreivės (10 °C/min, N_2 atmosfera)

Elektronų fotoemisijos ore metodu buvo išmatuoti mažamolekulinių junginių **STM24** ir **STM25** jonizacijos potencialai, kurie atitinkamai yra lygūs 4,84 ir 4,82 eV.

Dreifinis judris buvo išmatuotas kserografiniu laiko lėkio metodu. Junginio **STM24** silpname elektriniame lauke jis siekė $1{,}8\times10^{-6}$ cm^2/Vs, o analogo su didesne konjuguota sistema **STM25** – $2{,}4\times10^{-5}$ cm^2/Vs (žr. 21 lentelę).

Prieš konstruojant SE su tiksliniais monomerais **STM24** ir **STM25** buvo atlikti terminio tinklinimo eksperimentai. Bandymo pradžioje ant stiklinių plokštelių suformuojamas junginio sluoksnis ir kaitinama medžiagos polimerizacijos temperatūroje (**STM24** – 200 °C, **STM25** – 300 °C) skirtingą laiko tarpą (0, 30, 60, 90, 120 min). Po atkaitinimo visos plokštelės yra pamerkiamos į THF, kuris nuplauna nesusipolimerinusią medžiagos dalį, o 3D polimerinis sluoksnis lieka ant plokštelės. Iš gautų THF tirpalų užrašomi UV-RŠ sugerties spektrai 3D polimerizacijos konversijai įvertinti. **STM24** junginys susipolimerina per 90 min (žr. 34 pav., a), o aukštesnėje temperatūroje polimerintas **STM25** per vieną valandą (žr. 34 pav., b).

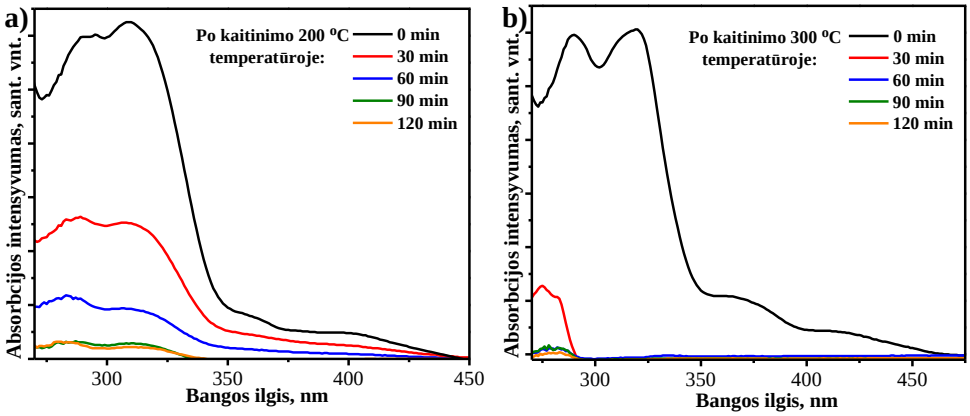

34 pav. STM24 (a) ir **STM25** (b) terminės polimerizacijos tyrimo UV-RŠ sugerties spektrai

Sutinklinti polimerai buvo panaudoti konstruojant *p-i-n* struktūros saulės elementus. Konstrukciją sudaro: ITO / polimeras STM arba monomeras STM / perovskitas – $Cs_{0,05}(FA_{0,83}MA_{0,17})_{0,95}Pb(I_{0,83}Br_{0,17})_3$ / LiF / C_{60} / BCP / Ag. Visos PSE fotovoltinės charakteristikos susistemintos ir pateiktos 22 lentelėje. Pastebima tendencija, kad 3D polimerų pagrindu sukonstruoti SE pasižymi aukštesniais šviesos konversijos efektyvumo rezultatais. Su junginiu **STM24** gauti perspektyviausi rezultatai – efektyvumas siekė 16,9 %. Monomeriniai puslaidininkiai dažniausiai nėra tinkami *p-i-n* konstrukcijos SE formuoti, nes būna neatsparūs DMSO:DMF tirpiklių mišiniui, kuris reikalingas perovskitui padengti. Atlikti monomerinių STM tirpumo tyrimai parodė, kad monomeras **STM24** yra dvigubai tirpesnis nei jo analogas **STM25**, todėl pastarojo pagrindu pagaminto SE efektyvumo rezultatai yra nepalyginti didesni.

22 lentelė. Perovskitinių saulės elementų, kuriuose naudoti puslaidininkiai **STM24** ir **STM25**, fotovoltinės charakteristikos ir efektyvumai

STM	V_{OC}, V	J_{SC}, mA/cm^2	*FF*	PSE, %
STM24 monomeras	0,285	15,6	0,251	1,1
STM24 polimeras	0,979	20,6	0,844	16,9
STM25 monomeras	0,819	18,6	0,808	11,8
STM25 polimeras	0,944	19,0	0,823	14,6

Buvo įvertintas **STM24** 3D polimero pagrindu sukonstruoto saulės elemento stabilumas. Eksperimentas truko 30 dienų aplinkos sąlygomis kambario temperatūroje. Prietaisas pasirodė stabilus ir eksperimento pabaigoje jo veikimo efektyvumas sumažėjo tik 3 %.

Apibendrinant galima pasakyti, kad dvi naujos karbazolo pagrindu susintetintos STM **STM24** ir **STM25** pasižymėjo paprasta sinteze, geru terminiu stabilumu, aukštu skylių dreifiniu judriu ir tinkamu HOMO lygmeniu. Dėl trijų vinilo grupių puslaidininkiai gali dalyvauti 3D polimerinimo procese. Po terminės polimerizacijos junginių plėvelės tampa atsparios organiniams tirpikliams, todėl jie yra perspektyvūs *p-i-n* konstrukcijos perovskitinių saulės elementų gamyboje.

3.7. Tinklintis galinčio puslaidininkio, turinčio spirobifluoreno centrinį fragmentą, sintezė bei panaudojimas skirtingų konfigūracijų perovskitiniuose saulės elementuose

Šis skyrius yra parašytas remiantis publikuotu straipsniu: „In situ thermal cross-linking of 9,9′-spirobifluorene-based hole-transporting layer for perovskite solar cells“, *ACS Appl. Mater. Interfaces*, 2024, 16, 1, 1206-1216, Š. Daškevičiūtė-Gegužienė, M. A. Truong, K. Rakštys, M. Daškevičienė, R. Hashimoto, R. Murdey, T. Yamada, Y. Kanemitsu, V. Jankauskas, A. Wakamiya, V. Getautis.

Šiame skyriuje aprašomos naujai susintetinto etaloninio Spiro-OMeTAD analogo **STM26** (žr. 35 pav.) panaudojimo galimybės skirtingų konstrukcijų (*n-i-p* ir *p-i-n*) naujos kartos PSE.

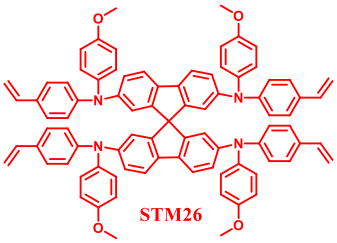

35 pav. Naujo Spiro-OMeTAD analogo su polimerintis galinčiomis grupėmis struktūra

Spiro-OMeTAD analogas **STM26** su keturiomis erdviniame tinklinime galinčiomis dalyvauti vinilgrupėmis buvo gautas išbandžius skirtingas reakcijų schemas ir sąlygas. Pirmuoju būdu naudota daugiapakopė sintezė (žr. 9 schemą). Pirmoje reakcijos stadijoje naudojant komercinius junginius 2-(4-bromofenil)-1,3-dioksolaną ir *p*-anizidiną Buchwaldo reakcijos metu buvo išskirtas aminas **18**, turintis užblokuotą aldehidinę grupę. Reakcijos metu susidarė pašalinių produktų, kurie apsunkino šio junginio kolonėlinės chromatografijos gryninimo procedūrą, o galutinė tarpinio junginio išeiga siekė vos 40 %. Taip pat buvo pastebėta, kad junginys ilgainiui atmosferos sąlygomis tampa nestabilus. Kitame sintezės etape gautas junginys **18** paladžiu katalizuojamos Buchwaldo reakcijos sąlygomis buvo prijungtas prie centrinio 2,2‘,7,7‘-tetrabrom-9,9‘-spirobifluoreno fragmento. Išskirtas tarpinis junginys **19** su keturiomis užblokuotomis aldehidinėmis ir metoksigrupėmis. Trečiajame etape naudojant 10 % HCl tirpalą vykdyta Boc- apsauginės grupės numušimo reakcija. Pastaroji įvyko per 20 min. kambario temperatūroje, išskiriant keturias aldehidines grupes turintį tarpinį junginį **20**. Wittigo reakcijos metu, naudojant natrio hidridą ir katalizatorių, per 23 val. visos aldehidinės grupės buvo transformuotos į keturias polimerintis galinčias vinilgrupes, susintetinant Spiro-OMeTAD analogą **STM26**.

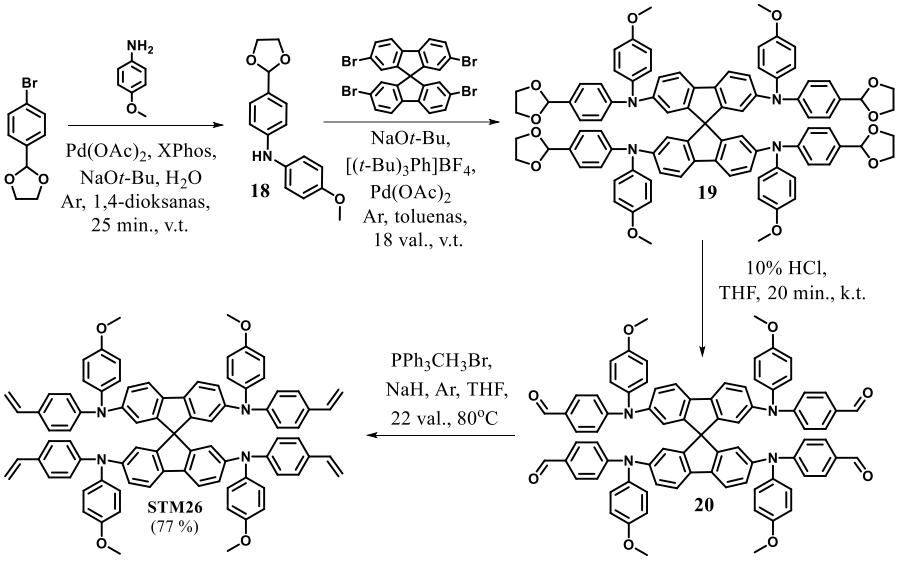

9 schema. Organinio puslaidininkio su vinilgrupėmis **STM26** sintezės schema

Kadangi aukščiau aprašytas polimerintis galinčio Spiro-OMeTAD anlogo sintezės būdas pareikalavo daug laiko ir didelių gamybos kaštų, buvo išbandytas dviejų pakopų sintezės metodas (žr. 10 schemą). Naudojant komercines pradines medžiagas – 2,2‘,7,7‘-tetrabrom-9,9‘-spirobifluoreną ir *p*-anizidiną, Buchwaldo reakcijos sąlygomis buvo gautas tarpinis junginys **21** su 70 % išeiga. Pastarajam identiškomis reakcijos sąlygomis reaguojant su 4-bromstirenu, buvo išskirtas tikslinis keturias nesočias bei polimerintis galinčias vinilgrupes turintis puslaidininkis **STM26**

su 51 % išeiga. Tikslinio junginio **STM26** gausinimui buvo pasirinktas būtent šis vos dviejų pakopų sintezės kelias.

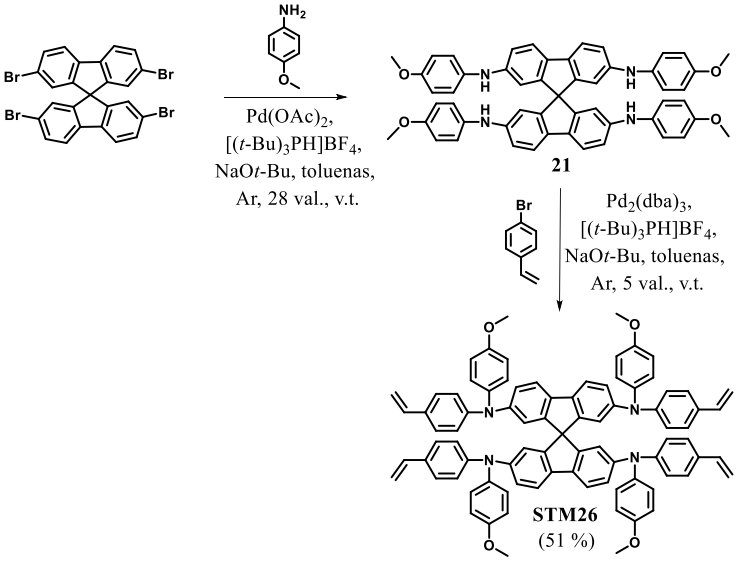

10 schema. Spiro-OMeTAD analogo su vinilgrupėmis **STM26** sintezės schema

Susintetintų junginių struktūros buvo patvirtintos ^{1}H ir ^{13}C BMR, masių spektroskopijos ir elementinės analizės būdais. Apskaičiuota bendra naujojo puslaidininkio kaina ~ 42 Eur/g yra daug mažesnė nei kitų plačiai naudojamų STM[143]. Tai rodo šio junginio didelį komercinį potencialą.

Buvo atlikti terminiai, optiniai ir fotofizikiniai tyrimai (žr. 23 lentelę).

23 lentelė. Puslaidininkio **STM26** terminės, optinės ir fotofizikinės savybės

STM	T_{poli} [a], °C	T_{sk} [a], °C	λ_{abs} [b], nm	λ_{em} [b], nm	I_P [c], eV	μ_0 [d], cm^2/Vs
STM26	253, 265	460	336, 395	419	5,29	$8,7\times10^{-5}$
STM26 po kaitinimo 255 °C temperatūroje	-	-	335, 394	-	5,38	$1,3\times10^{-5}$
STM26 + ditiolis po kaitinimo 103 °C temperatūroje	-	-	303, 383	-	5,35	$1,3\times10^{-5}$

[a]Polimerizacijos (T_{poli}) ir 5 % masės praradimo (T_{sk}) temperatūros, nustatytos iš DSK bei TGA kreivių (10 °C/min, N_2 atmosfera); [b]absorbcijos bei emisijos spektrų maksimumai (THF, 10^{-4} M); [c]jonizacijos potencialas, išmatuotas iš puslaidininkių plėvelių PESA metodu; [d]dreifinio judrio reikšmės esant 0 elektrinio lauko stiprio reikšmei.

TGA rezultatai parodė, kad puslaidininkio 5 % masės nuostolių atsiranda ties 460 °C. Tai rodo gerą terminį stabilumą, nes junginio skilimo temperatūra yra daug

aukštesnė nei įprastinė įrenginio veikimo temperatūra. Atlikus DSK analizę buvo nustatyta tikslinio monomero polimerizacijos temperatūra. Pirmojo kaitinimo metu užfiksuota, kad STM polimerinasi ties 253 °C temperatūra. Antrojo kaitinimo metu jokių virsmų nepastebėta, todėl galima teigti, kad polimerizacijos procesas iki galo įvyko pirmo kaitinimo metu (žr. 36 pav., a). Yra žinoma, kad aukštesnė nei 150 °C temperatūra sukelia perovskito destrukciją, o tai neigiamai veikia *n-i-p* konstrukcijos prietaiso efektyvumą. Deja, tikslinio **STM26** monomero polimerizacijos temperatūra yra aukštesnė, negu perovskitas gali toleruoti. Mokslinėje literatūroje yra duomenų, jog vykdant kopolimerizaciją su alifatiniais arba aromatiniais tioliais galima smarkiai sumažinti 3D polimero susidarymo temperatūrą[144]. Todėl buvo atlikta organinio puslaidininkio **STM26** ir 4,4‘-tiobisbenzentiolio (ditiolio) polimerizacijos reakcija, kurios metu susidarė C-S-C ryšius turintis 3D struktūros kopolimeras (žr. 11 schemą).

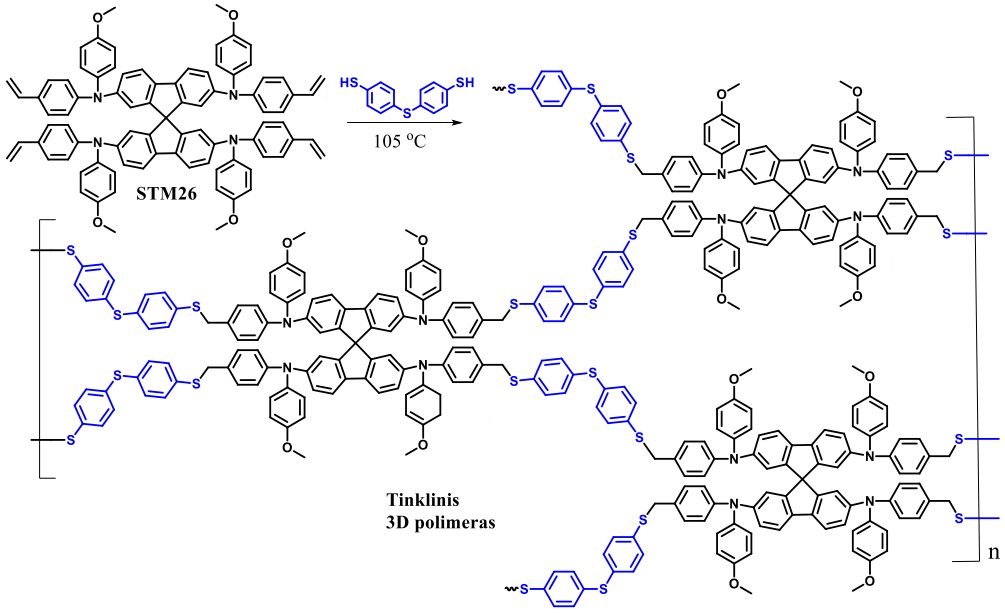

11 schema. Organinio puslaidininkio **STM26** ir 4,4‘-tiobisbenzentiolio polimerizacijos schema

DSK terminiu metodu buvo nustatyta, kad netirpus 3D polimerų tinklas susidaro 103 °C temperatūroje. Verta paminėti, kad tai PSE pritaikyme yra iki šiol žemiausia pasiekta 3D polimero susidarymo temperatūra, leidžianti panaudoti šį kopolimerą tiek *p-i-n*, tiek *n-i-p* architektūros elementuose atsisakant polimerizacijos iniciatorių[145-149].

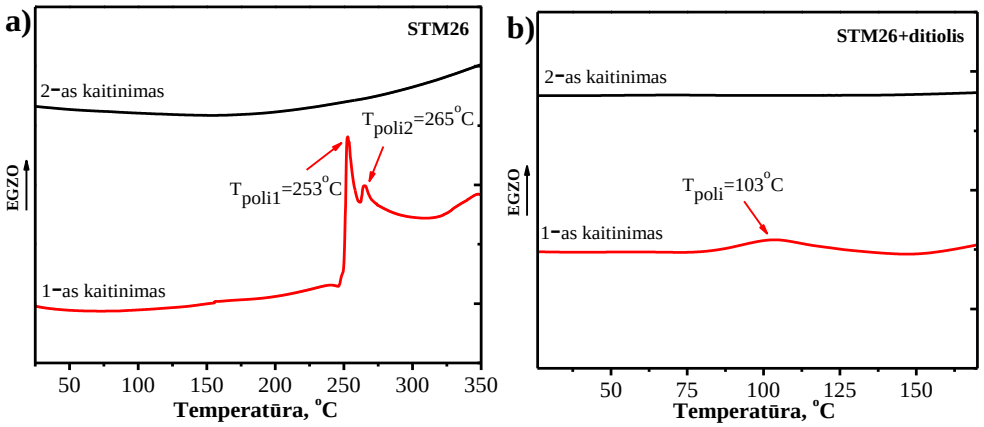

36 pav. STM26 (a) ir **STM26+ditiolis** (b) diferencinės skenuojamosios kalorimetrijos kreivės (10 °C/min, N_2 atmosfera)

Monomero, polimero ir kopolimero UV-RŠ sugerties ir FL emisijos spektrų rezultatai susisteminti ir pateikti 23 lentelėje. Organinio puslaidininkio **STM26** absorbcijos maksimumai matomi esant 336 ir 395 nm bangos ilgiui. Mažiau intensyvi absorbcijos smailė ties 336 nm gali būti priskiriama π-π^* elektronų perėjimams, o intensyvesnė – n-π^* delokalizuotiems elektronų šuoliams. Po organinio puslaidininkio polimerizacijos 253 °C temperatūroje ryškių pakitimų absorbcijos spektruose nepastebėta. Po terminio kryžminio sujungimo su ditioliu 103 °C temperatūroje UV-RŠ spektre buvo matomos dvi vienodai intensyvios smailės ties 303 ir 383 nm. Taip pat buvo pastebimas monomero emisijos maksimumas, esantis ties 419 nm. Apskaičiuota Stokso poslinkio vertė lygi 24 nm.

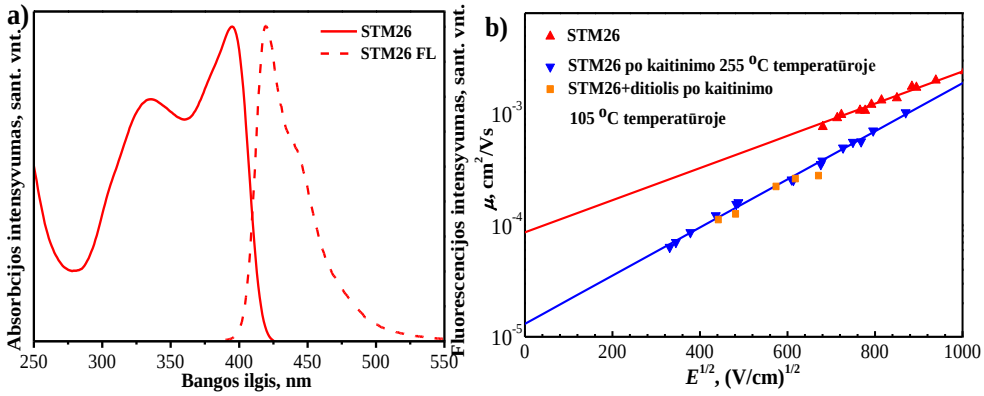

37 pav. Naujo organinio puslaidininkio **STM26**: a) UV-RŠ spinduliuotės sugerties (ištisinė linija) ir fluorescencijos (punktyrinė linija) spektrai THF tirpiklyje (10^{-4} M); b) dreifinio judrio priklausomybė nuo elektrinio lauko stiprio

Elektronų fotoemisijos ore metodu buvo išmatuoti mažamolekulinio junginio **STM26** monomero, polimero ir kopolimero jonizacijos potencialai, kurie atitinkamai lygūs 5,29, 5,38 ir 5,39 eV. Puslaidininkio skylių transportavimo savybės apibūdintos naudojant kserografinį laiko lėkio metodą. Esant nuliniam lauko stipriui monomero

mobilumas lygus $8,7\times10^{-5}$ cm^2/Vs. Po terminio kaitinimo tiek polimero, tiek kopolimero skylių dreifiniai judriai nedaug sumažėjo, tačiau vis dar yra palyginami su populiariais PSE skirtais puslaidininkiais (žr. 37 pav., b)[150-151].

Prieš konstruojant PSE buvo įvertinta polimerizacijos konversija. Bandymo pradžioje ant stikliukų buvo formuojamos plėvelės iš **STM26** polimero ir **STM26** su ditiolio mišinio. Padengti stikliukai kaitinti skirtingą laiką – 0, 15, 30, 45, 60 ir 140 minučių. Po atkaitinimo visos stiklinės plokštelės pamerktos į THF, kuris nuplauna nesusipolimerinusį monomerą bei linijinės struktūros polimerus. Ant plokštelės pasilieka tinklinio polimero sluoksnis. Norint įvertinti 3D polimerizacijos efektyvumo priklausomybę nuo kaitinimo laiko, iš gautų tirpalų buvo užrašyti UV-RŠ spektrai (žr. 38 pav., a, ir 38 pav., b). Išanalizavus sutinklinto spiro analogo sugerties spektrus galima teigti, kad monomeras buvo sutinklintas po 15 minučių kaitinimo. ~ 90 % kopolimero iš puslaidininkio **STM26** ir ditiolio mišinio (1:2) susidarė taip pat po 15 minučių kaitinimo. Taigi, susidarė 3D struktūros netirpus polimerinis tinklas, kurį galima panaudoti efektyvių *n-i-p* ir *p-i-n* struktūrų PSE konstravime.

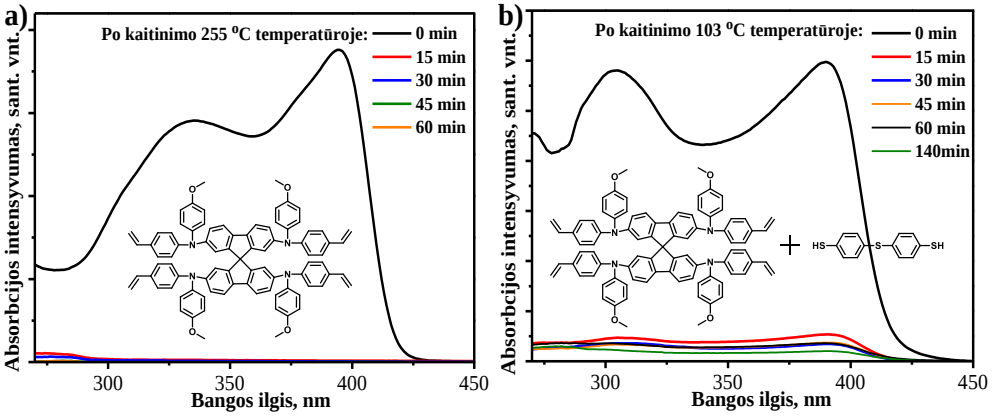

38 pav. STM26 (a) ir **STM26+ditiolis** (b) terminės polimerizacijos tyrimo UV-RŠ sugerties spektrai

Sutinklintas kopolimeras buvo panaudotas kaip STM *p-i-n* tipo PSE. Konstrukciją sudaro: FTO / **STM26**+ditiolis (kopolimeras) / perovskitas – $Cs_{0,05}FA_{0,80}MA_{0,15}PbI_{2,75}Br_{0,25}$ / $EDAI_2$ / C_{60} / BCP / Ag (žr. 39 pav., a). Buvo išbandytos skirtingos STM koncentracijos ir nustatyta, kad geriausi rezultatai pasiekti, kai kopolimero koncentracija siekė 2 mg/ml. Sukonstruoto elemento efektyvumas buvo lygus 19,3 %, ir tai prilygo įrenginiui, kuris buvo pagamintas naudojant gerai ištirtą polimerinį analogą PTAA.

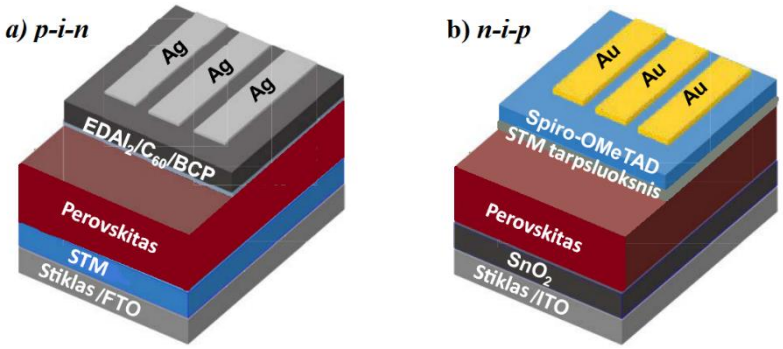

39 pav. Perovskitinių saulės elementų konstrukcijos *p-i-n* (a) ir *n-i-p* (b)

STM26 ir ditiolio kopolimeras taip pat panaudotas *n-i-p* tipo konfigūracijos PSE kaip tarpsluoksnis, apsaugantis perovskitą nuo drėgmės. Konstrukciją sudaro: ITO / SnO_2 / perovskitas – $Cs_{0,05}FA_{0,80}MA_{0,15}PbI_{2,75}Br_{0,25}$ / **STM26**+ditiolis (kopolimeras) / Spiro-OMeTAD / Au (žr. 39 pav., b). Spiro-OMeTAD buvo legiruotas LiTFSI, Co (III) druskų kompleksu ir *t*BP. Nustatyta optimali kopolimero koncentracija buvo 1 mg/ml. Sukonstruoto elemento su tarpsluoksniu efektyvumas siekė 19,1 % ir pralenkė palyginamojo elemento be tarpsluoksnio konversijos efektyvumą (18,9 %). Visos abiejų konstrukcijų PSE fotovoltinės charakteristikos susistemintos ir pateiktos 24 lentelėje.

24 lentelė. Skirtingų konstrukcijų perovskitinių saulės elementų, kuriuose naudotas puslaidininkio **STM26** ir ditiolio kopolimeras, fotovoltinės charakteristikos

	STM	V_{OC}, V	J_{SC}, mA/cm^2	*FF*	PSE, %
p-i-n	**STM26+ditiolis (kopolimeras)**	1,09	23,0	0,77	19,3
	PTAA	1,05	23,3	0,79	19,3
n-i-p	**STM26+ditiolis (kopolimeras)/Spiro-OMeTAD**	1,10	22,4	0,77	19,1
	Spiro-OMeTAD	1,08	22,6	0,77	18,9

Buvo atlikti *p-i-n* ir *n-i-p* konstrukcijos elementų stabilumo tyrimai. Buvo testuojami PSE, kur kaip STM buvo naudojami **STM26**/ditiolio kopolimeras ir etaloninis PTAA. PTAA pagrindu veikiančio PSE stabilumas po 30 valandų nukrito iki 80 % pradinio konversijos efektyvumo. O **STM26** ir ditiolio pagrindu pagamintas prietaisas po 200 valandų išlaikė 84 % pradinio savo našumo (žr. 40 pav., a). 40 pav., b, parodo *n-i-p* konstrukcijos PSE, pagamintų su ir be **STM26**/ditiolio kopolimero tarpsluoksnio, stabilumus. Prietaiso be tarpsluoksnio tarp perovskito ir Spiro-OMeTAD konversijos našumas po 16 valandų sumažėjo net iki 60 %, o elementas su kryžminiu tarpsluoksniu po 24 valandų išlaikė 84 % pradinio savo efektyvumo.

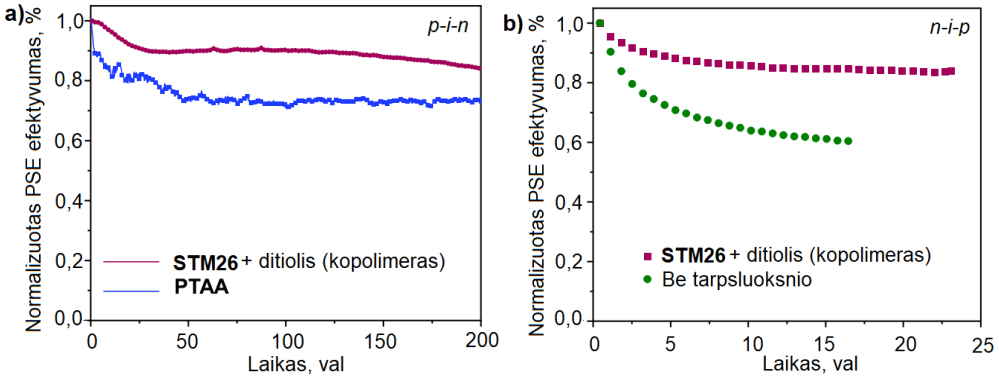

40 pav. Perovskitinių saulės elementų *p-i-n* (a) ir *n-i-p* (b) struktūros stabilumų tyrimai

Šio tyrimo rezultatai patvirtina galimybę sėkmingai vystyti mažamolekulinių organinių puslaidininkių ir ditiolių kopolimerų pritaikymą įvairių konstrukcijų PSE. Buvo patvirtinta teorija, kad tinkliniai 3D kopolimerų ryšiai sistemingai prisideda prie įrenginių našumo ir stabilumo gerinimo. Šio tyrimo svarbą liudija trys tarptautinės patentinės paraiškos „In-Situ crosslinking of 9,9′-spirobifluorene-based compounds for use in optoelectronic and/or in photoelectrochemical devices and manufacture thereof“, kurios pateiktos skirtinguose patentų biuruose – Amerikos (USPTO, Reg. Nr. 18/134,751, 2023-04-14), Europos (EPO, Reg. Nr. EP23168712.0, 2023-04-19) ir Japonijos (JP, Reg. Nr. 2023-068376, 2023-04-19).

4. IŠVADOS

Šioje disertacijoje pristatyti perspektyvūs fluorenilo, karbazolilo arba spirobisindano chromoforus turintys *p*-tipo organiniai puslaidininkiai. Darbo metu suformuluotos išvados:

1. Trijų stadijų sintezės metu susintetinti mažamolekuliniai *p*-tipo organiniai puslaidininkiai su fluoreno centriniu fragmentu. Atlikus šių junginių savybių tyrimus nustatyta, kad:
   1.1. Susintetinti organiniai puslaidininkiai yra termiškai stabilūs – 5 % savo masės svorio praranda aukštesnėje nei 400 ^{o}C temperatūroje.
   1.2. Trečiojo karbazolilo chromoforo prijungimas į centrinio fragmento 4-ą padėtį užtikrina stabilesnę amorfinę būseną.
   1.3. Šių organinių puslaidininkių jonizacijos potencialo (5,1 – 5,11 eV) ir skylių dreifinio judrio silpnuosiuose elektriniuose laukuose (10^{-6} cm^2/Vs) vertės yra tinkamos juos panaudoti perovskitiniuose saulės elementuose.
   1.4. Perovskitinio saulės elemento, kuriame naudojamas puslaidininkis **STM1**, galios konversijos efektyvumas siekė 18,3 % ir buvo artimas prietaiso su Spiro-OMeTAD našumui (18,9 %).
2. Kondensacijos reakcijos metu susintetintas enaminas **STM3**, kurio 9-oji fluoreno padėtis vėliau alkilinama skirtingais alkilfragmentais. Nustatyta, kad:
   2.1. Šie organiniai puslaidininkiai egzistuoja tiek kristalinės, tiek ir amorfinės būsenos, tačiau po antro kaitinimo fiksuojama tik stiklėjimo temperatūra.
   2.2. Propilpakaitą turinčio puslaidininkio **STM5** skylininkų judrio reikšmė (μ_0 = $3{,}3\times10^{-4}$ cm^2/Vs) buvo didžiausia ir aplenkė etalono Spiro-OMeTAD vertę ($\mu_0 = 1{,}3\times10^{-4}$ cm^2/Vs).
   2.3. Geriausiais efektyvumo rezultatais tiek su priedais legiruotoje struktūroje, tiek ir be priedų pasižymėjo puslaidininkio **STM3** pagrindu gauti perovskitiniai saulės elementai, kurių efektyvumo reikšmės atitinkamai buvo 19,3 % ir 17,1 %.
3. Naudojant kondensacijos reakcijas susintetinti fluorenilo chromoforus bei puslaidininkio centre akceptorines grupes turintys enaminai. Ištyrus jų savybes nustatyta, kad:
   3.1. Didesnę konjuguotąją dvigubųjų ryšių sistemą turintys junginiai pasižymi didesniu terminiu stabilumu. Aukščiausia skilimo temperatūra (412 ^{o}C) pasižymėjo puslaidininkis **STM14** su keturiomis difeniletenilgrupėmis ir fluorenono fragmentu molekulės centre.
   3.2. Jonizacijos potencialo reikšmės varijavo ~5,4–5,5 eV intervale, o geriausia krūvio pernaša silpnuose elektriniuose laukuose pasižymėjo junginys **STM13** ($\mu_0 = 4\times10^{-6}$ cm^2/Vs).
   3.3. Su keturias difeniletenilgrupes ir malononitrilo akceptoriaus fragmentą molekulės centre turinčiu puslaidininkiu **STM13** buvo pasiektas rekordinis saulės elemento našumas, lygus 22,03 %.

4. Naudojant įvairias reakcijų metodikas susintetinti spirobisindano centrinį fragmentą turintys organiniai puslaidininkiai. Nustatyta, kad:
   4.1. Junginiai **STM15** ir **STM16** egzistuoja tik amorfinės būsenos ir gali užtikrinti geresnį sluoksnių morfologinį stabilumą nei etalonas Spiro-OMeTAD. Jų stiklėjimo temperatūros atitinkamai yra 167 ^{o}C ir 157 ^{o}C.
   4.2. **STM15** ir **STM16** jonizacijos potencialo reikšmės atitinkamai yra 5,34 eV ir 5,30 eV ir patenka į pageidaujamą skylių transportinių medžiagų HOMO lygmens verčių intervalą. O junginio **STM15** dreifinis judris silpname elektriniame lauke lygus beveik 10^{5} cm^2/Vs, o jo *meta*-pakeisto analogo **STM16** – šiek tiek mažesnis ($\mu_0 = 2{,}6\times10^{-6}$ cm^2/Vs).
   4.3. Perovskitinio saulės elemento su teigiamus krūvininkus transportuojančiu junginiu **STM15** rezultatai gauti perspektyviausi – efektyvumas siekė 16,4 %
5. Remiantis žaliosios chemijos principais susintetintos naujos skylių transportinės medžiagos, molekulės centre turinčios fotodimerizuoto 9-vinilkarbazolo fragmentą. Atlikus junginių savybių tyrimus nustatyta, kad:
   5.1. Tiksliniai junginiai yra amorfiniai, išskyrus puslaidininkį **STM18**, turintį tiek amorfinę, tiek ir kristalinę būsenas.
   5.2. Junginių dreifinių judrių silpnuosiuose elektriniuose laukuose vertės varijavo nuo 10^{-4} cm^2/Vs iki 10^{-7} cm^2/Vs.
   5.3. Puslaidininkio **STM22** ir etalono Spiro-OMeTAD saulės elementų energijos konversijos efektyvumai buvo labai panašūs, t.y. atitinkamai 21 % ir 21,64 %. **STM22** pagrindu sukonstruotas saulės modulis (6,5×7 cm) pasiekė 19,06 % efektyvumą, kuris buvo rekordinis tarp Spiro-OMeTAD klasei nepriklausančių *p*-tipo puslaidininkių.
6. Naudojant alkilinimo ir Buchwaldo paladžio katalizuojamų reakcijų metodikas susintetintos fotolaidžius karbazolilchromoforus bei tinklintis galinčias tris vinilgrupes turinčios skyles transportuojančios medžiagos. Nustatyta, kad:
   6.1. Monomeras **STM24** polimerinasi 196 ^{o}C temperatūroje, o analogo su didesne konjuguotąja dvigubųjų ryšių sistema **STM25** tinklinimosi procesas fiksuojamas ties 300 ^{o}C.
   6.2. Junginių **STM24** ir **STM25** jonizacijos potencialai atitinkamai yra lygūs 4,84 eV ir 4,82 eV, o dreifiniai judriai silpnuose elektriniuose laukuose – $1{,}8\times10^{-6}$ cm^2/Vs ir $2{,}4\times10^{-5}$ cm^2/Vs.
   6.3. Monomero **STM24** konversija į 3D struktūros polimerą įvyksta per 90 min, o jo analogo **STM25** per vieną valandą.
   6.4. Terminės polimerizacijos metu gautas netirpus 3D struktūros *p*-tipo puslaidininkio **STM24** sluoksnis gali būti sėkmingai panaudotas invertuotos struktūros *(p-i-n)* perovskitiniuose saulės elementuose su beveik 17 % energijos konversijos efektyvumu.
7. Ištyrus, optimizavus ir parinkus geriausią sintezės kelią, Buchwaldo paladžio katalizuojamų reakcijų metu susintetintas 9,9′-spirobifluoreno centrinį

fragmentą bei keturias tinklintis galinčias vinilgrupes turintis *p*-tipo organinis puslaidininkis. Nustatyta, kad:

7.1. Silpnuosiuose elektriniuose laukuose monomero **STM26** teigiamų krūvininkų judris siekia beveik 10^{-4} cm^2/Vs, o po terminio tinklinimo sumažėja nedaug.

7.2. Monomeras **STM26** vos per 15 minučių 253 ^oC temperatūroje tinklinasi į 3D struktūros *p*-tipo polimerinį puslaidininkį. Invertuotos struktūros *(p-i-n)* perovskitiniai saulės elementai su pastaruoju polimeru pasižymi 19,3 % energijos konversijos efektyvumu, prilygstančiu naudojant etaloninį polimerinį puslaidininkį PTAA.

7.3. **STM26** polimerizacija su tinklinimo agentu 4,4′-tiobisbenzentioliu susidarant 3D struktūros polimerui vyksta sklandžiai (15 minučių) daug žemesnėje temperatūroje (107 ^oC). Tai leido jį panaudoti įprastos struktūros *(n-i-p)* perovskitiniuose saulės elementuose kaip tarpsluoksnį tarp Spiro-OMeTAD bei perovskito ir pagerinti pastarojo ilgaamžiškumą. Prietaisas pasižymėjo smarkiai padidėjusiu stabilumu ir 19,1 % energijos konversijos efektyvumu, viršijančiu prietaiso be šio tinklinės struktūros tarpsluoksnio (18,9 %) našumą.

5. SUMMARY

5.1. Introduction

In recent decades, energy consumption has been attracting considerable attention worldwide. Its extraction accounts for more than three-quarters of the greenhouse gas emissions produced by the European Union (EU). To reduce the amount of pollutants emitted by the energy sector, it is important to harness the potential of renewable energy. Currently, the EU obtains just over 20% of its energy from renewable sources. The goal is to reach 42.5% of the total EU consumption of renewable energy by 2030, and achieve climate neutrality by 2050, which means level zero of greenhouse gas emissions[1].

The Sun is the most powerful renewable source of energy. Solar cells (SCs) convert solar energy into electricity. It has been projected that, by the middle of the 21st century, solar energy could satisfy about 45% of the world's total energy needs[2]. Currently, polycrystalline silicon solar cells are the dominant photovoltaic technology (approx. 90%), but they are relatively expensive and complicated to produce[3]. Organic and hybrid solar cells of the third generation are rapidly gaining ground as a low-cost alternative. Among the latter, *Perovskite Solar Cells* (PSCs) stand out as a breakthrough as they have demonstrated impressive efficiency, which has been increasing sensationally from 3.8%[4] to over 26%[5] over the past decade.

PSCs are characterized by simplicity of construction, the low cost of raw materials, and the ability of the perovskite layer to absorb a wide range of light wavelengths[6]. In these solar cells, the organic hole transporting layer is one of the key components which is responsible for extracting holes from the perovskite layer and transporting them towards the electrode. An organic semiconductor codenamed *Spiro-OMeTAD*, which is most used for hole transporting, is very expensive because it is synthesized in a multistep synthesis procedure. In addition, expensive rare metal catalysts and aggressive reagents that are extremely sensitive to environmental effects are used for its synthesis[7-8]. However, the biggest problem is the insufficient long-term stability of these devices. All these disadvantages open wide opportunities to search for more promising *Hole Transporting Materials* (HTMs).

In this dissertation, HTMs, containing fluorene, carbazole or spirobisindane fragments, that have been synthesized and investigated by the author are reviewed. The low cost and commercial availability of the starting materials, simpler synthesis, lower production costs, and better results in terms of PSCs efficiency and stability make many of them attractive and promising HTMs in the modern PSC market.

The aim of this work is the design, synthesis, and characterization of efficient and economical fluorene-, carbazole-, and spirobisindane-based hole transporting materials for hybrid perovskite solar cells.

The following objectives were outlined to achieve the aim of the dissertation:

1. To synthesize novel low molecular mass organic semiconductors bearing a fluorene central fragment, to study their thermal, optical, and photophysical

properties, and to investigate the photovoltaic characteristics of the perovskite solar cells constructed on their basis.

2. To synthesize novel hole transporting materials bearing a fluorene core with enamine-linked diphenyl branches, to characterize their properties, and to investigate their application possibilities in doped and dopant-free perovskite solar cells.

3. To synthesize novel low molecular mass organic compounds bearing a fluorene core with an acceptor group and diphenylethylene moieties, to characterize their properties, and to investigate the influence of different acceptors on perovskite passivation, and on the efficiency and stability of solar cells.

4. To synthesize novel organic semiconductors bearing a spirobisindane core with diphenylethylene groups, to investigate their thermal, optical, and photophysical properties, and to study their performance in perovskite solar cells.

5. To investigate the application possibilities of green synthesis for new hole transporting materials with a central carbazole core, to characterize the properties of the synthesized compounds, and to investigate their performance in perovskite solar cells.

6. To synthesize novel cross-linking organic semiconductors bearing a central carbazole core, to investigate their thermal, optical and photophysical properties, and to study the efficiency of the perovskite solar cells constructed on their basis.

7. To synthesize a novel hole transporting material bearing a 9,9′-spirobifluorene central fragment and polymerizable groups, to characterize its properties, and to investigate the possibilities of its application in perovskite solar cells of various structures.

Scientific novelty and relevance of the work

Currently, hybrid PSCs are one of the fastest-growing types of solar cells. In these devices, HTM is one of the key components determining efficient conversion of solar energy. Organic semiconductors must have a relatively high drift mobility, suitable energy levels (HOMO, LUMO), a high decomposition temperature, an amorphous state, while also being cost-effective[9-11]. Despite significant efforts by researchers to develop new HTMs, currently, to the best of the knowledge of the author, the highest efficiency (26.1%[5]) has been achieved in PSCs employing the expensive molecule 2,2',7,7'-tetrakis[*N*,*N*-di(4-methoxyphenyl)amino]-9,9'-spirobifluorene (Spiro-OMeTAD). Its high cost is attributed to a five-step synthesis, which requires inert conditions, a low temperature, aggressive reagents that are extremely sensitive to environmental effects, as well as a lengthy and costly purification by employing the sublimation procedure[7-8]. Another significant drawback of Spiro-OMeTAD is its crystallinity, which negatively impacts the stability of PSCs and the light conversion efficiency[12]. Therefore, the search for new organic semiconductors continues, aiming for simpler, more environmentally friendly, and cost-effective synthesis methods. The goal is to develop PSCs based on these materials with an improved stability and efficiency.

Considering these criteria, new HTMs have been synthesized, their properties have been studied, and PSCs have been constructed. All the research results have been reported in seven scientific articles by the author of this dissertation.

The first publication reports two new organic semiconductors bearing a fluorene core. The low-molecular mass compounds were synthesized by using a simple three-step synthetic route. Upon characterization, it has been revealed that the HTMs are amorphous and possess high glass transition temperatures, a suitable thermal stability, and excellent photoelectric properties. The device containing a compound with an enlarged π conjugated system demonstrated an efficiency of more than 18% and a superior long-term stability compared to the device based on the reference Spiro-OMeTAD.

The second publication presents a new series of compounds based on a fluorene core with enamine-linked diphenyl branches. The hydrogen atoms at the 9th position of this chromophore are chemically active and well-suited for alkylation reactions enabling the functionalization of the compounds to obtain target photoactive HTMs. It is of importance to note that the best-performing organic semiconductor **STM3** was synthesized from commercial starting materials by using an economical condensation reaction. The PSC based on it exhibited promising efficiency results, i.e., 19.3% in the doped structure, and 17.1% in the dopant-free configuration, thereby outperforming the PSC with Spiro-OMeTAD.

The third publication also presents a new series of HTMs based on a fluorene core with acceptor groups attached at the 9th position and enamine-linked diphenyl branches. The donor-acceptor-donor interaction and the influence of the acceptor on perovskite passivation, as well as PSC efficiency and stability were investigated. The PSC containing compound **STM13** as HTM demonstrated an efficiency higher than 22%, which decreased only by 4 percentage points after 500 hours. Importantly, this device outperformed the PSC based on Spiro-OMeTAD when tested under identical environmental conditions. Additionally, the low-molecular mass compound **STM13** was synthesized by using a simple synthetic route, thus making it a cost-effective alternative to the reference HTM.

In the fourth scientific article, novel organic semiconductors based on a spirobisindane core with diphenylethylene groups were reported. The new compounds exhibit a high thermal stability, and good optical and photophysical properties. They are in a stable amorphous state, which ensures morphological stability in PSCs. SC containing the low-molecular mass compound **STM15** as a positive charge transporter showed promising performance results; therefore, the latter could be an excellent alternative to the reference Spiro-OMeTAD.

In the fifth publication, a photodimerized carbazole, which is attractive because of its simple and green synthesis, was chosen as the central core of the HTM. The influence of different substituents on the thermal, optical, and photophysical properties of the new organic semiconductors, as well as on the photovoltaic parameters of PSCs, was systematically investigated. An efficiency of 21% was achieved, and long-term stability under atmospheric conditions was improved compared to those of the devices based on Spiro-OMeTAD. The best-performing HTM **STM22** was used in the construction of a perovskite solar module (6.5 × 7 cm),

and a power conversion efficiency above 19% was achieved, thus setting a record at the time for compounds of the non-spiro class. The practical significance of these semiconductors has been demonstrated by patent applications filed in the US (US2023157158), Japan (JP2023072638), China (CN116133444), and Europe (EP4181225) patent offices.

The sixth scientific article focuses on organic semiconductors containing low-cost commercially available carbazole chromophores and cross-linking vinyl groups. After thermal processing, the molecules were used in the inverted (*p*-*i*-*n*) PSCs. The use of polymers in this type of PSCs makes it possible to eliminate doping additives which contribute to SC degradation over a long time. The optical, thermal, and photophysical properties of the newly synthesized compounds were investigated, and PSCs, which showed promising efficiency and stability results, were constructed.

The final publication reports a new Spiro-OMeTAD analogue **STM26** which has cross-linkable groups. After thermal cross-linking, a smooth and solvent-resistant three-dimensional (3D) polymer network was formed. It was used as an HTM in the inverted (*p*-*i*-*n*) PSC and as an interlayer between the perovskite and the hole transporting layer in regular (*n*-*i*-*p*) PSC. Both devices demonstrated record-breaking power conversion and long-term stability results compared to the benchmarks PTAA and Spiro-OMeTAD. The organic semiconductor was patented, with patent applications filed in the US (USPTO, Reg. No. 18/134,751), Japan (JP, Reg. No. 2023-068376), and Europe (EPO, Reg. No. EP23168712.0) patent offices.

5.2. Review of Published Articles

5.2.1. Fluorene-based organic semiconductors for hole transporting layers in efficient and stable perovskite solar cells

This subchapter is based on the published article: "Nonspiro, Fluorene-Based, Amorphous Hole Transporting Materials for Efficient and Stable Perovskite Solar Cells," *Adv. Sci., 2018, 5*, 1700811, Q1, by S. Daskeviciute, N. Sakai, M. Franckevicius, M. Daskeviciene, A. Magomedov, V. Jankauskas, H. J. Snaith, V. Getautis; cited 44 times.

As mentioned in the previous sections, the organic semiconductor Spiro-OMeTAD is used as a reference material in the PSC hole transporting layer. HTM is estimated to represent a large fraction of the cost of a solar cell[120]; therefore, due to tedious synthetic procedures, complicated purification steps, and increased production costs, Spiro-OMeTAD is not suitable for the production of commercial devices. Many organic semiconductors have been developed, the synthesis path of which is much shorter, and purification procedures are simple. One such example is the low-molecular mass compound **V886**[105]. Its structure consists of two 4,4'-dimethoxydiphenylamine and 3,6-diphenylcarbazole fragments connected by a benzene ring. The synthesis of this semiconductor is very simple, and the efficiency of the solid-state solar cell based on it was almost equal to that of the device with Spiro-OMeTAD. Based on these data, new low-molecular mass compounds **STM1** and **STM2** bearing two or three carbazolyl chromophores and a fluorene fragment in the center of the molecule (Figure 41) have been synthesized. These organic

semiconductors were synthesized by a simple three-step synthesis procedure. Novel HTMs were amorphous, thermally stable, and exhibited a high power conversion efficiency. It is of importance to note that devices with these materials demonstrated better stability levels than the device with Spiro-OMeTAD.

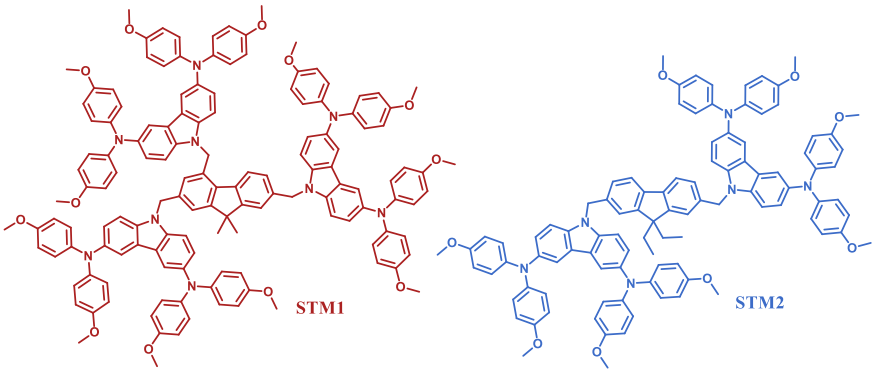

Figure 41. Structures of new HTMs **STM1** and **STM2**

Commercially available differently alkylated fluorenes were used as central cores in the synthesis of the target compounds. According to an already known methodology[121], the latter reacted with paraformaldehyde and HBr in acetic acid to obtain intermediate compounds **1** and **3** with varying numbers of bromine substituents (Scheme 12). In their reaction with 3,6-dibromocarbazole in THF in the presence of KOH, fluorene derivatives **2** and **4**, featuring three and two carbazole chromophores, respectively, were isolated. The final products, **STM1** and **STM2**, were obtained through palladium-catalyzed Buchwald cross-coupling reactions. The structures of the new compounds were confirmed by ^{1}H and ^{13}C NMR spectroscopy and elemental analysis methods.

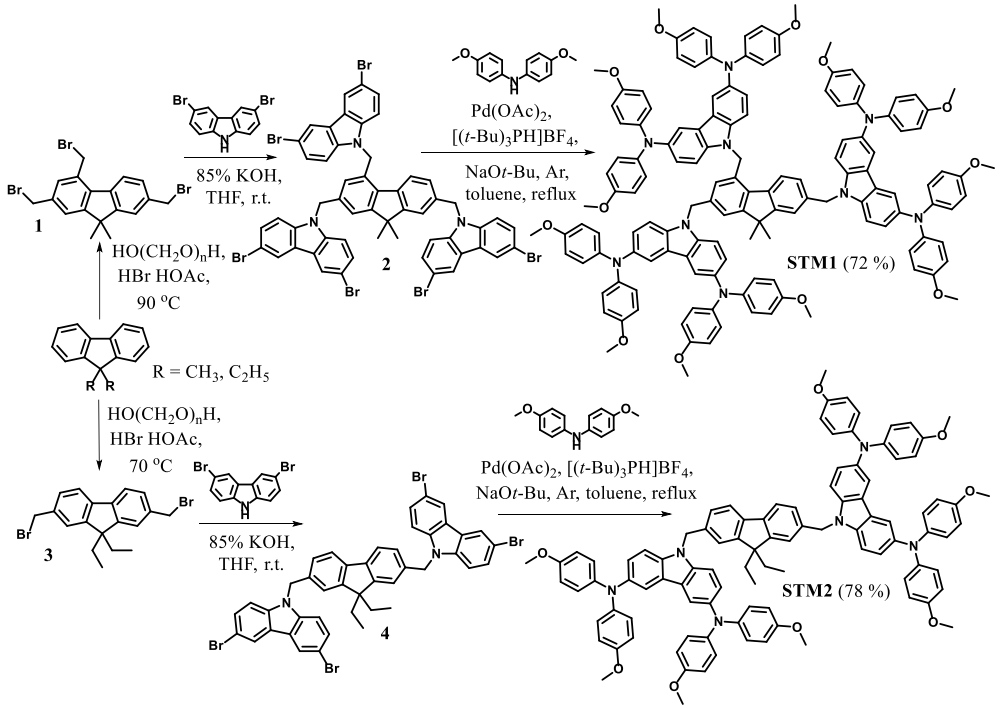

Scheme 12. Synthesis route to new HTMs **STM1** and **STM2**

On the basis of the optical, thermal, and photophysical properties of the synthesized HTMs (Table 25), their potential application in PSCs has been evaluated.

Table 25. Thermal, optical, and photoelectrical properties of **STM1**, **STM2**, and Spiro-OMeTAD

HTM	T_g [a], °C	T_{dec} [a], °C	λ_{abs} [b], nm	I_P [c], eV	μ_0 [d], cm^2/Vs
STM1	166	400	305, 375	5.11	1.5×10^{-6}
STM2	146	420	303, 373	5.10	3.0×10^{-6}
Spiro-OMeTAD	126	449	303, 387	5.00	4.1×10^{-5}

[a]Glass transition (T_g) and decomposition (T_{dec}) temperatures were observed from DSC and TGA, respectively (10 °C/min, N_2 atmosphere); [b]Absorption (excitation = $\lambda_{abs\ max}$) spectra were measured in THF solution (10^{-4} M); [c]Ionization energies of the films were measured by using PESA; [d]Mobility value at zero-field strength.

*Thermogravimetric A*nalysis (TGA) and *Differential Scanning Calorimetry* (DSC) methods were applied to determine the thermal stability of the HTMs. TGA showed that a 5% weight loss of **STM1**, containing three substituents, occurred at approx. 400 °C, while its analogue with two carbazole chromophores, **STM2**, lost 5% of its mass at 420 °C. The compounds are sufficiently thermally stable and are suitable for the application in PSCs. DSC analysis of **STM1** and **STM2** has shown that the

target products exist in an amorphous state. Their glass transition temperatures are 166 °C and 146 °C, respectively. These temperature values support one of Wirth's postulates, according to which the glass transition temperature increases as the size of the molecule increases, i.e., when an additional substituent is attached to the central fragment at the 4th position[122]. The glass transition temperature of the low-molecular mass compound **STM1** is higher by as much as 40 °C than that of Spiro-OMeTAD. The high glass transition temperature is an indicator of a more stable amorphous state and a reduced tendency to crystallize.

Ultraviolet and visible light radiation absorption spectra (UV-vis) of the new HTMs containing the central fluorene fragment and Spiro-OMeTAD were measured in THF solutions; the spectra are presented in Figure 42a. The absorption spectra of semiconductors **STM1** and **STM2** are almost identical, thus confirming that there is no conjugation between individual disubstituted carbazole-based branches. An intense π-π^* absorption band with the maximum at 305 nm is observed in the spectra of both HTMs. Weak absorption at 375 nm corresponds to n-π^* transitions. Since new HTMs have the highest absorption in the UV region and only very low absorption in the visible spectral region, they are very attractive for application in PSCs[123].

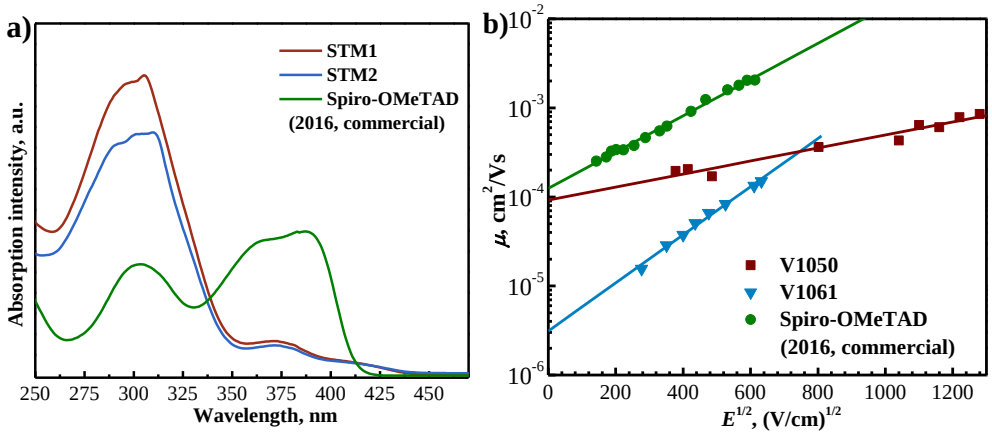

Figure 42. New HTMs **STM1**, **STM2** and Spiro-OMeTAD: a) UV-vis absorption spectra in THF solution (10^{-4} M); b) Electric field dependencies of the hole-drift mobilities

To determine the HOMO energy level of the new semiconductors, the solid state ionization potential (I_P) was measured by the photoelectron spectroscopy in air method. The results are presented in Table 25. Compounds **STM1** and **STM2** have nearly identical I_P values, 5.11 and 5.10 eV, respectively. The calculated values are very close to the ionization potential value of Spiro-OMeTAD (5.00 eV). The new semiconductors could ensure an efficient hole transfer in devices and, therefore, are suitable for use in PSCs. Another important photophysical property of semiconductors is the charge mobility, which was measured by using the xerographic time-of-flight technique (Figure 42b). The charge mobility values of compounds **STM1** and **STM2** were similar to that of Spiro-OMeTAD and reached 1.5×10^{-6} and 3.0×10^{-6} cm^2/Vs, respectively, in a weak electric field.

The new V-series compounds were tested in PSCs with the *n-i-p* structure. The device architecture was set up as follows: FTO / SnO_2 / perovskite – $FA_{0.83}Cs_{0.17}Pb(I_{0.8}Br_{0.2})_3$ / HTM / Au. The optimized photovoltaic characteristics data of the solar cells from the current-voltage (*J-V*) curves are presented in Table 26. The power conversion efficiency of the device based on semiconductor **STM1** reached 18.3%, which is a very similar value to the one obtained by PSC with Spiro-OMeTAD (18.9%). In the case of **STM2**, a slightly lower efficiency (16.7%) was recorded.

Table 26. Photovoltaic parameters of the new HTMs **STM1**, **STM2** and Spiro-OMeTAD extracted from the best-performing devices

HTM	V_{OC}, V	J_{SC}, mA/cm^2	*FF*	PCE, %
STM1	1.05	22.0	79.5	18.3
STM2	0.96	21.6	79.7	16.7
Spiro-OMeTAD	1.08	22.4	77.9	18.9

The stability of all constructed PSCs was investigated as well (Figure 43). The devices were without any encapsulation, at a relative humidity ~60%, and a temperature of 22 °C. The PCE values decreased by 20% after 270 h for Spiro-OMeTAD-based devices. However, the devices with semiconductors **STM1** and **STM2** were more stable with an observed reduction of efficiency by only 6% under the same conditions. The results of stability could be attributed to a better HTM morphology, since the new semiconductors uniformly cover the perovskite surface, thus protecting it from the effects of moisture.

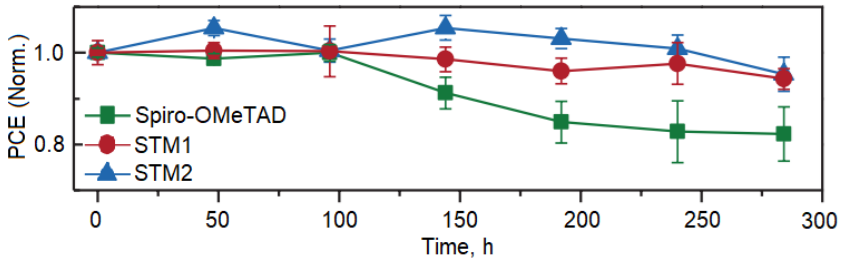

Figure 43. Stability test of PSCs devices with **STM1**, **STM2**, and Spiro-OMeTAD

In conclusion, a new promising organic semiconductor **STM1** can be a useful alternative to Spiro-OMeTAD. This would bring the commercialization of perovskite solar cells closer.

5.2.2. Fluorene-based enamines as hole transporting layers in efficient and stable perovskite solar cells

This subchapter is based on the published article: "Fluorene-based enamines as low-cost and dopant-free hole transporting materials for high performance and stable perovskite solar cells," *J. Mater. Chem. A, 2021, 9*, 301–309, Q1, by Š. Daškevičiūtė,

C. Momblona, K. Rakštys, A. A. Sutanto, M. Daškevičienė, V. Jankauskas, A. Gruodis, G. Bubnienė, V. Getautis, M. K. Nazeeruddin; cited 30 times.

High-performing PSCs most often contain organic semiconductors synthesized by cross-coupling reactions. Synthesis is carried out with expensive ligands or palladium catalysts under inert reaction conditions, and the workup procedures of the target products are complex. In the search for a low-cost and effective synthesis procedure, a simple condensation reaction was carried out while using cheap commercial starting materials that provided enamine molecules with good semiconducting properties (Figure 44). The cost of these final hole transporting materials is only a few Euros per gram, while the reference Spiro-OMeTAD costs ~92 Eur/g[124]. The enamines synthesized from fluorene diamines showed extremely high hole-drift mobility, whose values reached up to 3.3×10^{-4} cm^2/Vs. This is one of the most important physical characteristics of semiconductors, leading to the excellent efficiency results of the constructed PSCs, i.e., 19.3% in the doped structure and 17.1% without doping. In addition, the SCs of both structures showed excellent long-term stability compared to the one based on Spiro-OMeTAD.

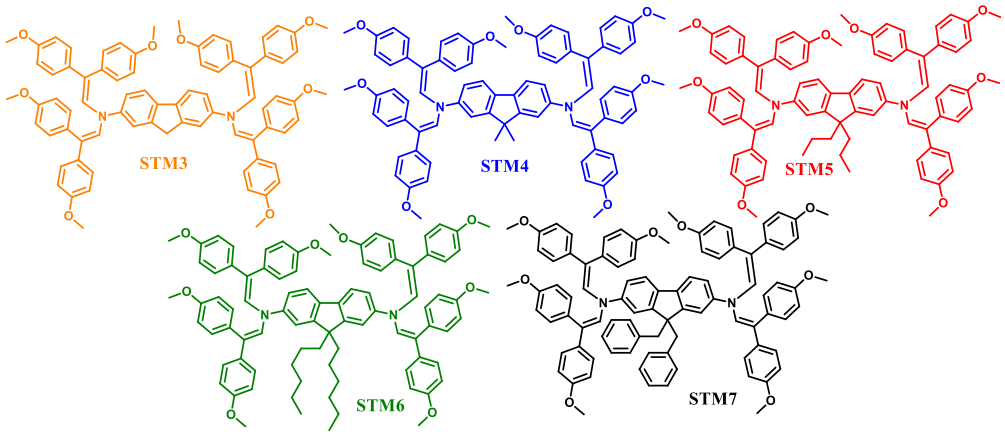

Figure 44. Structures of new enamines

The synthesis of the target enamines containing fluorene chromophore was carried out based on the methodology of the reaction of the primary amine with acetaldehydes. Therefore, 2,7-diamino-9*H*-fluorene reacted with 2,2-bis(4-methoxyphenyl)acetaldehyde in THF at reflux in the presence of camphor-10-sulfonic acid (CSA) as a catalyst. Enamine **STM3** was obtained and subsequently alkylated at the 9th position with halides of various chain lengths, yielding the target products **STM4, STM5, STM6**, and **STM7** (Scheme 13). The structures of the synthesized compounds were confirmed by ^1H and ^{13}C NMR spectroscopy and elemental analysis data.

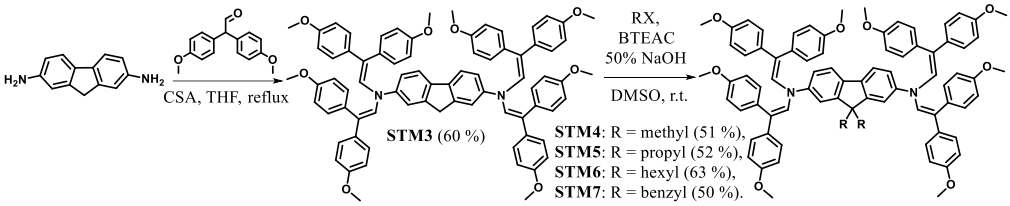

Scheme 13. Reaction scheme of fluorene enamines HTMs

In order to estimate the cost of the new materials, a synthesis cost analysis was performed. The predicted price of the semiconductor **STM3** is ~10 Eur/g, and the one for the alkylated analogue **STM5** is ~22 Eur/g, which is only a quarter of the market price of Spiro-OMeTAD.

The optical, thermal, and photophysical properties of the newly synthesized HTMs were investigated (Table 27), and the possibilities of their use in PSCs were evaluated.

Table 27. Thermal, optical, and photoelectrical properties of fluorene enamines HTMs

HTM	T_m [a], °C	T_c [a], °C	T_g [a], °C	T_{dec} [a], °C	λ_{abs} [b], nm	λ_{em} [b], nm	E_g [c], eV
STM3	255	–	150	403	262, 381, 401	508	2.79
STM4	247, 267, 272	198	153	285	265, 382, 404	510	2.79
STM5	272	159	120	399	266, 382, 404	509	2.81
STM6	173, 195	–	90	393	265, 383, 404	508	2.79
STM7	330	–	116	321	265, 384, 400	507	2.79

[a]Melting (T_m), crystallization (T_c), glass transition (T_g) and decomposition (T_{dec}) temperatures were observed from DSC and TGA, respectively (10 °C/min, N_2 atmosphere); [b]Absorption and emission (excitation = $\lambda_{abs\ max}$) spectra were measured in THF solution (10^{-4} M); [c]Eg was estimated from the intersection of absorption and emission spectra of solid films.

First, thermal tests were performed, during which, the state of the materials and their resistance to high temperatures were evaluated. TGA showed that compound **STM3** lost 5% of its weight at 403 °C, and its thermal stability was the highest among the enamines in this series. The introduction of aliphatic substituents at the 9th position of fluorene worsened the thermal stability of the new semiconductors, but the decomposition temperature of all of them was significantly higher than that of Spiro-OMeTAD (T_{dec} = 288 °C[125]). The thermal transitions of semiconductors were determined by using the DSC method. Interestingly, compounds **STM3**, **STM6**, and **STM7** exist in both crystalline and amorphous states, and **STM4** and **STM5** are more likely to crystallize. However, after the second heating, only the glass transition temperature was recorded, thus indicating that all the compounds also have an

amorphous state. The most stable amorphous state was identified for the organic semiconductor **STM4**, as its glass transition temperature is the highest (153 °C).

π electrons are particularly important in the charge transfer process of hole transporting materials[126]. In order to study their state in more detail, the electromagnetic radiation absorption spectra of organic semiconductors derived from fluorene diamines were recorded (Figure 45a). The spectra of all HTMs have two main absorption peaks at ~260 nm and ~400 nm. A less intense absorption peak at shorter wavelengths reflects localized electron π-π^* transitions. Meanwhile, the ~400 nm wavelength peak is the result of more intense delocalization from the central fragment of the molecule and is attributed to n-π^* transitions. It is also noticeable that the addition of different alkyl fragments did not significantly affect the conjugated system; therefore, the absorption spectra remained almost identical. The photoluminescence spectra (PL) were recorded after valence electron excitation (Figure 45a). The PL spectra of all enamines are similar, and the emission maximum was recorded at ~510 nm. The observed very large Stokes shifts (~100 nm) indicate that the material is characterized by large geometrical changes in the excited state. The higher is the Stokes shift, the more suitable the compound is for hole transporting, since a higher mobility of charge carriers can be expected[127].

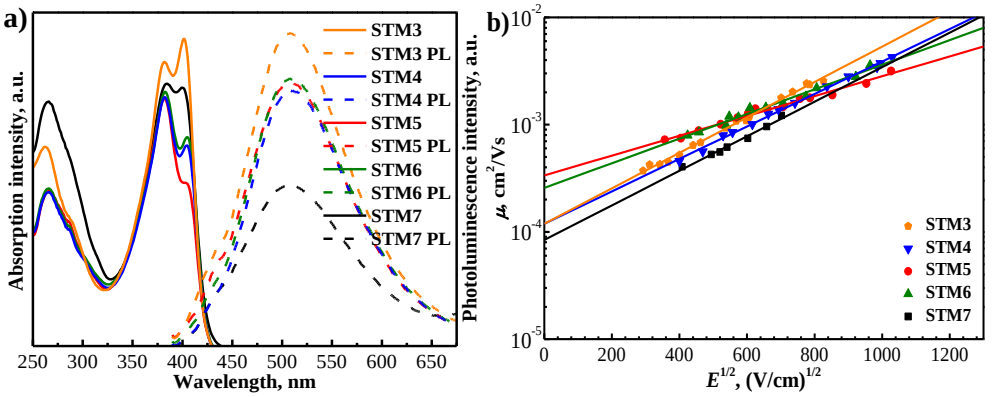

Figure 45. New enamines HTMs: a) UV-vis absorption (solid line) and photoluminescence (dashed line) spectra in THF solution (10^{-4} M); b) Electric field dependencies of hole-drift mobilities

Regarding the ionization potentials (I_P), the HOMO energy levels were measured by the electron photoemission in air method to elucidate the compatibility of the HTM energy levels (Table 28). The I_P values for **STM3, STM4**, **STM5**, **STM6**, and **STM7** were 5.01, 5.0, 5.03, 5.03, and 4.9 eV, respectively. They are ideally compatible with the perovskite valence band energy (5.70 eV). This compatibility ensures efficient hole transfer from the perovskite to the cathode[128]. The E_{ea} values (the LUMO energy level) were calculated by using the E_g and I_P values (Table 28). The electron affinity values for all compounds are between 2.1 and 2.2 eV. Importantly, they are significantly lower than the conduction band energy of the perovskite (4.1 eV), thus ensuring efficient blocking of electrons from the perovskite towards the anode[128].

Table 28. Photoelectrical properties of the new fluorene enamines HTMS

HTM	I_P [a], eV	I_P [b], eV	E_{ea} [c], eV	μ_0 [d], cm^2/Vs
STM3	5.01	5.39	2.22	1.2×10^{-4}
STM4	5.0	5.32	2.21	1.2×10^{-4}
STM5	5.03	5.39	2.22	3.3×10^{-4}
STM6	5.03	5.25	2.24	2.6×10^{-4}
STM7	4.9	5.34	2.11	8×10^{-5}

[a]Ionization energies of the films were measured by using PESA without doping; [b]Ionization energies of the films were measured by using PESA with doping; [c]$E_{ea} = I_P - E_g$; [d]Mobility value at zero-field strength.

By using the xerographic time-of-flight technique, the drift mobilities of positive charges in the new organic semiconductors were measured. Their dependence on the strength of the electric field is shown in Figure 45b. At a zero-field, the hole-drift mobility (μ_0) of the compounds **STM3**, **STM4**, **STM5**, and **STM6** was in the order of 10^{-4} cm^2/Vs, and the highest value of 3.3×10^{-4} cm^2/Vs was recorded for the propyl-substituted semiconductor **STM5**. It is of importance to note that higher hole mobility values than that of the reference Spiro-OMeTAD ($\mu_0 = 1.3\times10^{-4} cm^2/Vs$)[129] were achieved. The introduction of an aromatic benzyl substituent at the 9th position of fluorene had a negative effect on the drift mobility of holes as it decreased by more than one order compared to the other analogues.

As a conclusion based on the results of all the conducted studies, it can be stated that the obtained fluorene enamines are thermally stable, have an amorphous state and high hole-drift mobility in weak electric fields. The HOMO/LUMO energy levels of these organic semiconductors make them suitable hole transporting materials for application in perovskite solar cells.

The new V-series HTMs were tested as positive charge transporting materials in PCSs of the *n-i-p* architecture. The device construction was as follows: FTO / compact TiO_2 layer / mesoporous TiO_2 / amorphous SnO_2 / perovskite – $[(FAPbI_3)_{0.87}(MAPbBr_3)_{0.13}]_{0.92}(CsPbI_3)_{0.08}$ / HTM / Au. HTMs were doped with *t*BP, LiTFSI, and FK209 additives. All organic semiconductor-based PSCs were subjected to cross-sectional *Scanning Electron Microscopy* (SEM). This analysis showed that the hole transporting layers from enamines were compactly covered on the perovskite and were of ~120 nm thickness, while the thickness of the reference Spiro-OMeTAD layer was ~260 nm. The best efficiency results were demonstrated by **STM3**-based PSC (19.3%). The SCs efficiencies of the prealkylated enamine analogues **STM4**, **STM5**, and **STM6** were 19.2%, 19.2%, and 19.1%, respectively. The efficiency of the device based on the compound bearing the benzyl substituent was significantly lower and reached only 12.6%. It can be noted that this lower performance could be predicted because the drift mobility value and the filling factor of the holes of this semiconductor were incomparably lower than those of its analogues. It is of importance to mention that the efficiency of the Spiro-OMeTAD-based PSC

constructed under the same conditions was 19.7% and was only 0.4% higher than the efficiency of the PSC based on **STM3**, which was obtained by a simple condensation reaction.

Doped additives are known to have a negative effect on the long-term stability of PSCs. Lithium salts are hygroscopic, and 4-*tert*-butylpyridine tends to form complexes with PbI_2, leading to faster degradation of perovskite[130]. Therefore, SCs were also produced without additives. It should be noted that, when measuring the power conversion efficiency of PSCs without additives, the efficiency of SC based on the newly synthesized compounds was significantly higher than that of the compound with the reference semiconductor Spiro-OMeTAD. Compound **STM3** showed the best efficiency (17.1%). All results are collected from the graphs of *J-V* curves and presented in Table 29.

Table 29. Photovoltaic parameters of new fluorene enamines HTMs extracted from the best-performing devices

	HTM	V_{OC}, V	J_{SC}, mA/cm^2	*FF*	PCE, %
With doping	**STM3**	1.077	23.24	0.77	19.3
	STM4	1.090	22.97	0.76	19.2
	STM5	1.089	22.86	0.77	19.2
	STM6	1.094	22.95	0.76	19.1
	STM7	1.024	22.32	0.55	12.6
	Spiro-OMeTAD	1.115	22.97	0.77	19.7
Without doping	**STM3**	1.033	22.95	0.72	17.1
	STM4	1.038	22.98	0.71	16.9
	STM5	1.029	23.09	0.70	16.6
	STM6	1.022	23.02	0.69	16.2
	Spiro-OMeTAD	0.972	22.83	0.47	10.4

The stability of all the constructed PSCs was evaluated, except for the SC based on **STM7**, which showed results of a lower efficiency. For comparison, the stability of the device obtained with Spiro-OMeTAD was also evaluated. All the devices were unencapsulated, and continuously exposed to sunlight under a nitrogen atmosphere for 500 hours. The long-term stability results of the devices are presented in Figure 46. The PSCs of all new enamine class compounds showed better stability results than the Spiro-OMeTAD-based SC.

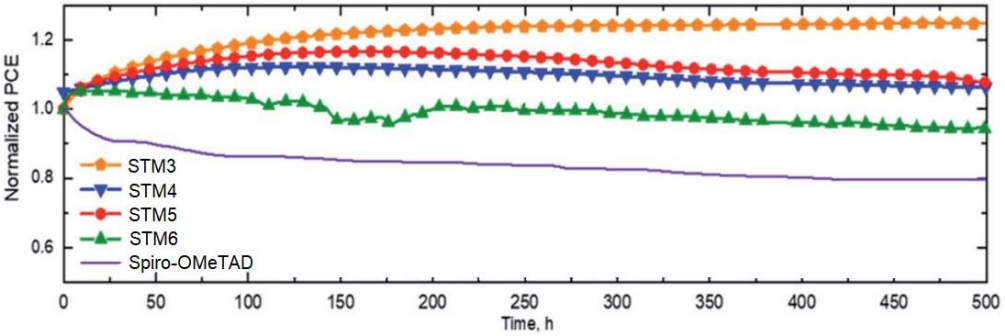

Figure 46. Stability test of the PSCs devices with new enamines and Spiro-OMeTAD

The functionality capabilities of these V-series enamines have also been demonstrated by their use in semi-transparent Sb_2S_3 solar cells whose application is currently quite limited due to a low power conversion efficiency and expensive HTMs. The most commonly used standard HTM is poly-3-hexylthiophene polymer (P3HT). The use of the semiconductor **STM6** and P3HT to construct antimony sulfide SCs has been reported by N. Juneja, S. Daškevičiūtė-Gegužienė et al. in the article "Sb_2S_3 Solar Cells with Economical and Additive-Free Fluorene-Based Enamine as Hole Transport Material," *Sustainable Energy Fuels, 2022, 6*, 3220–3229. The power conversion efficiency of the solar cell with enamine **STM6** was 17% higher than that of P3HT, and the transparency of the devices increased by 20%. It is of importance to note that the price of this device was significantly lower (for comparison: P3HT is valued ~45 Eur/g, **STM6** yields ~17 Eur/g).

The application possibilities of new enamine class semiconductors were also described by N. Juneja, S. Daskeviciute-Geguziene et al. in another article "Employment of Dopant-Free Fluorene-Based Enamines as Innovative Hole Transporting Materials to Boost the Transparency and Performance of Sb_2S_3 Based Solar Cells," *Materials Science in Semiconductor Processing*, *2024*, *169*, 107934. New organic semiconductors **STM3** and **STM5** were applied in the hole transporting layers of Sb_2S_3 solar cells. The power conversion efficiencies of these SCs were 3.9% and 4.3%, respectively, thus surpassing the efficiency of the standard P3HT-based device, which is equal to 3.8%.

5.2.3. Synthesis and application of enamines with fluorene chromophores and acceptor groups for efficient and stable perovskite solar cells

This subchapter is based on the published article: "Passivating Defects of Perovskite Solar Cells with Functional Donor-Acceptor-Donor Type Hole Transporting Materials," *Adv. Funct. Mater., 2022, 3*, 1–8, Q1, by Š. Daškevičiūtė-Gegužienė, Y. Zhang, K. Rakštys, C. Xiao, J. Xia, Z. Qiu, M. Daškevičienė, T. Paškevičius, V. Jankauskas, A. M. Asiri, V. Getautis, M. K. Nazeeruddin; cited 10 times.

This section describes a study of the influence of the donor-acceptor-donor (D-A-D) interaction on the passivation of perovskite defects. Organic semiconductors

based on units of fluorene and phenylethenyl enamine, which were distinguished by different acceptors, were synthesized for this purpose (Figure 47). The PSC based on the semiconductor **STM13** achieved the highest power conversion efficiency, exceeding 22%, which is higher than that of the Spiro-OMeTAD-based device under identical conditions. Incorporation of the malononitrile acceptor units has been shown to be beneficial not only for carrier transportation, but also for the passivation defects of perovskite, leading to a better stability of the SCs. The cost of HTM **STM13** is comparatively very low, i.e., 21 Eur/g. It is obvious, that these organic semiconductors are an excellent alternative to expensive Spiro-OMeTAD.

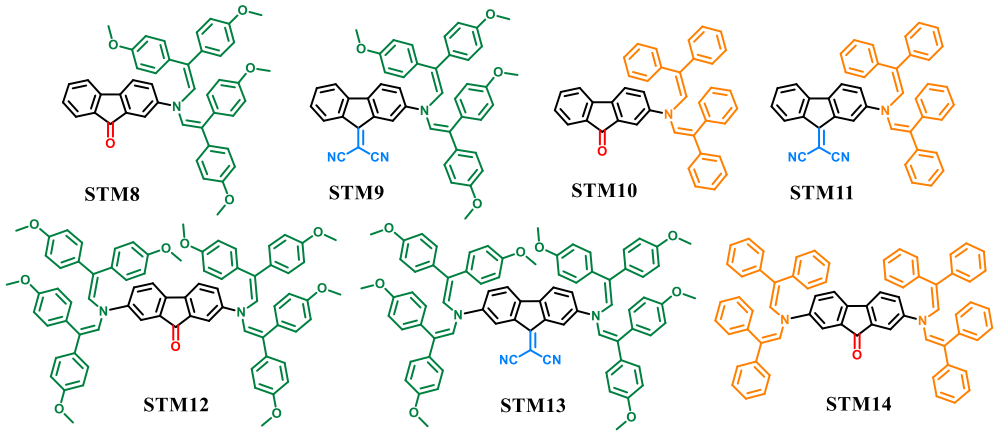

Figure 47. Chemical structures of synthesized D-A-D type organic semiconductors

By using a simple condensation reaction, in which water is the only by-product, fluorenone-based organic semiconductors with one (**STM8** and **STM10**) or two (**STM12** and **STM14**) enamine fragments were synthesized by condensing low-cost commercial reagents 2-aminofluorenone or 2,7-diaminofluorenone with 2,2-bis-(4-methoxyphenyl)acetaldhyde in the presence of CSA under ambient conditions. To obtain compounds with stronger ciano acceptor groups, the keto group was converted to malononitrile by Knoevenagel condensation, thus providing the semiconductors **STM9**, **STM11**, and **STM13**. A detailed synthetic pathway is reported in Scheme 14. It is of importance to highlight that condensation chemistry presents an excellent potential in moving away from transition metal-based cross-coupling reactions and the usage of metal catalysts while providing simplified product workup and purification. The structures of the new compounds were confirmed by ^{1}H and ^{13}C NMR spectroscopy, mass spectrometry, infrared spectroscopy, and elemental analysis data.

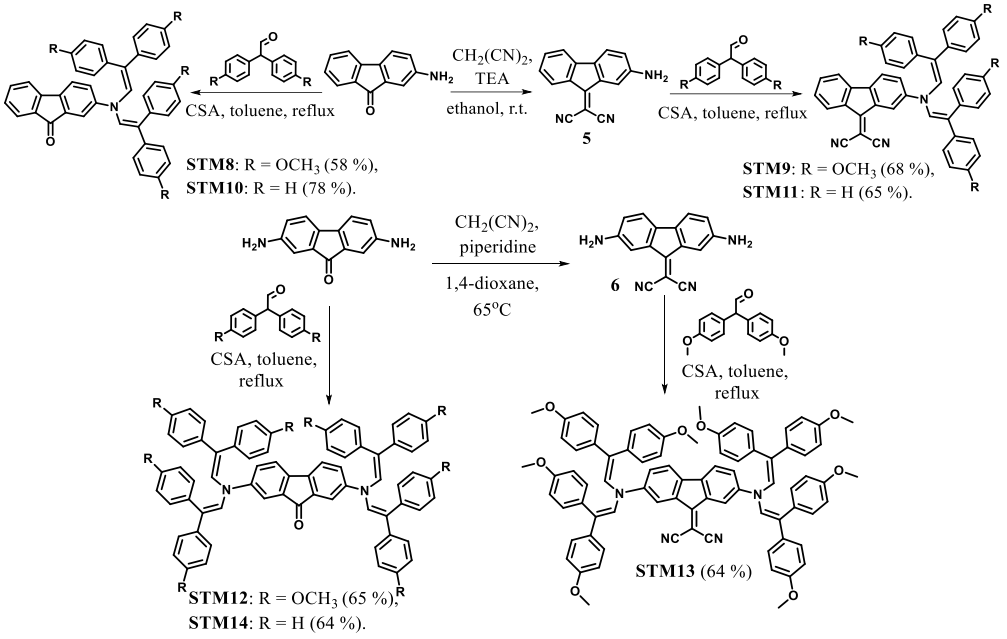

Scheme 14. Reaction scheme for fluorenone/dicianofluorenylidene enamine-based HTMs

In order to estimate the cost of the synthesized *p*-type semiconductors, a synthesis cost analysis was performed. The estimated cost of the semiconductor **STM13** with two enamine fragments is ~21 Eur/g, while that of the semiconductor with one enamine fragment **STM10** is ~18 Eur/g, which is only a quarter of the price of Spiro-OMeTAD.

The optical, thermal, and photophysical properties of new fluorenone and dicyanofluorenylidine enamines were investigated (Table 30), and the potential applications in PSCs were evaluated.

The thermal properties of the compounds were evaluated by using the TGA and DSC analysis methods (Table 30). Thermogravimetric analysis showed that organic semiconductors with higher aromatic systems have a higher thermal stability[131-133]. The highest decomposition temperature, when the compound loses 5% of its mass, was recorded for the semiconductor **STM14** (T_{dec} = 412 °C). All the synthesized compounds have a higher T_{dec} than that of Spiro-OMeTAD[125]. The thermal transitions of the compounds were determined by DSC. A clear trend was observed between methoxy-substituted and non-methoxy compounds. Organic semiconductors **STM10**, **STM11**, and **STM14** are crystalline, their melting points were recorded in both heating scans. Compounds bearing methoxy groups can exist in both crystalline and amorphous states. For all compounds containing methoxy groups in their structure, a glass transition temperature was recorded during the second heating scan. The organic semiconductors **V1351** and **STM13** have the most stable amorphous state with a glass transition temperature detected at 140 °C.

Table 30. Thermal, optical, and photoelectrical properties of new D-A-D type HTMs

HTM	T_m [a], °C	T_c [a], °C	T_g [a], °C	T_{dec} [a], °C	λ_{abs} [b], nm	I_P [c], eV	μ_0 [d], cm^2/Vs
STM8	171, 186, 208	–	92	376	259, 299, 313, 370, 538	5.44	1.3×10^{-7}
STM9	245	–	111	379	265, 345	5.44	1.1×10^{-7}
STM10	244, 247	202	111	338	255, 285, 313, 363, 513	5.49	1.4×10^{-6}
STM11	236, 248, 239, 248	175	115	347	268, 341	5.53	1.3×10^{-6}
STM12	221, 232	–	143	403	261, 299, 313, 385, 403, 598	5.43	4×10^{-6}
STM14	339, 351, 348	217	157	412	270, 288, 311, 378, 395, 570	5.39	2.8×10^{-6}
STM13	166	–	134	389	263, 323, 349, 409	5.41	4.6×10^{-6}

[a]Melting (T_m), crystallization (T_c), glass transition (T_g) and decomposition (T_{dec}) temperatures were observed from DSC and TGA, respectively (10 °C/min, N_2 atmosphere); [b]Absorption (excitation = $\lambda_{abs\ max}$) spectra were measured in THF solution (10^{-4} M); [c]Ionization energies of the films were measured by using PESA; [d]Mobility value at zero-field strength.

The UV-vis absorption spectra of the synthesized HTMs in THF solutions are presented in Figure 48a. When comparing **STM8** with **STM9**, **STM10** with **STM11**, and **STM12** with **STM13**, the red-shift of the absorption maxima was observed. The differences in the absorption maxima arise from different =O and $=C-(CN)_2$ acceptor fragments. The malononitrile functional group is a stronger electron acceptor. Compounds **STM12**, **STM14**, and **STM13** have a two-times-larger conjugated system; therefore, their absorption spectra display a significant hyperchromic shift compared to the enamines of a single fragment. Broad optical absorption in the visible region corresponds to the interaction of the donor-acceptor charge transfer[134-135]. The fluorescence spectra of all the molecules were measured in THF solutions; however, emission was not detected.

To determine the energy levels of semiconductors, the solid-state ionization potential was measured by using the electron photoemission in air of the thin films. The experimental data are presented in Table 30. Different I_P values, in the range of approximately 5.4–5.5 eV, were determined forD-A-D type semiconductors.

The charge carrier mobility of the synthesized molecules was measured by using the xerographic time-of-flight technique. The dependence of the hole-drift mobility on the electric field strength is shown in Figure 48 and Table 30. It was not possible to measure the drift mobility of **STM9** and **STM14** from pure layers; therefore, the charge transfer in layers of blends with bisphenol Z-polycarbonate (PC-Z) in mass

ratios of 1:1, 1:2, 1:3 or 1:4 was prepared. The quality of the obtained layers was suitable for measurements. Based on the exponential dependence of the charge carrier mobility on the average distance between the charge transporting molecules, interpolated mobility values were determined for pure materials[136]. At zero-field, the compound **STM13** exhibited the highest hole-drift mobility $\mu_0 = 4\times10^{-6}$ cm^2/Vs. The lower molecular conjugation negatively affected the hole-drift mobility. The organic semiconductor with a single enamine fragment **STM9** showed the lowest result of 1.1×10^{-7} cm^2/Vs.

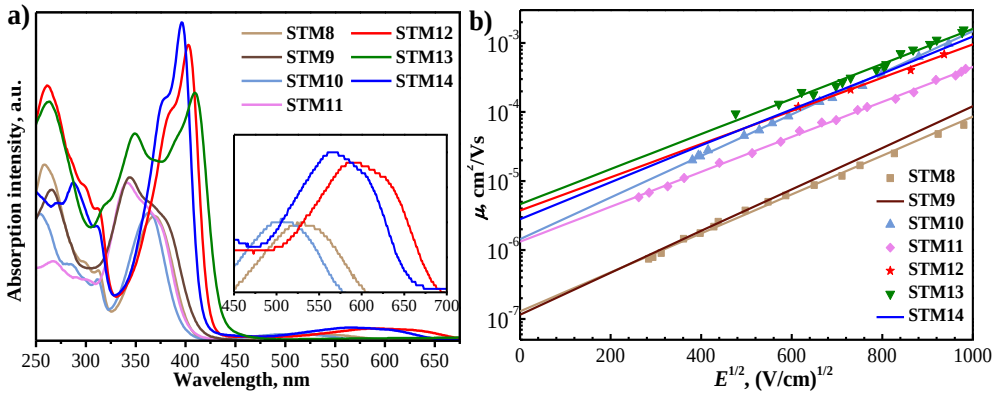

Figure 48. New D-A-D type HTMs: a) UV-vis absorption spectra in THF solution (10^{-4} M); b) Electric field dependencies of the hole-drift mobilities

After the properties of the new compounds had been studied, PSCs were constructed. The device construction of the *n-i-p* architecture was as follows: FTO / SnO_2 / perovskite – $(FAPbI_3)_{0.85}(MAPbBr_3)_{0.15}$ / HTM / Au. The SEM images of a cross-sectional view of all the PSC devices were recorded. The thickness of the layers of the new organic semiconductors were ~80 nm, while that of Spiro-OMeTAD was ~220 nm. The difference in thickness was due to the optimized concentrations of the new HTMs. The optimized photovoltaic characteristics data of the solar cells from *J-V* curves are systematized and presented in Table 31. It can be argued that the molecular structure, particularly, an increased conjugation, has a significant influence on the efficiency parameters of the devices. Devices with single-arm compounds (**STM8**, **STM9**, **STM10**, and **STM11**) as the HTMs exhibited a lower power conversion efficiency compared to the reference alternative Spiro-OMeTAD. The opposite situation was observed with the double-arm molecules. The efficiency results of devices with **STM12** and **STM12** as HTMs were 19.92% and 20.53%, respectively, and almost matched the efficiency value of Spiro-OMeTAD. The most efficient perovskite device contained **STM13**, achieving a power conversion efficiency of more than 22% and outperforming Spiro-OMeTAD. The reason for this record efficiency could have been a high fill factor (*FF*), indicating a good quality of the hole transporting layer. The acceptor =C-$(CN)_2$ group interacts with uncoordinated lead ions (Pb^{2+}), and this interaction reduces perovskite defects resulting in an improved efficiency and stability of PSCs[137-139].

Table 31. Photovoltaic parameters of the new D-A-D type HTMs extracted from the best-performing devices

HTM	V_{OC}, V	J_{SC}, mA/cm^2	*FF*	PCE, %
STM8	0.963	22.80	0.687	14.97
STM9	0.991	23.25	0.670	15.37
STM10	0.895	23.01	0.662	13.54
STM11	0.871	1.59	0.497	0.68
STM12	1.089	23.77	0.769	19.92
STM13	1.112	24.34	0.813	22.03
STM14	1.070	24.2	0.792	20.53
Spiro-OMeTAD	1.121	24.16	0.793	21.48

Another issue of importance for the commercialization is the large-scale production when upscaling from laboratory to manufacturing scale. Therefore, a 6.5 × 7 cm perovskite solar module was fabricated by using the compound **STM13**, and its power conversion efficiency was 18.61%.

The stabilities of the PSCs based on the semiconductor **STM13** and Spiro-OMeTAD were evaluated (Figure 49). The devices were kept without encapsulation at room temperature and 12% relative humidity under illumination for 500 hours. The device based on **STM13** maintained 95% of its initial efficiency after 500 h, while the device based on spiro-OMeTAD maintained only 85%.

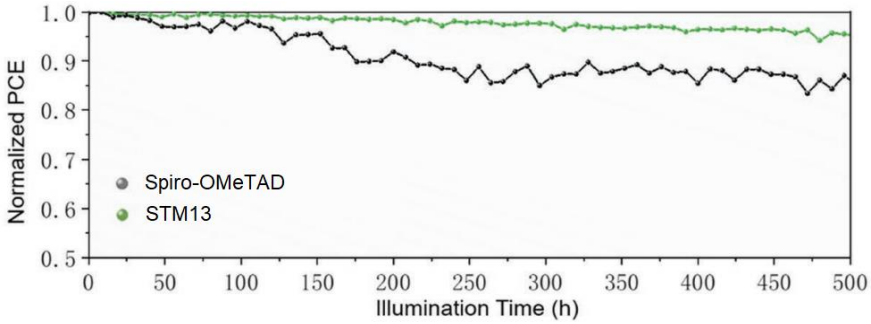

Figure 49. Stability test of PSCs with **STM13** and Spiro-OMeTAD

In this section, fluorene-based D-A-D type HTMs, synthesized by using simple condensation reactions, are described. Thermal, optical, photophysical, and photovoltaic measurements revealed that the incorporation of the malononitrile acceptor units is beneficial not only for carrier transportation, but also for the efficiency and stability of PSCs. The efficiency and stability of the device based on the organic semiconductor **STM13** was better than that of the reference Spiro-OMeTAD. The results of this study show that simple molecular engineering of hole

transporting materials contributed to a significant improvement of the PSC efficiency and stability.

5.2.4. Synthesis of spirobisindane-based enamines and their application in perovskite solar cells

This subchapter is based on the published article: "Design, Synthesis and Theoretical Simulations of Novel Spiroindane-Based Enamines as *p*-Type Semiconductors," *R. Soc. Open Sci., 2024, 11*, 232019, Q2, by Š. Daškevičiūtė-Gegužienė, M. Daškevičienė, K. Kantminienė, V. Jankauskas, E. Kamarauskas, A. Gruodis, S. Karazhanov, V. Getautis.

In this section, two new organic semiconductors **STM15** and **STM16** containing a spirobisindane fragment as a central core are described (Figure 50). The new compounds were synthesized by using commercially available starting materials without the use of costly metal catalysts and by combining different aniline substituents. After the thermal properties had been investigated, it was determined that the semiconductors are amorphous, thus making them an excellent alternative to the crystalline Spiro-OMeTAD.

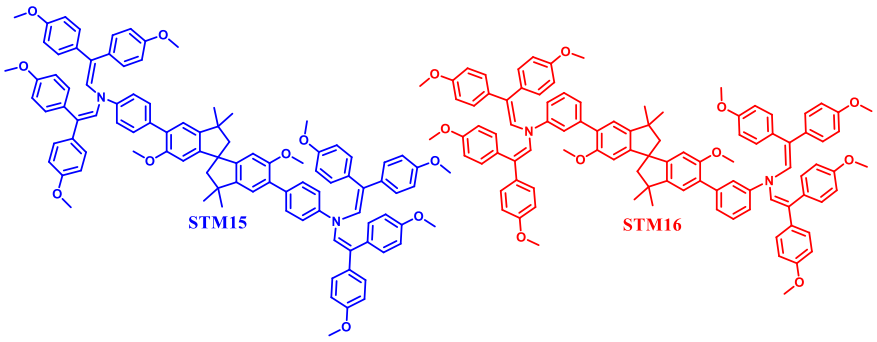

Figure 50. Structures of new HTMs **STM15** and **STM16**

The general synthesis procedure of new HTMs **STM15** and **STM16** is shown in Scheme 15. Low-cost and commercially available bisphenol A was used as a starting material. In the simple initial cyclization step, it was heated in methanesulfonic acid. The obtained spirobisindane **7** was alkylated with iodomethane and a base potassium carbonate in dimethylformamide. The intermediate product **8** was then brominated by using *N*-bromosuccinimide, and thus eliminating aggressive bromine. These three steps of synthesis were performed according to a known methodology described in the literature[99]. Enamine precursors **10** and **11** with benzene substituents in different positions (*para* and *meta*) were obtained by performing Suzuki cross-coupling reactions. By using a simple condensation reaction, of which the only byproduct is water, the target organic semiconductors **STM15** and **STM16** were synthesized by condensing the respective precursors with 2,2-bis(4-methoxyphenyl)acetaldehyde, in the presence of CSA. The structures of the new compounds were confirmed by ^{1}H, ^{13}C NMR, mass spectroscopy, and elemental analysis data.

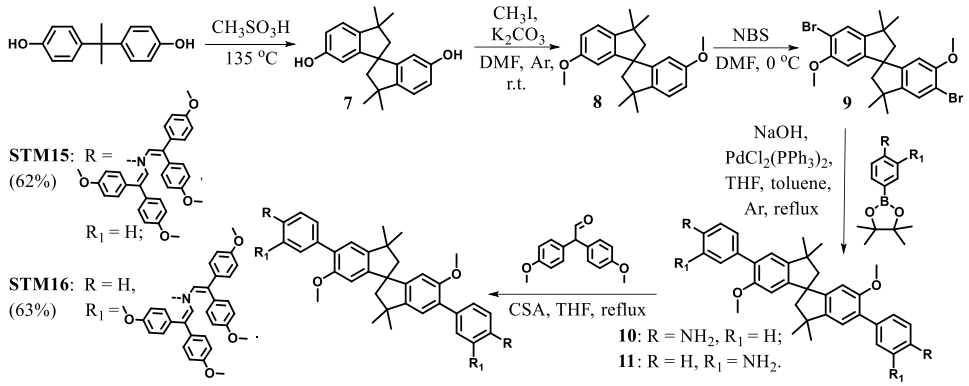

Scheme 15 Synthesis route to new HTMs **STM15** and **STM16**

In the study, the optical, thermal, and photophysical properties of HTMs were investigated (Table 32), and their potential applications in PSCs were evaluated.

Table 32. Thermal, optical, and photoelectrical properties of new HTMs **STM15** and **STM16**

STM	T_g [a], °C	T_{dec} [a], °C	λ_{abs} [b], nm	λ_{em} [b], nm	I_P [c], eV	E_g [d], eV	E_{ea} [e], eV	μ_0 [f], cm^2/Vs
STM15	167	403	265, 355	502	5.34	3.02	2.32	9.0×10^{-6}
STM16	157	389	260, 335, 365	502	5.30	3.07	2.23	2.6×10^{-6}

[a]Glass transition (T_g) and decomposition (T_{dec}) temperatures were observed from DSC and TGA, respectively (10 °C/min, N_2 atmosphere); [b]Absorption and emission (excitation = $\lambda_{abs\ max}$) spectra were measured in THF solution (10^{-4} M); [c]Ionization energies of the films were measured by using PESA; [d]Eg was estimated from the intersection of the absorption and emission spectra of solid films; [e]$E_{ea} = I_P - E_g$; [f]Mobility value at zero-field strength.

The thermal characteristics of the organic semiconductors were evaluated by TGA and DSC. TGA revealed that the compound **STM15** loses 5% of its weight at 403 °C and exhibits a higher thermal stability compared to the meta-substituted analogue **STM16** (T_{dec} = 389 °C). In particular, both synthesized enamines possess higher decomposition temperatures than that of Spiro-OMeTAD (T_{dec} = 288 °C). The DSC method was used to determine the thermal transitions of the target compounds. The results demonstrated that both enamines are amorphous. The glass transition temperatures recorded for **STM15** and **STM16** are 167 °C and 157 °C, respectively. It is of importance to note that the T_g value of the new HTMs is higher than that of the reference Spiro-OMeTAD (T_g = 124 °C), thus indicating that spirobisindane-based organic semiconductors are likely to possess a better morphological stability. It is also important to emphasize that the amorphous state of Spiro-OMeTAD is not stable; over time, this compound tends to crystallize, which adversely affects the long-term stability of PSCs.

The UV-vis absorption spectra of spirobisindane-based HTMs were recorded from THF solutions (Figure 51a). The spectra of both organic semiconductors have two main absorption peaks at ~265 and ~360 nm. The absorption peak at 265 nm corresponds to the localized π-π^* electron transitions originating from the central spirobisindane scaffold. Meanwhile, peaks of unequal intensity at ~360 nm are due to the delocalization of different substituents (*meta* and *para*) and are attributed to π-π^* and n-π^* electron transitions. Upon excitation of the valence electrons, the PL spectra were recorded (Table 32). The emission maxima for both compounds were recorded at 502 nm. The observed very large Stokes shifts (~150 nm) indicate significant geometric changes in the excited state of the molecules. The optical gaps (E_g) of **STM15** and **STM16** were calculated from the intersection of the absorption and PL spectra of thin films and are equal to 3.02 and 3.07 eV, respectively (Table 32).

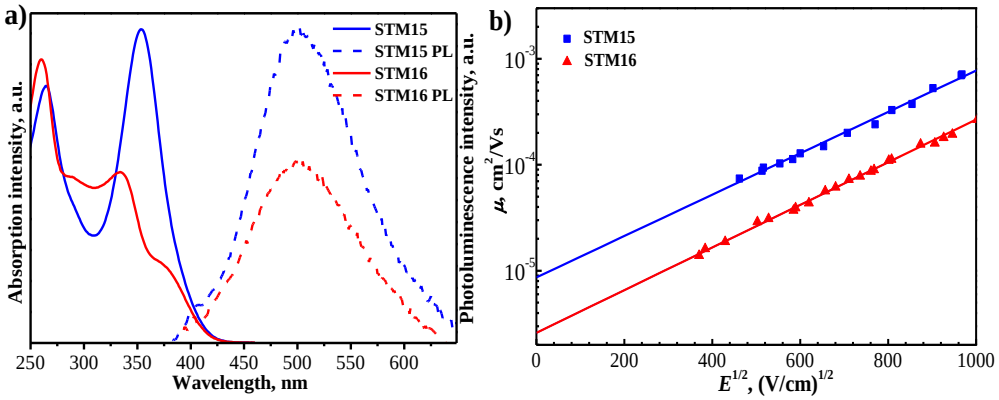

Figure 51. New HTMs **STM15** and **STM16**: a) UV-vis absorption (solid line) and photoluminescence (dashed line) spectra in THF solution (10^{-4} M); b) Electric field dependencies of the hole-drift mobilities

In order to determine the HOMO energy level of the new HTMs, the solid state ionization potential (I_P) was measured by the photoelectron spectroscopy in air method. The I_P values of **STM15** and **STM16** are 5.34 and 5.30 eV, respectively. They are in the same range as the preferred I_p values of HTMs used in perovskite solar cells. The LUMO energy level values were determined by calculating the E_{ea} value (2.32 eV for **STM15** and 2.23 eV for **STM16**) (Table 32).

The charge carrier mobility of the new organic semiconductors was measured by the xerographic time-of-flight technique. The experimental data illustrating the dependence of the hole-drift mobility on the electric field strength are shown in Figure 51b. The zero-field hole-drift mobility of the compound **STM15** reached almost 10^{-5} cm^2/Vs, while its meta-substituted analogue **STM16** exhibited a slightly lower mobility ($\mu_0 = 2.6\times10^{-6}$ cm^2/Vs).

Following a comprehensive evaluation of their thermal, optical, and photophysical properties, it is evident that the synthesized low-molecular mass compounds **STM15** and **STM16** emerge as promising candidates for applications in organic perovskite solar cells.

Table 33. Photovoltaic parameters of new HTMs **STM15** and **STM16** extracted from the best-performing devices

HTM	V_{OC}, V	J_{SC}, mA/cm^2	*FF*	PCE, %
STM15	1.11	22.6	0.66	16.4
STM16	1.10	22.3	0.60	14.7
Spiro-OMeTAD	1.09	22.8	0.77	19.1

The new spirobisindane-based enamines were used as positive charge transport materials in the *n-i-p* structure PSCs. The device architecture was as follows: ITO / SnO_2 / perovskite – $Cs_{0.05}FA_{0.87}MA_{0.08}PbI_{2.76}Br_{0.24}$ / HTM / Au. All the PSC photovoltaic characteristics are summarized in Table 33. The PSC with the positive charge transporting compound **STM15** showed the most promising results with an efficiency of 16.4%. This semiconductor is thermally more stable than Spiro-OMeTAD, and it exists only in an amorphous state. Therefore, it can be a promising alternative to Spiro-OMeTAD upon the appropriate improvement of the manufacturing conditions of PSCs.

5.2.5. Green-chemistry-inspired synthesis of hole transporting materials for efficient and stable perovskite solar cells and modules

This subchapter is based on the published article: "Green-Chemistry-Inspired Synthesis of Cyclobutane-Based Hole-Selective Materials for Highly Efficient Perovskite Solar Cells and Modules," *Angew. Chem. Int. Ed.*, *2022*, *61*, e202113207, Q1, by Š. Daškevičiūtė-Gegužienė, Y. Zhang, K. Rakštys, G. Kreiza, S. B. Khan, H. Kanda, S. Paek, M. Daškevičienė, E. Kamarauskas, V. Jankauskas, A. M. Asiri, V. Getautis, M. K. Nazeeruddin; cited 20 times.

This section describes HTMs synthesized by using green-chemistry inspired protocols so that to reduce hazardous and aggressive reagents and solvents. It is known that photodimerized carbazoles are attractive scaffolds because of their simple and green synthesis, and their various derivatives exhibit high hole-drift mobility[140-142]. Therefore, new cyclobutane-based organic semiconductors, which are suitable for PSC production due to their energy levels, were synthesized (Figure 52).

Systematic investigation of the influence of various carbazole substitutes on the properties of the new hole transporting materials was carried out. New cyclobutane-based HTMs were successfully applied in perovskite solar cells. An efficiency of 21% was achieved, along with an improved device stability compared to Spiro-OMeTAD. Most importantly, a **STM22**-based perovskite solar module (6.5 cm × 7 cm) was fabricated and exhibited a record efficiency of over 19%.

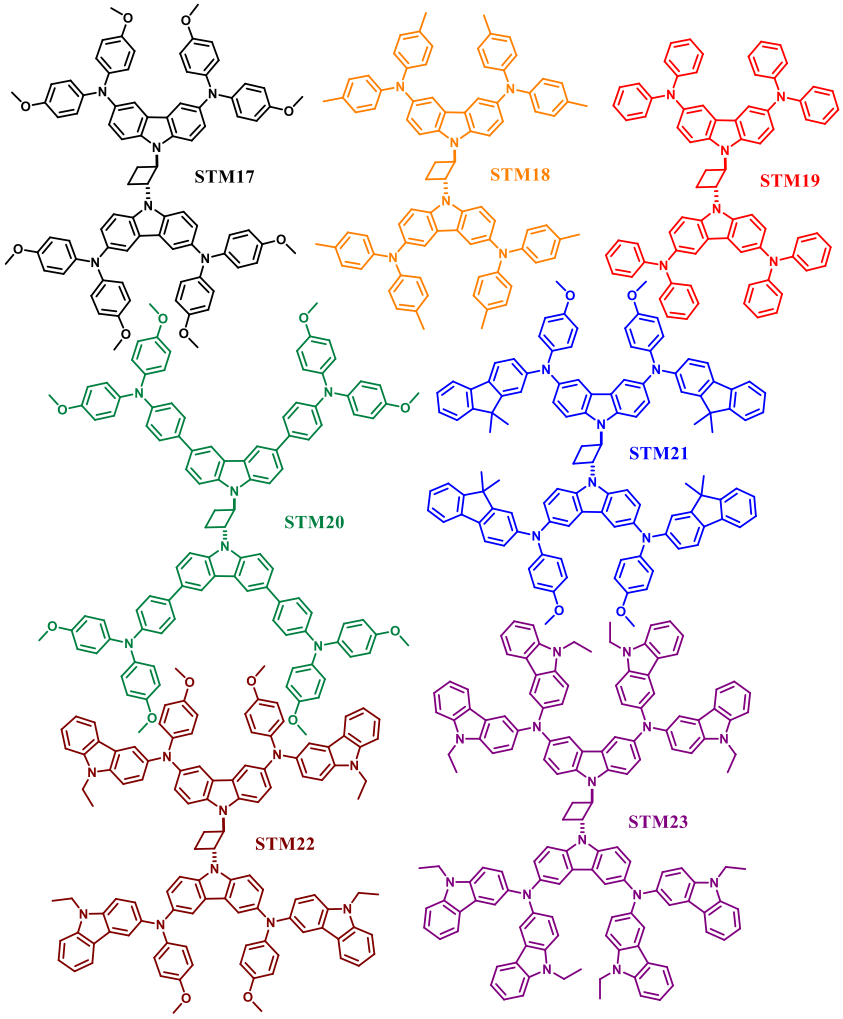

Figure 52. Structures of new HTMs based on substituted cyclobutane

The general synthesis procedure for the preparation of cyclobutane-based HTMs is shown in Scheme 16. Low-cost commercially available 9-vinylcarbazole was used as a starting reagent. Its photodimerization readily occurred under UV light in green solvent acetone at ambient temperature. Next, *trans*-1,2-bis(9-carbazolyl)cyclobutane (**12**) was brominated by using an aqueous solution of potassium bromate and bromide, thus eliminating the use of aggressive bromine. To obtain **STM20**, an aqueous/THF four-fold Suzuki cross-coupling procedure was applied. These three steps of synthesis demonstrated that **STM20** was obtained, and the use of hazardous substances to the environment and human health was completely eliminated. For the final synthesis step of other hole transporting materials described in this work, the standard Buchwald reaction conditions were used. The structures of the new compounds were confirmed by ^{1}H, ^{13}C NMR, mass spectroscopy, and elemental analysis data.

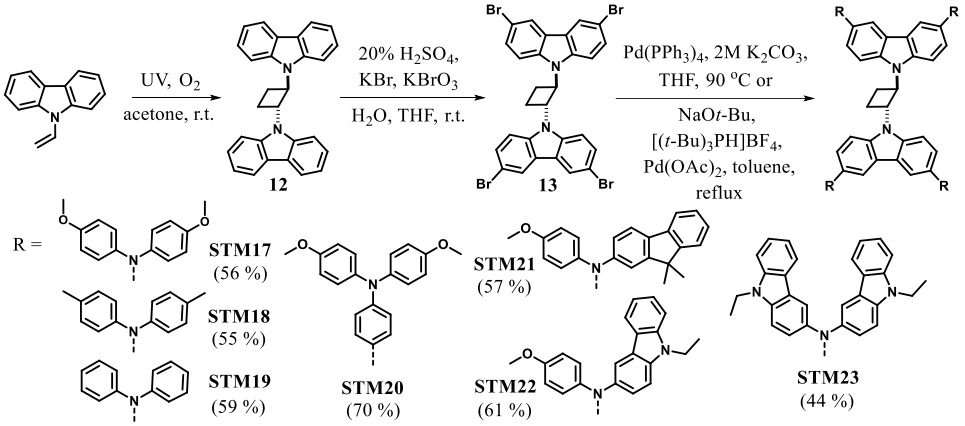

Scheme 16. Synthesis route to novel HTMs based on substituted cyclobutane

Thermal, optical, and photophysical studies of the new HTMs were performed (Table 34), and their potential applications in PSCs were evaluated.

Table 34. Thermal, optical, and photoelectrical properties of new HTMs based on substituted cyclobutane

HTM	T_m [a], °C	T_g [a], °C	T_{dec} [a], °C	λ_{abs} [b], nm	λ_{em} [b], nm	I_P [c], eV	E_g [d], eV	E_{ea} [e], eV	μ_0 [f], cm^2/Vs
STM17	–	122	416	291, 303	450	5.07	2.91	2.12	7.9×10^{-6}
STM18	320	159	406	291, 304	435	5.37	2.98	2.48	1.7×10^{-4}
STM19	–	162	382	289, 302	427	5.48	3.05	2.43	3.3×10^{-7}
STM20	–	148	421	291, 306, 334	420	5.34	3.13	2.21	1×10^{-5}
STM21	–	157	432	291, 315, 354	445	5.28	2.93	2.35	2.5×10^{-5}
STM22	–	173	439	291, 309	459	4.77	2.83	1.94	3.5×10^{-5}
STM23	–	215	477	291, 318	471	4.78	2.79	1.99	2.5×10^{-6}

[a]Melting (T_m), glass transition (T_g) and decomposition (T_{dec}) temperatures were observed from DSC and TGA, respectively (10 °C/min, N_2 atmosphere); [b]Absorption and emission (excitation = $\lambda_{abs\ max}$) spectra were measured in THF solution (10^{-4} M); [c]Ionization energies of the films were measured by using PESA; [d]Eg was estimated from the intersection of absorption and emission spectra of solid films; [e]$E_{ea} = I_P - E_g$; [f]Mobility value at zero-field strength.

The TGA results showed that a 5% weight loss of the HTMs occurs within a range of 380–480 °C, which is much higher than the usual operating temperature of the devices (Table 34). There is a clear trend that the thermal decomposition temperature increases with the increasing molar mass of the synthesized compounds.

DSC measurements revealed that all new compounds are amorphous, except for the semiconductor **STM18** which exhibits both amorphous and crystalline states. It is of importance to note that all the synthesized HTMs have glass transition temperatures higher than that of Spiro-OMeTAD (124 °C). Therefore, cyclobutane-based organic semiconductors are expected to have better morphological stability.

The UV-vis absorption and PL spectra of the new HTMs in THF solutions are shown in Figure 53a. The spectra of all the compounds have at least two main absorption peaks. An absorption maximum at 290 nm corresponds to localized π-π^* valence electron transitions arising from the central scaffold. The absorption peak maxima detected in the range from 303 nm to 354 nm are assigned to n-π^* delocalized electron transitions. The differences in the UV-vis spectra arise from the presence of different conjugated substituents in organic semiconductors. The PL spectra showed that significantly large Stokes shifts (100–150 nm) are observed for all the molecules; therefore, changes in the geometry of the molecules are expected upon excitation. The optical gaps (E_g) were calculated from the intersection of the absorption and photoluminescence spectra of thin films; they range from 2.79 to 3.13 eV (Table 34).

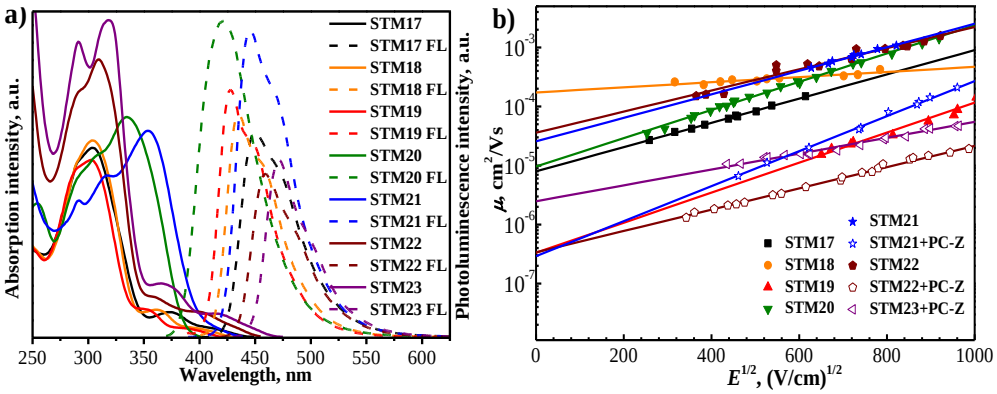

Figure 53. New HTMs based on substituted cyclobutane: a) UV-vis absorption (solid line) and photoluminescence (dashed line) spectra in THF solution (10^{-4} M); b) Electric field dependencies of the hole-drift mobilities

The HOMO energy levels of the new semiconductors were measured by the photoelectron spectroscopy in air method. Different I_P values in a range of 4.7–5.5 eV were determined for all the compounds (Table 34). Based on the E_g and I_P values, electron affinity values (E_{ea}) in the range of 1.9–2.5 eV were calculated. These values also indicate the level of LUMO energy. It must be lower than the energy of the perovskite layer (4.1 eV) to ensure the effective electron blocking from the perovskite to the electrode.

The data on the dependence of the hole-drift mobility of the new HTMs on the electric field strength are shown in Figure 53b. At zero-field, the compound **STM18** exhibited the highest hole-drift mobility ($\mu_0 = 1.7\times10^{-4}$ cm^2/Vs), thus outperforming Spiro-OMeTAD ($\mu_0 = 1.3\times10^{-4}$ cm^2/Vs)[129]. **STM20**, **STM21**, and **STM22** showed one order of magnitude lower μ_0 values.

The new V-series compounds were tested in PSCs with the *n-i-p* structure. The device architecture was as follows: FTO / SnO_2 / perovskite – $(FAPbI_3)_{0.85}(MAPbBr_3)_{0.15}$ / HTM / Au. The concentrations of the semiconductor solutions were optimized during the device construction. The thickness of the HTM layer was 100 nm, while that of Spiro-OMeTAD was 200 nm. The efficiencies of the devices based on **STM22** and the reference Spiro-OMeTAD were very similar, i.e.,. 21% and 21.64%, respectively. High device efficiency results were also demonstrated by the compounds **STM17** (19.11%) and **STM20** (18.53%). Unfortunately, PSCs with the semiconductors **STM18** and **STM19** exhibited a very low power conversion efficiency. This could be attributed to the relatively low HOMO levels of these compounds. Moreover, very low device fill factor values were also observed.

Table 35. Photovoltaic parameters of new HTMs based on substituted cyclobutane extracted from the best-performing devices

HTM	V_{OC}, V	J_{SC}, mA/cm^2	*FF*	PCE, %
STM17	1.073	24.01	0.750	19.11
STM18	0.942	6.49	0.198	1.21
STM19	0.506	12.00	0.217	1.32
STM20	1.057	24.22	0.752	18.53
STM21	1.061	21.11	0.693	15.26
STM22	1.092	24.38	0.791	21.00
STM23	0.927	22.99	0.584	12.44
Spiro-OMeTAD	1.114	24.17	0.803	21.64

The stability of the devices based on **STM22** and Spiro-OMeTAD was evaluated. The experiment was carried out under ambient conditions for 550 hours at a relative humidity of 15–20%. In the reference device which used Spiro-OMeTAD as an HTM, the conversion efficiency decreased by more than 1.5%, while almost no change was observed in the device based on **STM22** (Figure 54).

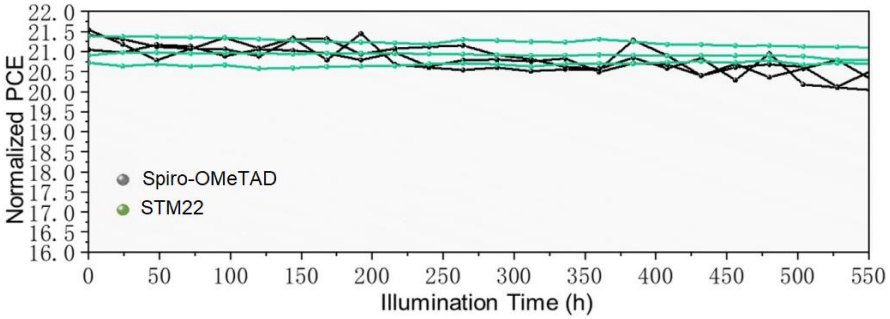

Figure 54. Stability test of PSCs with **STM22** and Spiro-OMeTAD

Another issue of importance to commercialization is large-scale production. Having achieved excellent efficiency results for the PSC with the semiconductor **STM22** under laboratory conditions, a prototype solar module of a size of 6.5 × 7 cm was manufactured. The module exhibited a PCE value of 19.06%. This result is the highest PCE ever reported for a non-Spiro-OMeTAD-based perovskite module.

The results of this study confirm the possibility of the successful development of manufacturing technologies for perovskite solar cells while using environmentally friendly green semiconductors.

The practical importance of V-series organic semiconductors is evidenced by four international patent applications "Photovoltaic Devices Containing Cyclobutane-Based Hole Transporting Materials," which were submitted in different patent offices: The United States (US2023157158), European (EP4181225), China (CN116133444), and Japan (JP2023072638).

5.2.6. Synthesis and application of cross-linkable carbazole-based hole transporting materials for inverted perovskite solar cells

This subchapter is based on the published article: "Cross-Linkable Carbazole-Based Hole Transporting Materials for Perovskite Solar Cells," *Chem. Commun., 2022, 58, 7495–7498*, Q2, by Š. Daškevičiūtė-Gegužienė, A. Magomedov, M. Daškevičienė, K. Genevičius, N. Nekrašas, V. Jankauskas, K. Kantminienė, M. D. McGehee, V. Getautis; cited 6 times. The cover of this issue of the journal *Chemical Communications* was illustrated with the theme of this particular article.

This chapter describes new HTMs that have been used in the construction of the increasingly popular inverted (*p-i-n*) perovskite solar cells. In this case, the *p*-type semiconductor is coated prior to the perovskite layer; therefore, it should withstand a mixture of polar DMSO:DMF solvents used in the casting of the light absorber layer. For this reason, polymer materials are most commonly used, especially those capable of forming solvent-resistant 3D structures. For this purpose, in this study, two new carbazole-based molecules with vinyl groups were synthesized (Figure 55).

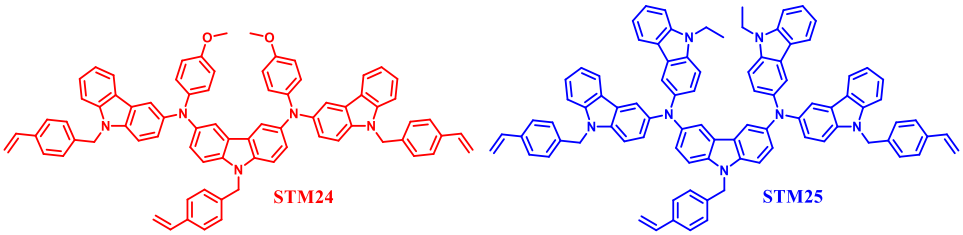

Figure 55. Molecular structures of the synthesized cross-linkable HTMs **STM24** and **STM25**

The general synthesis pathway of new polymerizable HTMs is shown in Scheme 17. Commercially available 3-bromo-9*H*-carbazole and 3,6-dibromo-9*H*-carbazole were chosen as the starting reagents. Intermediate compounds **14** and **16** with vinyl groups were synthesized by using a simple alkylation methodology. Then, Hartwig-Buchwald palladium-catalyzed reactions were performed. Compound **14** was coupled

with *p*-anisidine to yield secondary amine **15**, which was then reacted with precursor **16** to provide the target product **STM24** with three cross-linking groups. Similarly, 3-amino-9-ethylcarbazole reacted with compound **14** to produce a secondary amine **17**, which was then reacted with precursor **16** to provide the second target product **STM25**. The structures of the new compounds were confirmed by ^{1}H, ^{13}C NMR spectroscopy, and elemental analysis methods.

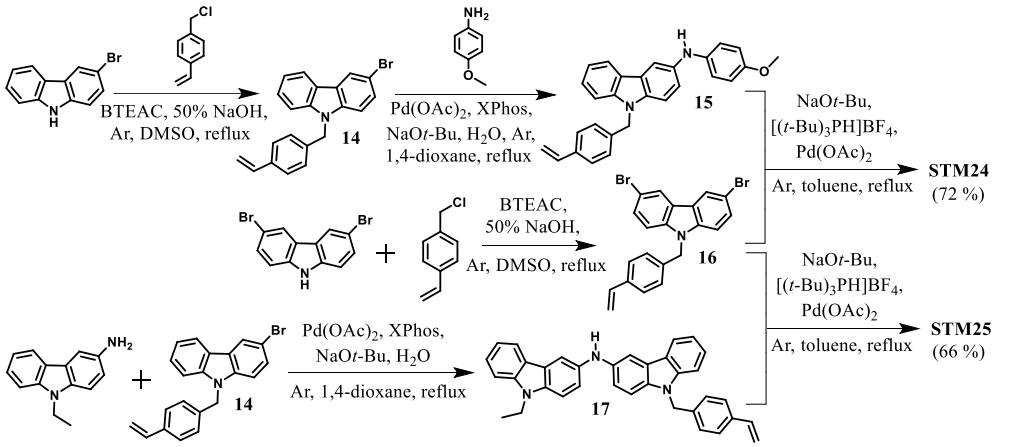

Scheme 17. Synthesis route to novel HTMs **STM24** and **STM25**

Thermal, optical, and photophysical studies of the new HTMs were performed (Table 36), and their potential applications in the *p-i-n* configuration PSCs were evaluated.

Table 36. Thermal, optical, and photoelectrical properties of HTMs **STM24** and **STM25**

HTM	T_g [a], °C	T_{poly} [a], °C	T_{dec} [a], °C	λ_{abs} [b], nm	λ_{em} [b], nm	I_P [c], eV	E_g [d], eV	E_{ea} [e], eV	μ_0 [f], cm^2/Vs
STM24	117	196	443	295, 309	458	4.84	2.90	1.94	1.8×10^{-6}
STM25	56	300	404	291, 319	470	4.82	2.84	1.98	2.4×10^{-5}

[a]Glass transition (T_g), polymerization (T_{poly}), and decomposition (T_{dec}) temperatures were observed from DSC and TGA, respectively (10 °C/min, N_2 atmosphere); [b]Absorption and emission (excitation = $\lambda_{abs\ max}$) spectra were measured in THF solution (10^{-4} M); [c]Ionization energies of the films were measured by using PESA; [d]Eg was estimated from the intersection of the absorption and emission spectra of solid films; [e]$E_{ea} = I_P - E_g$; [f]Mobility value at zero-field strength.

The results of thermogravimetric analysis showed that the thermal stability of both compounds is sufficiently high. T_{dec} of 443 °C for the compound **STM24** and 404 °C for **STM25** (Table 36) were recorded. The DSC analysis revealed that both synthesized compounds exist only in an amorphous state, and polymerization temperatures were observed during the first heating scan. The thermal polymerization

of the compound **STM24** of a lower molecular mass occurred at 196 °C, while the cross-linking process of the analogue with a larger conjugated double bond system was detected at 300 °C. During the second heating cycle, no phase transitions were observed, thus confirming that cross-linking processes occurred fully during the first heating cycle (Figure 56a). It should be noted that this cross-linking process does not require any use of initiators or dopants which are detrimental to the device efficiency and stability.

To evaluate the optical properties of the synthesized semiconductors, UV-vis absorption and PL spectra were recorded from the solutions (Figure 56b). The UV-vis spectra showed that the absorption maxima of both monomers are in the UV range at ~320 nm, while the absorption in the visible range of electromagnetic radiation is very insignificant. Due to the larger π-conjugated electron system, the absorption and emission maxima of the compound **STM25** are slightly red-shifted by ~10 nm.

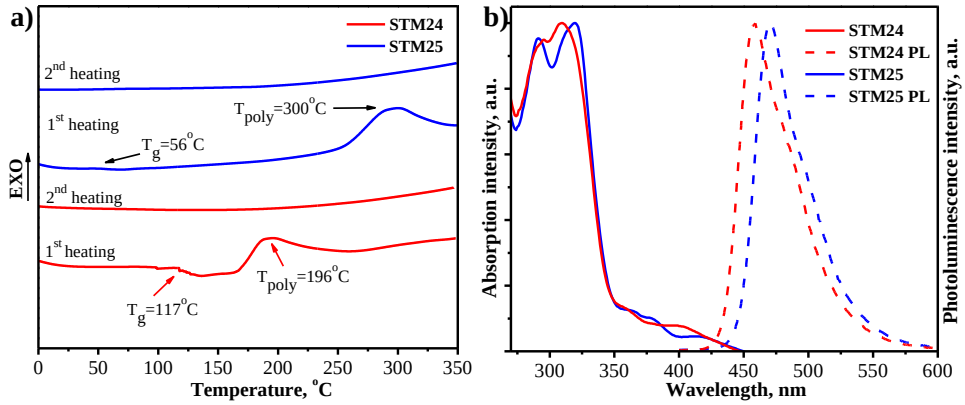

Figure 56. New HTMs **STM24** and **1206**: a) First and second scan heating curves (heating rate 10 °C/min, N_2, atmosphere, the *y*-axis is showing a heat flux); b) UV-vis absorption (solid line) and photoluminescence (dashed line) spectra in THF solution (10^{-4} M)

By using the method of photoelectron spectroscopy in air, the ionization potentials of the low molecular mass compounds **STM24** and **STM25** were recorded to be 4.84 eV and 4.82 eV, respectively. The hole-drift mobility was evaluated by the xerographic time-of-flight technique. The charge transporting properties of the compound **STM24** reached 1.8×10^{-6} cm^2/Vs at zero electrical fields, while the analogue with a larger π-conjugated electron system, **STM25**, showed a better hole-drift mobility, i.e., its value was 2.4×10^{-5} cm^2/Vs (Table 36).

Before fabricating PSCs with the targer monomers **STM24** and **STM25**, thermal cross-linking experiments were carried out. At the beginning of the experiment, a layer of the compound was formed on glass substrates and heated at the polymerization temperature of the HTM (200 °C for **STM24** and 300 °C for **STM25**) for the respective duration (0, 30, 60, 90, and 120 min). Subsequently, the layers were rinsed with THF, and the amount of the washed material was analyzed from the absorption spectra. The results indicated that the thermal polymerization process of

STM24 and **STM25** to 3D networks was complete after 90 minutes (Figure 57a) and 1 hour (Figure 57b), respectively.

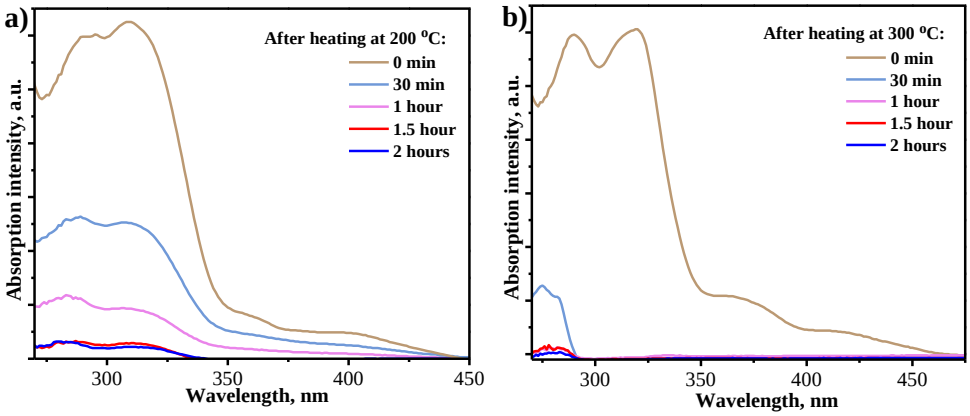

Figure 57. UV-vis absorption spectra after thermal cross-linking study of **STM24** (a) and **STM25** (b)

The cross-linked polymers were used in PSC devices with the *p-i-n* architecture. The device architecture was as follows: ITO / HTM or cross-linked HTM / perovskite – $Cs_{0.05}(FA_{0.83}MA_{0.17})_{0.95}Pb(I_{0.83}Br_{0.17})_3$ / LiF / C_{60} / BCP / Ag. All the photovoltaic characteristics of PSCs are summarized in Table 37. The PSCs constructed on the basis of 3D polymers exhibited higher power conversion efficiency results. The most promising results were obtained with the compound **STM24**; its efficiency was determined as 16.9%. Monomeric semiconductors are often not suitable for fabricating PSCs of the *p-i-n* configuration because they are not resistant to the DMSO:DMF mixture which is used during the formation of the perovskite layer. The solubility of the monomer **STM24** was almost two times higher than that of the monomer **STM25**, therefore, the efficiency results of SC based on the latter are incomparably higher.

Table 37. Photovoltaic parameters of the new HTMs **STM24** and **STM25** extracted from the best-performing devices

HTM	V_{OC}, V	J_{SC}, mA/cm^2	*FF*	PCE, %
STM24 monomer	0.285	15.6	0.251	1.1
STM24 cross-linked	0.979	20.6	0.844	16.9
STM25 monomer	0.819	18.6	0.808	11.8
STM25 cross-linked	0.944	19.0	0.823	14.6

The stability of the fabricated device with the best performing cross-linked **STM24** was evaluated (30 days, room temperature). The device showed good stability, and, at the end of the experiment, its power conversion efficiency decreased by as little as 3%.

In summary, two novel carbazole-based hole transporting materials **STM24** and **STM25** were synthesized by simple synthesis procedures, exhibited good thermal stabilities, high hole-drift mobilities, and the appropriate HOMO levels. Due to the presence of three vinyl groups, the semiconductors were able to thermally polymerize to the 3D networks. After thermal polymerization, the deposited films became resistant toward organic solvents making their application in inverted type PSCs promising.

5.2.7. Synthesis and application of 9,9′-spirobifluorene-based thermal cross-linking semiconductor for various configurations of perovskite solar cells

This subchapter is based on the published article: "In Situ Thermal Cross-Linking of 9,9′-Spirobifluorene-Based Hole-Transporting Layer for Perovskite Solar Cells," *ACS Appl. Mater. Interfaces, 2024, 16, 1*, 1206–1216, Q1, by Š. Daškevičiūtė-Gegužienė, M. A. Truong, K. Rakštys, M. Daškevičienė, R. Hashimoto, R. Murdey, T. Yamada, Y. Kanemitsu, V. Jankauskas, A. Wakamiya, V. Getautis.

This chapter describes the possibilities of using the newly synthesized Spiro-OMeTAD analogue **STM26** (Figure 58) in next-generation PSCs of various configurations (*n-i-p* and *p-i-n*).

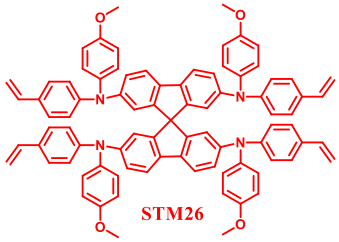

Figure 58. Structure of new Spiro-OMeTAD analogue with vinyl groups

The Spiro-OMeTAD analogue **STM26** bearing four vinyl cross-linkable groups was synthesized in a facile two-step synthesis procedure from commercially available starting materials (Scheme 18). The palladium-catalyzed Buchwald-Hartwig amination reaction of 2,2′,7,7′-tetrabromo-9,9′-spirobifluorene and *p*-anisidine was carried out to give intermediate compound **1** in 70% yield. The latter was then vinyl-functionalized by using 4-bromostyrene to generate the target product **STM26** in 51% yield. The structure of the new compound was confirmed by ^{1}H, ^{13}C NMR, mass spectroscopy, and elemental analysis methods. The total cost of the new semiconductor was estimated to be ~ 42 Eur/g, what is much cheaper than the widely used HTMs[143]. This indicates the high commercial potential of this compound.

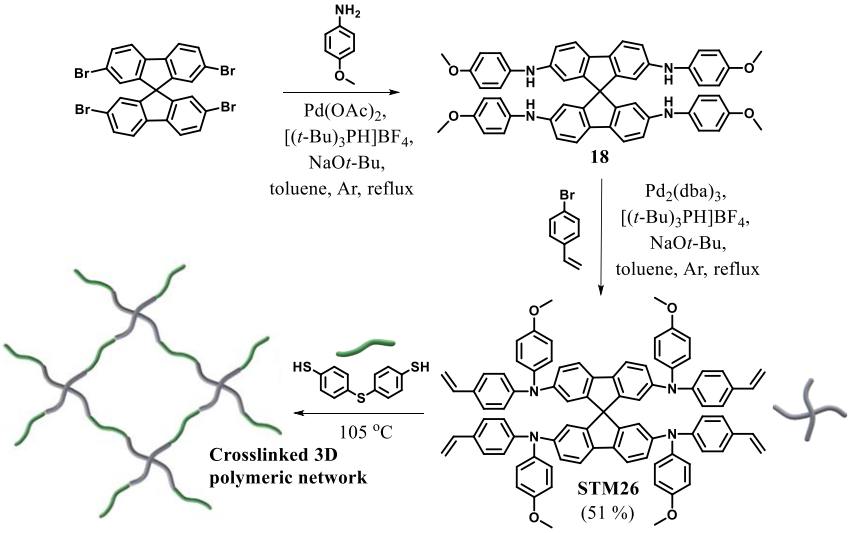

Scheme 18. Synthetic route and polymerization scheme of the organic semiconductor with vinyl groups **STM26**

Thermal, optical, and photophysical studies were performed (Table 38).

Table 38. Thermal, optical, and photoelectrical properties of novel organic semiconductor **STM26**

HTM	T_{poly} [a], °C	T_{dec} [a], °C	λ_{abs} [b], nm	λ_{em} [b], nm	I_P [c], eV	μ_0 [d], cm^2/Vs
STM26	253, 265	460	336, 395	419	5.29	8.7×10^{-5}
STM26 after heating at 255 °C	-	-	335, 394	-	5.38	1.3×10^{-5}
STM26 + dithiol After heating at 103 °C	-	-	303, 383	-	5.35	1.3×10^{-5}

[a]Polymerization (T_{poly}) and decomposition (T_{dec}) temperatures were observed from DSC and TGA respectively (10 °C/min, N_2 atmosphere); [b]Absorption and emission (excitation = $\lambda_{abs\ max}$) spectra were measured in THF solution (10^{-4} M); [c]Ionization energies of the films were measured by using PESA; [d]Eg was estimated from the intersection of the absorption and emission spectra of solid films; [e]$E_{ea} = I_P - E_g$; [f]Mobility value at zero-field strength.

The TGA results showed that a 5% weight loss of the synthesized semiconductor occurs at 460 °C, thus confirming that **STM26** possesses good thermal stability, as the decomposition temperature of the compound is much higher than the usual operating temperature of the device. DSC analysis was carried out to determine the polymerization temperature of the monomer. The polymerization temperature was recorded to be 253 °C during the first heating scan. During the second heating cycle,

no phase transitions were observed, which confirmed that cross-linking processes occurred fully during the first heating cycle (Figure 59a). It is known that temperatures above 150 °C can generate perovskite degradation, which negatively affects the efficiency of the *n-i-p* structure devices. Unfortunately, the polymerization temperature of the monomer **STM26** is higher than the levels which perovskite can tolerate. Data have been presented in the scientific literature that the temperature of 3D polymer formation can be significantly reduced during copolymerization with aliphatic or aromatic thiols[144]. Therefore, the polymerization reaction of the organic semiconductor **STM26** and 4,4'-thiobisbenzenethiol (dithiol) was performed. It was determined that the insoluble 3D polymer network forms at 103 °C. It is worth noting that this is the lowest cross-linking temperature reported in the PSC field, enabling the application of this semiconductor in PSC of both *p-i-n* and *n-i-p* architectures without polymerization initiators[145-149].

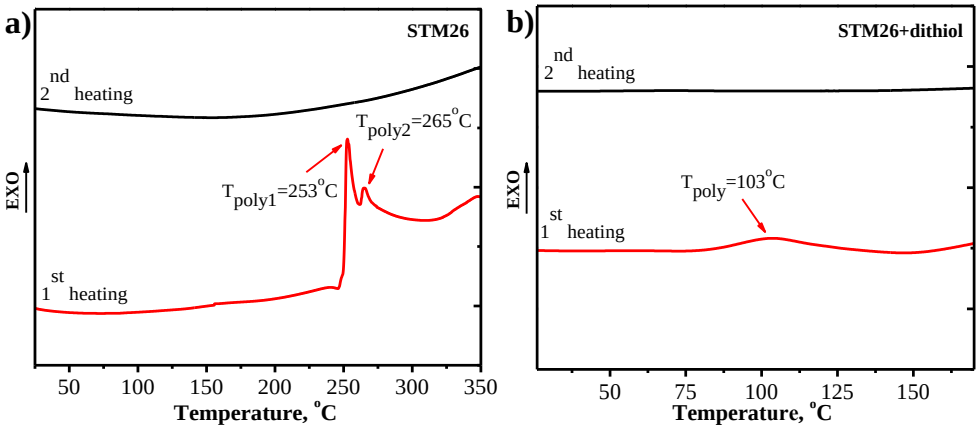

Figure 59. First and second scan heating curves (heating rate 10 °C/min, N_2, atmosphere, the *y*-axis is showing heat flux) for **STM26** (a) and **STM26+dithiol** (b)

The results of the UV-vis absorption and photoluminescense spectra of the **STM26** monomer, polymer, and copolymer are presented in Table 38. The absorption maxima of the organic semiconductor **STM26** are observed at 336 and 395 nm. The less intensive absorption peak at 336 nm can be attributed to the π-π^* electron transitions, while the more intense peak corresponds to the *n*-π^* delocalized electron transitions. After the polymerization of **STM26** at 253 °C, no significant changes in the absorption spectra were observed. After thermal cross-linking with dithiol at 103 °C, two equally intense peaks were present in the UV-vis spectrum at 303 and 383 nm. In addition, the emission maximum of the monomer was observed at 419 nm. The calculated Stokes shift value is 24 nm.

By using the method of photoelectron spectroscopy in air, the ionization potentials of the low-molecular mass compound **STM26** monomer, polymer, and copolymer were measured, which were found to equal 5.29, 5.38, and 5.39 eV, respectively. The hole transporting properties of the HTMs were characterized by using the xerographic time-of-flight method. At the zero-field strength, the monomer hole-drift mobility is equal to 8.7×10^{-5} cm^2/Vs. After thermal heating, the hole

mobility values of both the polymer and the copolymer slightly decreased but were still comparable to those of widely used PSC materials[150-151].

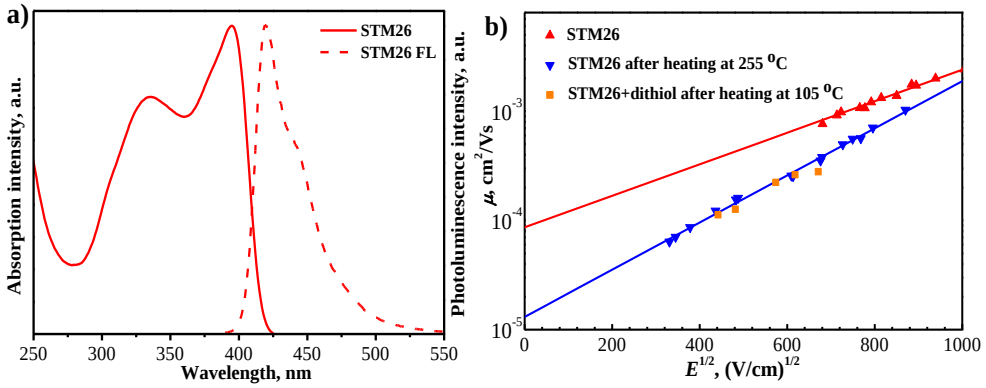

Figure 60. New HTM **STM26**: a) UV-vis absorption (solid line) and photoluminescence (dashed line) spectra in THF solution (10^{-4} M); b) Electric field dependencies of the hole-drift mobilities

Before PSCs were made, the polymerization conversion was evaluated. At the beginning of the experiment, a layer of **STM26** with and without 4,4′-thiobisbenzenethiol cross-linker were prepared on glass substrates and heated for the respective duration (0, 15, 30, 45, 60, and 140 min). Afterwards, the layers were rinsed with THF, and the amount of material washed was analyzed from the UV-vis absorption spectra (Figure 61a and 61b). The results indicated that the thermal polymerization process of the cross-linking spiro-OMeTAD analogue **STM26** to the 3D network was completed after 15 minutes. Approximately 90% of the copolymer from the semiconductor **STM26** and dithiol mixture (1:2) also formed after 15 minutes of heating. Therefore, a non-soluble 3D polymer network structure formed, which can be used in the construction of efficient *n-i-p* or *p-i-n* PCSs.

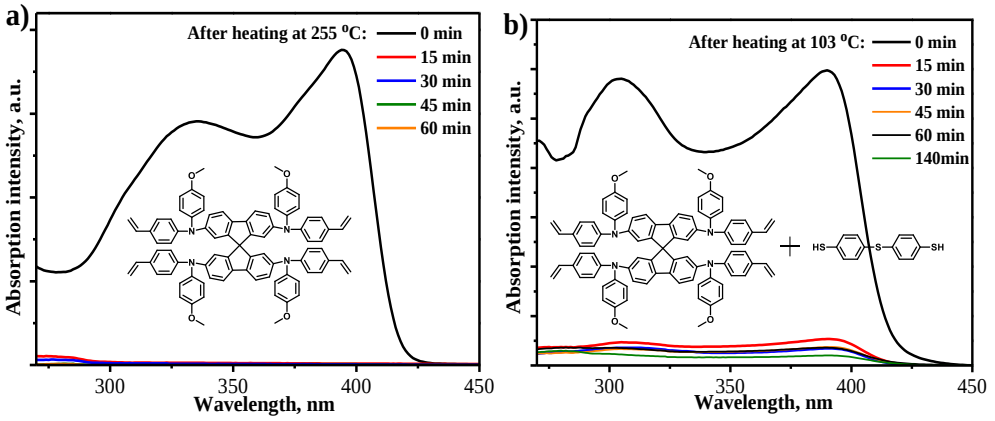

Figure 61. UV-vis absorption spectra after thermal cross-linking study of **STM26** (a) and **STM26+dithiol** (b)

The cross-linked copolymer was used as the HTM in PSC devices with the *p-i-n* architecture. The device architecture was as follows: FTO / **STM26**+dithiol (copolymer) / perovskite – $Cs_{0.05}FA_{0.8}MA_{0.15}PbI_{2.75}Br_{0.25}$ / $EDAI_2$ / C_{60} / BCP / Ag (Figure 62a). The concentration of the copolymer was optimized to be 2.0 mg/ml. The efficiency of the constructed device was 19.3%, which is comparable to a device fabricated by using the well-studied polymer analogue PTAA.

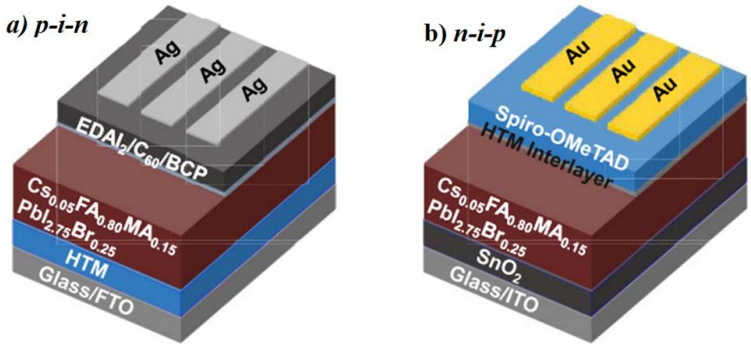

Figure 62. Structures of *p-i-n* and *n-i-p* PSCs

The cross-linked **STM26** and dithiol copolymer was also used in PSC devices with the *p-i-n* architecture as an interlayer protecting the perovskite from moisture. The device architecture was as follows: ITO / SnO_2 / perovskite – $Cs_{0.05}FA_{0.8}MA_{0.15}PbI_{2.75}Br_{0.25}$ / **STM26**+dithiol (copolymer) / Spiro-OMeTAD / Au (Figure 62b). Spiro-OMeTAD was doped with LiTFSI, the Co(III) complex, and *t*BP. The concentration of the cross-linking copolymer was optimized and determined to be 1 mg/ml. The device with the cross-linked interlayer exhibited a PCE of 19.1%, thus surpassing the power conversion efficiency of the reference device without the interlayer (18.9%). The photovoltaic characteristics of both PSC constructions are listed in Table 39.

Table 39. Photovoltaic parameters of the new HTM **STM26** and dithiol copolymer extracted from the best-performing devices

	HTM	V_{OC}, V	J_{SC}, mA/cm^2	*FF*	PCE, %
p-i-n	**STM26+dithiol (copolymer)**	1.09	23.0	0.77	19.3
	PTAA	1.05	23.3	0.79	19.3
n-i-p	**STM26+dithiol (copolymer)/Spiro-OMeTAD**	1.10	22.4	0.77	19.1
	Spiro-OMeTAD	1.08	22.6	0.77	18.9

The stability tests of the fabricated *p-i-n* and *n-i-p* devices were evaluated. The operational stability of *p-i-n* devices using the cross-linked **STM26**/dithiol copolymer and reference PTAA HTMs was tested. The power conversion efficiency of the PTAA-based reference device decreased to 80% of its initial value after 30 hours.

Meanwhile, the cross-linked **STM26**/dithiol copolymer-based device still retained 84% of the initial output after 200 hours (Figure 63a). Figure 63b shows the stabilities of *n-i-p* PCSs fabricated with and without the **STM26**/dithiol copolymer interlayer. The PCE of the reference device (without interlayer) decreased to 60% of its initial value after 16 hours, while the device with the cross-linked interlayer still maintained 84% of its initial output after 24 hours.

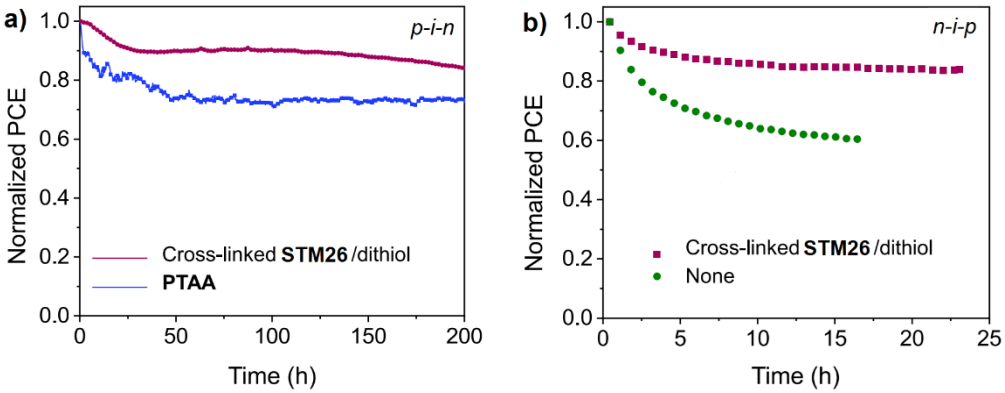

Figure 63. Stability test of the PSCs devices of *p-i-n* (a) and *n-i-p* (b) architectures

The results of this study confirm the possibility to successfully develop the application of low-molecular mass organic semiconductors and dithiol copolymers for various PSCs constructions. A three-dimensional copolymer network systematically contributes to an improved device performance and stability. The importance of this research has been evidenced by three international patent applications "In-Situ crosslinking of 9,9′-spirobifluorene-based compounds for use in optoelectronic and/or in photoelectrochemical devices and manufacture thereof," which were submitted in different patent offices: the United States (USPTO, Reg. No. 18/134,751, 14-04-2023), Europe (EPO, Reg. No. EP23168712.0, 19-04-2023), and Japan (JP, Reg. No. 2023-068376, 19-04-2023).

5.3. Conclusions

To conclude, this work presents promising *p*-type organic semiconductors containing fluorene or carbazole chromophores. In particular:

1. Low-molecular mass *p*-type organic semiconductors based on a fluorene core were synthesized during a three-step synthesis. It has been determined that:
   1.1. The synthesized organic semiconductors are thermally stable; the thermal decomposition temperature corresponding to a 5% weight loss of their mass occurs at temperatures higher than 400 °C.
   1.2. The addition of a third carbazole chromophore at the 4th position of the central fragment not only increases a π-conjugated double bond system of a molecule but also ensures a fully amorphous state of the compound.
   1.3. The ionization potentials (5.1–5.11 eV) and hole-drift mobility values at the zero-field hole-drift mobility (10^{-6} cm^2/Vs) of these organic

semiconductors are suitable for their application in perovskite solar cells.

1.4. The power conversion efficiency of the device based on the semiconductor **STM1** reached 18.3%, which is very similar to that of the device with Spiro-OMeTAD (18.9%).

2. The enamine **STM3**, which was subsequently alkylated with different alkyl fragments at the 9th position of the fluorene moiety, was synthesized by the condensation reaction, and its investigation has revealed that:
   2.1. All organic semiconductors exist in both crystalline and amorphous states, but, after the second heating, only the glass transition temperature has been recorded.
   2.2. The best charge transporting properties ($\mu_0 = 3.3\times10^{-4}$ cm^2/Vs) have been demonstrated by the propyl-substituted semiconductor **STM5**, and they surpassed the value of the reference Spiro-OMeTAD ($\mu_0 = 1.3\times10^{-4}$cm^2/Vs).
   2.3. The best power conversion efficiency results were demonstrated by both structures of **STM3**-based perovskite solar cells (with a dopant and dopant-free), respectively, 19.3% and 17.1%.
3. New enamines based on fluorene chromophores with an acceptor group in the center of molecules have been synthesized by condensation reactions. The investigation of their properties has revealed that:
   3.1. Organic semiconductors with the higher conjugated double-bond systems are denoted by a higher thermal stability. The highest decomposition temperature (412 ^{o}C) was observed for the semiconductor **STM14** with four diphenylethenyl groups and a fluorenone fragment in the center.
   3.2. The values of the ionization potential of different semiconductors varied within the range of ~5.4–5.5 eV, and the compound **STM13** exhibited the best charge transport properties at zero-field ($\mu_0 = 4\times10^{-6}$ cm^2/Vs).
   3.3. The perovskite solar cell based on the semiconductor **STM13**, bearing four diphenylethene groups and a malononitrile acceptor fragment at the center of the molecule, achieved a record-breaking solar cell efficiency of 22.03%.
4. Novel organic semiconductors containing the central fragment of spirobisindane were synthesized by using various synthesis methods, and their investigation has revealed that:
   4.1. Compounds **STM15** and **STM16** exist only in the amorphous state and can ensure a better morphological stability of the layers than the reference Spiro-OMeTAD. Their glass transition temperatures are 167 ^{o}C and 157 ^{o}C, respectively.
   4.2. The ionization potential values of **STM15** and **STM16** are 5.34 and 5.30 eV, respectively. They are in the same range as the preferred values of HTMs used in perovskite solar cells. Meanwhile, the zero-field hole-drift mobility of the compound **STM15** almost reaches 10^{-5} cm^2/Vs,

while its meta-substituted analogue **STM16** exhibits a slightly lower mobility ($\mu_0 = 2.6\times10^{-6}$ cm^2/Vs).

4.3. The perovskite solar cell based on the positive charge transporting compound **STM15** showed the most promising results with a power conversion efficiency of 16.4%.

5. New hole transporting materials containing the photodimerized 9-vinylcarbazole fragment as a central core have been synthesized based on the principles of green chemistry. It has been determined that:
   5.1. All the new compounds are amorphous, except for semiconductor **STM18**, which can be in both amorphous and crystalline states.
   5.2. The values of the compound hole-drift mobilities at zero-field ranged from 10^{-4} cm^2/Vs to 10^{-7} cm^2/Vs.
   5.3. The power conversion efficiencies of the solar cells based on **STM22** and reference Spiro-OMeTAD were very similar, i.e.,. 21% and 21.64%, respectively. The **STM22**-based solar module (6.5 × 7 cm) exhibited a power conversion efficiency of 19.06%, which is the highest efficiency ever reported for a non-Spiro-OMeTAD based perovskite module.
6. A series of new cross-linkable carbazole-derived hole transporting materials bearing three vinyl groups have been synthesized *via* alkylation and Buchwald palladium-catalyzed reactions. It has been found that:
   6.1. The monomer **STM24** underwent thermal polymerization at 196 °C, while the cross-linking process of its analogue with a larger conjugated double bond system was detected at 300 °C.
   6.2. The ionization potential values of the compounds **STM24** and **STM25** are 4.84 and 4.82 eV, respectively. The charge drift mobility values reached 1.8×10^{-6} cm^2/Vs and 2.4×10^{-5} cm^2/Vs, respectively, at zero-field.
   6.3. The conversion of the monomer **STM24** into a 3D structure polymer occurred within 90 minutes, while the one of its analogues **STM25** was completed within one hour.
   6.4. The insoluble layer of the 3D *p*-type semiconductor **STM24** obtained by thermal polymerization can be successfully used in the inverted structure *(p-i-n)* perovskite solar cells with a nearly 17% power conversion efficiency.
7. After analyzing, optimizing, and selecting the best synthesis route, a 9,9′-spirobifluorene-based *p*-type organic semiconductor bearing four cross-linkable vinyl groups has been synthesized during Buchwald palladium-catalyzed reactions. The investigation of its properties has shown that:
   7.1. The hole-drift mobility at the zero-field strength of the monomer **STM26** is equal to 8.7×10^{-5} cm^2/Vs. After thermal heating, the hole mobility slightly decreased.
   7.2. The monomer **STM26** cross-links and forms three-dimensional networks in as little as 15 minutes at 253 °C. The power conversion efficiency of the inverted *(p-i-n)* structure perovskite solar cells with

the formed polymer was 19.3%, which is comparable to one of the devices fabricated by using the well-studied reference polymer PTAA.

7.3. The polymerization of **STM26** with the crosslinking agent 4,4′-thiobisbenzenethiol proceeded smoothly (15 minutes) at a significantly lower temperature (107 °C). This enabled the usage of a three-dimensional polymer in perovskite solar cells of a regular structure *(n-i-p)* as an interlayer between Spiro-OMeTAD and perovskite, thus increasing the longevity of the latter. The device with the cross-linked interlayer demonstrated a significantly increased stability and 19.1% power conversion efficiency, thus surpassing the conversion efficiency of the reference device without the interlayer (18.9%).

6. LITERATŪROS SĄRAŠAS

1. Europarl. https://www.europarl.europa.eu/news/lt/headlines/society/20221128STO58001/kaip-es-skatina-atsinaujinancia-energija?
2. Deshmukh Md K. G.; M. Sameeroddin; D. Abdul; M. A. Sattar. Renewable energy in the 21st century: A review. *Materials Today: Proceedings*, 80(3), 2023, 1756-1759. Interaktyvus. ISSN 2214-7853 Prieiga per: https://doi.org/10.1016/j.matpr.2021.05.501
3. Prishya A. S. A.; L. Chopra; Manikanika. Comprehensive review on uses od silicon dioxide in solar cells. *Materials Today: Proceedings*, 72(3), 2023, 1471-1478. Interaktyvus. ISSN 2214-7853 Prieiga per: https://doi.org/10.1016/j.matpr.2022.09.348
4. Kojima A.; K. Teshima; Y. Shirai Y; T. Miyasaka. Organometal halide perovskites as visible-light sensitizers for photovoltaic cells. *Journal ot the American Chemical Society*, 131(17), 2009, 6050-6051. Interaktyvus. ISSN 0002-7863. Prieiga per: https://doi.org/10.1021/ja809598r
5. Szabó G.; N.-G. Park; F. De Angelis; P. V. Kamat. Are Perovskite Solar Cells Reaching the Efficiency and Voltage Limits? *ACS Energy Letters*, 8(9), 2023, 3829-3831. Interaktyvus. ISSN 2380-8195. Prieiga per: https://doi.org/10.1021/acsenergylett.3c01649
6. Roy P.; A. Ghosh; F. Barclay; A. Khare; E. Cuce. Perovskite Solar Cells: A Review of the Recent Advantages. C*oatings*, 12(8), 2022, 1089. Interaktyvus. ISSN 2079-6412. Prieiga per: https://doi.org:/0.3390/coatings12081089
7. Saragi T. P. I.; T. Spehr; A. Siebert; T. Fuhrmann-Lieker; J. Salbeck. Spiro Compounds for Organic Optoelectronics. *Chemicals Reviews*, 107(4), 2007; 1011-1065. Interaktyvus. ISSN 1520-6890. Prieiga per: https://doi.org/10.1021/cr0501341
8. Mattiello S.; G. Lucarelli; A. Calascibetta; L. Polastri; E. Ghiglietti ir kt. Sustainable, Efficient, and Scalable Preparation of Pure and Performing Spiro-OmeAD for Perovskite Solar Cells. *ACS Sustainable Chemistry & Engineering*, 10(14), 2022, 4750-4757. Interaktyvus. ISSN 2168-0485. Prieiga per: https://doi.org/10.1021/acssuschemeng.2c00493
9. Shahnawaz; S. S. Swayamprabha; M. R. Nagar; R. A. K. Yadav; S. Gull ir kt. Hole-transporting materials for organic light-emitting diodes: an overview. *Journal of Materials Chemistry C*. 7, 2019, 7144-7158. Interaktyvus. ISSN 2050-7526. Prieiga per: https://doi.org/10.1039/ C9TC01712G
10. Anagnostou K.; M. M. Stylianakis; K. Petridis; E. Kymakis. Building an organic solar cell: fundamental procedures for device fabrication. *Energies*. 12(11), 2019, 2188. Interaktyvus. ISSN 1996-1073. Prieiga per: https:// doi.org/10.3390/en12112188
11. Miao J.; Y. Wang; J. Liu; L. Wang. Organoboron molecules and polymers for organic solar cell applications. *Chemical Society Reviews*. 51, 2022, 153-187. Interaktyvus. ISSN 1460-4744. Prieiga per: https://doi.org/10.1039/D1CS00974E

12. Hawash Z.; L. K. Ono; S. R. Raga; M. V. Lee; Y. Qi. Air-Exposure Induced Dopant Redistribution and Energy Level Shifts in Spin-Coated Spiro-MeOTAD Films. *Chemistry of Materials*. 27(2), 2015, 562-569. Interaktyvus. ISSN 1520-5002. Prieiga per: https://doi.org/10.1021/cm504022q
13. Cui J.; H. Yuan; J. Li; X. Xu; Y. Shen ir kt. Recent progress in efficient hybrid lead halide perovskite solar cells. *Science Technology of Advanced Materials*. 16(3), 2016, 036004. Interaktyvus. ISSN 1468-6996. Prieiga per: https://doi.org/10.1088/1468-6996/16/3/036004
14. Jung H. S.; N. G. Park. Perovskite solar cells from materials to devices. *Small.* 11(1), 2015, 10-25. Interaktyvus. ISSN 1468-6996. Prieiga per: https://doi.org/10.1002/smll.201402767
15. Lee J.-W.; S. Seo; P. Nandi; H. S. Jung; N.-G. Park ir kt. Dynamic structural property of organic-inorganic metal halide perovskite. *Cel Press*. 24(1), 2021, 101959. ISSN 2211-1247. Prieiga per: https://doi.org/10.1016/j.isci.2020.101959
16. Masood, M. Talha. Solution-Processable Compact and Mesoporous Titanium Dioxide Thin Films as Electron-Selective Layers for Perovskite Solar Cells. 2020. Prieiga per: https://urn.fi/URN:ISBN:978-952-12-3956-4
17. Noh J. H.; S. H. Im; J. H. Heo; T. N. Mandal; S. I. Seok. Chemical Management for Colorful, Efficient, and Stable Inorganic-Organic Hybrid Nanostructured Solar Cells. *Nano Letters*. 13(4), 2013, 1764-1769. Interaktyvus. ISSN 1530-6984. Prieiga per: https://doi.org/10.1021/nl400349b
18. Kojima A.; K. Teshima; Y. Shirai; T. Miyasaka. Organometal halide perovskites as visible-light sensitizers for photovoltaic cells. *Journal of the American Chemical Society*. 131(17), 2019, 6050-6051. Interaktyvus. ISSN 1520-5126. Prieiga per: https://doi.org/10.1021/ja809598r
19. Cho A.-N.; N.-G. Park. Impact of Interfacial Layers in Perovskite Solar Cells. *ChemSusChem.* 10(19), 2017, 3687-3704. Interaktyvus. ISSN 1864-564X Prieiga per: https://doi.org/10.1002/cssc.201701095
20. Fortunato E.; D. Ginley; H. Hosono, DC. Paine. Transparent conducting oxides for photovoltaic. *MRS Bulletin*. 32, 2007, 242-247. Interaktyvus. ISSN 0883-7694. Prieiga per: https://doi.org/10.1557/mrs2007.29
21. Ellmer K. Resistivity of polycrystalline zinc oxide films: current status and physical limit. *Journal of Physics D: Applied Physics*. 34, 2001, 3097. Interaktyvus. ISSN 1361-6463. Prieiga per: https://doi.org/10.1088/0022-3727/34/21/301
22. Dutta J.; J. Perrin; T. Emeraud; J.-M. Laurent; A. Smith. Pyrosol deposition of fluorine-doped tin dioxide thin films. *Journal of Materials Science*. 30, 1995, 53-62. Interaktyvus. ISSN 2321-6212. Prieiga per: https://doi.org/ 10.1007/BF00352131
23. Zhu L.; J. Ye; X. Zhang; H. Zheng; G. Liu ir kt. Performance enhancement of perovskite solar cells using a La-doped $BaSnO_3$ electron transport layer. *Journal of Materials Chemistry A.* 5, 2017, 3675-3682. Interaktyvus. ISSN 2050-7488. Prieiga per: https://doi.org/10.1039/C6TA09689A

24. Wang Q.; C. C. Chueh; M. Eslamian; A. K. Jen. Modulation of PEDOT:PSS pH for Efficient Inverted Perovskite Solar Cells with Reduced Potential Loss and Enhanced Stability. *ACS Applied Materials & Interfaces.* 8, 2016, 32068-32076. Interaktyvus. ISSN 1944-8244. Prieiga per: https://doi.org/10.1021/acsami.6b11757
25. Sauvé G.; R. Fernando. Beyond Fullerenes: Designing Alternative Molecular Electron Acceptors for Solution-Processable Bulk Heterojunction Organic Photovoltaics. *Journal of Physical Chemistry Letters.* 6(18), 2015, 3770-3780. ISSN 1948-7185. Prieiga per: https://doi.org/10.1021/acs.jpclett.5b01471
26. Nielsen C. B.; S. Holliday; H.-Y. Chen; S. J. Cryer; I. McCulloch. Non-Fullerene Electron Acceptors for Use in Organic Solar Cells. *Accounts Chemical Research.* 48(11), 2015, 2803-2812. Interaktyvus. ISSN 2167-7956. Prieiga per: https://doi.org/10.1021/acs.accounts.5b00199
27. Huang J.; Z. Gu; L. Zuo; T. Ye; H. Chen. Morphology control of planar heterojunction perovskite solar cells with fluorinated PDI films as organic electron transport layer. *Solar Energy*. 133, 2016, 331-338. Interaktyvus. ISSN 0038-092X. Prieiga per: https://doi.org/10.1016/j.solener.2016.04.017
28. Zhang H.; L. Xue; J. Han; Y. Q. Fu; Y. Shen ir kt. New generation perovskite solar cells with solution-processed amino-substituted perylene diimide derivative as electron-transport layer. *Journal of Materials Chemistry A.* 4, 2016, 8724-8733. Interaktyvus. ISSN 2050-7488. Prieiga per: https://doi.org/10.1039/C6TA03119F
29. Leijtens T.; G. E. Eperon; S. Pathak; A. Abate; M. M. Lee ir kt. Overcoming ultraviolet light instability of sensitized TiO_2 with meso-superstructured organometal tri-halide perovskite solar cells. *Nature Communications.* 4, 2013, 2885. Interaktyvus. ISSN 2041-1723. Prieiga per: https://doi.org/10.1038/ncomms3885
30. Park M.; J. Y. Kim; H. J. Son; C. H. Lee; S. S. Jang ir kt. Low- ure solution-processed Li-doped SnO_2 as an effective electron transporting layer for high-performance flexible and wearable perovskite solar cells. *Nano Energy*. 26, 2016, 208-215. Interaktyvus. ISSN 2211-3282. Prieiga per: https://doi.org/10.1016/j.nanoen.2016.04.060
31. Tseng Z. L.; C. H. Chiang; S. H. Chang; C. G. Wu. Surface engineering of ZnO electron transporting layer via Al doping for high efficiency planar perovskite solar cells. *Nano Energy*. 28, 2016, 311-318. Interaktyvus. ISSN 2211-3282. Prieiga per: https://doi.org/10.1016/j.nanoen.2016.08.035
32. Liu J.; C. Gao; L. Luo; Q. Ye; X. He ir kt. Low-temperature, solution processed metal sulfide as an electron transport layer for efficient planar perovskite solar cells. *Journal of Materials Chemistry A.* 3, 2015, 11750-11755. Interaktyvus. ISSN 2050-7488. Prieiga per: https://doi.org/10.1039/C5TA01200G
33. Wang L.; W. Fu; Z. Gu; C. Fan; X. Yang ir kt. Low temperature solution processed planar heterojunction perovskite solar cells with a CdSe nanocrystal as an electron transport/extraction layer. *Journal of Materials Chemistry C.* 2, 2014, 9087-9090. Interaktyvus. ISSN 2050-7534. Prieiga per: https://doi.org/10.1039/C4TC01875C

34. Ghosh P.; S. Senthilarasu; T. P. Nixon; K. Satheesh. Influence of Nanostructures in Perovskite Solar Cells. *Encyclopedia of Smart Materials.* 2, 2022, 646-660. Prieiga per: https://doi.org/10.1016/B978-0-12-815732-9.00054-1
35. Park K.; J. Y. Kim; H. J. Son; C. H. Lee; S. S. Jang ir kt. Low-temperature solution-processed Li-doped SnO_2 as an effective electron transporting layer for high-performance flexible and wearable perovskite solar cells. *Nano Energy*. 26, 2016, 208-215. Interaktyvus. ISSN 2211-3282. Prieiga per: https://doi.org/10.1016/j.nanoen.2016.04.060
36. Snaith H. J. ir C. Ducati. SnO_2-Based Dye-Sensitized Hybrid Solar Cells Exhibiting Near Unity Absorbed Photon-to-Electron Conversion Efficiency. *Nano Letters.* 10, 2010, 1259-1265. Interaktyvus. ISSN 1530-6984. Prieiga per: https://doi.org/10.1021/nl903809r
37. Giorgi G. ir K. Yamashita. Organic-inorganic halide perovskites: an ambipolar class of materials with enhanced photovoltaic performances. *Journal of Materials Chemistry A.* 3, 2015, 8981-8991. Interaktyvus. ISSN 2050-7488. Prieiga per: https://doi.org/10.1039/C4TA05046K
38. Belous A. G.; A. A. Ishchenko; O. I. V'yunov; P. V. Torchyniuk. Preparation and Properties of Films of Organic-Inorganic Perovskites $MAPbX_3$ (MA = CH_3NH_3; X = Cl, Br, I) for Solar Cells: A Review. *Theoretical and Experimental Chemistry.* 56, 2021, 359-386. Interaktyvus. ISSN 0040-5760. Prieiga per: https://doi.org/10.1007/s11237-021-09666-6
39. Dualeh A.; N. Tetreault; T. Moehl; P. Gao; M. K. Nazeeruddin ir kt. Effect of Annealing Temperature on Film Morphology of Organic-Inorganic Hybrid Perovskite Solid-State Solar Cells. *Advanced Functional Mater*ials. 24, 2014, 3250-3258. Interaktyvus. ISSN 1616-3028. Prieiga per: https://doi.org/10.1002/adftn.201304022
40. Zhao Y.; A. M. Nardes; K. Zhu. Solid-State Mesostructured Perovskite $CH_3NH_3PbI_3$ Solar Cells: Charge Transport, Recombination, and Diffusion Length. *The Journal of Physical Chemistry Letters.* 5, 2014, 490-494. Interaktyvus. ISSN 1948-7185. Prieiga per: https://doi.org/10.1021/jz500003v
41. Wu Y.; A. Islam; X. Yang; C. Qin; J. Liu ir kt. Retarding the crystallization of PbI_2 for highly reproducible planar-structured perovskite solar cells *via* sequential deposition. *Energy & Environmental Science.* 7, 2014, 2934-2938. Interaktyvus. ISSN 1754-5692. Prieiga per: https://doi.org/10.1039/C4EE01624F
42. Seo J.; S. Park; Y. C. Kim; N. J.Jeon; J. H. Noh ir kt. Benefits of very thin PCBM and LiF layers for solution-processed p-i-n perovskite solar cells. *Energy & Environmental Science.* 7, 2014, 2642-2646. Interaktyvus. ISSN 1754-5692. Prieiga per: https://doi.org/10.1039/C4EE01216J.
43. Endres J.; D. A. Egger; M. Kulbak; R. A. Kerner; L. Zhao ir kt. Valence and Conduction Band Densities of States of Metal Halide Perovskites A Combined Experimental–Theoretical Study. *The Journal of Physical Chemistry Letters.* 7(14), 2016, 2722-2729. Interaktyvus. ISSN 1948-7185. Prieiga per: https://doi.org/10.1021/acs.jpclett.6b00946

44. Krishna A. ir A. C. Grimsdale. Hole transporting materials for mesoscopic perovskite solar cells – towards a rational design? *Journal of Materials Chemistry A.* 5, 2017, 16446-16466. Interaktyvus. ISSN 2050-7488. Prieiga per: https://doi.org/10.1039/c7ta01258f
45. Shahnawaz; S. S. Sudheendran; M. R. Nagar; R. A. K. Yadav; S. Gull ir kt. Hole-transporting materials for organic light-emitting diodes: an overview. *Journal of Materials Chemistry C*. 7, 2019, 7144-7158. Interaktyvus. ISSN 2050-7534. Prieiga per: https://doi.org/10.1039/ C9TC01712G
46. Anagnostou K.; M. M. Stylianakis; K. Petridis; E. Kymakis. Building an organic solar cell: fundamental procedures for device fabrication. *Energies*. 12(11), 2019, 2188. Interaktyvus. ISSN 1996-1073. Preiga per: https://doi.org/10.3390/en12112188
47. Singh R.; P. K. Singh; B. Bhattacharya; H.-W. Rhee. Review of current progress in inorganic-organic hole-transport materials for perovskite solar cells. *Applied Materials Today*. 14, 2019, 175-200. Interaktyvus. ISSN 2352-9407. Prieiga per: https://doi.org/10.1016/j.apmt.2018.12.011
48. Rajeswari R.; M. Mrinalini; S. Prasanthkumar; L. Giribabu. Emerging of Inorganic Hole Transporting Materials for Perovskite Solar Cells. *The Chemical Record*. 17(7), 2017, 681-699. Interaktyvus. ISSN 1528-0691. Prieiga per: https://doi.org/10.1002/tcr.201600117
49. Arora N.; M. I. Dar; A. Hinderhofer; N. Pellet; F. Schreiber ir kt. Perovskite solar cells with CuSCN hole extraction layers yield stabilized efficiencies greater than 20%. *Science* 358, 2017, 768-771. Interaktyvus. ISSN 1095-9203. Prieiga per: https://doi.org/10.1126/science.aam565
50. Li M.-H.; P.-S. Shen; K.-C. Wang; T.-F. Guo; P. Chen. Inorganic p-type contact materials for perovskite-based solar cells. *Journal of Materials Chemistry A*. 3, 2015, 9011-9019. Interaktyvus. ISSN 2050-7488. Prieiga per: https://doi.org/10.1039/C4TA06425A
51. You J.; L. Meng; T. B. Song; T. F. Guo; Y. M. Yang ir kt. Improved air stability of perovskite solar cells via solution-processed metal oxide transport layers. *Nature Nanotechnology*. 11, 2016, 75-81. Interaktyvus. ISSN 1748-3387. Prieiga per: https://doi.org/10.1038/nnano.2015.230
52. Wu Y.; X. Yang; W. Chen; Y. Yue; M. Cai ir kt. Perovskite solar cells with 18.21% efficiency and area over 1 cm^2 fabricated by heterojunction engineering. *Nature Energy*. 1, 2016, 16148. Interaktyvus. ISSN 2058-7546. Prieiga per: https://doi.org/10.1038/nenergy.2016.148
53. Bach U.; D. Lupo; P. Comte; J. E. Moser; F. Weissortel ir kt.. Solid-state dye-sensitized mesoporous TiO_2 solar cells with high photon-to-electron conversion efficiencies. *Nature*. 395, 1998, 583-585. Interaktyvus. ISSN STM15-4687. Prieiga per: https://doi.org/10.1038/26936
54. Ono L. K.; P. Schulz; J. J. Endres; G. O. Nikiforov; Y. Kato ir kt. Air-Exposure-Induced Gas-Molecule Incorporation into Spiro-MeOTAD Films. *The Journal of Physical Chemistry Letters.* 5, 2014, 1374-1379. Interaktyvus. ISSN 1948-7185. Prieiga per: https://doi.org/10.1021/jz500414m

55. Hawash Z.; L. K. Ono; S. R. Raga; M. V. Lee; Y. Qi. Air-Exposure Induced Dopant Redistribution and Energy Level Shifts in Spin-Coated Spiro-MeOTAD films. *Chemistry of Materials.* 27, 2015, 562-569. Interaktyvus. ISSN 1520-5002. Prieiga per: https://doi.org/10.1021/cm504022q
56. Salbeck J.; N. Yu; J. Bauer; F. Weissörtel; H. Bestgen. Low molecular organic glasses for blue electroluminescence. *Synthetic Metals.* 91, 1997, 209-215. Interaktyvus. ISSN 0379-6779. Prieiga per: https://doi.org/10.1016/S0379-6779(98)80033-7
57. Salbeck J.; F. Weissörtel; J. Bauer. Spiro linked compounds for use as active materials in organic light emitting diodes. *Macromolecular Symposia.* 125, 1998, 121-132. Interaktyvus. ISSN 1521-3900. Prieiga per: https://doi.org/10.1002/masy.19981250110
58. Hawash Z.; L. K. Ono; Y. Qi. Recent Advances in Spiro-MeOTAD Hole Transport Material and Its Applications in Organic-Inorganic Halide Perovskite Solar Cells. *Advanced Materials Interfaces.* 5, 2018, 1700623. Interaktyvus. ISSN 2196-7350. Prieiga per: https://doi.org/ 10.1002/admi.201700623
59. Kamino B. A.; B. Mills; C. Reali; M. J. Gretton; M. A. Brook ir kt. Liquid Triarylamines: The Scope and Limitations of Piers-Rubinsztajn Conditions for Obtaining Triarylamine-Siloxane Hybrid Materials. *The Journal of Organic Chemistry.* 77(4), 2012, 1663-1674. Interaktyvus. ISSN 0022-3263. Prieiga per: https://doi.org/10.1021/jo202090611
60. Tobat P. I. S.; T. Spehr; A. Siebert; T. Fuhrmann-Lieker; J. Salbeck. Spiro Compounds for Organic Optoelectronics. *Chemical Reviews.* 107, 2007, 1011-1065. Interaktyvus. ISSN 0009-2665. Prieiga per: https://doi.org/ 10.1021/cr0501341
61. MSE Supplies LLC. https://www.msesupplies.com/products/high-purity-spiro-ometad-spiro-meotad-1g?variant=39718816546874
62. Malinauskas T.; D. Tomkute-Luksiene; R. Sens; M. Daskeviciene; R. Send ir kt. Enhancing Thermal Stability and Lifetime of Solid-State Dye-Sensitized Solar Cells via Molecular Engineering of the Hole-Transporting Material Spiro-OMeTAD. *ACS Applied Materials & Interfaces.* 7, 2015, 11107-11116. Interaktyvus. ISSN 1944-8244. Prieiga per: https://doi.org/ 10.1021/am5090385
63. Hawash Z.; L. K. Ono; S. R. Raga; M. V. Lee; Y. Qi. Air-Exposure Induced Dopant Redistribution and Energy Level Shifts in Spin-Coated Spiro-OMeTAD films. *Chemistry of Materials.* 27, 2015, 562-569. Interaktyvus. ISSN 1520-5002. Prieiga per: https://doi.org/10.1021/cm504022q
64. Poplavskyy D. ir J. Nelson. Nondispersive hole transport in amorphous films of methoxy-spirofluorene-arylamine organic compound. *Journal of Applied Physics.* 93, 2002, 341-346. Interaktyvus. ISSN 0021-8979. Prieiga per: https://doi.org/10.1063/1.1525866
65. Krüger J.; R. Plass; L. Cevey; M. Piccirelli; M. Grätzel ir kt. High efficiency solid-state photovoltaic device due to inhibition of interface charge recombination. *Applied Physics Letters.* 79, 2001, 2085-2087. Interaktyvus. ISSN 0003-6951. Prieiga per: https://doi.org/10.1063/1.1406148

66. Snaith H. J. ir M. Grätzel. Enhanced charge mobility in a molecular hole transporter via addition of redox inactive ionic dopant: Implication to dye-sensitized solar cells. *Applied Physics Letters.* 89, 2006, 262114. Interaktyvus. ISSN 0003-6951. Prieiga per: https://doi.org/10.1063/1.2424552
67. Abate A.; T. Leijtens; S. Pathak; J. Teuscher; R. Avolio ir kt. Lithium salts as "redox active" p-type dopants for organic semiconductors and their impact in solid-state dye-sensitized solar cells. *Physical Chemistry Chemical Physics.* 15, 2013, 2572-2579. Interaktyvus. ISSN 1463-9076. Prieiga per: https://doi.org/10.1039/C2CP44397J
68. Juarez-Perez E. J.; M. R. Leyden; S. Wang; L. K. Ono; Z. Hawash ir kt. Role of the Dopants on the Morphological and Transport Properties of Spiro-MeOTAD Hole Transport Layer. *Chemistry of Materials*. 2016, 28, 5702-5709. Interaktyvus. ISSN 1520-5002. Prieiga per: https://doi.org/10.1021/acs.chemmater.6b01777
69. Hawash Z.; L. K. Ono; Y. B. Qi. Moisture and Oxygen Enhance Conductivity of LiTFSI-Doped Spiro-MeOTAD Hole Transport Layer in Perovskite Solar Cells. *Advanced Materials Interfaces*. 3, 2016, 1600117. Interaktyvus. ISSN 2196-7350. Prieiga per: https://doi.org/10.1002/admi.201600117
70. Zhao Q.; R. Wu; Z. Zhang; J. Xiong; Z. He ir kt. Achieving efficient inverted planar perovskite solar cells with nondoped PTAA as a hole transport layer. *Organic Electronics.* 71, 2019, 106-112. Interaktyvus. ISSN 1566-1199. Prieiga per: https://doi.org/10.1016/j.orgel.2019.05.019
71. Kim Y.; E. H. Jung; G. Kim; D. Kim; B. J. Kim ir kt. Sequentially Fluorinated PTAA Polymers for Enhancing V_{OC} of High-Performance Perovskite Solar Cells. *Advanced Energy Materials.* 8, 2018, 1801668. Interaktyvus. ISSN 1614-6840. Prieiga per: https://doi.org/10.1002/aenm.201801668
72. Heo J. H.; S. H. Im; J. H. Noh; T. N. Mandal; C.-S. Lim ir kt. Efficient inorganic-organic hybrid heterojunction solar cells containing perovskite compound and polymeric hole conductors. *Nature Photonics.* 7, 2013, 486-491. Interaktyvus. ISSN 1749-4885. Prieiga per: https://doi.org/ 10.1038/nphoton.2013.80
73. Li F.; X. Deng; F. Qi; Z. Li; D. Liu ir kt. Regulating Surface Termination for Efficient Inverted Perovskite Solar Cells with Greater Than 23% Efficiency. *Journal of the American Chemical Society.* 142, 2020, 20134-20142. Interaktyvus. ISSN 0002-7863. Prieiga per: https://doi.org/ 10.1021/jacs.0c09845
74. Bi C.; B. Chen; H. Wei; S. DeLuca; J. Huang. Efficient Flexible Solar Cell based on Composition-Tailored Hybrid Perovskite. *Advanced Materials.* 29, 2017, 1605900. Interaktyvus. ISSN 1521-4095. Prieiga per: https://doi.org/ 10.1002/adma.201605900
75. Zhang Y.; A. Kirs; F. Ambroz; C.-T. Lin; A. S. R. Bati ir kt. Ambient Fabrication of Organic-Inorganic Hybrid Perovskite Solar Cells. *Small Methods.* 5, 2021, 2000744. Interaktyvus. ISSN 2366-9608. Prieiga per: https://doi.org/10.1002/smtd.202000744
76. Park I. J.; G. Kang; M. A. Park; J. S. Kim; S. W. Seo ir kt. Highly Efficient and Uniform 1 cm^2 Perovskite Solar Cells with an Electrochemically Deposited

NiO_x Hole-Extraction Layer. *ChemSusChem*. 10, 2017, 2660-2667. Interaktyvus. ISSN 1864-5631. Prieiga per: https://doi.org/10.1002/cssc.201700612
77. Zhang W.; J. Smith; R. Hamilton; M. Heeney; J. Kirkpatrick ir kt. Systematic Improvement in Charge Carrier Mobility of Air Stable Triarylamine Copolymers. *Journal of the American Chemical Society*. 131, 2009, 10814-10815. Interaktyvus. ISSN 0002-7863. Prieiga per: https://doi.org/10.1021/ja9034818
78. Lim K. G.; H. B. Kim; J. Jeong; H. Kim; J. Y. Kim ir kt. Boosting the Power Conversion Efficiency of Perovskite Solar Cells Using Self-Organized Polymeric Hole Extraction Layers with High Work Function. *Advanced Materials*. 26, 2014, 6461-6466. Interaktyvus. ISSN 1521-4095. Prieiga per: https://doi.org/10.1002/adma.201401775
79. Yang W. S.; B. W. Park; E. H. Jung; N. J. Jeon; Y. C. Kim ir kt. Iodide management in formamidinium-lead-halide-based perovskite layers for efficient solar cells. *Science*. 356, 2017, 1376-1379. Interaktyvus. ISSN 1095-9203. Prieiga per: https://doi.org/10.1126/science.aan2301
80. DeLongchamp D. M.; R. J. Kline; Y. Jung; E. K. Lin; D. A. Fischer ir kt. Molecular Basis of Mesophase Ordering in a Thiophene-Based Copolymer. *Macromolecules*. 41(15), 2008, 5709-5715. Interaktyvus. ISSN 0024-9297. Prieiga per: https://doi.org/10.1021/ma800440f
81. Sigma Aldrich. https://www.sigmaaldrich.com/LT/en/product/aldrich/702471
82. Ouyang J.; Q. Xu; C. Chu; Y. Yang; G. Li ir kt. On the mechanism of conductivity enhancement in poly (3,4-ethylenedioxythiophene):poly (styrenesulfonate) film through solvent treatment. *Polymer*. 45(25), 2004, 8443-8450. Interaktyvus. ISSN 2073-4360. Prieiga per: https://doi.org/10.1016/j.polymer.2004.10.001
83. Nardes A. M.; R. A. J. Janssen; M. A. Kemerin. A morphological model for the solvent-enhanced conductivity of PEDOT: PSS thin films. *Advanced Functional Materials*. 18(6), 2008, 865-871. Interaktyvus. ISSN 1616-3028. Prieiga per: https://doi.org/10.1002/adfm.200700796
84. Xia Y.; K. Sun; J. Chang; J. Ouyang. Effects of organic inorganic hybrid perovskite materials on the electronic properties and morphology of poly (3, 4-ethylenedioxythiophene): poly(styrenesulfonate) and the photovoltaic performance of planar perovskite solar cells. *Journal of Materials Chemistry A*. 3, 2015, 15897-15904. Interaktyvus. ISSN 2050-7488. Prieiga per: https://doi.org/10.1039/C5TA03456F
85. Sigma Aldrich. https://www.sigmaaldrich.com/LT/en/product/aldrich/655201
86. Wang Q.; C. C. Chueh; M. Eslamian; A. K. Jen. Modulation of PEDOT:PSS pH for Efficient Inverted Perovskite Solar Cells with Reduced Potential Loss and Enhanced Stability. *ACS Applied Materials & Interfaces*. 8, 2016, 32068-32076. Interaktyvus. ISSN 1944-8244. Prieiga per: https://doi.org/10.1021/acsami.6b11757
87. Kato Y.; L. K. Ono; M. V. Lee; S. Wang; S. R. Raga ir kt. Silver Iodide Formation in Methyl Ammonium Lead Iodide Perovskite Solar Cells with Silver

Top Electrodes. *Advanced Materials Interfaces.* 2, 2015, 1500195. Interaktyvus. ISSN 2196-7350. Prieiga per: https://doi.org/ 10.1002/admi.201500195
88. Back H.; G. Kim; J. Kim; J. Kong; T. K. Kim ir kt. Achieving long-term stable perovskite solar cells *via* ion neutralization. *Energy & Environmental Science.* 9, 2016, 1258-1263. Interaktyvus. ISSN 1754-5692. Prieiga per: https://doi.org/10.1039/C6EE00612D
89. Huja Y.; J. Zhang; B. Xu; P. Liu; M. Cheng ir kt. Facile synthesis of fluorene-based hole transport materials for highly efficient perovskite solar cells and solid-state dye-sensitized solar cells. *Nano Energy*. 26, 2016, 108-113. Interaktyvus. ISSN 2211-2855. Prieiga per: https://doi.org/ 10.1016/j.nanoen.2016.05.006
90. Xu B.;, H. Tian; D. Bi; E. Gabrielsson; E. M. J. Johansson ir kt. Efficient solid state dye-sensitized solar cells based on an oligomer hole transport material and an organic dye. *Journal of Materials Chemistry A.* 1, 2013, 14467-14470. Interaktyvus. ISSN 2050-7488. Prieiga per: https://doi.org/ 10.1039/C3TA13646A
91. Zhang D.; T. Wu; P. Xu; Y. Ou; A. Sun ir kt. Importance of terminated groups in 9,9-bis(4-methoxyphenyl)-substituted fluorene-based hole transport materials for highly efficient organic-inorganic hybrid and all-inorganic perovskite solar cells. *Journal of Materials Chemistry A*. 7, 2019, 10319-10324. Interaktyvus. ISSN 2050-7488. Prieiga per: https://doi.org/ 10.1039/C9TA01452G
92. Hua Y.; J. B. Zhang; B. Xu; P. Liu; M. Cheng ir kt. Facile synthesis of fluorene-based hole transport materials for highly efficient perovskite solar cells and solid-state dye-sensitized solar cells. *Nano Energy*. 26, 2016, 108-113. Interaktyvus. ISSN 2211-2855. Prieiga per: https://doi.org/ 10.1016/j.nanoen.2016.05.006
93. Xu B.; J. B. Zhang; Y. Hua; P. Liu; L. Q. Wang ir kt. Tailor-Making Low-Cost Spiro[fluorene-9,9′-xanthene]-Based 3D Oligomers for Perovskite Solar Cells. *Chemistry.* 2, 2017, 676-687. Interaktyvus. ISSN 2451-9294. Prieiga per: https://doi.org/10.1016/j.chempr.2017.03.011
94. Chen W.; H. Yang; F. Guo; C. Shi; X. Sun ir kt. Simply designed nonspiro fluorene-based hole-transporting materials for high performance perovskite solar cells. *Synthetic Metals.* 250, 2019, 42-48. Interaktyvus. ISSN 0379-6779. Prieiga per: https://doi.org/10.1016/j.synthmet.2019.02.011
95. Qian-Qing G.; S. Jiang-Yang; D. Jie; D. Li-Ye; Z. Wen-Ke ir kt. A Two-Dimensional Hole-Transporting Material for High-Performance Perovskite Solar Cells with 20 % Average Efficiency. *Angewandte Chemie*. 57, 2018, 11125-11131. Interaktyvus. ISSN 1521-3773. Prieiga per: https://doi.org/ 10.1002/ange.201806392
96. Chen H.; D. Bryant; J. Troughton; M. Kirkus; M. Neophytou ir kt. One-Step Facile Synthesis of a Simple Hole Transport Material for Efficient Perovskite Solar Cells. *Chemistry of Materials*. 28(8), 2016, 2515-2518. Interaktyvus. ISSN 1520-5002. Prieiga per: https://doi.org/10.1021/acs.chemmater.6b00858
97. Gayathri R. D.; T. Gokulnath; H.-Y. Park; Z. Xie; S.-H. Jin ir kt. Facile and Stable Fluorene Based Organic Hole Transporting Materials for Efficient

Perovskite Solar Cells. *Macromolecular Research.* 30(10), 2022, 745-750. Interaktyvus. ISSN 1598-5032. Prieiga per: https://doi.org/10.1007/s13233-022-0080-2

98. Jegorove A.; C. Momblona; M. Daskeviciene; A. Magomedov; R. Degutyte ir kt. Molecular Engineering of Fluorene-Based Hole-transporting Materials for Efficient Perovskite Solar Cells. *Solar RRL*. 6, 2022, 2100990. Interaktyvus. ISSN 2367-198X. Prieiga per: https://doi.org/10.1002/solr.202100990
99. Wang X.; J. Zhang; S. Yu; W. Yu; P. Fu ir kt. Lowering Molecular Symmetry to Improve the Morphological Properties of the Hole-Transport Layer for Stable Perovskite Solar Cells. *Angewandte Chemie*. 57(38), 2018, 12529-12533. Interaktyvus. ISSN 1521-3773. Prieiga per: https://doi.org/10.1002/anie.201807402
100. Agarwala P. ir D. Kabra. A review on triphenylamine (TPA) based organic hole transport materials (HTMs) for dye sensitized solar cells (DSSCs) and perovskite solar cells (PSCs): evolution and molecular engineering. *Journal of Materials Chemistry A.* 5, 2017, 1348-1373. Interaktyvus. ISSN 2050-7488. Prieiga per: https://doi.org/10.1039/C6TA08449D
101. Juarez-Perez E. J.; M. R. Leyden; S. Wang; L. K. Ono; Z. Hawash ir kt. Role of the Dopants on the Morphological and Transport Properties of Spiro-MeOTAD Hole Transport Layer. *Chemistry of Materials.* 28(16), 2016, 5702-5709. Interaktyvus. ISSN 1520-5002. Prieiga per: https://doi.org/10.1021/acs.chemmater.6b01777
102. Richards J. J.; A. H. Rice; R. D. Nelson; F. S. Kim; S. A. Jenekhe ir kt. Modification of PCBM Crystallization via Incorporation of C_{60} in Polymer/Fullerene Solar Cells. *Advanced Functional Materials.* 23(4), 2013, 514-522. Interaktyvus. ISSN 1616-3028. Prieiga per: https://doi.org/10.1002/adfm.201201100
103. Bakr Z. H.; Q. Wali; A. Fakharuddin; L. Schmidt-Mende; T. M. Brown ir kt. Advances in hole transport materials engineering for stable and efficient perovskite solar cells. *Nano Energy*. 34, 2017, 271-305. Interaktyvus. ISSN 2211-2855. Prieiga per: https://doi.org/10.1016/j.nanoen.2017.02.025
104. Prachumrak N.; S. Pojanasopa; S. Namuangruk; T. Kaewin; S. Jungsuttiwong ir kt. Novel Bis[5-(fluoren-2-yl)thiophen-2-yl]benzothiadiazole End-Capped with Carbazole Dendrons as Highly Efficient Solution-Processed Nondoped Red Emitters for Organic Light-Emitting Diodes. *ACS Applied Materials & Interfaces.* 5, 2013, 8694-8703. ISSN 1944-8244. Prieiga per: https://doi.org/10.1021/am402349v
105. Gratia P.; A. Magomedov; T. Malinauskas; M. Daskeviciene; A. Abate ir kt. A Methoxydiphenylamine-Substituted Carbazole Twin Derivative: An Efficient Hole-Transporting Material for Perovskite Solar Cells. *Angewandte Chemie*. 54(39), 2015, 11409-11413. Interaktyvus. ISSN 1521-3773. Prieiga per: https://doi.org/10.1002/anie.201504666
106. Leijtens T.; I.-K. Ding; T. Giovenzana; J. T. Bloking; M. D. McGehee ir kt. Hole Transport Materials with Low Glass Transition Temperatures and High Solubility for Application in Solid-State Dye-Sensitized Solar Cells. *ACS Nano*.

6, 2012, 1455-1462. Interaktyvus. ISSN 1936-0851. Prieiga per: https://doi.org/10.1021/nn204296b
107. Gao W.-J.; H.-J. Yu; J. Chen; J. Xiao; J.-K. Fang ir kt. Simple hole-transporting materials containing twin-carbazole moiety and unconjugated flexible linker for efficient and stable perovskite solar cells. *Chemical Engineering Journal*. 405, 2021, 126434. Interaktyvus. ISSN 1385-8947. Prieiga per: https://doi.org/10.1016/j.cej.2020.126434
108. Petrus M. L.; K. Schutt; M. T. Sirtl; E. M. Hutter; A. C. Closs ir kt. New generation hole transporting materials for perovskite solar cells: amide-based small-molecules with nonconjugated backbones. *Advanced Energy Materials*. 8, 2018, 1801605. Interaktyvus. ISSN 1614-6840. Prieiga per: https://doi.org/10.1002/aenm.201801605
109. Lu H.; B. He; Y. Ji; Y. Shan; C. Zhong ir kt. Dopant-free hole transport materials processed with green solvent for efficient perovskite solar cells. *Chemical Engineering Journal*. 385, 2020, 123976. Interaktyvus. ISSN 1385-8947. Prieiga per: https://doi.org/10.1016/j.cej.2019.123976
110. Gao L.; T. H. Schloemer; F. Zhang; X. Chen; C. Xiao ir kt. Carbazole-Based Hole-Transport Materials for High-Efficiency and Stable Perovskite Solar Cells. *ACS Applied Energy Materials*. 3(5), 2020, 4492-4498. Interaktyvus. ISSN 2574-0962. Prieiga per: https://doi.org/10.1021/acsaem.0c00179
111. Zhang Y.; C. Kou; J. Zhang; Y. Liu; W. Li ir kt. Crosslinked and dopant free hole transport materials for efficient and stable planar perovskite solar cells. *Journal of Materials Chemistry A*. 7, 2019, 5522-5529. Interaktyvus. ISSN 2050-7488. Prieiga per: https://doi.org/10.1039/C8TA12060A
112. Zhang C.; Q. Liao; J. Chen; B. Li; C. Xu ir kt. Thermally Crosslinked Hole Conductor Enables Stable Inverted Perovskite Solar Cells with 23.9% Efficiency. *Advanced Materials*. 35(9), 2023, 2209422. Interaktyvus. ISSN 1521-4095. Prieiga per: https://doi.org/10.1002/adma.202209422
113. Choi Y.; D. Koo; G. Jeong; U. Kim; H. Kim ir kt. A vertically oriented two-dimensional Ruddlesden-Popper phase perovskite passivation layer for efficient and stable inverted perovskite solar cells. *Energy & Environmental Science.* 15, 2022, 3369-3378. Interaktyvus. ISSN 1754-5692. Prieiga per: https://doi.org/10.1039/D2EE00759B
114. Lin X.; D. Cui; X. Luo; C. Zhang; Q. Han ir kt. Efficiency progress of inverted perovskite solar cells. *Energy & Environmental Science.* 13, 2020, 3823-3847. Interaktyvus. ISSN 1754-5692. Prieiga per: https://doi.org/ 10.1039/D0EE02017F
115. Yu H.; D. Li; H. Bao; Z. Zhang; H. Liu ir kt. Multifunctional Cross-Linked Hole Transporting Interfacial Layer for Efficient and Stable Perovskite Solar Cells. *ACS Applied Energy Materials*. 5(9), 2022, 10742-10750. Interaktyvus. ISSN 2574-0962. Prieiga per: https://doi.org/10.1021/acsaem.2c01470
116. Zhang H.; Z. Chen; M. Qin; Z. Ren; K. Liu ir kt. Multifunctional Crosslinking-Enabled Strain-Regulating Crystallization for Stable, Efficient α-FAPbI3 -Based Perovskite Solar Cells. *Advanced Materials.* 33, 2021, e2008487.

Interaktyvus. ISSN 1521-4095. Prieiga per: https://doi.org/10.1002/adma.202008487
117. Li X.; S. Fu; S. Liu; Y. Wu; W. Zhang ir kt. Suppressing the ions-induced degradation for operationally stable perovskite solar cells. *Nano Energy*. 64, 2019, 103962. Interaktyvus. ISSN 2211-2855. Prieiga per: https://doi.org/10.1016/j.nanoen.2019.103962
118. Wang L.; F. Zhang; T. Liu; W. Zhang; Y. Li ir kt. A crosslinked polymer as dopant-free hole-transport material for efficient n-i-p type perovskite solar cells. *Journal of Energy Chemistry*. 55, 2021, 211-218. Interaktyvus. ISSN 2095-4956. Prieiga per: https://doi.org/10.1016/j.jechem.2020.06.062
119. Onozawa-Komatsuzaki N.; D. Tsuchiya; S. Inoue; A. Kogo; T. Funaki ir kt. Highly Efficient Dopant-Free Cyano-Substituted Spiro-Type Hole-Transporting Materials for Perovskite Solar Cells. *ACS Applied Energy Materials*. 5(6), 2022, 6633-6641. Interaktyvus. ISSN 2574-0962. Prieiga per: https://doi.org/10.1021/acsaem.2c00078
120. Binek A.; M. L. Petrus; N. Huber; H. Bristow; Y. Hu ir kt. Recycling Perovskite Solar Cells To Avoid Lead Waste. *ACS Applied Materials & Interfaces*. 8(20), 2016, 12881-12886. Interaktyvus. ISSN 1944-8244. Prieiga per: https://doi.org/10.1021/acsami.6b03767
121. Yao S. ir K. D. Belfield. Synthesis of Two-Photon Absorbing Unsymmetrical Branched Chromophores through Direct Tris(bromomethylation) of Fluorene. *The Journal of Organic Chemistry*. 70, 2005, 5126-5132. Interaktyvus. ISSN 0022-3263. Prieiga per: https://doi.org/10.1021/jo0503512
122. Wirth H. O. Organische Glaser mit hohen Glasumwandlungstemperaturen auf Basis niedermolekularer Verbindungen. *Die Angewandte Makromolekulare Chemie*. 185(1), 1991, 329-334. Interaktyvus. ISSN 1522-9505. Prieiga per: https://doi.org/10.1002/apmc.1991.051850132
123. Augulis R.; M. Franckevicius; V. Abramavicius; D. Abramavicius; S. M. Zakeeruddin ir kt. Multistep Photoluminescence Decay Reveals Dissociation of Geminate Charge Pairs in Organolead Trihalide Perovskites. *Advanced Energy. Materials*. 7(17), 2017, 1700405. Interaktyvus. ISSN 1614-6840. Prieiga per: https://doi.org/10.1002/aenm.201700405
124. Petrus M. L.; T. Bein; T. J. Dingemans; P. Docampo. A low cost azomethine-based hole transporting material for perovskite photovoltaics. *Journal of Materials Chemistry A*. 3, 2015, 12159-12162. Interaktyvus. ISSN 2050-7496. Prieiga per: https://doi.org/10.1039/C5TA03046C
125. Liu F.; F. Wu; W. Ling; Z. Tu; J. Zhang ir kt. Facile-Effective Hole-Transporting Materials Based on Dibenzo[*a,c*]carbazole: The Key Role of Linkage Position to Photovoltaic Performance of Perovskite Solar Cells. *ACS Energy Letters*. 4(10), 2019, 2514-2521. Interaktyvus. ISSN 2380-8195. Prieiga per: https://doi.org/10.1021/acsenergylett.9b01539
126. Undzėnas A. Organinių junginių fotonikos pagrindai. Vilnius, 1993, 271
127. Chi W.-J.; P.-P. Sun; Z.-S. Li. A strategy to improve the efficiency of hole transporting materials: introduction of a highly symmetrical core. *Nanoscale*. 8,

2016, 17752-17756. Interaktyvus. ISSN 2040-3372. Prieiga per: https://doi.org/10.1039/C6NR06116H
128. Urieta-Mora J.; I. Garcia-Benito; I. Zimmermann; J. Arag´o; J. Calbo ir kt. Saddle-liek, π-conjugated, cyclooctatetrathiophene-based, hole-transporting material for perovskite solar cells. *Journal of Materials Chemistry C*. 2019, 7, 6656-6663. Interaktyvus. ISSN 2050-7526. Prieiga per: https://doi.org/10.1039/C9TC00437H
129. Rakstys K.; M. Saliba; P. Gao; P. Gratia; E. Kamarauskas ir kt. Highly Efficient Perovskite Solar Cells Employing an Easily Attainable Bifluorenylidene-Based Hole-Transporting Material. *Angewandte Chemie*. 128, 2016, 7590-7594. Interaktyvus. ISSN 1521-3773. Prieiga per: https://doi.org/10.1002/ange.201602545
130. Lee K.-M.; W.-H. Chiu; Y. H. Tsai; C.-S. Wang; Y.-T. Tao ir kt. High-performance perovskite solar cells based on dopant-free hole-transporting materials fabricated by a thermal-assisted blade-coating method with efficiency exceeding 21%. *Chemical Engineering Journal*. 247, 2022, 31609. Interaktyvus. ISSN 1385-8947. Prieiga per: https://doi.org/10.1016/J.CEJ.2021.131609
131. Daskeviciute-Geguziene S.; Y. Zhang; K. Rakstys; G. Kreiza; S. B. Khan ir kt. Green-Chemistry-Inspired Synthesis of Cyclobutane-Based Hole-Selective Materials for Highly Efficient Perovskite Solar Cellsand Modules. *Angewandte Chemie*. 61, 2022, e202113207 . Interaktyvus. ISSN 1521-3773. Prieiga per: https://doi.org/10.1002/anie.202113207
132. Rakstys K.; A. Abate; M. I. Dar; P. Gao; V. Jankauskas ir kt. Triazatruxene-Based Hole Transporting Materials for Highly Efficient Perovskite Solar Cells. *Journal of the American Chemical Society*. 137, 2015, 16172-16178. Interaktyvus. ISSN 0002-7863. Prieiga per: https://doi.org/10.1021/jacs.5b11076
133. Vaitukaityte D.; C. Momblona; K. Rakstys; A. A. Sutanto; B. Ding ir kt. Cut from the Same Cloth: Enamine-Derived Spirobifluorenes as Hole Transporters for Perovskite Solar Cells. *Chemistry of Materials*. 33(15), 2021, 6059-6067. Interaktyvus. ISSN 1520-5002. Prieiga per: https://doi.org/10.1021/acs.chemmater.1c01486
134. Rakstys K.; S. Paek; G. Grancini; P. Gao; V. Jankauskas ir kt. Low-Cost Perovskite Solar Cells Employing Dimethoxydiphenylamine-Substituted Bistricyclic Aromatic Enes as Hole Transport Materials. *ChemSusChem*. 10(19), 2017, 3825-3832. Interaktyvus. ISSN 1864-564X. Prieiga per: https://doi.org/10.1002/cssc.201700974
135. Levy A.; P. U. Biedermann; I. Agranat. Interplay of Twisting and Folding in Overcrowded Heteromerous Bistricyclic Aromatic Enes. *Organic Letters*. 2(13), 2000, 1811-1814. Interaktyvus. ISSN 1523-7060. Prieiga per: https://doi.org/10.1021/ol005827c
136. Matoliukstyte A.; E. Burbulis; J. V. Grazulevicius; V. Gaidelis; V. Jankauskas. Carbazole-containing enamines as charge transport materials for

electrophotography. *Synthetic Metals*. 158(11), 2008, 462-467. Interaktyvus. ISSN 0379-6779. Prieiga per: https://doi.org/ 10.1016/j.synthmet.2008.03.020
137. Li Y.; F. Wu; M. Han; Z. Li,; L. Zhu ir kt. Merocyanine with Hole-Transporting Ability and Efficient Defect Passivation Effect for Perovskite Solar Cells. *ACS Energy Letters*. 6(3), 2021, 869-876. Interaktyvus. ISSN 2380-8195. Prieiga per: https://doi.org/10.1021/acsenergylett.1c00124
138. Lu H.; J. Xu; X. Liu; F. Wu; L. Zhu. Effect of isomeric hole-transporting materials on perovskite solar cell performance. *Materials Today Energy*. 21, 2021, 100780. Interaktyvus. ISSN 2468-6069. Prieiga per: https://doi.org/ 10.1016/j.mtener.2021.100780
139. Liu C.; C. Igci; Y. Yang; O. A. Syzgantseva; M. A. Syzgantseva ir kt. Dopant-Free Hole Transport Materials Afford Efficient and Stable Inorganic Perovskite Solar Cells and Modules. *Angewandte Chemie*. 60(37), 2021, 20489-20497. Interaktyvus. ISSN 1521-3773. Prieiga per: https://doi.org/10.1002/anie.202107774
140. Tsutsumi N.; M. Yamamoto; Y. Nishijima. Hole transport of *trans*-1,2-biscarbazolylcyclobutane-doped poly(bisphenol A carbonate) film. *Journal of Polymer Science. P art B.* 25(10), 1987, 2139-2148. Interaktyvus. ISSN 0887-6266. Prieiga per: https://doi.org/10.1002/polb.1987.090251008
141. Sasakawa S.; T. Ikeda; S. Tazuke. Effect of polymer matrices on hole transport of 1,2-*trans*-bis(9H-carbazole-9-yl) cyclobutane dissolved in a polymer binder. *Journal of Applied Physics*. 65, 1989, 2750-2755. Interaktyvus. ISSN 1089-7550. Prieiga per: https://doi.org/10.1063/1.342764
142. Ikeda T.; H. Mochizuki; Y. Hayashi; M. Sisido; T. Sasakawa. Hole transport in liquid-crystalline media. I. Effect of matrices on hole drift mobilities of 1,2-*trans*-bis (9*H*-carbazol-9-yl)-cyclobutane doped in polymer liquid crystals. *Journal of Applied Physics*. 70, 1991, 3689-3695. Interaktyvus. ISSN 1089-7550. Prieiga per: https://doi.org/10.1063/1.349218
143. Wang Y.; Q. Liao; J. Chen; W. Huang; X. Zhuang ir kt. Teaching an Old Anchoring Group New Tricks: Enabling Low-Cost, Eco-Friendly Hole-Transporting Materials for Efficient and Stable Perovskite Solar Cells. *Journal of the American Chemical Society*. 142(39), 2020, 16632-16643. Interaktyvus. ISSN 0002-7863. Prieiga per: https://doi.org/10.1021/jacs.0c06373
144. Li Z.; Z. Zhu; C. C. Chueh; J. Luo; A. K. Y. Jen. Facile Thiol-Ene Thermal Crosslinking Reaction Facilitated Hole-Transporting Layer for Highly Efficient and Stable Perovskite Solar Cells. *Advanced Energy Materials*. 6(21), 2016, 1601165. Interaktyvus. ISSN 1614-6832. Prieiga per: https://doi.org/10.1002/aenm.201601165
145. Zhang C.; Q. Liao; J. Chen; B. Li; C. Xu ir kt. Thermally Crosslinked Hole Conductor Enables Stable Inverted Perovskite Solar Cells with 23.9% Efficiency. *Advanced Materials*. 35(9), 2023, 2209422. Interaktyvus. ISSN 1521-4095. Prieiga per: https://doi.org/10.1002/adma.202209422
146. Wang Y.; S. Gu; G. Liu; L. Zhang; Z. Z. Liu ir kt. Cross-Linked Hole Transport Layers for High-Efficiency Perovskite Tandem Solar Cells. *Science China*

Chemistry. 64(11), 2021, 2025-2034. Interaktyvus. ISSN 1674-7291 Prieiga per: https://doi.org/10.1007/s11426-021-1059-1
147. Daskeviciute-Geguziene S.; A. Magomedov; M. Daskeviciene; K. Genevicius; N. Nekrasas ir kt. Cross-Linkable Carbazole-Based Hole Transporting Materials for Perovskite Solar Cells. *Chemical Communication*. 58(54), 2022, 7495-7498. Interaktyvus. ISSN 1359-7345. Prieiga per: https://doi.org/ 10.1039/D2CC02612K
148. Wu J.; M. Hu; L. Zhang; G. Song; Y. Li ir kt. Fluorinated Cross-Linkable and Dopant-Free Hole Transporting Materials for Efficient and Stable Perovskite Solar Cells. *Chemical Engineering Journal*. 422, 2021, 130124. Interaktyvus. ISSN 1385-8947. Prieiga per: https://doi.org/10.1016/j.cej.2021.130124
149. Zhang Y.; C. Kou; J. Zhang; Y. Liu; W. Li ir kt. Crosslinked and Dopant Free Hole Transport Materials for Efficient and Stable Planar Perovskite Solar Cells. *Journal of Materials Chemistry A.* 7(10), 2019, 5522-5529. Interaktyvus. ISSN 1364-5501. Prieiga per: https://doi.org/ 10.1039/C8TA12060A
150. Malinauskas T.; M. Saliba; T. Matsui; M. Daskeviciene; S. Urnikaite ir kt. Branched Methoxydiphenylamine-Substituted Fluorene Derivatives as Hole Transporting Materials for High-Performance Perovskite Solar Cells. *Energy & Environmental Science*. 9(5), 2016, 1681-1686. Interaktyvus. ISSN 1754-5692. Prieiga per: https://doi.org/10.1039/C5EE03911H
151. Gratia P.; A. Magomedov; T. Malinauskas; M. Daskeviciene; A. Abate ir kt. Methoxydiphenylamine-Substituted Carbazole Twin Derivative: An Efficient Hole-Transporting Material for Perovskite Solar Cells. *Angewandte Chemie*. 54(39), 2015, 11409-11413. Interaktyvus. ISSN 1433-7851. Prieiga per: https://doi.org/10.1002/anie.201504666

7. MOKSLINIAI STRAIPSNIAI

FULL PAPER

Solar Cells

ADVANCED SCIENCE Open Access

www.advancedscience.com

Nonspiro, Fluorene-Based, Amorphous Hole Transporting Materials for Efficient and Stable Perovskite Solar Cells

Šarūnė Daškevičiūtė, Nobuya Sakai, Marius Franckevičius, Marytė Daškevičienė, Artiom Magomedov, Vygintas Jankauskas, Henry J. Snaith, and Vytautas Getautis**

Novel nonspiro, fluorene-based, small-molecule hole transporting materials (HTMs) V1050 and V1061 are designed and synthesized using a facile three-step synthetic route. The synthesized compounds exhibit amorphous nature with a high glass transition temperature, a good solubility, and decent thermal stability. The planar perovskite solar cells (PSCs) employing V1050 generated an excellent power conversion efficiency of 18.3%, which is comparable to 18.9% obtained with the state-of-the-art Spiro-OMeTAD. Importantly, the devices based on V1050 and V1061 show better stability compared to devices based on Spiro-OMeTAD when aged without any encapsulation under uncontrolled humidity conditions (relative humidity around 60%) in the dark and under continuous full sun illumination.

1. Introduction

Due to the merits of intense absorption in an almost entire visible spectral region, perovskite materials first emerged as dye substitutes for dye-sensitized solar cells with the liquid electrolyte showing a power conversion efficiency (PCE) around 4%.[1] Since the first perovskite-based solar cells (PSCs) suffered from fast degradation their architecture was shifted from liquid electrolyte-based low PCE devices to solid-state devices using small organic hole transporting molecule 2,2′,7,7′-tetrakis(*N*,*N*-di-*p*-methoxyphenylamine)-9,9′-spirobifluorene (Spiro-OMeTAD).[2] In consequence, the photovoltaic performances have skyrocketed to 21.1% for small-area cells[3] and 20.5% for cells[4] with the active area larger than 1 cm^2 in just a few years. Since then, Spiro-OMeTAD became a standard material for the development of the new hole transporting materials (HTMs) for PSCs. In the majority of the state-of-the-art devices, Spiro-OMeTAD is used as a hole transporting material.[5–8] However, the tedious synthetic procedures and purification processes of this HTM make it cost ineffective and thus limit its application and commercialization.[9] Moreover, the study by A. Binek et al. showed that Spiro-OMeTAD can significantly contribute to the overall cost of materials required for the PSC manufacturing.[10]

To engineer HTMs which are considerably cheaper than Spiro-OMeTAD, shorter reaction schemes with simple purification procedures are required. Successful examples include azomethine derivative EDOT-OMeTPA,[11] branched methoxydiphenylamine-substituted fluorene derivatives V859 and V862,[12] enamine derivative V950,[13] and spiro[fluorene-9,9′-xanthene] (SFX)-based materials SFXMeOTAD[14] or X60,[15] and X59.[16] Some of them are reported to have equal or slightly better performance in comparison to that of Spiro-OMeTAD.[12,15]

Besides the low cost, HTMs should meet a number of other requirements, including excellent charge transporting properties, good energy matching with the perovskite, transparency to solar radiation, large Stokes shift, good solubility in organic solvents, morphologically stable film formation, and others. Meanwhile, numerous investigations are being carried out aiming to improve the efficiency of HTMs, however until now only few concrete recommendations have been made with regard to the molecular structure modification.[17–24]

Recently, we have presented the synthesis of a new class of efficient HTMs.[25,26] Their structure consists of two 4,4′-dimethoxydiphenylamine 3,6-disubstituted carbazole fragments linked by a nonplanar unit. Synthesis of these HTMs was performed by a simple two-step synthetic procedure providing a target product in high yield. Conveniently, the first step is a basic "click" type reaction and high reaction rates (≈10 min at room temperature), simple purification procedure (only filtration is required) and high yields are typical for this step. The

Š. Daškevičiūtė, Dr. M. Daškevičienė, A. Magomedov, Prof. V. Getautis
Department of Organic Chemistry
Kaunas University of Technology
Radvilenų pl. 19, Kaunas LT-50254, Lithuania
E-mail: vytautas.getautis@ktu.lt

Dr. N. Sakai, Prof. H. J. Snaith
Department of Physics Clarendon Laboratory
University of Oxford
Parks Road, Oxford OX1 3PU, UK
E-mail: henry.snaith@physics.ox.ac.uk

Dr. M. Franckevičius
Center for Physical Sciences and Technology
Saulėtekio Ave. 3, Vilnius LT-10257, Lithuania

Dr. V. Jankauskas
Institute of Chemical Physics Vilnius University
Saulėtekio al.3, Vilnius LT-10257, Lithuania

The ORCID identification number(s) for the author(s) of this article can be found under https://doi.org/10.1002/advs.201700811.

DOI: 10.1002/advs.201700811

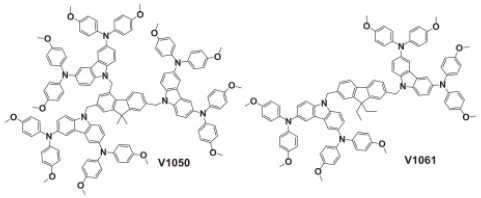

Figure 1. Structures of HTMs: **V1050** and **V1061**.

performance of $CH_3NH_3PbI_3$-based PSC with these branched compounds was close to that of the Spiro-OMeTAD in the same conditions.

In this work, we present the synthesis, characterization and photovoltaic performance of two new hole transporting materials, namely **V1050** and **V1061** possessing 4,4′-dimethoxydiphenylamine 3,6-disubstituted carbazole-based hole transporting moieties and 9,9-dialkyl-9*H*-fluorene as a central linking fragment (**Figure 1**).

The coplanar central core was chosen in order to improve the efficiency of HTM, as was previously shown by Li and coworkers.[17] Furthermore, the properties and performance of newly synthesized HTMs were additionally compared to that of the state-of-the-art Spiro-OMeTAD.

2. Results and Discussions

2.1. Synthesis

The fluorene derivatives **V1050** and **V1061** were synthesized by a simple two-step reaction from the key intermediates, the bromomethylfluorenes **1** and **3**, as illustrated in **Scheme 1**. To synthesize intermediate **3**, a slightly modified literature procedure was employed to perform the tris(bromomethylation) of 9,9-dimethylfluorene.[27] In the next step, 3,6-dibromo-9*H*-carbazole was reacted with 2,4,7-tris(bromomethyl)-9,9-dimethyl-9*H*-fluorene (**3**) in the presence of KOH powder to provide the intermediate compound **4**. Finally, the desired product **V1050** was obtained by the palladium-catalyzed Buchwald–Hartwig C–N cross-coupling reaction of

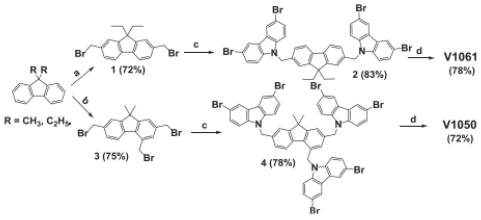

Scheme 1. Synthesis route to HTMs **V1050** and **V1061**: a) paraformaldehyde (2.2 equiv.), 33% HBr in HOAc, 65 –70 °C; b) paraformaldehyde (10.0 equiv), 33% HBr in HOAc, 85 –90 °C; c) 3,6-dibromocarbazole, 85% KOH, THF, at r.t.; d) 4,4′-dimethoxydiphenylamine, $Pd(OAc)_2$, P(*t*-Bu)$_3$·BF_3, NaO*t*-Bu, at reflux of anhydrous toluene.

compound **4** with 4,4′-dimethoxydiphenylamine. Surprisingly, di(bromomethylation) of 9,9-dimethyl-9*H*-fluorene was unsuccessful and inseparable mixture of the reaction products was obtained by using two equivalents of paraformaldehyde. Presumably, the presence of the small methyl substituents at the 9th position markedly stipulates the formation of trisubstituted product as well. Therefore, as the reference compound, the hole transporting material **V1061**, containing 9,9-diethyl-9*H*-fluorene as a central linking fragment and two equivalent 4,4′-dimethoxydiphenylamine 3,6-disubstituted carbazole-based branches was also prepared according to the same approach. The final compounds **V1050** and **V1061** were isolated by column chromatography and precipitated from toluene or tetrahydrofuran into 15-fold excess of *n*-hexane. Obtained by such a procedure **V1050** and **V1061** were amorphous compounds. All our attempts to crystallize them were unsuccessful. The chemical structure of the synthesized **V1050** and **V1061** products were confirmed by ^{1}H and ^{13}C NMR as well as elemental analysis data. A more detailed procedure for the synthesis of hole transport materials is included in the Supporting Information.

2.2. Thermal Properties

Thermal gravimetric analysis (TGA) and differential scanning calorimetry (DSC) were applied to measure the thermal stability of the above obtained HTMs. The weight loss as a function of temperature of **V1050** and **V1061** compounds is presented in **Figure 2**a. A significant weight loss appears at around 400 °C and proceeds until complete decomposition of both materials at 600 °C.

The decomposition temperature corresponding to a 5% weight loss (T_d) is about 400 °C, indicating good thermal stability of **V1050**. HTM possessing two 4,4′-dimethoxydiphenylamine 3,6-disubstituted carbazole-based branches shows slightly better thermal stability because T_d is about 420 °C. From TGA measurements we conclude, that both fluorene-based compounds are suitable for the application in the perovskite solar cells. Initial small (2–3%) weight loss at <150 °C can be attributed to the evaporation of the solvent traces remaining after the purification procedure.

DSC analysis of the **V1050** and **V1061** has shown (Figure 2b) that after purification, the target compounds exist in an amorphous state with the glass transition temperatures of about 166 and 146 °C, respectively. The high glass transition temperature is in good agreement with one of Wirth postulates[28] demonstrating that the glass transition temperature can be raised by increasing molecular size, incorporating additional bulky substituent into 4th position of the molecule, and enhancing molecular interaction, which can hinder molecular motions. To the best of our knowledge, **V1050** exhibits one of the highest glass transition temperatures among amorphous HTMs applied in the PSCs, being 40 °C higher than that of Spiro-OMeTAD (126 °C). A high glass transition temperature is an indicator of the more stable amorphous state and reduced tendency to crystallize. Recently, it has been observed that Spiro-OMeTAD tends to crystallize in perovskite solar cells under device operating conditions,[29] which in turn can lead to device degradation and failure over the longer term. Whereas, both **V1050** and

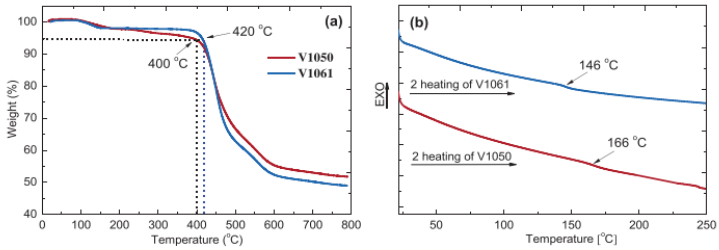

Figure 2. a) TGA curves of the **V1050** and **V1061** (heating rate 10 °C min^{-1}), b) DSC second heating curves for the **V1050** and **V1061** (heating rate 10 °C min^{-1}).

V1061 are entirely amorphous and do not show characteristic transitions of the crystalline state (Figures S1 and S2, Supporting Information). The superior properties of new HTMs can be attributed to the presence of the branched 4,4′-dimethoxydiphenylamine 3,6-disubstituted carbazole-based moieties linked by bulky central fluorene core.

2.3. Optical and Photophysical Properties

The UV–vis absorption spectra of a new fluorene-based organic HTMs measured in tetrahydrofuran (THF) solution is shown in **Figure 3**a and compared with Spiro-OMeTAD. The absorption spectra for both **V1050** and **V1061** HTMs are almost identical. This confirms that conjugation between 4,4′-dimethoxydiphenylamine 3,6-disubstituted carbazole-based branches is absent. Both HTMs show intense π–π^* absorption band with the maximum at 305 nm and weak low energy absorption at 375 nm corresponding to n–π^* transitions. Furthermore, absorption of both compounds lies mainly in the UV region with a very weak undesirable absorption in the visible spectral range. Because a new hole transporting materials are more transparent to solar radiation, they become even more advantageous for the application in the PSC.[30] The steady state absorption spectra of perovskite $FA_{0.83}Cs_{0.17}Pb(I_{0.8}Br_{0.2})_3$ films deposited on TiO_2 with and without hole transporting materials are shown in Figure 3b. The absorption spectra show characteristic absorption onset at around 775 nm due to exciton absorption. All films reveal very similar signatures when measured above 550 nm, indicating that there is no apparent contribution of HTMs to the light absorption of perovskite solar cells.

Here, we additionally performed time resolved photoluminescence (PL) decay measurements to study charge–carrier transport properties in perovskite films deposited on glass with and without HTMs (**Figure 4**). For pristine perovskite films, PL decays during 58 ns and reflects nongeminate electron–hole recombination[30] being the dominating radiative channel in the neat perovskite films. When the perovskite films are covered with hole transporting materials, the PL decay rate for all three films becomes significantly reduced. The strong photoluminescence quenching indicates efficient extraction of holes at the perovskite/HTM interfaces.

To evaluate the efficiency of the charge transfer properties from perovskite to HTMs from time-resolved PL measurements, we used previously proposed protocol.[31] The calculated charge-transfer time and efficiency values are presented in **Table 1**. The charge transfer efficiency values of perovskite solar cell devices comprising new HTMs are comparable to that obtained with commercially available Spiro-OMeTAD. The superior hole collection was also consistent with photovoltaic measurements of devices, which showed similar power conversion efficiencies between all devices.

2.4. Photoelectrical Properties

Xerographic time-of-flight technique was used to characterize charge transporting properties of the synthesized HTMs. The

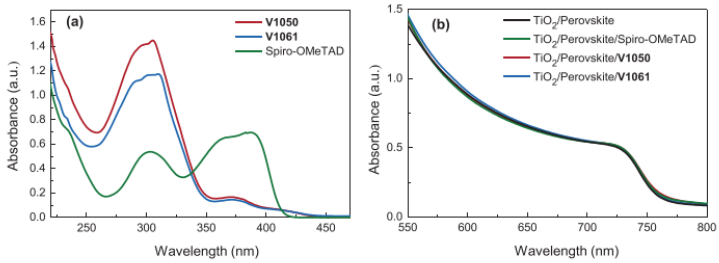

Figure 3. a) UV–vis absorption spectra of **V1050**, **V1061**, and Spiro-OMeTAD, b) UV–vis absorption spectra of TiO_2/perovskite ($FA_{0.83}Cs_{0.17}Pb(I_{0.8}Br_{0.2})_3$) film and perovskite ($FA_{0.83}Cs_{0.17}Pb(I_{0.8}Br_{0.2})_3$) deposited with Spiro-OMeTAD and **V1050**, and **V1061** hole transporting materials.

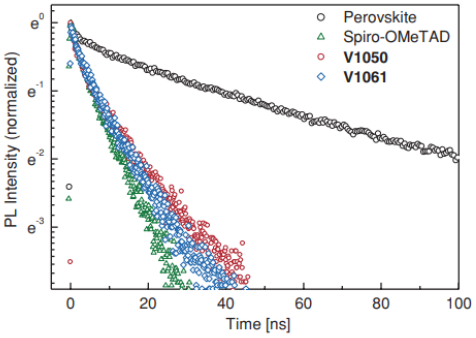

Figure 4. Photoluminescence decay kinetics of lead halide perovskite ($FA_{0.83}Cs_{0.17}Pb(I_{0.8}Br_{0.2})_3$) films deposited on glass substrates comprising **V1050**, **V1061**, and Spiro-OMeTAD hole transporting layers. Photoluminescence lifetimes were monitored at the emission maximum at 770 nm upon excitation at 470 nm.

measured charge mobility values of **V1050** and **V1061** are found to be comparable to the values measured for Spiro-OMeTAD. Values of charge mobility defining parameters: zero field mobility (μ_0) and the mobility at the electric field of 6.4×10^5 V cm^{-1} are given in **Table 2.** The measured hole–drift mobility for **V1061** was 3.0×10^{-6} cm^2 V^{-1} s^{-1}, while for **V1050** – 1.5×10^{-6} cm^2 V^{-1} s^{-1} at weak electric fields. Interestingly, the charge mobility values of the new HTMs at strong field strength coming closer to the values measured for Spiro-OMeTAD (**Figure 5**, Table 2). Lower hole drift mobility values could be attributed to the presence of the bulky central fluorene fragment, which is linked to the 4,4′-dimethoxydiphenylamine 3,6-disubstituted carbazole-based hole transporting moieties by nonconjugated bonds. Conformational freedom increases disorder of molecules in the films, thus lowering mobility values.

To determine the highest occupied molecular orbital (HOMO) energy level of **V1050** and **V1061**, solid state ionization potential (I_p) was measured by photoelectron spectroscopy in air method[32] and results are presented in Table 2; the measurement error is evaluated as 0.03 eV. Compounds **V1050** and **V1061** have almost the same I_p values, 5.11 and 5.10 eV, respectively (Figures S3 and S4, Supporting Information). The estimated I_p values are very closed to the value of Spiro-OMeTAD (5.00 eV) and compatible for application in perovskite solar cell devices to ensure efficient hole transfer at the interface.

2.5. Perovskite Solar Cells

Currently one of the best and most reproducible results are obtained with "triple-cation" composition of perovskite,

Table 1. Charge–transfer time (τCT) and efficiency (CTE) calculated for perovskite films employing various HTMs.

HTM	τ [ns]	CTE [%]
V1050	12.8	81.9
V1061	15.9	78.4
Spiro-OMeTAD	9.6	85.8

Table 2. Thermal and photoelectrical properties of **V1050**, **V1061**, and Spiro-OMeTAD.

HTM	T_g[a] [°C]	T_{dec}[b] [°C]	I_p[c] [eV]	μ_0[d] [cm^2 V^{-1} s^{-1}]	μ[e] [cm^2 V^{-1} s^{-1}]
V1050	166	400	5.11	1.5×10^{-6}	1.7×10^{-4}
V1061	146	420	5.10	3.0×10^{-6}	2.0×10^{-4}
Spiro-OMeTAD[26]	126	449	5.00	4.1×10^{-5}	5.0×10^{-4}

[a]Determined by DSC: scan rate = 10 °C min^{-1}, N_2 atmosphere; second run; [b]Thermal decomposition temperature was registered at 5% weight loss; [c]Ionization potential was measured by the photoemission in air method from films; [d]Mobility value at zero field strength; [e]Mobility value at 6.4×10^5 V cm^{-1} field strength.

containing MA^+, FA^+, and inorganic Cs^+ cations.[3] However, MA^+ is a volatile cation and can cause degradation of the perovskite absorber film. Thus, during the last years, MA^+-free architectures have been extensively studied, where FA^+ cation is combined with Cs^+, which provides higher stability.[33–36] SnO_2 was used as an electron transporting layer, as it can be deposited at low temperatures (annealing temperature–180 °C), and thus is suitable material for the application in tandem solar cells.[37]

The nonspiro, fluorene-based compounds **V1050** and **V1061** were tested in perovskite solar cells employing planar FTO/SnO_2/$FA_{0.83}Cs_{0.17}Pb(I_{0.8}Br_{0.2})_3$/HTM/Au architecture. **Figure 6** shows current–voltage characteristics of the best devices employing **V1050**, **V1061**, and Spiro-OMeTAD in planar PSC. The optimized champion device efficiency for **V1050**, **V1061**, Spiro-OMeTAD, and corresponding photovoltaic performance parameters are shown in Figure 6. The **V1050** HTM-based device shows the device efficiency of 18.3% (J_{sc} = 22.0 mA cm^{-2}, V_{OC} = 1.05 V, and FF = 79.5%). This is comparable to the state-of-the-art material Spiro-OMeTAD on a like-to-like comparison (PCE = 18.9%, J_{sc} = 22.4 mA cm^{-2}, V_{OC} = 1.08 V, and FF = 77.9%). A bit lower PCE of 16.7%

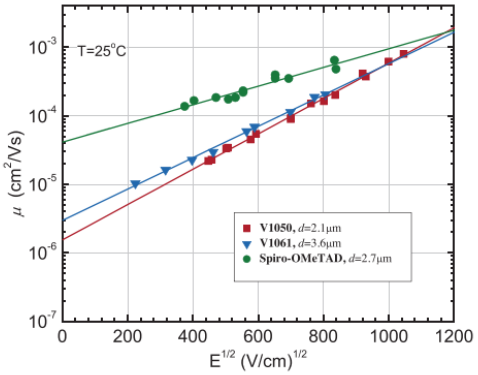

Figure 5. Electric field dependencies of the hole-drift mobilities (μ) in charge transport layers of **V1050**, **V1061**, and Spiro-OMeTAD, with corresponding linear fits represented by solid lines.

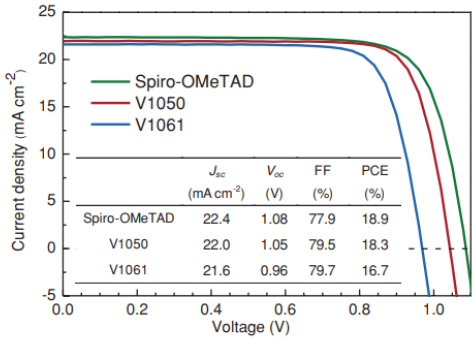

	J_{sc} (mA cm^{-2})	V_{oc} (V)	FF (%)	PCE (%)
Spiro-OMeTAD	22.4	1.08	77.9	18.9
V1050	22.0	1.05	79.5	18.3
V1061	21.6	0.96	79.7	16.7

Figure 6. Best performing *J–V* characteristics (reverse scan) of the best devices employing **V1050**, **V1061**, and Spiro-OMeTAD.

(Figure 6) was recorded with J_{sc} = 21.6 mA cm^{-2}, V_{OC} = 0.96 V, and *FF* = 79.7% in case of **V1061**. Efficiencies at stabilized power output (SPO) of tested compounds are shown in Figure S5 in the Supporting Information and are 16.1%, 15.0%, and 17.3%, respectively. External quantum efficiency (EQE) spectra were recorded for typical device for each HTMs in Figure S6 (Supporting Information). The same trend was observed from the measured *J–V* curves. The statistical distribution of the PSC parameters employing investigated HTMs is shown in Figure S7 in the Supporting Information and is indicating high reproducibility of PSC devices. Furthermore, Figure S8 (Supporting Information) shows *J–V* curves from both forward-bias to short-circuit and short-circuit to forward-bias current–voltage sweeps of typical device from both sweeps. While hysteresis is quite pronounced, it is comparable between the mentioning HTMs, thus reverse scans can be used as representatives for the HTMs performance analysis.

From the SEM cross-section images, it can be seen, that new fluorene-based compounds form a uniform morphology on top of perovskite layer as similar as Spiro-OMeTAD (**Figure 7**).

To give good performance, HTM should effectively block the electrons and transport holes from perovskite to the Au electrode. Thus, it is important for the HTMs to have excellent film forming ability. As from the SEM cross-section images no significant difference could be observed, contact angle measurement of the HTM droplets on the perovskite film was performed (Figure S9, Supporting Information). From the results it can be seen, that **V1050** solution has the lowest contact angle of 9°, which could potentially lead to a better film forming ability of **V1050**.

Additionally, we also studied the stability of fabricated champion devices without any encapsulation at uncontrollable humidity conditions (relative humidity ≈ 60%, temperature 22 °C, in dark condition) for our newly developed **V1050**, **V1061** and standard Spiro-OMeTAD HTMs. It can be seen (**Figure 8**) that the PCE values diminished down ≈20% after 330 h for Spiro-OMeTAD based devices. However, the devices based on **V1050** and **V1061** are seen to be more stable with observed efficiency reduced only ≈6% at the same conditions. The device stability

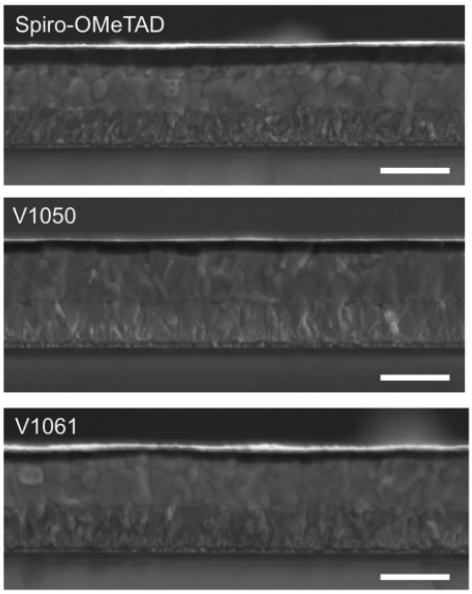

Figure 7. Cross-sectional SEM microscopy image of the devices with Spiro-OMeTAD, **V1050**, and **V1061** as a HTM. Scale bar equals to 1000 nm.

test results revealed that the improved stability of **V1050** and **V1061**-based cells compared to Spiro-OMeTAD-based device could be attributed to the uniform HTM capping layer on the top of the perovskite layer, preventing the moisture penetration into the perovskite layer, which is in agreement with the result from HTM contact angle measurement on top of perovskite film. The overall good performance of PCE and stability of **V1050** over Spiro-OMeTAD provide a promising alternative replacement for high performance PSCs.

3. Conclusions

In conclusion, a new promising nonspiro fluorene-based hole transport materials **V1050** and **V1061** were synthesized and characterized. The synthesis of these HTMs consists of three steps starting from the commercially available materials. Solar cells using **V1050** exhibit PCEs of 18.3% which is comparable to the performance of PSC comprising Spiro-OMeTAD (18.9%) as HTM. Compared with Spiro-OMeTAD, new HTM additionally shows several significant advantages: it has much facile synthesis, has high glass transition temperature (166 °C) and does not form the crystalline state. Moreover, this new HTM also exhibits better environmental stability compared to Spiro-OMeTAD. We believe that the **V1050** can be a useful alternative HTM to Spiro-OMeTAD for perovskite solar cells, thus bringing PSCs closer to commercial production.

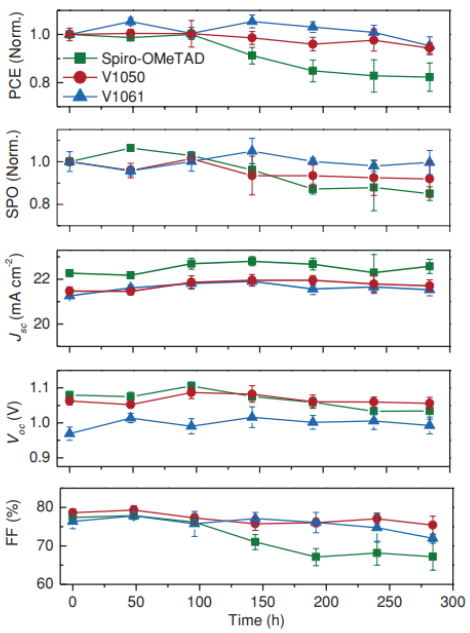

Figure 8. Transition of the PV performance parameters (PCE, SPO, J_{sc}, V_{oc}, and *FF*) of the PSCs with **V1050**, **V1061**, and Spiro-OMeTAD.

Supporting Information

Supporting Information is available from the Wiley Online Library or from the author.

Acknowledgements

Š.D. and N.S. contributed equally to this work. The authors acknowledge funding from the Research Council of Lithuania via grant (Grant No. LAT-07/2016), funding from the European Union Seventh Framework Programme [FP7/2007–2013] under grant agreement no. 604032 of the MESO project, and E. Kamarauskas for measurements of ionization potential.

Conflict of Interest

The authors declare no conflict of interest.

Keywords

fluorene, materials science, organic conductor, perovskite, solar cells

Received: November 2, 2017
Revised: December 29, 2017
Published online: January 31, 2018

[1] A. Kojima, K. Teshima, Y. Shirai, T. Miyasaka, *J. Am. Chem. Soc.* **2009**, *131*, 6050.
[2] S. D. Stranks, H. J. Snaith, *Nat. Nanotechnol.* **2015**, *10*, 391.
[3] M. Saliba, T. Matsui, J.-Y. Seo, K. Domanski, J.-P. Correa-Baena, M. K. Nazeeruddin, S. M. Zakeeruddin, W. Tress, A. Abate, A. Hagfeldt, M. Grätzel, *Energy Environ. Sci.* **2016**, *9*, 1989.
[4] X. Li, D. Bi, C. Yi, J.-D. Décoppet, J. Luo, S. M. Zakeeruddin, A. Hagfeldt, M. Grätzel, *Science* **2016**, *353*, 58.
[5] M. Saliba, T. Matsui, K. Domanski, J.-Y. Seo, A. Ummadisingu, S. M. Zakeeruddin, J.-P. Correa-Baena, W. R. Tress, A. Abate, A. Hagfeldt, M. Grätzel, *Science* **2016**, *354*, 206.
[6] D.-Y. Son, J.-W. Lee, Y. J. Choi, I.-H. Jang, S. Lee, P. J. Yoo, H. Shin, N. Ahn, M. Choi, D. Kim, N.-G. Park, *Nat. Energy* **2016**, *1*, 16081.
[7] Y. Zhang, G. Grancini, Y. Feng, A. M. Asiri, M. K. Nazeeruddin, *ACS Energy Lett.* **2017**, *2*, 802.
[8] G. Grancini, C. Rolda-Carmona, I. Zimmermann, E. Mosconi, X. Lee, D. Martineau, S. Narbey, F. Oswald, F. De Angelis, M. Graetzel, M. K. Nazeeruddin, *Nat. Commun.* **2017**, *8*, 15684.
[9] P. Liu, B. Xu, Y. Hua, M. Cheng, K. Aitola, K. Sveinbjörnsson, J. Zhang, G. Boschloo, L. Sun, L. Kloo, *J. Power Sources* **2017**, *344*, 11.
[10] A. Binek, M. L. Petrus, N. Huber, H. Bristow, Y. Hu, T. Bein, P. Docampo, *ACS Appl. Mater. Interfaces* **2016**, *8*, 12881.
[11] M. L. Petrus, T. Bein, T. J. Dingemans, P. Docampo, *J. Mater. Chem. A* **2015**, *3*, 12159.
[12] T. Malinauskas, M. Saliba, T. Matsui, M. Daskeviciene, S. Urnikaite, P. Gratia, R. Send, H. Wonneberger, I. Bruder, M. Graetzel, V. Getautis, M. K. Nazeeruddin, *Energy Environ. Sci.* **2016**, *9*, 1681.
[13] M. Daskeviciene, S. Paek, Z. Wang, T. Malinauskas, G. Jokubauskaite, K. Rakstys, K. T. Cho, A. Magomedov, V. Jankauskas, S. Ahmad, H. J. Snaith, V. Getautis, M. K. Nazeeruddin, *Nano Energy* **2017**, *32*, 551.
[14] M. Maciejczyk, A. Ivaturi, N. Robertson, *J. Mater. Chem. A* **2016**, *4*, 4855.
[15] B. Xu, D. Bi, Y. Hua, P. Liu, M. Cheng, M. Grätzel, L. Kloo, A. Hagfeldt, L. Sun, *Energy Environ. Sci.* **2016**, *9*, 873.
[16] D. Bi, B. Xu, P. Gao, L. Sun, M. Grätzel, A. Hagfeldt, *Nano Energy* **2016**, *23*, 138.
[17] W.-J. Chi, P.-P. Sun, Z.-S. Li, *Nanoscale* **2016**, *8*, 17752.
[18] L. Zhu, Y. Shan, R. Wang, D. Liu, C. Zhong, Q. Song, F. Wu, *Chem. Eur. J.* **2017**, *23*, 4373.
[19] I. García-Benito, I. Zimmermann, J. Urieta-Mora, J. Aragó, A. Molina-Ontoria, E. Ortí, N. Martín, M. K. Nazeeruddin, *J. Mater. Chem. A* **2017**, *5*, 8317.
[20] H. Nishimura, N. Ishida, A. Shimazaki, A. Wakamiya, A. Saeki, L. T. Scott, Y. Murata, *J. Am. Chem. Soc.* **2015**, *137*, 15656.
[21] C. Huang, W. Fu, C.-Z. Li, Z. Zhang, W. Qiu, M. Shi, P. Heremans, A. K.-Y. Jen, H. Chen, *J. Am. Chem. Soc.* **2016**, *138*, 2528.
[22] S.-D. Sung, M.-S. Kang, I.-T. Choi, H.-M. Kim, H. Kim, M.-P. Hong, H.-K. Kim, W.-I. Lee, *Chem. Commun.* **2014**, *50*, 14161.
[23] M.-S. Kang, S.-D. Sung, I.-T. C.-H. Kim, M.-P. Hong, J. Kim, W.-I. Lee, H.-K. Kim, *ACS Appl. Mater. Interfaces* **2015**, *7*, 22213.
[24] C. Lu, I.-T. Choi, J. Kim, H.-K. Kim, *J. Mater. Chem. A* **2017**, *5*, 20263.
[25] P. Gratia, A. Magomedov, T. Malinauskas, M. Daskeviciene, A. Abate, S. Ahmad, M. Grätzel, V. Getautis, M. K. Nazeeruddin, *Angew. Chem., Int. Ed.* **2015**, *54*, 11409.
[26] A. Magomedov, N. Sakai, E. Kamarauskas, G. Jokubauskaitė, M. Franckevičius, V. Jankauskas, H. J. Snaith, V. Getautis, *Chem. - Asian J.* **2017**, *12*, 958.
[27] S. Yao, K. D. Belfield, *J. Org. Chem.* **2005**, *70*, 5126.

[28] H. O. Wirth, *Angew. Makromol. Chem.* **1991**, *185*, 329.
[29] T. Malinauskas, D. Tomkute-Luksiene, R. Sens, M. Daskeviciene, R. Send, H. Wonneberger, V. Jankauskas, I. Bruder, V. Getautis, *ACS Appl. Mater. Interfaces* **2015**, *7*, 11107.
[30] R. Augulis, M. Franckevičius, V. Abramavičius, D. Abramavičius, S. M. Zakeeruddin, M. Grätzel, V. Gulbinas, *Adv. Energy. Mater.* **2017**, *6*, 1700405.
[31] M. S. Kang, S. D. Sung, I. T. Choi, H. Kim, M. P. Hong, J. Kim, W. I. Lee, H. K. Kim, *ACS Appl. Mater. Interfaces* **2015**, *7*, 22213.
[32] M. Kirkus, M.-H. Tsai, J. V. Grazulevicius, C.-C. Wu, L.-C. Chi, K.-T. Wong, *Synth. Met.* **2009**, *159*, 729.
[33] D. P. McMeekin, G. Sadoughi, W. Rehman, G. E. Eperon, M. Saliba, M. T. Hörantner, A. Haghighirad, N. Sakai, L. Korte, B. Rech, M. B. Johnston, L. M. Herz, H. J. Snaith, *Science* **2016**, *351*, 151.
[34] Z. Li, M. Yang, J.-S. Park, S.-H. Wei, J. J. Berry, K. Zhu, *Chem. Mater.* **2016**, *28*, 284.
[35] C. Yi, J. Luo, S. Meloni, A. Boziki, N. Ashari-Astani, C. Grätzel, S. M. Zakeeruddin, U. Röthlisberger, M. Grätzel, *Energy Environ. Sci.* **2016**, *9*, 656.
[36] W. Qiu, A. Ray, M. Jaysankar, T. Merckx, J. P. Bastos, D. Cheyns, R. Gehlhaar, J. Poortmans, P. Heremans, *Adv. Funct. Mater.* **2017**, *27*, 1700920.
[37] S. Albrecht, M. Saliba, J. P. Correa Baena, F. Lang, L. Kegelmann, M. Mews, L. Steier, A. Abate, J. Rappich, L. Korte, R. Schlatmann, M. K. Nazeeruddin, A. Hagfeldt, M. Gratzel, B. Rech, *Energy Environ. Sci.* **2016**, *9*, 81.

ADVANCED SCIENCE
Open Access

Supporting Information

for *Adv. Sci.*, DOI: 10.1002/advs.201700811

Nonspiro, Fluorene-Based, Amorphous Hole Transporting Materials for Efficient and Stable Perovskite Solar Cells

Šaruūnė Daškevičiūtė, Nobuya Sakai, Marius Franckevičius, Marytė Daškevičienė, Artiom Magomedov, Vygintas Jankauskas, Henry J. Snaith, and Vytautas Getautis**

General methods and materials

Chemicals were purchased from Sigma-Aldrich and TCI Europe and used as received without further purification. The ^{1}H and ^{13}C NMR spectra were taken on Bruker Avance III (400 MHz) spectrometer at RT. All the data are given as chemical shifts in δ (ppm). The course of the reactions products was monitored by TLC on ALUGRAM SIL G/UV254 plates and developed with UV light. Silica gel (grade 9385, 230–400 mesh, 60 Å, Aldrich) was used for column chromatography. Elemental analysis was performed with an Exeter Analytical CE-440 elemental analyser, Model 440 C/H/N/. Differential scanning calorimetry (DSC) was performed on a Q10 calorimeter (TA Instruments) at a scan rate of 10 K min^{-1} in the nitrogen atmosphere. The glass transition temperatures for the investigated compounds were determined during the second heating scan. Electrothermal MEL-TEMP capillary melting point apparatus was used for determination of melting points. UV/vis spectra were recorded on Shimadzu UV-3600 spectrometer. A scanning electron microscope (SEM; Hitachi, S-4300) was used to acquire cross section SEM image of the perovskite solar cells. Contact angle measurement was performed by Kruss, Drop Shape Analysis System DSA25.

Synthesis

2,7-Bis(bromomethyl)-9,9-diethyl-9*H*-fluorene (1)

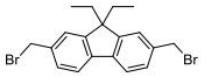

A mixture of 9,9-diethyl-9*H*-fluorene (1.11 g, 5 mmol), paraformaldehyde (0.33 g, 11 mmol), and 33% HBr solution in acetic acid (10 ml) was heated at 60-70 °C for 20 h. Upon cooling, the precipitates were filtered off and tree times washed with water and dried in vacuum, affording 1.47 g of pale white solid (72.0%). The product was recrystallized from toluene/*n*-hexane 1:1 gave as white crystals. Mp 148-150°C.
The NMR spectra were identical to the corresponding spectra of the product referred in [1];
Anal. calcd for C19H20Br2: C, 55.91; H, 4.94; found: C, 55.68; H, 4.81.

2,7-Bis(3,6-dibromo-9*H*-carbazol-9-methyl)-9,9-diethyl-9*H*-fluorene (2)

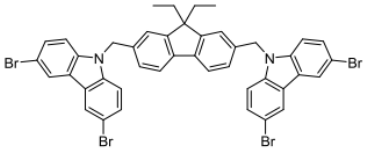

A mixture of compound **1** (0.82 g, 2 mmol) and 3,6-dibromo-9*H*-carbazole (1,30 g, 4 mmol) was dissolved in 15 ml of tetrahydrofurane and 0.68 g (12 mmol) of 85% powdered potassium hydroxide was added in small portions during 2-3 minutes. The obtained mixture was stirred at room temperature for 6 h. The part of solvent was removed in vacuum. Then obtained crystals of product **2** were filtered off and washed with water until it was neutral and three times with ethanol. The product was recrystallized from ethanol/tetrahydrofurane 2:1 gave as white crystals (1.82 g, 83.1%), Mp 293-295°C.

^{1}H NMR (400 MHz, DMSO-d_6) δ: 8.49 (s, 4H), 7.72-7.48 (m, 10H), 7.35 (s, 2H), 6.94 (d, J = 7.8 Hz, 2H), 5.70 (s, 4H), 1.83 (q, J = 7.2 Hz, 2H), 1.81 (d, J = 7.9 Hz, 4H), 0.10 (t, J = 7.2 Hz, 6H) ppm.
^{13}C NMR (101 MHz, DMSO) δ: 150.09, 139.95, 139.49, 136.31, 129.08, 125.65, 123.73, 123.37, 122.21, 120.21,112.21, 111.79, 55.43, 46.59, 31.77, 8.47 ppm.
Anal. calcd for C43H32Br4N2: C, 57.64; H, 3.60; N, 3.13; found: C, 57.18; H, 3.31; N, 2.98.

2,4,7-Tris(bromomethyl)-9,9-dimethyl-9*H*-fluorene (3)

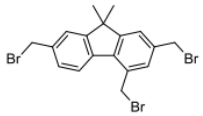

A mixture of 9,9-dimethyl-9*H*-fluorene (1) (2.50 g, 12.9 mmol), paraformaldehyde (3.86 g, 129 mmol), and 33% HBr solution in acetic acid (25 mL) was heated at 85-90 ºC for 45 h. Upon cooling, the precipitate was collected by filtration, carefully washed with water and then with ether. The brown crude product was purified by column chromatography on silica gel, using 1:24 v/v acetone/n-hexane as an eluent, affording 3.90 g of white solid (64.1%). The product was recrystallized from *n*-hexane gave as white crystals. Mp 164-165°C.
^{1}H NMR (400 MHz, DMSO-d_6) δ: 7.95 (d, J = 8.0 1H), 7.79-7.64 (m, 2H), 7.61-7.48 (m, 2H), 5.09 (s, 2H), 4.82 (s, 2H), 4.78 (s, 2H), 1.48, 1.44 (two s, 6H) ppm.
^{13}C NMR (101 MHz, DMSO) δ: 152.21, 151.30, 139.87, 139.11, 137.89, 137.79, 132.88, 131,12, 129.18, 124.63, 124.58, 124.13, 55.74, 34.93, 34.72, 33.86, 32.27 ppm.

Anal. calcd for C18H17Br3: C, 45.70; H, 3.62; found: C, 45.58; H, 3.51.

2,4,7-Tris(3,6-dibromo-9*H*-carbazol-9-methyl)-9,9-dimethyl-9*H*-fluorene (4)

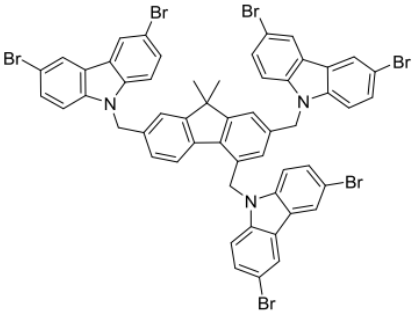

A mixture of compound **3** (1.42 g, 3 mmol) and 3,6-dibromo-9*H*-carbazole (2.93 g, 9 mmol) was dissolved in 30 ml of tetrahydrofurane and 1,52 g (27 mmol) of 85% powdered potassium hydroxide was added in small portions during 2-3 minutes. The obtained mixture was stirred at room temperature for 6 h. The resulting solid was dissolved in 80 mL tetrahydrofurane and washed with water (3 × 50 mL). Then the organic layer was separated and dried over Na_2SO_4. The crude product was purified by column chromatography on silica gel using 4:21 v/v tetrahydrofurane/*n*-hexane as an eluent gave the product **4** as white crystals (2.83 g, 78.3%), Mp 204-205°C.

^{1}H NMR (400 MHz, DMSO-d_6) δ: 8.52 (s, 2H), 8.19 (d, J = 18.2 Hz, 4H), 7.81 (d, J = 8.0 Hz 1H), 7.71 (d, J = 8.0 Hz, 2H), 7.66-7.59 (m, 3H), 7.47 (s, 1H), 7.24-7.16 (m, 4H), 7.00 (dd, J = 19.4 Hz, J = 8.8 Hz, 4H), 5.78 (s, 4H), 5.32 (s, 2H), 4.84 (s, 1H), 1.42 (s, 6H) ppm.
Anal. calcd for C54H35Br6N3: C, 53.81; H, 2.93; N, 3.49; found: C, 53.48; H, 2.61; N, 3.18.

2,7-Bis[3,6-di(4,4`-dimethoxy)diphenylamino-9*H*-carbazol-9-methyl]-9,9-diethyl-9*H*-fluorene (V1061)

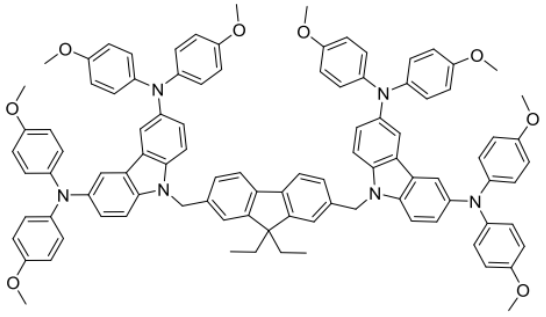

A solution of compound **2** (1.34 g, 1.5 mmol), 4,4`-dimethoxydiphenylamine (2.06 g, 9 mmol) in anhydrous toluene (17 mL) was purged with argon for 30 minutes. Afterwards, palladium(II) acetate (6.7 mg, 0.03 mmol), tri-*tert*-butylphosphonium tetrafluoroborate (11.7 mg, 0.04 mmol) and sodium *tert*-butoxide (0.86 g, 9 mmol) were added and the solution was refluxed under argon atmosphere for 24 hours. After cooling to room temperature, reaction mixture was filtered through Celite, 50 mL of distilled water were added and extraction was done with ethyl acetate and distilled water. The organic layer was dried over anhydrous Na_2SO_4, filtered and solvent evaporated. The crude product was purified by column chromatography using 1:4 v/v acetone/*n*-hexane as an eluent. The obtained product was precipitated from tetrahydrofurane into 15-fold excess of hexane. The precipitate was filtered off and washed with hexane to collect **V1061** as a pale yellow – green solid. (1.70 g, 77.6%).

^{1}H NMR (400 MHz, DMSO-d_6) δ: 7.65 (s, 4H), 7.57 (d, J = 7.8 Hz, 2H), 7.50 (d, J = 8.8 Hz, 4H), 7.34 (s, 2H), 7.04 (d, J = 8.4, 6H), 6.90 – 6.69 (m, 32H), 5.58 (s, 4H), 3.65 (s, 24H), 1.81 (m, 4H), 0.12 (t, J = 7.3 Hz, 6H) ppm.
^{13}C NMR (101 MHz, DMSO) δ: 154.63, 150.38, 142.50, 140.69, 140.10, 137.88, 137.07, 126.09, 125.79, 124.76, 124.15, 123.36, 122.56, 120.40, 117.27, 115.06, 111.18, 55.60, 46.90, 31.96, 26.81, 8.79 ppm.
Anal. calcd for C99H88N6O8: C, 79.81; H, 5.95; N, 5.64; found: C, 79.48; H, 5.71; N, 5.68.

2,4,7-Tris[3,6-di(4,4`-dimethoxy)diphenylamino-9*H*-carbazol-9-methyl]-9,9-dimethyl-9*H*-fluorene (V1050)

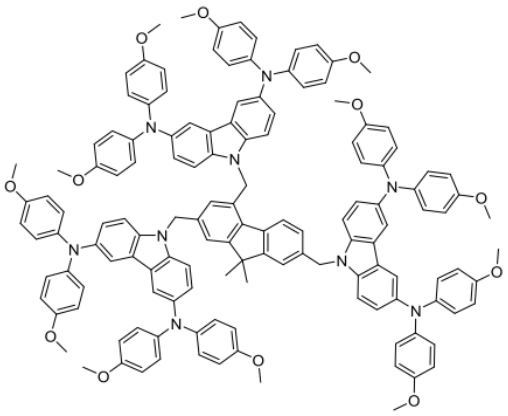

A solution of compound **4** (2.50 g, 2 mmol), 4,4‘-dimethoxydiphenylamine (4.19 g, 18 mmol) in anhydrous toluene (35 mL) was purged with argon for 30 minutes. Afterwards, palladium(II) acetate (9.3 mg, 0.04 mmol), tri-*tert*-butylphosphonium tetrafluoroborate (6.5 mg, 0.02 mmol) and sodium *tert*-butoxide (1.8 g, 18 mmol) were added and the solution was refluxed under argon atmosphere for 52 hours. After cooling to room temperature, reaction mixture was filtered

through Celite, 50 mL of distilled water were added and extraction was done with ethyl acetate and distilled water. The organic layer was dried over anhydrous Na_2SO_4, filtered and solvent evaporated. The crude product was purified by column chromatography using 6:3.5:15.5 v/v acetone/tetrahydrofurane/*n*-hexane as an eluent. The obtained product was precipitated from toluene into 15-fold excess of hexane. The precipitate was filtered off and washed with hexane to collect **V1050** as a pale yellow – green solid (3.03 g, 71.8%).

^{1}H NMR (400 MHz, DMSO-d_6) δ 7.85 (d, J = 8.2 Hz, 1H), 7.73 – 7.44 (m, 9H), 7.33 (s, 1H), 7.26 – 6.56 (m, 60H), 6.34 (s, 1H), 5.88 (s, 2H), 5.61 (s, 2H), 5.14 (s, 2H), 3.77 – 3.50 (m, 36H), 1.28 (s, 6H).
^{13}C NMR (101 MHz, DMSO) δ 154.64, 154.60, 154.58, 142.50, 142.45, 140.78, 140.54, 137.97, 137.82, 137.68, 135.04, 124.84, 124.20, 124.14, 123.34, 123.22, 117.08, 115.07, 115.02, 114.97, 55.59, 55.55, 55.53, 46.36, 40.67, 40.62, 40.47, 40.41, 40.26, 40.21, 40.05, 40.00, 39.79, 39.58, 39.37, 27.41.
Anal. calcd for C138H1194N9O12: C, 79.10; H, 5.72; N, 6.02; found: C, 78.88; H, 5.61; N, 5.88.

Journal of Materials Chemistry A

ROYAL SOCIETY OF CHEMISTRY

PAPER

View Article Online
View Journal

Cite this: DOI: 10.1039/d0ta08452b

Fluorene-based enamines as low-cost and dopant-free hole transporting materials for high performance and stable perovskite solar cells†

Sarune Daskeviciute,‡[a] Cristina Momblona,‡[b] Kasparas Rakstys,[a] Albertus Adrian Sutanto,[b] Maryte Daskeviciene,[a] Vygintas Jankauskas,[c] Alytis Gruodis,[c] Giedre Bubniene,[a] Vytautas Getautis *[a] and Mohammad Khaja Nazeeruddin *[b]

The power conversion efficiency of perovskite solar cells is approaching the Shockley–Queisser limit, and therefore this technology is next to the commercialization stage. Inexpensive and stable hole transporting materials are highly desirable for the successful scale-up. Most high performing devices generally employ expensive hole conductors that are synthesized *via* cross-coupling reactions which require expensive catalysts, inert reaction conditions and time-consuming sophisticated product purification. In a quest to employ cost-effective chemistry to combine the building blocks, we explore enamine-based small molecules that can be synthesized in a simple condensation reaction from commercially available materials leading to an estimated material cost of a few euros per gram. The synthesized fluorene-based enamines exhibit a very high hole mobility up to 3.3×10^{-4} cm^2 V^{-1} s^{-1} and enable the fabrication of perovskite solar cells with a maximum power conversion efficiency of 19.3% in a doped configuration and 17.1% without doping. In addition, both PSC systems demonstrate superior long-term stability compared to spiro-OMeTAD. This work shows that hole transporting materials prepared *via* a simple condensation protocol have the potential to compete in terms of performance with materials obtained *via* expensive cross-coupling methods at a fraction of their cost and deliver exceptional stability of the final device. This work provides a design strategy for the further development of novel, low-cost semiconductors.

Received 28th August 2020
Accepted 21st November 2020

DOI: 10.1039/d0ta08452b

rsc.li/materials-a

Introduction

In their first decade, hybrid organic–inorganic halide perovskite-based solar cells (PSCs) continually improved. They are now approaching the Shockley–Queisser power conversion efficiency (PCE) limit with the current best certified PCE of 25.5%.[1] The improvement in PCE can be attributed to the outstanding optoelectronic properties such as high absorption coefficient, long carrier diffusion length, small exciton binding energy, and high charge carrier mobility of the perovskite material and rapid advances in the device engineering.[2–6] Owing to the combination of highly abundant precursor materials and simple preparation methods it is believed that the commercialization of PSC technology during the second decade is inevitable.[7–9]

While the very high efficiency obtained using perovskites is a significant achievement, issues related to the high price of the device components such as hole transporting materials (HTMs) and long-term stability against moisture, heat, and light are still a concern for the commercial application of the technology; therefore, breaking these bottlenecks is a must for the realization of cost-effective and stable devices.[10–14]

Until now, most of the highly efficient PSCs are based on either the small organic molecule 2,2′,7,7′-tetrakis(*N*,*N*-di-*p*-methoxyphenylamine)-9,9′-spirobifluorene (spiro-OMeTAD) or conjugated macromolecule poly[bis(4-phenyl)(2,4,6-trimethylphenyl)amine] (PTAA) HTMs, both of which are very expensive.[14–17] For example, spiro-OMeTAD is synthesized in a multi-step reaction scheme that requires a low temperature (−78 °C) and sensitive (*n*-butyllithium) and aggressive (Br_2) reagents, resulting in a relatively high material cost and consequently leading to a significant contribution to the total device cost.[18–20] Additionally, the tedious synthesis hampers

[a]Department of Organic Chemistry, Kaunas University of Technology, Radvilenu pl. 19, Kaunas 50254, Lithuania. E-mail: vytautas.getautis@ktu.lt
[b]Group for Molecular Engineering of Functional Material, Institute of Chemical Sciences and Engineering, École Polytechnique Fédérale de Lausanne, CH-1951 Sion, Switzerland, . E-mail: mdkhaja.nazeeruddin@epfl.ch
[c]Institute of Chemical Physics, Vilnius University, Sauletekio al. 3, Vilnius 10257, Lithuania

† Electronic supplementary information (ESI) available. See DOI: 10.1039/d0ta08452b

‡ These authors contributed equally to this work.

large scale production and thereby could impede the commercial success of PSCs.

Therefore, huge interest of many research groups has been directed towards new HTM candidates to find an ideal HTM, which would be easily scalable for reasonable cost, including spiroxanthene-,[21–23] fluorene-,[24,25] carbazole-,[26–31] silane-,[32] bifluorene-,[33] pyrene-,[34,35] and bifluorenylidene-based[36] examples. However, most of the conjugated HTMs are generally designed by linking together building blocks of the conjugated central core with costly diphenylamine- or triphenylamine-containing methoxy-substituted side groups using C–N or C–C cross-coupling chemistry, respectively. These coupling reactions generally require stringent reaction conditions resulting in several disadvantages, such as inert reaction conditions, expensive transition metal catalysts and extensive purification procedures. The commonly used purification methods involve sublimation or repeated column chromatography due to the inherent formation of side products that are usual for this type of reaction and a tiny amount of metal catalyst residues that may remain in the hole transporting layer. The metal catalyst residues act as traps that deteriorate the charge-transporting properties of the synthesized HTMs and negatively affect the performance of the resulting devices as well as greatly reducing the material yield and therefore further increasing the final product costs. Also the high processing cost in turn results in a significant cost contribution of HTMs, making them industrially less interesting.

To this extent, significant effort is now being put towards finding simplified synthetic protocols to reduce the cost of HTM synthesis without sacrificing the efficiency. Recently, several research groups have focussed on tuning the structure by decreasing the number of synthetic steps, thus reducing the synthetic complexity, cost of materials and the environmental impact.[37,38] This includes reports based on azomethine,[39] hydrazone,[40] and amide[41] by Petrus *et al.* and our previously explored aniline[42] and carbazole[43,44] enamines prepared by a facile condensation reaction. In this sense, condensation chemistry is an excellent perspective moving away from palladium-catalysed reactions since water is the only side-product and expensive catalysts are not required. Moreover, simple product workup and purification drastically reduce the cost of the final product.

In this work, we further explore the potential of enamine family HTMs employing fluorene as the central scaffold. Five different substituents containing fluorene-based HTMs were successfully synthesised employing facile synthesis using commercially available and cheap reagents. Their optical, thermal, electrophysical, and photovoltaic properties were thoroughly investigated by combining experimental and simulation methods. Moreover, the impact of the differently substituted central fluorene core on different properties of the synthesized molecules, in comparison to our earlier reports, has been systematically investigated. All these enamine-based HTMs have been successfully applied in PSCs with and without additives, showing a photovoltaic performance of up to 19.3% and 17.1%, respectively, with excellent long-term stability in both cases. With this we demonstrate that both simple chemistry and product purification result in estimated material costs of a few euros per gram without sacrificing the efficiency and in contrast enhancing the stability.

Results and discussion

Fluorene enamines were synthesized using straightforward chemistry with excellent yields and high purity. As shown in Fig. 1, **V1275** only required one-pot reaction condensing inexpensive commercially available reagents 2,7-diaminofluorene and 2,2-bis(4-methoxyphenyl)acetaldehyde in the presence of camphor sulfonic acid. The reaction is performed under ambient conditions and water is the only by-product separated from the reaction mixture using a Dean–Stark trap, accelerating the formation of the final product and significantly reducing the reaction duration. Moreover, we note that column chromatography or vacuum sublimation processes are avoided for the purification, and the simplicity of the condensation chemistry reduces batch-to-batch variations.

V1275 was further reacted with different alkylating agents to yield methyl-, propyl-, hexyl-, and benzyl-substituted fluorene enamines as final HTMs **V1237**, **V1235**, **V1236**, and **V1227**, respectively. The chemical structures of the synthesized products were verified by NMR spectroscopy and elemental analysis. Detailed synthetic procedures and analysis are reported in the ESI.† In order to assess the price of the synthesized materials, we performed a cost-analysis on a lab-scale synthesis (Table S1†).[45] The estimated cost of **V1275** is ~10€ per g and that of the alkylated product **V1235** is around 22€ per g, which are a fraction of the cost of spiro-OMeTAD (~92€ per g)[46] and less than that of our previously developed double-armed carbazole enamines mainly due to the less expensive 2,7-diaminofluorene starting reagent.[44]

Quantum chemical calculations were performed with Gaussian 09 software to establish the most probable molecular geometry and absorption spectrum.[47] The density functional theory (DFT) method B3LYP/6-31G was used for geometry optimization. **V1275**, **V1237**, and **V1227** have been chosen as model compounds for computations, and as the different lengths of the aliphatic substituents should not affect the electronic properties they were ignored. Due to fragmental motions, a large number of different conformers could be formed. Only two typical and the most probable conformers of each compound (a and b, after ground state geometry optimization) are presented in Fig. S1–S3.† Conformers could be formed due to the following condition: enamine subfragments are formed as quite well expressed π-conjugated fragments >C═CH–N*–CH═C< oriented quasi linearly, and this bridge between two O–Ph subfragments must be treated as the important factor for fragment displacement in space. Two chains of O–Ph subfragments of the left and right fragments could be oriented in the shape of the upper-side roof according to the fluorene core (see **V1237** and **V1275**, a and b, bottom part), but other O–Ph subfragments are oriented chaotically (see **V1227**, a and b, top part). Due to the presence of benzyl substituents in **V1227**, it is necessary to conclude that phenyl fragments are not included in the core π-conjugated system

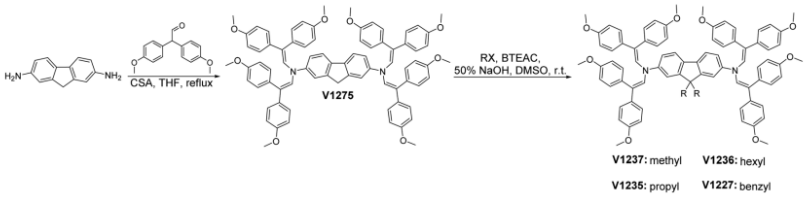

Fig. 1 Straightforward reaction scheme of fluorene enamine HTMs and their molecular structures.

(connection through two single –C–C– bonds with high lability). The possibility to orient the phenyl on the fluorene core could be realized in many ways. This factor of indeterminacy of the phenyl position creates the condition of non-ordered distribution of enamine subfragments in the **V1227** structure. For all three derivatives, b conformers are more ordered than a conformers. The semiempirical TD method (for singlets only) was used for the simulation of the electronic absorption spectrum. Table S2† shows the excitation parameters for the three lowest excited states S_1, S_2, and S_3: transition energy and oscillator strength. For all compounds (including both conformers), $S_0 \rightarrow S_1$ transitions are allowed and partially allowed (oscillator strength in the interval 0.57–0.71) and the transition energy is approximately 2.89–2.92 eV. Table S3† presents the scheme of the population of excited electronic states and the corresponding set of MO.

Distributions of electron density for the HOMO−1 and HOMO as well as the LUMO and LUMO+1 for **V1275**, **V1237**, and **V1227** structures are presented in Fig. S4–S6.† Any pure CT charge redistribution behaviour was established for both a and b conformers, and only charge redistribution between the first and second enamine subfragments of the left fragment takes place. It is necessary to point out that the enamine subfragments could play the role of charge donors and charge acceptors, depending on the fragment orientation to the central core fluorene unit (a conformer, HOMO → LUMO transition). Also, charge redistributions between the enamine fragment and fluorene core take place (b conformer, HOMO → LUMO transition

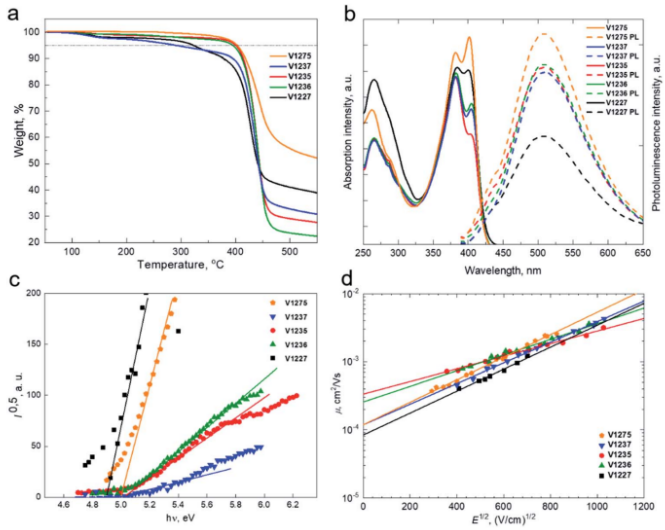

Fig. 2 (a) Thermogravimetric analysis (TGA) data (heating rate of 10 °C min^{-1}, N_2 atmosphere); (b) UV-Vis absorption (solid line) and photoluminescence (dashed line) spectra of V-series HTMs in THF solution (10^{-4} M); (c) photoemission in air spectra of the charge transporting layers **V1275**, **V1237**, **V1235**, **V1236**, and **V1227**; (d) electric field dependencies of the hole-drift mobility in the synthesized HTMs.

and a conformer, HOMO → LUMO+1 transition). In general, charge redistribution between the left and right enamine substituents and the central core fluorene unit is typical for both conformers.

The thermal behaviour of HTMs was evaluated by thermogravimetric analysis (TGA) (Fig. 2a) and differential scanning calorimetry (DSC) (Fig. S7†) techniques. TGA analysis has shown that **V1275** has the highest thermal stability among the series with a decomposition temperature (T_{dec}) of 403 °C at 5% weight loss. The introduction of the aliphatic substituents to the central fluorene position has led to the deteriorated thermal resistance. However, we note that the instant weight loss at around 400 °C is observed for all new materials suggesting that they may undergo sublimation rather than decomposition, enabling them to be vacuum-deposited. The thermal transitions of V-series molecules were determined by DSC. Interestingly, it was found that **V1275**, **V1236**, and **V1227** exist both in the crystalline and the amorphous state, while **V1237** and **V1235** tend to crystallize. Only the glass transition temperature (T_g) was investigated for all compounds during the second heating scan, while **V1237** has the most stabilized amorphous state with the glass transition detected at 153 °C.

The UV-visible absorption and photoluminescence (PL) spectra of the synthesized HTMs in THF solutions and solid films are depicted in Fig. 2b and S8,† respectively. All HTMs have two major absorption peaks at approximately 260 nm and 400 nm. The less intense absorption peak at the shorter wavelength corresponds to localised π–π* transitions. The longer wavelength arises from more intensive delocalisation from the conjugated scaffold and is assigned to n–π* transitions. Change of the different aliphatic fragments has not influenced the conjugation, and therefore, spectra of all molecules are almost identical; however, there is a significant difference in the absorption intensity ratio of **V1227** peaks arising from benzyl moieties. The PL spectra of all compounds are similar to the peak at 510 nm, showing that significantly large Stokes shifts of approximately 100 nm are observed for all molecules, and therefore, significant changes in the geometry of the molecules are desired upon excitation. The optical gaps (E_g) of HTMs were calculated from the intersection of absorption and PL spectra of thin films and were found to be identical for all the materials at around 2.8 eV.

To understand the energy level alignment of the HTMs in PSCs, we next measured solid-state ionization potential (I_P) using the electron photoemission in air of the thin films (PESA) with the experimental data shown in Fig. 2c. **V1275**, **V1237**, **V1235**, **V1236**, and **V1227** were found to have I_P values of 5.01, 5.0, 5.03, 5.03 and 4.9 eV, respectively, which ideally align with the valence band (VB) energy of the triple cation-based perovskite (~5.70 eV), and therefore, efficient hole transfer from the perovskite to the cathode should be ensured.[48] Spiro-OMeTAD has been measured as well and was found to have a very similar ionization potential of 5.00 eV (Fig. S9†). Additionally, to reveal the effect of the p-dopant as the electron acceptor we have evaluated the ionization potentials of doped layers (I_P^*) since they are known to control the HOMO energy level by removing electrons from the HOMO to generate holes of an intrinsic HTM, enhancing the device efficiency.[14,49–51] HTMs were doped in the same manner as in the device fabrication part detailed in the ESI.† As expected, upon doping, ionization potentials were stabilized by around 0.3 eV further reducing the overpotential with the VB of the perovskite thus expectedly increasing the V_{OC} in doped HTL-containing devices including spiro-OMeTAD (Fig. S10 and S11†). Based on the solid-state optical gap and I_P values, we calculated the electron affinities (E_{ea}) of the enamine materials to be 2.22, 2.21, 2.22, 2.24, and 2.11 eV for **V1275**, **V1237**, **V1235**, **V1236**, and **V1227**, respectively. Importantly, the electron affinities of the compounds are smaller than the conduction band energy of the perovskite (−4.10 eV), and therefore, they should effectively block the electron transfer from the perovskite to the anode.[48] We next measured the charge mobility of the V-series using the xerographic time of flight (XTOF) technique. Dependences of hole drift mobility on electric field strength are depicted in Fig. 2d. The zero-field hole drift mobility (μ_0) for **V1275**, **V1237**, **V1235**, and **V1236** was determined to be at 10^{-4} cm^2 V^{-1} s^{-1}, while the propyl-substituted **V1235** was found to have the highest hole mobility of 3.3×10^{-4} cm^2 V^{-1} s^{-1} among the series. We note that this is also the highest hole mobility compared with that of our previous aniline and carbazole enamine reports and it outperforms that of spiro-OMeTAD ($\mu_0 = 1.3 \times 10^{-4}$ cm^2 V^{-1} s^{-1}).[36,44] Switching to the aromatic benzyl substitution has negatively influenced the hole drift mobility as **V1227** showed the lowest result of 8×10^{-5} cm^2 V^{-1} s^{-1} due to the larger energetic disorder. The thermal, optical, and photoelectrical properties of the novel HTMs are listed in Table 1.

The new V-series HTMs were implemented in n–i–p solar cells with the following layout: fluorine-doped tin oxide (FTO)/

Table 1 Thermal, optical and photophysical properties of the newly synthesized enamines

ID	T_m[a] (°C)	T_c[a] (°C)	T_g[a] (°C)	T_{dec}[a] (°C)	λ_{abs}[b] (nm)	λ_{em}[b] (nm)	I_P[c] (eV)	I_P^*[d] (eV)	E_g[e] (eV)	E_{ea}[f] (eV)	μ_0[g] (cm^2 V^{-1} s^{-1})
V1275	255	—	150	403	262, 381, 401	508	5.01	5.39	2.79	2.22	1.2×10^{-4}
V1237	247, 267, 272	198	153	285	265, 382, 404	510	5.0	5.32	2.79	2.21	1.2×10^{-4}
V1235	273	159	120	399	266, 382, 404	509	5.03	5.39	2.81	2.22	3.3×10^{-4}
V1236	173, 195	—	90	393	265, 383, 404	508	5.03	5.25	2.79	2.24	2.6×10^{-4}
V1227	330	—	116	321	265, 384, 400	507	4.9	5.34	2.79	2.11	8×10^{-5}

[a] Melting (T_m), crystallization (T_c), glass transition (T_g) and decomposition (T_{dec}) temperatures observed from DSC and TGA, respectively (10 °C min^{-1}, N_2 atmosphere). [b] Absorption and emission (excitation = $\lambda_{abs\ max}$) spectra were measured in THF solution (10^{-4} M). [c] Ionization energies of the films measured using PESA without doping. [d] Ionization energies of the films measured using PESA with doping. [e] E_g estimated from the intersection of absorption and emission spectra of solid films. [f] $E_{ea} = I_P - E_g$. [g] Mobility value at zero field strength.

compact TiO_2 (c-TiO_2)/mesoporous TiO_2 (m-TiO_2)/SnO_2/perovskite/HTM/Au, where the HTMs were doped with *tert*-butylpyridine (*t*BP), tris(bis(trifluoromethylsulfonyl)imide) (LiTFSI) and tris(2-(1*H*-pyrazol-1-yl)-4-*tert*-butylpyridine)cobalt(III) (FK209). The detailed fabrication procedure can be found in the ESI.†

Cross-sectional scanning electron microscopy (SEM) imaging was performed on the complete devices fabricated with the V-series and spiro-OMeTAD (Fig. 3a and S12†). The analysis of the images shows that the HTM layers are compact and uniform on top of the perovskite layer with a thickness of ~150 nm for **V1275**, **V1237**, **V1235** and **V1236**, ~120 nm for **V1227**, and ~260 nm for spiro-OMeTAD. The surface morphology was evaluated by scanning electron microscopy (Fig. S13†), with the doped-HTM layers deposited on top of FTO-glass under the same deposition conditions as in the device fabrication. All the images of doped-HTM thin films show homogeneous and complete surface coverage without the presence of material aggregation.[52] The energy levels of the complete devices with the studied HTMs as well as spiro-OMeTAD can be found in Fig. 3b.[48,53]

The initial *J*–*V* curves and the corresponding photovoltaic parameters are presented in Fig. S14 and Table S4.† The initial PCEs are 15.9% for **V1275** (non-alkylated HTM), 18.0% for **V1237** and **V1235** (methyl- and propyl-based, respectively) and 17.8% for **V1236** hexyl-based devices. This initial performance of the devices might indicate that the alkyl functionalization of the HTM is required for an appropriate perovskite/HTM interface for enhanced charge extraction through the device. Once the maximum efficiency was reached, the corresponding photovoltaic parameters were extracted and are presented in Table 2. The devices containing **V1275**, alkylated-HTMs **V1237**, **V1235**, and **V1236**, and spiro-OMeTAD present comparable photovoltaic behaviour with the maximum PCE around 19%. The comparison of the devices at the best performing efficiency is confirmed by statistical data (Fig. S15†). The performance is greater than that of the benzyl-substituted **V1227**-based device with 12.5% efficiency. Note that this trend can be related to the hole mobility values obtained for the HTMs, ranging from 1.2×10^{-4} cm^2 V^{-1} s^{-1} to 3.3×10^{-4} cm^2 V^{-1} s^{-1} for **V1275** and **V1235**, and the value for spiro-OMeTAD (1.3×10^{-4} cm^2 V^{-1} s^{-1}) is similar, but lower for the bulky analogue **V1227** with a hole mobility value of 8×10^{-5} cm^2 V^{-1} s^{-1}.[44]

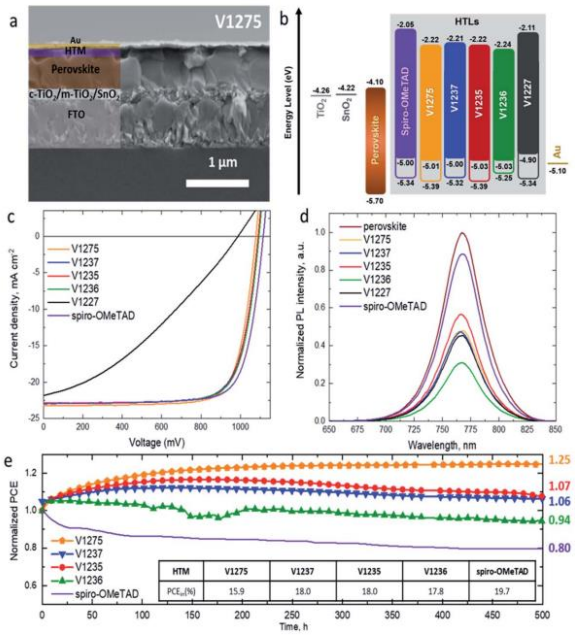

Fig. 3 (a) Cross-sectional SEM image of the photovoltaic device fabricated with the doped **V1275** HTM; (b) schematic energy level diagram of the device representing the HOMO/LUMO and the stabilized HOMO of doped layers; (c) *J*–*V* curves recorded for the champion devices for each doped HTM; (d) normalized steady-state photoluminescence spectra of perovskite and perovskite/HTM layers deposited on glass (λ_{exc} = 625 nm); (e) stability test of unencapsulated devices under continuous 1 sun illumination with the initial PCE values shown in the insert.

Table 2 Photovoltaic parameters, series resistance, and thickness of the fluorene-based enamine HTMs extracted from the best-performing devices (short-circuit current density calculated from the corresponding EQE)

	HTM	V_{OC} (mV)	J_{SC} (mA cm^{-2})	FF	PCE (%)	R_S (Ω)	HTM thickness (nm)
Doped-HTM	**V1275**	1077	23.24 (23.11)	0.77	19.3	5.9	~150
	V1237	1090	22.97 (22.74)	0.76	19.2	6.2	~150
	V1235	1089	22.86 (22.85)	0.77	19.2	5.1	~150
	V1236	1094	22.95 (22.94)	0.76	19.1	5.2	~150
	V1227	1024	22.32 (21.82)	0.55	12.6	26.0	~120
	Spiro-OMeTAD	1115	22.97 (21.86)	0.77	19.7	5.7	~260
Dopant-free HTM	**V1275**	1033	22.95 (22.81)	0.72	17.1	22.2	~70
	V1237	1038	22.98 (22.93)	0.71	16.9	22.9	~70
	V1235	1029	23.09 (22.81)	0.70	16.6	24.5	~70
	V1236	1022	23.02 (22.88)	0.69	16.2	25.2	~70
	Spiro-OMeTAD[58]	972	22.83	0.47	10.4		

The highest efficiency reached for each HTM (Table 2) shows that the **V1275** and alkyl-based devices have almost identical short-circuit current density values (J_{SC}) in the range from 23.24 mA cm^{-2} for **V1275** to 22.86 mA cm^{-2} for **V1235**, respectively. This suggests that the substitution with an alkyl chain and the increasing alkyl chain length from methyl to hexyl do not strongly influence the charge collection properties of the perovskite layer. However, the benzyl-based **V1227** results in devices having a slightly lower J_{SC} value of 22.32 mA cm^{-2}. Such behaviour is also confirmed by the external quantum efficiency (EQE) spectra (Fig. S16†). The corresponding integrated current densities from the respective EQEs (Fig. S16†) are presented in Table 2 in brackets, and the values are in good agreement with the measured values from the *J–V* characteristics (within 5% error). Similar fill-factor (FF) values are obtained for the devices employing **V1275**, **V1237**, **V1235** and **V1236**, with values ranging between 0.76 and 0.77. However, the FF in the device with **V1227** is reduced to 0.55, this can be explained by the presence of benzyl groups in **V1227**, which causes a less ordered packing of the molecules in the film and in the interface with the perovskite, and this also leads to a greater dispersion of solar cell parameters (Fig. S15†).[54] The main parameter leading to the slightly lower performance of the V-series in comparison to spiro-OMeTAD is the open-circuit voltage (V_{OC}). The cells incorporating **V1275**, **V1237**, **V1235** and **V1236** exhibit lower values of V_{OC} (1077, 1090, 1089 and 1094 mV, respectively) than the reference device containing spiro-OMeTAD (1115 mV).

In order to evaluate the photogenerated hole extraction efficiency of the new HTMs, we performed thin-film steady-state PL measurements. Perovskite layers were deposited on top of glass and the PL spectra of the films were recorded under 625 nm excitation wavelength. Afterwards, the HTMs were deposited on top of the pristine perovskite layers under the same conditions as in the device fabrication. The quenching effect was analysed in comparison with the corresponding pristine perovskite layer and it is presented in Fig. 3d, and the percentage of PL quenching for each HTM is shown in Table S5.† In spite of the perovskite/HTM energy level mismatch, the decrease of PL intensity suggests a good hole-extraction capability and confirms the efficient extraction of holes across the interface from the VB of the perovskite into the HOMO of enamine-based HTMs, which is attributed to good perovskite/HTM contact.[55]

The device stability was evaluated for the solar cells containing **V1275** and the alkyl-substituted HTMs (**V1237**, **V1235** and **V1236**) due to their higher efficiency than that of the benzyl-substituted HTM **V1227**. As a reference, the long-term stability of the spiro-OMeTAD-based device was also evaluated. All the devices were unencapsulated and kept under constant 1 sun illumination in a N_2 atmosphere for 500 hours. The results of the long-term stability tests of the devices are presented in Fig. 3e. For comparison, the study was carried out with all the devices kept under the same light source. The device containing the non-substituted **V1275** HTM shows a continuous increase of PCE achieving 125% of its original efficiency after 500 h under operation, being not only the device having the most thermally stable HTM of the series but also the most stable device under constant light illumination among them. The introduction of the methyl and propyl groups (**V1237** and **V1235**) reduces this increase, obtaining 107 and 106% of its original efficiency after 500 h. However, the PCE of the device containing the longest insulating hexyl chain **V1236** of the series is only reduced to 94% of its initial efficiency after 500 h under illumination. Interestingly, although the length of the alkyl chains only slightly influences the maximum device performance (see Table 2), it displays an influence on the time to reach this value and the long-term device stability. The introduction of an alkyl group and with a longer alkyl chain results in a shorter time to reach the highest efficiency, but the long-term light stability is deteriorated. Such behaviour may suggest that the stabilization/degradation of the layer is enhanced with a higher/lower degree of packing due to the longer insulating chains. In addition, these changes might also be influenced by different relaxation processes in the thin film[56] and/or photo/oxygen-doping during operation.[57]

The outstanding light stability of the doped V-series HTMs is increased when compared with the most widely used HTM in PSCs, spiro-OMeTAD, whose efficiency is reduced to 80% from its initial performance after 500 h under constant illumination. With this result we can confirm that the use of dopants does not negatively affect the long-term stability of PSCs, and this fact contradicts previously reported studies.[14]

In order to evaluate if the dopants chemically interact with the HTMs and detrimentally affect the long-term stability of the

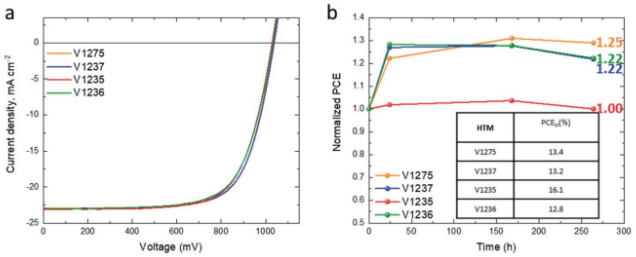

Fig. 4 (a) *J–V* curves recorded for the champion devices for each dopant-free HTM; (b) shelf-lifetime of unencapsulated devices fabricated with each dopant-free HTM (stored in the dark and dry environment RH < 10%) with the initial PCE values shown in the insert.

devices, the most promising HTMs from the series, **V1275**, **V1237**, **V1235** and **V1236**, were studied without the use of additives.[59–61] The initial *J–V* curves are presented in Fig. S17† and the corresponding photovoltaic parameters are listed in the insert of Fig. 4b and Table S6.† Once the maximum efficiency is reached, all of them showed efficiencies exceeding 16% (Fig. 4a and Table 2) with improved device performance compared with the reported 10.39% PCE for dopant-free spiro-OMeTAD-based devices previously reported by our group (Table 2).[58] The corresponding EQEs and the integrated short-circuit current density are presented in Fig. S16b† and the values in Table 2. The statistical data (Fig. S18†) compared at the maximum efficiency show that the gradual increase of the length of the alkyl substituents results in a slight deterioration of the device performance. Devices fabricated with the non-alkylated HTM **V1275** are the most efficient of the series, whereas the efficiency is gradually reduced by the introduction of the methyl, propyl, and hexyl groups, **V1237**, **V1235** and **V1236**, respectively, mainly due to lower V_{OC} and FF values. This difference can be attributed to different packing of the molecules compared to the equivalent doped devices.

While the J_{SC} is similar to that of the equivalent doped devices, the V_{OC} and FF values are significantly lower. The series resistance (R_S) of the devices was calculated from the corresponding *J–V* curves. The R_S is reduced with the incorporation of dopants in the HTM layer due to the increase of the hole mobility in the layer.[62,63] The lowest series resistance values of 5.9, 6.2, 5.1 and 5.2 Ω are obtained for devices made with doped-**V1275**, **V1237**, **V1235** and **V1236** HTMs and are comparable to the value registered for the spiro-OMeTAD device (5.7 Ω). The series resistance in the doped **V1227**-based device is similar to the values obtained in the dopant-free series, denoting a charge carrier transport issue in the device. The presence of the bulky benzyl group can induce a less ordered packing of the molecules in the film, also confirmed by DFT calculations, hence resulting in a possible poor charge transfer between the perovskite and the doped **V1227** layer. This interface issue might reduce the transport of charge carriers through the perovskite/HTM interface ultimately limiting the overall solar cell performance.[56]

On the other hand, devices containing the dopant-free HTMs suffer from 4–5 times higher resistance than the doped counterparts. The dopant-free HTM layer presents higher resistance values even when we tried to reduce the series resistance by lowering the HTM solution concentration from 20 mM for the doped HTM to 15 mM for the dopant-free HTM to generate a thinner HTM layer. These higher values are reflected in the lower device performance for dopant-free HTMs. The use of the longer alkyl chain for the devices containing dopant-free HTMs increases the series resistance of the device. This suggests less ordered packing of the molecules in the film reducing the carrier transport through the perovskite/HTM interface, and therefore the HTM layer itself. This trend is not observed for the doped HTM counterparts.[56] The higher resistance of the dopant-free HTM layer reduces the hole extraction and increases the interfacial recombination at the perovskite/HTM contact reflected in the drop of FF and V_{OC} in all the devices.[64]

The HTM thicknesses of the dopant-free devices were extracted from their respective cross-sectional SEM images (Fig. S19†), obtaining films of ~70 nm. To shed light on the surface morphology, scanning electron microscopy was performed (Fig. S20†). As mentioned above, the dopant-free HTM layers were deposited on top of FTO-glass under the same deposition conditions as in the device fabrication. A homogeneous surface morphology was observed for the dopant-free HTM layers, but due to the thinner layer thickness than in the doped counterparts, the layer underneath can be intuited. The stability of the dopant-free devices was tested by storing non-encapsulated devices in the dark under dry air (RH < 10%) and periodically testing under a relative humidity of 45% (Fig. 4b). The PCE of all HTMs shows no degradation after 250 h from their fabrication. After 250 h, the device efficiency increases to reach 125%, 122%, 100%, and 122% from the initial device efficiency for the **V1275**, **V1237**, **V1235** and **V1236** HTMs, respectively. This result demonstrates that V-series HTMs can also efficiently work as dopant-free HTMs in PSCs with excellent stability.

Conclusions

We report the synthesis and a systematic study of the fluorene-based hole transporting enamines. Novel HTMs are easily

attainable by a straightforward synthetic scheme ensuring cost-effective scale-up; in particular, **V1275** only required a one-pot reaction condensing inexpensive commercially available reagents leading to the extremely low synthetic cost of approximately 10€ per g. The impact of different substitution in the central fluorene was revealed through the optical, electrochemical, photophysical, and photovoltaic measurements. PSCs using the V-series compounds were fabricated in doped and dopant-free configurations. The synthesized materials exhibit a very high hole mobility up to 3.3×10^{-4} cm^2 V^{-1} s^{-1} leading to a light-to-energy power conversion efficiency exceeding 19% with the doped non-functionalized **V1275**, which is on par with that of the widely researched spiro-OMeTAD, with a remarkable improvement in the long-term stability. While the efficiency of the spiro-based device dropped down to 80% of the original PCE after 500 h without encapsulation and constant light illumination, the doped V-based devices achieved up to 125% of the original PCE in the same ageing time. The devices fabricated with dopant-free HTMs showed high efficiency, exceeding 17%, and also excellent shelf-lifetime stability. The results presented here show that HTMs prepared *via* a simple condensation protocol can compete in performance with materials obtained *via* expensive cross-coupling methods at a fraction of their cost and may be very attractive low-cost and stable semiconductors solving one of the concerns for the near future commercialization.

Conflicts of interest

There are no conflicts to declare.

Acknowledgements

This project has received funding from the European Union's Horizon 2020 Research and Innovation Programme under the Marie Skłodowska-Curie grant agreement no. 754462. We acknowledge the Swiss National Science Foundation (SNSF) funding through the Synergia Grant EPISODE (Grant No. CRSII5_171000). The authors (M. Daskeviciene and G. Bubniene) acknowledge the funding from the Research Council of Lithuania (grant no. MIP-19-14). Computations were performed on resources at the High Performance Computing Center "HPC Sauletekis" (Faculty of Physics, Vilnius University). Prof. R. Buonsanti is acknowledged for the use of the Fluorolog system and Dr E. Kamarauskas is acknowledged for ionisation potential measurements. KR acknowledges the funding received from the MJJ Foundation.

Notes and references

1 NREL, *Photovoltaic Research: Best Research Cell Efficiency Chart*, https://www.nrel.gov/pv/cell-efficiency.html, accessed 28 April 2020.
2 J. Burschka, N. Pellet, S. J. Moon, R. Humphry-Baker, P. Gao, M. K. Nazeeruddin and M. Grätzel, *Nature*, 2013, **499**, 316–319.
3 N. J. Jeon, J. H. Noh, W. S. Yang, Y. C. Kim, S. Ryu, J. Seo and S. Il Seok, *Nature*, 2015, **517**, 476–480.
4 M. M. Lee, J. Teuscher, T. Miyasaka, T. N. Murakami and H. J. Snaith, *Science*, 2012, **338**, 643–647.
5 C. Wehrenfennig, G. E. Eperon, M. B. Johnston, H. J. Snaith and L. M. Herz, *Adv. Mater.*, 2014, **26**, 1584–1589.
6 M. Saliba, T. Matsui, J. Y. Seo, K. Domanski, J. P. Correa-Baena, M. K. Nazeeruddin, S. M. Zakeeruddin, W. Tress, A. Abate, A. Hagfeldt and M. Grätzel, *Energy Environ. Sci.*, 2016, **9**, 1989–1997.
7 M. A. Green, A. Ho-Baillie and H. J. Snaith, *Nat. Photonics*, 2014, **8**, 506–514.
8 B. Chen, Z. J. Yu, S. Manzoor, S. Wang, W. Weigand, Z. Yu, G. Yang, Z. Ni, X. Dai, Z. C. Holman and J. Huang, *Joule*, 2020, **4**, 850–864.
9 W. S. Yang, B. W. Park, E. H. Jung, N. J. Jeon, Y. C. Kim, D. U. Lee, S. S. Shin, J. Seo, E. K. Kim, J. H. Noh and S. Il Seok, *Science*, 2017, **356**, 1376–1379.
10 W. W. Liu, T. H. Wu, M. C. Liu, W. J. Niu and Y. L. Chueh, *Adv. Mater. Interfaces*, 2019, **6**, 1801758.
11 D. H. Kim, J. B. Whitaker, Z. Li, M. F. A. M. van Hest and K. Zhu, *Joule*, 2018, **2**, 1437–1451.
12 L. Qiu, L. K. Ono and Y. Qi, *Mater. Today Energy*, 2018, **7**, 169–189.
13 Y. Rong, Y. Hu, A. Mei, H. Tan, M. I. Saidaminov, S. Il Seok, M. D. McGehee, E. H. Sargent and H. Han, *Science*, 2018, **361**, 6408.
14 K. Rakstys, C. Igci and M. K. Nazeeruddin, *Chem. Sci.*, 2019, **10**, 6748–6769.
15 U. Bach, D. Lupo, P. Comte, J. E. Moser, F. Weissörtel, J. Salbeck, H. Spreitzer and M. Grätzel, *Nature*, 1998, **395**, 583–585.
16 W. S. Yang, J. H. Noh, N. J. Jeon, Y. C. Kim, S. Ryu, J. Seo and S. Il Seok, *Science*, 2015, **348**, 1234–1237.
17 G. W. Kim, H. Choi, M. Kim, J. Lee, S. Y. Son and T. Park, *Adv. Energy Mater.*, 2020, **10**, 1903403.
18 T. P. I. Saragi, T. Spehr, A. Siebert, T. Fuhrmann-Lieker and J. Salbeck, *Chem. Rev.*, 2007, **107**, 1011–1065.
19 J. Salbeck, F. Weissörtel and J. Bauer, *Macromol. Symp.*, 1998, **125**, 121–132.
20 J. Salbeck, N. Yu, J. Bauer, F. Weissörtel and H. Bestgen, *Synth. Met.*, 1997, **91**, 209–215.
21 B. Xu, D. Bi, Y. Hua, P. Liu, M. Cheng, M. Grätzel, L. Kloo, A. Hagfeldt and L. Sun, *Energy Environ. Sci.*, 2016, **9**, 873–877.
22 D. Bi, B. Xu, P. Gao, L. Sun, M. Grätzel and A. Hagfeldt, *Nano Energy*, 2016, **23**, 138–144.
23 B. Xu, J. Zhang, Y. Hua, P. Liu, L. Wang, C. Ruan, Y. Li, G. Boschloo, E. M. J. Johansson, L. Kloo, A. Hagfeldt, A. K. Y. Jen and L. Sun, *Chem*, 2017, **2**, 676–687.
24 T. Malinauskas, M. Saliba, T. Matsui, M. Daskeviciene, S. Urnikaite, P. Gratia, R. Send, H. Wonneberger, I. Bruder, M. Graetzel, V. Getautis and M. K. Nazeeruddin, *Energy Environ. Sci.*, 2016, **9**, 1681–1686.
25 K. Rakstys, S. Paek, G. Grancini, P. Gao, V. Jankauskas, A. M. Asiri and M. K. Nazeeruddin, *ChemSusChem*, 2017, **10**, 3825–3832.

26 A. Magomedov, S. Paek, P. Gratia, E. Kasparavicius, M. Daskeviciene, E. Kamarauskas, A. Gruodis, V. Jankauskas, K. Kantminiene, K. T. Cho, K. Rakstys, T. Malinauskas, V. Getautis and M. K. Nazeeruddin, *Adv. Funct. Mater.*, 2018, **28**, 1704351.
27 J. A. Christians, P. Schulz, J. S. Tinkham, T. H. Schloemer, S. P. Harvey, B. J. Tremolet De Villers, A. Sellinger, J. J. Berry and J. M. Luther, *Nat. Energy*, 2018, **3**, 68–74.
28 X. Li, M. Cai, Z. Zhou, K. Yun, F. Xie, Z. Lan, J. Hua and L. Han, *J. Mater. Chem. A*, 2017, **5**, 10480–10485.
29 L. Guan, X. Yin, D. Zhao, C. Wang, Q. An, J. Yu, N. Shrestha, C. R. Grice, R. A. Awni, Y. Yu, Z. Song, J. Zhou, W. Meng, F. Zhang, R. J. Ellingson, J. Wang, W. Tang and Y. Yan, *J. Mater. Chem. A*, 2017, **5**, 23319–23327.
30 F. Wu, Y. Shan, J. Qiao, C. Zhong, R. Wang, Q. Song and L. Zhu, *ChemSusChem*, 2017, **10**, 3833–3838.
31 C. Lu, I. T. Choi, J. Kim and H. K. Kim, *J. Mater. Chem. A*, 2017, **5**, 20263–20276.
32 R. Xue, M. Zhang, G. Xu, J. Zhang, W. Chen, H. Chen, M. Yang, C. Cui, Y. Y. Li and Y. Y. Li, *J. Mater. Chem. A*, 2018, **6**, 404–413.
33 J. Zhang, Y. Hua, B. Xu, L. Yang, P. Liu, M. B. Johansson, N. Vlachopoulos, L. Kloo, G. Boschloo, E. M. J. Johansson, L. Sun and A. Hagfeldt, *Adv. Energy Mater.*, 2016, **6**, 1601062.
34 D. Li, J. Y. Shao, Y. Y. Li, Y. Y. Li, L. Y. Deng, Y. W. Zhong and Q. Meng, *Chem. Commun.*, 2018, **54**, 1651–1654.
35 B. Bin Cui, C. Zhu, S. Yang, Y. Han, N. Yang, L. Zhang, Y. Wang, Y. Jia, L. Zhao and Q. Chen, *ACS Omega*, 2018, **3**, 10791–10797.
36 K. Rakstys, M. Saliba, P. Gao, P. Gratia, E. Kamarauskas, S. Paek, V. Jankauskas and M. K. Nazeeruddin, *Angew. Chem., Int. Ed.*, 2016, **55**, 7464–7468.
37 F. Zhang, Z. Wang, H. Zhu, N. Pellet, J. Luo, C. Yi, X. Liu, H. Liu, S. Wang, X. Li, Y. Xiao, S. M. Zakeeruddin, D. Bi and M. Grätzel, *Nano Energy*, 2017, **41**, 469–475.
38 F. Zhang, S. Wang, H. Zhu, X. Liu, H. Liu, X. Li, Y. Xiao and S. M. Zakeeruddin, *ACS Energy Lett.*, 2018, **3**, 1145–1152.
39 M. L. Petrus, A. Music, A. C. Closs, J. C. Bijleveld, M. T. Sirtl, Y. Hu, T. J. Dingemans, T. Bein and P. Docampo, *J. Mater. Chem. A*, 2017, **5**, 25200–25210.
40 M. L. Petrus, M. T. Sirtl, A. C. Closs, T. Bein and P. Docampo, *Mol. Syst. Des. Eng.*, 2018, **3**, 734–740.
41 M. L. Petrus, K. Schutt, M. T. Sirtl, E. M. Hutter, A. C. Closs, J. M. Ball, J. C. Bijleveld, A. Petrozza, T. Bein, T. J. Dingemans, T. J. Savenije, H. Snaith and P. Docampo, *Adv. Energy Mater.*, 2018, **8**, 1–11.
42 D. Vaitukaityte, Z. Wang, T. Malinauskas, A. Magomedov, G. Bubniene, V. Jankauskas, V. Getautis and H. J. Snaith, *Adv. Mater.*, 2018, **30**, 1–7.
43 M. Daskeviciene, S. Paek, Z. Wang, T. Malinauskas, G. Jokubauskaite, K. Rakstys, K. T. Cho, A. Magomedov, V. Jankauskas, S. Ahmad, H. J. Snaith, V. Getautis and M. K. Nazeeruddin, *Nano Energy*, 2017, **32**, 551–557.
44 M. Daskeviciene, S. Paek, A. Magomedov, K. T. Cho, M. Saliba, A. Kizeleviciute, T. Malinauskas, A. Gruodis, V. Jankauskas, E. Kamarauskas, M. K. Nazeeruddin and V. Getautis, *J. Mater. Chem. C*, 2019, **7**, 2717–2724.
45 T. P. Osedach, T. L. Andrew and V. Bulović, *Energy Environ. Sci.*, 2013, **6**, 711–718.
46 M. L. Petrus, T. Bein, T. J. Dingemans and P. Docampo, *J. Mater. Chem. A*, 2015, **3**, 12159–12162.
47 A. C. Recommendations, *Gaussian 09 Citation, Gaussian.com*, https://gaussian.com/g09citation/, accessed 15 May 2020.
48 J. Urieta-Mora, I. García-Benito, I. Zimmermann, J. Aragó, J. Calbo, G. Grancini, A. Molina-Ontoria, E. Ortí, N. Martin and M. K. Nazeeruddin, *J. Mater. Chem. C*, 2019, **7**, 6656–6663.
49 K. Walzer, B. Männig, M. Pfeiffer and K. Leo, *Chem. Rev.*, 2007, **107**, 1233–1271.
50 B. Lüssem, M. Riede and K. Leo, *Phys. Status Solidi A*, 2013, **210**, 9–43.
51 I. Salzmann, G. Heimel, M. Oehzelt, S. Winkler and N. Koch, *Acc. Chem. Res.*, 2016, **49**, 370–378.
52 J. Y. Feng, K. W. Lai, Y. S. Shiue, A. Singh, C. H. P. Kumar, C. T. Li, W. T. Wu, J. T. Lin, C. W. Chu, C. C. Chang and C. C. Su, *J. Mater. Chem. A*, 2019, **7**, 14209–14221.
53 Y. Lee, S. Paek, K. T. Cho, E. Oveisi, P. Gao, S. Lee, J. S. Park, Y. Zhang, R. Humphry-Baker, A. M. Asiri and M. K. Nazeeruddin, *J. Mater. Chem. A*, 2017, **5**, 12729–12734.
54 K. Rakstys, A. Abate, M. I. Dar, P. Gao, V. Jankauskas, G. Jacopin, E. Kamarauskas, S. Kazim, S. Ahmad, M. Grätzel and M. K. Nazeeruddin, *J. Am. Chem. Soc.*, 2015, **137**, 16172–16178.
55 G. Xing, N. Mathews, S. Sun, S. S. Lim, Y. M. Lam, M. Grätzel, S. Mhaisalkar and T. C. Sum, *Science*, 2013, **342**, 344–347.
56 N. Drigo, C. Roldan-Carmona, M. Franckevičius, K. H. Lin, R. Gegevičius, H. Kim, P. A. Schouwink, A. A. Sutanto, S. Olthof, M. Sohail, K. Meerholz, V. Gulbinas, C. Corminboeuf, S. Paek and M. K. Nazeeruddin, *J. Am. Chem. Soc.*, 2020, **142**, 1792–1800.
57 W. Zhou, Z. Wen and P. Gao, *Adv. Energy Mater.*, 2018, **8**, 1702512.
58 T. Braukyla, R. Xia, T. Malinauskas, M. Daskeviciene, A. Magomedov, E. Kamarauskas, V. Jankauskas, Z. Fei, C. Roldán-Carmona, C. Momblona, M. K. Nazeeruddin, P. J. Dyson and V. Getautis, *Sol. RRL*, 2019, **3**, 1900224.
59 A. Magomedov, E. Kasparavičius, K. Rakstys, S. Paek, N. Gasilova, K. Genevičius, G. Juška, T. Malinauskas, M. K. Nazeeruddin and V. Getautis, *J. Mater. Chem. C*, 2018, **6**, 8874–8878.
60 E. Kasparavicius, A. Magomedov, T. Malinauskas and V. Getautis, *Chem.–Eur. J.*, 2018, **24**, 9910–9918.
61 A. K. Jena, M. Ikegami and T. Miyasaka, *ACS Energy Lett.*, 2017, **2**, 1760–1761.
62 D. Shi, X. Qin, Y. Li, Y. He, C. Zhong, J. Pan, H. Dong, W. Xu, T. Li, W. Hu, J. L. Brédas and O. M. Bakr, *Sci. Adv.*, 2016, **2**, e1501491.
63 M. Namatame, M. Yabusaki, T. Watanabe, Y. Ogomi, S. Hayase and K. Marumoto, *Appl. Phys. Lett.*, 2017, **110**, 123904.
64 J. Zhang, Q. Daniel, T. Zhang, X. Wen, B. Xu, L. Sun, U. Bach and Y. B. Cheng, *ACS Nano*, 2018, **12**(10), 10452–10462.

Supporting Information

Fluorene-based enamines as low-cost and dopant-free hole transporting materials for high performance and stable perovskite solar cells

Sarune Daskeviciute, Cristina Momblona, Kasparas Rakstys, Albertus Adrian Sutanto, Maryte Daskeviciene, Vygintas Jankauskas, Alytis Gruodis, Giedre Bubniene, Vytautas Getautis, Mohammad Khaja Nazeeruddin**

EXPERIMENTAL SECTION

Synthetic methods and procedures: Chemicals required for the synthesis were purchased from Sigma-Aldrich and TCI Europe and used as received without additional purification. ^{1}H NMR spectra were recorded at 400 MHz on a Bruker Avance III spectrometer with a 5 mm double resonance broad band BBO z-gradient room temperature probe, ^{13}C NMR spectra were collected using the same instrument at 101 MHz. The chemical shifts, expressed in ppm, were relative to tetramethylsilane (TMS). All the NMR experiments were performed at 25 °C. Reactions were monitored by thin-layer chromatography on ALUGRAM SIL G/UV254 plates and developed with UV light. Silica gel (grade 9385, 230–400 mesh, 60 Å, Aldrich) was used for column chromatography. Elemental analysis was performed with an Exeter Analytical CE-440 elemental analyzer, Model 440 C/H/N/. Melting points were measured with Electrothermal MEL-TEMP capillary melting point apparatus.

N^2,N^2,N^7,N^7-tetrakis[2,2-bis(4-methoxyphenyl)vinyl]-9*H*-fluorene-2,7-diamine (V1275)

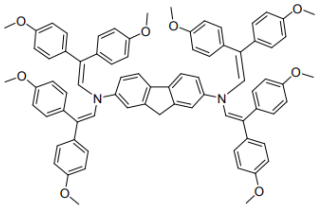

2,7-diaminofluorene (0.3 g, 1.5 mmol) was dissolved in tetrahydrofuran (9 mL + volume of the Dean-Stark trap), (+/-)camphor-10-sulphonic acid (0.36 g, 1.5 mmol) was added and the mixture was heated at reflux for 20 minutes. Afterwards, 2,2-bis(4-methoxyphenyl)acetaldehyde (2.4 g, 9.2 mmol) was added and reflux was continued using a Dean-Stark trap for 6 hours. After cooling to room temperature, reaction mixture was extracted with ethyl acetate. The organic layer was dried over anhydrous Na_2SO_4, filtered and solvent evaporated. The

crude product was crystallized from ethanol (30 mL). The obtained crystals were filtered off and washed with hot ethanol for three times. The product was recrystallized from acetone/ethanol 1:1 gave as light yellow-green crystals (1.14 g, 60%). ^{1}H NMR (400 MHz, $CDCl_3$) δ 7.60 (d, J = 8.4 Hz, 2H), 7.34 – 7.20 (m, 2H), 7.19 – 6.94 (m, 10H), 6.84 (d, J = 8.4 Hz, 8H), 6.67 (d, J = 8.4 Hz, 8H), 6.49 (d, J = 8.4 Hz, 8H), 5.82 (s, 4H), 4.04 – 3.57 (m, 26H). ^{13}C NMR (101 Mhz, $CDCl_3$) δ 159.01, 158.71, 144.37, 132.82, 130.66, 130.18, 128.85, 114.43, 113.92, 113.63, 113.05, 55.46, 55.26, 37.05 ppm. Anal. calcd for $C_{77}H_{68}N_2O_8$: C, 80.46; H, 5.96; N, 2.44; found: C, 80.14; H, 5.82; N, 2.48.

9,9-dibenzyl-*N*^{2},*N*^{2},*N*^{7},*N*^{7}-tetrakis[2,2-bis(4-methoxyphenyl)vinyl]-9*H*-fluorene-2,7-diamine (V1227)

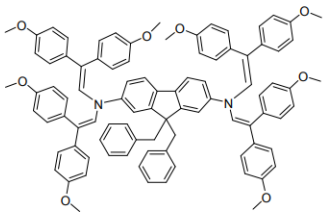

Compound **V1275** (0.5 g, 0.4 mmol) in dimethylsulfoxyde (20 mL) was dissolved and purged with argon for 30 minutes. Afterwards, benzyltriethylammonium chloride (0.01 g, 0.04 mmol) and 50% NaOH (0.15 mL) solution were added. The color of the reaction turned black and then benzyl bromide (0.16 g, 1.0 mmol) was slowly added dropwise under argon atmosphere and stirred at room temperature for 96 hours. The reaction mixture was filtered off and washed with water three times. The crude product was purified by column chromatography using 1:4 v/v tetrahydrofuran/*n*-hexane as an eluent to collect **V1227** as a pale brown solid (0.29 g, 50%). ^{1}H NMR (400 MHz, acetone-d_6) δ 7.56 (d, J = 8.0 Hz, 2H), 7.31 – 6.78 (m, 30H), 6.71 (d, J = 8.4 Hz, 8H), 6.50 (d, J = 8.4 Hz, 8H), 5.97 – 5.66 (m, 4H), 3.85 (d, J = 48.8 Hz, 24H), 3.53 – 3.14 (m, 4H). ^{13}C NMR (101 MHz, acetone) δ 159.35, 159.03, 148.60, 136.29, 134.30, 132.53, 130.68, 130.54, 128.84, 127.22, 127.14, 126.52, 113.86, 113.50, 112.98, 60.05, 54.88, 54.61, 10.95 ppm. Anal. calcd for $C_{91}H_{80}N_2O_8$: C, 82.20; H, 6.06; N, 2.11; found: C, 82.54; H, 6.11; N, 2.15.

***N*²,*N*²,*N*⁷,*N*⁷-tetrakis[2,2-bis(4-methoxyphenyl)vinyl]-9,9-dipropyl-9*H*-fluorene-2,7-diamine (V1235)**

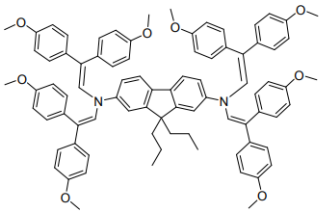

Compound **V1275** (0.5 g, 0.4 mmol) in dimethylsulfoxyde (20 mL) was dissolved and purged with argon for 30 minutes. Afterwards, benzyltriethylammonium chloride (0.01 g, 0.04 mmol) and 50% NaOH (0.15 mL) solution were added. The color of the reaction turned black and then bromopropane (0.12 g, 1.0 mmol) was slowly added dropwise under argon atmosphere and stirred at room temperature for 72 hours. The reaction mixture was filtered off and washed with water three times. The crude product was purified by column chromatography using 1:4 v/v tetrahydrofuran/*n*-hexane as an eluent to collect **V1235** as a yellow solid (0.28 g, 52%). ^{1}H NMR (400 MHz, $CDCl_3$) δ 7.48 (d, *J* = 8.0 Hz, 2H), 7.12 – 6.94 (m, 12H), 6.85 (d, *J* = 8.8 Hz, 8H), 6.66 (d, *J* = 8.8 Hz, 8H), 6.51 (d, *J* = 8.8 Hz, 8H), 5.81 (s, 4H), 3.81 (d, *J* = 37.2 Hz, 24H), 1.99 – 1.81 (m, 4H), 0.88 – 0.60 (m, 10H). ^{13}C NMR (101 MHz, $CDCl_3$) δ 158.79, 158.54, 149.08, 134.23, 132.65, 130.45, 128.79, 119.03, 113.71, 112.84, 111.90, 59.52, 55.25, 55.07, 17.74, 14.12, 11.52 ppm. Anal. calcd for $C_{83}H_{80}N_2O_8$: C, 80.82; H, 6.54; N, 2.27; found: C, 80.64; H, 6.61; N, 2.30.

***N*²,*N*²,*N*⁷,*N*⁷-tetrakis[2,2-bis(4-methoxyphenyl)vinyl]-9,9-dihexyl-9*H*-fluorene-2,7-diamine (V1236)**

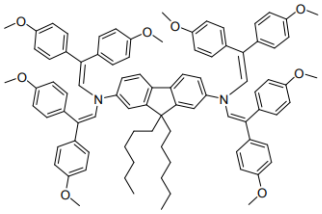

Compound **V1275** (0.5 g, 0.4 mmol) in dimethylsulfoxyde (20 mL) was dissolved and purged with argon for 30 minutes. Afterwards, benzyltriethylammonium chloride (0.01 g, 0.04 mmol) and 50% NaOH (0.15 mL) solution were added. The color of the reaction turned black and then bromohexane (0.16 g, 1.0 mmol) was slowly added dropwise under argon atmosphere and stirred at room temperature for 26 hours. The reaction mixture was filtered off and washed repeatedly with water three times. The crude product was purified by column chromatography

using 4:21 v/v tetrahydrofuran/*n*-hexane as an eluent to collect **V1236** as a yellow solid (0.36 g, 63%). ^{1}H NMR (400 MHz, $CDCl_3$) δ 7.52 (d, J = 8.0 Hz, 2H), 7.12 – 6.93 (m, 12H), 6.85 (d, J = 8.4 Hz, 8H), 6.65 (d, J = 8.4 Hz, 8H), 6.50 (d, J = 8.8 Hz, 8H), 5.81 (s, 4H), 3.81 (d, J = 38.0 Hz, 24H), 1.97 – 1.82 (m, 4H), 1.21 – 1.01 (m, 12H), 0.85 – 0.66 (m, 10H) ppm. ^{13}C NMR (101 MHz, $CDCl_3$) δ 158.99, 158.69, 152.04, 134.48, 132.95, 130.64, 128.90, 119.25, 115.91, 113.92, 113.02, 111.31, 55.38, 55.26, 40.11, 31.39, 29.38, 23.62, 22.48, 14.12 ppm. Anal. calcd for $C_{89}H_{92}N_2O_8$: C, 81.12; H, 7.04; N, 2.13; found: C, 81.24; H, 7.11; N, 2.10.

***N*²,*N*²,*N*⁷,*N*⁷-tetrakis[2,2-bis(4-methoxyphenyl)vinyl]-9,9-dimethyl-9*H*-fluorene-2,7-diamine (V1237)**

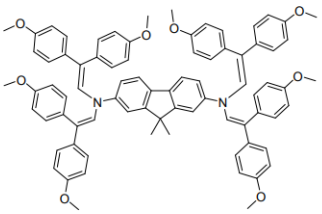

Compound **V1275** (0.5 g, 0.4 mmol) in dimethylsulfoxyde (20 mL) was dissolved and purged with argon for 30 minutes. Afterwards, benzyltriethylammonium chloride (0.01 g, 0.04 mmol) and 50% NaOH (0.15 mL) solution were added. The color of the reaction turned black and then iodomethane (0.14 g, 1.0 mmol) was slowly added dropwise under argon atmosphere and stirred at room temperature for 120 hours. The reaction mixture was filtered off and washed with water three times. The crude product was purified by column chromatography using 1:4 v/v tetrahydrofuran/*n*-hexane as an eluent to collect **V1237** as a yellow solid (0.26 g, 51%). ^{1}H NMR (400 MHz, $CDCl_3$) δ 7.54 (d, J = 8.0 Hz, 2H), 7.19 – 6.94 (m, 12H), 6.87 (d, J = 8.4 Hz, 8H), 6.66 (d, J = 8.4 Hz, 8H), 6.53 (d, J = 8.4 Hz, 8H), 5.96 – 5.70 (m, 4H), 3.84 (d, J = 36.8, 24H), 1.46 (s, 6H). ^{13}C NMR (101 MHz, $CDCl_3$) δ 158.98, 158.68, 155.02, 132.82, 132.23, 130.65, 128.90, 116.10, 113.90, 113.01, 111.03, 55.43, 55.24, 47.14, 27.56 ppm. Anal. calcd for $C_{79}H_{72}N_2O_8$: C, 80.59; H, 6.16; N, 2.38; found: C, 80.74; H, 6.11; N, 2.35.

ADVANCED FUNCTIONAL MATERIALS
www.afm-journal.de

Passivating Defects of Perovskite Solar Cells with Functional Donor-Acceptor–Donor Type Hole Transporting Materials

Sarune Daskeviciute-Geguziene, Yi Zhang, Kasparas Rakstys, Chuanxiao Xiao, Jianxing Xia, Zhiheng Qiu, Maryte Daskeviciene, Tomas Paskevicius, Vygintas Jankauskas, Abdullah M. Asiri, Vytautas Getautis,* and Mohammad Khaja Nazeeruddin**

In this study, a series of donor–acceptor–donor (D-A-D) type small molecules based on the fluorene and diphenylethenyl enamine units, which are distinguished by different acceptors, as holetransporting materials (HTMs) for perovskite solar cells is presented. The incorporation of the malononitrile acceptor units is found to be beneficial for not only carrier transportation but also defects passivation via Pb–N interactions. The highest power conversion efficiency of over 22% is achieved on cells based on V1359, which is higher than that of spiro-OMeTAD under identical conditions. This st shows that HTMs prepared via simplified synthetic routes are not only a low-cost alternative to spiro-OMeTAD but also outperform in efficiency and stability state-of-art materials obtained via expensive cross-coupling methods.

1. Introduction

Due to the outstanding photovoltaic properties, simple fabrication process, abundant precursors, and extraordinary power conversion efficiency (PCE), perovskite solar cells (PSCs) have attracted tremendous attention all over the world.[1–9] While the very high efficiency using perovskites is a significant achievement, issues relating to the high price of device components such as hole transporting material (HTM) and long-term stability against moisture, heat, and light are still a concern for commercial application of the technology, therefore currently the research is directed to the realization of cost-effective and stable devices.[10–14]

Compositional engineering and crystallization control of perovskites, interface modification, and charge transport layer optimization are manifested to be effective ways to improve the photovoltaic performance of PSCs.[15–21] It has been widely recognized that the defects as well as their density would cause undesired charge recombination and carrier scattering limiting the further improvement of device performance because of a significant loss of the open-circuit voltage (Voc) and fill factor (FF). Besides, the presence of defects also causes serious stability issues due to the phase segregation during cell operation and induced ion migration at the perovskite/HTM interface.[22–25] Therefore, developing novel HTMs with added extra functionality to passivate the perovskite defects is essential.

It is known, the introduction of electron-acceptor functional groups in the HTM structure increases the dipole moment, which is beneficial for intramolecular charge transfer (ICT) and increases hole mobility of the resulting HTM.[26–29] Moreover, the strong interaction in donor–acceptor (D–A) systems effectively suppresses the nonradiative recombination loss and improves the device performance. On the other hand, previous studies have revealed that the uncoordinated Pb^{2+} ions at the surface of perovskite are one of the primary sources of defects in the perovskite layer, which could act as charge recombination centers to hinder charge transfer. In addition, molecules containing electron-deficient groups have been shown to interact with uncoordinated lead ions (Pb^{2+}), thereby passivating the defects of halide vacancies.[30–38]

S. Daskeviciute-Geguziene, K. Rakstys, M. Daskeviciene, V. Getautis
Department of Organic Chemistry
Kaunas University of Technology
Radvilenu pl. 19, Kaunas 50254, Lithuania
E-mail: vytautas.getautis@ktu.lt
Y. Zhang, J. Xia, M. K. Nazeeruddin
Group for Molecular Engineering of Functional Material
Institute of Chemical Sciences and Engineering
École Polytechnique Fédérale de Lausanne
Sion CH-1951, Switzerland
E-mail: yi.zhang@epfl.ch; mdkhaja.nazeeruddin@epfl.ch
C. Xiao, Z. Qiu
Ningbo Institute of Materials Technology and Engineering
Chinese Academy of Sciences
Ningbo, Zhejiang 315201, China
C. Xiao, Z. Qiu
Ningbo New Materials Testing and Evaluation Center CO., Ltd
Ningbo, Zhejiang 315201, China
T. Paskevicius
Department of Organic Chemistry
Center for Physical Sciences and Technology
Akademijos g. 7, Vilnius 08412, Lithuania
V. Jankauskas
Institute of Chemical Physics
Vilnius University
Sauletekio al. 3, Vilnius 10257, Lithuania
A. M. Asiri
Center of Excellence for Advanced Materials Research (CEAMR)
King Abdulaziz University
P.O. Box 80203, Jeddah 21589, Saudi Arabia
The ORCID identification number(s) for the author(s) of this article can be found under https://doi.org/10.1002/adfm.202208317.

DOI: 10.1002/adfm.202208317

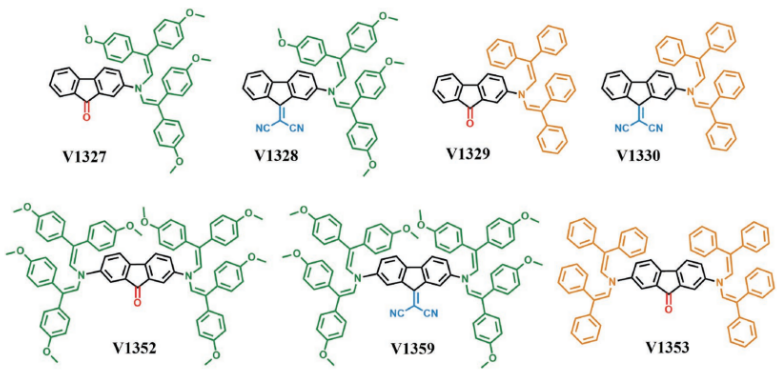

Figure 1. Chemical structures of synthesized D–A–D type hole transporting materials having different structural units.

However, most conjugated D–A–D type HTMs are generally designed by linking together donor and acceptor building blocks using cross-coupling chemistry. Such coupling reactions generally require stringent reaction conditions resulting in several disadvantages, such as inert reaction conditions, expensive transition metal catalysts and extensive purification procedures due to the inherent formation of side products that are prone to this type of reaction. Tiny amount of metal catalyst residues may remain in the hole transporting layer serving as traps that deteriorate the charge-transporting properties of the synthesized HTMs and negatively affect the performance of the resulting devices. To this extent, a significant effort is to find the simplified synthetic protocols to reduce the cost of HTM synthesis without sacrificing efficiency. Recently, several research groups have focused on tuning the structure by decreasing the number of synthetic steps, thus reducing the synthetic complexity, cost of materials and environmental impact.[39–48] In this sense, condensation chemistry is an excellent perspective moving away from transition metal-based cross-coupling reactions, as water is the only side-product and metal catalysts are not required simplifying product workup and purification.

In this work, we explore D–A–D type HTMs employing fluorene as the central scaffold, diphenylethenyl enamine donating arms and ketone/dicyanoylidene acceptors. Combining different substituents, seven fluorene-based HTMs shown in **Figure 1** were designed and successfully synthesized employing facile condensation chemistry using commercially available and cheap reagents. Their optical, thermal, electrophysical, and photovoltaic properties were thoroughly investigated. Moreover, the impact of a different number of enamine arms and methoxy group presence, as well as different acceptors on the central core were examined and various properties of newly synthesized molecules were systematically investigated. All these enamine-based HTMs have been applied in PSCs, showing a PCE of over 22% with improved stability once compared with spiro-OMeTAD. With this, we demonstrate simple chemistry resulting in low-cost semiconductors without sacrificing the photovoltaic performance.

2. Results and Discussion

Fluorenone/dicyanofluorenylidine enamines were prepared using straightforward synthesis with high purity and excellent yields. As shown in **Figure 2**, single- and double-arm enamines only required a one-step reaction condensing low-cost commercial reagents 2-aminofluorenone or 2,7-diaminofluorenone with 2,2-bis(4-methoxyphenyl)acetaldehyde in the presence of camphor sulfonic acid under ambient conditions. It is worth mentioning that water is the only by-product, which was separated using a Dean-Stark trap. To obtain cyanated compounds, the keto group was converted to malononitrile by Knoevenagel condensation under basic media. The chemical structures of the synthesized compounds were verified by NMR spectroscopy, mass spectrometry, elemental analysis, and infrared spectroscopy. A detailed synthetic procedures and analysis are reported in the Supporting Information.

The thermal properties of HTMs were evaluated using thermogravimetric analysis (TGA) (**Figure 3**a) and differential scanning calorimetry (DSC) (Figure S3, Supporting Information) measurements. TGA analysis has shown that double enamine arm containing compounds have higher thermal stability among the series due to the higher aromatic system,[48–50] with the highest decomposition temperature (T_{dec}) of 412°C at 5% weight loss for **V1353**. In addition, all synthesized compounds have a higher T_{dec} than that of the spiro-OMeTAD (T_{dec} = 288°C).[51] The thermal transitions were determined by DSC. A clear trend between methoxy-substituted and non-methoxy compounds were observed. Diphenylethenyl-substituted compounds **V1329**, **V1330**, and **V1353** are fully crystalline, having a melting temperature (T_m) in both heating scans, while during the second heating, a glass transition is observed followed by recrystallization. The introduction of the methoxy groups allows existence in

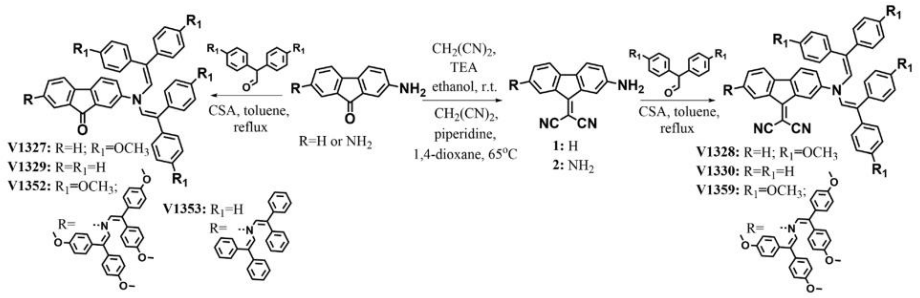

Figure 2. Reaction scheme of fluorenone/dicianofluorenylidene enamine HTMs and their molecular structures.

both crystalline and amorphous states. Only the glass transition temperature (T_g) was investigated for all methoxy-containing compounds during the second heating scan, while **V1352** and **V1359** have the most stabilized amorphous state, with the glass transition detected at around 140 °C.

The UV–vis absorption spectra of the synthesized HTMs in THF solutions are depicted in Figure 3b. Directly comparing **V1327** with **V1328**, **V1329** with **V1330**, and **V1352** with **V1359**, a wider and red-shifted optical bands could be noticed. The absorption spectral difference is clearly owed to the difference

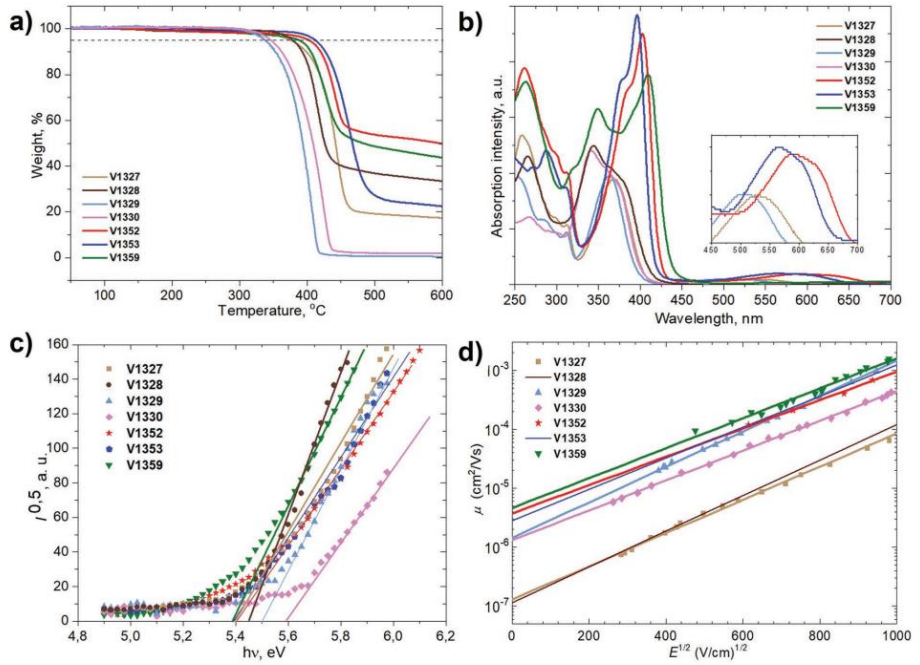

Figure 3. a) Thermogravimetric analysis (TGA) data (heating rate of 10 °Cmin^{-1}, N_2 atmosphere); b) UV–vis absorption spectra of V-series HTMs in THF solutions (10^{-4} M); c) Photoemission in air spectra of the charge transporting layers; d) Electric field dependencies of the hole-drift mobility in synthesized HTMs.

in electron-accepting power between =O and =C-$(CN)_2$ fragments, confirming that malononitrile is a stronger electron acceptor. As expected, the change from mono to disubstituted enamine fragments has influenced the conjugation; therefore, spectra of all double-arm molecules **V1352**, **V1353**, and **V1359** have a significant hyperchromic shift. Broad optical absorption in the visible region reveals push-pull communication through the 9-ylidene double bond, in which the fluorene and the keto/dicyanoylidene moieties serve as a donor and an acceptor, respectively.[52,53] Photoluminescence (PL) of the molecules in solution was measured, but no detectable emission was observed.

For a better interpretation of the energy level alignment of the HTMs in PSCs, solid-state ionization potential (I_P) was measured using the electron photoemission in the air of the thin films (PESA) with the experimental data shown in Figure 3c. As expected, D–A–D type HTMs were found to have a quite low-lying I_P values around 5.4 eV, which should have enough overpotential with the valence band (VB) energy of the triple cations-based perovskite (≈5.70 eV) ensuring efficient hole transfer from perovskite to the cathode.

We next measured the hole drift mobility using the xerographic time of flight (XTOF) technique. The dependences of hole drift mobility on electric field strength are shown in Figure 3d and Figure S4 (Supporting Information). Some of the materials were not able to be measured from pure layers; therefore, the charge transfer in layers of blends with bisphenol Z-polycarbonate (PC-Z), in weight ratios of 1:1, 1:2, 1:3 or 1:4, which were of suitable quality, was studied in detail. Based on the exponential dependence of the charge carrier mobility on the average distance between the charge transporting molecules, interpolated mobility values were found for the case when the material is pure.[54] The validity of such interpolation has been confirmed in several cases where hole mobility in samples of pure material has been measured.[55] The highest zero-field hole drift mobility of 4.6×10^{-6} cm^2 Vs^{-1} among the series was found for **V1359**. Switching to the single-arm compounds had a negative influence on the hole drift mobility as **V1328** showed the lowest result of 1.1×10^{-7} cm^2 Vs^{-1}. The thermal, optical, and photoelectrical properties of the V-series charge transporting materials are summarized in **Table 1**.

Figure 4a,b represents the scanning electron microscopy (SEM) images of a cross-sectional view of PSC devices with spiro-OMeTAD and **V1359**, providing a direct view of the PSCs individual layers: FTO/SnO_2/perovskite/HTM/Au (see Supporting Information for all experimental details). The thickness of the perovskite films is ≈ 750–800 nm with 90 nm of Au layer. However, the thickness of the **V1359** layer is ≈ 80 nm which is much thinner than that of the spiro-OMeTAD layer (≈220 nm). This is due to the smaller molecule bulk and lowers optimized concentration of the **V1359** solution. Due to the absence of a carrier transport layer, as shown in Figure 4c, higher continuous-wave photoluminescence (CWPL) intensity is found in the perovskite thin film. When the HTM layers are covered, the CWPL intensities decrease sharply, and the **V1359** exhibit higher hole extraction capabilities. Time-resolved photoluminescence (TRPL) measurement of the films are performed, and the results fit with a bi-exponential decay formula: $f(t) = A_1 \exp(-t/\tau_1) + A_2 \exp(-t/\tau_2)$ were shown in Figure 4d and Table S2 (Supporting Information). The PL lifetime shown in Figure 4d obtained from perovskite thin films was 349 ns, which is much longer than the results from perovskite/spiro-OMeTAD (246 ns) and perovskite/**V1359** films (155 ns). Photoluminescence measurements clearly show much improved hole extraction properties using **V1359** that could be ascribed to an extra passivation functionality having built-in CN units.

PSC devices using the different HTMs were fabricated by sandwiching the perovskite thin films between an FTO/SnO_2 anode and an HTM/Au cathode. **Figure 5**a shows the typical current-density–voltage (*J–V*) curves (reverse scan) for the PSCs with spiro-OMeTAD as a reference, **V1352**, **V1353**, and **V1359**, respectively. Devices having synthesized HTMs exhibit photoelectric conversion performance comparable to spiro-OMeTAD, especially for the **V1359**, which showed even higher photocurrent. However, the devices with **V1327**, **V1328**, **V1329**, and **V1330** as the HTMs exhibit relatively low PCE (Figure S5, Supporting Information). The PCE of 22.03% consisting a J_{SC} of 24.34 mA cm^{-2}, a V_{OC} of 1.112 V, and an FF of 81.3% was achieved for the **V1359**-based device in comparison to 21.48% for the spiro-OMeTAD with a J_{SC} of 24.16 mA cm^{-2}, a V_{OC} of 1.121 V, and an FF of 79.3%, showing that molecular engineering of side-arm and acceptor units fully dictates the performance of the final device. The *J–V* hysteresis of the best devices is shown in Figure 5b. A similar hysteresis index of 1.11 for spiro-OMeTAD and 1.09 for **V1359** device was found (Table S4, Supporting Information). A total of 30 solar cells in two groups were fabricated under the same conditions with spiro-OMeTAD or **V1359** as the HTM. Figure 5c demonstrates the statistical distribution of all

Table 1. Thermal, optical and photophysical properties of newly synthesized enamines.

ID	T_m, [°C][a)]	T_c, [°C][a)]	T_g, [°C][a)]	T_{dec}, [°C][a)]	λ_{abs}, [nm][b)]	I_p, [eV][c)]	μ_0, [cm^2 V^{-1} s^{-1}][d)]
V1327	171, 186, 208	–	92	376	259, 299, 313, 370, 538	5.44	$1.3 \cdot 10^{-7}$
V1328	245	–	111	379	265, 345	5.44	$1.1 \cdot 10^{-7}$
V1329	244, 247	202	111	338	255, 285, 313, 363, 513	5.49	$1.4 \cdot 10^{-6}$
V1330	236, 248 239, 248	175	115	347	268, 341	5.53	$1.3 \cdot 10^{-6}$
V1352	221, 232	–	143	403	261, 299, 313, 385, 403, 598	5.43	$4 \cdot 10^{-6}$
V1353	339, 351, 348	217	157	412	270, 288, 311, 378, 395, 570	5.39	$2.8 \cdot 10^{-6}$
V1359	166	–	134	389	263, 323, 349, 409	5.41	$4.6 \cdot 10^{-6}$

[a)]Melting (T_m), crystallization (T_c), glass transition (T_g) and decomposition (T_{dec}) temperatures were observed from DSC and TGA, respectively (10 °C/min, N_2 atmosphere); [b)]Absorption spectra were measured in THF solutions (10^{-4} M); [c)]Ionization energies of the films measured using PESA; [d)]Mobility value at zero field strength.

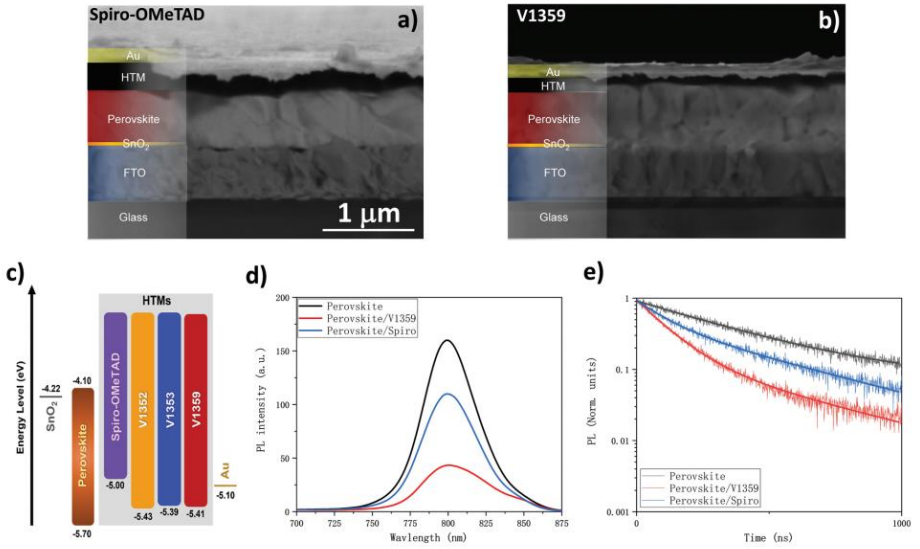

Figure 4. Cross-sectional SEM images of the sample comprising FTO/SnO_2/perovskite/ a) spiro-OMeTAD/Au and b) **V1359**/Au layers, c) the energy level diagram of the devices based on different HTMs, d) CWPL spectra excited at 480 nm and e) TRPL of the perovskite thin films with or without spiro-OMeTAD or **V1359**.

four photovoltaic parameters of the two groups of solar cells to show the reproducibility of each condition. All the photovoltaic parameters of them show a similar half-width, which means the reproducibility of **V1359**-based devices is comparable to that of spiro-OMeTAD (Table S5, Supporting Information).

Another issue of importance to commercialization is the large-scale production when translating from laboratory to manufacturing scale. To characterize the upscaling performance of the new HTM, we fabricated **V1359**-based perovskite modules sized 6.5 × 7 cm. The module exhibited a PCE of 18.61% with a J_{SC} of 2.63 mA cm^{-2}, a V_{OC} of 8.78 V, and an FF of 80.6%, as shown in Figure 5d (an aperture area ≈29 cm^2, corresponding to 20.45% with the active area, a geometric fill factor of 91%).

In addition to the PCE, the chemical stability was also evaluated, showing the increased stability of **V1359**-based device, which represents another important advantage of the new HTM. We reported the long-term operational stability of devices without encapsulation based on the spiro-OMeTAD, or **V1359** HTMs maintained in an argon atmosphere under a constant illumination of 100 mW cm^{-2} (Figure 5e). The device based on **V1359** HTM maintained ≈ 95% of its initial efficiency after 500 h, whereas the device based on spiro-OMeTAD was < 85%. And the long-term device stability was tested every 24 h at about 12% RH, room temperature as shown in Figure S6 (Supporting Information). While the spiro-OMeTAD based device shows a decrease of > 7% in PCE after 500 h, almost no PCE loss is observed for the **V1359** based PSC, demonstrating the enhanced device stability at air.

To explore the effect of **V1359** on the perovskite/HTM interface, we use Kelvin probe force microscopy (KPFM) to elucidate the electric junction characteristic affected by the different HTMs, and to understand how electric field distribution impacts cell performance (Figure S7, Supporting Information). In the measurements, we scan the cross-sectional surface of both control and target cells. By applying small bias voltages (0, −0.5, −1, +0.5 V), KPFM spatially maps surface potential across the whole device stack; and we subtract the 0-V profile to obtain bias-voltage-induced potential change in the bulk of the cell. Further, we calculate the electric-field changes by extracting the derivative of the potential change. As bias voltage is applied, the electric current must be the same throughout the whole device. The KPFM mapped potential distribution is determined by the equivalent resistance of different layers and interfaces of the device, which relates to the junction characteristics (including reverse saturation current J_0, and diode ideality factor n). On both cells, the electric-field peaks locate at the perovskite/HTM and the ETM/perovskite interfaces, indicating the cells have p-i-n junction structure.[56] We assume the ETM/perovskite interfaces are identical, hence we normalized the ETM/perovskite electric-field peaks for better comparison of the two cells. On the target cell, the perovskite/HTM junction is much stronger than the ones on the control cell. We ascribe this electric-field enhancement at HTM layer. The enhanced perovskite/HTM junction is beneficial for charge separation, where electron-hole pairs recombine less at the perovskite/HTM interface. The reduced

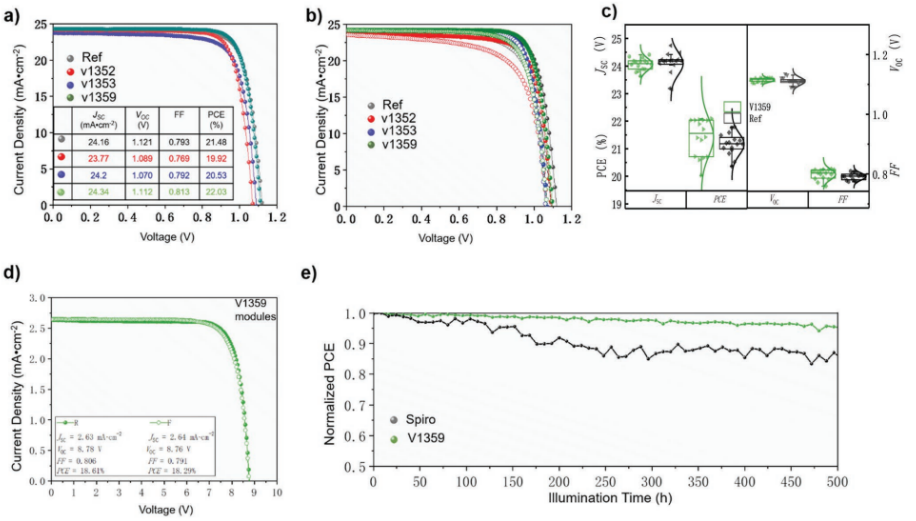

Figure 5. a) *J–V* curves (reverse-scan) of and b) *J–V* hysteresis (Reverse scan: filled circles and Forward scan: hollow circles) of the PSCs based on **V1352**, **V1353**, and **V1359** as HTMs and spiro-OMeTAD as the reference. c) Statistical deviation of the photovoltaic parameters for solar cells with **V1359** or spiro-OMeTAD respectively (15 different solar cells of each type) d) *J-V* hysteresis (Reverse scan "R" and Forward scan "F") of **V1359**-based PSC module, the aperture area was estimated as 30 cm^2. Inset is the maximum-power-point power output of this module. e) Long-term stability study shows in situ measured PCEs of the unsealed solar modules over 500 h under Ar.

recombination rate at the treated perovskite/HTM interface is consistent with FF improvement in cell performance and the electrochemical impedance spectroscopy (EIS) was executed for quantifying the parameters of charge transport in solar cells, such as chemical capacitance, recombination resistance and charge conductivity (Figure S8, Supporting Information). These parameters are imperative to aid in the explanation of the factors that determine the performance metrics of the HTMs in the corresponding solar cells. The inset of Figure S8 (Supporting Information) shows the fitting of the EIS spectra to an appropriate equivalent circuit model. Typically, Nyquist plots were separated into two main regions or arcs at high and low frequencies. As the devices predominantly differ with respect to the HTM, the high frequency range arc is attributed to R_{CT} and C_{CT} at the interface between perovskite and HTMs. It can be seen that the R_{CT} value of the perovskite solar cell with **V1359** as HTM are a little larger than those of that with spiro-OMeTAD as HTM, which may be due to the passivation of **V1359**. Moreover, to validate that charge-carrier recombination process is suppressed, we preformed the light-intensity-dependent *J–V* measurements. The dependence of V_{oc} on light intensity for the spiro-OMeTAD and **V1359** based devices is described in Figure S9 (Supporting Information), where *K*, *T*, and *e* are the Boltzmann constant, temperature in Kelvin, and the elementary charge, respectively. the slope of this plot is correlated with the ideality factor (*n*) in the form of $nkBT/e$, which is the reflex of trap-induced recombination behaviour in PSCs.[57] The slope for **V1359** based device (1.31 KT/e) is lower than that of the spiro-OMeTAD based device (1.39 KT/e), indicating the suppressed trap-induced recombination in the **V1359** based device.

3. Conclusion

To sum up, we report the synthesis and a systematic study of the fluorene-based donor–acceptor–donor hole transporting materials that are synthesized by simple and "green" chemistry. The impact of the different side-arm and acceptor fragments onto fluorene central core was revealed through the optical, electrochemical, photophysical, and photovoltaic measurements. It was found that the incorporation of the malononitrile acceptor units has been found to be beneficial for not only carrier transportation but also defects passivation via Pb–N interactions. The most efficient perovskite devices contained **V1359** reaching the PCE of over 22% and excellent long-term stability outperforming spiro-OMeTAD. In addition, we fabricated perovskite solar mini-modules (6.5 × 7 cm) exhibiting efficiency of 18.6%. The results of this study show that simple molecular engineering of hole transporting materials with an extra functionality contributes to the significant improvement of perovskite solar cell efficiency and stability.

Supporting Information

Supporting Information is available from the Wiley Online Library or from the author.

Acknowledgements

KR acknowledges funding from the Research Council of Lithuania via Grant no. 09.3.3-LMT-K-712-19-0061 and the funding received from the MJJ Foundation. This publication was made possible by NPRP grant No. NPRP11S-1231-170150 from the Qatar National Research Fund (a member of Qatar Foundation). Dr. E. Kamarauskas is acknowledged for ionization potential measurements.

Conflict of Interest

The authors declare no conflict of interest.

Data Availability Statement

The data that support the findings of this study are available on request from the corresponding author. The data are not publicly available due to privacy or ethical restrictions.

Keywords

defects passivation, donor-acceptor-donor, fluorene, malononitrile, perovskite solar cells

Received: July 20, 2022
Revised: September 20, 2022
Published online:

[1] H. Min, D. Y. Lee, J. Kim, G. Kim, K. S. Lee, J. Kim, M. J. Paik, Y. K. Kim, K. S. Kim, M. G. Kim, T. J. Shin, S. Il Seok, *Nature* **2021**, *598*, 444.
[2] J. Burschka, N. Pellet, S. J. Moon, R. Humphry-Baker, P. Gao, M. K. Nazeeruddin, M. Grätzel, *Nature* **2013**, *499*, 316.
[3] N. J. Jeon, J. H. Noh, W. S. Yang, Y. C. Kim, S. Ryu, J. Seo, S. Il Seok, *Nature* **2015**, *517*, 476.
[4] M. M. Lee, J. Teuscher, T. Miyasaka, T. N. Murakami, H. J. Snaith, *Science* **2012**, *338*, 643.
[5] C. Wehrenfennig, G. E. Eperon, M. B. Johnston, H. J. Snaith, L. M. Herz, *Adv. Mater.* **2014**, *26*, 1584.
[6] M. Saliba, T. Matsui, J. Y. Seo, K. Domanski, J. P. Correa-Baena, M. K. Nazeeruddin, S. M. Zakeeruddin, W. Tress, A. Abate, A. Hagfeldt, M. Grätzel, *Energy Environ. Sci.* **2016**, *9*, 1989.
[7] M. A. Green, A. Ho-Baillie, H. J. Snaith, *Nat. Photonics* **2014**, *8*, 506.
[8] B. Chen, Z. J. Yu, S. Manzoor, S. Wang, W. Weigand, Z. Yu, G. Yang, Z. Ni, X. Dai, Z. C. Holman, J. Huang, *Joule* **2020**, *4*, 850.
[9] W. S. Yang, B. W. Park, E. H. Jung, N. J. Jeon, Y. C. Kim, D. U. Lee, S. S. Shin, J. Seo, E. K. Kim, J. H. Noh, S. Il Seok, *Science* **2017**, *356*, 1376.
[10] W. W. Liu, T. H. Wu, M. C. Liu, W. J. Niu, Y. L. Chueh, *Adv. Mater. Interfaces* **2019**, *6*, 1801758.
[11] D. H. Kim, J. B. Whitaker, Z. Li, M. F. A. M. van Hest, K. Zhu, *Joule* **2018**, *2*, 1437.
[12] L. Qiu, L. K. Ono, Y. Qi, *Mater. Today Energy* **2018**, *7*, 169.
[13] Y. Rong, Y. Hu, A. Mei, H. Tan, M. I. Saidaminov, S. Il Seok, M. D. McGehee, E. H. Sargent, H. Han, *Challenges for commercializing perovskite solar cells*, Vol. *361*, American Association for the Advancement of Science, NY **2018**.
[14] K. Rakstys, C. Igci, M. K. Nazeeruddin, *Chem. Sci.* **2019**, *10*, 6748.
[15] C. Liu, Y. Yang, K. Rakstys, A. Mahata, M. Franckevicius, E. Mosconi, R. Skackauskaite, B. Ding, K. G. Brooks, O. J. Usiobo, J. N. Audinot, H. Kanda, S. Driukas, G. Kavaliauskaite, V. Gulbinas, M. Dessimoz, V. Getautis, F. De Angelis, Y. Ding, S. Dai, P. J. Dyson, M. K. Nazeeruddin, *Nat. Commun.* **2021**, *12*, 6394.
[16] A. R. Bin Mohd Yusoff, M. Vasilopoulou, D. G. Georgiadou, L. C. Palilis, A. Abate, M. K. Nazeeruddin, *Energy Environ. Sci.* **2021**, *14*, 2906.
[17] A. Mahapatra, D. Prochowicz, M. M. Tavakoli, S. Trivedi, P. Kumar, P. Yadav, *J. Mater. Chem. A* **2020**, *8*, 27.
[18] X. Liu, Z. Yu, T. Wang, K. L. Chiu, F. Lin, H. Gong, L. Ding, Y. Cheng, *Adv. Energy Mater.* **2020**, *10*, 2001958.
[19] Y. Cai, J. Cui, M. Chen, M. Zhang, Y. Han, F. Qian, H. Zhao, S. Yang, Z. Yang, H. Bian, T. Wang, K. Guo, M. Cai, S. Dai, Z. Liu, S. Liu, *Adv. Funct. Mater.* **2021**, *31*, 2005776.
[20] G. Sathiyan, A. A. Syed, C. Chen, C. Wu, L. Tao, X. Ding, Y. Miao, G. Li, M. Cheng, L. Ding, *Nano Energy* **2020**, *72*, 104673.
[21] F. Li, X. Deng, F. Qi, Z. Li, D. Liu, D. Shen, M. Qin, S. Wu, F. Lin, S. H. Jang, J. Zhang, X. Lu, D. Lei, C. S. Lee, Z. Zhu, A. K. Y. Jen, *J. Am. Chem. Soc.* **2020**, *142*, 20134.
[22] C. C. Boyd, R. Cheacharoen, T. Leijtens, M. D. McGehee, *Chem. Rev.* **2019**, *119*, 3418.
[23] S. G. Motti, D. Meggiolaro, S. Martani, R. Sorrentino, A. J. Barker, F. De Angelis, A. Petrozza, *Adv. Mater.* **2019**, *31*, 1901183.
[24] E. Aydin, M. De Bastiani, S. De Wolf, *Adv. Mater.* **2019**, *31*, 1900428.
[25] C. M. Wolff, P. Caprioglio, M. Stolterfoht, D. Neher, *Adv. Mater.* **2019**, *31*, 1902762.
[26] B. Wang, H. Wang, G. Sathiyan, C. Chen, Y. Xu, M. Cheng, *ACS Appl. Energy Mater.* **2022**, *5*, 5901.
[27] C. Igci, H. Kanda, S. M. Yoo, A. A. Sutanto, O. A. Syzgantseva, M. A. Syzgantseva, V. Jankauskas, K. Rakstys, M. Mensi, H. Kim, A. M. Asiri, M. K. Nazeeruddin, *Sol. RRL* **2022**, *6*, 2100667.
[28] K. Rakstys, J. Solovjova, T. Malinauskas, I. Bruder, R. Send, A. Sackus, R. Sens, V. Getautis, *Dye. Pigment* **2014**, *104*, 211.
[29] Y. Wang, Q. Chen, J. Fu, Z. Liu, Z. Sun, S. Zhang, Y. Zhu, X. Jia, J. Zhang, N. Yuan, Y. Zhou, B. Song, Y. Li, *Chem. Eng. J.* **2022**, *433*, 133265.
[30] Y. Li, F. Wu, M. Han, Z. Li, L. Zhu, Z. Li, *ACS Energy Lett.* **2021**, *6*, 869.
[31] H. Lu, J. Xu, X. Liu, F. Wu, L. Zhu, *Mater. Today Energy* **2021**, *21*, 100780.
[32] J. Yuan, Y. Chen, X. Liu, S. Xue, *ACS Appl. Energy Mater.* **2021**, *4*, 5756.
[33] Y. Sun, C. Zhao, J. Zhang, Y. Peng, R. Ghadari, L. Hu, F. Kong, *Synth. Met.* **2022**, *285*, 117027.
[34] Y. Wang, Q. Liao, J. Chen, W. Huang, X. Zhuang, Y. Tang, B. Li, X. Yao, X. Feng, X. Zhang, M. Su, Z. He, T. J. Marks, A. Facchetti, X. Guo, *J. Am. Chem. Soc.* **2020**, *142*, 16632.
[35] C. Igci, S. Paek, K. Rakstys, H. Kanda, N. Shibayama, V. Jankauskas, C. Roldán-Carmona, H. Kim, A. M. Asiri, M. K. Nazeeruddin, *Sol RRL* **2020**, *4*, 2000173.
[36] C. Liu, C. Igci, Y. Yang, O. A. Syzgantseva, M. A. Syzgantseva, K. Rakstys, H. Kanda, N. Shibayama, B. Ding, X. Zhang, V. Jankauskas, Y. Ding, S. Dai, P. J. Dyson, M. K. Nazeeruddin, *Angew. Chemie – Int. Ed.* **2021**, *60*, 20489.
[37] K. Rakstys, S. Paek, P. Gao, P. Gratia, T. Marszalek, G. Grancini, K. T. Cho, K. Genevicius, V. Jankauskas, W. Pisula, M. K. Nazeeruddin, *J. Mater. Chem. A* **2017**, *5*, 7811.

[38] B. Chen, P. N. Rudd, S. Yang, Y. Yuan, J. Huang, *Chem. Soc. Rev.* **2019**, *48*, 3842.
[39] F. Zhang, Z. Wang, H. Zhu, N. Pellet, J. Luo, C. Yi, X. Liu, H. Liu, S. Wang, X. Li, Y. Xiao, S. M. Zakeeruddin, D. Bi, M. Grätzel, *Nano Energy* **2017**, *41*, 469.
[40] F. Zhang, S. Wang, H. Zhu, X. Liu, H. Liu, X. Li, Y. Xiao, S. M. Zakeeruddin, *ACS Energy Lett.* **2018**, *3*, 1145.
[41] M. L. Petrus, A. Music, A. C. Closs, J. C. Bijleveld, M. T. Sirtl, Y. Hu, T. J. Dingemans, T. Bein, P. Docampo, *J. Mater. Chem. A* **2017**, *5*, 25200.
[42] M. L. Petrus, M. T. Sirtl, A. C. Closs, T. Bein, P. Docampo, *Mol. Syst. Des. Eng.* **2018**, *3*, 734.
[43] M. L. Petrus, K. Schutt, M. T. Sirtl, E. M. Hutter, A. C. Closs, J. M. Ball, J. C. Bijleveld, A. Petrozza, T. Bein, T. J. Dingemans, T. J. Savenije, H. Snaith, P. Docampo, *Adv. Energy Mater.* **2018**, *8*, 1614.
[44] D. Vaitukaityte, Z. Wang, T. Malinauskas, A. Magomedov, G. Bubniene, V. Jankauskas, V. Getautis, H. J. Snaith, *Adv. Mater.* **2018**, *30*, 1803735.
[45] M. Daskeviciene, S. Paek, Z. Wang, T. Malinauskas, G. Jokubauskaite, K. Rakstys, K. T. Cho, A. Magomedov, V. Jankauskas, S. Ahmad, H. J. Snaith, V. Getautis, M. K. Nazeeruddin, *Nano Energy* **2017**, *32*, 551.
[46] M. Daskeviciene, S. Paek, A. Magomedov, K. T. Cho, M. Saliba, A. Kizeleviciute, T. Malinauskas, A. Gruodis, V. Jankauskas, E. Kamarauskas, M. K. Nazeeruddin, V. Getautis, *J. Mater. Chem. C* **2019**, *7*, 2717.
[47] S. Daskeviciute, C. Momblona, K. Rakstys, A. A. Sutanto, M. Daskeviciene, V. Jankauskas, A. Gruodis, G. Bubniene, V. Getautis, M. K. Nazeeruddin, *J. Mater. Chem. A* **2021**, *9*, 301.
[48] S. Daskeviciute-Geguziene, Y. Zhang, K. Rakstys, G. Kreiza, S. B. Khan, H. Kanda, S. Paek, M. Daskeviciene, E. Kamarauskas, V. Jankauskas, A. M. Asiri, V. Getautis, M. K. Nazeeruddin, *Angew. Chemie – Int. Ed.* **2022**, *61*, e202113207.
[49] K. Rakstys, A. Abate, M. I. Dar, P. Gao, V. Jankauskas, G. Jacopin, E. Kamarauskas, S. Kazim, S. Ahmad, M. Grätzel, M. K. Nazeeruddin, *J. Am. Chem. Soc.* **2015**, *137*, 16172.
[50] D. Vaitukaityte, C. Momblona, K. Rakstys, A. A. Sutanto, B. Ding, C. Igci, V. Jankauskas, A. Gruodis, T. Malinauskas, A. M. Asiri, P. J. Dyson, V. Getautis, M. K. Nazeeruddin, *Chem. Mater.* **2021**, *33*, 6059.
[51] F. Liu, F. Wu, W. Ling, Z. Tu, J. Zhang, Z. Wei, L. Zhu, Q. Li, Z. Li, *ACS Energy Lett.* **2019**, *4*, 2514.
[52] K. Rakstys, S. Paek, G. Grancini, P. Gao, V. Jankauskas, A. M. Asiri, M. K. Nazeeruddin, *ChemSusChem* **2017**, *10*, 3825.
[53] A. Levy, P. U. Biedermann, I. Agranat, *Org. Lett.* **2000**, *2*, 1811.
[54] A. Matoliukstyte, E. Burbulis, J. V. Grazulevicius, V. Gaidelis, V. Jankauskas, *Synth. Met.* **2008**, *158*, 462.
[55] A. Jegorovė, C. Momblona, M. Daškevičienė, A. Magomedov, R. Degutyte, A. M. Asiri, V. Jankauskas, A. A. Sutanto, H. Kanda, K. Brooks, N. Klipfel, M. K. Nazeeruddin, V. Getautis, *Sol. RRL* **2022**, 2100990.
[56] C. Xiao, Q. Zhao, C. S. Jiang, Y. Sun, M. M. Al-Jassim, S. U. Nanayakkara, J. M. Luther, *Nano Energy* **2020**, *78*, 105319.
[57] G. J. A. H. Wetzelaer, M. Scheepers, A. M. Sempere, C. Momblona, J. Ávila, H. J. Bolink, *Adv. Mater.* **2015**, *27*, 1837.

ADVANCED FUNCTIONAL MATERIALS

Supporting Information

for *Adv. Funct. Mater.*, DOI: 10.1002/adfm.202208317

Passivating Defects of Perovskite Solar Cells with Functional Donor-Acceptor–Donor Type Hole Transporting Materials

Sarune Daskeviciute-Geguziene, Yi Zhang, Kasparas Rakstys, Chuanxiao Xiao, Jianxing Xia, Zhiheng Qiu, Maryte Daskeviciene, Tomas Paskevicius, Vygintas Jankauskas, Abdullah M. Asiri, Vytautas Getautis,* and Mohammad Khaja Nazeeruddin**

EXPERIMENTAL SECTION

Chemicals were purchased from Sigma-Aldrich, TCI Europe and BLDpharm and used as received without further purification. 2,2-bis(4-methoxyphenyl)acetaldehyde was synthesized as described in the literature.[1] ^{1}H NMR spectra were recorded at 400 MHz on a Bruker Avance III spectrometer with a 5 mm double resonance broad band BBO z-gradient room temperature probe, ^{13}C NMR spectra were collected using the same instrument at 101 MHz. The chemical shifts, expressed in ppm, were relative to tetramethylsilane (TMS). All the NMR experiments were performed at 25 °C. Reactions were monitored by thin-layer chromatography on ALUGRAM SIL G/UV254 plates and developed with UV light. Silica gel (grade 9385, 230–400 mesh, 60 Å, Aldrich) was used for column chromatography. Elemental analysis was performed with an Exeter Analytical CE-440 elemental analyzer, Model 440 C/H/N/. MS were recorded on Waters SQ Detector 2 Spectrometer using electrospray ionization (ESI) technique. FT-IR spectra were recorded by using a Perkin–Elmer Frontier spectrophotometer with a single reflectance horizontal ATR (Attenuated Total Reflectance) cell equipped with a diamond crystal. The data were recorded in the spectral range from 655 to 4000 cm^{-1} by accumulating 5 scans with a resolution of 4 cm^{-1}.

DETAILED SYNTHETIC PROCEDURES

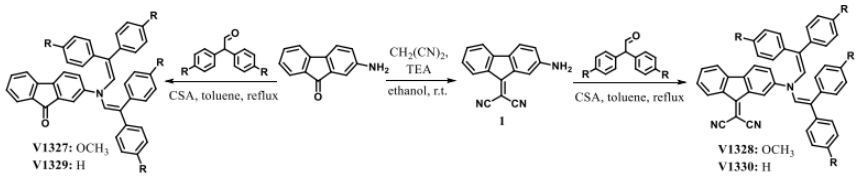

Figure S1. Synthesis pathway of single-substituted derivatives.

2-(2-amino-9*H*-fluoren-9-ylidene)malononitrile (1)

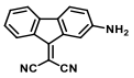

To a solution of the mixture of 2-amino-9-fluorenone (0.5 g, 2.6 mmol, 1 eq) and malononitrile (0.19 g, 2.8 mmol, 1.1 eq) in ethanol (3 mL) triethylamine (1 eq) was slowly dropped. The mixture

was stirred at 35 °C temperature for 16 hours. After completing the reaction, the resulting mixture was poured into water (7 mL), and the pH was adjusted to neutral by adding acetic acid. The precipitate was filtered off and washed with water and ethanol to collect **1** as a moss color solid (0.54 g, 87.1%). Spectral data is in agreement with the values reported in the literature.[2]

2-{bis[2,2-bis(4-methoxyphenyl)ethenyl]amino}-9*H*-fluoren-9-one (V1327)

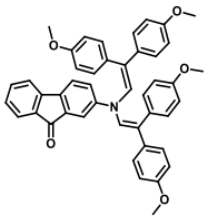

2-amino-9-fluorenone (1 g, 5.1 mmol, 1 eq) was dissolved in toluene (9 mL + volume of the Dean-Stark trap), (+/-)camphor-10-sulphonic acid (1.2 g, 5.1 mmol, 1 eq) was added and the mixture was heated at reflux for 20 minutes. Afterwards, 2,2-bis(4-methoxyphenyl)acetaldehyde (3.3 g, 12.8 mmol, 2.5 eq) was added and reflux was continued using a Dean-Stark trap for 10 minutes. After cooling to room temperature, the reaction mixture was extracted with ethyl acetate. The organic layer was dried over anhydrous Na_2SO_4, filtered and solvent evaporated. The crude product was purified by column chromatography using 3:22 v/v tetrahydrofuran/*n*-hexane as an eluent to collect **V1327** as a dark raspberry color solid (1.98 g, 57.6%). ^{1}H NMR (400 MHz, THF-d_6) δ 7.74 (d, J = 8.4 Hz, 1H), 7.58 – 7.50 (m, 3H), 7.44 (t, J = 7.6 Hz, 1H), 7.33 – 7.27 (m, 1H), 7.21 – 7.17 (m, 1H), 6.99 (d, J = 8.4 Hz, 4H), 6.87 (d, J = 8.4 Hz, 4H), 6.61 (d, J = 8.4 Hz, 4H), 6.46 (d, J = 8.4 Hz, 4H), 5.82 (s, 2H), 3.84 (s, 6H), 3.73 (s, 6H). ^{13}C NMR (101 MHz, THF) δ 190.58, 157.42, 145.56, 143.25, 134.80, 133.82, 132.74, 131.92, 130.50, 128.59, 126.96, 125.68, 124.12, 121.75, 118.86, 117.66, 111.93, 110.93, 109.51, 52.76, 52.52. FTIR ν (cm^{-1}): 3000 ($CH_{arom.}$); 2932, 2834 ($CH_{alif.}$); 1712 (C=O); 1239 (C-O-C). Anal. calcd for $C_{45}H_{37}NO_5$: C, 80.46; H, 5.55; N, 2.09; found: C, 80.67; H, 5.51; N, 2.11. $C_{45}H_{37}NO_5[M^+]$ exact mass = 671.27, MS (ESI) = 672.21.

2-/2-{bis[2,2-bis(4-methoxyphenyl)ethenyl]amino}-9*H*-fluoren-9-ylidene/malononitrile (V1328)

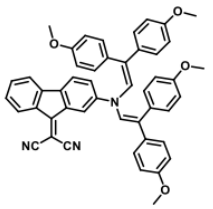

Compound **1** (0.5 g, 2.1 mmol, 1 eq) was dissolved in toluene (5 mL + volume of the Dean-Stark trap), (+/-)camphor-10-sulphonic acid (0.48 g, 2.1 mmol, 1 eq) was added and the mixture was heated at reflux for 20 minutes. Afterwards, 2,2-bis(4-methoxyphenyl)acetaldehyde (1.3 g, 5.1 mmol, 2.5 eq) was added and reflux was continued using a Dean-Stark trap for 20 minutes. After cooling to room temperature, the obtained product was filtered off and washed with water and ethanol. The product was recrystallized from acetone/THF/ethanol 3:1:1 to collect **V1328** as green crystals (1 g, 67.6%). ^{1}H NMR (400 MHz, THF-d_6) δ 8.28 (d, J = 8.0 Hz, 1H), 8.14 (s, 1H), 7.56 (d, J = 8.0 Hz, 2H), 7.45 (t, J = 7.6 Hz, 1H), 7.27 – 7.15 (m, 2H), 7.00 (d, J = 8.4 Hz, 4H), 6.85 (d, J = 8.4 Hz, 4H), 6.63 (d, J = 8.5 Hz, 4H), 6.50 (d, J = 8.5 Hz, 4H), 5.85 (s, 2H), 3.81 (s, 6H), 3.71 (s, 6H). ^{13}C NMR (101 MHz, THF) δ 160.93, 159.21, 147.37, 143.20, 135.47, 134.67, 134.07, 133.77, 132.68, 132.23, 130.46, 128.88, 127.52, 126.30, 126.04, 121.49, 119.89, 114.85, 113.71, 112.75, 75.94, 54.59, 54.32. FTIR ν (cm^{-1}): 3009 ($CH_{arom.}$); 2956, 2838 ($CH_{alif.}$); 2223 (CN); 1238 (C-O-C). Anal. calcd for $C_{48}H_{37}N_3O_4$: C, 80.09; H, 5.18; N, 5.84; found: C, 80.27; H, 5.15; N, 5.81. $C_{48}H_{37}N_3O_4$ [M^+] exact mass = 719.28, MS (ESI) = 720.29.

2-[bis(2,2-diphenylethenyl)amino]-9*H*-fluoren-9-one (V1329)

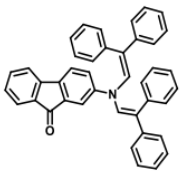

2-amino-9-fluorenone (0.5 g, 2.6 mmol, 1 eq) was dissolved in toluene (5 mL + volume of the Dean-Stark trap), (+/-)camphor-10-sulphonic acid (0.59 g, 2.6 mmol, 1 eq) was added and the mixture was heated at reflux for 20 minutes. Afterwards, diphenylacetaldehyde (1.3 g, 6.4 mmol, 2.5 eq) was added and reflux was continued using a Dean-Stark trap for 35 minutes. After cooling to room

temperature, the obtained product was filtered off and washed with water and ethanol. The product was recrystallized from toluene to collect **V1329** as dark raspberry color crystals (1.1 g, 78.1%). ^{1}H NMR (400 MHz, THF-d_6) δ 7.61 – 7.52 (m, 3H), 7.46 (t, J = 7.6 Hz, 1H), 7.38 – 7.29 (m, 7H), 7.26 – 7.16 (m, 4H), 7.15 – 7.11 (m, 4H), 7.08 – 7.01 (m, 4H), 6.49 (d, J = 7.6 Hz, 4H), 5.98 (s, 2H). ^{13}C NMR (101 MHz, THF) δ 190.42, 145.05, 143.07, 139.18, 138.14, 133.82, 132.78, 131.34, 127.63, 126.84, 126.62, 125.84, 124.86, 123.21, 121.81, 119.56, 119.42, 117.82, 110.04. FTIR ν (cm^{-1}): 3055, 3022 ($CH_{arom.}$); 1713 (C=O). Anal. calcd for $C_{41}H_{29}NO$: C, 89.26; H, 5.30; N, 2.54; found: C, 89.17; H, 5.34.; N, 2.51. $C_{41}H_{29}NO$ [M^+] exact mass = 551.22, MS (ESI) = 552.24.

2-{2-[bis(2,2-diphenylethenyl)amino]-9*H*-fluoren-9-ylidene}malononitrile (V1330)

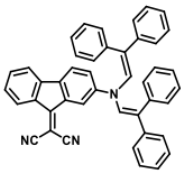

Compound **1** (0.5 g, 2.1 mmol, 1 eq) was dissolved in toluene (5 mL + volume of the Dean-Stark trap), (+/-)camphor-10-sulphonic acid (0.48 g, 2.1 mmol, 1 eq) was added and the mixture was heated at reflux for 20 minutes. Afterwards, diphenylacetaldehyde (1 g, 5.1 mmol, 2.5 eq) was added and reflux was continued using a Dean-Stark trap for 20 minutes. After cooling to room temperature, the obtained product was filtered off and washed with water and ethanol. The product was recrystallized from acetone to collect **V1330** as green color crystals (0.8 g, 65.1%). ^{1}H NMR (400 MHz, THF-d_6) δ 8.26 (d, J = 7.8 Hz, 1H), 8.16 (s, 1H), 7.59 (d, J = 7.8 Hz, 2H), 7.46 (t, J = 7.4 Hz, 1H), 7.34 – 7.21 (m, 8H), 7.15 – 7.01 (m, 10H), 6.55 (d, J = 7.6 Hz, 4H), 6.01 (s, 2H). ^{13}C NMR (101 MHz, THF) δ 158.83, 144.95, 141.08, 139.22, 137.97, 133.59, 133.53, 132.85, 131.41, 127.66, 126.49, 125.90, 125.53, 125.28, 124.82, 120.42, 119.64, 118.22, 113.70, 111.18, 74.30. FTIR ν (cm^{-1}): 3057, 3023 ($CH_{arom.}$); 2225 (CN). Anal. calcd for $C_{44}H_{29}N_3$: C, 88.12; H, 4.87; N, 7.01; found: C, 88.37; H, 4.84.; N, 6.91. $C_{44}H_{29}N_3$ [M^+] exact mass = 599.24, MS (ESI) = 600.17.

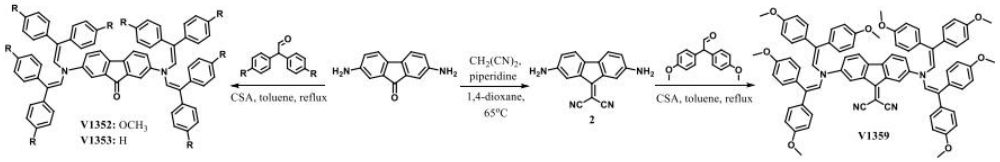

Figure S2. Synthesis pathway of double-substituted derivatives.

2-(2,7-diamino-9*H*-fluoren-9-ylidene)malononitrile (2)

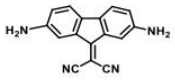

A solution of 2,7-diamino-9-fluorenone (0.5 g, 2.4 mmol, 1 eq) and malononitrile (0.79 g, 11.1 mmol, 5 eq) in anhydrous 1,4-dioxane (6 mL) was purged with argon for 10 minutes. Afterwards, was slowly dropped piperidine (2 eq). The mixture was stirred at 65 °C temperature for 22 hours. After cooling to room temperature, the obtained product was filtered off and washed with ethanol to collect **2** as a moss color solid. (0.48 g, 78.2%). ^{1}H NMR (400 MHz, THF-d_6) δ ^{1}H NMR (400 MHz, THF) δ 7.48 (s, 2H), 7.00 (d, J = 8.2 Hz, 2H), 6.54 (d, J = 8.2 Hz, 2H), 2.91 (s, 4H). ^{13}C NMR (101 MHz, THF) δ 163.01, 148.24, 135.09, 132.94, 119.51, 119.02, 113.64, 112.42, 73.66. FTIR ν (cm^{-1}): 3566, 3419, 3326 (NH_2); 3210 ($CH_{arom.}$); 2225 (CN).

2,7-bis{bis[2,2-bis(4-methoxyphenyl)ethenyl]amino}-9*H*-fluoren-9-one (V1352)

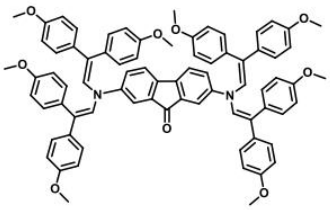

2,7-diamino-9-fluorenone (0.5 g, 2.4 mmol, 1 eq) was dissolved in toluene (7 mL + volume of the Dean-Stark trap), (+/-)camphor-10-sulphonic acid (0.55 g, 2.4 mmol, 1 eq) was added and the mixture was heated at reflux for 20 minutes. Afterwards, 2,2-bis(4-methoxyphenyl)acetaldehyde (3 g, 11.9 mmol, 5 eq) was added and reflux was continued using a Dean-Stark trap for 40 minutes. After cooling to room temperature, the reaction mixture was precipitated into 15 times excess of

ethanol. The obtained product was filtered off and washed with water and ethanol. The crude product was purified by column chromatography using 1:4 v/v THF/*n*-hexane as an eluent to collect **V1352** as a dark green solid (1.8 g, 65.2%). ^{1}H NMR (400 MHz, THF-d_6) δ 7.46 (d, J = 8.2 Hz, 2H), 7.26 (s, 2H), 7.15 (d, J = 8.2 Hz, 2H), 6.99 (d, J = 8.2 Hz, 8H), 6.87 (d, J = 8.2 Hz, 8H), 6.62 (d, J = 8.2 Hz, 8H), 6.46 (d, J = 8.2 Hz, 8H), 5.80 (s, 4H), 3.83 (s, 12H), 3.70 (s, 12H). ^{13}C NMR (101 MHz, THF) δ 192.53, 159.50, 146.35, 137.65, 135.65, 133.91, 131.96, 130.47, 128.79, 126.00, 120.40, 113.77, 112.76, 54.62, 54.37. FTIR ν (cm^{-1}): 3034 ($CH_{arom.}$); 2997, 2930, 2833 ($CH_{alif.}$); 1714 (C=O); 1239 (C-O-C). Anal. calcd for $C_{77}H_{66}N_2O_9$: C, 79.50; H, 5.72; N, 2.41; found: C, 79.66; H, 5.68.; N, 2.47. $C_{77}H_{66}N_2O_9$ [M^+] exact mass = 1162.46, MS (ESI) = 1162.97.

2,7-bis[bis(2,2-diphenylethenyl)amino]-9*H*-fluoren-9-one (V1353)

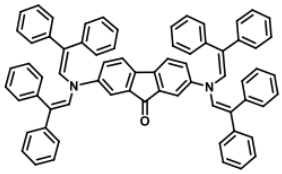

2,7-diamino-9-fluorenone (0.5 g, 2.4 mmol, 1 eq) was dissolved in toluene (6 mL + volume of the Dean-Stark trap), (+/-)camphor-10-sulphonic acid (0.55 g, 2.4 mmol, 1 eq) was added and the mixture was heated at reflux for 20 minutes. Afterwards, diphenylacetaldehyde (2.3 g, 11.9 mmol, 5 eq) was added and reflux was continued using a Dean-Stark trap for 15 minutes. After cooling to room temperature, the obtained product was filtered off and washed with water and ethanol. The product was recrystallized from toluene to collect **V1353** as green crystals (1.4 g, 63.6%). ^{1}H NMR (400 MHz, THF-d_6) δ 7.51 (d, J = 8.2 Hz, 2H), 7.38 – 7.26 (m, 14H), 7.20 (d, J = 8.2 Hz, 2H), 7.14 – 6.99 (m, 20H), 6.48 (d, J = 7.6 Hz, 8H), 5.96 (s, 4H). ^{13}C NMR (101 MHz, THF) δ 190.40, 144.11, 139.26, 138.15, 136.28, 131.01, 127.66, 126.59, 125.82, 124.79, 119.99, 118.74, 110.39. FTIR ν (cm^{-1}): 3081, 3054, 3022 ($CH_{arom.}$); 1712 (C=O). Anal. calcd for $C_{69}H_{50}N_2O$: C, 89.77; H, 5.46; N, 3.03; found: C, 89.66; H, 5.48.; N, 3.07. $C_{69}H_{50}N_2O$ [M^+] exact mass = 922.32, MS (ESI) = 923.35.

2-/2,7-bis{bis[2,2-bis(4-methoxyphenyl)ethenyl]amino}-9*H*-fluoren-9-ylidene/malononitrile (V1359)

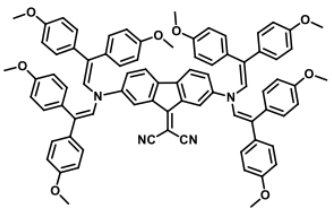

Compound **2** (0.4 g, 1.5 mmol, 1 eq) was dissolved in toluene (6 mL + volume of the Dean-Stark trap), (+/-)camphor-10-sulphonic acid (0.36 g, 1.5 mmol, 1 eq) was added and the mixture was heated at reflux for 20 minutes. Afterwards, 2,2-bis(4-methoxyphenyl)acetaldehyde (2 g, 7.7 mmol, 5 eq) was added and reflux was continued using a Dean-Stark trap for 25 minutes. After cooling to room temperature, the reaction mixture was precipitated into 15 times excess of ethanol. The obtained product was filtered off and washed with water and ethanol. The crude product was purified by column chromatography using 1:3 v/v THF/*n*-hexane as an eluent to collect **V1359** as a green solid (1.2 g, 64.2%). ^{1}H NMR (400 MHz, THF-d_6) δ 8.05 (s, 2H), 7.45 (d, J = 8.4 Hz, 2H), 7.15 (d, J = 8.4 Hz, 2H), 6.99 (d, J = 8.4 Hz, 8H), 6.84 (d, J = 8.4 Hz, 8H), 6.62 (d, J = 8.8 Hz, 8H), 6.48 (d, J = 8.8 Hz, 8H), 5.81 (s, 4H), 3.82 (s, 12H), 3.70 (s, 12H). ^{13}C NMR (101 MHz, THF) 161.35, 159.14, 146.23, 135.32, 133.89, 132.29, 130.49, 128.84, 126.11, 121.85, 120.53, 115.11, 113.69, 112.73, 75.78, 54.60, 54.31. FTIR ν (cm^{-1}): 3034 ($CH_{arom.}$); 2997, 2931, 2833 ($CH_{alif.}$); 2225 (CN); 1238 (C-O-C). Anal. calcd for $C_{80}H_{66}N_4O_8$: C, 79.32; H, 5.49; N, 4.62; found: C, 79.56; H, 5.48; N, 4.67. $C_{80}H_{66}N_4O_8$ [M^+] exact mass = 1210.49, MS (ESI) = 1211.10.

ROYAL SOCIETY OPEN SCIENCE

royalsocietypublishing.org/journal/rsos

Research

Cite this article: Daskeviciute-Geguziene S, Daskeviciene M, Kantminienė K, Jankauskas V, Kamarauskas E, Gruodis A, Karazhanov S, Getautis V. 2024 Design, synthesis and theoretical simulations of novel spiroindane-based enamines as *p*-type semiconductors. *R. Soc. Open Sci.* **11**: 232019.
https://doi.org/10.1098/rsos.232019

Received: 11 January 2024
Accepted: 27 February 2024

Subject Category:
Chemistry

Subject Areas:
organic chemistry, computational chemistry, materials science

Keywords:
spirobisindane, enamines, hole-transporting materials, solar cells

Author for correspondence:
Vytautas Getautis
e-mail: vytautas.getautis@ktu.lt

This article has been edited by the Royal Society of Chemistry, including the commissioning, peer review process and editorial aspects up to the point of acceptance.

Electronic supplementary material is available online at https://doi.org/10.6084/m9.figshare.c.7123857.

ROYAL SOCIETY OF CHEMISTRY

THE ROYAL SOCIETY PUBLISHING

Design, synthesis and theoretical simulations of novel spiroindane-based enamines as *p*-type semiconductors

Sarune Daskeviciute-Geguziene[1], Maryte Daskeviciene[1], Kristina Kantminienė[2], Vygintas Jankauskas[3], Egidijus Kamarauskas[3], Alytis Gruodis[3], Smagul Karazhanov[4] and Vytautas Getautis[1]

[1]Department of Organic Chemistry, and [2]Department of Physical and Inorganic Chemistry, Kaunas University of Technology, Kaunas, 50254, Lithuania
[3]Institute of Chemical Physics, Vilnius University, Vilnius, 10257, Lithuania
[4]Institute for Energy Technology (IFE), Kjeller 2027, Norway

KK, 0000-0002-0266-8608

The search for novel classes of hole-transporting materials (HTMs) is a very important task in advancing the commercialization of various photovoltaic devices. Meeting specific requirements, such as charge-carrier mobility, appropriate energy levels and thermal stability, is essential for determining the suitability of an HTM for a given application. In this work, two spirobisindane-based compounds, bearing terminating hole transporting enamine units, were strategically designed and synthesized using commercially available starting materials. The target compounds exhibit adequate thermal stability; they are amorphous and their glass-transition temperatures (>150°C) are high, which minimizes the probability of direct layer crystallization. V1476 stands out with the highest zero-field hole-drift mobility, approaching 1×10^{-5} cm^2 V s^{-1}. To assess the compatibility of the highest occupied molecular orbital energy levels of the spirobisindane-based HTMs in solar cells, the solid-state ionization potential (I_p) was measured by the electron photoemission in air of the thin-film method. The favourable morphological properties, energy levels and hole mobility in combination with a simple synthesis make V1476 and related compounds promising materials for HTM applications in antimony-based solar cells and triple-cation-based perovskite solar cells.

1. Introduction

Since the use of the first device incorporating an organic semiconductor (OS) in the latter part of the twentieth century [1], a number of innovative devices using organic materials for charge transport have been developed. These include organic field-effect transistors (OFETs) [2], organic light-emitting diodes (OLEDs) [3] and various types of organic or hybrid solar cells (SCs) [4–6]. Typically, these devices comprise multiple layers of OSs, each serving a distinct function, such as light emission, light absorption and charge transfer [6,7].

In recent decades, antimony- and triple-cation-based SCs have been significantly improved, resulting in notably enhanced efficiencies. Hole-transporting materials (HTMs) play a pivotal role in all types of SCs as they transport photogenerated holes to contact [8,9]. High hole-drift mobility, appropriate energy levels and the capacity to create high-quality thin films are essential attributes of effective HTMs [10–12]. Small molecules as HTMs have attracted a lot of attention due to their well-defined structures, facile synthesis/purification, high chemical purity and reproducible film forming ability [13,14]. Until recently, the organic low-molecular-mass spiro-OMeTAD, derived from 9,9′-spirobifluorene, has been central to the development of highly efficient SCs. The following factors are characteristic of spiro-OMeTAD. (i) It has a large band gap (approx. 3.0 eV) and a relatively deep-lying HOMO energy level, which provides good electronic alignment with the perovskite layers; its band gap can be further tuned to the electronic structure of a chosen perovskite [15,16]. (ii) Spiro-OMeTAD benefits from a thoroughly researched synthesis and solution method, making it advantageous for manufacturing both rigid and flexible SCs on a large scale. (iii) Its high melting point contributes to the thermal stability of a device [17,18]. (iv) Pure spiro-OMeTAD hole transporting layer (HTL) exhibits low conductivity and hole mobility [19]. A commonly used method includes the use of additives, such as 4-*tert*-butylpyridine (TBP) and LiTFSI, to enhance electrical properties of spiro-OMeTAD films [20–22]. For these reasons, HTMs based on spiro-OMeTAD undeniably have a significant impact on the advancement of antimony-based and triple-cation-based SCs.

Despite its numerous advantages, the crystallization tendency of spiro-OMeTAD, owing to the symmetry of its central spirobifluorene fragment [23], limits its ability to form films, potentially impacting device stability [24]. Taking into account this criterion, a logical approach involves removing two arms of the spirobifluorene core [25] to transform it into the spirobisindane core [26] with reduced symmetry. Additionally, the advantages of spirobisindane are its synthesis from a cheap commercially available bisphenol A in high yield and simple purification.

It is imperative to synthesize new OSs via simple and green chemistry methods without compromising the efficiency of the solar cell [27–29]. One of the approaches is the preparation of enamines by a facile condensation reaction because condensation chemistry offers a promising alternative to palladium-catalysed reactions since it produces water as the only by-product and eliminates the need for expensive catalysts. In addition, it includes facile product workup and purification [30–32]. Furthermore, enamines have been successfully applied in antimony- or triple-cation-based SCs with and without additives, showing excellent efficiency and long-term stability [32–34].

This study is devoted to further exploration of the enamine family HTMs using spirobisindane as the central core. By combining different aniline substituents, two spirobisindane-based HTMs shown in figure 1 were designed and synthesized from commercially available compounds without the use of costly metal catalysts. The optical, thermal and electrophysical properties of V1476 and V1481 were thoroughly investigated. Both HTMs exhibited high thermal stability and relatively high hole-drift mobility, making them viable candidates for application as HTMs in SCs. Density functional theory (DFT) Cam-B3LYP method and 6-31G(d) basis set (supplemented with polarization functions (d)) were used for ground-state optimization that supplemented the experimental study.

2. Experimental section

2.1. Chemical reagents and instruments

Information about chemical reagents used for synthesis of the target compounds V1476 and V1481 and instruments used for their characterization is provided in the electronic supplementary material.

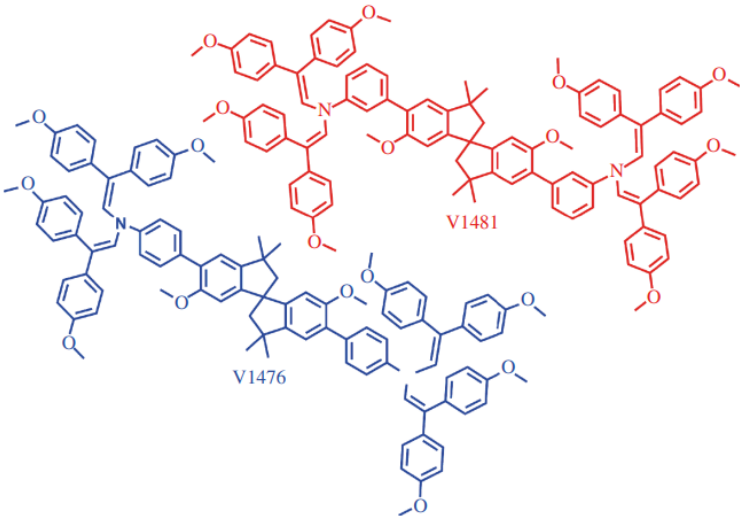

Figure 1. Chemical structures of the synthesized hole-transporting materials V1476 and V1481.

2.2. Synthesis

2.2.1. 3,3,3′,3′-Tetramethyl-1,1′-spirobisindane-6,6′-diol (**1**), 6,6′-dimethoxy-3,3,3′,3′-tetramethyl-1,1′-spirobisindane (**2**) and 5,5′-dibromo-6,6′-dimethoxy-3,3,3′,3′-tetramethyl-1,1′-spirobisindane (**3**)

3,3,3′,3′-Tetramethyl-1,1′-spirobisindane-6,6′-diol (**1**), 6,6′-dimethoxy-3,3,3′,3′-tetramethyl-1,1′-spirobisindane (**2**) and 5,5'-dibromo-6,6′-dimethoxy-3,3,3′,3′-tetramethyl-1,1′-spirobisindane (**3**) were prepared according to the synthesis procedures described in [35]. Detailed synthesis procedures are provided in the electronic supplementary material.

2.2.2. 5,5′-Bis(4-aminophenyl)-6,6′-dimethoxy-3,3,3′,3′-tetramethyl-1,1′-spirobisindane (**4**)

A mixture of **3** (1 g, 2 mmol, 1 eq) and 4-(4,4,5,5-tetramethyl-1,3,2-dioxaborolan-2-yl)aniline (1 g, 4.5 mmol, 2.2 eq) in 40 ml of anhydrous solvent mixture of tetrahydrofuran (THF) and toluene (1:1) was purged with argon for 10 min. Afterwards, sodium hydroxide (1.2 g, 30.3 mmol, 15 eq) and $PdCl_2(PPh_3)_2$ (0.7 g, 1 mmol, 0.5 eq) were added, and the reaction mixture was heated under reflux under argon atmosphere for 23 h. After the reaction mixture was cooled to room temperature, it was filtered, and solvent was evaporated *in vacuo*. The crude product was purified by column chromatography (THF/*n*-hexane; 8:17 v/v) to obtain **4** as a pale yellow solid. Yield 0.94 g (89.5%). ^{1}H NMR (400 MHz, DMSO-d_6) δ 7.18 (*d*, *J* = 8.2 Hz, 4H), 7.05 (*s*, 2H), 6.59 (*d*, *J* = 8.2 Hz, 4H), 6.39 (*s*, 2H), 5.03 (*s*, 4H), 3.58 (*s*, 6H), 2.32 (*d*, *J* = 12.8 Hz, 2H), 2.22 (*d*, *J* = 12.8 Hz, 2H), 1.39 (*s*, 6H), 1.32 (*s*, 6H). ^{13}C NMR (101 MHz, DMSO) δ 156.46, 149.21, 147.92, 144.56, 130.39, 130.32, 126.46, 123.54, 113.87, 107.12, 59.66, 58.08, 56.21, 42.99, 31.94, 30.90.

2.2.3. 5,5′-Bis/{4[(4-methoxyphenyl)etenyl]amino}phenyl/-6,6′-dimethoxy-3,3,3′,3′-tetramethyl-1,1′-spirobisindane (**V1476**)

To a solution of **4** (0.6 g, 1.2 mmol, 1 eq) in THF (5 ml + volume of the Dean–Stark trap), (+/−)camphor-10-sulfonic acid (0.27 g, 1.2 mmol, 1 eq) was added, and the reaction mixture was heated under reflux for 20 min. Afterwards, 2,2-bis(4-methoxyphenyl)acetaldehyde (1.8 g, 6.9 mmol, 6 eq) was added, and heating under reflux was continued with the removal of water using a Dean–Stark trap for 40 min. After cooling down, the reaction mixture was poured into 15-fold excess of ethanol. The obtained precipitate was filtered off and washed with water and ethanol. The crude product was purified by column chromatography (THF/*n*-hexane; 6.5:18.5 v/v) to obtain V1476 as a yellow solid.

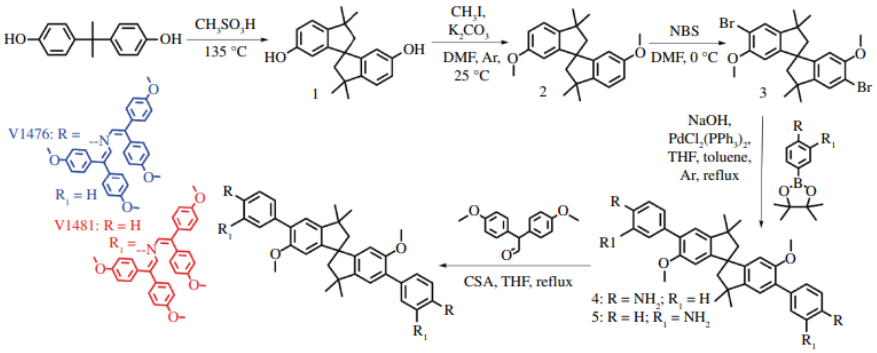

Figure 2. Synthesis route towards the target hole-transporting materials V1476 and V1481.

Yield 1.05 g (61.8%). ^{1}H NMR (400 MHz, DMSO-d_6) δ 7.41 (*d*, *J* = 8.0 Hz, 4H), 7.09 (*s*, 2H), 7.00 (*d*, *J* = 8.0 Hz, 4H), 6.94–6.83 (*m*, 16H), 6.64 (*d*, *J* = 8.6 Hz, 8H), 6.42 (*s*, 2H), 6.38 (*d*, *J* = 8.6 Hz, 8H), 5.71 (*s*, 4H), 3.81 (*s*, 12H), 3.68 (*s*, 12H), 3.57 (*s*, 6H), 2.31 (*d*, *J* = 12.6 Hz, 2H), 2.24 (*d*, *J* = 12.6 Hz, 2H), 1.37 (*s*, 6H), 1.32 (*s*, 6H). ^{13}C NMR (101 MHz, DMSO) δ 159.24, 158.90, 156.49, 150.14, 144.67, 134.06, 132.38, 130.79, 130.60, 129.52, 128.80, 126.59, 116.22, 114.46, 113.55, 107.09, 59.53, 58.24, 56.18, 55.75, 55.49, 43.03, 31.93, 30.84. Anal. calcd for $C_{99}H_{94}N_2O_{10}$: C, 80.79; H, 6.44; N, 1.9; found: C, 80.55; H, 6.49; N, 1.9. $C_{99}H_{94}N_2O_{10}$ [M^+] exact mass = 1470.69, MS (ESI) = 1472.10.

2.2.4. 5,5′-Bis(3-aminophenyl)-6,6′-dimethoxy-3,3,3′,3′-tetramethyl-1,1′-spirobisindane (**5**)

A mixture of **3** (0.7 g, 1.4 mmol, 1 eq) and 3-(4,4,5,5-tetramethyl-1,3,2-dioxaborolan-2-yl)aniline (0.7 g, 3.1 mmol, 2.2 eq) in 28 ml of anhydrous solvent mixture of THF and toluene (1:1) was purged with argon for 10 min. Afterwards, sodium hydroxide (0.9 g, 21.2 mmol, 15 eq) and $PdCl_2(PPh_3)_2$ (0.5 g, 0.7 mmol, 0.5 eq) were added, and the solution was heated under reflux under argon atmosphere for 22 h. After cooling down, the reaction mixture was filtered and solvent was evaporated *in vacuo*. The crude product was purified by column chromatography (THF/*n*-hexane; 2:3 v/v) to obtain **5** as a pale yellow solid. Yield 0.68 g (93.2%). ^{1}H NMR (400 MHz, DMSO-d_6) δ 7.08 (*s*, 2H), 7.03 (*t*, *J* = 7.6 Hz, 2H), 6.69 (*s*, 2H), 6.62 (*d*, *J* = 7.4 Hz, 2H), 6.52 (*d*, *J* = 7.4 Hz, 2H), 6.44 (*s*, 2H), 5.03 (*s*, 4H), 3.59 (*s*, 6H), 2.34 (*d*, *J* = 13.0 Hz, 2H), 2.26 (*d*, *J* = 13.0 Hz, 2H), 1.41 (*s*, 6H), 1.34 (*s*, 6H). ^{13}C NMR (101 MHz, DMSO) δ 156.55, 150.14, 148.69, 144.47, 139.85, 130.75, 128.74, 124.09, 117.69, 115.55, 112.82, 107.15, 59.57, 58.19, 56.25, 43.02, 31.94, 30.87.

2.2.5. 5,5′-Bis/{3[(4-methoxyphenyl)etenyl]amino}phenyl/-6,6′-dimethoxy-3,3,3′,3′-tetramethyl-1,1′-spirobisindane (**V1481**)

To a solution of **5** (0.6 g, 1.2 mmol, 1 eq) in THF (5 ml + volume of the Dean–Stark trap), (+/−)camphor-10-sulfonic acid (0.27 g, 1.2 mmol, 1 eq) was added, and the reaction mixture was heated under reflux for 20 min. Afterwards, 2,2-bis(4-methoxyphenyl)acetaldehyde (1.8 g, 6.9 mmol, 6 eq) was added, and heating under reflux was continued with the removal of water using a Dean–Stark trap for 40 min. After cooling down, the reaction mixture was poured into 15-fold excess of ethanol. The formed precipitate was filtered off and washed with water and ethanol. The crude product was purified by column chromatography (THF/*n*-hexane; 6.5:18.5 v/v) to obtain V1481 as a yellow solid. Yield 1.08 g (63.3%). ^{1}H NMR (400 MHz, DMSO-d_6) δ 7.32 (*t*, *J* = 7.8 Hz, 2H), 7.16–7.03 (*m*, 6H), 6.97–6.81 (*m*, 18H), 6.63 (*d*, *J* = 8.4 Hz, 8H), 6.46–6.30 (*m*, 10H), 5.73 (*s*, 4H), 3.78 (*s*, 12H), 3.67 (*s*, 12H), 3.52 (*s*, 6H), 2.29 (*d*, *J* = 12.8 Hz, 2H), 2.17 (*d*, *J* = 12.8 Hz, 2H), 1.34 (*s*, 6H), 1.27 (*s*, 6H). ^{13}C NMR (101 MHz, DMSO) δ 159.20, 158.85, 156.42, 150.63, 145.68, 144.68, 140.27, 134.08, 132.39, 130.68, 130.59, 129.77, 128.75, 126.77, 118.07, 114.46, 113.54, 107.34, 59.46, 58.29, 56.23, 55.72, 55.47, 43.01, 31.88, 30.80. Anal. calcd for $C_{99}H_{94}N_2O_{10}$: C, 80.79; H, 6.44; N, 1.9; found: C, 80.59; H, 6.48; N, 1.9. $C_{99}H_{94}N_2O_{10}$ [M^+] exact mass = 1470.69, MS (ESI) = 1472.18.

3. Results and discussion

3.1. Synthesis

The overall synthesis procedure for the preparation of new HTMs V1476 and V1481 is depicted in figure 2. A readily available low-cost bisphenol A is used as a starting compound. In the simple initial cyclization step, bisphenol A was heated in methanesulfonic acid. Next, spirobisindane (**1**) was alkylated using iodomethane and a base in dimethylformamide as a solvent at room temperature. The intermediate product **2** was then brominated using *N*-bromosuccinimide, eliminating the need for aggressive bromine. To obtain enamines, an amino group was introduced into the molecule through an aqueous/THF/toluene twofold Suzuki cross-coupling procedure to yield precursors **4** and **5** with different benzene substitutions at the *para* and *meta* positions. Subsequently, the aminated precursors were condensed with the commercially available reagent 2,2-bis(4-methoxyphenyl)acetaldehyde in the presence of camphor sulfonic acid to produce the target products V1476 and V1481. Water was the only by-product, which was removed from the reaction mixture using a Dean–Stark trap. The chemical structures of the synthesized compounds were confirmed based on the ^{1}H NMR, mass spectrometry, and elemental analysis data (electronic supplementary material, figures S1 and S2). It should be noted that attempts to synthesize the target analogue with the amino group at the *ortho* position failed. Presumably, steric hindrance prevented the formation of such an enamine derivative.

3.2. Thermal and optical properties

The thermal characteristics of the HTMs were evaluated by thermogravimetric analysis (TGA) (figure 3*a*) and differential scanning calorimetry (DSC) (figure 3*b*) measurements. Understanding these characteristics is crucial, especially in the context of processing temperatures, as they can potentially impact the long-term stability of SCs. TGA has revealed that V1476 exhibits higher thermal stability with a decomposition temperature (T_{dec}) of 403°C at 5% weight loss than *meta*-substituted HTM V1481 (T_{dec} = 389°C). Notably, both synthesized enamines possess higher T_{dec} than that of spiro-OMeTAD (T_{dec} = 288°C) [23]. The DSC measurements were employed to identify the thermal changes in the new HTMs. The results have demonstrated that the new compounds are entirely non-crystalline with only a glass transition temperature (T_g) recorded (V1476 T_g = 167°C and V1481 T_g = 157°C). Interestingly, T_g of both synthesized HTMs are higher than that of spiro-OMeTAD (T_g = 124°C), indicating that the spirobisindane-based HTMs are likely to possess better morphological stability. Furthermore, it is worth noting that spiro-OMeTAD is not fully amorphous; it has a crystallization temperature and a melting point, factors that can compromise the long-term stability of SCs [23].

The ultraviolet–visible (UV–Vis) absorption spectra of spirobisindane-based HTMs were recorded in THF solutions and are depicted in figure 4*a*. Two major absorption peaks at approximately 265 and 360 nm are present in the spectra of both HTMs. The absorption peak at 265 nm corresponds to the localized π–π^* transitions originating from the central spirobisindane scaffold. The more intensive delocalization of the different conjugated substituents (*meta* and *para*) gives rise to longer wavelength peaks and indicates conjugated π–π^* and n–π^* transitions. The significant changes in molecular geometry of the synthesized molecules upon excitation have been proven by the presence of peaks at 500 nm, showing markedly large Stokes shifts of approximately 150 nm, in the photoluminescence spectra of both compounds. The optical gaps (E_g) of new HTMs were calculated from the crossing of absorption and photoluminescence spectra of thin films (figure 4*b*) to be similar for both HTMs at approximately 3 eV (table 1). Notably, no shift in absorption can be observed in the spectra of the same compounds in solution in comparison with the ones of those acting as thin films. This one more advantageous property of the novel HTMs is likely attributed to their stereostructure. These compounds do not form aggregates in the layers, which is the usual form for use of such materials in SCs [36].

Furthermore, contact angle (θ) measurements were carried out to assess the hydrophobicity of the HTMs (electronic supplementary material, figure S3). No obvious difference in θ values between the films of the synthesized spirobisindane-based enamines V1476, V1481 and that of spiro-OMeTAD can be observed, implying that their surface hydrophobicity is almost the same. Therefore, it may be assumed that the device stability should be similar.

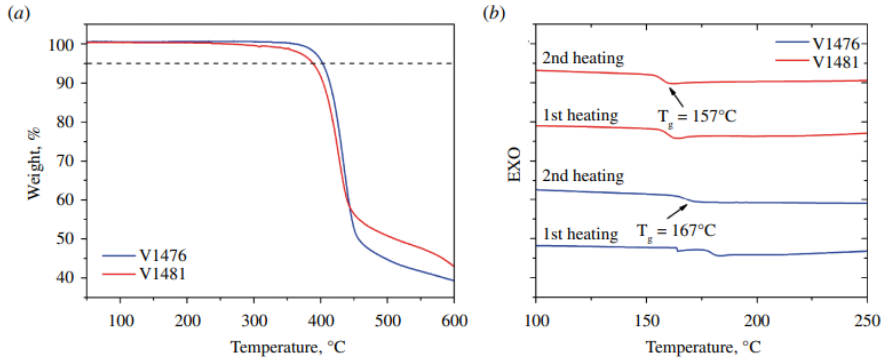

Figure 3. (*a*) Thermogravimetric analysis (TGA) data for V1476 and V1481 (heating rate of 10°C min^{-1}, N_2 atmosphere). (*b*) First and second heating curves of differential scanning calorimetry (DSC) for V1476 and V1481 (scan rate 10°C min^{-1}, N_2 atmosphere).

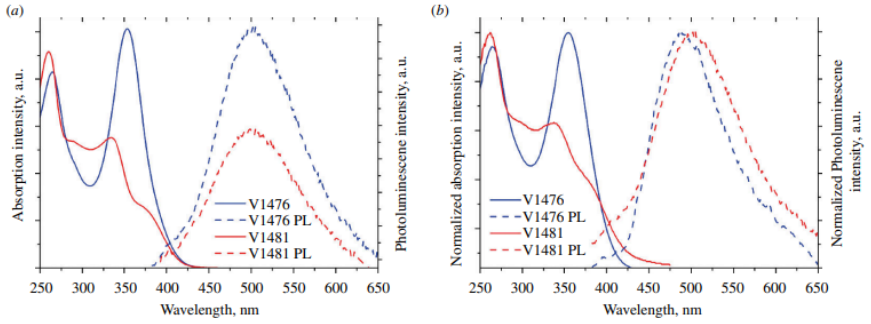

Figure 4. (*a*) UV–Vis absorption (solid line) and photoluminescence (dashed line) spectra of V1476 and V1481 in THF solutions (10^{-4} M). (*b*) UV–Vis absorption (solid line) and photoluminescence (dashed line) spectra of thin films of V1476 and V1481.

Table 1. Parameters of electronic excitations (transition energy ΔE_n and corresponding oscillator strength f_n) simulated using semiempirical TD method (for singlets).

compound	$\Delta E_1(S_0 \rightarrow S_1)$ (eV)	f_1	$\Delta E_2(S_0 \rightarrow S_2)$ (eV)	f_2	$\Delta E_3(S_0 \rightarrow S_3)$ (eV)	f_3
V1476a	3.71	0.289	3.83	0.522	3.96	1.612
V1481a	3.84	0.266	3.85	0.904	4.14	0.428
V1481b	3.83	0.469	3.85	0.687	4.11	0.343

3.3. Theoretical calculations

Software *Gaussian 16* was used to determine the most probable molecular conformation using quantum chemistry methods. DFT Cam-B3LYP method and 6-31G(d) basis set (supplemented with polarization functions (d)) were used for ground-state optimization [37]. Due to the large volume of molecular structures, solvation effects were not considered in all cases. The three most probable molecular conformations are presented in figure 5. Total molecular symmetry is absent. Substituents are oriented in a chaotic manner resulting in a vast array of different conformers. All structures depicted in figure 5 were derived using the grad optimization technique, ensuring convergence of all parameters such as Maximum Force, RMS Force, Maximum Displacement and RMS Displacement.

Electronic excitations of fully optimized structures were simulated using the semiempirical TD method (for singlets). Table 1 presents the parameters of electronic excitations (transition energies $\Delta E_1(S_0 \rightarrow S_1)$, $\Delta E_2(S_0 \rightarrow S_2)$, $\Delta E_3(S_0 \rightarrow S_3)$ and corresponding oscillator strengths f_1, f_2, f_3) for all structures. The population of low-lying excited molecular states S_1 and S_2 was achieved through partially allowed

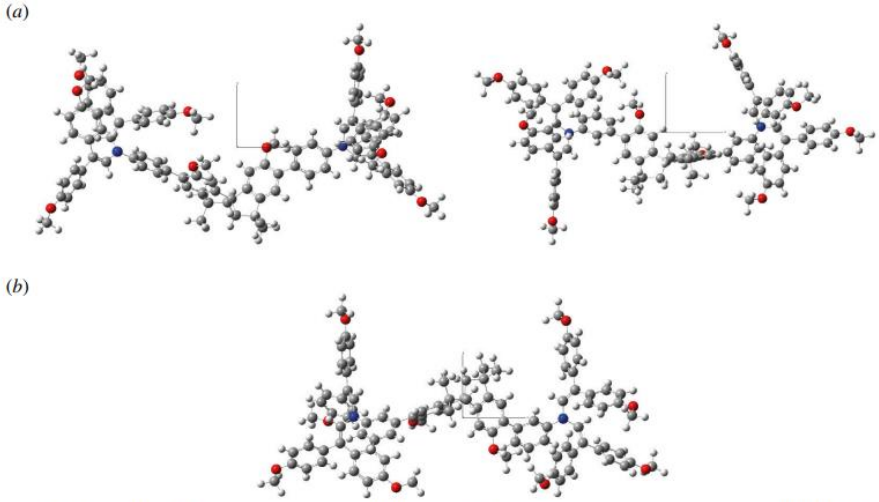

Figure 5. Most stable conformations of V1476 and V1481 obtained after ground-state energy optimization. B3LYP/6-31G(d). Projection *xy*.

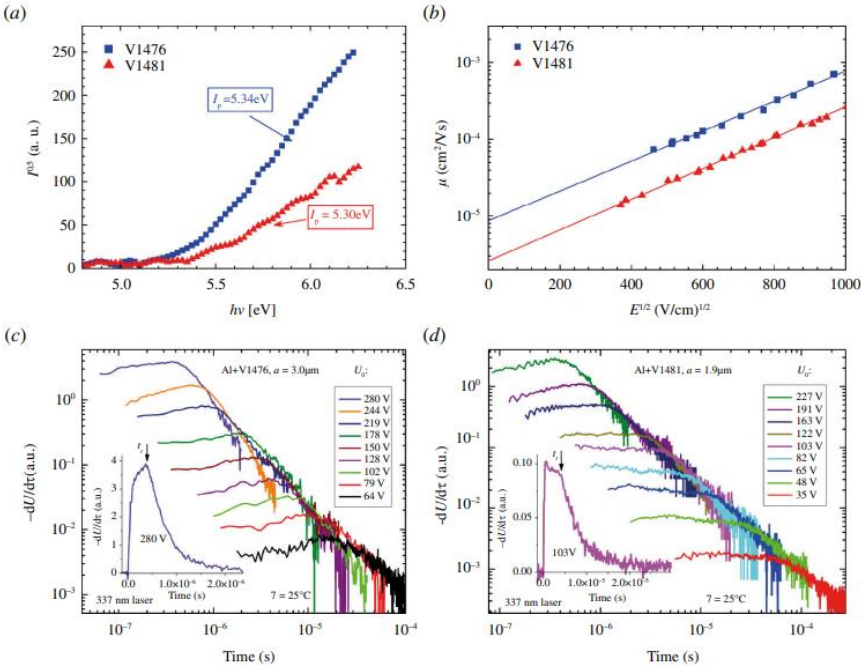

Figure 6. (*a*) Photoemission in air spectra of the charge transporting layers. (*b*) Electric field dependencies of the hole-drift mobility in V1476 and V1481. (*c*) Photocurrent XTOF transients of holes in V1476. (*d*) Photocurrent XTOF transients of holes in V1481.

transitions $S_0 \rightarrow S_n$, n = 1, 2 (oscillator strengths $f_n > 0.2$). The experimental absorption spectra of both solutions and thin films, as depicted in figure 4, exhibit excellent agreement with simulated spectra. Electronic supplementary material, figure S4, represents the molecular orbitals of V1476 and V1481 which are involved in 'spectroscopic' transitions (population of 'spectroscopic' states S_1, S_2). In all instances, the predominant and most significant electron jump of the CT transition (π–π^*) type occurs between the highest occupied molecular orbital (HOMO) and the lowest unoccupied molecular orbital

Table 2. Thermal, optical and photophysical properties of V1476 and V1481.

Compound	T_g (°C)[a]	T_{dec} (°C)[a]	λ_{abs} (nm)[b]	λ_{em} (nm)[b]	I_P (eV)[c]	E_g (eV)[d]	E_{ea} (eV)[e]	μ_0 (cm^2 V^{-1} s^{-1})[f]
V1476	167	403	265, 355	502	5.34	3.02	2.32	9.0×10^{-6}
V1481	157	389	260, 335, 365	502	5.30	3.07	2.23	2.6×10^{-6}

[a]Glass transition (T_g) and decomposition (T_{dec}) temperatures determined through DSC and TGA, respectively (10°C min^{-1}, N_2 atmosphere).
[b]Absorption and emission spectra were recorded for THF solutions with a concentration of10^{-4} M.
[c]Ionization energies of the films were measured using photoemission of electrons in air (PESA) method.
[d]The optical bandgap (E_g) was estimated from the intersection of absorption and emission spectra of solid films.
[e]Electron affinity (E_{ea}) was calculated as the difference IP – E_g.
[f]Mobility value at zero field strength.

(LUMO). Electronic supplementary material, table S1, lists the spatial distributions of electron density for the HOMO-1, HOMO, LUMO and LUMO+1 of each compound, while transition parameters between molecular orbitals (MOs) related to the population of 'spectroscopic' state are detailed in table 1. Based on such simulations, it can be argued that the central core fragment (two pentarings oriented at an angle of about 80° instead of perpendicular) does not participate in CT excitations, and the molecular charge redistribution is provided between substituents only. In all cases, the orientation of the substituents (relative to each other) is not ideal, but the presence of many phenyl moieties associated with the single bond (each with no significant rotational barrier) creates the possibility of quite effective partially allowed charge redistribution.

3.4. Photoelectric properties

The HOMO energy level of the material stands out as one of the most important parameters when selecting HTMs for device applications. To assess the compatibility of the HOMO energy levels of the spirobisindane-based HTMs for application in SCs, the solid-state ionization potential (I_p) was measured through the electron photoemission in air of thin films (PESA) method. The experimental results are presented in figure 6*a*. I_p values for V1476 and V1481 are 5.34 and 5.3 eV, respectively. They are in the same range as the preferred I_p values (4.9–5.5 eV) of HTMs used in antimony-based and triple-cation-based perovskite SCs [34,38,39]. The LUMO energy level was determined by calculating E_{ea} (electron affinity, table 2) from the interaction of absorption and emission spectra of solid films after determination of the optical bandgap (E_g).

Another essential characteristic for an effective charge-transporting material is its charge carrier mobility, determining the speed at which electrons or holes move in the device. Normally, hole-mobility values at zero field are 10^{-4} cm^2 V s^{-1} and higher values are desired for SCs. Xerographic time of flight (XTOF) measurements were employed to measure the charge mobility of the newly developed HTM layers. Experimental data illustrating the dependence of hole-drift mobility on electric field strength are depicted in figure 6*b*. The relationship between hole drift mobility and electric field strength is characterized by a Bässler-type dependence, which is typical for organic HTMs in most cases [40]. The zero-field hole drift mobility of V1476, almost reaching 1×10^{-5} cm^2 V s^{-1}, is higher than the hole drift mobility of *meta*-substituted HTM V1481 which is 2×10^{-6} cm^2 V s^{-1}. Meanwhile, the mobility values at strong electric fields are approximately 10^{-4} and 10^{-5} cm^2 V^{-1} s^{-1} for V1476 and V1481, respectively. Both materials are characterized by Gaussian charge transport: the transit time t_t was determined by the kink on the curve of the dU/dt transient in linear scale (insets in figure 6*c*,*d*). This indicates that the molecules pack closely ensuring efficient charge transfer in the layers of these materials. In the V1481 material, at weaker electric fields, the signal kinetics (figure 6*d*) show slight hole trapping, which may be related to a less ordered packing of the molecules. This is also in accordance with the lower T_g of V1481 compared with that of V1476.

Table 2 summarizes the thermal, optical and photoelectrical properties of the spirobisindane-based HTMs.

4. Conclusions

In this work, two novel spirobisindane-based enamines were designed and synthesized from commercially available starting materials. Following a comprehensive assessment of their thermal, optical and photophysical properties, and a comparative analysis with those of the HTMs utilized in SCs reported in the scientific literature, it is evident that compounds V1476 and V1481 emerge as promising candidates for applications in organic or hybrid electronics. The synthesized materials exhibit noteworthy thermal and electrochemical stability, possess suitable energy levels and demonstrate sufficiently high drift carrier mobility, reaching 10^{-4} cm^2 V^{-1} s^{-1} (V1476) at strong electric fields. These characteristics position them favourably as HTMs for use in perovskite SCs and antimony selenide SCs. The experimental findings were complemented by the DFT Cam-B3LYP method. It has been determined that, in the three most probable molecular conformations, the central core fragment does not participate in charge transfer excitations, and the molecular charge redistribution occurs solely between substituents.

Ethics. This work did not require ethical approval from a human subject or animal welfare committee.

Data accessibility. Supporting information is available online at Dryad [41].

Electronic supplementary material is available online [42].

Declaration of AI use. We have not used AI-assisted technologies in creating this article.

Authors' contributions. S.D.-G.: formal analysis, investigation, visualization, writing—original draft; M.D.: formal analysis, project administration, resources; K.K.: writing—original draft, writing—review and editing; V.J.: formal analysis, investigation; E.K.: formal analysis, investigation; A.G.: formal analysis, investigation, visualization, writing—original draft; S.K.: funding acquisition; V.G.: conceptualization, funding acquisition, methodology, resources, supervision, writing—review and editing.

All authors gave final approval for publication and agreed to be held accountable for the work performed therein.

Conflict of interest declaration. We declare we have no competing interests.

Funding. The 'Development of Semi-Transparent Bifacial Thin Film Solar Cells for Innovative Applications' benefits from a €1 000 000 grant from Iceland, Liechtenstein and Norway through EEA grants. The aim of the project is to develop materials for semi-transparent bifacial cost-effective solar cells, which operate in full and faint sunlight, as well as in backlit by snow-reflected conditions. Project contract with the Research Council of Lithuania (LMTLT) no. S-BMT-21-1(LT08-2-LMT K-01-003).

Acknowledgements. Computations were performed using resources at the High Performance Computing Center 'HPC Saulėtekis' (Faculty of Physics, Vilnius University, Lithuania).

References

1. McGinness J, Corry P, Proctor P. 1974 Amorphous semiconductor switching in melanins. *Science* **183**, 853–855. (doi:10.1126/science.183.4127.853)
2. Wang Y, Gong Q, Miao Q. 2020 Structured and functionalized organic semiconductors for chemical and biological sensors based on organic field effect transistors. *Mater. Chem. Front.* **4**, 3505–3520. (doi:10.1039/D0QM00202J)
3. Sudheendran Swayamprabha S, Dubey DK, Yadav RAK, Nagar MR, Sharma A, Tung FC, Jou JH. 2020 Approaches for long lifetime organic light emitting diodes. *Adv. Sci.* **8**, 2002254. (doi:10.1002/advs.202002254)
4. Lei H, Chen J, Tan Z, Fang G. 2019 Review of recent progress in antimony chalcogenide-based solar cells: materials and devices. *Sol. RRL* **3**, 1900026. (doi:10.1002/solr.201900026)
5. Liu Q *et al*. 2020 18% Efficiency organic solar cells. *Sci. Bull.* **65**, 272–275. (doi:10.1016/j.scib.2020.01.001)
6. Rakstys K, Igci C, Nazeeruddin MK. 2019 Efficiency *vs.* stability: dopant-free hole transporting materials towards stabilized perovskite solar cells. *Chem. Sci.* **10**, 6748–6769. (doi:10.1039/c9sc01184f)
7. Zou SJ, Shen Y, Xie FM, Chen JD, Li YQ, Tang JX. 2020 Recent advances in organic light-emitting diodes: toward smart lighting and displays. *Mater. Chem. Front.* **4**, 788–820. (doi:10.1039/C9QM00716D)
8. Idrissi A, Elfakir Z, Atir R, Bouzakraoui S. 2023 Small thiophene-based molecules with favorable properties as HTMs for perovskite solar cells or as active materials in organic solar cells. *J. Phys. Chem. Solids* **181**, 111492. (doi:10.1016/j.jpcs.2023.111492)
9. Li Z, Zhu Z, Chueh CC, Jo SB, Luo J, Jang SH, Jen AKY. 2016 Rational design of dipolar chromophore as an efficient dopant-free hole-transporting material for perovskite solar cells. *J. Am. Chem. Soc.* **138**, 11833–11839. (doi:10.1021/jacs.6b06291)
10. Shahnawaz S, Sudheendran Swayamprabha S, Nagar MR, Yadav RAK, Gull S, Dubey DK, Jou JH. 2019 Hole-transporting materials for organic light-emitting diodes: an overview. *J. Mater. Chem. C* **7**, 7144–7158. (doi:10.1039/C9TC01712G)
11. Anagnostou K, Stylianakis MM, Petridis K, Kymakis E. 2019 Building an organic solar cell: fundamental procedures for device fabrication. *Energies* **12**, 2188. (doi:10.3390/en12112188)

12. Miao J, Wang Y, Liu J, Wang L. 2022 Organoboron molecules and polymers for organic solar cell applications. *Chem. Soc. Rev.* **51**, 153–187. (doi:10.1039/d1cs00974e)
13. Kayaa İC, Ozdemir R, Usta H, Sonmezoglu S. 2022 A dopant-free 2,7-dioctyl[1]benzothieno[3,2-*b*][1]benzothiophene (C8-BTBT)-based hole transporting layer for highly stable perovskite solar cells with efficiency over 22%. *J. Mater. Chem. A* **10**, 12464–12472. (doi:10.1039/D2TA01541B)
14. Kong F, Güzel E, Sonmezoglu S. 2023 Hydrophobic 4-(isopropylbenzyl)oxy-substituted metallophthalocyanines as a dopant-free hole selective material for high-performance and moisture-stable perovskite solar cells. *Mater. Today Energy* **35**, 101324. (doi:10.1016/j.mtener.2023.101324)
15. Ono LK, Schulz P, Endres JJ, Nikiforov GO, Kato Y, Kahn A, Qi Y. 2014 Air-exposure-induced gas-molecule incorporation into spiro-MeOTAD films. *J. Phys. Chem. Lett.* **5**, 1374–1379. (doi:10.1021/jz500414m)
16. Hawash Z, Ono LK, Raga SR, Lee MV, Qi Y. 2015 Air-exposure induced dopant redistribution and energy level shifts in spin-coated spiro-MeOTAD films. *Chem. Mater.* **27**, 562–569. (doi:10.1021/cm504022q)
17. Salbeck J, Yu N, Bauer J, Weissörtel F, Bestgen H. 1997 Low molecular organic glasses for blue electroluminescence. *Synth. Met.* **91**, 209–215. (doi:10.1016/S0379-6779(98)80033-7)
18. Salbeck J, Weissörtel F, Bauer J. 1998 Spiro linked compounds for use as active materials in organic light emitting diodes. *Macromol. Symp.* **125**, 121–132. (doi:10.1002/masy.19981250110)
19. Poplavskyy D, Nelson J. 2003 Nondispersive hole transport in amorphous films of methoxy-spirofluorene-arylamine organic compound. *J. Appl. Phys.* **93**, 341–346. (doi:10.1063/1.1525866)
20. Krüger J, Plass R, Cevey L, Piccirelli M, Grätzel M, Bach U. 2001 High efficiency solid-state photovoltaic device due to inhibition of interface charge recombination. *Appl. Phys. Lett.* **79**, 2085–2087. (doi:10.1063/1.1406148)
21. Snaith HJ, Grätzel M. 2006 Enhanced charge mobility in a molecular hole transporter via addition of redox inactive ionic dopant: implication to dye-sensitized solar cells. *Appl. Phys. Lett.* **89**, 262114. (doi:10.1063/1.2424552)
22. Abate A *et al*. 2013 Lithium salts as 'redox active' p-type dopants for organic semiconductors and their impact in solid-state dye-sensitized solar cells. *Phys. Chem. Chem. Phys.* **15**, 2572–2579. (doi:10.1039/c2cp44397j)
23. Malinauskas T, Tomkute-Luksiene D, Sens R, Daskeviciene M, Send R, Wonneberger H, Jankauskas V, Bruder I, Getautis V. 2015 Enhancing thermal stability and lifetime of solid-state dye-sensitized solar cells via molecular engineering of the hole-transporting material spiro-OMeTAD. *ACS Appl. Mater. Interfaces* **7**, 11107–11116. (doi:10.1021/am5090385)
24. Hawash Z, Ono LK, Raga SR, Lee MV, Qi Y. 2015 Air-exposure induced dopant redistribution and energy level shifts in spin-coated spiro-MeOTAD films. *Chem. Mater.* **27**, 562–569. (doi:10.1021/cm504022q)
25. Matuszná K, Breza M, Pálszegi T. 2008 On electronic structure of neutral and monocharged 9,9′-spirobifluorene. *J. Mol. Struct. Theochem.* **851**, 277–283. (doi:10.1016/j.theochem.2007.11.020)
26. Tamao K, Nakamura K, Ishii H, Yamaguchi S, Shiro M. 1996 Axially chiral spirosilanes via catalytic asymmetric intramolecular hydrosilation. *J. Am. Chem. Soc.* **118**, 12469–12470. (doi:10.1021/ja962754c)
27. Petrus ML, Music A, Closs AC, Bijleveld JC, Sirtl MT, Hu Y, Dingemans TJ, Bein T, Docampo P. 2017 Design rules for the preparation of low-cost hole transporting materials for perovskite solar cells with moisture barrier properties. *J. Mater. Chem. A* **5**, 25200–25210. (doi:10.1039/C7TA06452G)
28. Petrus ML et al. 2018 New generation hole transporting materials for perovskite solar cells: amide-based small-molecules with nonconjugated backbones. *Adv. Energy Mater.* **8**, 1–11. (doi:10.1002/aenm.201801605)
29. Rakstys K *et al*. 2020 Carbazole-terminated isomeric hole-transporting materials for perovskite solar cells. *ACS Appl. Mater. Interfaces* **12**, 19710–19717. (doi:10.1021/acsami.9b23495)
30. Daskeviciene M *et al*. 2017 Carbazole-based enamine: low-cost and efficient hole transporting material for perovskite solar cells. *Nano Energy* **32**, 551–557. (doi:10.1016/j.nanoen.2017.01.015)
31. Vaitukaityte D, Wang Z, Malinauskas T, Magomedov A, Bubniene G, Jankauskas V, Getautis V, Snaith HJ. 2018 Efficient and stable perovskite solar cells using low-cost aniline-based enamine hole-transporting materials. *Adv. Mater.* **30**, e1803735. (doi:10.1002/adma.201803735)
32. Daskeviciute S *et al*. 2021 Fluorene-based enamines as low-cost and dopant-free hole transporting materials for high performance and stable perovskite solar cells. *J. Mater. Chem. A* **9**, 301–309. (doi:10.1039/D0TA08452B)
33. Daskeviciute-Geguziene S, et al. 2023 Passivating Defects of Perovskite Solar Cells with Functional Donor-Acceptor–Donor Type Hole Transporting Materials. *Adv. Funct. Materials* **33**, 2208317. (doi:10.1002/adfm.202208317)
34. Juneja N. 2022 Sb2S3 solar cells with a cost-effective and dopant-free fluorene-based enamine as a hole transport material. *Sustain. Energy Fuels* **6**, 3220–3229. (doi:10.1039/D2SE00356B)
35. Wang X, Zhang J, Yu S, Yu W, Fu P, Liu X, Tu D, Guo X, Li C. 2018 Lowering molecular symmetry to improve the morphological properties of the hole-transport layer for stable perovskite solar cells. *Angew. Chem. Int. Ed. Engl.* **57**, 12529–12533. (doi:10.1002/anie.201807402)
36. Sapagovas VJ, Gaidelis V, Kovalevskij V, Undzenas A. 2006 3,4,9,10-Perylenetetracarboxylic acid derivatives and their photophysical properties. *Dyes Pigm.* **71**, 178–187. (doi:10.1016/j.dyepig.2005.06.012)
37. Frisch MJ *et al*. 2019 *Gaussian 16, revision C.01*. Wallingford CT: Gaussian, Inc.
38. Xiang Y, Guo H, Cai Z, Jiang C, Zhu C, Wu Y, Zhu WH, Chen T. 2022 Dopant-free hole-transporting materials for stable $Sb_2(S,Se)_3$ solar cells. *Chem. Commun.* **58**, 4787–4790. (doi:10.1039/D1CC07041J)
39. Urieta-Mora J, García-Benito I, Molina-Ontoria A, Martín N. 2018 Hole transporting materials for perovskite solar cells: a chemical approach. *Chem. Soc. Rev.* **47**, 8541–8571. (doi:10.1039/c8cs00262b)

40. Matoliukstyte A, Burbulis E, Grazulevicius JV, Gaidelis V, Jankauskas V. 2008 Carbazole-containing enamines as charge transport materials for electrophotography. *Synth. Met.* **158**, 462–467. (doi:10.1016/j.synthmet.2008.03.020)
41. Daskeviciute-Geguziene S, Daskeviciene M, Kantminienė K, Jankauskas V, Kamarauskas E, Gruodis A, Karazhanov S, Getautis V. 2024 Data from: Design, synthesis and theoretical simulations of novel spiroindane-based enamines as p-type semiconductors. Dryad. (doi:10.5061/dryad.0rxwdbs7j)
42. Daskeviciute-Geguziene S, Daskeviciene M, Kantminienė K, Jankauskas V, Kamarauskas E, Gruodis A. 2024 Supplementary Material from: Design, synthesis and theoretical simulations of novel spiroindane-based enamines as p-type semiconductors. FigShare (doi:10.6084/m9.figshare.c.7123857)

How to cite: *Angew. Chem. Int. Ed.* **2022**, *61*, e202113207
International Edition: doi.org/10.1002/anie.202113207
German Edition: doi.org/10.1002/ange.202113207

Perovskite Solar Cells

Green-Chemistry-Inspired Synthesis of Cyclobutane-Based Hole-Selective Materials for Highly Efficient Perovskite Solar Cells and Modules

Sarune Daskeviciute-Geguziene, Yi Zhang, Kasparas Rakstys, Gediminas Kreiza, Sher Bahadar Khan, Hiroyuki Kanda, Sanghyun Paek, Maryte Daskeviciene, Egidijus Kamarauskas, Vygintas Jankauskas, Abdullah M. Asiri, Vytautas Getautis,* and Mohammad Khaja Nazeeruddin**

Abstract: *Hybrid lead halide perovskite solar cells (PSCs) have emerged as potential competitors to silicon-based solar cells with an unprecedented increase in power conversion efficiency (PCE), nearing the breakthrough point toward commercialization. However, for hole-transporting materials, it is generally acknowledged that complex structures often create issues such as increased costs and hazardous substances in the synthetic schemes, when translated from the laboratory to manufacture on a large scale. Here, we present cyclobutane-based hole-selective materials synthesized using simple and green-chemistry inspired protocols in order to reduce costs and adverse environmental impact. A series of novel semiconductors with molecularly engineered side arms were successfully applied in perovskite solar cells.* ***V1366****-based PSCs feature impressive efficiency of 21 %, along with long-term operational stability under atmospheric environment. Most importantly, we also fabricated perovskite solar modules exhibiting a record efficiency over 19 % with an active area of 30.24 cm^2.*

Introduction

Although organic–inorganic perovskites have been known since the 19th century, they have currently gained substantial attention in the field of photovoltaics and optoelectronics.[1] Over the recent years, organic-inorganic hybrid perovskite solar cells (PSCs) have been attracting massive worldwide attention due to their low cost and facile fabrication.[2] Since 2009, when Miyasaka and co-workers reported 3.8 % power conversion efficiency (PCE) of PSC,[3] the performance of these photovoltaic devices has increased dramatically and currently PCE exceeds 25 %.[4] Despite PSCs have skyrocketed in PCE, there are still several device issues that need to be resolved especially improving the long-term stability.[5–10] HTM is one of the quintessential components required for efficient and stable PSC devices. These materials are responsible for the transport of the photo-generated carriers from the absorber towards the electrode. HTMs should demonstrate sufficient charge transport properties, adequate energy levels, especially HOMO level, and good thermal stability. Despite significant research efforts devoted to developing new HTMs, these materials are still a weak spot in the PSC devices. In this context, small organic molecules are particularly appealing since they offer a wide range of structural modifications leading to the desired properties, and are easy to synthesize, purify, and process.[11–14] Numerous approaches in the development of such HTMs including linear, star-shaped, or spiro-centered structures were reported in order to match the required hydrophobicity, energy levels, and the charge carrier mobility.[15–20] To date, 2,2′,7,7′-tetrakis-(*N*,*N*-di-*p*-methoxyphenylamine)-9,9′-spirobifluorene (spiro-OMeTAD) dominates the field and despite its high price is routinely used as the gold standard for the research interests due to commercialization decades ago.[21]

[*] S. Daskeviciute-Geguziene, Dr. K. Rakstys, Dr. M. Daskeviciene, Prof. V. Getautis
Department of Organic Chemistry, Kaunas University of Technology
Radvilenu pl. 19, Kaunas 50254 (Lithuania)
E-mail: vytautas.getautis@ktu.lt
Dr. Y. Zhang, Dr. H. Kanda, Prof. M. K. Nazeeruddin
Institute of Chemical Sciences and Engineering
École Polytechnique Fédérale de Lausanne
1951 Sion (Switzerland)
E-mail: yi.zhang@epfl.ch
mdkhaja.nazeeruddin@epfl.ch
Dr. G. Kreiza
Institute of Photonics and Nanotechnology, Vilnius University
Saulėtekio al. 3, 10257 Vilnius (Lithuania)
Dr. E. Kamarauskas, Dr. V. Jankauskas
Institute of Chemical Physics, Vilnius University
Saulėtekio al. 3, 10257 Vilnius (Lithuania)
Dr. S. B. Khan, Prof. A. M. Asiri
Center of Excellence for Advanced Materials Research (CEAMR)
King Abdulaziz University
P.O. Box 80203, 21589 Jeddah (Saudi Arabia)
Dr. S. Paek
Department of Chemistry and Energy Engineering
Sangmyung University
Seoul 03016 (Republic of Korea)
Supporting information and the ORCID identification number(s) for the author(s) of this article can be found under: https://doi.org/10.1002/anie.202113207.

As of the success of spiro-OMeTAD, many research groups have been focused on spiro-type compounds, expecting to improve the PCE with slight structural modifications.[22,23] Several groups studied central 9,9′-spirobifluorene-linked HTMs including dimethylfluorenyl-, ethylcarbazolyl-, and fluorinated methoxyphenyl-terminated examples recently reported by Seo,[24] Chen,[25] and Yang,[26] respectively, as well as the development of new central spiro-cored structures such as spiro[fluorene-9,9′-xanthene],[27–31] spirobisacridine,[32] thiophene-containing spiro cores[33–35] and other spiro-type derivatives.[36,37] However, the synthesis of such spiro-type compounds typically requires a multi-step reaction scheme involving low temperature (−78 °C), sensitive (*n*-butyllithium), and aggressive (Br_2) reagents resulting in a relative high material cost, consequently leading to a significant contribution to the total device cost and non-negligible environmental impact.[38–40] The tedious synthesis and costly purification of HTMs may hamper large scale production and thereby could impede the overall commercial success of PSCs.

Therefore, the hunt is now on for new organic semiconductors that are prepared by simple, cost-effective, and green chemistry without sacrificing the efficiency and would be easily scalable for a reasonable cost.[41,42] In this sense, the utilization of a synthetic protocols that reduces or eliminates the use of hazardous substances is highly desirable. Moreover, simple product work up and purification may also significantly reduce the final synthesis cost and the environmental issues.[43–45] Recently, several research groups have focussed on tuning the structure by decreasing the number of synthetic steps, thus reducing the synthetic complexity, cost of materials and environmental impact.[46,47]

Carbazole is known to be a promising core unit for molecular design since it can be substituted with a wide range of desired groups, allowing fine-tuning of optical and electrochemical properties.[48] Various carbazole-containing scaffolds as electron donating units in the periphery were routinely used to tune the HOMO level and applied in PSCs, showing comparable photovoltaic performance.[49–51] This includes star-shaped SGT series,[52,53] benzodithiazole,[54] bismethylenebenzene,[55,56] bipyridine,[57] pyrene-based[58] examples. Photodimerized carbazole is an attractive building block due to the simple, elegant and green synthesis and has been studied as excimer-free and high hole carrier mobility material in early works.[59–61]

Herein, we disclose the development of novel HTMs, which comprises cyclobutane as a new structural core element for HTMs flanked by two differently substituted photodimerized carbazole arms in a branched fashion. The specific arrangement of carbazolyl groups onto cyclobutane core is also likely to facilitate the carrier transport process. Moreover, bulkiness and sterically hindered rigid *trans*-configuration result in competition between the planarization and repulsive steric hindrance leading to a pseudo spiro type arrangement and diversified torsion angles. The effects of different peripheral carbazole substituents on various properties of newly synthesized molecules have been systematically investigated. Novel cyclobutane-based HTMs have been successfully applied in PSCs, showing PCE up to 21% and improved long-term stability under atmospheric environment comparing to spiro-OMeTAD. We also fabricated **V1366**-based perovskite solar modules (6.5 cm × 7 cm) exhibiting a record efficiency over 19.0% with an active area of 30.24 cm^2 (corresponding to 16.78% with an aperture area ≈34.36 cm^2, a geometric fill factor of 88%, the active area is used hereafter). Most importantly, to obtain novel HTMs we have applied protocols inspired by green chemistry, for the first time presenting that HTMs for PSCs could be synthesised eliminating the use of hazardous substances in order to reduce the adverse environmental impact without sacrificing the efficiency.

Results and Discussion

The general synthesis procedure for the preparation of cyclobutane-based HTMs is shown in Figure 1. The synthesis

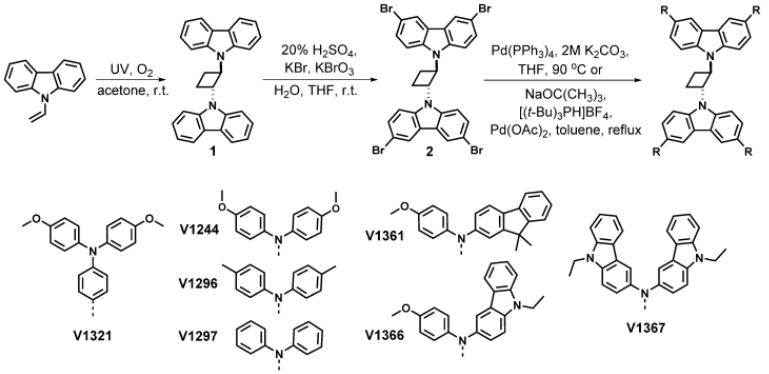

Figure 1. Synthetic route to novel hole-transporting materials based on substituted cyclobutane.

starts with the photochemical cyclodimerization of low-cost commercially available 9-vinyl carbazole. This step only required photoirradiation of starting material in green solvent acetone at ambient temperature. Next, *trans*-1,2-bis(9-carbazolyl)cyclobutane (**1**) was brominated using an aqueous bromate-bromide mixture as a green brominating agent to eliminate the use of aggressive bromine. To yield **V1321**, an aqueous/THF four-fold Suzuki cross-coupling procedure was applied. With this we demonstrate that all 3 synthetic steps required to obtain **V1321** were selected to reduce or eliminate the use of hazardous substances. Therefore, it could be classified as "green" HTM. To synthesise other HTMs presented in this work, **2** was reacted with the desired diarylamine-based coupling partner under the standard Buchwald reaction conditions. Detailed synthetic protocols and full characterization of the compounds (NMR spectroscopy, mass spectrometry, and elemental analysis) are described in the Supporting Information.

Thermal gravimetric analysis (TGA) and differential scanning calorimetry (DSC) were used to determine thermal properties of the HTMs which are important to explore for processing temperatures and might affect the long-term stability of the PSCs. TGA suggests that novel HTMs decompose in a range between 380–470 °C (Figure 3a), far above the temperature for conventional device operation. From TGA results, there is a clear trend that higher molecular weight increases the thermal decomposition temperature (T_{dec}). DSC measurements indicated that all new compounds are fully amorphous and have a glass transition temperature (T_g) around 160 °C except **V1296**, which could exist in both crystalline and amorphous states as shown in Figure S9. Interestingly, all synthesized HTMs have higher T_g than spiro-OMeTAD (124 °C) meaning that the cyclobutane-based HTMs should have better morphological stability. In comparison, **V1367** has the highest T_g of 215 °C and should result in improved quality of the HTM layer. Moreover, microscope pictures revealed that among the series only **V1296** was prone for rapid formation of crystallization centers on the glass substrate, while other compounds resulted in fully transparent and amorphous films (Figure S10).

V1296 has been chosen as a model compound for X-ray crystallography due to the highest crystallinity among the series to confirm the *trans*-cyclobutane configuration and study the arrangement of carbazole substituents as the different electron donors around the carbazole should not affect the central core geometry and were ignored. **V1296** packs in orthorhombic spacegroup (*Pbcn;* No. 60) when grown by acetone vapor diffusion into chloroform solution. The following cell parameters were determined by single-crystal X-ray diffraction measurements: $a = 10.54500(10)$ Å, $b = 20.7442(4)$ Å, $c = 31.1322(4)$ Å, $\alpha = \beta = \gamma = 90°$, $V = 6810.09(17)$ Å3. The cell consists of four **V1296** molecules ($Z = 4$) with an asymmetric unit equalling to half molecule ($Z' = 0.5$). Molecular geometry and packing are visualized in Figure 2, whereas detailed crystallographic data is provided in Table S1. As visualized in Figure 2a, two carbazole units were found to be attached to the central cyclobutane core with the same bond angles of 119° and −119°, respectively, indicating the *trans*-configuration. Moreover, as shown in Figure 2b, the dihedral angle between the cyclobutane-connected carbazoles is measured to be 98° revealing a pseudo spiro conformation and being close to the dihedral angle between spiro-connected fluorenes in spiro-OMeTAD (90°).[62] In addition, central cyclobutane ring was found to be not completely flat as demonstrated by different torsion angles shown in Figure 2c.

The ultraviolet-visible absorption (UV/Vis) spectra in THF solutions of cyclobutane V-series HTMs are shown in Figure 3b. All new compounds have at least two major absorption peaks. The same absorption peak at 290 nm

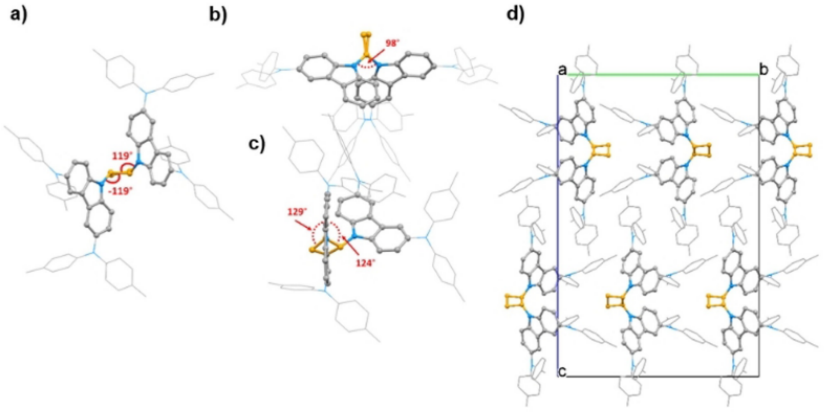

Figure 2. Molecular geometries of **V1296** obtained by X-ray diffraction analysis with an indicated bond (a) and torsional angles (b and c). d) View down crystallographic *a*-axis of the molecular packing model. For clarity, diphenylamine groups are shown as wireframe, the cyclobutane ring is coloured in orange, and hydrogen atoms are omitted.

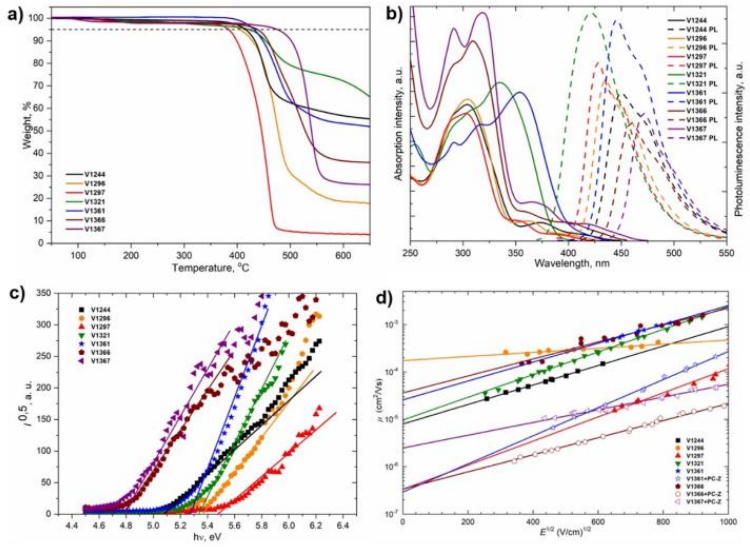

Figure 3. a) Thermogravimetric analysis (TGA) data (heating rate of 10 °C min^{-1}, N_2 atmosphere). b) UV/Vis absorption (solid line) and photoluminescence (dashed line) spectra of V-series HTMs in THF solution (10^{-4} M). c) Photoemission spectra of the charge transporting layers measured in air. d) Electric field dependencies of the hole-drift mobility in synthesized HTMs.

corresponds to localized π-π* transitions arising from *trans*-1,2-bis(9-carbazolyl)cyclobutane central scaffold, while absorption peaks at longer wavelengths arise from more intensive delocalization from the different conjugated substituents and are assigned to n-π* transitions. The PL spectra revealed that significantly large Stokes shifts (100–150 nm) are observed for all molecules, therefore changes in the geometry of the molecules are expected upon excitation. The optical gaps (E_g) were calculated from the intersection of absorption and photoluminescence spectra of thin films. They were found to be similar for all the compounds at around 3 eV (Figure S11).

The solid-state ionization potentials (I_P) of HTMs were determined using electron photoemission spectroscopy in air (PESA) of the thin films to assess the HOMO energy levels (Figure 3c). I_P values of novel cyclobutanes were found to be lower than 5.7 eV, which equals to the valence band (VB) energy of the triple cation-based perovskite, therefore efficient hole transfer from perovskite to the cathode should be ensured. Based on E_g and I_P values, we calculated the electron affinities (E_{ea}) in the range of 1.9–2.5 eV. Importantly, calculated E_{ea} are smaller than the conduction band (CB) energy of the perovskite (−4.10 eV), ensuring the effective electron blocking from the perovskite to the electrode.

Xerographic time of flight (XTOF) measurements were used to determine the charge mobility of the V-series layers. Dependences of hole drift mobility on electric field strength are shown in Figure 3d. **V1296** exhibited the highest zero-field hole drift mobility (μ_0) among the series having the values of 1.7×10^{-4} cm^{2}Vs^{-1}, outperforming that of spiro-OMeTAD ($\mu_0 = 1.3\times10^{-4}$ cm^{2}Vs^{-1}).[63] The highest hole drift mobility of **V1296** could be explained due to its crystalline nature, however, the rapid crystallization in the film might result poor film forming properties and deteriorated PSC performance. **V1321**, **V1361**, and **V1366** showed one order of magnitude lower μ_0 values. The thermal, optical, and photoelectrical properties of the cyclobutanes are summarized in Table 1.

The schematic energy level diagram of the devices containing different HTLs is shown in Figure 4a, and the detailed preparation process is described in the see the Supporting Information. Figure S12 and Figure 4b represent the SEM of a cross-sectional view of PSC devices with spiro-OMeTAD and **V1366**, providing a direct view of the PSCs individual layers: FTO/SnO_2/perovskite/HTM/Au. Thickness of the perovskite films are about 700 nm with 70 nm of Au layer. However, the thickness of the **V1366** layer is about 100 nm which is much thinner than that of the spiro-OMeTAD layer (≈200 nm). This is due to the smaller molecule bulk and lower optimized concentration of the **V1366** solution. Due to the absence of carrier transport layer, as shown in Figure 4c, higher continuous-wave photoluminescence (CWPL) intensity is found in the perovskite thin film. When the HTM layers are covered, the CWPL intensities decrease sharply, and both HTM materials exhibit similar hole extraction capabilities. Also, the PL lifetime

Table 1: Thermal, optical, and photophysical properties of newly synthesized compounds.

Cmpd.	T_m [°C][a]	T_g [°C][a]	T_{dec} [°C][a]	λ_{abs} [nm][b]	λ_{em} [nm][b]	I_P [eV][c]	E_g [eV][d]	E_{ea} [eV][e]	μ_0 [$cm^2\,V^{-1}\,s^{-1}$][f]
V1244	–	122	416	291, 303	450	5.07	2.91	2.12	7.9×10^{-6}
V1296	320	159	406	291, 304	435	5.37	2.98	2.48	1.7×10^{-4}
V1297	–	162	382	289, 302	427	5.48	3.05	2.43	3.3×10^{-7}
V1321	–	148	421	291, 306, 334	420	5.34	3.13	2.21	1×10^{-5}
V1361	–	157	432	291, 315, 354	445	5.28	2.93	2.35	2.5×10^{-5}
V1366	–	173	439	291, 309	459	4.77	2.83	1.94	3.5×10^{-5}
V1367	–	215	477	291,318	471	4.78	2.79	1.99	2.5×10^{-6}

[a] Melting (T_m), glass transition (T_g), and decomposition (T_{dec}) temperatures determined by DSC and TGA, respectively (10 °C min^{-1}, N_2 atmosphere). [b] Absorption and emission spectra were measured in THF solution (10^{-4} M). [c] Ionization energies of the films measured using PESA. [d] E_g estimated from the intersection of absorption and emission spectra of solid films. [e] $E_{ea}=I_P-E_g$. [f] Mobility value at zero field strength.

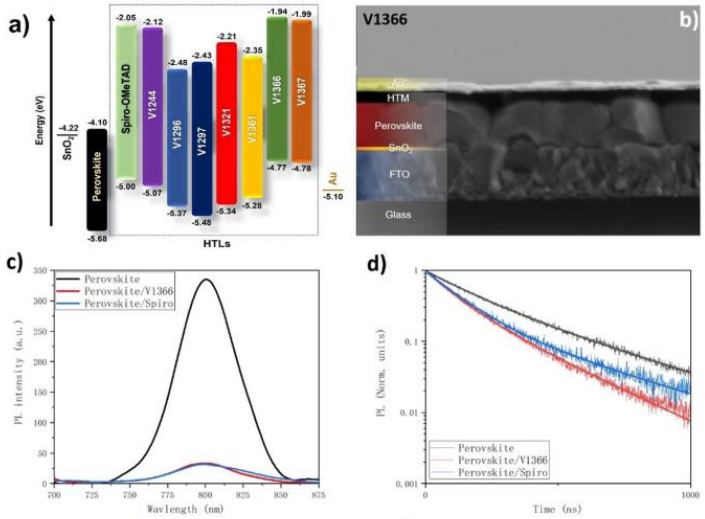

Figure 4. a) Schematic energy level diagram of the devices containing different HTLs. b) Cross-sectional SEM image of the sample comprising FTO/SnO_2/perovskite/**V1366**/Au layers. c) CW-PL spectra (excitation: 480 nm) and d) PL lifetime of the perovskite thin films with or without spiro-OMeTAD or **V1366**.

shown in Figure 4d obtained from perovskite thin films was 286 ns (Table S2), which is almost 2 times longer than the results from perovskite/spiro-OMeTAD and perovskite/**V1366** films.

PSC devices using the different HTM materials were fabricated by sandwiching the perovskite thin films between an FTO/SnO_2 anode and an HTM/Au cathode. Figure 5a shows the typical current density—voltage (*J-V*) curves (reverse scan) for the PSCs with spiro-OMeTAD as a reference, **V1244**, **V1321**, and **V1366**, respectively. Devices having synthesised HTMs exhibit photoelectric conversion performance comparable to spiro-OMeTAD, especially for the **V1366**, which showed even higher photocurrent. However, the devices with **V1296**, **V1297**, **V1361** and **V1367** as the HTMs exhibit relatively low PCE (Figure S14). Such deteriorated performance of **V1296** and **V1297** could be explained by quite deep HOMO levels, which could lead to the mismatch with the perovskite VB, while **V1367** has one of the lowest hole drift mobility among the series. On the other hand, the PCE of 21% consisting of J_{SC} of 24.38 mA cm^{-2}, a V_{OC} of 1.092 V, and an FF of 79.1% was achieved for the **V1366**-based device in comparison to 21.64% for the spiro-OMeTAD with J_{SC} of 24.17 mA cm^{-2}, a V_{OC} of 1.114 V, and an FF of 80.3%, showing that molecular engineering of side-arms fully dictates the performance of the final device. The *J-V* hysteresis of the best devices is shown in Figure 5b. A similar hysteresis index of 1.08 for spiro-OMeTAD and 1.12 for **V1366** device was found. A total of 20 solar cells in two groups were fabricated under the same conditions with spiro-OMeTAD or **V1366** as the HTM. Figure 5c demonstrates the

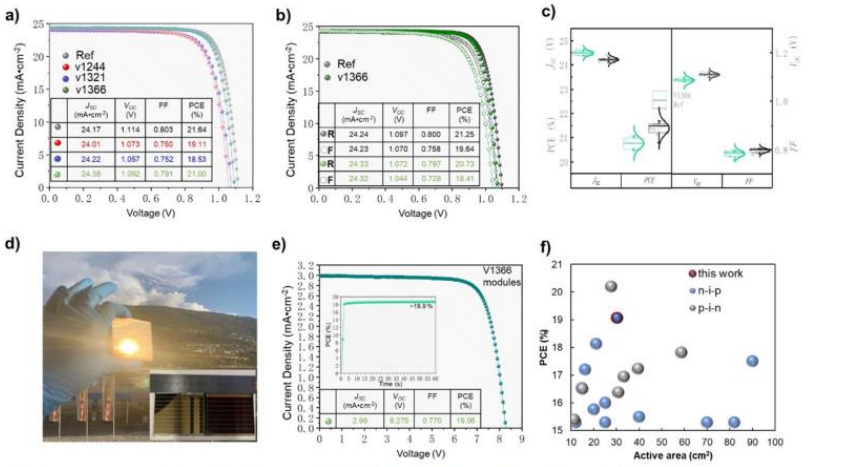

Figure 5. a) *J-V* curves (reverse-scan) of the PSCs based on **V1244**, **V1321**, and **V1366** as HTMs and spiro-OMeTAD as the reference. b) *J-V* hysteresis of spiro-OMeTAD and **V1366**. c) Statistical deviation of the photovoltaic parameters for solar cells with **V1366** or spiro-OMeTAD, respectively (10 different solar cells of each type). d) Photograph of the unsealed 6.5×7 cm solar module. e) *J-V* curves of **V1366**-based PSC module; the designated illumination area was estimated as 30.24 cm^2; inset is the maximum-power-point power output of this module. f) Recently reported PCEs of perovskite solar modules with an active area of 10–100 cm^2 and PCE over 15% for both n-i-p and p-i-n architectures.

statistical distribution of all four photovoltaic parameters of the two groups of solar cells to show the reproducibility of each condition. All the photovoltaic parameters of them show a similar half-width, which means the reproducibility of **V1366**-based devices is comparable to that of spiro-OMeTAD (Table S3). As shown in the Figure S13, we observe an iodine/lead atoms ratio (1.84) in the spiro-OMeTAD/perovskite layer while a constant iodine/lead atoms ratio (1.42) is observed in the **V1366**/perovskite layer, which means more iodine should be diffused into the spiro-OMeTAD between the interface of perovskite thin films and HTL.

Another issue of importance to commercialization is the large-scale production when translating from laboratory to manufacturing scale. To characterize the upscaling performance of the new HTM, we fabricated **V1366**-based perovskite modules sized of 6.5×7 cm as shown in Figure 5d. The module exhibited a PCE of 19.06% with J_{SC} of 2.99 mA cm^{-2}, a V_{OC} of 8.275 V, and an FF of 77% as shown in Figure 5e. And the PCE of

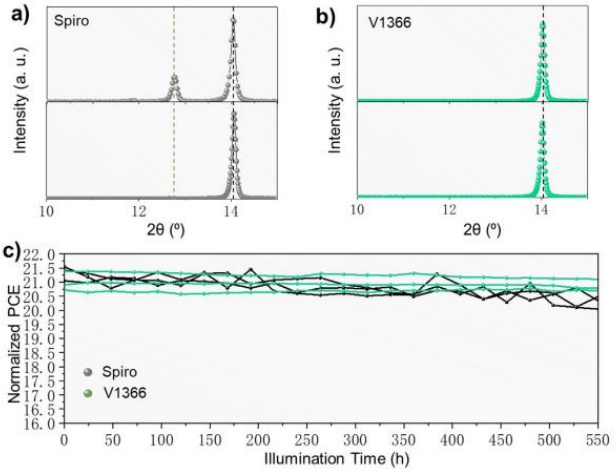

Figure 6. Long-term stability of the perovskite thin films and devices. Representative XRD patterns of the perovskite thin films with different HTMs before and after 5 h heating (85 °C) under ambient conditions (60% RH): a) spiro-OMeTAD, b) **V1366**. The green and black dashed lines indicate the peak positions of the 001 reflection of the PbI_2 crystal phase and the 110 reflection of the perovskite phase, respectively. c) Long-term stability of PSC devices (stored in the drawer, tested every 24 hours, 15%–20% RH, RT) made with spiro-OMeTAD and **V1366**.

the module stabilizes at ≈19%, consistent with the reverse-scan *J-V* curve. To the best of our knowledge, the PCE value over 19% is the highest PCE ever reported for non-spiro-OMeTAD based perovskite module. This is also illustrated in Figure 5 f and Table S4, to facilitate the comparison of the device itself, we summarized the recent reports with photovoltaic performance and device structure of perovskite solar modules prepared by different methods with an active area of 10–100 cm^2 and PCE over 15% including both n-i-p and p-i-n architectures. In addition, from the broader view, the highly efficient module using **V1366** not only shows one of the state-of-the-art performances for both n-i-p and p-i-n architectures but also clearly shows the proficient scalability and combined advantages of green-chemistry approach developed **V1366** HTM.

In addition to the PCE, the chemical stability was also evaluated showing the increased stability of **V1366**-based device, which represents another important advantage of the new HTM. Figure 6 a, b shows representative XRD patterns of the perovskite thin films with spiro-OMeTAD and **V1366** before and after 5 h heating (85 °C) under ambient conditions (60% RH). While the reference perovskite thin-film shows decomposition to PbI_2 after storage, the **V1366**-based film maintains its good phase purity. It is most likely that the **V1366** slows the moisture ingression kinetics, due to denser layer structure and less doping. The long-term device stability is tested every 24 hours by operating the three PSCs per condition. While the reference device shows a decrease of more than 5% in PCE after 550 h, almost no PCE loss is observed for the **V1366**-based PSC, demonstrating the enhanced device stability.

Conclusion

Drawing the results together, we report the synthesis and a systematic study of the cyclobutane-based hole-transporting materials that are synthesized by simple and "green" chemistry. The impact of the different side-arm fragments onto cyclobutane central core was revealed through the optical, electrochemical, photophysical, and photovoltaic measurements. It was found that cyclobutane fragment increases the glass transition temperature of final HTMs being more amorphous and morphologically stable. Additionally, hole drift mobility values of cyclobutane-centered HTMs up to 10^{-4} $cm^2 Vs^{-1}$ order of magnitude, have been reached which outperforms spiro-OMeTAD. The most efficient perovskite devices contained **V1366** reaching the PCE of 21% and excellent long-term stability. Most importantly, we fabricated perovskite solar modules exhibiting a record efficiency over 19% with an active area of 30.24 cm^2. The results of this study cover the main requirements for the successful implementation of perovskite solar cell technology.

Acknowledgements

S.D.-G., M.D., and V.G. acknowledge funding from the Research Council of Lithuania under grant agreement Nr. 01.2.2-LMT-K-718-03-0040 (SMARTMOLECULES). The authors extend their appreciation to the Deputyship for Research & Innovation, Ministry of Education in Saudi Arabia for funding this research work through the project number 526. K.R. acknowledges the funding received from MJJ Foundation. Open access funding provided by Ecole Polytechnique Federale de Lausanne.

Conflict of Interest

The authors declare no conflict of interest.

Keywords: cyclobutane · green chemistry · hole-transporting materials · perovskites · solar cells

[1] B. Saparov, D. B. Mitzi, *Chem. Rev.* **2016**, *116*, 4558.
[2] Y. Rong, Y. Hu, A. Mei, H. Tan, M. I. Saidaminov, S. Il Seok, M. D. McGehee, E. H. Sargent, H. Han, *Science* **2018**, *361*, 1214.
[3] A. Kojima, K. Teshima, Y. Shirai, T. Miyasaka, *J. Am. Chem. Soc.* **2009**, *131*, 6050.
[4] J. J. Yoo, G. Seo, M. R. Chua, T. G. Park, Y. Lu, F. Rotermund, Y. K. Kim, C. S. Moon, N. J. Jeon, J. P. Correa-Baena, V. Bulović, S. S. Shin, M. G. Bawendi, J. Seo, *Nature* **2021**, *590*, 587.
[5] G. Divitini, S. Cacovich, F. Matteocci, L. Cinà, A. Di Carlo, C. Ducati, *Nat. Energy* **2016**, *1*, 15012.
[6] Y. Han, S. Meyer, Y. Dkhissi, K. Weber, J. M. Pringle, U. Bach, L. Spiccia, Y. B. Cheng, *J. Mater. Chem. A* **2015**, *3*, 8139.
[7] N. Aristidou, I. Sanchez-Molina, T. Chotchuangchutchaval, M. Brown, L. Martinez, T. Rath, S. A. Haque, *Angew. Chem. Int. Ed.* **2015**, *54*, 8208; *Angew. Chem.* **2015**, *127*, 8326.
[8] T. Leijtens, G. E. Eperon, S. Pathak, A. Abate, M. M. Lee, H. J. Snaith, *Nat. Commun.* **2013**, *4*, 2885.
[9] S. Ma, W. Qiao, T. Cheng, B. Zhang, J. Yao, A. Alsaedi, T. Hayat, Y. Ding, Z. Tan, S. Dai, *ACS Appl. Mater. Interfaces* **2018**, *10*, 3902.
[10] Y. Yang, H. Peng, C. Liu, Z. Arain, Y. Ding, S. Ma, X. Liu, T. Hayat, A. Alsaedi, S. Dai, *J. Mater. Chem. A* **2019**, *7*, 6450.
[11] X. Lian, Z. Zhao, D. Cheng, *Mol. Cryst. Liq. Cryst.* **2017**, *648*, 223.
[12] P. Agarwala, D. Kabra, *J. Mater. Chem. A* **2017**, *5*, 1348.
[13] J. D. Myers, J. Xue, *Polym. Rev.* **2012**, *52*, 1.
[14] T. P. I. Saragi, T. Spehr, A. Siebert, T. Fuhrmann-Lieker, J. Salbeck, *Chem. Rev.* **2007**, *107*, 1011.
[15] T. Swetha, S. P. Singh, *J. Mater. Chem. A* **2015**, *3*, 18329.
[16] J. Urieta-Mora, I. García-Benito, A. Molina-Ontoria, N. Martín, *Chem. Soc. Rev.* **2018**, *47*, 8541.
[17] W. Yan, S. Ye, Y. Li, W. Sun, H. Rao, Z. Liu, Z. Bian, C. Huang, *Adv. Energy Mater.* **2016**, *6*, 1600474.
[18] C. H. Teh, R. Daik, E. L. Lim, C. C. Yap, M. A. Ibrahim, N. A. Ludin, K. Sopian, M. A. M. Teridi, *J. Mater. Chem. A* **2016**, *4*, 15788.
[19] K. Rakstys, C. Igci, M. K. Nazeeruddin, *Chem. Sci.* **2019**, *10*, 6748.
[20] Z. H. Bakr, Q. Wali, A. Fakharuddin, L. Schmidt-Mende, T. M. Brown, R. Jose, *Nano Energy* **2017**, *34*, 271.
[21] U. Bach, D. Lupo, P. Comte, J. E. Moser, F. Weissörtel, J. Salbeck, H. Spreitzer, M. Grätzel, *Nature* **1998**, *395*, 583.
[22] Z. Hawash, L. K. Ono, Y. Qi, *Adv. Mater. Interfaces* **2018**, *5*, 1700623.
[23] S. Gangala, R. Misra, *J. Mater. Chem. A* **2018**, *6*, 18750.
[24] N. J. Jeon, H. Na, E. H. Jung, T. Y. Yang, Y. G. Lee, G. Kim, H. W. Shin, S. Il Seok, J. Lee, J. Seo, *Nat. Energy* **2018**, *3*, 682.

[25] Z. Deng, M. He, Y. Zhang, F. Ullah, K. Ding, J. Liang, Z. Zhang, H. Xu, Y. Qiu, Z. Xie, T. Shan, Z. Chen, H. Zhong, C. C. Chen, *Chem. Mater.* **2021**, *33*, 285.

[26] M. Jeong, I. W. Choi, E. M. Go, Y. Cho, M. Kim, B. Lee, S. Jeong, Y. Jo, H. W. Choi, J. Lee, J. H. Bae, S. K. Kwak, D. S. Kim, C. Yang, *Science* **2020**, *369*, 1615.

[27] D. Bi, B. Xu, P. Gao, L. Sun, M. Grätzel, A. Hagfeldt, *Nano Energy* **2016**, *23*, 138.

[28] B. Xu, D. Bi, Y. Hua, P. Liu, M. Cheng, M. Grätzel, L. Kloo, A. Hagfeldt, L. Sun, *Energy Environ. Sci.* **2016**, *9*, 873.

[29] J. Zhang, B. Xu, L. Yang, C. Ruan, L. Wang, P. Liu, W. Zhang, N. Vlachopoulos, L. Kloo, G. Boschloo, L. Sun, A. Hagfeldt, E. M. J. Johansson, *Adv. Energy Mater.* **2018**, *8*, 1701209.

[30] B. Xu, J. Zhang, Y. Hua, P. Liu, L. Wang, C. Ruan, Y. Li, G. Boschloo, E. M. J. Johansson, L. Kloo, A. Hagfeldt, A. K. Y. Jen, L. Sun, *Chem* **2017**, *2*, 676.

[31] V. A. Chiykowski, Y. Cao, H. Tan, D. P. Tabor, E. H. Sargent, A. Aspuru-Guzik, C. P. Berlinguette, *Angew. Chem. Int. Ed.* **2018**, *57*, 15529; *Angew. Chem.* **2018**, *130*, 15755.

[32] N. Drigo, C. Roldan-Carmona, M. Franckevičius, K. H. Lin, R. Gegevičius, H. Kim, P. A. Schouwink, A. A. Sutanto, S. Olthof, M. Sohail, K. Meerholz, V. Gulbinas, C. Corminboeuf, S. Paek, M. K. Nazeeruddin, *J. Am. Chem. Soc.* **2020**, *142*, 1792.

[33] M. Saliba, S. Orlandi, T. Matsui, S. Aghazada, M. Cavazzini, J. P. Correa-Baena, P. Gao, R. Scopelliti, E. Mosconi, K. H. Dahmen, F. De Angelis, A. Abate, A. Hagfeldt, G. Pozzi, M. Graetzel, M. K. Nazeeruddin, *Nat. Energy* **2016**, *1*, 15017.

[34] K. Rakstys, S. Paek, M. Sohail, P. Gao, K. T. Cho, P. Gratia, Y. Lee, K. H. Dahmen, M. K. Nazeeruddin, *J. Mater. Chem. A* **2016**, *4*, 18259.

[35] K. Gao, B. Xu, C. Hong, X. Shi, H. Liu, X. Li, L. Xie, A. K. Y. Jen, *Adv. Energy Mater.* **2018**, *8*, 1800809.

[36] X. D. Zhu, X. J. Ma, Y. K. Wang, Y. Li, C. H. Gao, Z. K. Wang, Z. Q. Jiang, L. S. Liao, *Adv. Funct. Mater.* **2019**, *29*, 1807094.

[37] X. Wang, J. Zhang, S. Yu, W. Yu, P. Fu, X. Liu, D. Tu, X. Guo, C. Li, *Angew. Chem. Int. Ed.* **2018**, *57*, 12529; *Angew. Chem.* **2018**, *130*, 12709.

[38] See ref. [14].

[39] J. Salbeck, F. Weissörtel, J. Bauer, *Macromol. Symp.* **1998**, *125*, 121.

[40] J. Salbeck, N. Yu, J. Bauer, F. Weissörtel, H. Bestgen, *Synth. Met.* **1997**, *91*, 209.

[41] M. L. Petrus, A. Music, A. C. Closs, J. C. Bijleveld, M. T. Sirtl, Y. Hu, T. J. Dingemans, T. Bein, P. Docampo, *J. Mater. Chem. A* **2017**, *5*, 25200.

[42] M. L. Petrus, K. Schutt, M. T. Sirtl, E. M. Hutter, A. C. Closs, J. M. Ball, J. C. Bijleveld, A. Petrozza, T. Bein, T. J. Dingemans, T. J. Savenije, H. Snaith, P. Docampo, *Adv. Energy Mater.* **2018**, *8*, 1801605.

[43] M. Daskeviciene, S. Paek, Z. Wang, T. Malinauskas, G. Jokubauskaite, K. Rakstys, K. T. Cho, A. Magomedov, V. Jankauskas, S. Ahmad, H. J. Snaith, V. Getautis, M. K. Nazeeruddin, *Nano Energy* **2017**, *32*, 551.

[44] D. Vaitukaityte, Z. Wang, T. Malinauskas, A. Magomedov, G. Bubniene, V. Jankauskas, V. Getautis, H. J. Snaith, *Adv. Mater.* **2018**, *30*, 1803735.

[45] S. Daskeviciute, C. Momblona, K. Rakstys, A. A. Sutanto, M. Daskeviciene, V. Jankauskas, A. Gruodis, G. Bubniene, V. Getautis, M. K. Nazeeruddin, *J. Mater. Chem. A* **2021**, *9*, 301.

[46] F. Zhang, Z. Wang, H. Zhu, N. Pellet, J. Luo, C. Yi, X. Liu, H. Liu, S. Wang, X. Li, Y. Xiao, S. M. Zakeeruddin, D. Bi, M. Grätzel, *Nano Energy* **2017**, *41*, 469.

[47] F. Zhang, S. Wang, H. Zhu, X. Liu, H. Liu, X. Li, Y. Xiao, S. M. Zakeeruddin, *ACS Energy Lett.* **2018**, *3*, 1145.

[48] H. Jiang, J. Sun, J. Zhang, *Curr. Org. Chem.* **2012**, *16*, 2014.

[49] Z. Chen, H. Li, X. Zheng, Q. Zhang, Z. Li, Y. Hao, G. Fang, *ChemSusChem* **2017**, *10*, 3111.

[50] X. X. Liu, X. Ding, Y. Ren, Y. Yang, Y. Ding, X. X. Liu, A. Alsaedi, T. Hayat, J. Yao, S. Dai, *J. Mater. Chem. C* **2018**, *6*, 12912.

[51] W. Yu, Q. Yang, J. Zhang, D. Tu, X. Wang, X. Liu, G. Li, X. Guo, C. Li, *ACS Appl. Mater. Interfaces* **2019**, *11*, 30065.

[52] M. S. Kang, S. Do Sung, I. T. Choi, H. Kim, M. Hong, J. Kim, W. I. Lee, H. K. Kim, *ACS Appl. Mater. Interfaces* **2015**, *7*, 22213.

[53] C. Lu, I. T. Choi, J. Kim, H. K. Kim, *J. Mater. Chem. A* **2017**, *5*, 20263.

[54] F. Wu, Y. Ji, C. Zhong, Y. Liu, L. Tan, L. Zhu, *Chem. Commun.* **2017**, *53*, 8719.

[55] A. Magomedov, S. Paek, P. Gratia, E. Kasparavicius, M. Daskeviciene, E. Kamarauskas, A. Gruodis, V. Jankauskas, K. Kantminiene, K. T. Cho, K. Rakstys, T. Malinauskas, V. Getautis, M. K. Nazeeruddin, *Adv. Funct. Mater.* **2018**, *28*, 1704351.

[56] K. Rakstys, S. Paek, A. Drevilkauskaite, H. Kanda, S. Daskeviciute, N. Shibayama, M. Daskeviciene, A. Gruodis, E. Kamarauskas, V. Jankauskas, V. Getautis, M. K. Nazeeruddin, *ACS Appl. Mater. Interfaces* **2020**, *12*, 19710.

[57] F. Wu, Y. Shan, J. Qiao, C. Zhong, R. Wang, Q. Song, L. Zhu, *ChemSusChem* **2017**, *10*, 3833.

[58] D. Li, J. Y. Shao, Y. Y. Li, Y. Y. Li, L. Y. Deng, Y. W. Zhong, Q. Meng, *Chem. Commun.* **2018**, *54*, 1651.

[59] N. Tsutsumi, M. Yamamoto, Y. Nishijima, *J. Polym. Sci. Part B* **1987**, *25*, 2139.

[60] T. Sasakawa, T. Ikeda, S. Tazuke, *J. Appl. Phys.* **1989**, *65*, 2750.

[61] T. Ikeda, H. Mochizuki, Y. Hayashi, M. Sisido, T. Sasakawa, *J. Appl. Phys.* **1991**, *70*, 3689.

[62] P. Ganesan, K. Fu, P. Gao, I. Raabe, K. Schenk, R. Scopelliti, J. Luo, L. H. Wong, M. Grätzel, M. K. Nazeeruddin, *Energy Environ. Sci.* **2015**, *8*, 1986.

[63] K. Rakstys, M. Saliba, P. Gao, P. Gratia, E. Kamarauskas, S. Paek, V. Jankauskas, M. K. Nazeeruddin, *Angew. Chem. Int. Ed.* **2016**, *55*, 7464; *Angew. Chem.* **2016**, *128*, 7590.

Manuscript received: October 1, 2021
Version of record online: December 16, 2021

Angewandte Chemie
Eine Zeitschrift der Gesellschaft Deutscher Chemiker

Supporting Information

Green-Chemistry-Inspired Synthesis of Cyclobutane-Based Hole-Selective Materials for Highly Efficient Perovskite Solar Cells and Modules

Sarune Daskeviciute-Geguziene, Yi Zhang, Kasparas Rakstys, Gediminas Kreiza, Sher Bahadar Khan, Hiroyuki Kanda, Sanghyun Paek, Maryte Daskeviciene, Egidijus Kamarauskas, Vygintas Jankauskas, Abdullah M. Asiri, Vytautas Getautis,* and Mohammad Khaja Nazeeruddin**

anie_202113207_sm_miscellaneous_information.pdf

Supporting Information

Experimental section

Chemicals required for the synthesis were purchased from Sigma-Aldrich, TCI Europe, and Fluorochem and were used as received without additional purification. ^{1}H NMR spectra were recorded at 400 MHz on a Bruker Avance III spectrometer with a 5 mm double resonance broad band BBO z-gradient room temperature probe, ^{13}C NMR spectra were collected using the same instrument at 101 MHz. The chemical shifts, expressed in ppm, were relative to tetramethylsilane (TMS). All the NMR experiments were performed at 25 °C. Reactions were monitored by thin-layer chromatography on ALUGRAM SIL G/UV254 plates and developed with UV light. Silica gel (grade 9385, 230–400 mesh, 60 Å, Aldrich) was used for column chromatography. Elemental analysis was performed with an Exeter Analytical CE-440 elemental analyser, Model 440 C/H/N/.

Detailed synthetic procedures

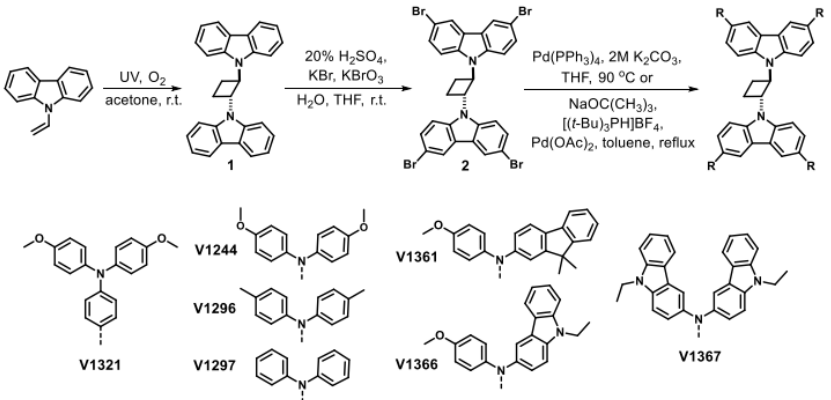

Figure S1. Synthesis scheme for final HTMs.

1,2-di(9*H*-carbazol-9-yl)cyclobutane (1)

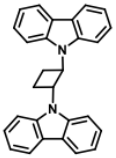

A solution of 9-vinylcarbazole (12 g, 62 mmol) in acetone (125 mL) was irradiated (GR.E. 125W helios italquartz) for 15 hours at room temperature. Air was bubbled through the solution continuously. The precipitated product was filtered and recrystallized from acetone to give pale creamy crystals. (8.5 g, 70.8%). ^{1}H NMR (400 MHz, THF-d_6) δ 8.02 (d, J = 8.0 Hz, 4H), 7.72 (d, J = 8.0 Hz, 4H), 7.34 (t, J = 7.6 Hz, 4H), 7.13 (t, J = 7.6 Hz, 4H), 6.53 – 6.29 (m, 2H), 3.22 – 2.99 (m, 2H), 2.80 – 2.63 (m, 2H). ^{13}C NMR (101 MHz, THF) 138.27, 123.59, 121.69, 118.15, 117.15, 107.88, 52.48, 18.59.

1,2-bis(3,6-dibromo-9*H*-carbazol-9-yl)cyclobutane (2)

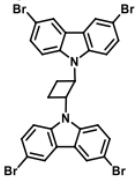

Compound **(1)** (1.9 g, 4.9 mmol) was dissolved in THF (50 mL). Afterwards, 20% H_2SO_4 (50 mL) solution was added, following by dropwise addition (10mL/min) of KBr and $KBrO_3$ solution (69 mL H_2O, KBr 4.1 g, $KBrO_3$ 1.15 g) and stirred at room temperature for 72 hours. The precipitate was collected by filtration, washed with water and hot methanol for three times to give **2** as white crystals. (3.1 g, 88.6%). ^{1}H NMR (400 MHz, THF-d_6) δ 8.26 (s, 4H), 7.65 (d, J = 8.8 Hz, 4H), 7.50 (d, J = 8.8 Hz, 4H), 6.41 – 6.13 (m, 2H), 3.14 – 2.96 (m, 2H), 2.85 – 2.64 (m, 2H). ^{13}C NMR (101 MHz, THF) δ 139.05, 129.02, 124.33, 123.45, 112.47, 111.59, 54.51, 20.75.

1,2-bis[3,6-bis(4,4'-dimethoxy)diphenylamino-9*H*-carbazol-9-yl]cyclobutane (V1244)

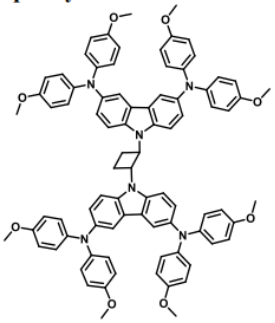

A solution of compound **2** (0.5 g, 0.7 mmol, 1 eq) and 4,4'-dimethoxydiphenylamine (0.98 g, 4.3 mmol, 6 eq) in anhydrous toluene (7 mL) was purged with argon for 30 minutes. Afterwards, palladium (II) acetate (0.02 eq), tri-*tert*-butylphosphonium tetrafluoroborate (0.027 eq) and sodium *tert*-butoxide (6 eq) were added and the solution was refluxed under argon atmosphere for 5 hours. After cooling to room temperature, reaction mixture was filtered through celite, extracted with ethylacetate and distilled water. The organic layer was dried over anhydrous Na_2SO_4, filtered and solvent evaporated. The crude product was purified by column chromatography using 3:9.5 v/v THF/*n*-hexane as an eluent. The obtained product was dissolved in acetone and precipitated into 15 times excess of ethanol. The precipitate was filtered off and washed with ethanol to collect **V1244** as a pale green solid. (0.52 g, 56.3%). ^{1}H NMR (400 MHz, THF-d_6) δ 7.66 – 7.51 (m, 8H), 7.08 (d, J = 8.8, 1.7 Hz, 4H), 6.88 (d, J = 8.8 Hz, 16H), 6.71 (d, J = 8.8 Hz, 16H), 6.34 – 6.18 (m, 2H), 3.69 (s, 24H), 3.03 – 2.91 (m, 2H), 2.70 – 2.60 (m, 2H). ^{13}C NMR (101 MHz, THF) δ 154.95, 142.47, 141.24, 137.03, 124.27, 124.13, 123.92, 116.39, 114.17, 110.55, 54.75, 54.54, 20.62. Anal. calcd for $C_{84}H_{74}N_6O_8$: C, 77.88; H, 5.76; N, 6.49; found: C, 77.97; H, 5.72; N, 6.41. $C_{84}H_{74}N_6O_8[M^+]$ exact mass = 1294.56, MS (ESI) = 1294.97.

1,2-bis[3,6-bis(4,4'-dimethyl)diphenylamino-9*H*-carbazol-9-yl]cyclobutane (V1296)

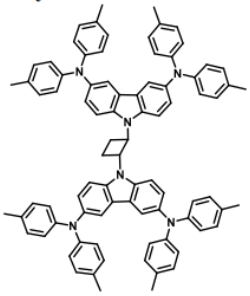

A solution of compound **2** (0.5 g, 0.7 mmol, 1 eq) and 4,4'-dimethyldiphenylamine (0.84 g, 4.3 mmol, 6 eq) in anhydrous toluene (7 mL) was purged with argon for 30 minutes. Afterwards, palladium (II) acetate (0.02 eq), tri-*tert*-butylphosphonium tetrafluoroborate (0.027 eq) and sodium *tert*-butoxide (6 eq) were added and the solution was refluxed under argon atmosphere for 22 hours. After cooling to room temperature, reaction mixture was filtered through celite, extracted with ethylacetate and distilled water. The organic layer was dried over anhydrous Na_2SO_4, filtered and solvent evaporated. The crude product was recrystallized from ethanol/toluene 1:1 to give **V1296** as pale green crystals. (0.46 g, 55.4%). ^{1}H NMR (400 MHz, THF-d_6) δ 7.67 (s, 4H), 7.66 (d, J = 8.8 Hz, 4H), 7.12 (d, J = 8.8 Hz, 4H), 6.93 (d, J = 8.4 Hz, 16H), 6.85 (d, J = 8.4 Hz, 16H), 6.39 – 6.25 (m, 2H), 3.09 – 2.92 (m,

2H), 2.79 – 2.59 (m, 2H), 2.22 (s, 24H). ^{13}C NMR (101 MHz, THF) δ 144.59, 138.67, 135.70, 128.59, 127.45, 123.16, 122.52, 120.71, 116.07, 108.91, 52.89, 18.84, 17.92. Anal. calcd for $C_{84}H_{74}N_6$: C, 86.41; H, 6.39; N, 7.20; found: C, 86.24; H, 6.45; N, 7.31. $C_{84}H_{74}N_6[M^+]$ exact mass = 1166.60, MS (ESI) = 1167.06.

1,2-bis(3,6-bisdiphenylamino-9*H*-carbazol-9-yl)cyclobutane (V1297)

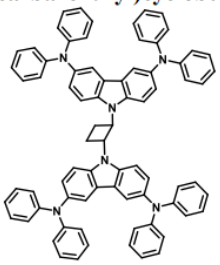

A solution of compound **2** (0.5 g, 0.7 mmol, 1 eq) and diphenylamine (0.72 g, 4.3 mmol, 6 eq) in anhydrous toluene (7 mL) was purged with argon for 30 minutes. Afterwards, palladium (II) acetate (0.02 eq), tri-*tert*-butylphosphonium tetrafluoroborate (0.027 eq) and sodium *tert*-butoxide (6 eq) were added and the solution was refluxed under argon atmosphere for 27 hours. After cooling to room temperature, reaction mixture was filtered through celite, extracted with ethylacetate and distilled water. The organic layer was dried over anhydrous Na_2SO_4, filtered and solvent evaporated. The crude product was purified by column chromatography using 1:9 v/v THF/*n*-hexane as an eluent. The obtained product was dissolved in THF and precipitated into 15 times excess of *n*-hexane. The precipitate was filtered off and washed with hexane to collect **V1297** as a pale green solid. (0.44 g, 58.7%). ^{1}H NMR (400 MHz, DMSO-d_6) δ 7.89 (d, J = 9.2 Hz, 4H), 7.83 (d, J = 2.0 Hz, 4H), 7.27 – 7.05 (m, 20H), 6.97 – 6.79 (m, 24H), 6.39 – 6.24 (m, 2H), 2.93 – 2.75 (m, 2H), 2.70 – 2.55 (m, 2H). ^{13}C NMR (101 MHz, DMSO) δ 148.42, 139.76, 138.02, 129.65, 126.33, 124.09, 122.46, 122.02, 119.67, 112.27, 54.24, 21.65. Anal. calcd for $C_{76}H_{58}N_6$: C, 86.50; H, 5.54; N, 7.96; found: C, 86.65; H, 5.50; N, 7.85. $C_{76}H_{58}N_6[M^+]$ exact mass = 1054.47, MS (ESI) = 1054.90.

1,2-bis|3,6-bis{4-[*N*,*N*-bis(4-methoxyfenil)amino]fenil}-9*H*-carbazol-9-yl|cyclobutane (V1321)

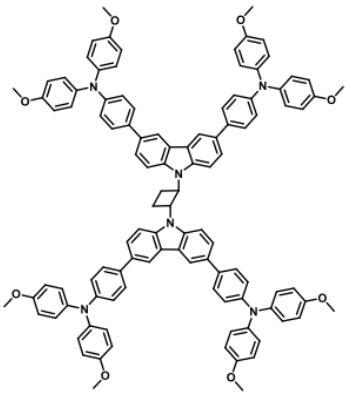

A solution of compound **2** (0.1 g, 0.14 mmol, 1 eq) and 4-methoxy-*N*-(4-methoxyphenyl)-*N*-(4-(4,4,5,5-tetramethyl-1,3,2-dioxaborolan-2-yl)phenyl)aniline (0.61 g, 1.4 mmol, 10 eq) in anhydrous THF (10 mL) was purged with argon for 10 minutes. Afterwards,

tetrakis(triphenylphosphine)-palladium(0) (0.115 eq) and 2M K_2CO_3 (4 mL) were added and the solution was heated for 3 hours at 90 °C. After cooling to room temperature, reaction mixture was filtered through celite, extracted with ethylacetate and distilled water. The organic layer was dried over anhydrous Na_2SO_4, filtered and solvent evaporated. The crude product was purified by column chromatography using 4:8.5 v/v THF/*n*-hexane as an eluent. The obtained product was dissolved in THF into 15 times excess of *n*-hexane. The precipitate was filtered off and washed with hexane to collect **V1321** as a pale yellow - green solid. (0.16 g, 70.2%). ^{1}H NMR (400 MHz, THF-d_6) δ 8.34 (s, 4H), 7.76 (d, J = 8.8 Hz, 4H), 7.59 (d, J = 8.8 Hz, 4H), 7.51 (d, J = 8.6 Hz, 8H), 7.02 (d, J = 8.8 Hz, 16H), 6.97 (d, J = 8.6 Hz, 8H), 6.82 (d, J = 8.8 Hz, 16H), 6.50 – 6.35 (m, 2H), 3.74 (s, 24H), 3.19 – 3.02 (m, 2H), 2.86 – 2.68 (m, 2H). ^{13}C NMR (101 MHz, THF) δ 154.17, 145.70, 139.26, 137.80, 132.26, 130.62, 125.34, 124.20, 122.65, 122.48, 119.37, 115.94, 112.55, 108.21, 52.85, 52.74, 18.86. Anal. calcd for $C_{108}H_{90}N_6O_8$: C, 81.08; H, 5.67; N, 5.25; found: C, 81.35; H, 5.54; N, 5.23. $C_{108}H_{90}N_6O_8[M^+]$ exact mass = 1598.68, MS (ESI) = 1599.45.

_N_-(4-methoxyphenyl)-9,9-dimethyl-9_H_-fluoren-2-amine (3)

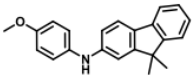

Anhydrous dioxane (12 mL) with few drops of distilled water (0.02 eq) was purged with argon for 20 minutes. After that, the temperature was raised to 80 °C, palladium (II) acetate (0.005 eq) and XPhos (0.015 eq) were added. The mixture was stirred for 1.5 minutes and temperature was raised to 110 °C. 2-bromo-9,9-dimethylfluorene (2.7 g, 9.9 mmol, 1 eq), *p*-Anisidine (1.5 g, 11.9 mmol, 1.2 eq) and sodium *tert*-butoxide (1.4 eq) were added and stirred for 1 hour. After cooling to room temperature, reaction mixture was extracted with ethyl acetate and distilled water. The organic layer was dried over anhydrous Na_2SO_4, filtered and the solvent evaporated. The crude product was purified by column chromatography using 1:12.5 v/v THF/*n*-hexane as an eluent. Pale brown crystals were collected as a final product. (2.45 g, 78.7 %). ^{1}H NMR (400 MHz, DMSO-d_6) δ 8.01 (s, 1H), 7.68 – 7.53 (m, 2H), 7.44 (d, J = 7.6 Hz, 1H), 7.25 (t, J = 7.4 Hz, 1H), 7.16 (t, J = 7.4 Hz, 1H), 7.14 – 7.02 (m, 3H), 6.97 – 6.84 (m, 3H), 3.73 (s, 3H), 1.38 (s, 6H). ^{13}C NMR (101 MHz, DMSO) δ 155.29, 154.30, 152.89, 145.47, 139.65, 136.60, 129.78, 127.34, 125.89, 122.90, 121.36, 120.86, 119.02, 115.07, 114.19, 109.53, 55.69, 46.63, 27.63. Anal. calcd. for: $C_{22}H_{21}NO$: C, 83.78; H, 6.71; N, 4.44; found: C, 83.94; H, 6.66; N, 4.42.

1,2-bis{3,6-bis[_N_-(9,9-dimethylfluoren-2-yl)-_N_-(4-methoxyfenil)amino]-9_H_-carbazol-9-yl}cyclobutane (V1361)

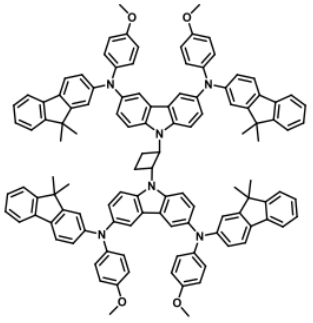

A solution of compound **2** (0.5 g, 0.7 mmol, 1 eq) and **3** (1.35 g, 4.3 mmol, 6 eq) in anhydrous toluene (10 mL) was purged with argon for 30 minutes. Afterwards, palladium (II) acetate (0.02 eq), tri-*tert*-butylphosphonium tetrafluoroborate (0.027 eq) and sodium *tert*-butoxide (6

eq) were added and the solution was refluxed under argon atmosphere for 5 hours. After cooling to room temperature, reaction mixture was filtered through celite, extracted with ethylacetate and distilled water. The organic layer was dried over anhydrous Na_2SO_4, filtered and solvent evaporated. The crude product was purified by column chromatography using 5.5:19.5 v/v THF/*n*-hexane as an eluent. The obtained product was dissolved in THF and precipitated into 15 times excess of *n*-hexane. The precipitate was filtered off and washed with hexane to collect **V1361** as a yellow-green solid. (0.67 g, 57.3%). ^{1}H NMR (400 MHz, DMSO-d_6) δ 7.88 (d, J = 8.4 Hz, 4H), 7.78 (s, 4H), 7.55 (d, J = 7.8 Hz, 4H), 7.49 (d, J = 7.8 Hz, 4H), 7.28 (d, J = 7.2 Hz, 4H), 7.24 – 7.16 (m, 8H), 7.11 (t, J = 7.4 Hz, 4H), 7.00 (d, J = 8.6 Hz, 8H), 6.93 (s, 4H), 6.80 (d, J = 8.6 Hz, 8H), 6.69 (d, J = 8.4 Hz, 4H), 6.42 – 6.23 (m, 2H), 3.64 (s, 12H), 2.92 – 2.77 (m, 2H), 2.76 – 2.56 (m, 2H), 1.17 (s, 24H). ^{13}C NMR (101 MHz, DMSO) δ 155.83, 154.82, 153.15, 149.03, 141.15, 140.42, 139.09, 137.50, 131.40, 127.37, 126.76, 126.35, 125.32, 123.94, 122.86, 121.12, 119.41, 119.19, 118.17, 115.27, 114.25, 111.87, 55.55, 53.96, 46.56, 27.29, 27.25. Anal. calcd for $C_{116}H_{98}N_6O_2$: C, 84.95; H, 6.02; N, 5.12; found: C, 84.85; H, 6.06; N, 5.15. $C_{116}H_{98}N_6O_2[M^+]$ exact mass = 1638.76, MS (ESI) = 1639.48.

1,2-bis{3,6-bis[*N*-(9-ethylcarbazol-3-yl)-N-(4-methoxyfenil)amino]-9*H*-carbazol-9-yl}cyclobutane (V1366)

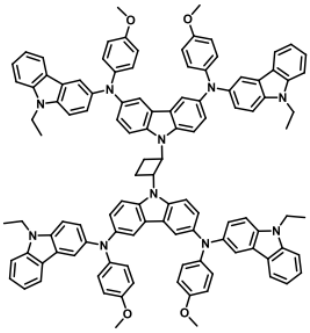

A solution of compound **2** (0.5 g, 0.7 mmol, 1 eq) and 9-ethyl-*N*-(4-methoxyphenyl)-9*H*-carbazol-3-amine[1] (1.35 g, 4.3 mmol, 6 eq) in anhydrous toluene (10 mL) was purged with argon for 30 minutes. Afterwards, palladium (II) acetate (0.02 eq), tri-*tert*-butylphosphonium tetrafluoroborate (0.027 eq) and sodium *tert*-butoxide (6 eq) were added and the solution was refluxed under argon atmosphere for 5 hours. After cooling to room temperature, reaction mixture was filtered through celite, extracted with ethylacetate and distilled water. The organic layer was dried over anhydrous Na_2SO_4, filtered and solvent evaporated. The crude product was purified by column chromatography using 4.5:8 v/v THF/*n*-hexane as an eluent. The obtained product was dissolved in THF and precipitated into 15 times excess of *n*-hexane. The precipitate was filtered off and washed with hexane to collect **V1366** as a yellow-green solid. (0.71 g, 60.7%). ^{1}H NMR (400 MHz, THF-d_6) δ 7.84 (d, J = 8.0 Hz, 4H), 7.75 (s, 4H), 7.69 – 7.58 (m, 8H), 7.37 (d, J = 8.4 Hz, 4H), 7.33 – 7.25 (m, 8H), 7.19 – 7.11 (m, 8H), 6.97 (t, J = 7.4 Hz, 4H), 6.92 (d, J = 8.8 Hz, 8H), 6.68 (d, J = 8.8 Hz, 8H), 6.38 – 6.26 (m, 2H), 4.31 (q, J = 7.0 Hz, 8H), 3.65 (s, 12H), 3.08 – 2.93 (m, 2H), 2.71 – 2.58 (m, 2H), 1.33 (t, J = 7.0 Hz, 12H). ^{13}C NMR (101 MHz, THF) δ 154.55, 143.30, 141.94, 141.50, 140.44, 136.86, 136.20, 125.19, 124.98 124.35, 123.79, 123.69, 123.56, 122.77, 120.21, 118.13, 116.09, 115.97, 114.11, 110.49, 108.88, 108.19, 54.74, 54.52, 37.04, 20.57, 13.14. Anal. calcd for $C_{112}H_{94}N_{10}O_4$: C, 81.82; H, 5.76; N, 8.52; found: C, 81.91; H, 5.70; N, 7.50. $C_{112}H_{94}N_{10}O_4[M^+]$ exact mass = 1642.75, MS (ESI) = 1643.47.

Bis(9-ethyl-9*H*-carbazol-3-yl)amine (4)

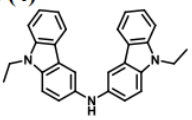

Anhydrous dioxane (14 mL) with few drops of distilled water (0.02 eq) was purged with argon for 20 minutes. After that, the temperature was raised to 80 °C, palladium (II) acetate (0.005 eq) and XPhos (0.015 eq) were added. The mixture was stirred for 1.5 minutes and temperature was raised to 110 ºC. 3-bromo-9-ethylcarbazole (2.7 g, 9.8 mmol, 1 eq), 3-amino-9-ethylcarbazole (2.5 g, 11.8 mmol, 1.2 eq) and sodium *tert*-butoxide (1.4 eq) were added and stirred for 30 minutes. After cooling to room temperature, reaction mixture was extracted with ethyl acetate and distilled water. The organic layer was dried over anhydrous Na_2SO_4, filtered and the solvent evaporated. The crude product was purified by column chromatography using 3:22 v/v THF/*n*-hexane as an eluent. Light orange brown crystals were collected as a final product. (3.24 g, 81.6 %). ^{1}H NMR (400 MHz, THF-d_6) δ 7.94 (d, J = 7.6 Hz, 2H), 7.81 (s, 2H), 7.42–7.30 (m, 6H), 7.24 (d, J = 8.4 Hz, 2H), 7.06 (t, J = 7.2 Hz, 2H), 6.89 (s, 1H), 4.37 (q, J = 7.2 Hz, 4H), 1.38 (t, J = 7.2 Hz, 6H). ^{13}C NMR (101 MHz, THF) δ 140.46, 138.61, 135.27, 124.98, 123.66, 122.90, 119.98, 118.30, 117.79, 108.76, 108.17, 37.04, 13.13. Anal. calcd. for: $C_{28}H_{25}N_3$: C, 83.34; H, 6.24; N, 10.41; found: C, 83.14; H, 6.29; N, 10.49.

1,2-bis{3,6-bis[*N*,*N*-bis(9-ethylcarbazol-3-yl) amino]-9*H*-carbazol-9-yl}cyclobutane (V1367)

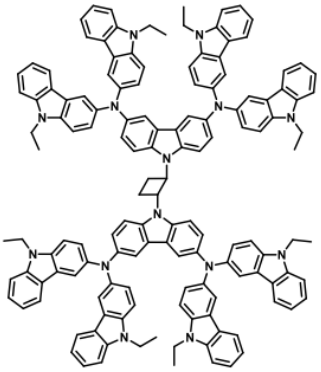

A solution of compound **2** (0.5 g, 0.7 mmol, 1 eq) and **4** (1.72 g, 4.3 mmol, 6 eq) in anhydrous toluene (12 mL) was purged with argon for 30 minutes. Afterwards, palladium (II) acetate (0.02 eq), tri-*tert*-butylphosphonium tetrafluoroborate (0.027 eq) and sodium *tert*-butoxide (6 eq) were added and the solution was refluxed under argon atmosphere for 6 hours. After cooling to room temperature, reaction mixture was filtered through celite and diluted with ethylacetate and distilled water resulting in solid precipitate formed, that was filtered and crude precipitate was purified by column chromatography using 4.5:8 v/v THF/*n*-hexane as an eluent. The obtained product was dissolved in THF and precipitated into 15 times excess of ethanol. The precipitate was filtered off and washed with ethanol to collect **V1367** as a yellow-green solid. (0.62 g, 43.7%). ^{1}H NMR (400 MHz, THF-d_6) δ 7.92 – 7.50 (m, 24H), 7.38 – 7.10 (m, 36H), 6.93 (t, J = 7.4 Hz, 8H), 6.46 – 6.29 (m, 2H), 4.24 (q, J = 6.8 Hz, 16H), 3.11 – 2.94 (m, 2H), 2.70 – 2.57 (m, 2H), 1.28 (t, J = 6.8 Hz, 24H). ^{13}C NMR (101 MHz, THF) δ 142.76, 142.40, 140.41, 136.70, 135.94, 128.72, 127.96, 125.07, 124.46, 123.66, 123.32, 122.85, 120.24, 118.04, 115.74, 115.44, 110.45, 108.83, 108.10, 54.73, 37.01, 13.17. Anal. calcd for $C_{140}H_{114}N_{14}$: C, 84.39; H, 5.77; N, 9.84; found: C, 84.28; H, 5.83; N, 9.89. $C_{140}H_{114}N_{14}[M^+]$ exact mass = 1990.94, MS (ESI) = 1991.12.

Volume 58
Number 54
11 July 2022
Pages 7441–7582

ChemComm

Chemical Communications

rsc.li/chemcomm

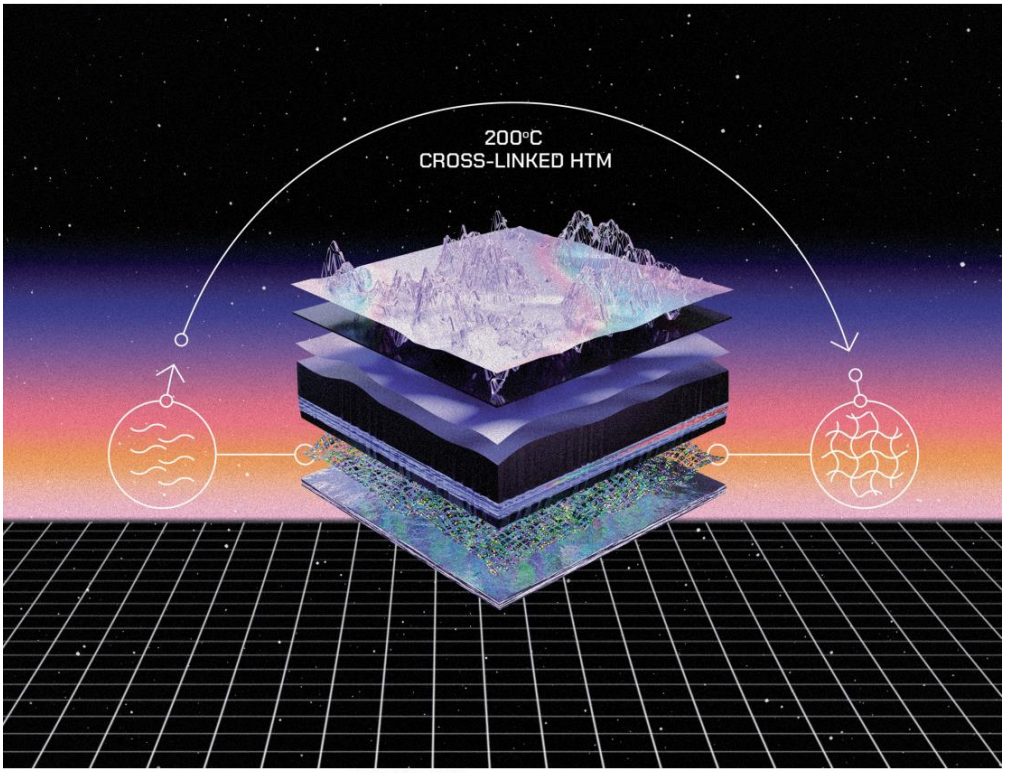

ISSN 1359-7345

ROYAL SOCIETY OF CHEMISTRY

COMMUNICATION

Vytautas Getautis *et al.*

Cross-linkable carbazole-based hole transporting materials for perovskite solar cells

ChemComm

COMMUNICATION

View Article Online
View Journal | View Issue

Cite this: *Chem. Commun.*, 2022, **58**, 7495

Received 7th May 2022,
Accepted 8th June 2022

DOI: 10.1039/d2cc02612k

rsc.li/chemcomm

Cross-linkable carbazole-based hole transporting materials for perovskite solar cells†

Sarune Daskeviciute-Geguziene,[a] Artiom Magomedov,[ab] Maryte Daskeviciene,[a] Kristijonas Genevičius,[c] Nerijus Nekrašas,[c] Vygintas Jankauskas,[c] Kristina Kantminiene,[d] Michael D. McGehee[b] and Vytautas Getautis*[a]

Carbazole-based molecules V1205 and V1206 capable of cross-linking *via* three vinyl groups were synthesized by a simple process and applied as hole-transporting materials (HTMs) in inverted perovskite solar cells (PSC). Novel HTMs were thermally polymerized to provide films resistant to organic solvents. A PSC with V1205 exhibited a photovoltaic conversion efficiency of 16.9% with good stability.

Organic–inorganic hybrid perovskite solar cells (PSCs) have been attracting increasing worldwide attention as a competitive alternative to conventional silicon-based solar cells[1] owing to their low-cost constituent materials, solution processing[2] and high power conversion efficiencies (PCEs).[3] Currently, the highest PCE of 25.8% (certified 25.5%) under standard illumination published in peer-reviewed journals was achieved in a so-called "regular", or n–i–p configuration, where HTM is deposited on top of the perovskite absorber layer.[4] As an alternative, in recent years, also p–i–n (or "inverted") configuration of PSCs has been explored with efficiencies getting close to those of the best regular PSCs (the highest published PCE value is 25.0%).[5] Moreover, inverted PSCs have an advantage in tandem applications where atomic layer deposition of SnO_x if often used to provide a functional protective contact that enables sputtering of transparent conducting oxides.[6] The advantages of PSCs with the inverted p–i–n architecture over n–i–p ones include the absence of dopants in the hole transporting layer, negligible hysteresis behavior, and compatibility with organic electronics manufacturing processes.[7] However, in the case of p–i–n devices, solution-processing of the perovskite absorber layer adds additional constraints on the choice of HTMs, as it usually should withstand a mixture of polar DMF:DMSO solvents. Therefore, so far the most popular choice of organic HTMs for such devices are polymers, such as PEDOT:PSS[8] and PTAA,[9] or combination of them.[10] As an alternative, several strategies have been reported, *e.g.* use of self-assembled monolayers,[11] change of the perovskite precursor solvent[12] or use of soluble precursors that are subsequently transformed into insoluble films.[13] Recently, cross-linkable fluorene-based HTMs have been introduced into inverted PSCs devices resulting in relatively high performances.[14] These small-molecule-based HTMs can be *in situ* converted into solvent-resistant, cross-linked networks. This approach provides an ideal solution to avoid tedious synthesis and purification that are often encountered for polymers.

On the other hand, the low-cost 9*H*-carbazole as a starting material is interesting due to its excellent charge-transport properties, high chemical stability, and simple functionalization of the structure with a variety of functional groups, which enable fine-tuning of the optical and electronic properties of target HTMs.[15] Therefore, carbazole-based derivatives have been employed in organic light-emitting diodes,[16] organic thin film transistors,[17] and dye-sensitized solar cells.[18] In recent years, carbazole-based HTMs have also attracted much attention in perovskite solar cells.[19]

In this work, cross-linkable carbazole-based HTMs **V1205** and **V1206** (Fig. 1), containing three vinyl groups, were synthesized in the simple reactions from commercially available materials and their properties were investigated. The new

[a] *Department of Organic Chemistry, Kaunas University of Technology, Kaunas 50254, Lithuania. E-mail: vytautas.getautis@ktu.lt*
[b] *Department of Chemical and Biological Engineering, University of Colorado, Boulder, CO, 80309, USA*
[c] *Institute of Chemical Physics, Vilnius University, Vilnius 10257, Lithuania*
[d] *Department of Physical and Inorganic Chemistry, Kaunas University of Technology, Kaunas 50254, Lithuania*

† Electronic supplementary information (ESI) available. See DOI: https://doi.org/10.1039/d2cc02612k

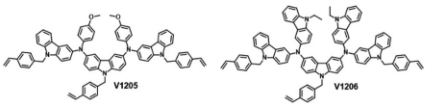

Fig. 1 Molecular structures of the synthesized carbazole-based cross-linkable HTMs **V1205** and **V1206**.

compounds underwent thermal polymerization to form solvent-resistant films. As a proof of concept, PSCs of p–i–n configuration were constructed, and a promising PCE of 16.7% was reached for a device with polymerized **V1205**, indicating a great potential of the presented class of cross-linkable dopant-free HTMs.

For the target materials to undergo *in situ* cross-linking, it is required to incorporate at least two groups that can undergo polymerization into the structure of the final cross-linked networks. Therefore, commercially available 3-bromo-9*H*-carbazole and 3,6-dibromo-9*H*-carbazole were chosen as starting compounds and two precursors **1** and **2** were synthesized by using a simple alkylation reaction scheme (Scheme 1). Next, in a sequential Hartwig–Buchwald palladium-catalyzed amination, *p*-anisidine was first coupled with **1** to yield compound **3**, which was then reacted with precursor **2** to provide the target product **V1205** containing three cross-linking 4-vinylbenzyl groups. Similarly, the precursor **1** reacted with 3-amino-9-ethylcarbazole to produce compound **4**, which could be treated with compound **2** to provide the final product **V1206** bearing cross-linking 4-vinylbenzyl groups. **V1206** was designed by replacing 4-methoxyphenyl groups in **V1205** with carbazolyl moieties. Structures of the synthesized compounds were confirmed by NMR and elemental analysis data. Detailed synthesis procedures and analysis data are reported in the ESI.†

To evaluate the optical properties of the synthesized compounds, UV/vis and photoluminescence (PL) spectra were recorded from the solutions (Fig. 2a). The UV spectra for both monomers, **V1205** and **V1206**, show an absorption maximum (λ_{max}) in the UV range at 325 nm, while only negligible absorption in the visible range of electromagnetic radiation has been recorded. The latter property is particularly important in devices with a p–i–n architecture, in which the light first passes through the HTM layer. Furthermore, it can be seen from the PL spectra that the emission of **V1206** is slightly red-shifted by 9 nm, compared to that of **V1205**, which corresponds to the increased π-conjugated electron system.

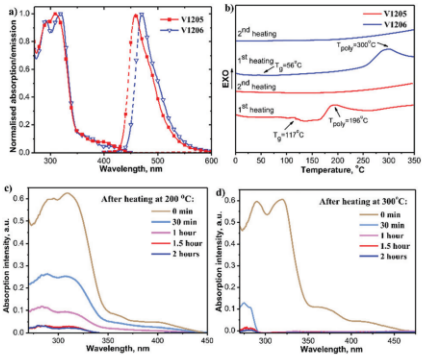

Fig. 2 (a) UV/vis and PL spectra of the solutions of **V1205** and **V1206** (THF, 10^{-4} M); (b) first and second scan heating curves of **V1205** and **V1206** (heating rate 10 °C min^{-1}, the *y*-axis is showing a heat flux). Cross-linking experiment of **V1205** (c) and **V1206** (d) films. The UV/vis spectra of the solutions prepared by dipping spin coated HTM films into THF after heating at 200 °C (c) and 300 °C (d) for the respective duration.

For the evaluation of the thermal stability of the synthesized carbazole-based materials and their ability to undergo a cross-linking process, thermal properties were studied by means of thermogravimetric analysis (TGA) and differential scanning calorimetry (DSC). Both compounds showed excellent thermal stability, with a T_{dec} of 443 °C for **V1205** and 404 °C for **V1206**, as seen from the TGA analysis (Fig. S1, ESI†). The DSC curves have shown that both investigated compounds exist only in an amorphous state since no endothermic melting peaks were detected during both heating cycles (Fig. 2b). For **V1205**, during the first DSC heating cycle, the glass transition process was detected at 117 °C, followed by an exothermic process at 196 °C, suggesting that thermal polymerization occurred at this

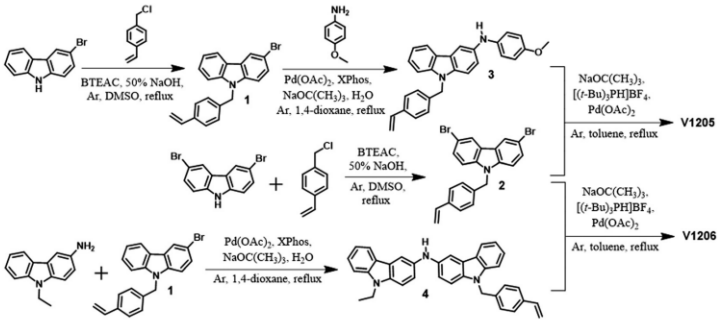

Scheme 1 Synthetic route to **V1205** and **V1206**.

temperature. During the second heating cycle, no phase transitions were observed, confirming the formation of the cross-linked polymer. For compound **V1206**, with higher molecular weight, a lower T_g of 56 °C was detected and the cross-linking process started at ~270 °C with a peak at ~300 °C (Fig. 2b). Again, during the second heating cycle, no phase transitions were detected. It should be noted that this cross-linking process does not require any use of initiators or dopants, and consequently, no unexpected impurities and defects that are detrimental to the device efficiency and stability can be introduced.

To evaluate the cross-linking ability of the thin films of the carbazole-based HTMs, the amount of washed material from the spin-coated film was evaluated by means of UV/vis spectroscopy detailed cross- into an insoluble polymer while in the case of **V1206** this process was faster – it took only 30 min. For both films, the cross-linking was completed roughly after 1.5 h of heating. The cross-linked films have shown to be resistant to the DMF : DMSO (4 : 1) solvent mixture, as after exposure to them the UV/vis absorption spectra of the films remained almost the same (Fig. S7 and S8, ESI†).

Next, the ability of new HTMs to transport charges was evaluated by the xerographic time-of-flight (XTOF) technique. The measured electric field dependencies of the hole drift mobilities in **V1205** and **V1206** are presented in Fig. 3. For both new HTMs, measurements from pure layers were not possible due to their insufficient quality, therefore, the charge transfer in layers of blends with bisphenol Z-polycarbonate (PC-Z), in weight ratios of 1 : 1, 1 : 2 or 1 : 3, which were of suitable quality, were studied in detail (Fig. S2–S5, ESI†). Based on the exponential dependence of the charge carrier mobility on the average distance between the charge transporting molecules,[20] interpolated mobility values were calculated for the case of pure material. Compound **V1206** bearing higher number of carbazolyl chromophores showed good charge transporting properties, *i.e.* reached 10^{-3} cm^2 V^{-1} s^{-1} at strong electrical fields (Fig. 3a). The simpler compound **V1205** showed slightly lower hole drift mobilities, yet still comparable to that of popular HTMs for PSCs. Since the cross-linking process does not affect the chromophoric system of the HTMs, it had only a minor influence on the hole drift mobility. Hole drift mobility of **V1205** even increased slightly after cross-linking (Fig. S6, ESI†), as was confirmed by the time-of-flight (TOF) method, as no measurement results were obtained by the XTOF method. Unfortunately, it was not possible to measure the hole drift mobility of **V1206** after cross-linking using neither the XTOF nor the TOF method. In addition to charge transporting properties, ionization potentials were measured through photoelectron spectroscopy in air (PESA). The values were 4.97 eV and 5.00 eV for **V1205** and **V1206**, respectively (Fig. 3b and c). As expected, these values changed negligibly after cross-linking (Fig. 3b and c). The recorded ionization potential values are consistent with the values reported for other HTMs used in PSCs.

To evaluate the performance of materials acting as hole-selective layers in PSCs, devices with p–i–n architecture (Fig. 4a) were fabricated and characterized. As an absorber material, triple-cation perovskite was used, with a nominal precursor solution composition of $Cs_{0.05}(FA_{0.83}MA_{0.17})_{0.95}Pb(I_{0.83}Br_{0.17})_3$. The films of the organic HTMs were prepared by spin-coating from toluene followed by the annealing at 200 °C (1.5 h) for **V1205** and 300 °C (1 h) for **V1206** to achieve cross-linking, as was determined previously. A detailed description of the fabrication and characterization of the devices can be found in the ESI.† The photovoltaic performance of the perovskite solar cells was evaluated from their photocurrent density–voltage (*J*–*V*) characteristics. The cross-linked **V1205** allowed for higher open-circuit voltages (V_{OC}) and current density (J_{SC}) and, as a consequence, the higher PCE of 16.9% than that of **V1206** (Fig. 4b and Table 1). As seen from Fig. 4c, only minor hysteresis was recorded. Performance of the employing thermally cross-linked HTM films was compared with that of neat films. As

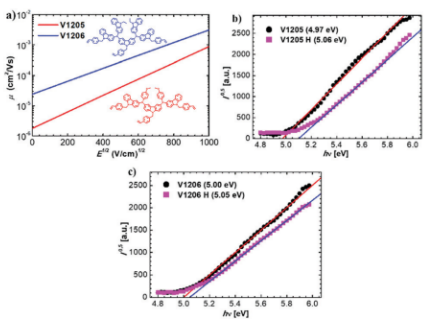

Fig. 3 (a) Charge mobility of **V1205** and **V1206**; (b) UV emission spectra of not heated (**V1205**) and cross-linked (**V1205H**) samples; (c) UV emission spectra of not heated (**V1206**) and cross-linked (**V1206H**) samples.

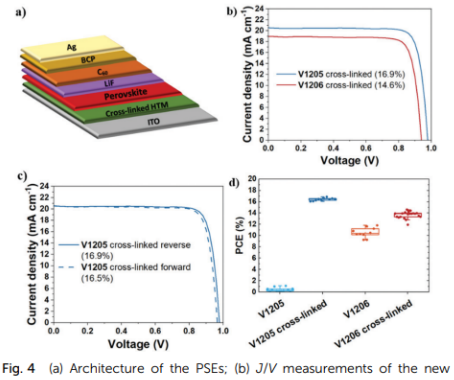

Fig. 4 (a) Architecture of the PSEs; (b) *J*/*V* measurements of the new HTMs (cross-linked), reverse scan; (c) *J*/*V* measurements of the cross-linked **V1205**, showing reverse and forward scans; (d) statistical distribution of the PCE for the HTMs studied.

Table 1 Performance parameters of the measured devices. The data extracted from *J*/*V* scans (reverse and forward), and includes average with standard deviation, as well as best value (in brackets)

HTM	J_{SC} (mA cm^{-1})	V_{OC} (mV)	FF (%)	PCE (%)
V1205	14.6 ± 0.5 (15.6)	120 ± 81 (285)	24.5 ± 0.4 (25.1)	0.4 ± 0.3 (1.1)
V1205 cross-linked	20.4 ± 0.2 (20.6)	971 ± 6 (979)	82.8 ± 1.1 (84.4)	16.4 ± 0.2 (16.9)
V1206	18.3 ± 0.2 (18.6)	759 ± 33 (819)	75.7 ± 3.1 (80.8)	10.5 ± 0.8 (11.8)
V1206 cross-linked	18.6 ± 0.2 (19.0)	911 ± 23 (944)	80.4 ± 1.7 (82.3)	13.7 ± 0.6 (14.6)

presented in Fig. 4d, PCE recorded for the devices employing monomer films of **V1206** was lower (by 10.0% on average) compared with that of the devices with crosslinked same HTM. Lowering of PCE can be attributed to the formation of direct contact between perovskite and ITO due to the damage of the HTM film during solution-processing of the perovskite film. This in turn led to an increased interfacial recombination, which reduced V_{OC}. Interestingly, devices with the monomer **V1205** practically did not function. Apparently, the HTM layer was severely damaged in this case. The solubility of both monomers was tested in a DMF and DMSO mixture (4 : 1) since this mixture of solvents is used during the formation of the perovskite layer. Solubility of monomer **V1205** was almost twice higher (10 mg/50 μl) than that of monomer **V1206** (10 mg/80 μl) what is in accordance with the obtained results. In order to estimate the stability of the fabricated devices with the best performing cross-linked **V1205**, we have retested the devices after 30 days (N_2 atmosphere, dark, room temperature). Overall, the devices have shown a good shelf lifetime. For the best pixel, 97% of the initial performance was retained. The main reason behind the slightly lower performance was a drop in V_{OC} (Fig. S9, ESI†), which could be attributed to the increased number of defects in the bulk of perovskite. A more detailed statistical analysis of the aged devices can be found in Table S1 (ESI†).

In summary, two novel carbazole-based hole-transporting materials, namely **V1205** and **V1206**, were synthesized by a simple process with high yield and investigated. The synthesized compounds exhibit good thermal stabilities, high hole-drift mobilities and appropriate HOMO levels, indicating that these materials can be promising HTMs in PSCs. Due to the presence of three vinyl groups, compounds **V1205** and **V1206** are able to undergo thermal cross-linking during the heating at 200 °C and 300 °C, respectively. After thermal polymerization the deposited films became resistant towards organic solvents. By employing cross-linked **V1205** and **V1206** as HTM layers between perovskite and ITO in inverted type perovskite solar cells, the PCE is improved to 16.9% (**V1205**) and to 14.6% (**V1206**) under AM 1.5G 100 mW cm^{-2} illumination. To achieve higher efficiency, further optimization of the concentration of the cross-linkable HTMs is under investigation and will be reported later.

We acknowledge the financial support from the Research Council of Lithuania (grant no. MIP-19-14). A. M. acknowledges funding from the Fulbright Scholar Program.

Conflicts of interest

There are no conflicts to declare.

Notes and references

1 G. Hodes, *Science*, 2013, **342**, 317.
2 Y. Rong, Y. Hu, A. Mei, H. Tan, M. I. Saidaminov, S. Il Seok, M. D. McGehee, E. H. Sargent and H. Han, *Science*, 2018, **361**, 1214.
3 **https://www.nrel.gov/pv/cell-efficiency.html**, accessed 06-2022.
4 H. Min, D. Y. Lee, J. Kim, G. Kim, K. S. Lee, J. Kim, M. J. Paik, Y. K. Kim, K. S. Kim, M. G. Kim, T. J. Shin and S. I. Seok, *Nature*, 2021, **598**, 444.
5 Z. Li, B. Li, X. Wu, S. A. Sheppard, S. Zhang, D. Gao, N. J. Long and Z. Zhu, *Science*, 2022, **376**, 416.
6 (*a*) J. Xu, C. C. Boyd, Z. J. Yu, A. F. Palmstrom, D. J. Witter, B. W. Larson, R. M. France, J. Werner, S. P. Harvey, E. J. Wolf, W. Weigand, S. Manzoor, M. F. A. M. Van Hest, J. J. Berry, J. M. Luther, Z. C. Holman and M. D. McGehee, *Science*, 2020, **367**, 1097; (*b*) Y. Hou, E. Aydin, M. De Bastiani, C. Xiao, F. H. Isikgor, D. J. Xue, B. Chen, H. Chen, B. Bahrami, A. H. Chowdhury, A. Johnston, S. W. Baek, Z. Huang, M. Wei, Y. Dong, J. Troughton, R. Jalmood, A. J. Mirabelli, T. G. Allen, E. Van Kerschaver, M. I. Saidaminov, D. Baran, Q. Qiao, K. Zhu, S. De Wolf and E. H. Sargent, *Science*, 2020, **367**, 1135.
7 L. Meng, J. You, T.-F. Guo and Y. Yang, *Acc. Chem. Res.*, 2016, **49**, 155.
8 (*a*) M. Wang, W. Li, H. Wang, K. Yang, X. Hu, K. Sun, S. Lu and Z. Zang, *Adv. Electron. Mater.*, 2020, **6**, 2000604; (*b*) W. Li, H. Wang, X. Hu, W. Cai, C. Zhang, M. Wang and Z. Zang, *Sol. RRL*, 2021, **5**, 2000573.
9 M. Stolterfoht, C. M. Wolff, J. A. Márquez, S. Zhang, C. J. Hages, D. Rothhardt, S. Albrecht, P. L. Burn, P. Meredith, T. Unold and D. Neher, *Nat. Energy*, 2018, **3**, 847.
10 M. Wang, H. Wang, W. Li, X. Hu, K. Sun and Z. Zang, *J. Mater. Chem. A*, 2019, **7**, 26421.
11 A. Magomedov, A. Al-Ashouri, E. Kasparavičius, S. Strazdaite, G. Niaura, M. Jošt, T. Malinauskas, S. Albrecht and V. Getautis, *Adv. Energy Mater.*, 2018, **8**, 1801892.
12 C. Wang, J. Hu, C. Li, S. Qiu, X. Liu, L. Zeng, C. Liu, Y. Mai and F. Guo, *Sol. RRL*, 2019, **4**, 1900389.
13 K. Rakstys, M. Stephen, J. Saghaei, H. Jin, M. Gao, G. Zhang, K. Hutchinson, A. Chesman, P. L. Burn, I. Gentle and P. E. Shaw, *ACS Appl. Energy Mater.*, 2020, **3**, 889.
14 D. Vaitukaitytė, A. Al-Ashouri, M. Daškevičienė, E. Kamarauskas, J. Nekrasovas, V. Jankauskas, A. Magomedov, S. Albrecht and V. Getautis, *Sol. RRL*, 2021, **5**, 2000597.
15 S.-i Kato, H. Noguchi, A. Kobayashi, T. Yoshihara, S. Tobita and Y. Nakamura, *J. Org. Chem.*, 2012, **77**, 9120.
16 B. Wex and B. R. Kaafarani, *J. Mater. Chem. C*, 2017, **5**, 8622.
17 M. Reig, J. Puigdollers and D. Velasco, *J. Mater. Chem. C*, 2015, **3**, 506.
18 J. An, X. Yang, B. Cai, L. Zhang, K. Yang, Z. Yu, X. Wang, A. Hagfeldt and L. Sun, *ACS Appl. Mater. Interfaces*, 2020, **12**, 46397.
19 S. Zhou, M. Daskeviciene, M. Steponaitis, G. Bubniene, V. Jankauskas, K. Schutt, P. Holzhey, A. R. Marshall, P. Caprioglio, G. Christoforo, J. M. Ball, T. Malinauskas, V. Getautis and H. J. Snaith, *Sol. RRL*, 2022, **6**, 2100984.
20 A. Matoliukstyte, E. Burbulis, J. V. Gražulevičius, V. Gaidelis and V. Jankauskas, *Synth. Met.*, 2008, **158**(11), 462.

Electronic Supplementary Information

Cross-Linkable Carbazole-Based Hole Transporting Materials for Perovskite Solar Cells

Sarune Daskeviciute-Geguziene,[1] Artiom Magomedov,[1,2] Maryte Daskeviciene,[1] Kristijonas Genevičius,[3] Nerijus Nekrašas,[3] Kristina Kantminiene,[4] Michael D. McGehee,[2] Vytautas Getautis[1]*

[1]Department of Organic Chemistry, Kaunas University of Technology, Kaunas 50254, Lithuania.

[2]Department of Chemical and Biological Engineering, University of Colorado, Boulder, CO, 80309 USA

[3]Institute of Chemical Physics, Vilnius University, Vilnius 10257, Lithuania.

[4]Department of Physical and Inorganic Chemistry, Kaunas University of Technology, Kaunas 50254, Lithuania.

E-mail: vytautas.getautis@ktu.lt

Table of Contents

General methods	S2
Detailed synthetic procedures	S2–S6
Thermal Properties	S7
Ionization Potential Measurements	S7
Hole Drift Mobility Measurements	S7-S10
Fabrication of the devices	S11
UV/vis spectra of the not heated and cross-linked HTM films, before and after washing with DMF:DMSO	S11-S12
Stability of the devices	S12
References	S13

Materials and HTMs synthesis

Chemicals were purchased from Sigma-Aldrich, TCI Europe and used as received without further purification. ^{1}H NMR spectra were recorded at 400 MHz on a Bruker Avance III spectrometer with a 5 mm double resonance broad band BBO z-gradient room temperature probe, ^{13}C NMR spectra were collected using the same instrument at 101 MHz. The chemical shifts, expressed in ppm, were relative to tetramethylsilane (TMS). All the NMR experiments were performed at 25 °C. Reactions were monitored by thin-layer chromatography on ALUGRAM SIL G/UV254 plates and developed with UV light. Silica gel (grade 9385, 230–400 mesh, 60 Å, Aldrich) was used for column chromatography. Elemental analysis was performed with an Exeter Analytical CE-440 elemental analyser, Model 440 C/H/N/.

Thermogravimetric analysis (TGA) was performed on a Q50 thermogravimetric analyzer (TA Instruments) at a scan rate of 10 °C min^{-1} under nitrogen atmosphere. The values are given for a weight-loss of 5% (T_{d5}). Differential scanning calorimetry (DSC) was performed on a TA Instruments Q2000 differential scanning calorimeter under nitrogen atmosphere. Heating and cooling rate is 10 °C min^{-1}.

UV–vis spectral analysis of the sample in solution (THF, 10^{-4} mol l^{-1}) was performed on a Perkin Elmer Lambda 35 UV/VIS spectrophotometer. Diffraction grating crack width is 2 nm. Spectral recording speed is 2 nm s^{-1}. The layer thickness of the solution is d = 1 cm. The wavelength λ is given in nm. The time-resolved fluorescence spectra of the sample in solution (THF, 10^{-4} mol l^{-1}) were recorded on an Edinburgh Instruments FLS920 light emission intensity spectrophotometer. The layer thickness of the solution is d = 1 cm. The crack width of the diffraction grating is 1.5 nm. The wavelength λ is given in nm.

3-bromo-9-(4-vinylbenzyl)-9*H*-carbazole (1)

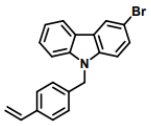

3-bromocarbazole (1 g, 4.1 mmol, 1 eq) was dissolved in dimethylsulfoxyde (25 mL) and purged with argon for 30 minutes. Afterwards, benzyltriethylammonium chloride (0.1 eq) and 50% NaOH (0.4 mL) solution were added. When the reaction mixture turned red 4-vinylbenzylchloride (0.63 mL, 4.5

mmol, 1.1 eq) was slowly dropped and the mixture was stirred at room temperature for 3 hours under argon atmosphere. The obtained product was filtered off and washed with ethanol to collect **2** as a white solid (1.25 g, 85%). ^{1}H NMR (400 MHz, DMSO-d_6) δ 8.44 (s, 1H), 8.21 (d, J = 7.6 Hz, 1H), 7.69 – 7.59 (m, 2H), 7.56 (d, J = 8.4 Hz, 1H), 7.47 (t, J = 7.6 Hz, 1H), 7.36 (d, J = 8.0 Hz, 2H), 7.24 (t, J = 7.6 Hz, 1H), 7.12 (d, J = 8.0 Hz, 2H), 6.65 (2d, J_1 = 17.6, J_2 = 10.9 Hz, 1H), 5.74 (d, J = 17.6 Hz, 1H), 5.66 (s, 2H), 5.20 (d, J = 10.9 Hz, 1H). ^{13}C NMR (101 MHz, DMSO) 140.98, 139.34, 137.63, 136.75, 136.59, 128.63, 127.47, 127.15, 126.84, 124.68, 123.44, 121.73, 121.41, 119.97, 114.76, 112.08, 111.70, 110.32, 45.93.

3,6-dibromo-9-(4-vinylbenzyl)-9*H*-carbazole (2)

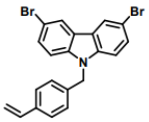

3,6-dibromocarbazole (1.5 g, 4.6 mmol, 1 eq) was dissolved in dimethylsulfoxyde (40 mL) and purged with argon for 30 minutes. Afterwards, benzyltriethylammonium chloride (0.1 eq) and 50% NaOH (0.5 mL) solution were added. When the reaction mixture turned dark yellow 4-vinylbenzylchloride (0.72 mL, 5.1 mmol, 1.1 eq) was slowly dropped and the mixture was stirred at room temperature for 12 hours under argon atmosphere. After that, was extracted with ethyl acetate. The organic layer was dried over anhydrous Na_2SO_4, filtered and solvent evaporated. The obtained product was white crystals. The product washed three times with ethanol and filtered off to collect **2** as white crystals (1.84 g, 90%). Spectral data is in agreement with the values reported in the literature [1].

***N*-(4-methoxyphenyl)-9-(4-vinylbenzyl)-9*H*-carbazol-3-amine (3)**

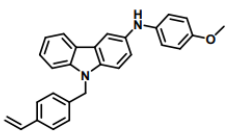

Anhydrous dioxane (10 mL) with few drops of distilled water (0.02 eq) was purged with argon for 20 minutes. After that, the temperature was raised to 80 °C, palladium (II) acetate (0.005 eq) and XPhos (0.015 eq) were added. The mixture was stirred for 1.5 minutes and temperature was raised to 110 °C. Compound **1** (2 g, 5.5 mmol, 1 eq), *p*-Anisidine (0.8 g, 6.6 mmol, 1.2 eq) and sodium *tert*-butoxide

(1.4 eq) were added and stirred for 5 minutes. After cooling to room temperature, reaction mixture was extracted with ethyl acetate and distilled water. The organic layer was dried over anhydrous Na_2SO_4, filtered and the solvent evaporated. The crude product was purified by column chromatography using 1:9 v/v THF/*n*-hexane as an eluent. Pale gray solid were collected as a final product (1.74 g, 78%). ^{1}H NMR (400 MHz, DMSO-d_6) δ 8.02 (d, J = 7.6 Hz, 1H), 7.75 (s, 1H), 7.65 (s, 1H), 7.52 (d, J = 8.4 Hz, 1H), 7.46 (d, J = 8.4 Hz, 1H), 7.38 – 7.28 (m, 3H), 7.16 – 7.06 (m, 4H), 6.99 (d, J = 8.6 Hz, 2H), 6.81 (d, J = 8.6 Hz, 2H), 6.62 (2d, J_1 = 17.6, J_2 = 10.9 Hz, 1H), 5.70 (d, J = 17.6 Hz, 1H), 5.54 (s, 2H), 5.16 (d, J = 10.9 Hz, 1H), 3.67 (s, 3H). ^{13}C NMR (101 MHz, DMSO) δ 153.16, 141.02, 139.32, 138.20, 137.83, 136.66, 136.63, 135.67, 127.51, 126.79, 126.09, 123.28, 122.50, 120.78, 118.92, 118.87, 118.12, 115.10, 114.64, 110.58, 109.87, 108.63, 55.72, 45.87.

9-ethyl-*N*-[9-(4-vinylbenzyl)-9*H*-carbazol-3-yl]- 9*H*-carbazol-3-amine (4)

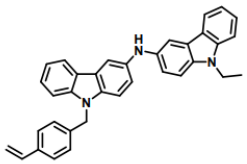

Anhydrous dioxane (10 mL) with few drops of distilled water (0.02 eq) was purged with argon for 20 minutes. After that, the temperature was raised to 80 °C, palladium (II) acetate (0.005 eq) and XPhos (0.015 eq) were added. The mixture was stirred for 1.5 minutes and temperature was raised to 110 °C. Compound **1** (2 g, 5.5 mmol, 1 eq), 3-amino-9-ethylcarbazole (1.4 g, 6.6 mmol, 1.2 eq) and sodium *tert*-butoxide (1.4 eq) were added and stirred for 10 minutes. After cooling to room temperature, reaction mixture was extracted with ethyl acetate and distilled water. The organic layer was dried over anhydrous Na_2SO_4, filtered and the solvent evaporated. The crude product was purified by column chromatography using 1:9 v/v THF/*n*-hexane as an eluent. Pale green solid were collected as a final product (1.82 g, 67%). ^{1}H NMR (400 MHz, DMSO-d_6) δ 8.11 – 7.90 (m, 2H), 7.85 – 7.74 (m, 3H), 7.56 – 7.44 (m, 4H), 7.41 – 7.30 (m, 4H), 7.29 – 7.18 (m, 2H), 7.17 – 7.03 (m, 4H), 6.62 (2d, J_1 = 17.6, J_2 = 10.9 Hz, 1H), 5.71 (d, J = 17.6 Hz, 1H), 5.56 (s, 2H), 5.17 (d, J = 10.9 Hz, 1H), 4.46 – 4.27 (m, 2H), 1.37 – 1.19 (m, 3H). ^{13}C NMR (101 MHz, DMSO) δ 141.02, 140.38, 138.99, 138.25, 138.17, 136.67, 136.63, 135.51, 135.14, 127.53, 126.79, 126.03, 125.89, 123.37, 123.26, 122.55, 122.45, 120.80, 118.87, 118.80, 118.50, 118.34, 114.64, 110.63, 110.14, 109.85, 109.65, 109.36, 108.79, 107.89, 45.89, 37.39, 14.24.

N^3,N^6-bis(4-methoxyphenyl)-9-(4-vinylbenzyl)-N^3,N^6-bis[9-(4-vinylbenzyl)-9*H*-carbazol-3-yl]-9*H*-carbazole-3,6-diamine (V1205)

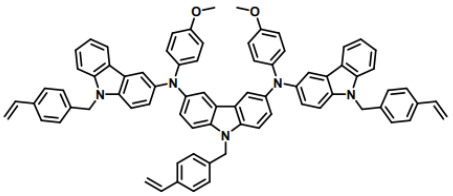

A solution of compound **2** (0.5 g, 1.1 mmol, 1 eq) and compound **3** (1.4 g, 3.4 mmol, 3 eq) in anhydrous toluene (12 mL) was purged with argon for 30 minutes. Afterwards, palladium (II) acetate (0.02 eq), tri-*tert*-butylphosphonium tetrafluoroborate (0.027 eq) and sodium *tert*-butoxide (3 eq) were added and the solution was refluxed under argon atmosphere for 8 hours. After cooling to room temperature, reaction mixture was extracted with ethylacetate and distilled water, filtered through celite. The organic layer was dried over anhydrous Na_2SO_4, filtered and solvent evaporated. The crude product was purified by column chromatography using 3:22 v/v acetone/*n*-hexane as an eluent. The obtained product was precipitated from acetone into 15 times excess of *n*-hexane. The precipitate was filtered off and washed with ethanol to collect **V1205** as a pale green solid (0.89 g, 72%). ^{1}H NMR (400 MHz, DMSO-d_6) δ 7.95 (d, J = 8.0 Hz, 2H), 7.75 (d, J = 8.0 Hz, 4H), 7.59 – 7.43 (m, 6H), 7.40 – 7.30 (m, 8H), 7.21 (d, J = 8.0 Hz, 2H), 7.18 – 7.03 (m, 10H), 6.83 (d, J = 8.9 Hz, 4H), 6.75 (d, J = 8.9 Hz, 4H), 6.70 – 6.57 (m, 3H), 5.81 – 5.66 (m, 3H), 5.54 (s, 6H), 5.26 – 5.11 (m, 3H), 3.65 (s, 6H). ^{13}C NMR (101 MHz, DMSO) δ ^{13}C NMR (101 MHz, DMSO) δ 154.19, 143.43, 141.74, 141.38, 141.09, 138.00, 137.67, 136.80, 136.72, 136.66, 136.61, 127.68, 127.56, 126.85, 126.79, 126.30, 124.91, 124.03, 123.48, 123.34, 123.30, 122.40, 120.95, 119.20, 117.21, 116.08, 115.04, 114.66, 110.96, 110.76, 109.94, 55.60, 45.94. Anal. calcd for $C_{77}H_{61}N_5O_2$: C, 84.98; H, 5.65; N, 6.43; found: C, 85.17; H, 5.54.; N, 6.41.

N^3,N^6-bis(9-ethyl-9*H*-carbazol-3-yl)-9-(4-vinylbenzyl)-N^3,N^6-bis[9-(4-vinylbenzyl)-9*H*-carbazol-3-yl]-9*H*-carbazole-3,6-diamine (V1206)

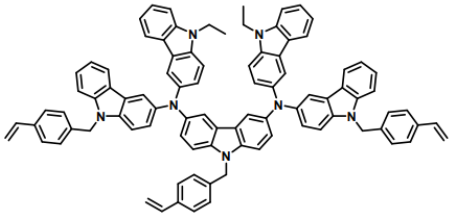

A solution of compound **2** (0.5 g, 1.1 mmol, 1 eq) and compound **4** (1.7 g, 3.4 mmol, 3 eq) in anhydrous toluene (13 mL) was purged with argon for 30 minutes. Afterwards, palladium (II) acetate (0.02 eq), tri-*tert*-butylphosphonium tetrafluoroborate (0.027 eq) and sodium *tert*-butoxide (3 eq) were added and the solution was refluxed under argon atmosphere for 23 hours. After cooling to room temperature, reaction mixture was extracted with ethylacetate and distilled water, filtered through celite. The organic layer was dried over anhydrous Na_2SO_4, filtered and solvent evaporated. The crude product was purified by column chromatography using 1.1:3.9 v/v THF/*n*-hexane as an eluent. The obtained product was precipitated from THF into 15 times excess of *n*-hexane. The precipitate was filtered off and washed with ethanol to collect **V1206** as a pale green solid (0.94 g, 66%). ^{1}H NMR (400 MHz, DMSO-d_6) δ 7.83 – 7.77 (m, 4H), 7.75 – 7.70 (m, 6H), 7.52 – 7.43 (m, 6H), 7.39 – 7.26 (m, 14H), 7.20 (d, J = 8.0 Hz, 2H), 7.16 – 7.03 (m, 10H), 7.01 – 6.93 (m, 4H), 6.67 – 6.50 (m, 3H), 5.74 – 5.61 (m, 3H), 5.48 (s, 6H), 5.22 – 5.10 (m, 3H), 4.26 (q, J = 7.0 Hz, 4H), 1.19 (t, J = 7.0 Hz, 6H). ^{13}C NMR (101 MHz, DMSO) δ 142.82, 142.26, 141.05, 140.39, 137.99, 137.45, 136.59, 136.38, 136.00, 127.70, 127.55, 126.82, 126.74, 126.01, 123.73, 123.41, 123.32, 122.42, 122.30, 120.87, 119.05, 118.70, 115.67, 114.88, 114.60, 110.62, 110.24, 109.84, 109.36, 45.91, 37.35, 14.16. Anal. calcd for $C_{91}H_{71}N_7$: C, 86.57; H, 5.67; N, 7.77; found: C, 86.37; H, 5.64.; N, 7.81.

ACS APPLIED MATERIALS & INTERFACES

www.acsami.org
Research Article

In Situ Thermal Cross-Linking of 9,9′-Spirobifluorene-Based Hole-Transporting Layer for Perovskite Solar Cells

Sarune Daskeviciute-Geguziene,‖ Minh Anh Truong,‖ Kasparas Rakstys, Maryte Daskeviciene, Ruito Hashimoto, Richard Murdey, Takumi Yamada, Yoshihiko Kanemitsu, Vygintas Jankauskas, Atsushi Wakamiya,* and Vytautas Getautis*

Cite This: ACS Appl. Mater. Interfaces 2024, 16, 1206−1216
Read Online

ACCESS | Metrics & More | Article Recommendations | Supporting Information

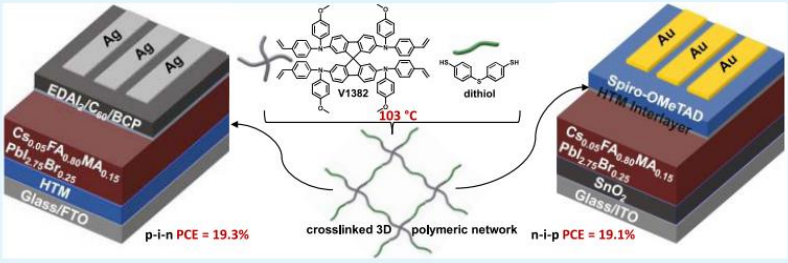

ABSTRACT: A novel 9,9′-spirobifluorene derivative bearing thermally cross-linkable vinyl groups (**V1382**) was developed as a hole-transporting material for perovskite solar cells (PSCs). After thermal cross-linking, a smooth and solvent-resistant three-dimensional (3D) polymeric network is formed such that orthogonal solvents are no longer needed to process subsequent layers. Copolymerizing **V1382** with 4,4′-thiobisbenzenethiol (dithiol) lowers the cross-linking temperature to 103 °C via the facile thiol−ene "click" reaction. The effectiveness of the cross-linked **V1382**/dithiol was demonstrated both as a hole-transporting material in p−i−n and as an interlayer between the perovskite and the hole-transporting layer in n−i−p PSC devices. Both devices exhibit better power conversion efficiencies and operational stability than devices using conventional **PTAA** or **Spiro-OMeTAD** hole-transporting materials.

KEYWORDS: *cross-linking, temperature, hole-transporting layer, perovskite solar cell, spirobifluorene*

INTRODUCTION

Organic−inorganic metal halide perovskite solar cells (PSCs) have received significant interest from the photovoltaic community due to their skyrocketing power conversion efficiencies (PCEs) from 3.8 to 26.1%,[1] to compete with established solar cell technologies such as crystalline silicon (c-Si) and copper indium gallium selenide (CIGS).[2,3] Moreover, PSCs may be scaled up using a low-cost solution process from widely available abundant precursors showing promise as a future mainstream photovoltaic (PV) technology.[4,5] PSCs can also be integrated as top cells into tandem solar cells when combined with existing mature PV technologies to increase efficiency beyond the Shockley−Queisser limit of single-junction devices.[6,7] However, besides impressive efficiency, the long-term stability of PSC devices under practical working conditions still requires further improvement to satisfy stringent market demands.

A typical PSC consists of a perovskite light absorber sandwiched between an n-type electron-transporting layer (ETL) and a p-type hole-transporting layer (HTL).[8] Hole-transporting materials (HTMs) play critical roles in efficiently extracting and transporting photogenerated holes from the perovskite layer to the electrode, as well as suppressing charge recombination in PSCs.[9,10] In general, HTMs should possess the following properties: (1) appropriate energy-level alignment with perovskite materials to guarantee effective hole extraction and electron blocking; (2) high hole mobility; (3) good solubility in common solvents; (4) excellent film-forming ability; (5) good thermal, photochemical, air, and moisture stability; and (6) low cost.[11] However, the requirements for HTMs vary depending on the device configurations.[12] For n−

Received: September 18, 2023
Revised: December 4, 2023
Accepted: December 7, 2023
Published: December 20, 2023

https://doi.org/10.1021/acsami.3c13950
ACS Appl. Mater. Interfaces 2024, 16, 1206−1216

Scheme 1. Synthetic Route of the 9,9′-Spirobifluorene Polymer Precursor V1382 and Its Schematic Thiol−Ene Cross-Linking Using 4,4′-Thiobisbenzenethiol as a Cross-Linker

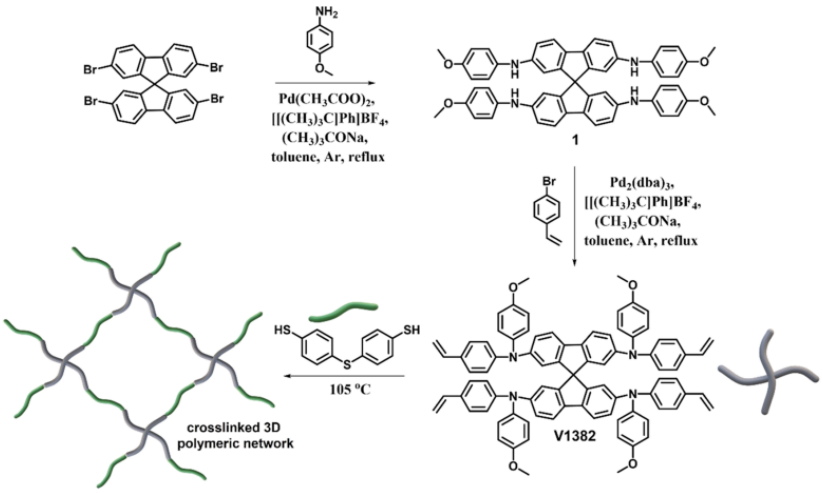

i−p PSCs, since the HTM layer is fabricated on top of the perovskite layer, a thick HTM film is required to ensure full coverage of the rough perovskite surface and suppress the diffusion of metal from the top electrode into the perovskite. Also, the HTM film should ideally be hydrophobic to protect the perovskite from moisture ingress. Although various kinds of HTMs have been developed, 2,2′,7,7′-tetrakis(*N*,*N*-di-*p*-methoxyphenylamino)-9,9′-spirobifluorene (**Spiro-OMeTAD**) has been proven to be the most reliable and effective HTM for use in n−i−p PSCs.[13,14] **Spiro-OMeTAD** has a large bandgap (about 3.0 eV) and a relatively shallow highest occupied molecular orbital (HOMO) energy level of around −5.1 eV,[12] which provides good electronic alignment with perovskite materials. In addition, the synthesis and solution-based film processing of **Spiro-OMeTAD** are well established and are well suited to the fabrication of large-area solar cells. On the other hand, chemical dopants or additives, such as lithium bis(trifluoromethanesulfonyl)imide (LiTFSI), cobalt(III) complexes, and 4-*tert*-butylpyridine (*t*BP), are needed to improve the conductivity and hole mobility of the pristine **Spiro-OMeTAD**. These hygroscopic dopants have an impact on the device's long-term stability due to moisture ingress and ion migration. Therefore, an interlayer that is hydrophobic[15] and/or able to block ion migration[16] between the perovskite layer and HTM layer would be helpful to improve the stability of PSCs.

In the case of p−i−n devices, solution-processing of the perovskite absorber layer puts additional constraints on the choice of HTMs, as the materials must now be made resistant to the perovskite precursor solution, commonly a mixture of polar dimethylformamide (DMF) and dimethyl sulfoxide (DMSO) solutions. So far, polymeric HTMs, such as poly(3,4-ethylenedioxythiophene):polystyrenesulfonate (**PEDOT:PSS**),[17] poly[3-(4-carboxylatebutyl)thiophene] (**P3CT**) derivatives,[18,19] and poly[bis(4-phenyl)(2,4,6-trimethylphenyl)amine] (**PTAA**)[20,21] or combinations thereof, are widely used for this application.[22,23] Among them, **PTAA**, with its excellent electrical properties and chemical neutrality, has attracted particular interest.[5,24−27] However, the strongly hydrophobic **PTAA** film surface results in the dewetting of the perovskite precursor solution and low-quality perovskite films.[28] Despite several attempts to modify **PTAA**, such as chemical doping,[29,30] surface post-treatment,[31] and interfacial functionalization,[32] the tedious synthetic process and batch-to-batch variation of **PTAA** remain significant issues restricting its application to large-scale device fabrication. In this regard, small molecular organic molecules offer potential advantages, such as a well-defined molecular weight, ease of synthesis, and good reproducibility. To insolubilize small molecular molecules, the use of molecules with anchoring groups such as phosphonic acid (−PO(OH)$_2$) or carboxylic acid (−COOH) that can spontaneously bind to the transparent conducting oxide surface to form a conformal hole-collecting monolayer has been demonstrated as an effective way by our groups and others.[33−36] An alternative approach is to polymerize the small molecules in situ via cross-linking reactions. Soluble small molecules bearing cross-linkable units, such as vinyl, acrylate, azide, and oxetane groups, can form insoluble cross-linked three-dimensional (3D) networks under thermal or ultraviolet (UV) treatment.[37−39] Such cross-linked 3D networks could enable solvent-resistant hole-transporting layers[40−46] and protective interlayers.[47,48] However, the reported cross-linkable systems would not be suitable for flexible p−i−n PSCs with film substrates or for n−i−p PSCs due to their high cross-linking temperatures (usually >180 °C), which exceed the tolerance of the underlying layers.

In this work, we report the development of a 9,9′-spirobifluorene-based molecule functionalized with four vinyl groups (**V1382**) for the targeted cross-linkable HTL (Scheme 1) and its application to PSCs. To lower the cross-linking temperature, the introduction of an aliphatic cross-linker containing four thiol groups, pentaerythritol tetrakis(3-

https://doi.org/10.1021/acsami.3c13950
ACS Appl. Mater. Interfaces 2024, 16, 1206−1216

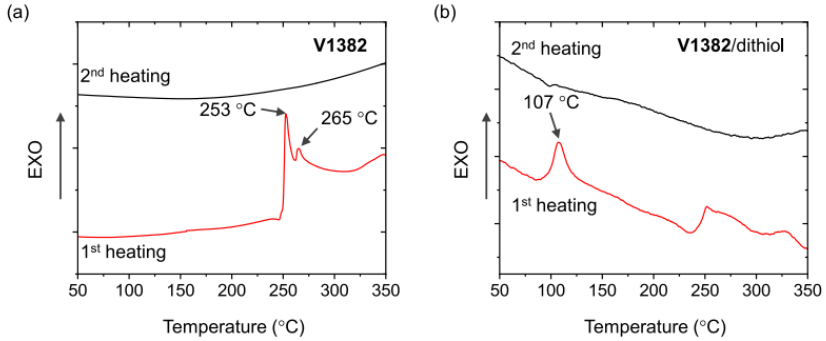

Figure 1. Differential scanning calorimetry curves (scan rate, 10 °C min^{-1}; N_2 atmosphere) of (a) **V1382** and (b) a mixture of **V1382** with 4,4′-thiobisbenzenethiol.

Table 1. Thermal, Optical, and Photophysical Properties of V1382 and V1382/Dithiol

	T_{poly} (°C)[a]	T_{dec} (°C)[a]	λ_{abs} (nm)[b]	λ_{em} (nm)[b]	I_P (eV)[c]	μ_0 (cm^2 V^{-1} s^{-1})[d]
V1382	253, 265	460	336, 395	419, 441	5.29	8.7×10^{-5}
V1382 after heating at 255 °C[e]	–	–	371	–	5.38	1.3×10^{-5}
V1382/dithiol after heating at 103 °C[e]	–	–	303, 383	–	5.35	1.3×10^{-5}

[a]Polymerization (T_{poly}) and decomposition (T_{dec}) temperatures observed from DSC and TGA, respectively (scan rate = 10 °C min^{-1}, N_2 atmosphere). [b]Absorption and emission spectra were measured in THF solutions (10^{-4} M) or thin films. [c]Ionization energies of the films measured using PESA. [d]Mobility value at zero field strength. [e]After annealing, films were rinsed with THF several times.

mercaptopropionate) (PETMP), has been reported.[49] We chose a dithiol-terminated diphenylsulfide, 4,4′-thiobisbenzenethiol, as a cross-linker since it has a shorter insulating part than PETMP and may generate a stable radical form to facilitate the thiol−ene "click" reaction with **V1382**. We found that the cross-linking between **V1382** and 4,4′-thiobisbenzenethiol (dithiol) can occur at a low temperature of 103 °C to form an insoluble 3D polymer network. To the best of our knowledge, this is the lowest cross-linking temperature reported for HTLs for PSCs. Benefiting from the mild cross-linking conditions, this cross-linkable system is suitable for applications in both p−i−n and n−i−p PSC architectures. Devices employing the cross-linked **V1382**/dithiol as the hole-transporting layer in p−i−n PSCs and as the interlayer between the perovskite layer and **Spiro-OMeTAD** in n−i−p PSCs have shown improved performance and long-term stability compared with devices using conventional HTMs. These results demonstrate cross-linking as an efficient strategy for low-cost and high-performance organic semiconducting materials, not only for photovoltaics but also for other optoelectronic devices such as light-emitting diodes, photo-transistors, photocells, and so on.

RESULTS AND DISCUSSION

The polymer precursor **V1382**, which possesses a 9,9′-spirobifluorene core and four vinyl cross-linkable groups, was synthesized in a facile 2-step synthetic procedure with commercially available starting materials as shown in Scheme 1. During the first step, the palladium-catalyzed Buchwald−Hartwig amination reaction of 2,2′,7,7′-tetrabromo-9,9′-spirobifluorene and *p*-anisidine was carried out to give aminated precursor **1** in 70% yield. Compound **1** was then vinyl-functionalized by using 4-bromostyrene to generate the target product **V1382** in 51% yield. Structures of the synthesized compounds were characterized by nuclear magnetic resonance (NMR), elemental analysis (EA), and mass spectrometry (MS). The total cost for **V1382** is estimated to be 42 € g^{-1}, much cheaper than widely used HTMs,[50] indicating its strong potential for large-scale manufacturing processes (Table S1). Detailed synthesis procedures and analysis data are given in the Supporting Information.

The thermal properties of **V1382** and its cross-linking reaction with 4,4′-thiobisbenzenethiol were investigated by thermogravimetric analysis (TGA) and differential scanning calorimetry (DSC). The decomposition temperature corresponding to 5% weight loss (T_{dec}) of **V1382** was estimated from the TGA curve to be 460 °C (Figure S1), confirming that **V1382** has good thermal stability. As shown in Figure 1a, an exothermic peak was detected at 253 °C during the first scan, while no distinct phase transition could be observed until 350 °C in the second heating scan, suggesting that thermal cross-linking of **V1382** occurs at 253 °C. In contrast, after mixing **V1382** with a dithiol cross-linker, 4,4′-thiobisbenzenethiol, in a molar ratio of 1:2, the exothermic peak shifted to the region of 103−120 °C, and the cross-linking temperature (T_{poly}) was detected at 107 °C (Figure 1b). The results imply that the fast thermal cross-linking occurs due to the facile thiol−ene "click" reaction. It is worth noting that this is the lowest cross-linking temperature reported in the PSC field,[40−52] enabling the application in both p−i−n and n−i−p PSC architectures.

To evaluate the optical properties of **V1382** and formed polymers, ultraviolet−visible (UV−vis) absorption and photoluminescence (PL) spectra were measured from tetrahydrofuran (THF) solutions and thin films. The results are shown in Figure S2 and summarized in Table 1. The absorption maxima (λ_{abs}) of **V1382** were observed at 336 and 395 nm. The less intense absorption peak at 336 nm can be assigned to the

https://doi.org/10.1021/acsami.3c13950
ACS Appl. Mater. Interfaces 2024, 16, 1206−1216

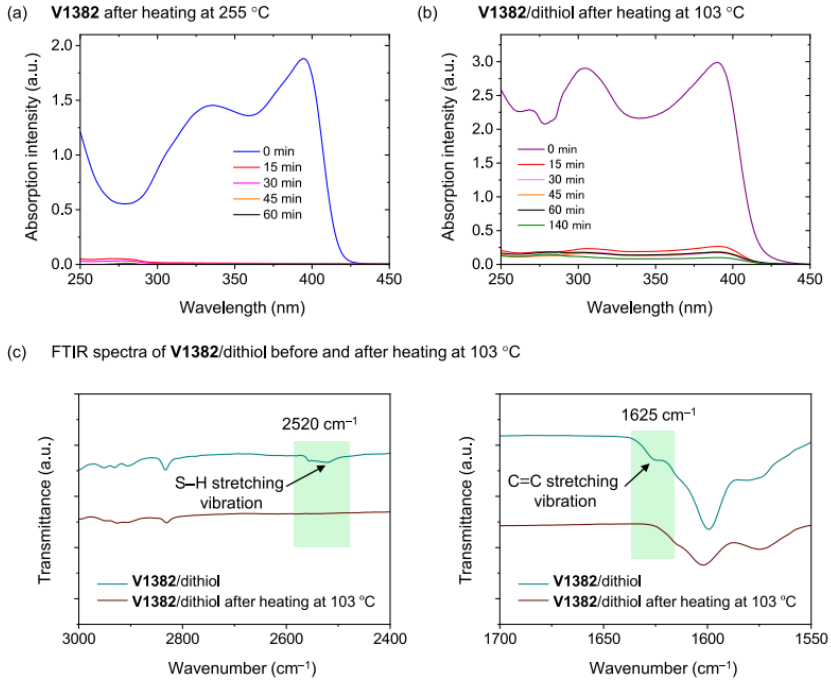

Figure 2. UV−vis spectra of (a) cross-linked **V1382** and (b) **V1382**/dithiol films with different annealing times. (c) FTIR spectra before and after cross-linking of **V1382** with dithiol.

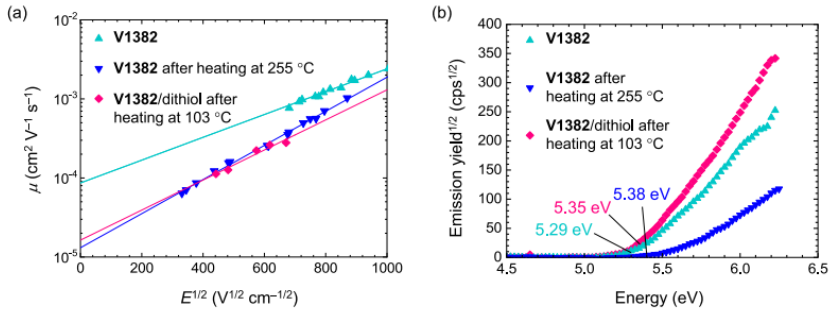

Figure 3. (a) Electric field dependencies of the hole-drift mobilities in charge transport layers and (b) photoelectron yield of **V1382** and cross-linked films measured in air.

$\pi-\pi^*$ transition, while the more intense absorption peak at 395 nm corresponds to the $n-\pi^*$ transition. After polymerization of **V1382** at 255 °C, wide absorption band ranging from 275 to 450 nm was observed, while after thermal cross-linking using dithiol at 103 °C, the absorption spectra of the polymer had two main peaks at around 303 and 383 nm. In addition, the emission maxima (λ_{em}) of **V1382** were observed at 419 and 441 nm with a Stokes shift value of 24 nm.

V1382 films with and without 4,4′-thiobisbenzenethiol cross-linker (molar ratio = 1:2) were prepared by spin-coating the corresponding materials in THF solutions (**V1382** 20 mg mL^{-1}). The ability to form insoluble cross-linked networks was evaluated by measuring the UV−vis absorption of these spin-coated films. The results are shown in Figure 2a,b. After annealing the films of **V1382** without and with the dithiol cross-linker for only 15 min at 255 and 103 °C, respectively, and rinsing with THF several times to remove soluble parts, absorbance from the films was still detected. It indicates that the cross-linking of these films occurred under these conditions, resulting in good solvent-resistant films. We note

https://doi.org/10.1021/acsami.3c13950
ACS Appl. Mater. Interfaces 2024, 16, 1206−1216

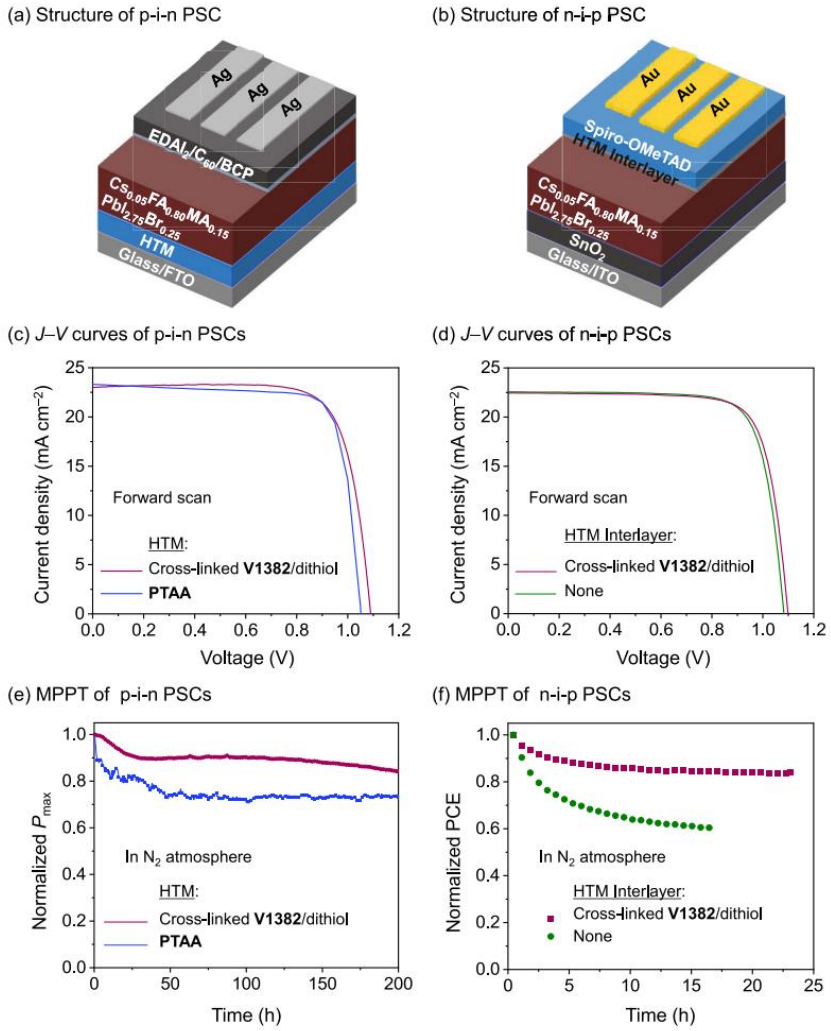

Figure 4. Structure of (a) p−i−n and (b) n−i−p PSCs. (c) *J*−*V* curves and (e) MPPT of p−i−n PSCs. (d) *J*−*V* curves and (f) MPPT of n−i−p PSCs.

that such rapid cross-linking is quite unusual for thiol−ene-type polymerization according to our previously reported works,[42,44] suggesting that spiro configuration might be sterically or energetically favorable for this type of reaction. A longer time frame was used to quantitatively cross-link the films. The cross-linking process in both cases was completed after annealing for 60 min.

Fourier transform infrared (FTIR) spectra (Figure 2c) were recorded to ascertain the occurrence of the cross-linking. After **V1382** cross-linking with dithiol at 103 °C, the peak of S−H stretching vibration at 2520 cm^{-1} and the peak of C=C stretching vibration at 1625 cm^{-1} disappeared compared with the peaks before heating confirming that fast thermal cross-linking occurs after heating **V1382** with a dithiol cross-linker at 103 °C.

The hole-transport properties of the HTMs were characterized with the aid of xenographic time-of-flight (XTOF) measurements (Figure 3a). At zero field strength, **V1382** demonstrates a hole-drift mobility of 8.7×10^{-5} cm^2 V^{-1} s^{-1}. After thermal annealing, regardless of using the dithiol cross-linker, the hole mobilities of cross-linked films slightly reduce to 1.3×10^{-5} cm^2 V^{-1} s^{-1}, yet are still comparable to those of popular HTMs for PSCs.[53,54] In addition, the solid-state ionization potential (I_p) of **V1382** and the cross-linked films

https://doi.org/10.1021/acsami.3c13950
ACS Appl. Mater. Interfaces 2024, 16, 1206−1216

Table 2. Photovoltaic Parameters of p−i−n and n−i−p PSCs Derived from *J*−*V* Measurements

p−i−n PSC Devices						
HTM[a]	scan[b]	J_{sc} (mA cm^{-2})[c]	V_{oc} (V)[c]	FF[c]	PCE (%)[c]	HI[d]
cross-linked **V1382**/dithiol	F	23.0 (22.6 ± 0.3)	1.09 (1.08 ± 0.01)	0.77 (0.77 ± 0.02)	19.3 (18.7 ± 0.4)	−0.027
	R	23.5 (22.8 ± 0.4)	1.07 (1.07 ± 0.01)	0.75 (0.74 ± 0.02)	18.8 (18.1 ± 0.8)	
PTAA	F	23.3 (21.5 ± 0.8)	1.05 (1.05 ± 0.01)	0.79 (0.77 ± 0.02)	19.3 (17.5 ± 1.0)	−0.090
	R	22.3 (21.1 ± 0.7)	1.06 (1.05 ± 0.01)	0.75 (0.75 ± 0.03)	17.7 (16.6 ± 1.1)	
n−i−p PSC Devices						
HTM[a]	scan[b]	J_{sc} (mA cm^{-2})[c]	V_{oc} (V)[c]	FF[c]	PCE (%)[c]	HI[d]
cross-linked **V1382**/dithiol/**Spiro-MeTAD**	F	22.4 (22.1 ± 0.4)	1.10 (1.05 ± 0.03)	0.77 (0.75 ± 0.01)	19.1 (17.6 ± 0.8)	−0.032
	R	22.4 (22.1 ± 0.4)	1.09 (1.06 ± 0.02)	0.76 (0.76 ± 0.01)	18.5 (17.8 ± 0.5)	
Spiro-OMeTAD	F	22.6 (22.2 ± 0.4)	1.08 (1.05 ± 0.02)	0.77 (0.75 ± 0.01)	18.9 (17.5 ± 0.8)	−0.050
	R	22.5 (22.1 ± 0.4)	1.07 (1.06 ± 0.01)	0.75 (0.74 ± 0.01)	18.0 (17.4 ± 0.5)	

[a]HTM (**V1382**/dithiol/1:2 molar ratio) were spin-coated on FTO substrates or on top of the perovskite layer from PhCl solution to fabricate p−i−n or n−i−p PSCs, respectively. The optimized concentration of **V1382** is 2.0 and 1.0 mg mL^{-1} for p−i−n and n−i−p PSCs, respectively. [b]Forward and reverse indicate the scan direction from J_{SC} to V_{OC} and from V_{OC} to J_{SC}, respectively. [c]The average and standard deviation values were given in parentheses. [d]Hysteresis index (HI) = $(PCE_{Reverse} - PCE_{Forward})/PCE_{Reverse}$.

were measured by using photoelectron spectroscopy in air (PESA). As shown in Figure 3b, the ionization potential of the **V1382** film was measured to be 5.29 eV. The I_p values slightly increase to 5.38 and 5.35 eV in the case of cross-linked **V1382** without and with 4,4′-thiobisbenzenethiol, respectively. The I_p values of the cross-linked **V1382** films are smaller than the valence band (VB) of typical perovskite materials such as $CH_3NH_3PbI_3$ ($MAPbI_3$, VB = 5.45 eV) or $Cs_{0.05}FA_{0.80}MA_{0.15}PbI_{2.75}Br_{0.25}$ (FA: formamidinium, VB = 5.56 eV)[34] and larger than those of conventional HTMs such as **PTAA** or **Spiro-OMeTAD**. As shown in energy-level diagrams of both p−i−n and n−i−p PSC devices (Figure S3), compared to conventional HTMs, the smaller energy-level offset between the cross-linked **V1382** and the perovskite suggests that more efficient hole transfer could be expected for the cross-linked **V1382**.

X-ray photoelectron spectroscopy (XPS) measurements were carried out to prove the interaction between the cross-linked **V1382**/dithiol and the perovskite ($Cs_{0.05}FA_{0.80}MA_{0.15}PbI_{2.75}Br_{0.25}$). Figure S4 presents the XPS spectra of Pb 4*f* peaks in the pristine perovskite film and the perovskite film with cross-linked polymer surface modification. Compared to the pristine film, the peaks of Pb $4f_{7/2}$ and Pb $4f_{5/2}$ in the modified perovskite film shifted 0.3 eV to a higher binding energy, implying an interaction between the cross-linked **V1382**/dithiol and the perovskite surface. This could benefit solar cell operational stability.

To evaluate the efficacy of the HTM formed by the cross-linking between **V1382** and 4,4′-thiobisbenzenethiol (named cross-linked **V1382**/dithiol) in PSCs, both p−i−n devices [fluorine-doped tin oxide (FTO)/HTM/perovskite/ethylenediammonium diiodide ($EDAI_2$)/C_{60}/bathocuproine (BCP)/Ag] (Figure 4a) and n−i−p devices [indium tin oxide (ITO)/SnO_2/perovskite/(with or without HTM interlayer)/**Spiro-OMeTAD**/Au] (Figure 4b) were fabricated. In the p−i−n PSCs, $EDAI_2$ was used as a post-treatment for the perovskite surface to improve the cell voltages.[55] A triple cation perovskite ($Cs_{0.05}FA_{0.80}MA_{0.15}PbI_{2.75}Br_{0.25}$) with a bandgap of 1.56 eV was selected as the light absorber material.[34,56] Cross-linked **V1382**/dithiol was used as the HTM and the HTM interlayer in p−i−n and n−i−p PSCs, respectively. The details for the device fabrication are provided in the Supporting Information. The current−voltage (*J*−*V*) curves of devices were measured under AM 1.5G illumination at 100 mW cm^{-2}, and detailed device parameters are listed in Table 2.

In the p−i−n PSCs, all HTMs are used without any dopants or additives. Devices with **PTAA** as the HTM were also fabricated as references. The performance of the cross-linked **V1382**/dithiol-based devices with different concentrations of **V1382** (0.125−4.0 mg mL^{-1}) is presented in Table S2 and Figures S5−S9 in the Supporting Information. The morphology of the perovskite films was characterized with the help of scanning electron microscopy (SEM) (Figures S10 and S11). All of the perovskite layers are smooth and pinhole-free, indicating that the perovskite films are not significantly affected by the concentration of **V1382** used for cross-linking.

The concentration of **V1382** used for cross-linking with dithiol was optimized to be 2.0 mg mL^{-1}. Devices with cross-linked **V1382**/dithiol fabricated by using <2.0 mg mL^{-1} of **V1382** exhibited a lower open-circuit voltage and a larger hysteresis, while those using >2.0 mg mL^{-1} of **V1382** showed a lower fill factor. Under the optimized conditions, in the forward scan, the cross-linked **V1382**/dithiol-based p−i−n devices exhibited a short-circuit current density (J_{SC}) of 23.0 mA cm^{-2}, an open-circuit voltage (V_{OC}) of 1.09 V, and a fill factor (FF) of 0.77, resulting in a PCE of 19.3%. The J_{SC} values derived from the *J*−*V* measurements were consistent with the values integrated from the incident photon-to-current efficiency (IPCE) spectra (Figures S6−S8). Compared to the reference devices based on **PTAA** (Figures 4c, S12, and S13), the cross-linked **V1382**/dithiol-based devices showed comparable PCE (19.3 vs 19.3%), higher V_{OC} (1.09 vs 1.05 V), and smaller hysteresis (−0.027 vs −0.090). The higher V_{OC} of the cross-linked **V1382**/dithiol-based devices could be attributed to the larger ionization potential (or deeper HOMO energy level), resulting in a better energy alignment with the VB of the perovskite material.

To compare the operational stability of p−i−n devices using cross-linked **V1382**/dithiol and reference **PTAA** HTMs, maximum power point tracking (MPPT) was carried out under AM 1.5G in an inert atmosphere (Figure 4e). The PCE of the **PTAA**-based reference device degraded to 80% of its initial value after 30 h. In contrast, the cross-linked **V1382**/dithiol-based device still retained 84% of the initial output after 200 h, indicating the superior long-term stability of the cross-linked HTMs. In addition, Figure S14 shows the much improved thermal stability of the unencapsulated device using

https://doi.org/10.1021/acsami.3c13950
ACS Appl. Mater. Interfaces 2024, 16, 1206−1216

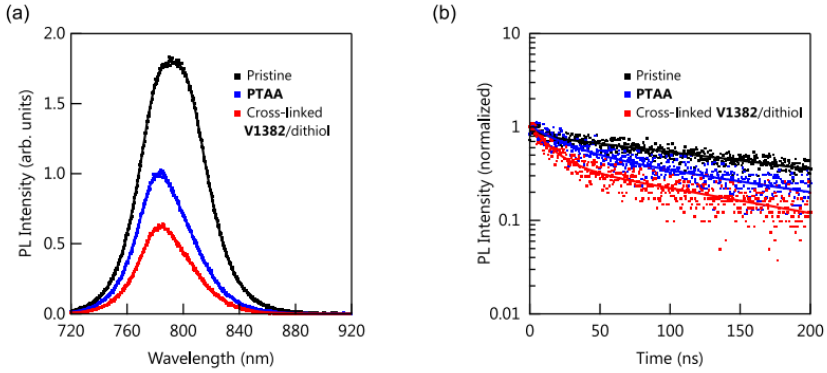

Figure 5. (a) Steady-state PL and (b) time-resolved PL spectra of the perovskite films ($Cs_{0.05}FA_{0.80}MA_{0.15}PbI_{2.75}Br_{0.25}$) fabricated on quartz, **PTAA**, and cross-linked **V1382**/dithiol substrates excited at 688 nm with an excitation fluence of 100 nJ cm^{-2}. The perovskite is probed through the glass side.

the cross-linked **V1382**/dithiol, which remained at 91% of its initial PCE after being heated at 85 °C in air for 50 h under a relative humidity of 40%, while the PCE of the **PTAA**-based device dropped to 76% of its initial value.

The electrical properties of the devices were investigated with the aid of impedance spectroscopy (AM 1.5G, zero applied bias; Figure S15). The data are analyzed with a simple equivalent circuit comprising series and parallel resistances together with a parallel capacitance element. At low bias voltages, the parallel resistance is determined by recombination and/or leakage currents, with larger values indicating either better quality of the perovskite layer or more efficient charge extraction from the perovskite absorber. The parallel resistance of the cross-linked **V1382**/dithiol-based device was estimated to be 228 cm^2, higher than that of the **PTAA**-based device (152 Ω cm^2). It indicates that the interfacial recombination could be suppressed in the case of the device with cross-linked **V1382**/dithiol. The results are in good agreement with the trend in V_{OC}.

The effect of the cross-linked **V1382**/dithiol as the interlayer between the perovskite layer and **Spiro-OMeTAD** on the performance of the n−i−p PSCs was investigated. In this case, **Spiro-OMeTAD** was doped with LiTFSI, the Co(III) complex, and *t*BP. Devices using the doped **Spiro-OMeTAD** without the interlayer were also fabricated as reference n−i−p devices (Figure S16). The concentration of **V1382** on the cross-linking precursor used for the interlayer was optimized and determined to be 1.0 mg mL^{-1} (Table S3, and Figures S17−S20). As shown in Figure 4d, after optimization, the device with the cross-linked interlayer exhibited a PCE of 19.1% with a J_{SC} of 22.4 mA cm^{-2}, a V_{OC} of 1.10 V, and an FF of 0.77 in the forward scan. For the reference device without the interlayer, slight drops in V_{OC} and PCE were observed (V_{OC} = 1.08 V and PCE = 18.9%). It implies that by inserting the cross-linked **V1382**/dithiol interlayer, the interfacial recombination could be suppressed. As confirmed by impedance spectroscopy (Figure S21), the parallel resistance of the device increased from 71 to 252 Ω cm^2 after inserting the cross-linked **V1382**/dithiol interlayer, supporting the above statement. The operational stability of the devices was assessed by running them at the maximum power point under AM 1.5G for 24 h. As shown in Figure 4f, the PCE of the reference device degraded to 60% of its initial value after 16 h, while the device with the cross-linked interlayer still maintained 84% of its initial output after 24 h. In addition, a thermal durability test on the unencapsulated devices was also carried out under an ambient atmosphere. The results are listed in Figure S22. After heating the devices at 100 °C for 1 h, the efficiency of the reference device without the interlayer dropped to 58% of the initial efficiency. In contrast, under the same conditions, the efficiency of the device using the cross-linked **V1382**/dithiol interlayer still retained 71%. Since the cross-linked **V1382**/dithiol with a water contact angle of 69° (Figure S23) shows similar hydrophobicity to doped **Spiro-OMeTAD**,[57,58] the better stability of the cross-linked **V1382**/dithiol-based PSCs could be attributed to the suppression of the metal diffusion[59] and the interfacial defect passivation,[60,61] caused by the insertion of the sulfur-rich interlayer.

In order to investigate the interfacial charge transfer kinetics, steady-state photoluminescence (PL) quenching and time-resolved PL (TRPL) decay on the perovskite films deposited on quartz, **PTAA**, and cross-linked **V1382**/dithiol were conducted.[62] As shown in Figure 5a, after fabricating perovskite on HTM layers, the PL peak intensity was reduced, falling to 56 and 35% for **PTAA** and cross-linked **V1382**/dithiol, respectively. The TRPL lifetime for the pristine perovskite film was found to be 196 ns, and the TRPL lifetime for HTM/perovskite films decreased to 120 and 75 ns for **PTAA** and cross-linked **V1382**/dithiol, respectively (Figure 5b). The stronger PL quenching together with the shorter PL lifetime indicates that cross-linked **V1382**/dithiol has a better hole extraction ability than **PTAA**. There is no significant difference between the PL properties of perovskite/**Spiro-OMeTAD** and perovskite/cross-linked **V1382** interlayer/**Spiro-OMeTAD** (Figure S24 and Table S4).

CONCLUSIONS

In summary, a low-cost 9,9′-spirobifluorene derivative bearing four vinyl groups (**V1382**) was designed and synthesized. Due to the presence of vinyl groups, **V1382** can undergo thermal cross-linking at 255 °C to form a solvent-resistant polymeric network. Importantly, by mixing **V1382** with 4,4′-thiobisben-

https://doi.org/10.1021/acsami.3c13950
ACS Appl. Mater. Interfaces 2024, 16, 1206−1216

zenethiol in a molar ratio of 1:2, the cross-linking temperature can occur at 103 °C via a facile thiol−ene reaction. The cross-linked **V1382**/dithiol film exhibits appropriate hole mobility and ionization potential, implying its potential as an HTM in PSCs. Taking advantage of the low cross-linking temperature, the cross-linked **V1382**/dithiol can be used as the HTM and HTM interlayer in p−i−n and n−i−p PSC devices, respectively. Devices with the cross-linked **V1382**/dithiol were found to show suppressed interfacial recombination, resulting in better power conversion efficiencies and operational stability than devices using conventional hole-transporting materials such as **PTAA** and **Spiro-OMeTAD**.

MATERIALS AND METHODS

Fabrication of p−i−n PSCs. *Preparation of Transparent Conductive Oxide Substrates.* Glass/FTO substrates (10 sq^{-1}, AGC, Inc.) were etched with zinc powder and HCl (6 M in deionized water) and consecutively cleaned with 15 min ultrasonic bath in water, acetone, detergent solution (Semico Clean 56, Furuuchi chemical), water, and isopropanol, followed by drying with an air gun, and finally plasma treatment. The substrates were transferred to an inert gas-filled glovebox for further processing.

Preparation of Hole-Transporting Layers. **V1382** was mixed with 4,4′-thiobisbenzenethiol (molar ratio = 1:2, concentration of **V1382** = 0.125−4 mg mL^{-1}) in chlorobenzene. The HTM solution (100 μL) was deposited on the FTO substrate using spin-coating (3000 rpm for 30 s, 5 s acceleration), followed by heating on a hot plate at 110 °C for 1 h. In the case of bare **V1382**, 8 mg mL^{-1} **V1382** was used. The hole-collecting material PTAA (2.0 mg mL^{-1} in anhydrous toluene) was deposited by using spin-coating (4000 rpm for 30 s, 5 s acceleration), followed by heating on a hot plate at 100 °C for 10 min.

Preparation of Perovskite Layer. The $Cs_{0.05}FA_{0.80}MA_{0.15}PbI_{2.75}Br_{0.25}$ precursor solution was prepared from CsI (69 mg, 0.27 mmol), MABr (85 mg, 0.76 mmol), PbI_2 (2.24 g, 4.85 mmol), $PbBr_2$ (96 mg, 0.26 mmol), and FAI (703 mg, 4.09 mmol) dissolved in a mixture of DMF (3.0 mL) and DMSO (0.90 mL). After stirring at 40 °C for 30 min, the solution was filtered with a 0.45 μm PTFE filter. 190 μL of the solution was placed on an FTO/HTM substrate and spread by spin-coating (slope 1 s, 1000 rpm 10 s, slope 5 s, 6000 rpm 20 s, slope 1 s) to make a thin film. 300 μL of chlorobenzene was dripped over the rotating substrate at 3 s before the end of the spinning at 6000 rpm. The films were then annealed on a hot plate at 150 °C for 10 min. These perovskite samples were moved under Ar to a vacuum deposition chamber, where 0.5 nm of ethylenediammonium diiodide ($EDAI_2$) (deposition rate 0.03 nm s^{-1}) was deposited by thermal evaporation.

Preparation of Electron-Transporting Layer and Metal Electrode. The above samples were moved under Ar to a vacuum deposition chamber, where 20 nm of C_{60} (deposition rate 0.05 nm s^{-1}) and 8 nm of BCP (deposition rate 0.01 nm s^{-1}) were deposited by thermal evaporation. The top electrode was prepared by depositing 100 nm of silver (deposition rate, 0.005 nm s^{-1}) through a shadow mask.

Fabrication of n−i−p PSCs. *Preparation of Transparent Conductive Oxide Substrates.* Glass/ITO substrates (10 sq^{-1}) were etched with zinc powder and HCl (6 M in deionized water) and consecutively cleaned with a 15 min ultrasonic bath in water, acetone, detergent solution (Semico Clean 56, Furuuchi chemical), water, and isopropanol, followed by drying with an air gun, and finally plasma treatment. The substrates were transferred to an inert gas-filled glovebox for further processing.

Preparation of the SnO_2 Layer. The SnO_2 layer was prepared by spin-coating a colloidal dispersion (15% in H_2O) diluted with deionized water (volume ratio = 1:1) on the ITO substrates (400 μL for each substrate, slope 2 s, 3000 rpm 20 s, slope 2 s) followed by annealing at 150 °C for 30 min. A plasma treatment was performed after cooling the substrate to room temperature, before transferring the samples to an inert gas-filled glovebox for further processing.

Preparation of Perovskite Layer. The $Cs_{0.05}FA_{0.80}MA_{0.15}PbI_{2.75}Br_{0.25}$ precursor solution was prepared from CsI (69 mg, 0.27 mmol), MABr (85 mg, 0.76 mmol), PbI_2 (2.24 g, 4.85 mmol), $PbBr_2$ (96 mg, 0.26 mmol), and FAI (703 mg, 4.09 mmol) dissolved in a mixture of DMF (3.0 mL) and DMSO (0.90 mL). After stirring at 40 °C for 30 min, the solution was filtered with a 0.45 μm PTFE filter. 190 μL of the solution was placed on a glass/ITO/SnO_2 substrate and spread by spin-coating (slope 1 s, 1000 rpm 10 s, slope 5 s, 6000 rpm 20 s, slope 1 s) to make a thin film. 300 μL of chlorobenzene was dripped over the rotating substrate at 3 s before the end of the spinning at 6000 rpm. The films were then annealed on a hot plate at 150 °C for 10 min.

Preparation of Cross-Linked V1382 Interlayer. **V1382** was mixed with 4,4′-thiobisbenzenethiol (molar ratio = 1:2, concentration of **V1382** = 1.0, 2.0 mg mL^{-1}) in chlorobenzene. 100 μL of the solution was spin-coated on top of the perovskite layer (3000 rpm for 30 s, 5 s acceleration), followed by heating on a hot plate at 110 °C for 1 h.

Preparation of Hole-Transporting Layer. Spiro-OMeTAD (0.06 M) was mixed with an oxidizing agent [tris(2-(1*H*-pyrazol-1-yl)-4-*tert*-butylpyridine)cobalt(III) tris(bis(trifluoromethylsulfonyl)imide)] (FK209, 0.15 equiv) into a solution of chlorobenzene, 4-*tert*-butylpyridine (*t*BP, 3.3 equiv), and lithium bis-(trifluoromethylsulfonyl)imide (LITFSI, 0.54 equiv). After being stirred at 70 °C for 30 min, the suspension was filtered with a 0.45 μm PTFE filter to remove insoluble Co(II) complexes. 90 μL of the solution was spin-coated on top of **V1382** (slope 4 s, 4000 rpm, 30 s, slope 4 s), followed by annealing at 70 °C for 30 min.

Preparation of Metal Electrode. Gold electrodes (80 nm) were thermally deposited on the top face of the devices by using a shadow mask.

ASSOCIATED CONTENT

Supporting Information

The Supporting Information is available free of charge at https://pubs.acs.org/doi/10.1021/acsami.3c13950.

Equipment and characterization; detailed synthetic procedures, DSC, UV−vis, PESA, XPS, and SEM data; detailed photovoltaic parameters along with *J*−*V* curves; and PL data (PDF)

AUTHOR INFORMATION

Corresponding Authors

Atsushi Wakamiya − *Institute for Chemical Research, Kyoto University, Uji, Kyoto 611-0011, Japan*; orcid.org/0000-0003-1430-0947; Email: wakamiya@scl.kyoto-u.ac.jp

Vytautas Getautis − *Department of Organic Chemistry, Kaunas University of Technology, Kaunas 50254, Lithuania*; orcid.org/0000-0001-7695-4677; Email: vytautas.getautis@ktu.lt

Authors

Sarune Daskeviciute-Geguziene − *Department of Organic Chemistry, Kaunas University of Technology, Kaunas 50254, Lithuania*

Minh Anh Truong − *Institute for Chemical Research, Kyoto University, Uji, Kyoto 611-0011, Japan*; orcid.org/0000-0003-2649-0282

Kasparas Rakstys − *Department of Organic Chemistry, Kaunas University of Technology, Kaunas 50254, Lithuania*; orcid.org/0000-0001-8016-9567

Maryte Daskeviciene − *Department of Organic Chemistry, Kaunas University of Technology, Kaunas 50254, Lithuania*

Ruito Hashimoto − *Institute for Chemical Research, Kyoto University, Uji, Kyoto 611-0011, Japan*

Richard Murdey – *Institute for Chemical Research, Kyoto University, Uji, Kyoto 611-0011, Japan*; orcid.org/0000-0001-7621-9664
Takumi Yamada – *Institute for Chemical Research, Kyoto University, Uji, Kyoto 611-0011, Japan*; orcid.org/0000-0002-6461-7363
Yoshihiko Kanemitsu – *Institute for Chemical Research, Kyoto University, Uji, Kyoto 611-0011, Japan*; orcid.org/0000-0002-0788-131X
Vygintas Jankauskas – *Institute of Chemical Physics, Vilnius University, Vilnius 10257, Lithuania*

Complete contact information is available at: https://pubs.acs.org/10.1021/acsami.3c13950

Author Contributions

‖S.D.-G. and M.A.T contributed equally to this work. The manuscript was written through contributions of all authors. All authors have given approval to the final version of the manuscript.

Notes

The authors declare no competing financial interest.

■ ACKNOWLEDGMENTS

This work was funded by the European Union. Views and opinions expressed are however those of the author(s) only and do not necessarily reflect those of the European Union or CINEA. Neither the European Union nor the granting authority can be held responsible for them. VALHALLA project has received funding from Horizon Europe Research and Innovation Action program under Grant Agreement no. 101082176. This work was also supported by the Japan Society for the Promotion of Science (JP20K22531, J22K14744, and JP21H04699), a research grant from the Iwatani Naoji Foundation, the Mazda Foundation, and JSPS Fellows (21J23253). The authors thank Yasuko Iwasaki (ICR, Kyoto University) for the SEM measurements. They also thank Prof. Toshiyuki Nohira and Dr. Takayuki Yamamoto (ICR, Kyoto University) for XPS measurements.

■ REFERENCES

(1) Best Research-Cell Efficiency Chart | Photovoltaic Research | NREL, 2023 https://www.nrel.gov/pv/cell-efficiency.html. (accessed September 11, 2023).
(2) Ramanujam, J.; Singh, U. P. Copper Indium Gallium Selenide Based Solar Cells - A Review. *Energy Environ. Sci.* **2017**, *10* (6), 1306–1319.
(3) Yang, Y. M.; Yu, A.; Hsu, B.; Hsu, W. C.; Yang, A.; Lan, C. W. Development of High-Performance Multicrystalline Silicon for Photovoltaic Industry. *Prog. Photovoltaics Res. Appl.* **2015**, *23* (3), 340–351.
(4) Chao, L.; Niu, T.; Gao, W.; Ran, C.; Song, L.; Chen, Y.; Huang, W. Solvent Engineering of the Precursor Solution toward Large-Area Production of Perovskite Solar Cells. *Adv. Mater.* **2021**, *33* (14), No. 2005410.
(5) Yao, Y.; Cheng, C.; Zhang, C.; Hu, H.; Wang, K.; De Wolf, S. Organic Hole-Transport Layers for Efficient, Stable, and Scalable Inverted Perovskite Solar Cells. *Adv. Mater.* **2022**, *34* (44), No. 2203794.
(6) Fu, F.; Li, J.; Yang, T. C. J.; Liang, H.; Faes, A.; Jeangros, Q.; Ballif, C.; Hou, Y. Monolithic Perovskite-Silicon Tandem Solar Cells: From the Lab to Fab? *Adv. Mater.* **2022**, *34* (24), No. 2106540.
(7) Rong, Y.; Hu, Y.; Mei, A.; Tan, H.; Saidaminov, M. I.; Seok, S. Il.; McGehee, M. D.; Sargent, E. H.; Han, H. Challenges for Commercializing Perovskite Solar Cells. *Science* **2018**, *361* (6408), No. eaat8235, DOI: 10.1126/science.aat8235.
(8) Kim, J. Y.; Lee, J. W.; Jung, H. S.; Shin, H.; Park, N. G. High-Efficiency Perovskite Solar Cells. *Chem. Rev.* **2020**, *120* (15), 7867–7918.
(9) Urieta-Mora, J.; García-Benito, I.; Molina-Ontoria, A.; Martín, N. Hole Transporting Materials for Perovskite Solar Cells: A Chemical Approach. *Chem. Soc. Rev.* **2018**, *47* (23), 8541–8571.
(10) Calió, L.; Kazim, S.; Grätzel, M.; Ahmad, S. Hole-Transport Materials for Perovskite Solar Cells. *Angew. Chem., Int. Ed.* **2016**, *55* (47), 14522–14545.
(11) Krishna, A.; Grimsdale, A. C. Hole Transporting Materials for Mesoscopic Perovskite Solar Cells-towards a Rational Design? *J. Mater. Chem. A* **2017**, *5* (32), 16446–16466.
(12) Yin, X.; Song, Z.; Li, Z.; Tang, W. Toward Ideal Hole Transport Materials: A Review on Recent Progress in Dopant-Free Hole Transport Materials for Fabricating Efficient and Stable Perovskite Solar Cells. *Energy Environ. Sci.* **2020**, *13* (11), 4057–4086.
(13) Ren, G.; Han, W.; Deng, Y.; Wu, W.; Li, Z.; Guo, J.; Bao, H.; Liu, C.; Guo, W. Strategies of Modifying Spiro-OMeTAD Materials for Perovskite Solar Cells: A Review. *J. Mater. Chem. A* **2021**, *9* (8), 4589–4625.
(14) Rakstys, K.; Igci, C.; Nazeeruddin, M. K. Efficiency: Vs. Stability: Dopant-Free Hole Transporting Materials towards Stabilized Perovskite Solar Cells. *Chem. Sci.* **2019**, *10* (28), 6748–6769.
(15) Li, Y.; Lim, E. L.; Xie, H.; Song, J.; Kong, T.; Zhang, Y.; Yang, M.; Wu, B.; Duan, C.; Bi, D. Hydrophobic Fluorinated Conjugated Polymer as a Multifunctional Interlayer for High-Performance Perovskite Solar Cells. *ACS Photonics* **2021**, *8* (11), 3185–3192.
(16) Webb, T.; Liu, X.; Westbrook, R. J. E.; Kern, S.; Sajjad, M. T.; Jenatsch, S.; Jayawardena, K. D. G. I.; Perera, W. H. K.; Marko, I. P.; Sathasivam, S.; Li, B.; Yavari, M.; Scurr, D. J.; Alexander, M. R.; Macdonald, T. J.; Haque, S. A.; Sweeney, S. J.; Zhang, W. A Multifaceted Ferrocene Interlayer for Highly Stable and Efficient Lithium Doped Spiro-OMeTAD-Based Perovskite Solar Cells. *Adv. Energy Mater.* **2022**, *12* (26), No. 2200666.
(17) Han, W.; Ren, G.; Liu, J.; Li, Z.; Bao, H.; Liu, C.; Guo, W. Recent Progress of Inverted Perovskite Solar Cells with a Modified PEDOT:PSS Hole Transport Layer. *ACS Appl. Mater. Interfaces* **2020**, *12* (44), 49297–49322.
(18) Li, X.; Zhang, W.; Guo, X.; Lu, C.; Wei, J.; Fang, J. Constructing Heterojunctions by Surface Sulfidation for Efficient Inverted Perovskite Solar Cells. *Science* **2022**, *375* (6579), 434–437.
(19) Li, X.; Zhang, W.; Wang, Y. C.; Zhang, W.; Wang, H. Q.; Fang, J. In-Situ Cross-Linking Strategy for Efficient and Operationally Stable Methylammoniun Lead Iodide Solar Cells. *Nat. Commun.* **2018**, *9* (1), No. 3806.
(20) Wang, Y.; Duan, L.; Zhang, M.; Hameiri, Z.; Liu, X.; Bai, Y.; Hao, X. PTAA as Efficient Hole Transport Materials in Perovskite Solar Cells: A Review. *Sol. RRL* **2022**, *6* (8), No. 2200234.
(21) Li, Z.; Li, B.; Wu, X.; Sheppard, S. A.; Zhang, S.; Gao, D.; Long, N. J.; Zhu, Z. Organometallic-Functionalized Interfaces for Highly Efficient Inverted Perovskite Solar Cells. *Science* **2022**, *376* (6591), 416–420, DOI: 10.1126/science.abm8566.
(22) Stolterfoht, M.; Wolff, C. M.; Márquez, J. A.; Zhang, S.; Hages, C. J.; Rothhardt, D.; Albrecht, S.; Burn, P. L.; Meredith, P.; Unold, T.; Neher, D. Visualization and Suppression of Interfacial Recombination for High-Efficiency Large-Area Pin Perovskite Solar Cells. *Nat. Energy* **2018**, *3* (10), 847–854.
(23) Li, W.; Wang, H.; Hu, X.; Cai, W.; Zhang, C.; Wang, M.; Zang, Z. Sodium Benzenesulfonate Modified Poly (3,4-Ethylenedioxythiophene):Polystyrene Sulfonate with Improved Wettability and Work Function for Efficient and Stable Perovskite Solar Cells. *Sol. RRL* **2021**, *5* (1), No. 2000573.
(24) Xu, C.; Liu, Z.; Lee, E. C. High-Performance Metal Oxide-Free Inverted Perovskite Solar Cells Using Poly(Bis(4-Phenyl)(2,4,6-Trimethylphenyl)Amine) as the Hole Transport Layer. *J. Mater. Chem. C* **2018**, *6* (26), 6975–6981.

(25) Zhao, Q.; Wu, R.; Zhang, Z.; Xiong, J.; He, Z.; Fan, B.; Dai, Z.; Yang, B.; Xue, X.; Cai, P.; Zhan, S.; Zhang, X.; Zhang, J. Achieving Efficient Inverted Planar Perovskite Solar Cells with Nondoped PTAA as a Hole Transport Layer. *Org. Electron.* **2019**, *71*, 106−112.
(26) Liu, Y.; Liu, Z.; Lee, E. C. High-Performance Inverted Perovskite Solar Cells Using Doped Poly(Triarylamine) as the Hole Transport Layer. *ACS Appl. Energy Mater.* **2019**, *2* (3), 1932−1942.
(27) Li, Y.; Liao, J. F.; Pan, H.; Xing, G. Interfacial Engineering for High-Performance PTAA-Based Inverted 3D Perovskite Solar Cells. *Sol. RRL* **2022**, *6* (12), No. 2200647.
(28) Liu, X.; Cheng, Y.; Liu, C.; Zhang, T.; Zhang, N.; Zhang, S.; Chen, J.; Xu, Q.; Ouyang, J.; Gong, H. 20.7% Highly Reproducible Inverted Planar Perovskite Solar Cells With Enhanced Fill Factor and Eliminated Hysteresis. *Energy Environ. Sci.* **2019**, *12* (5), 1622−1633.
(29) Xu, C. Y.; Hu, W.; Wang, G.; Niu, L.; Elseman, A. M.; Liao, L.; Yao, Y.; Xu, G.; Luo, L.; Liu, D.; Zhou, G.; Li, P.; Song, Q. Coordinated Optical Matching of a Texture Interface Made from Demixing Blended Polymers for High-Performance Inverted Perovskite Solar Cells. *ACS Nano* **2020**, *14* (1), 196−203.
(30) Wu, F.; Xiao, Q.; Sun, X.; Wu, T.; Hua, Y.; Li, Z.; Zhu, L. Hole Transporting Layer Engineering via a Zwitterionic Polysquaraine toward Efficient Inverted Perovskite Solar Cells. *Chem. Eng. J.* **2022**, *445*, No. 136760.
(31) Li, H.; Zhang, C.; Gong, C.; Zhang, D.; Zhang, H.; Zhuang, Q.; Yu, X.; Gong, S.; Chen, X.; Yang, J.; Li, X.; Li, R.; Li, J.; Zhou, J.; Yang, H.; Lin, Q.; Chu, J.; Grätzel, M.; Chen, J.; Zang, Z. 2D/3D Heterojunction Engineering at the Buried Interface towards High-Performance Inverted Methylammonium-Free Perovskite Solar Cells. *Nat. Energy* **2023**, *55*, 946−955.
(32) Xu, X.; Ji, X.; Chen, R.; Ye, F.; Liu, S.; Zhang, S.; Chen, W.; Wu, Y.; Zhu, W. H. Improving Contact and Passivation of Buried Interface for High-Efficiency and Large-Area Inverted Perovskite Solar Cells. *Adv. Funct. Mater.* **2022**, *32* (9), No. 2109968.
(33) Yalcin, E.; Can, M.; Rodriguez-Seco, C.; Aktas, E.; Pudi, R.; Cambarau, W.; Demic, S.; Palomares, E. Semiconductor Self-Assembled Monolayers as Selective Contacts for Efficient PiN Perovskite Solar Cells. *Energy Environ. Sci.* **2019**, *12* (1), 230−237.
(34) Truong, M. A.; Funasaki, T.; Ueberricke, L.; Nojo, W.; Murdey, R.; Yamada, T.; Hu, S.; Akatsuka, A.; Sekiguchi, N.; Hira, S.; Xie, L.; Nakamura, T.; Shioya, N.; Kan, D.; Tsuji, Y.; Iikubo, S.; Yoshida, H.; Shimakawa, Y.; Hasegawa, T.; Kanemitsu, Y.; Suzuki, T.; Wakamiya, A. Tripodal Triazatruxene Derivative as a Face-On Oriented Hole-Collecting Monolayer for Efficient and Stable Inverted Perovskite Solar Cells. *J. Am. Chem. Soc.* **2023**, *145* (13), 7528−7539.
(35) Al-Ashouri, A.; Köhnen, E.; Li, B.; Magomedov, A.; Hempel, H.; Caprioglio, P.; Márquez, J. A.; Vilches, A. B. M.; Kasparavicius, E.; Smith, J. A.; Phung, N.; Menzel, D.; Grischek, M.; Kegelmann, L.; Skroblin, D.; Gollwitzer, C.; Malinauskas, T.; Jošt, M.; Matič, G.; Rech, B.; Schlatmann, R.; Topič, M.; Korte, L.; Abate, A.; Stannowski, B.; Neher, D.; Stolterfoht, M.; Unold, T.; Getautis, V.; Albrecht, S. Monolithic Perovskite/Silicon Tandem Solar Cell with > 29% Efficiency by Enhanced Hole Extraction. *Science* **2020**, *370* (6522), 1300−1309.
(36) Magomedov, A.; Al-Ashouri, A.; Kasparavičius, E.; Strazdaite, S.; Niaura, G.; Jošt, M.; Malinauskas, T.; Albrecht, S.; Getautis, V. Self-Assembled Hole Transporting Monolayer for Highly Efficient Perovskite Solar Cells. *Adv. Energy Mater.* **2018**, *8* (32), No. 1801892.
(37) Kahle, F. J.; Saller, C.; Köhler, A.; Strohriegl, P. Crosslinked Semiconductor Polymers for Photovoltaic Applications. *Adv. Energy Mater.* **2017**, *7* (16), No. 1700306.
(38) Sun, Y.; Chien, S. C.; Yip, H. L.; Zhang, Y.; Chen, K. S.; Zeigler, D. F.; Chen, F. C.; Lin, B.; Jen, A. K. Y. Chemically Doped and Cross-Linked Hole-Transporting Materials as an Efficient Anode Buffer Layer for Polymer Solar Cells. *Chem. Mater.* **2011**, *23* (22), 5006−5015.
(39) Cheng, Y. J.; Liu, M. S.; Zhang, Y.; Niu, Y.; Huang, F.; Ka, J. W.; Yip, H. L.; Tian, Y.; Jen, A. K. Y. Thermally Cross-Linkable Hole-Transporting Materials on Conducting Polymer: Synthesis, Characterization, and Applications for Polymer Light-Emitting Devices. *Chem. Mater.* **2008**, *20* (2), 413−422.
(40) Zhang, C.; Liao, Q.; Chen, J.; Li, B.; Xu, C.; Wei, K.; Du, G.; Wang, Y.; Liu, D.; Deng, J.; Luo, Z.; Pang, S.; Yang, Y.; Li, J.; Yang, L.; Guo, X.; Zhang, J. Thermally Crosslinked Hole Conductor Enables Stable Inverted Perovskite Solar Cells with 23.9% Efficiency. *Adv. Mater.* **2023**, *35* (9), No. 2209422, DOI: 10.1002/adma.202209422.
(41) Wang, Y.; Gu, S.; Liu, G.; Zhang, L.; Liu, Z. Z.; Lin, R.; Xiao, K.; Luo, X.; Shi, J.; Du, J.; Meng, F.; Li, L.; Liu, Z. Z.; Tan, H. Cross-Linked Hole Transport Layers for High-Efficiency Perovskite Tandem Solar Cells. *Sci. China Chem.* **2021**, *64* (11), 2025−2034.
(42) Daskeviciute-Geguziene, S.; Magomedov, A.; Daskeviciene, M.; Genevičius, K.; Nekrašas, N.; Jankauskas, V.; Kantminiene, K.; McGehee, M. D.; Getautis, V. Cross-Linkable Carbazole-Based Hole Transporting Materials for Perovskite Solar Cells. *Chem. Commun.* **2022**, *58* (54), 7495−7498.
(43) Wu, J.; Hu, M.; zhang, L.; Song, G.; Li, Y.; Tan, W.; Tian, Y.; Xu, B. Fluorinated Cross-Linkable and Dopant-Free Hole Transporting Materials for Efficient and Stable Perovskite Solar Cells. *Chem. Eng. J.* **2021**, *422*, No. 130124.
(44) Vaitukaitytė, D.; Al-Ashouri, A.; Daškevičienė, M.; Kamarauskas, E.; Nekrasovas, J.; Jankauskas, V.; Magomedov, A.; Albrecht, S.; Getautis, V. Enamine-Based Cross-Linkable Hole-Transporting Materials for Perovskite Solar Cells. *Sol. RRL* **2021**, *5* (1), No. 2000597.
(45) Zhang, Y.; Kou, C.; Zhang, J.; Liu, Y.; Li, W.; Bo, Z.; Shao, M. Crosslinked and Dopant Free Hole Transport Materials for Efficient and Stable Planar Perovskite Solar Cells. *J. Mater. Chem. A* **2019**, *7* (10), 5522−5529.
(46) Li, S.; Chen, W.; Yang, Y.; Zhao, P.; Cui, H.; Huang, Y.; He, D.; Ning, Y.; Feng, Y.; Zhang, B. Regulating the Solvent Resistance of Hole Transport Layer for High-Performance Inverted Perovskite Solar Cells. *Sol. RRL* **2023**, *7*, No. 2300252.
(47) Chang, C. C.; Tao, J. H.; Tsai, C. E.; Cheng, Y. J.; Hsu, C. S. Cross-Linked Triarylamine-Based Hole-Transporting Layer for Solution-Processed PEDOT:PSS-Free Inverted Perovskite Solar Cells. *ACS Appl. Mater. Interfaces* **2018**, *10* (25), 21466−21471.
(48) Jhuo, H. J.; Yeh, P. N.; Liao, S. H.; Li, Y. L.; Sharma, S.; Chen, S. A. Inverted Perovskite Solar Cells with Inserted Cross-Linked Electron-Blocking Interlayers for Performance Enhancement. *J. Mater. Chem. A* **2015**, *3* (17), 9291−9297.
(49) Li, Z.; Zhu, Z.; Chueh, C. C.; Luo, J.; Jen, A. K. Y. Facile Thiol-Ene Thermal Crosslinking Reaction Facilitated Hole-Transporting Layer for Highly Efficient and Stable Perovskite Solar Cells. *Adv. Energy Mater.* **2016**, *6* (21), No. 1601165.
(50) Wang, Y.; Liao, Q.; Chen, J.; Huang, W.; Zhuang, X.; Tang, Y.; Li, B.; Yao, X.; Feng, X.; Zhang, X.; Su, M.; He, Z.; Marks, T. J.; Facchetti, A.; Guo, X. Teaching an Old Anchoring Group New Tricks: Enabling Low-Cost, Eco-Friendly Hole-Transporting Materials for Efficient and Stable Perovskite Solar Cells. *J. Am. Chem. Soc.* **2020**, *142* (39), 16632−16643.
(51) Rakstys, K.; Stephen, M.; Saghaei, J.; Jin, H.; Gao, M.; Zhang, G.; Hutchinson, K.; Chesman, A.; Burn, P. L.; Gentle, I.; Shaw, P. E. Precursor Route Poly(1,4-Phenylenevinylene)-Based Interlayers for Perovskite Solar Cells. *ACS Appl. Energy Mater.* **2020**, *3* (1), 889−899.
(52) Yu, H.; Li, D.; Bao, H.; Zhang, Z.; Liu, H.; Zhang, F.; Wang, S. Multifunctional Cross-Linked Hole Transporting Interfacial Layer for Efficient and Stable Perovskite Solar Cells. *ACS Appl. Energy Mater.* **2022**, *5* (9), 10742−10750.
(53) Malinauskas, T.; Saliba, M.; Matsui, T.; Daskeviciene, M.; Urnikaite, S.; Gratia, P.; Send, R.; Wonneberger, H.; Bruder, I.; Graetzel, M.; Getautis, V.; Nazeeruddin, M. K. Branched Methoxydiphenylamine-Substituted Fluorene Derivatives as Hole Transporting Materials for High-Performance Perovskite Solar Cells. *Energy Environ. Sci.* **2016**, *9* (5), 1681−1686.
(54) Gratia, P.; Magomedov, A.; Malinauskas, T.; Daskeviciene, M.; Abate, A.; Ahmad, S.; Grätzel, M.; Getautis, V.; Nazeeruddin, M. K. A Methoxydiphenylamine-Substituted Carbazole Twin Derivative: An

Efficient Hole-Transporting Material for Perovskite Solar Cells. *Angew. Chem., Int. Ed.* **2015**, *54* (39), 11409−11413.
(55) Hu, S.; Pascual, J.; Liu, W.; Funasaki, T.; Truong, M. A.; Hira, S.; Hashimoto, R.; Morishita, T.; Nakano, K.; Tajima, K.; Murdey, R.; Nakamura, T.; Wakamiya, A. A Universal Surface Treatment for P-i-n Perovskite Solar Cells. *ACS Appl. Mater. Interfaces* **2022**, *14* (50), 56290−56297.
(56) Ozaki, M.; Ishikura, Y.; Truong, M. A.; Liu, J.; Okada, I.; Tanabe, T.; Sekimoto, S.; Ohtsuki, T.; Murata, Y.; Murdey, R.; Wakamiya, A. Iodine-Rich Mixed Composition Perovskites Optimised for Tin(IV) Oxide Transport Layers: The Influence of Halide Ion Ratio, Annealing Time, and Ambient Air Aging on Solar Cell Performance. *J. Mater. Chem. A* **2019**, *7* (28), 16947−16953.
(57) Li, W.; Cariello, M.; Méndez, M.; Cooke, G.; Palomares, E. Self-Assembled Molecules for Hole-Selective Electrodes in Highly Stable and Efficient Inverted Perovskite Solar Cells with Ultralow Energy Loss. *ACS Appl. Energy Mater.* **2023**, *6* (3), 1239−1247.
(58) Jegorovė, A.; Xia, J.; Steponaitis, M.; Daskeviciene, M.; Jankauskas, V.; Gruodis, A.; Kamarauskas, E.; Malinauskas, T.; Rakstys, K.; Alamry, K. A.; Getautis, V.; Nazeeruddin, M. K. Branched Fluorenylidene Derivatives with Low Ionization Potentials as Hole-Transporting Materials for Perovskite Solar Cells. *Chem. Mater.* **2023**, *35* (5923), 5914−5923, DOI: 10.1021/acs.chemmater.3c00708.
(59) Yang, J.; Cao, Q.; Wang, T.; Yang, B.; Pu, X.; Zhang, Y.; Chen, H.; Tojiboyev, I.; Li, Y.; Etgar, L.; Li, X.; Hagfeldt, A. Inhibiting Metal-Inward Diffusion-Induced Degradation through Strong Chemical Coordination toward Stable and Efficient Inverted Perovskite Solar Cells. *Energy Environ. Sci.* **2022**, *15* (5), 2154−2163.
(60) Li, M. H.; Sun, T. G.; Shao, J. Y.; Wang, Y. D.; Hu, J. S.; Zhong, Y. W. A Sulfur-Rich Small Molecule as a Bifunctional Interfacial Layer for Stable Perovskite Solar Cells with Efficiencies Exceeding 22%. *Nano Energy* **2021**, *79*, No. 105462.
(61) Huang, Z.; Li, L.; Wu, T.; Xue, T.; Sun, W.; Pan, Q.; Wang, H.; Xie, H.; Chi, J.; Han, T.; Hu, X.; Su, M.; Chen, Y.; Song, Y. Wearable Perovskite Solar Cells by Aligned Liquid Crystal Elastomers. *Nat. Commun.* **2023**, *14* (1), No. 1204.
(62) Handa, T.; Tex, D. M.; Shimazaki, A.; Wakamiya, A.; Kanemitsu, Y. Charge Injection Mechanism at Heterointerfaces in CH3NH3PbI3 Perovskite Solar Cells Revealed by Simultaneous Time-Resolved Photoluminescence and Photocurrent Measurements. *J. Phys. Chem. Lett.* **2017**, *8* (5), 954−960.

Supporting Information

In Situ Thermal Cross-Linking of 9,9´-Spirobifluorene-Based Hole-Transporting Layer for Perovskite Solar Cells

Sarune Daskeviciute-Geguziene,[‡,a] Minh Anh Truong,[‡,b] Kasparas Rakstys,[a] Maryte Daskeviciene,[a] Ruito Hashimoto,[b] Richard Murdey,[b] Takumi Yamada,[b] Yoshihiko Kanemitsu,[b] Vygintas Jankauskas,[c] Atsushi Wakamiya,[,b] Vytautas Getautis*[,a]*

[a]Department of Organic Chemistry, Kaunas University of Technology, Radvilenu pl. 19, Kaunas 50254, Lithuania.
[b]Institute for Chemical Research, Kyoto University, Gokasho, Uji, Kyoto 611-0011, Japan.
[c]Institute of Chemical Physics, Vilnius University, Sauletekio al. 3, Vilnius 10257, Lithuania.

[‡]S.D.-G. and M.A.T. contributed equally to this work.

*Corresponding Authors:
wakamiya@scl.kyoto-u.ac.jp; vytautas.getautis@ktu.lt

EXPERIMENTAL SECTION

Equipment and Characterization

Chemicals were purchased from Sigma-Aldrich, TCI Europe and used as received without further purification.

^{1}H NMR spectra were recorded at 400 MHz on a Bruker Avance III spectrometer with a 5 mm double resonance broad band BBO *z*-gradient room temperature probe, ^{13}C NMR spectra were collected using the same instrument at 101 MHz. The chemical shifts, expressed in ppm, were relative to tetramethylsilane (TMS). All the NMR experiments were performed at 25 °C. Reactions were monitored by thin-layer chromatography on ALUGRAM SIL G/UV254 plates and developed with UV light. Silica gel (grade 9385, 230–400 mesh, 60 Å, Aldrich) was used for column chromatography.

Elemental analysis (EA) was performed with an Exeter Analytical CE-440 elemental analyser, Model 440 C/H/N/.

Mass spectrometry (MS) was performed on Waters SQ Detector 2 Spectrometer using electrospray ionization (ESI) technique.

Synthesis

Scheme S1. Synthetic route of the **V1382**.

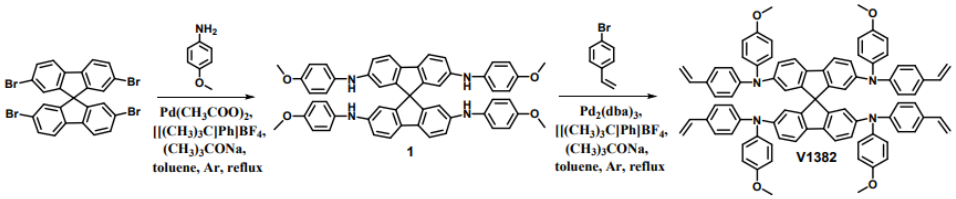

***N*²,*N*²',*N*⁷,*N*⁷'-tetrakis(4-methoxyphenyl)-9,9'-spirobi[fluorene]-2,2',7,7'-tetraamine (1)**

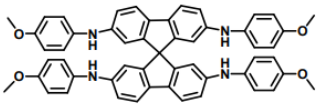

1

A solution of compound 2,2',7,7'-Tetrabromo-9,9'-spirobifluorene (3 g, 4.7 mmol, 1 equiv) and *p*-anisidine (5.9 g, 47.5 mmol, 10 equiv) in anhydrous toluene (47 mL) was purged with argon for 30 minutes. Afterwards, palladium (II) acetate (0.02 equiv), tri-*tert*-butylphosphonium tetrafluoroborate (0.027 equiv) and sodium *tert*-butoxide (8 equiv) were added and the resulted solution was refluxed under argon atmosphere for 28 hours. After cooling down to room temperature, the reaction mixture was extracted with ethyl acetate and distilled water. The organic layer was dried over anhydrous Na_2SO_4, filtered and solvent evaporated. The crude product was purified by column chromatography using 8:17 v/v THF/*n*-hexane as an eluent. Pale green solid were collected as a final product. (2.7 g, 71% yield). ^{1}H NMR (400 MHz, DMSO-d_6) δ 7.73 (s, 4H), 7.54 (d, J = 8.0 Hz, 4H), 7.00 – 6.87 (m, 12H), 6.79 (d, J = 8.4 Hz, 8H), 6.23 (s, 4H), 3.67 (s, 12H). ^{13}C NMR (101 MHz, DMSO-d_6) δ 154.14, 150.79, 144.28, 136.61, 132.96, 120.61, 119.86, 114.96, 113.37, 111.64, 65.48, 55.65 ppm. Anal. calcd for $C_{53}H_{44}N_4O_4$: C, 79.48; H, 5.54; N, 7.00; found: C, 79.77; H, 5.52; N, 7.04.

N^2,$N^{2'}$,N^7,$N^{7'}$-tetrakis(4-methoxyphenyl)-N^2,$N^{2'}$,N^7,$N^{7'}$-tetrakis(4-vinylphenyl)-9,9'-spirobi[fluorene]- 2,2',7,7'-tetraamine (V1382)

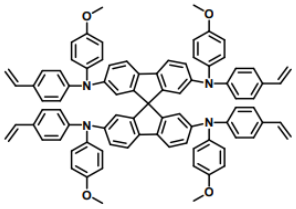

V1382

A solution of compound **1** (0.2 g, 0.2 mmol, 1 equiv) and 4-bromostyrene (0.2 g, 1.1 mmol, 4.5 equiv) in anhydrous toluene (22 mL) was purged with argon for 30 minutes. Afterwards, tris(dibenzylideneacetone)dipalladium(0) (0.063 equiv), tri-*tert*-butylphosphonium tetrafluoroborate (0.09 equiv) and sodium *tert*-butoxide (6 equiv) were added and the resulted solution was refluxed under argon atmosphere for 5 hours. After cooling down to room temperature, the reaction mixture was filtered through celite, extracted with ethylacetate and distilled water. The organic layer was dried over anhydrous Na_2SO_4, filtered and solvent evaporated. The crude product was purified by column chromatography using 1:4 v/v THF/*n*-hexane as an eluent. The obtained product was precipitated from THF into 15 times excess of ethanol. The precipitate was filtered off and washed with ethanol to collect **V1382** as a pale yellow solid. (0.15 g, 51% yield). ^{1}H NMR (400 MHz, THF-d_6) δ 7.51 (d, J = 8.4 Hz, 4H), 7.20 (d, J = 8.6 Hz, 8H), 6.97 (d, J = 8.6 Hz, 8H), 6.92 – 6.78 (m, 20H), 6.67 – 6.53 (m, 8H), 5.57 (d, J = 17.6 Hz, 4H), 5.05 (d, J = 10.9 Hz, 4H), 3.75 (s, 12H). ^{13}C NMR (101 MHz, THF-d_6) δ 154.68, 148.14, 146.11, 144.97, 138.45, 134.54, 134.47, 128.93, 124.82, 124.81, 122.14, 119.29, 118.32, 117.12, 112.68, 108.59, 63.78, 52.76 ppm. Anal. calcd for $C_{85}H_{68}N_4O_4$: C, 84.41; H, 5.67; N, 4.63; found: C, 84.27; H, 5.62; N, 4.65. $C_{85}H_{68}N_4O_4$[M^+] exact mass = 1208.52, MS (ESI) = 1208.61.

8. CURRICULUM VITAE

Šarūnė Daškevičiūtė
sarune.daskeviciute@ktu.lt

Išsilavinimas:

2002 – 2010	Jonavos Raimundo Samulevičiaus progimnazija
2010 – 2014	Jonavos Senamiesčio gimnazija
2014 – 2018	Kauno technologijos universitetas, Pramoninės biotechnologijos aukštasis bakalauro išsilavinimas
2018 – 2020	Kauno technologijos universitetas, Pramoninės biotechnologijos aukštasis magistro išsilavinimas
2020 – 2024	Kauno technologijos universitetas, Chemijos doktorantūra

Profesinė patirtis:

2019 – 2020	KTU Cheminės technologijos fakulteto Organinės chemijos katedros laborantė
2019 – 2020	KTU, LMT finansuojamo mokslininkų grupių projekto „Savitvarkiai krūvius transportuojantys monosluoksniai efektyviems perovskitiniams saulės elementams“ inžinierė
2020 – 2021	KTU, LMT finansuojamo mokslininkų grupių projekto „2D perovskitai efektyviems bei stabiliems 2D/3D saulės elementams“ inžinierė
2020 – 2023	KTU, projekto „Efektyvios bei tvarios krūvius transportuojančios molekulės energiją taupančioms technologijoms“ jaunesnioji mokslo darbuotoja
2020 – 2023	KTU, kompetencijų centro projekto „Funkcinės molekulės naujos kartos saulės elementams: nuo sintezės link komercializavimo“ jaunesnioji mokslo darbuotoja
2023 – 2023	tarptautinio projekto „Padidinto stabilumo ir taikomumo perovskitiniai saulės elementai“ jaunesnioji mokslo darbuotoja
2023 – dabar	KTU, tarptautinio projekto „Tandeminių Perovskito-Silicio modulių gamybos pramoniniu mastu bandomoji linija“ jaunesnioji mokslo darbuotoja
2023 – dabar	tarptautinio projekto „Racionaliai sukurti ploni kontaktiniai sluoksniai, įgalinantys didelio ploto perovskitų / silicio tandeminių saulės elementų gamybą“ jaunesnioji mokslo darbuotoja
2023 – dabar	tarptautinio projekto „Aukštu efektyvumu pasižymintys perovskitai lankstiems bei tvariems saulės elementams“ jaunesnioji mokslo darbuotoja

Mokslinė patirtis:

2021 – 2023	KTU Cheminės technologijos fakulteto modulio P390M112 „Biomolekulių spektriniai analizės metodai“ dėstytoja
2019 – 2020	KTU Cheminės technologijos fakulteto studijų programų komiteto narė
2015 – dabar	Vykdomi moksliniai tyrimai prof. Vytauto Getaučio vadovaujamoje mokslinėje grupėje „Organinių puslaidininkių sintezė“

Visuomeninė veikla:

2024	Prezidentūroje „Žaliųjų idėjų mugėje“ įvairaus amžiaus mokiniams demonstruoti eksperimentai apie saulės elementus.
2023	Šalčininkų mokyklų mokiniams dėstytos paskaitos ir demonstruoti eksperimentai apie saulės elementus.
2022	Vaškų miestelio mokyklų mokiniams dėstytos paskaitos ir demonstruoti eksperimentai apie saulės elementus.
2020–2021	KTU Cheminės technologijos fakulteto mokslo populiarinimo veikla – rengtos nuotolinės paskaitos mokiniams apie gamtos ir technologijų mokslus, demonstruoti eksperimentai.

Apdovanojimai:

2024	LMA jaunųjų mokslininkų ir doktorantų geriausių mokslinių darbų konkurse pelnytas pagyrimo raštas.
2023	Tarptautinėje mokslinėje konferencijoje „Chemistry & chemical technology 2023“ pelnytas laureato apdovanojimas už geriausią stendinį pranešimą.
2020	Mokslinėje konferencijoje „Fizinių ir technologijos mokslų tarpdalykiniai tyrimai: 10-oji jaunųjų mokslininkų konferencija“ pelnytas laureato apdovanojimas už geriausią žodinį pranešimą.
2019	Mokslinėje konferencijoje „Chemija ir cheminė technologija 2019“ pelnytas laureato apdovanojimas už geriausią žodinį pranešimą biotechnologijos sekcijoje.
2019	Tarptautinėje mokslinėje konferencijoje „Matematika ir gamtos mokslai: teorija ir taikymas“ pelnytas laureato apdovanojimas už geriausią žodinį pranešimą.

Stipendijos:

2022 – 2024	KTU mecenatų (Kazickų fondo) stipendijos laureatė (3 kartai).
2021 – 2023	KTU aktyviausių doktorantų konkurso laureatė (3 kartai).
2021 – 2023	LMT doktorantų stipendijos už mokslo rezultatus laureatė (3 kartai).
2022	LMA Teodoro Grotuso fondo vardinės stipendijos laureatė.
2020	INFOBALT ir „INVL Technology“ jaunųjų mokslininkų stipendijos už mokslo rezultatus laureatė.

2018, 2020	KTU rektoriaus skatinamosios stipendijos laureatė (2 kartai).
2017 – 2020	KTU talento stipendijos laureatė (4 kartai).
2016, 2019	KTU Cheminės technologijos fakulteto skatinamosios stipendijos laureatė (2 kartai).

Moksliniai straipsniai disertacijos tema:

1. **Daskeviciute-Geguziene, Sarune**; Daskeviciene, Maryte; Kantminienė, Kristina; Jankauskas, Vygintas; Kamarauskas, Egidijus; Gruodis, Alytis; Karazhanov, Smagul; Getautis, Vytautas. Design, synthesis and theoretical simulations of novel spiroindane-based enamines as p-type semiconductors // Royal Society Open science. London : Royal Society. ISSN 2054-5703. 2024, vol. 11, iss. 5, art. no. 232019, p. 1-11. DOI: 10.1098/rsos.232019. [Science Citation Index Expanded (Web of Science); Scopus; MEDLINE] [IF: 3,500; AIF: 7,200; IF/AIF: 0,486; Q2 (2022, InCites JCR SCIE)] [M.kr.: N 003] [Indėlis: 0,125]
2. **Daskeviciute-Geguziene, Sarune**; Truong, Minh Anh; Rakstys, Kasparas; Daskeviciene, Maryte; Hashimoto, Ruito; Murdey, Richard; Yamada, Takumi; Kanemitsu, Yoshihiko; Jankauskas, Vygintas; Wakamiya, Atsushi; Getautis, Vytautas. In situ thermal cross-linking of 9,9'-spirobifluorene-based hole-transporting layer for perovskite solar cells // ACS Applied materials & interfaces. Washington : American Chemical Society. ISSN 1944-8244. eISSN 1944-8252. 2024, vol. 16, iss. 1, p. 1206-1216. DOI: 10.1021/acsami.3c13950. [Science Citation Index Expanded (Web of Science); Scopus] [IF: 9,500; AIF: 7,550; IF/AIF: 1,258; Q1 (2022, InCites JCR SCIE)] [M.kr.: N 003, N 002] [Indėlis: 0,100]
3. Daskeviciute-Geguziene, Sarune; Zhang, Yi; Rakstys, Kasparas; Xiao, Chuanxiao; Xia, Jianxing; Qiu, Zhiheng; Daskeviciene, Maryte; Paskevicius, Tomas; Jankauskas, Vygintas; Asiri, Abdullah M.; Getautis, Vytautas; Nazeeruddin, Mohammad Khaja. Passivating defects of perovskite solar cells with functional donor-acceptor–donor type hole transporting materials // Advanced functional materials. Weinheim : Wiley-VCH. ISSN 1616-301X. eISSN 1616-3028. 2023, vol. 33, iss. 1, art. no. 2208317, p. 1-8. DOI: 10.1002/adfm.202208317. [Science Citation Index Expanded (Web of Science); Scopus] [IF: 19,000; AIF: 6,916; IF/AIF: 2,747; Q1 (2022, InCites JCR SCIE)] [M.kr.: N 003] [Indėlis: 0,087]
4. **Daskeviciute-Geguziene, Sarune**; Magomedov, Artiom; Daskeviciene, Maryte; Genevičius, Kristijonas; Nekrašas, Nerijus; Jankauskas, Vygintas; Kantminiene, Kristina; McGehee, Michael D.; Getautis, Vytautas. Cross-linkable carbazole-based hole transporting materials for perovskite solar cells // Chemical communications. Cambridge : Royal society of chemistry. ISSN 1359-7345. eISSN 1364-548X. 2022, vol. 58, iss. 54, p. 7495-7498. DOI: 10.1039/D2CC02612K. [Science Citation Index Expanded (Web of Science); Scopus; MEDLINE] [IF: 4,900; AIF: 6,900; IF/AIF: 0,710; Q2 (2022, InCites JCR SCIE)] [M.kr.: N 003, N 002] [Indėlis: 0,112]

5. **Daskeviciute-Geguziene**, Sarune; Zhang, Yi; Rakstys, Kasparas; Kreiza, Gediminas; Khan, Sher Bahadar; Kanda, Hiroyuki; Paek, Sanghyun; Daskeviciene, Maryte; Kamarauskas, Egidijus; Jankauskas, Vygintas; Asiri, Abdullah M.; Getautis, Vytautas; Nazeeruddin, Mohammad Khaja. Green-chemistry-inspired synthesis of cyclobutane-based hole-selective materials for highly efficient perovskite solar cells and modules // Angewandte chemie (international edition). Weinheim : Wiley-VCH. ISSN 1433-7851. eISSN 1521-3773. 2022, vol. 61, iss. 5, art. no. e202113207, p. 1-9. DOI: 10.1002/anie.202113207. [Science Citation Index Expanded (Web of Science); Scopus; MEDLINE] [IF: 16,600; AIF: 6,900; IF/AIF: 2,405; Q1 (2022, InCites JCR SCIE)] [M.kr.: N 003, N 002] [Indėlis: 0,088]
6. Daskeviciute, Sarune; Momblona, Cristina; Rakstys, Kasparas; Sutanto, Albertus Adrian; Daskeviciene, Marytė; Jankauskas, Vygintas; Gruodis, Alytis; Bubniene, Giedre; Getautis, Vytautas; Nazeeruddin, Mohammad Khaja. Fluorene-based enamines as low-cost and dopant-free hole transporting materials for high performance and stable perovskite solar cells // Journal of materials chemistry A. Cambridge : Royal society of chemistry. ISSN 2050-7488. eISSN 2050-7496. 2021, vol. 9, iss. 1, p. 301-309. DOI: 10.1039/D0TA08452B. [Science Citation Index Expanded (Web of Science); Scopus] [IF: 14,511; AIF: 7,496; IF/AIF: 1,935; Q1 (2021, InCites JCR SCIE)] [M.kr.: N 003, T 005] [Indėlis: 0,100]
7. **Daškevičiūtė, Šarūnė**; Sakai, Nobuya; Franckevičius, Marius; Daškevičienė, Marytė; Magomedov, Artiom; Jankauskas, Vygintas; Snaith, Henry J.; Getautis, Vytautas. Nonspiro, fluorene-based, amorphous hole transporting materials for efficient and stable perovskite solar cells // Advanced science. Weinheim : Wiley-VCH. ISSN 2198-3844. 2018, vol. 5, iss. 4, art. no. 1700811, p. 1-7. DOI: 10.1002/advs.201700811. [Science Citation Index Expanded (Web of Science); Scopus; MEDLINE] [IF: 15,804; AIF: 5,874; IF/AIF: 2,690; Q1 (2018, InCites JCR SCIE)] [M.kr.: N 003, N 002] [Indėlis: 0,125]

Kiti moksliniai straipsniai:

1. Kamarauskas, Egidijus; Jegorove, Aiste; Čepas, Romualdas J.; **Daskeviciute-Geguziene, Sarune**; Genevicius, Kristijonas; Franckevicius, Marius; Talaikis, Martynas; Dobuzinskas, Rokas; Scheler, Florian; Sveinbjornsson, Kari; Jankauskas, Vygintas; Getautis, Vytautas. Cross-linkable fluorene-based hole transporting materials for perovskite solar cells // Chemical physics. Amsterdam : Elsevier. ISSN 0301-0104. eISSN 1873-4421. 2024, vol. 579, art. no. 112183, p. 1-7. DOI: 10.1016/j.chemphys.2024.112183. [Science Citation Index Expanded (Web of Science); Scopus] [IF: 2,300; AIF: 5,600; IF/AIF: 0,410; Q3 (2022, InCites JCR SCIE)] [M.kr.: N 002, N 003] [Indėlis: 0,083]
2. Juneja, Nimish; **Daskeviciute-Geguziene, Sarune**; Spalatu, Nicolae; Mandati, Sreekanth; Katerski, Atanas; Grzibovskis, Raitis; Vembris,

Aivars; Karazhanov, Smagul; Getautis, Vytautas; Krunks, Malle; Oja Acik, Ilona. Employment of dopant-free fluorene-based enamines as innovative hole transport materials to boost the transparency and performance of Sb2S3 based solar cells // Materials science in semiconductor processing. Kidlington : Elsevier. ISSN 1369-8001. eISSN 1873-4081. 2024, vol. 169, art. no. 107934, p. 1-10. DOI: 10.1016/j.mssp.2023.107934. [Science Citation Index Expanded (Web of Science); Scopus] [IF: 4,100; AIF: 5,650; IF/AIF: 0,725; Q2 (2022, InCites JCR SCIE)] [M.kr.: N 003] [Indėlis: 0,090]

3. Juneja, Nimish; Mandati, Sreekanth; Katerski, Atanas; Spalatu, Nicolae; **Daskeviciute-Geguziene, Sarune**; Vembris, Aivars; Karazhanov, Smagul; Getautis, Vytautas; Krunks, Malle; Acik, Ilona Oja. Sb2S3 solar cells with a cost-effective and dopant-free fluorene-based enamine as a hole transport material // Sustainable energy & fuels. Cambridge : Royal society of chemistry. ISSN 2398-4902. 2022, vol. 6, iss. 13, p. 1-10. DOI: 10.1039/d2se00356b. [Science Citation Index Expanded (Web of Science); Scopus] [IF: 5,600; AIF: 7,033; IF/AIF: 0,796; Q2 (2022, InCites JCR SCIE)] [M.kr.: N 003] [Indėlis: 0,100]
4. Rakstys, Kasparas; Paek, Sanghyun; Drevilkauskaite, Aida; Kanda, Hiroyuki; **Daskeviciute, Sarune**; Shibayama, Naoyuki; Daskeviciene, Maryte; Gruodis, Alytis; Kamarauskas, Egidijus; Jankauskas, Vygintas; Getautis, Vytautas; Nazeeruddin, Mohammad Khaja. Carbazole-terminated isomeric hole transporting materials for perovskite solar cells // ACS applied materials & interfaces. Washington : American Chemical Society. ISSN 1944-8244. eISSN 1944-8252. 2020, vol. 12, iss. 17, p. 19710-19717. DOI: 10.1021/acsami.9b23495. [Science Citation Index Expanded (Web of Science); Scopus; MEDLINE] [IF: 9,229; AIF: 7,125; IF/AIF: 1,295; Q1 (2020, InCites JCR SCIE)] [M.kr.: N 003] [Indėlis: 0,083]

Patentų tarnybose įregistruotos patentinės paraiškos

1. Getautis, Vytautas (autorius, išradimo); Rakstys, Kasparas (autorius, išradimo); Daskeviciene, Maryte (autorius, išradimo); **Daskeviciute Geguziene, Sarune** (autorius, išradimo); Zgang, Yi (autorius, išradimo); Nazeeruddin, Mohammad Khaja (autorius, išradimo). Photovoltaic devices containing cyclobutane-based hole transporting materials : Japan patent application / inventors: V. Getautis, K. Rakstys, M. Daskeviciene, S. Daskeviciute Geguziene, Y. Zhang, M.K. Nazeeruddin; applicants: Kaunas University of Technology, Swiss Federal Institute of Technology Lausanne. JP 2023072638 A. 2023-05-24. [Espacenet] [M.kr.: N 003] [Indėlis: 0,166]
2. Getautis, Vytautas (autorius, išradimo); Rakstys, Kasparas (autorius, išradimo); Daskeviciene, Maryte (autorius, išradimo); **Daskeviciute-Geguziene, Sarune** (autorius, išradimo); Zgang, Yi (autorius, išradimo); Nazeeruddin, Mohammad Khaja (autorius, išradimo). Photovoltaic devices containing cyclobutane-based hole transporting materials : United States

patent application / inventors: V. Getautis, K. Rakstys, M. Daskeviciene, S. Daskeviciute-Geguziene, Y. Zhang, M.K. Nazeeruddin; applicants: Kaunas University of Technology, Swiss Federal Institute of Technology Lausanne. US 2023157158 A1. 2023-05-18. [Espacenet] [M.kr.: N 003] [Indėlis: 0,166]

3. Getautis, Vytautas (autorius, išradimo); Rakstys, Kasparas (autorius, išradimo); Daskeviciene, Maryte (autorius, išradimo); **Daskeviciute Geguziene, Sarune** (autorius, išradimo); Zgang, Yi (autorius, išradimo); Nazeeruddin, Mohammad Khaja (autorius, išradimo). Photovoltaic devices containing cyclobutane-based hole transporting materials : European patent application / inventors: V. Getautis, K. Rakstys, M. Daskeviciene, S. Daskeviciute Geguziene, Y. Zhang, M.K. Nazeeruddin; applicants: Kaunas University of Technology, Swiss Federal Institute of Technology Lausanne. EP 4181225 A1. 2023-05-17. [Espacenet] [M.kr.: N 003] [Indėlis: 0,166]
4. Getautis, Vytautas (autorius, išradimo); Rakstys, Kasparas (autorius, išradimo); Daskeviciene, Maryte (autorius, išradimo); **Daskeviciute Geguziene, Sarune** (autorius, išradimo); Zgang, Yi (autorius, išradimo); Nazeeruddin, Mohammad Khaja (autorius, išradimo). Photovoltaic devices containing cyclobutane-based hole transporting materials : Chinese patent application / inventors: V. Getautis, K. Rakstys, M. Daskeviciene, S. Daskeviciute Geguziene, Y. Zhang, M.K. Nazeeruddin; applicants: Kaunas University of Technology, Swiss Federal Institute of Technology Lausanne. CN 116133444 A. 2023-05-16. [Espacenet] [M.kr.: N 003] [Indėlis: 0,166]

Patentų tarnyboms pateiktos patentinės paraiškos:

1. 2023-04-14 pateikta Amerikos patentų biuro (USPTO) patento paraiška In-Situ crosslinking of 9,9′-spirobifluorene-based compounds for use in optoelectronic and/or in photoelectrochemical devices and manufacture thereof, Reg. Nr. 18/134,751
2. 2023-04-19 pateikta Japonijos patentų biuro (JP) patento paraiška In-Situ crosslinking of 9,9′-spirobifluorene-based compounds for use in optoelectronic and/or in photoelectrochemical devices and manufacture thereof, Reg. Nr. 2023-068376
3. 2023-04-19 pateikta Europos patentų biuro (EPO) patento paraiška In-Situ crosslinking of 9,9′-spirobifluorene-based compounds for use in optoelectronic and/or in photoelectrochemical devices and manufacture thereof, Reg. Nr. EP23168712.0

Mokslinės konferencijos:

1. Technorama’24: let‘s make it // plenarinis pranešimas ir mokslinės dirbtuvės moksleiviams – Organiniai puslaidininkiai naujos kartos saulės elementams: nuo idėjos link komercializavimo. Kaunas, 2024 m. gegužės 29 d.

2. Chemija ir cheminė technologija 2023: studentų mokslinė konferencija // plenarinis pranešimas – Šiuolaikinės medžiagos efektyviems saulės elementams. Klaipėda, 2023 m. gegužės 12 d.
3. Open readings 2023: 66th international conference for students of physics and natural sciences // stendinis pranešimas – Donor-acceptor-donor type enamines for perovskite solar cells. Vilnius, 2023 m. balandžio 18-21 d.
4. Fizinių ir technologijos mokslų tarpdalykiniai tyrimai: 11-oji jaunųjų mokslininkų konferencija // žodinis pranešimas – Žaliosios sintezės metodais pagaminti skyles transportuojantys ciklobutano dariniai efektyviems perovskitiniams saulės elementams ir moduliams. Vilnius, 2023 m. kovo 23 d.
5. Chemistry and chemical technology: international conference CCT-2023 // stendinis pranešimas – Passivating defects of perovskite solar cells with functional donor-acceptor-donor type hole transporting materials. Vilnius, 2023 m. kovo 10 d.
6. Chemistry and chemical technology: proceedings of international scientific conference // stendinis pranešimas – Carbazole-based cross-linkable hole-transporting materials for perovskite solar cells. Kaunas, 2022 m. spalio 14 d.
7. PhotoIUPAC // stendinis pranešimas – Cross-linkable carbazole-based HTM's for perovskite solar cells. Amsterdamas, 2022 m. liepos 17-22 d.
8. Balticum organicum syntheticum [BOS] 2022: in memory of prof. Victor Snieckus // stendinis pranešimas – High efficiency of perovskite solar cells and modules via green chemistry inspired hole selective materials. Vilnius, 2022 m. liepos 3-6 d.
9. Proceedings of international conference on hybrid and organic photovoltaics (HOPV22) // stendinis pranešimas – Green synthesis of cyclobutane-based hole-selective materials for efficient perovskite solar cells and modules. Valensija, Ispanija, 2022 m. gegužės 19-25 d.
10. Open readings 2022: 65th international conference for students of physics and natural sciences // stendinis pranešimas – Green chemistry inspired carbazole-flanked cyclobutanes as hole selective materials for solar cells and modules. Vilnius, 2022 m. kovo 15-18 d.
11. Proceedings of nanoGe Spring meeting 2022: AdvMatSyn22 // stendinis pranešimas – Fluorene-based enamines as low-cost and dopant-free hole transporting materials for high performance and stable perovskite solar cells. Ispanija (online), 2022 m. kovo 7-11 d.
12. Chemistry and chemical technology: 16th international conference of Lithuanian Chemical Society // stendinis pranešimas – Fluorene-based enamines as low-cost and dopant-free hole transporting materials for perovskite solar cells. Vilnius, 2021 m. rugėjo 24 d.
13. Technorama 2021: from vision to innovation // žodinis pranešimas – Green chemistry inspired carbazole-flanked cyclobutanes as hole selective materials for perovskite solar cells. Kaunas, 2021 m. gegužės 28 d.

14. Open readings 2021: 64th international conference for students of physics and natural sciences // stendinis pranešimas – Fluorene-based enamines as low-cost and dopant-free hole transporting materials for high performance and stable perovskite solar cells. Vilnius, 2021 m. kovo 16-19 d.
15. Fizinių ir technologijos mokslų tarpdalykiniai tyrimai: 10-oji jaunųjų mokslininkų konferencija // žodinis pranešimas – Naujų zondų sintezė ir jų pritaikymas merkaptoaminorūgščių atpažinimui. Vilnius, 2020 m. kovo 15 d.
16. Bioateitis: gamtos ir gyvybės mokslų perspektyvos: 13-oji jaunųjų mokslininkų konferencija // žodinis pranešimas – Nauji žymekliai biotioliams aptikti. Vilnius, 2020 m. gruodžio 4 d.
17. FM&NT-2020: virtual // stendinis pranešimas – Carbazole–terminated isomeric hole transporting materials for perovskite solar cells. Vilnius, 2020 m. lapkričio 23-26 d.
18. Open readings 2020: 63rd international conference for students of physics and natural sciences // stendinis pranešimas – Synthesis of new dyes for the detection of mercapto amino acids. Vilnius, 2020 m. kovo 17-20 d.
19. Lithuania-Poland workshop on physics and technology // stendinis pranešimas – p-type fluorene-based organic semiconductors for efficient perovskite solar cells. Vilnius, 2019 m. rugsėjo 26-27 d.
20. Mathematics and natural sciences: theory and applications: material of the 17th students // žodinis pranešimas – Naujų dažiklių sintezė ir panaudojimas merkaptoaminorūgščių identifikavimui. Kaunas, 2019 m. balandžio 4 d.
21. Respublikinė studentų mokslinė konferencija „Chemija ir cheminė technologija 2019“ // žodinis pranešimas – Naujų zondų kūrimas ir panaudojimas merkaptoaminorūgščių identifikavimui. Vilnius, 2019 m. gegužės 17 d.
22. Technorama 2019: from vision to innovation! // stendinis pranešimas – Nonspiro, fluorene-based, amorphous hole transporting materials for efficient and stable perovskite solar cells. Kaunas, 2019 m. gegužės 9 d.
23. Open readings 2019: 62nd international conference for students of physics and natural sciences // stendinis pranešimas – Fluorene-based hole transporting materials for efficient and stable perovskite solar cells. Vilnius, 2019 m. kovo 19-22 d.
24. Proceedings of international conference on hybrid and organic photovoltaics (HOPV18) // stendinis pranešimas – Amorphous, fluorene-based hole transporting materials for efficient and stable Perovskite solar cells. Benidormas, Ispanija, 2018 m. gegužės 28-31 d.
25. Chemija ir cheminė technologija: studentų mokslinė konferencija // žodinis pranešimas – Naujų dažiklių sintezė ir panaudojimas merkaptoaminorūgščių identifikavimui. Klaipėda, 2018 m. gegužės 18 d.
26. Studentų mokslinė konferencija „Chemija ir cheminė technologija“ // žodinis pranešimas – Molekulinių stiklų su fluorenilchromoforu molekulės centre sintezė ir savybės. Kaunas, 2017 m. balandžio 27 d.

9. PADĖKA

Nuoširdžiai dėkoju vadovui prof. V. Getaučiui už galimybę dirbti jo vadovaujamoje mokslinėje grupėje, suteiktas žinias, naudingus patarimus ir visokeriopą pasitikėjimą.
Vyr. m. d. M. Daškevičienei už įgūdžių ir žinių perdavimą dirbant laboratorijoje.
Dokt. A. Jegorovei už draugystę, palaikymą ir gerą atmosferą laboratorijoje.
Visiems kitiems grupės nariams už pagalbą, draugystę ir smagų laiką, praleistą kartu.
Savo šeimai už tikėjimą manimi, motyvaciją ir besąlygišką rūpestį.

UDK 547.759+547.678.3+621.383.51](043.3)

SL344. 2024-08-06, 30 leidyb. apsk. l. Tiražas 14 egz. Užsakymas 136.
Išleido Kauno technologijos universitetas, K. Donelaičio g. 73, 44249 Kaunas
Spausdino leidyklos „Technologija“ spaustuvė, Studentų g. 54, 51424 Kaunas